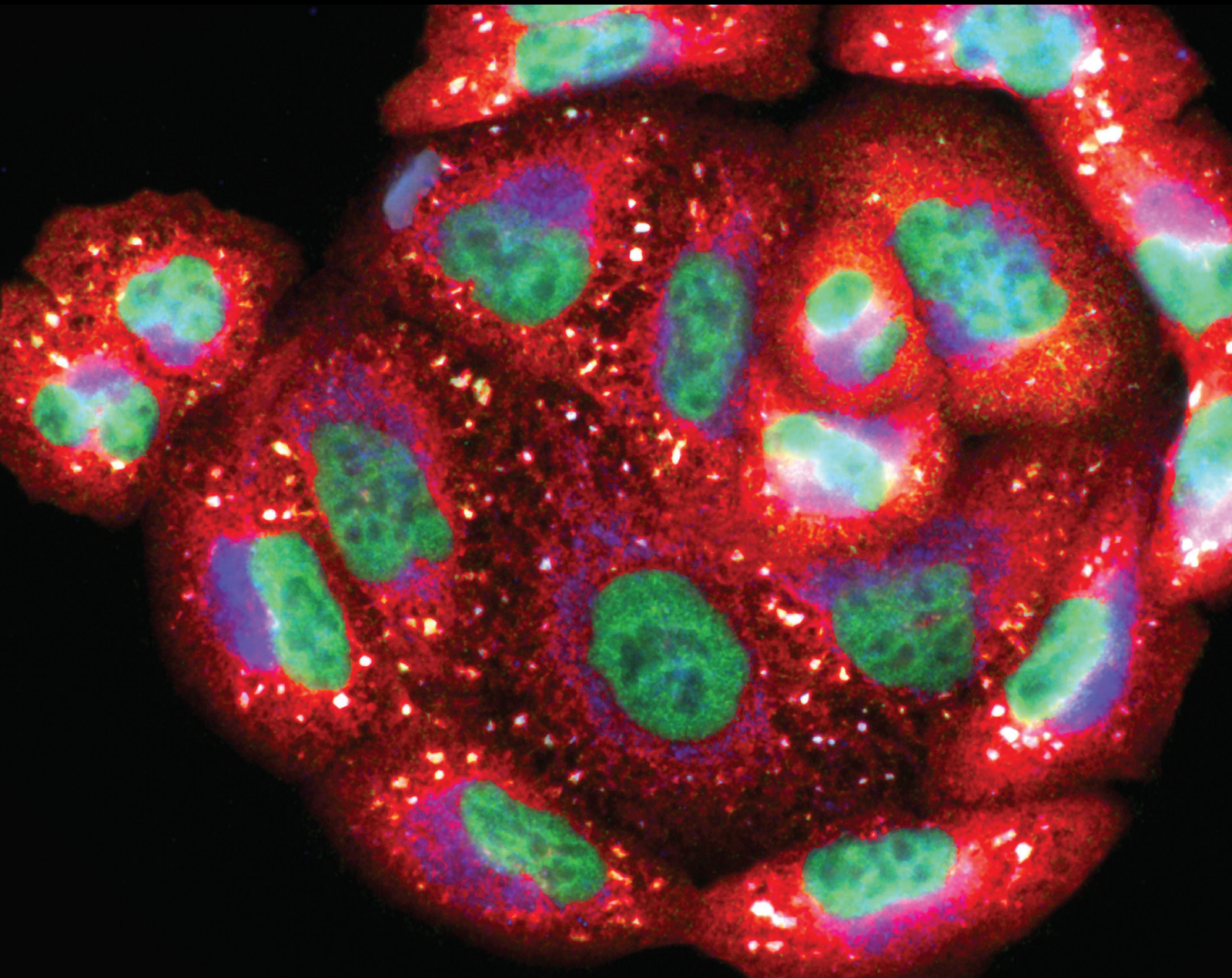


Targeting Redox Mechanisms for Novel Cardiopulmonary Therapeutics

Guest Editors: Bhagavatula Moorthy, Lynette K. Rogers, and Jason Richardson



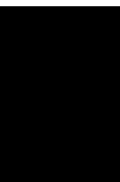


Targeting Redox Mechanisms for Novel Cardiopulmonary Therapeutics

Oxidative Medicine and Cellular Longevity

Targeting Redox Mechanisms for Novel Cardiopulmonary Therapeutics

Guest Editors: Bhagavatula Moorthy, Lynette K.
Rogers, and Jason Richardson



Copyright © 2020 Hindawi Limited. All rights reserved.

This is a special issue published in "Oxidative Medicine and Cellular Longevity" All articles are open access articles distributed under the Creative Commons Attribution License, which permits unrestricted use, distribution, and reproduction in any medium, provided the original work is properly cited.

Chief Editor

Jeannette Vasquez-Vivar, USA

Associate Editors

Amjad Islam Aqib, Pakistan
Angel Catalá , Argentina
Cinzia Domenicotti , Italy
Janusz Gebicki , Australia
Aldrin V. Gomes , USA
Vladimir Jakovljevic , Serbia
Thomas Kietzmann , Finland
Juan C. Mayo , Spain
Ryuichi Morishita , Japan
Claudia Penna , Italy
Sachchida Nand Rai , India
Paola Rizzo , Italy
Mithun Sinha , USA
Daniele Vergara , Italy
Victor M. Victor , Spain


Academic Editors

Ammar AL-Farga , Saudi Arabia
Mohd Adnan , Saudi Arabia
Ivanov Alexander , Russia
Fabio Altieri , Italy
Daniel Dias Rufino Arcanjo , Brazil
Peter Backx, Canada
Amira Badr , Egypt
Damian Bailey, United Kingdom
Rengasamy Balakrishnan , Republic of Korea
Jiaolin Bao, China
Ji C. Bihl , USA
Hareram Birla, India
Abdelhakim Bouyahya, Morocco
Ralf Braun , Austria
Laura Bravo , Spain
Matt Brody , USA
Amadou Camara , USA
Marcio Carochio , Portugal
Peter Celec , Slovakia
Giselle Cerchiaro , Brazil
Arpita Chatterjee , USA
Shao-Yu Chen , USA
Yujie Chen, China
Deepak Chhangani , USA
Ferdinando Chiaradonna , Italy

Zhao Zhong Chong, USA
Fabio Ciccarone, Italy
Alin Ciobica , Romania
Ana Cipak Gasparovic , Croatia
Giuseppe Cirillo , Italy
Maria R. Ciriolo , Italy
Massimo Collino , Italy
Manuela Corte-Real , Portugal
Manuela Curcio, Italy
Domenico D'Arca , Italy
Francesca Danesi , Italy
Claudio De Lucia , USA
Damião De Sousa , Brazil
Enrico Desideri, Italy
Francesca Diomede , Italy
Raul Dominguez-Perles, Spain
Joël R. Drevet , France
Grégory Durand , France
Alessandra Durazzo , Italy
Javier Egea , Spain
Pablo A. Evelson , Argentina
Mohd Farhan, USA
Ioannis G. Fatouros , Greece
Gianna Ferretti , Italy
Swaran J. S. Flora , India
Maurizio Forte , Italy
Teresa I. Fortoul, Mexico
Anna Fracassi , USA
Rodrigo Franco , USA
Juan Gambini , Spain
Gerardo García-Rivas , Mexico
Husam Ghanim, USA
Jayeeta Ghose , USA
Rajeshwary Ghosh , USA
Lucia Gimeno-Mallench, Spain
Anna M. Giudetti , Italy
Daniela Giustarini , Italy
José Rodrigo Godoy, USA
Saeid Golbidi , Canada
Guohua Gong , China
Tilman Grune, Germany
Solomon Habtemariam , United Kingdom
Eva-Maria Hanschmann , Germany
Md Saquib Hasnain , India
Md Hassan , India


Tim Hofer , Norway
John D. Horowitz, Australia
Silvana Hrelia , Italy
Dragan Hrnčić, Serbia
Zebo Huang , China
Zhao Huang , China
Tarique Hussain , Pakistan
Stephan Immenschuh , Germany
Norsharina Ismail, Malaysia
Franco J. L. , Brazil
Sedat Kacar , USA
Andleeb Khan , Saudi Arabia
Kum Kum Khanna, Australia
Neelam Khaper , Canada
Ramoji Kosuru , USA
Demetrios Kouretas , Greece
Andrey V. Kozlov , Austria
Chan-Yen Kuo, Taiwan
Gaocai Li , China
Guoping Li , USA
Jin-Long Li , China
Qiangqiang Li , China
Xin-Feng Li , China
Jialiang Liang , China
Adam Lightfoot, United Kingdom
Christopher Horst Lillig , Germany
Paloma B. Liton , USA
Ana Lloret , Spain
Lorenzo Loffredo , Italy
Camilo López-Alarcón , Chile
Daniel Lopez-Malo , Spain
Massimo Lucarini , Italy
Hai-Chun Ma, China
Nageswara Madamanchi , USA
Kenneth Maiese , USA
Marco Malaguti , Italy
Steven McAnulty, USA
Antonio Desmond McCarthy , Argentina
Sonia Medina-Escudero , Spain
Pedro Mena , Italy
V́ctor M. Mendoza-Núñez , Mexico
Lidija Milkovic , Croatia
Alexandra Miller, USA
Sara Missaglia , Italy

Premysl Mladenka , Czech Republic
Sandra Moreno , Italy
Trevor A. Mori , Australia
Fabiana Morroni , Italy
Ange Mouithys-Mickalad, Belgium
Iordanis Mourouzis , Greece
Ryoji Nagai , Japan
Amit Kumar Nayak , India
Abderrahim Nemmar , United Arab Emirates
Xing Niu , China
Cristina Nocella, Italy
Susana Novella , Spain
Hassan Obied , Australia
Pál Pacher, USA
Pasquale Pagliaro , Italy
Dilipkumar Pal , India
Valentina Pallottini , Italy
Swapnil Pandey , USA
Mayur Parmar , USA
Vassilis Paschalis , Greece
Keshav Raj Paudel, Australia
Ilaria Peluso , Italy
Tiziana Persichini , Italy
Shazib Pervaiz , Singapore
Abdul Rehman Phull, Republic of Korea
Vincent Pialoux , France
Alessandro Poggi , Italy
Zsolt Radak , Hungary
Dario C. Ramirez , Argentina
Erika Ramos-Tovar , Mexico
Sid D. Ray , USA
Muneeb Rehman , Saudi Arabia
Hamid Reza Rezvani , France
Alessandra Ricelli, Italy
Francisco J. Romero , Spain
Joan Roselló-Catafau, Spain
Subhadeep Roy , India
Josep V. Rubert , The Netherlands
Sumbal Saba , Brazil
Kunihiro Sakuma, Japan
Gabriele Saretzki , United Kingdom
Luciano Saso , Italy
Nadja Schroder , Brazil

Anwen Shao , China
Iman Sherif, Egypt
Salah A Sheweita, Saudi Arabia
Xiaolei Shi, China
Manjari Singh, India
Giulia Sita , Italy
Ramachandran Srinivasan , India
Adrian Sturza , Romania
Kuo-hui Su , United Kingdom
Eisa Tahmasbpour Marzouni , Iran
Hailiang Tang, China
Carla Tatone , Italy
Shane Thomas , Australia
Carlo Gabriele Tocchetti , Italy
Angela Trovato Salinaro, Italy
Rosa Tundis , Italy
Kai Wang , China
Min-qi Wang , China
Natalie Ward , Australia
Grzegorz Wegrzyn, Poland
Philip Wenzel , Germany
Guangzhen Wu , China
Jianbo Xiao , Spain
Qiongming Xu , China
Liang-Jun Yan , USA
Guillermo Zalba , Spain
Jia Zhang , China
Junmin Zhang , China
Junli Zhao , USA
Chen-he Zhou , China
Yong Zhou , China
Mario Zoratti , Italy


Contents

Follistatin-Like 1 Protects against Doxorubicin-Induced Cardiomyopathy through Upregulation of Nrf2

Yintao Zhao, Jingjing Sun, Wei Zhang, Meng Peng, Jun Chen, Lu Zheng, Xiangqin Zhang, Haibo Yang, and Yuan Liu 



Research Article (11 pages), Article ID 3598715, Volume 2020 (2020)

Dexmedetomidine Ameliorates Lung Injury Induced by Intestinal Ischemia/Reperfusion by Upregulating Cannabinoid Receptor 2, Followed by the Activation of the Phosphatidylinositol 3-Kinase/Akt Pathway

Meng Chen, Xue-Tao Yan, Li Ye, Jun-Jiao Tang, Zong-Ze Zhang, and Xiang-Hu He 




Research Article (14 pages), Article ID 6120194, Volume 2020 (2020)

Combination of Dichloroacetate and Atorvastatin Regulates Excessive Proliferation and Oxidative Stress in Pulmonary Arterial Hypertension Development via p38 Signaling

Tangzhiming Li , Suqi Li, Yilu Feng, Xiaofang Zeng, Shaohong Dong, Jianghua Li, Lihuang Zha, Hui Luo, Lin Zhao, Bin Liu, Ziwei Ou, Wenchao Lin, Mengqiu Zhang, Sheng Li, Qiuqiong Jiang, Qiangqiang Qi, Qingyao Xu, and Zaixin Yu 



Research Article (15 pages), Article ID 6973636, Volume 2020 (2020)

The Research Progress of Vascular Macrophages and Atherosclerosis

Yeqing Tong , Li Cai, Shiyu Yang, Shuang Liu, Zhihong Wang , and Jinqian Cheng 




Review Article (4 pages), Article ID 7308736, Volume 2020 (2020)

Asiatic Acid Protects against Doxorubicin-Induced Cardiotoxicity in Mice

Xiaoping Hu, Baijun Li , Luocheng Li, Bowen Li, Jinlong Luo , and Bin Shen




Research Article (12 pages), Article ID 5347204, Volume 2020 (2020)

DHA Supplementation Attenuates MI-Induced LV Matrix Remodeling and Dysfunction in Mice

I. Habicht, G. Mohsen, L. Eichhorn, S. Frede, C. Weisheit, T. Hilbert , H. Treede, E. Güresir, O. Dewald, G. D. Duerr , and M. Velten 




Research Article (14 pages), Article ID 7606938, Volume 2020 (2020)

The Role of DNMT and HDACs in the Fetal Programming of Hypertension by Glucocorticoids

J. Lamothe, S. Khurana , S. Tharmalingam, C. Williamson, C. J. Byrne, N. Khaper , S. Mercier, and T. C. Tai 

Research Article (17 pages), Article ID 5751768, Volume 2020 (2020)

Potential Role of Antioxidants as Adjunctive Therapy in Chagas Disease

Juana P. Sánchez-Villamil , Paula K. Bautista-Niño , Norma C. Serrano, Melvin Y. Rincon, and Nisha J. Garg 


Review Article (13 pages), Article ID 9081813, Volume 2020 (2020)

Norepinephrine Induces Lung Microvascular Endothelial Cell Death by NADPH Oxidase-Dependent Activation of Caspase-3





Andreia Z. Chignalia , Guy Weinberg, and Randal O. Dull 

Research Article (11 pages), Article ID 2563764, Volume 2020 (2020)






Resveratrol Prevents Right Ventricle Remodeling and Dysfunction in Monocrotaline-Induced Pulmonary Arterial Hypertension with a Limited Improvement in the Lung Vasculature

Eduardo Vázquez-Garza, Judith Bernal-Ramírez, Carlos Jerjes-Sánchez, Omar Lozano, Edgar Acuña-Morín, Mariana Vanoye-Tamez, Martín R. Ramos-González, Héctor Chapoy-Villanueva, Luis Pérez-Plata, Luis Sánchez-Trujillo, Guillermo Torre-Amione, Alicia Ramírez-Rivera, and Gerardo García-Rivas 
Research Article (13 pages), Article ID 1841527, Volume 2020 (2020)


Virgin Coconut Oil Supplementation Prevents Airway Hyperreactivity of Guinea Pigs with Chronic Allergic Lung Inflammation by Antioxidant Mechanism

Luiz Henrique C. Vasconcelos , Maria da Conceição C. Silva, Alana C. Costa, Giuliana A. de Oliveira, Iara Leão Luna de Souza, Renato F. Righetti , Fernando R. Queiroga, Glébia A. Cardoso, Alexandre S. Silva, Patrícia M. da Silva, Giciane C. Vieira, Iolanda de F. L. C. Tibério, Marta S. Madruga, Fabiana de A. Cavalcante , and Bagnólia A. da Silva 
Research Article (16 pages), Article ID 5148503, Volume 2020 (2020)


Melatonin Ameliorates MI-Induced Cardiac Remodeling and Apoptosis through a JNK/p53-Dependent Mechanism in Diabetes Mellitus

Linhe Lu , Jipeng Ma, Mingming Sun, Xiaowu Wang, Erhe Gao, Lintao Lu , Jun Ren , Lifang Yang , and Jian Yang 
Research Article (14 pages), Article ID 1535201, Volume 2020 (2020)


Toxic Acetaminophen Exposure Induces Distal Lung ER Stress, Proinflammatory Signaling, and Emphysematous Changes in the Adult Murine Lung

Jeryl Sandoval, David J. Orlicky, Ayesha Allawzi, Brittany Butler, Cynthia Ju, Caroline T. Phan, Roy Toston, Robyn De Dios, Leanna Nguyen, Sarah McKenna, Eva Nozik-Grayck, and Clyde J. Wright 
Research Article (15 pages), Article ID 7595126, Volume 2019 (2019)

Role of *HIF-1 α -miR30a-Snai1* Axis in Neonatal Hyperoxic Lung Injury

Yuhao Zhang, Xiaoyu Dong, and Krithika Lingappan 
Research Article (9 pages), Article ID 8327486, Volume 2019 (2019)

Cell Type- and Exposure-Specific Modulation of CD63/CD81-Positive and Tissue Factor-Positive Extracellular Vesicle Release in response to Respiratory Toxicants

Frank R. M. Stassen, Pascalle H. van Eijck, Paul H. M. Savelkoul, Emiel F. M. Wouters, Gernot G. U. Rohde, Jacco J. Briedé, Niki L. Reynaert, Theo M. de Kok, and Birke J. Benedikter 
Research Article (9 pages), Article ID 5204218, Volume 2019 (2019)

Protection against Doxorubicin-Induced Cytotoxicity by Geniposide Involves AMPK α Signaling Pathway

Yan-Yan Meng, Yu-Pei Yuan, Xin Zhang, Chun-Yan Kong , Peng Song, Zhen-Guo Ma , and Qi-Zhu Tang 
Research Article (12 pages), Article ID 7901735, Volume 2019 (2019)



Contents

miR-25 Promotes Cell Proliferation, Migration, and Invasion of Non-Small-Cell Lung Cancer by Targeting the LATS2/YAP Signaling Pathway

Tangwei Wu, Hui Hu, Tianzhu Zhang, Liyuan Jiang, Xiaoyi Li, Shuiyi Liu, Chao Zheng, Ge Yan, Weiqun Chen, Yong Ning , Yong Li , and Zhongxin Lu 

Research Article (14 pages), Article ID 9719723, Volume 2019 (2019)

Thioredoxin Reductase-1 Inhibition Augments Endogenous Glutathione-Dependent Antioxidant Responses in Experimental Bronchopulmonary Dysplasia

Stephanie B. Wall, Rachael Wood, Katelyn Dunigan, Qian Li, Rui Li, Lynette K. Rogers , and Trent E. Tipple 

Research Article (10 pages), Article ID 7945983, Volume 2019 (2019)

Research Article

Follistatin-Like 1 Protects against Doxorubicin-Induced Cardiomyopathy through Upregulation of Nrf2

Yintao Zhao,¹ Jingjing Sun,¹ Wei Zhang,² Meng Peng,¹ Jun Chen,¹ Lu Zheng,¹ Xiangqin Zhang,¹ Haibo Yang,¹ and Yuan Liu¹ 

¹Department of Cardiology, The First Affiliated Hospital of Zhengzhou University, Zhengzhou, China

²Department of Anesthesiology, The First Affiliated Hospital of Zhengzhou University, Zhengzhou, China

Correspondence should be addressed to Yuan Liu; fccliuy2@zzu.edu.cn

Received 29 March 2020; Revised 15 May 2020; Accepted 9 July 2020; Published 3 August 2020

Guest Editor: Bhagavatula Moorthy

Copyright © 2020 Yintao Zhao et al. This is an open access article distributed under the Creative Commons Attribution License, which permits unrestricted use, distribution, and reproduction in any medium, provided the original work is properly cited.

Doxorubicin- (DOX-) induced cardiomyocyte loss results in irreversible heart failure, which limits the clinical applications of DOX. Currently, there are no drugs that can effectively treat DOX-related cardiotoxicity. Follistatin-like 1 (FSTL1) has been reported to be a transforming growth factor-beta-inducible gene, and FSTL1 supplementation attenuated ischemic injury and cardiac apoptotic loss in mice. However, the effect of FSTL1 on DOX-induced cardiomyopathy has not been elucidated. We aimed to explore whether FSTL1 could prevent DOX-related cardiotoxicity in mice. Mice were intraperitoneally injected with a single dose of DOX to induce acute cardiotoxicity. We used an adeno-associated virus system to overexpress FSTL1 in the heart. DOX administration decreased FSTL1 mRNA and protein expression in the heart and in cells. FSTL1 prevented DOX-related cardiac injury and inhibited cardiac oxidative stress and apoptosis, thereby improving cardiac function in mice. FSTL1 also improved cardiomyocyte contractile functions in vitro. FSTL1 upregulated expression of nuclear factor (erythroid-derived 2)-like 2 (Nrf2) in DOX-treated hearts. FSTL1 was not capable of protecting against these toxic effects in Nrf2-deficient mice. In conclusion, FSTL1 protected against DOX-induced cardiotoxicity via upregulation of Nrf2 expression.

1. Introduction

Doxorubicin (DOX), a well-known and highly effective chemotherapy drug, can contribute to the development of cardiotoxicity and irreversible heart failure, which largely limits its clinical use [1]. Heart transplantation is the only approach to treating serious cardiomyopathy in patients that were administered with DOX [2]. The precise pathogenesis of DOX-related cardiotoxicity has not been completely elucidated, but several lines of evidence have suggested that oxidative damage and myocardial apoptotic loss are closely involved [3, 4]. Thus, finding a drug that can restrict DOX-induced cardiac apoptosis might be important in treating DOX-related cardiac injury.

Follistatin-like 1 (FSTL1) is an extracellular glycoprotein that plays key roles in cardiometabolic diseases. It has been reported that FSTL1 supplementation limits ischemic injury and cardiac apoptotic loss in mice [5]. Similarly, FSTL1 exerted therapeutic effects by decreasing

ventricle mass [6]. Moreover, elevated plasma FSTL1 concentrations are closely correlated with brain natriuretic peptide release [7]. In addition, FSTL1 has been found to upregulate protein kinase B (PKB/AKT) activity in mice [5]. However, there have been no reports describing the role of FSTL1 in DOX-related acute cardiotoxicity.

Herein, we sought to examine the hypothesis that FSTL1 could prevent DOX-related cardiotoxicity in mice. The results showed that FSTL1 expression was decreased in DOX-treated hearts and cells. FSTL1 restoration attenuated DOX-related cardiac injury and dysfunction and suppressed cardiac apoptosis in mice. Moreover, we found that the protective effect of FSTL1 was dependent on the restoration of nuclear factor (erythroid-derived 2)-like 2 (Nrf2).

2. Methods

2.1. Reagents. Recombinant human FSTL1 ($\geq 97\%$ purity, as determined by HPLC) was obtained from PeproTech Co.

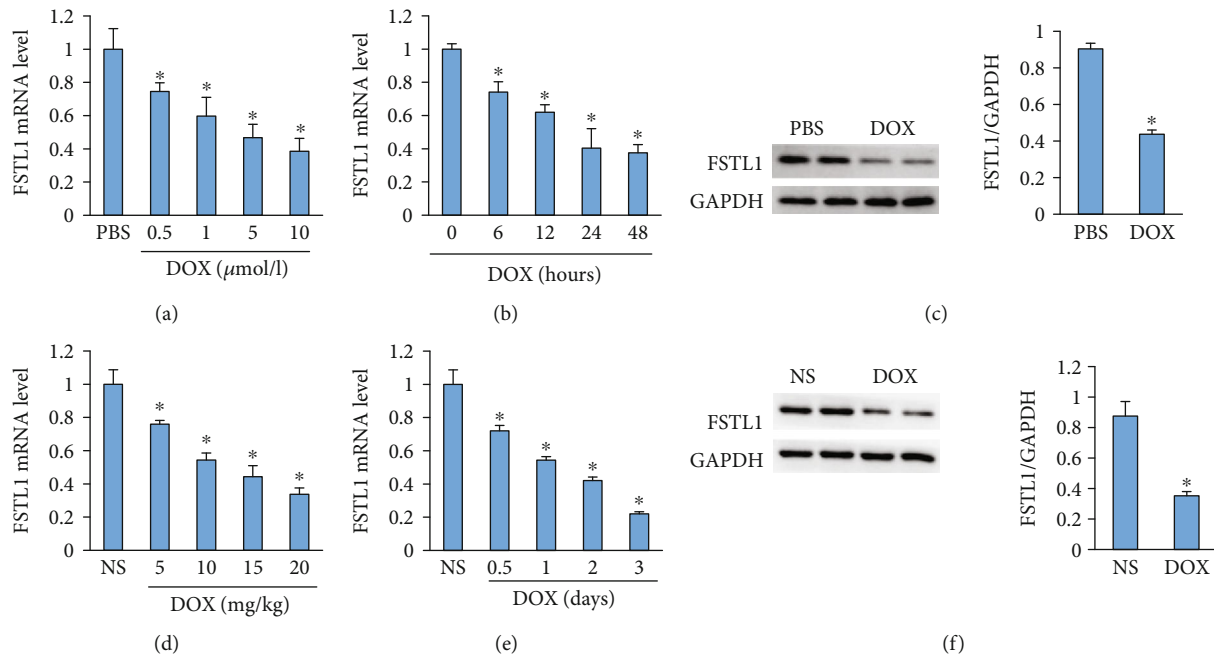


FIGURE 1: FSTL1 expression after DOX treatment. (a, b) The mRNA level of FSTL1 in DOX-treated NRCMs ($n = 6$). (c) Protein expression of FSTL1 in DOX-treated NRCMs ($n = 6$). (d, e) The mRNA level of FSTL1 in DOX-treated hearts ($n = 6$). (f) Protein expression of FSTL1 in DOX-treated hearts ($n = 6$). * $P < 0.05$ vs. the NS/PBS groups. The data were analyzed using two-tailed Student's t -tests.

(New Jersey, USA). Primary antibodies against FSTL1 (#ab11805, 1:1000), GAPDH (#ab181602, 1:1000), Nrf2 (#ab62352, 1:1000), and cleaved caspase-3 (#ab2302, 1:1000) were obtained from Abcam (Cambridge, UK). A mouse N-terminal brain natriuretic peptide precursor (NT-proBNP) assay kit was obtained from CUSABIO (#CSB-E05153m, Wuhan, China). DOX (#D1515) was provided by Sigma-Aldrich (MO, USA). A mouse cardiac troponin I (cTnI) ELISA kit was provided by CUSABIO (#CSB-E08421m). A mouse creatine kinase (CK) ELISA kit (#CSB-E14404m) and lactate dehydrogenase (LDH) ELISA kit (#CSB-E17733m) were also provided by CUSABIO.

2.2. Animal Studies. This study was approved by the Committee on Animal Care of the First Affiliated Hospital of Zhengzhou University and was carried out in accordance with the National Institutes of Health Guidelines on the Use of Laboratory Animals. All C57/BL6J mice (age: 12 weeks, 25–28 g, male) were provided by the Chinese Academy of Medical Sciences (Beijing, China). All mice ($n = 48$) were randomly divided into 4 groups ($n = 12$ in each group): normal saline (NS)+control (con), NS+FSTL1, DOX+con, and DOX+FSTL1. We used an adeno-associated virus (AAV9) system to overexpress FSTL1 in the heart. AAV9-FSTL1 and AAV9- β -gal were provided by Vigene Bioscience, and AAV9- β -gal was used as the control. To investigate the protective effects of FSTL1, mice in the FSTL1 group received a single tail vein injection of AAV9-FSTL1, and the control group received a single tail vein injection of AAV9- β -gal at a dose of 5×10^{11} particles 4 weeks before DOX injection [8–10]. Four weeks after AAV9 infection, all the animals were subjected to a single intraperitoneal injection of DOX (20 mg/kg) [11]. The efficacy of AAV9-FSTL1 was confirmed

by Western blotting at the endpoint of the study. Two days after DOX treatment, all mice were sacrificed immediately via an intraperitoneal injection of sodium pentobarbital (150 mg/kg). We collected heart samples for biochemical analysis. To confirm the hypothesis that FSTL1 exerted cardioprotective effects by activating Nrf2, mice were intramyocardially injected with adenoviral genome particles (1×10^9 plaque forming units) carrying small interfering RNAs targeting Nrf2 (siNrf2) in the left ventricle [3]. The efficacy of siNrf2 was confirmed by Western blotting. Seven days after intramyocardial injection, all mice were administered a single injection of DOX (20 mg/kg, once) as previously described. siNrf2 was obtained from Santa Cruz.

2.3. Hemodynamics Analysis. Left ventricle function was assessed by invasive hemodynamic monitoring. We exposed the left ventricle at the seventh intercostal space, and a 1.0 F catheter (SPR 839; Millar Instruments Inc.) was inserted into the left ventricle along the longitudinal axis. The data were analyzed using Labchart software. This experiment was performed in a blinded manner.

2.4. RNA Analysis. Total RNA samples were obtained from pulverized left ventricles with TRIzol reagent (Invitrogen). cDNA synthesis was achieved using the Superscript III reverse transcriptase kit (Invitrogen). Real-time PCR was performed using a LightCycler 480 SYBR Green master mix kit (Roche Diagnostics). GAPDH was selected as the internal control.

2.5. Western Blotting. Frozen heart samples were homogenized with RIPA lysis buffer. Proteins were loaded into 10% SDS-PAGE gels and then electrotransferred to Immobilon-

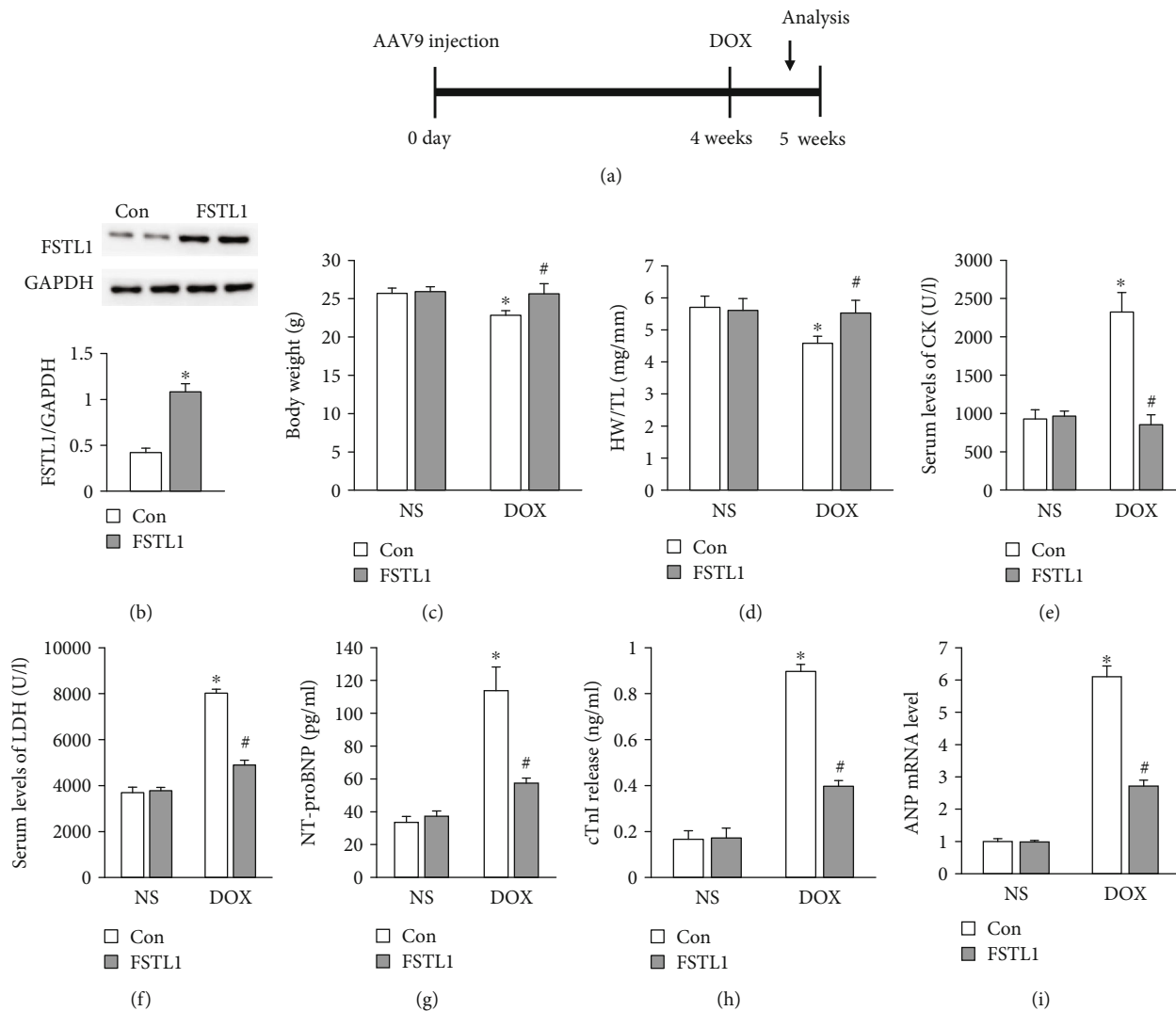


FIGURE 2: FSTL1 overexpression reduced myocardial injury in mice. (a) A diagram illustrating the study protocol. (b) FSTL1 protein expression in the heart ($n=6$). (c, d) Body weight and heart weight/tibia length ratio ($n=12$). (e, f) The levels of CK and LDH ($n=6$). (g, h) The levels of NT-proBNP and cTnI ($n=6$). (i) The mRNA level of ANP in the heart ($n=6$). The data are expressed as the mean \pm SD. * $P < 0.05$ vs. the NS/con group; # $P < 0.05$ vs. the DOX/con group. The data were analyzed using one-way ANOVA, followed by Tukey's post hoc analysis.

FL transfer membranes (Millipore, IPFL00010). Then, the Immobilon-FL transfer membranes were incubated with primary antibodies against FSTL1 (#ab11805, 1:1000), GAPDH (#ab181602, 1:1000), Nrf2 (#ab62352, 1:1000) and cleaved caspase-3 (1:1000, #ab2302) [12]. Band intensity was scanned and analyzed by NIH ImageJ software, and GAPDH was selected as the internal control.

2.6. Antioxidant Assay and Determination of Cardiac Injury Markers. To detect cardiac oxidative damage, fresh heart samples were homogenized. Superoxide dismutase (SOD) activity was detected using a commercially available kit (Nanjing Jiancheng Bioengineering Institute, Nanjing, China). Lipid peroxidation products, including malondialdehyde (MDA) and 4-hydroxynonenal (4-HNE), were also measured as a reflection of DOX-related oxidative damage. The MDA assay kit was provided by Nanjing Jiancheng Bio-

engineering Institute, and the 4-HNE detection kit was provided by Abcam (#ab238538).

To detect cardiac injury markers, blood was collected and measured for cTnI, NT-pro BNP, CK, and LDH levels using commercial kits.

2.7. Apoptotic Cell Death Assay. Fresh heart samples were collected and assayed for myocardial apoptotic cell death using terminal deoxynucleotidyl transferase-mediated dUTP nick-end labeling (TUNEL) staining with an in situ apoptosis detection kit (Roche Diagnostics Ltd., USA). Fresh heart samples were homogenized, and the activity of caspase3 in the heart was examined using a caspase3 activity assay kit from Nanjing Jiancheng Bioengineering Institute.

2.8. Adult Mouse Cardiomyocyte Isolation and Mechanics Detection. Adult ventricular myocyte isolation was achieved

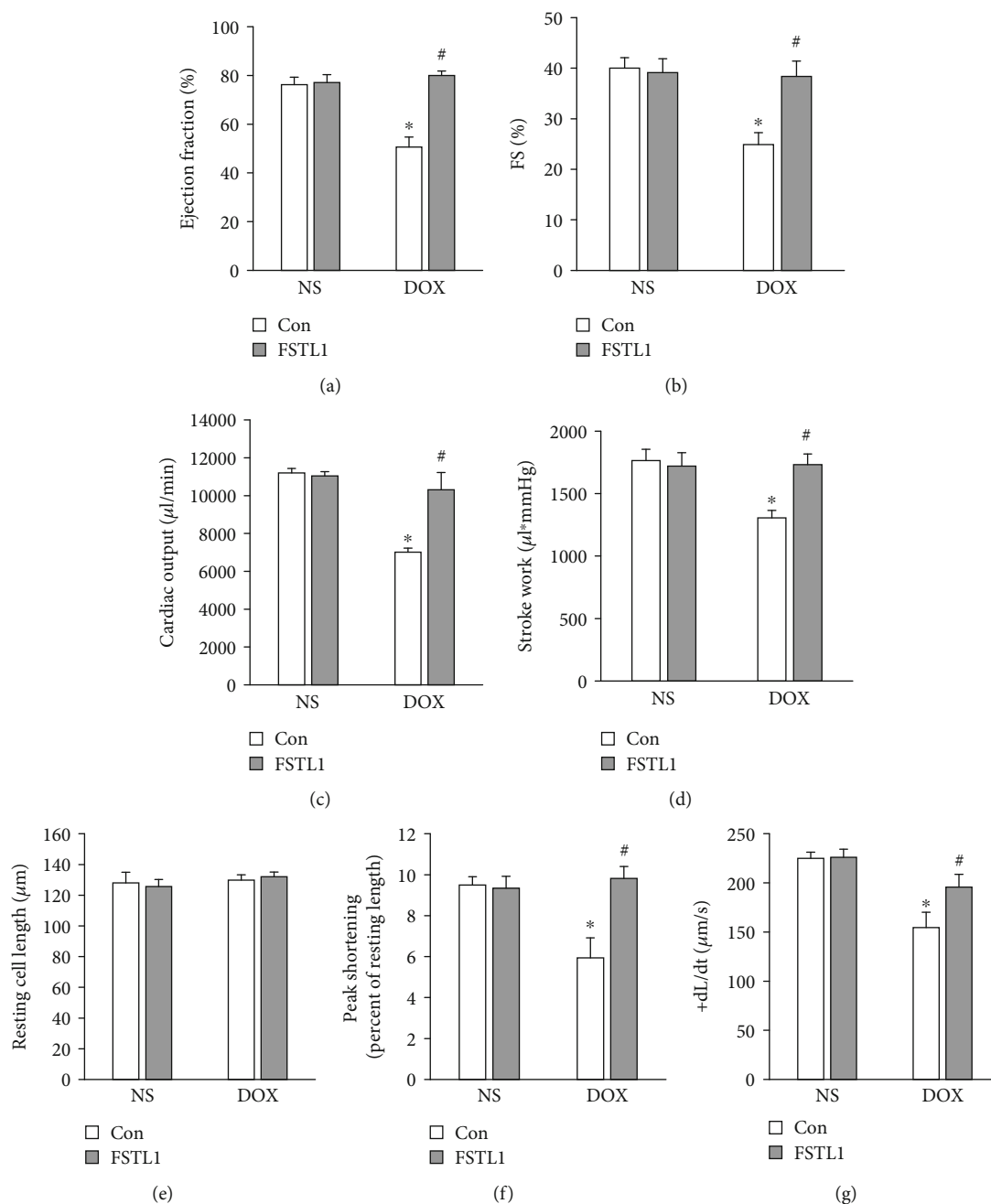
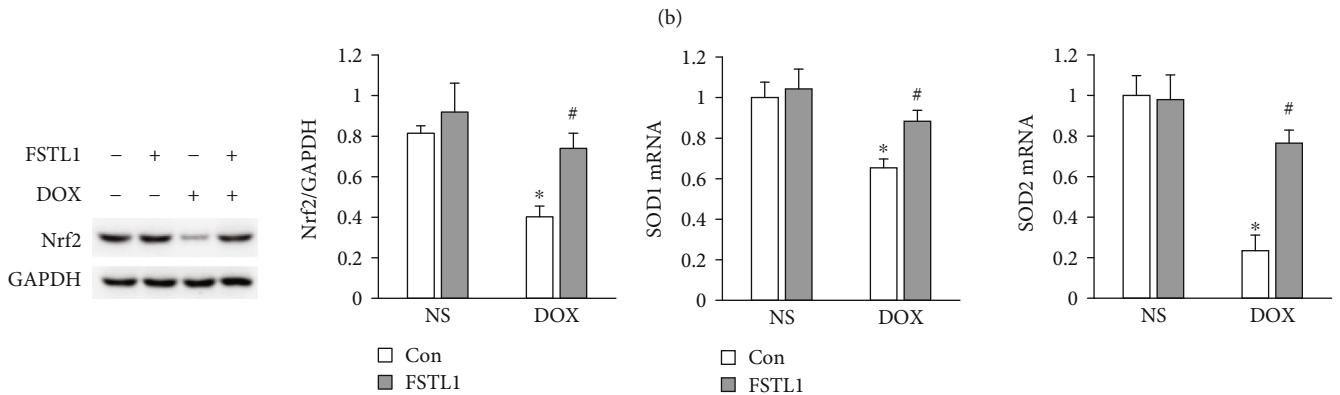
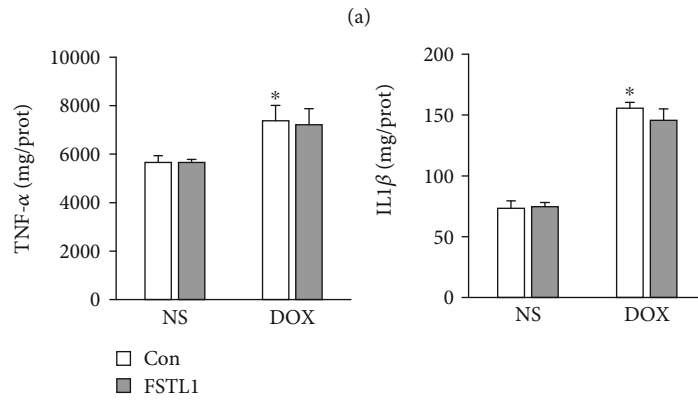
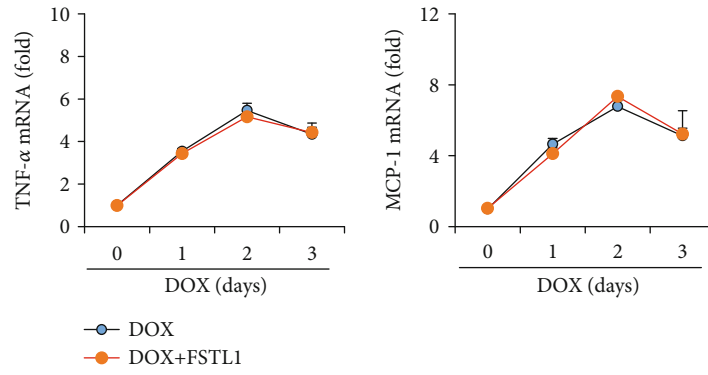


FIGURE 3: Effects of FSTL1 overexpression on DOX-induced cardiac dysfunction. (a, b) Ejection fraction and fraction shortening ($n = 8$). (c, d) Stroke work and cardiac output in mice ($n = 8$). (e) Resting cell length in isolated adult cells ($n = 5$). (f, g) Alterations in peak shortening and +dL/dt ($n = 5$). The data are expressed as the mean \pm SD. * $P < 0.05$ vs. the NS/con group; # $P < 0.05$ vs. the DOX/con group. The data were analyzed using one-way ANOVA, followed by Tukey's post hoc analysis.

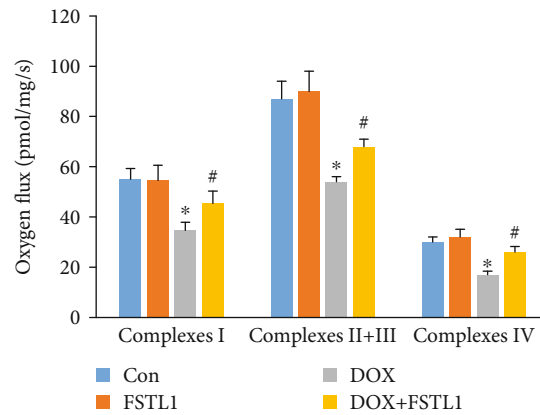
by a temperature-controlled Langendorff system. The fresh heart samples were incubated with liberase (0.1 mg/ml, Sigma-Aldrich) for 25 min. Only rod-shaped cardiomyocytes with clear edges were selected for further detection in our study. The IonOptix™ soft-edge system (IonOptix, MA, USA) was used to assess cardiomyocyte contractile properties. Cardiomyocyte mechanical properties were assessed in more than 200 cells per group ($n = 5$, more than 40 cells per mouse).

2.9. Neonatal Rat Cardiomyocyte Culture. Primary neonatal rat cardiomyocytes (NRCMs) were prepared as previously described [13]. These cells were cultured in DMEM (Gibco, NY, USA) containing 10% fetal bovine serum (Gibco). Human recombinant FSTL1 was dissolved in PBS. NRCMs were subjected to DOX treatment (5 μ mol/l) for 24 h. To explore the effect of FSTL1, NRCMs were incubated with FSTL1 (5 μ g/ml) or the same volume of PBS. For RNA interference analysis of Nrf2, siNrf2 (Invitrogen) was used, and



(c)

(d)



(e)

FIGURE 4: Continued.

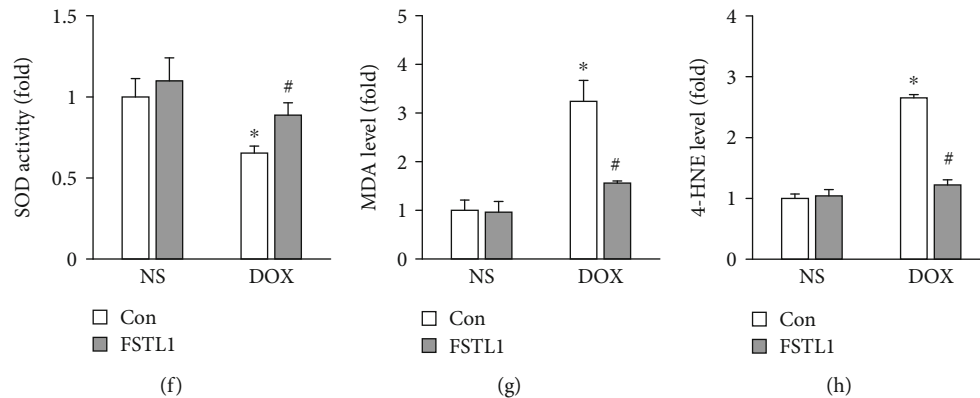


FIGURE 4: FSTL1 overexpression reduced DOX-induced myocardial oxidative damage. (a) The mRNA levels of TNF- α and IL-1 β ($n = 5$ for each time point). (b) Myocardial TNF- α and IL-1 β levels were determined by ELISA ($n = 6$). (c) Protein expression of Nrf2 in the heart ($n = 6$). (d) The mRNA levels of SOD1 and SOD2 ($n = 6$). (e) Mitochondrial complex activities ($n = 6$). (f) Alterations in SOD activity ($n = 6$). (g, h) MDA and 4-HNE levels ($n = 6$). The data are expressed as the mean \pm SD. * $P < 0.05$ vs. the NS/con group; # $P < 0.05$ vs. the DOX/con group. The data were analyzed using one-way ANOVA, followed by Tukey's post hoc analysis.

scrambled siRNA was used as a nonspecific control. NRCMs were treated with siNrf2 (50 nmol/l, 6 h) to achieve Nrf2 knockdown. To detect ROS production in NRCMs, cells were seeded in 96-well culture plates and then treated with DOX (5 μ mol/l) for 24 h. Then, the NRCMs were incubated with DCFH-DA (10 μ mol/l) at 37°C for 30 min, and ROS levels were examined by a microplate reader. Cell viability was assessed by a CCK-8 kit according to the manufacturer's instructions. Cells were also homogenized with PBS to measure the release of LDH after FSTL1 treatment.

2.10. Detection of Nuclear Nrf2 Activity. Frozen heart samples were homogenized with RIPA lysis buffer, and nuclear proteins in the heart samples were prepared using NE-PER™ nuclear and cytoplasmic extraction reagents. Then, Nrf2-binding activity was measured using the Nrf2 DNA-binding ELISA kit (TransAM Nrf2, Active Motif).

2.11. Mitochondrial Isolation and Complex Activity Detection. Fresh heart samples were homogenized, and mitochondria were isolated using a mitochondria isolation kit (#89801, Thermo Fisher Scientific). Myocardial mitochondrial complex activities were measured using the MitoCheck Complex I activity assay kit (#700930, Cayman), MitoCheck Complex II/III activity assay kit (#700950, Cayman), and MitoCheck Complex IV activity assay kit (#700990, Cayman).

2.12. Statistical Analysis. All data are shown as the means \pm SD. Comparisons between multiple groups were performed using one-way ANOVA followed by a post hoc Tukey's multiple comparisons test. Comparisons among two groups were performed using two-tailed Student's t tests. Statistical significance was accepted at a value of $P < 0.05$.

3. Results

3.1. FSTL1 Was Decreased in DOX-Treated Hearts and Cells. We first measured FSTL1 mRNA in NRCMs treated with DOX for 24 h. Interestingly, DOX decreased FSTL1 mRNA levels in a dose-dependent manner (Figure 1(a)). DOX

(5 μ mol/l) also decreased FSTL1 mRNA levels in a time-dependent manner (Figure 1(b)). FSTL1 protein expression in DOX-treated cells was reduced to approximately 48.7% of that in the PBS control (Figure 1(c)). Next, we detected FSTL1 mRNA levels in hearts that were treated with DOX for 2 days and found that FSTL1 mRNA levels in mice were also dose-dependently decreased after DOX treatment (Figure 1(d)). DOX (15 mg/kg) also decreased FSTL1 mRNA levels in a time-dependent manner in mice (Figure 1(e)). DOX injection also led to significant downregulation in FSTL1 protein expression in the heart (Figure 1(f)).

3.2. FSTL1 Overexpression Protected against Cardiac Injury in DOX-Treated Mice. AAV9 infection induced a 2.5-fold increase in FSTL1 expression in the heart (Figures 2(a) and 2(b)). DOX injection induced a decrease in body weight and the heart weight/tibia length ratio (Figures 2(c) and 2(d)). However, these pathological changes were abolished after FSTL1 overexpression in mice (Figures 2(c) and 2(d)). FSTL1 overexpression decreased the levels of plasma CK, LDH, NT-proBNP, and cTnI in DOX-treated hearts (Figures 2(e)–2(h)). FSTL1 overexpression also significantly decreased the mRNA level of atrial natriuretic peptide in DOX-treated mice (Figure 2(i)).

3.3. FSTL1 Improved Cardiac Function and Adult Cardiomyocyte Contractile Function. Hemodynamic parameters were evaluated, and ejection fraction (EF), fraction shortening (FS), cardiac output, and stroke work were significantly decreased in DOX-injected mice compared with NS-injected mice in all groups. These markers were significantly preserved after FSTL1 overexpression in DOX-treated mice (Figures 3(a)–3(d)). Next, we detected the effect of FSTL1 overexpression on the contractile function of isolated single adult cardiomyocytes. FSTL1 overexpression did not affect resting cell length in any of the groups (Figure 3(e)). Adult cardiomyocytes isolated from DOX-treated hearts showed decreased contractile function, as indicated by alterations in peak shortening and the maximal velocity of shortening/

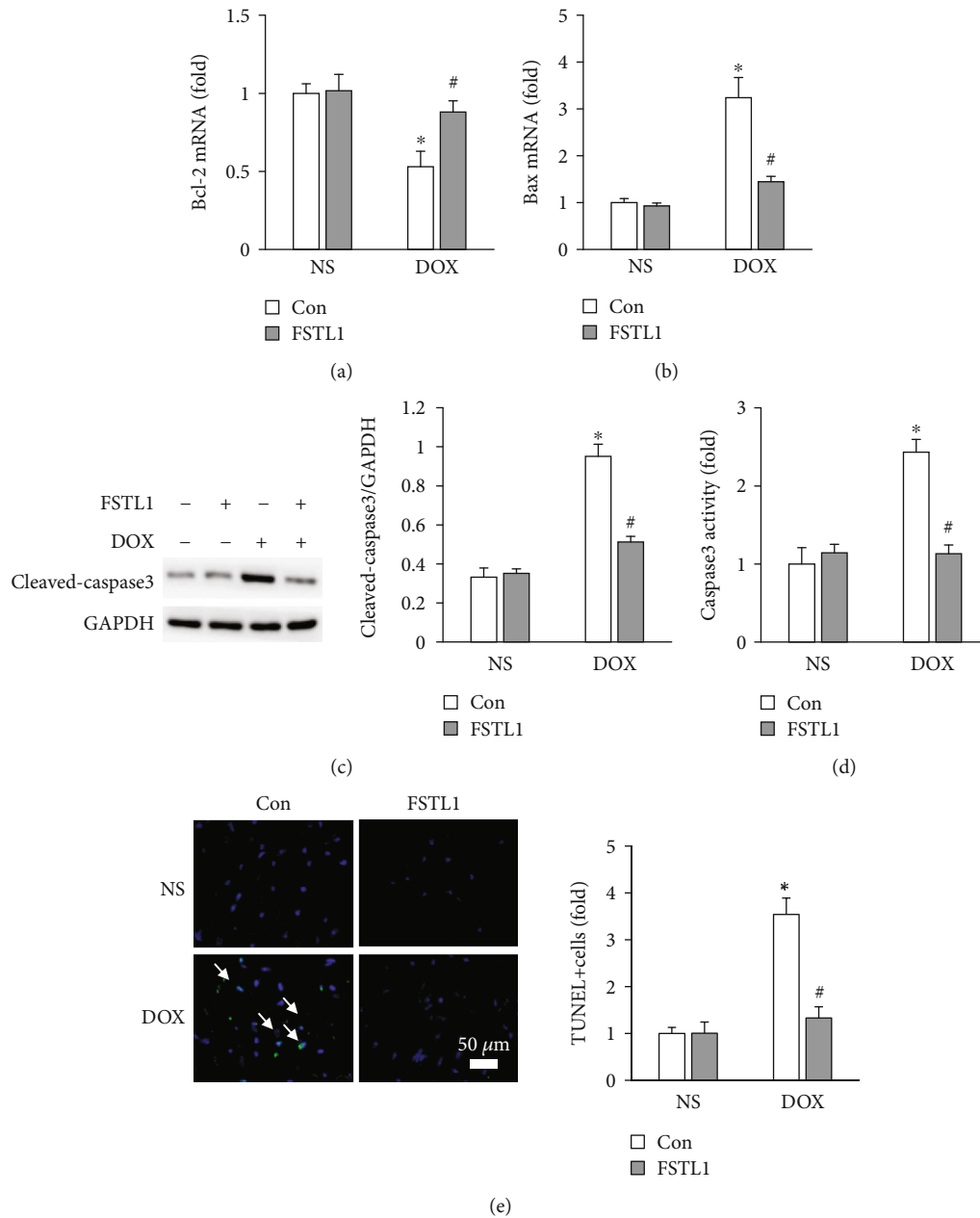


FIGURE 5: FSTL1 overexpression attenuated DOX-induced myocardial apoptosis. (a, b) The mRNA levels of Bcl-2 and Bax in the hearts ($n = 6$). (c, d) Cleaved caspase-3 and caspase-3 activity in the heart ($n = 6$). (e) TUNEL staining ($n = 6$). The data are expressed as the mean \pm SD. * $P < 0.05$ vs. the NS/con group; # $P < 0.05$ vs. the DOX/con group. The data were analyzed using one-way ANOVA, followed by Tukey's post hoc analysis.

relengthening (+dL/dt). However, FSTL1 supplementation restored cardiomyocyte contractile function in DOX-treated hearts (Figures 3(f) and 3(g)).

3.4. FSTL1 Attenuated DOX-Induced Oxidative Damage in Mice. Proinflammatory mediators contribute to the development of acute DOX-induced toxicity [14]. We first measured tumor necrosis factor- ($\text{TNF-}\alpha$) and monocyte chemotactic protein 1 (MCP-1) mRNA levels and found that FSTL1 did not decrease expression of these two pro-inflammatory factors (Figure 4(a)). We used ELISA to

measure myocardial $\text{TNF-}\alpha$ and interleukin- 1β (IL- 1β) production. There was no difference in the concentration of $\text{TNF-}\alpha$ or IL- 1β between the DOX and DOX+FSTL1 groups (Figure 4(b)). DOX decreased the protein expression of Nrf2, and FSTL1 overexpression largely restored the protein level of Nrf2 (Figure 4(c)). FSTL1 also increased SOD1 and SOD2 mRNA levels in DOX-treated hearts (Figure 4(d)). Next, fresh heart samples were collected to assess the electron transport chain. We showed that DOX treatment significantly impaired complex I, II+III, and IV activities in mice. However, FSTL1 supplementation restored

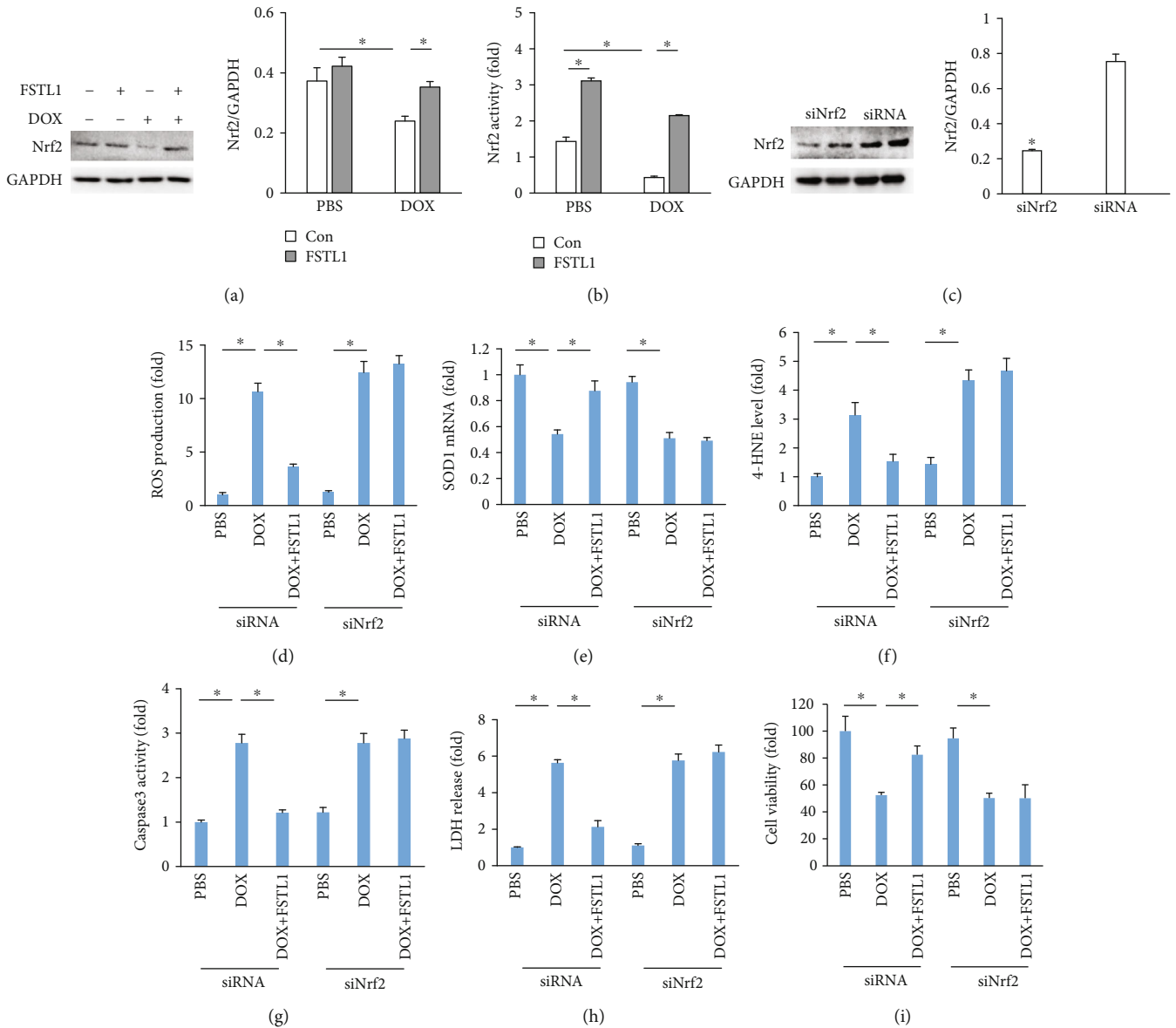


FIGURE 6: FSTL1 overexpression attenuated DOX-induced damage in vitro. (a, b) Nrf2 expression and Nrf2 activity in NRCMs ($n = 6$). (c) Nrf2 expression after siRNA infection ($n = 6$). (d) ROS production in NRCMs ($n = 6$). (e) The mRNA levels of SOD1 in NRCMs ($n = 6$). (f) The level of 4-HNE in NRCMs ($n = 6$). (g, h) Caspase 3 activity and LDH release ($n = 6$). (i) Cell viability ($n = 6$). * $P < 0.05$. For (c), the data were analyzed using two-tailed Student's t -tests. For the others, the data were analyzed using one-way ANOVA, followed by Tukey's post hoc analysis.

these functions in mice (Figure 4(e)). We also measured total SOD activity and found that FSTL1 increased SOD activity in DOX-treated hearts (Figure 4(f)). DOX increased MDA and 4-HNE levels, and FSTL1 supplementation reduced myocardial MDA and 4-HNE levels in DOX-treated mice (Figures 4(g) and 4(h)).

3.5. FSTL1 Supplementation Reduced Cardiac Apoptosis in DOX-Treated Hearts. Next, we detected whether FSTL1 could decrease DOX-related cardiac apoptosis in mice. FSTL1 upregulated the Bcl-2 mRNA level but decreased the Bax mRNA level in DOX-treated hearts (Figures 5(a) and 5(b)). DOX treatment upregulated the protein level of

cleaved caspase-3; however, this pathological alteration was attenuated by FSTL1 supplementation (Figure 5(c)). Further evaluation also found that FSTL1 supplementation decreased caspase-3 activity in DOX-treated hearts (Figure 5(d)). To further confirm the antiapoptotic effect of FSTL1, we used the TUNEL assay to assess cardiac apoptosis. FSTL1 supplementation substantially decreased the number of TUNEL-positive cells in DOX-treated mice (Figure 5(e)).

3.6. Nrf2 Deficiency Antagonized FSTL1-Mediated Protection. In view of the restoration of Nrf2 by FSTL1 in vivo, we measured Nrf2 protein expression in vitro. FSTL1 supplementation also significantly increased Nrf2 protein expression in

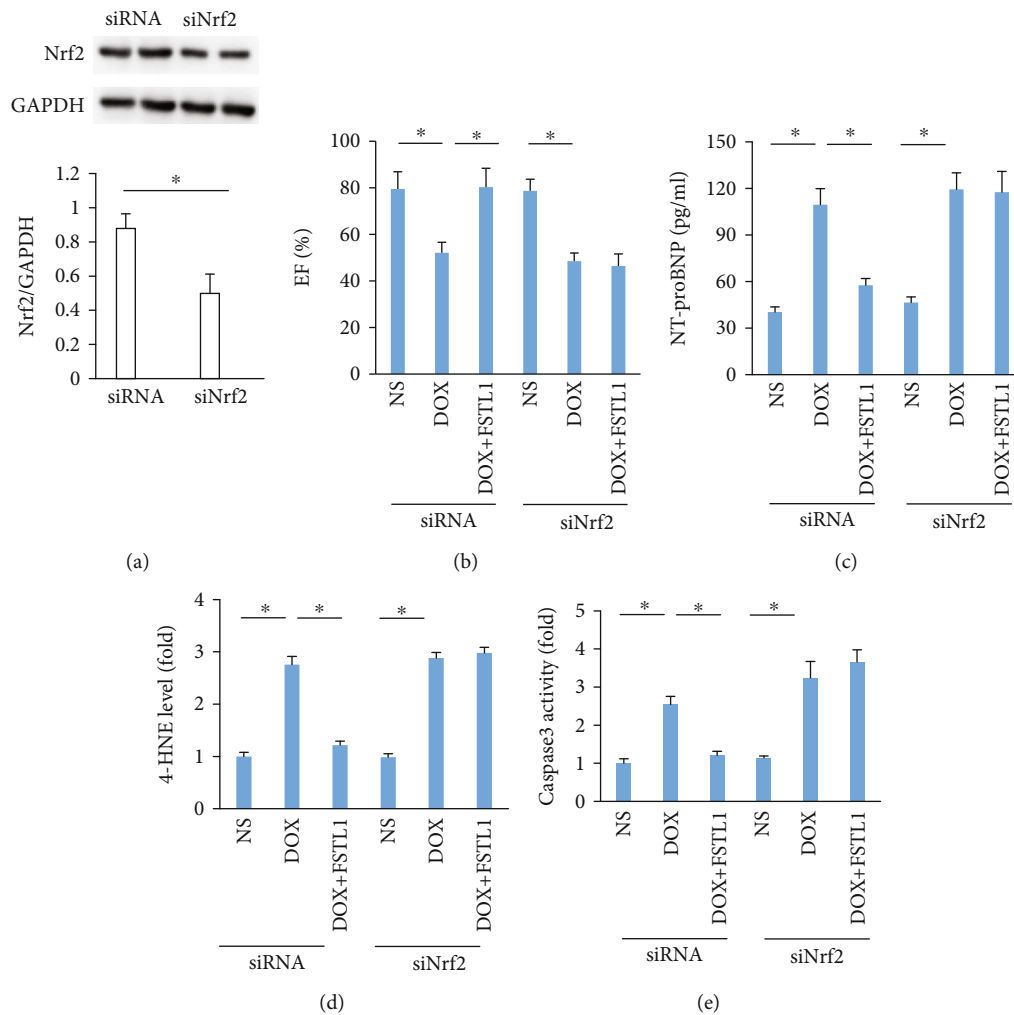


FIGURE 7: FSTL1 lost its cardioprotective effect in Nrf2-deficient hearts. (a) Nrf2 expression after siRNA infection ($n = 6$). (b) Ejection fraction ($n = 6$). (c) The level of NT-proBNP ($n = 6$). (d) The level of 4-HNE ($n = 6$). (e) Caspase-3 activity in the hearts ($n = 6$). * $P < 0.05$. For (a), the data were analyzed using two-tailed Student's t -tests. For the others, the data were analyzed using one-way ANOVA, followed by Tukey's post hoc analysis.

DOX-treated NRCMs (Figure 6(a)). FSTL1 enhanced Nrf2 activity even in the absence of any stimuli. FSTL1 also increased nuclear Nrf2 activity in DOX-treated cells (Figure 6(b)). Next, we confirmed the hypothesis that FSTL1 exerted its protective effects by activating Nrf2. FSTL1 supplementation in vitro attenuated DOX-induced ROS production, upregulated SOD1 mRNA levels, and blocked the production of 4-HNE in NRCMs. However, this protection was abolished by Nrf2 deficiency (Figures 6(c)–6(f)). The inhibitory effects of FSTL1 on caspase-3 activity and LDH release were also lost in Nrf2-deficient NRCMs (Figures 6(g) and 6(h)). FSTL1 improved cell viability after DOX treatment, and siNrf2 antagonized this effect of FSTL1 (Figure 6(i)). To further verify the hypothesis that FSTL1 exerted its protective effects via activation of Nrf2 in mice, we used siRNAs to knock down Nrf2 expression in the heart. Our data suggested that FSTL1 could not exert cardioprotective effects in DOX-treated hearts, as indicated by the alterations in EF, plasma NT-proBNP, cardiac 4-HNE, and caspase-3 activity in mice (Figures 7(a)–7(e)).

4. Discussion

We showed for the first time that FSTL1 expression was decreased in DOX-treated hearts and that FSTL1 overexpression prevented acute DOX-induced injury in the heart. We found that FSTL1 overexpression prevented DOX-related cardiac atrophy, oxidative damage, and apoptosis, thus improving cardiac function. We also found that FSTL1 exerted cardioprotective effects by activating the Nrf2 signaling pathway in mice. Our study provide experimental evidence that FSTL1 possesses the potential to be a drug that can limit DOX-caused toxicity.

The pathogenesis of DOX-related cardiomyopathy is still unclear. Moreover, heart transplantation is the only approach for serious DOX-induced injury [2]. Therefore, devising a novel strategy to block DOX-induced cardiomyopathy would have tremendous benefits in clinical practice. Previous studies have found that several natural products that act as ROS scavengers have the ability to suppress acute cardiotoxicity caused by DOX, but there has been little

success in clinical trials due to the low bioavailability of these drugs and secondary reactions with other molecules [15–17]. FSTL1 also inhibited pressure overload-induced cardiac hypertrophy in mice [18]. Another study found that FSTL1 alleviated myocardial damage caused by ischemia-reperfusion [5]. In the present study, we found that FSTL1, which was originally identified in a murine osteoblastic cell line, prevented DOX-induced body weight loss and cardiac atrophy and reduced cardiac injury marker release, thus improving cardiac function in mice. Moreover, overexpression of FSTL1 did not affect cardiac function or body weight in mice in the absence of DOX treatment. These observations suggest that FSTL1 might be a potential drug that can treat DOX-related cardiac injury.

One of the landmarks in acute cardiotoxicity caused by DOX is acute inflammation [14]. A previous study found that inhibition of myocardial inflammation accumulation suppressed DOX-related cardiac apoptosis in mice [4]. We also detected alterations in cardiac inflammation after FSTL1 overexpression, and our data showed that FSTL1 did not restrict myocardial inflammation in DOX-treated hearts, suggesting that the cardioprotective effect of FSTL1 was not dependent on attenuation of inflammation. It has been reported that free radical lesions are closely involved in DOX-related cardiac damage [19]. Overexpression of catalase or metallothionein could suppress DOX-related cardiotoxicity in mice [20, 21], suggesting a key role of oxidative damage in DOX-related cardiac injury. Highly reactive DOX metabolites induce mitochondrial injury and 4-HNE production, which could modify several mitochondrial proteins [22]. In the present study, we found that FSTL1 restored cardiac Nrf2 protein expression and SOD activity and reduced cardiac 4-HNE and MDA production in DOX-induced mice. Moreover, we found that FSTL1 restored cardiac mitochondrial complex activities to normal levels in mice treated with DOX. Moreover, we found that FSTL1 lost its cardioprotective effect against oxidative stress *in vitro* and *in vivo* after Nrf2 deficiency, suggesting that FSTL1 protects against DOX-related cardiac injury by activating the Nrf2 signaling pathway.

There is a direct correlation between the degree of myocardial apoptosis and the severity of DOX-induced cardiac injury [23]. Apoptotic cell death is a typical feature of DOX-induced cardiotoxicity. DOX induces cardiomyocyte apoptotic cell death by activating caspase-3 *in vivo* [24]. DOX treatment results in cytochrome C release and cardiomyocyte apoptosis and changes the Bcl-2/Bax ratio in mice [25]. Moreover, suppressing the degree of myocardial apoptosis could prevent DOX-related cardiac injury in mice [3]. In the present study, we found that FSTL1 overexpression upregulated Bcl-2 mRNA but decreased Bax mRNA levels, reduced cleaved-caspase3 protein expression, and decreased caspase3 activity in mice. Moreover, we found that FSTL1 lost these antiapoptotic effects *in vitro* and *in vivo* after Nrf2 deficiency, suggesting that FSTL1 protects against DOX-related apoptosis by activating the Nrf2 signaling pathway.

Overall, our results suggest that FSTL1 protects against DOX-induced acute toxicity by activating Nrf2 to suppress oxidative damage and apoptotic cell death, thus improving

cardiac function. The present findings suggest that FSTL1 supplementation might represent a new cardioprotective strategy against DOX-induced cardiotoxicity.

Data Availability

The data that support the findings of this study are available from the corresponding author upon reasonable request.

Conflicts of Interest

The authors declare that they have no conflicts of interest.

Authors' Contributions

Yintao Zhao and Jingjing Sun are cofirst authors.

Acknowledgments

This study was supported by the Scientific and Technological Project of Henan Province (182102310099 and 182102310495).

References

- [1] P. K. Singal, N. Iliskovic, T. Li, and D. Kumar, "Adriamycin cardiomyopathy: pathophysiology and prevention," *The FASEB Journal*, vol. 11, no. 12, pp. 931–936, 1997.
- [2] A. H. Blaes, P. Gaillard, B. A. Peterson, D. Yee, and B. Virnig, "Angiotensin converting enzyme inhibitors may be protective against cardiac complications following anthracycline chemotherapy," *Breast Cancer Research and Treatment*, vol. 122, no. 2, pp. 585–590, 2010.
- [3] X. Zhang, C. Hu, C.-Y. Kong et al., "FNDC5 alleviates oxidative stress and cardiomyocyte apoptosis in doxorubicin-induced cardiotoxicity via activating AKT," *Cell Death and Differentiation*, vol. 27, no. 2, pp. 540–555, 2020.
- [4] Y. P. Yuan, Z. G. Ma, X. Zhang et al., "CTRP3 protected against doxorubicin-induced cardiac dysfunction, inflammation and cell death via activation of Sirt1," *Journal of Molecular and Cellular Cardiology*, vol. 114, pp. 38–47, 2018.
- [5] Y. Oshima, N. Ouchi, K. Sato, Y. Izumiya, D. R. Pimentel, and K. Walsh, "Follistatin-like 1 is an Akt-regulated cardioprotective factor that is secreted by the heart," *Circulation*, vol. 117, no. 24, pp. 3099–3108, 2008.
- [6] K. Tanaka, M. Valero-Muñoz, R. M. Wilson et al., "Follistatin-Like 1 Regulates Hypertrophy in Heart Failure With Preserved Ejection Fraction," *JACC: Basic to Translational Science*, vol. 1, no. 4, pp. 207–221, 2016.
- [7] A. El-Armouche, N. Ouchi, K. Tanaka et al., "Follistatin-like 1 in chronic systolic heart failure: a marker of left ventricular remodeling," *Circulation. Heart Failure*, vol. 4, no. 5, pp. 621–627, 2011.
- [8] Z.-G. Ma, J. Dai, Y.-P. Yuan et al., "T-bet deficiency attenuates cardiac remodeling in rats," *Basic Research in Cardiology*, vol. 113, no. 3, p. 19, 2018.
- [9] Z. G. Ma, X. Zhang, Y. P. Yuan et al., "A77 1726 (leflunomide) blocks and reverses cardiac hypertrophy and fibrosis in mice," *Clinical Science*, vol. 132, no. 6, pp. 685–699, 2018.
- [10] Z. G. Ma, Y. P. Yuan, S. C. Xu et al., "CTRP3 attenuates cardiac dysfunction, inflammation, oxidative stress and cell death in

- diabetic cardiomyopathy in rats," *Diabetologia*, vol. 60, no. 6, pp. 1126–1137, 2017.
- [11] G. C. Fan, X. Zhou, X. Wang et al., "Heat shock protein 20 interacting with phosphorylated Akt reduces doxorubicin-triggered oxidative stress and cardiotoxicity," *Circulation Research*, vol. 103, no. 11, pp. 1270–1279, 2008.
- [12] Z. G. Ma, Y. P. Yuan, X. Zhang et al., "C1q-tumour necrosis factor-related protein-3 exacerbates cardiac hypertrophy in mice," *Cardiovascular Research*, vol. 115, no. 6, pp. 1067–1077, 2019.
- [13] N. Koitabashi, T. Aiba, G. G. Hesketh et al., "Cyclic GMP/PKG-dependent inhibition of TRPC6 channel activity and expression negatively regulates cardiomyocyte NFAT activation novel mechanism of cardiac stress modulation by PDE5 inhibition," *Journal of Molecular and Cellular Cardiology*, vol. 48, no. 4, pp. 713–724, 2010.
- [14] G. Takemura and H. Fujiwara, "Doxorubicin-induced cardiomyopathy from the cardiotoxic mechanisms to management," *Progress in Cardiovascular Diseases*, vol. 49, no. 5, pp. 330–352, 2007.
- [15] G. C. Pereira, A. M. Silva, C. V. Diogo, F. S. Carvalho, P. Monteiro, and P. J. Oliveira, "Drug-induced cardiac mitochondrial toxicity and protection: from doxorubicin to carvedilol," *Current Pharmaceutical Design*, vol. 17, no. 20, pp. 2113–2129, 2011.
- [16] L. Xi, S. G. Zhu, A. Das et al., "Dietary inorganic nitrate alleviates doxorubicin cardiotoxicity: mechanisms and implications," *Nitric Oxide*, vol. 26, no. 4, pp. 274–284, 2012.
- [17] P. Singh, R. Sharma, K. McElhanon et al., "Sulforaphane protects the heart from doxorubicin-induced toxicity," *Free Radical Biology & Medicine*, vol. 86, pp. 90–101, 2015.
- [18] N. Ouchi, Y. Oshima, K. Ohashi et al., "Follistatin-like 1, a secreted muscle protein, promotes endothelial cell function and revascularization in ischemic tissue through a nitric-oxide synthase-dependent mechanism," *The Journal of Biological Chemistry*, vol. 283, no. 47, pp. 32802–32811, 2008.
- [19] E. Monti, E. Prosperi, R. Supino, and G. Bottiroli, "Free radical-dependent DNA lesions are involved in the delayed cardiotoxicity induced by adriamycin in the rat," *Anticancer Research*, vol. 15, no. 1, pp. 193–197, 1995.
- [20] Y. J. Kang, Y. Chen, A. Yu, M. Voss-McCowan, and P. N. Epstein, "Overexpression of metallothionein in the heart of transgenic mice suppresses doxorubicin cardiotoxicity," *The Journal of Clinical Investigation*, vol. 100, no. 6, pp. 1501–1506, 1997.
- [21] Y. J. Kang, Y. Chen, and P. N. Epstein, "Suppression of doxorubicin cardiotoxicity by overexpression of catalase in the heart of transgenic mice," *The Journal of Biological Chemistry*, vol. 271, no. 21, pp. 12610–12616, 1996.
- [22] Y. Zhao, S. Miriyala, L. Miao et al., "Redox proteomic identification of HNE-bound mitochondrial proteins in cardiac tissues reveals a systemic effect on energy metabolism after doxorubicin treatment," *Free Radical Biology & Medicine*, vol. 72, pp. 55–65, 2014.
- [23] T. G. Neilan, D. S. Jassal, T. M. Perez-Sanz et al., "Tissue Doppler imaging predicts left ventricular dysfunction and mortality in a murine model of cardiac injury," *European Heart Journal*, vol. 27, no. 15, pp. 1868–1875, 2006.
- [24] M. Ueno, Y. Kakinuma, K. Yuhki et al., "Doxorubicin induces apoptosis by activation of caspase-3 in cultured cardiomyocytes in vitro and rat cardiac ventricles in vivo," *Journal of Pharmacological Sciences*, vol. 101, no. 2, pp. 151–158, 2006.
- [25] A. C. Childs, S. L. Phaneuf, A. J. Dirks, T. Phillips, and C. Leeuwenburgh, "Doxorubicin treatment in vivo causes cytochrome C release and cardiomyocyte apoptosis, as well as increased mitochondrial efficiency, superoxide dismutase activity, and Bcl-2:Bax ratio," *Cancer Research*, vol. 62, no. 16, pp. 4592–4598, 2002.

Research Article

Dexmedetomidine Ameliorates Lung Injury Induced by Intestinal Ischemia/Reperfusion by Upregulating Cannabinoid Receptor 2, Followed by the Activation of the Phosphatidylinositol 3-Kinase/Akt Pathway

Meng Chen,¹ Xue-Tao Yan,² Li Ye,¹ Jun-Jiao Tang,¹ Zong-Ze Zhang,¹ and Xiang-Hu He¹ 

¹Department of Anesthesiology, Zhongnan Hospital of Wuhan University, Wuhan, Hubei 430071, China

²Department of Anesthesiology, Shenzhen Bao'an Maternity and Child Health hospital, Shenzhen 518133, China

Correspondence should be addressed to Xiang-Hu He; hexh1220@aliyun.com

Received 8 February 2020; Revised 27 April 2020; Accepted 5 May 2020; Published 22 June 2020

Guest Editor: Bhagavatula Moorthy

Copyright © 2020 Meng Chen et al. This is an open access article distributed under the Creative Commons Attribution License, which permits unrestricted use, distribution, and reproduction in any medium, provided the original work is properly cited.

Intestinal ischemia/reperfusion (I/R) is a clinical emergency, which often causes lung injury with high morbidity and mortality. Although dexmedetomidine has been identified to have a protective effect on lung injury caused by intestinal I/R, its specific mechanism is still elucidated. In recent years, the cannabinoid (CB₂) receptor pathway has been found to be involved in I/R injury of some organs. In the current study, we investigated whether the CB₂ receptor pathway contributes to the protective effect of dexmedetomidine on the intestinal I/R-induced lung injury in rats. Dexmedetomidine treatment upregulated the expression of CB₂ receptor and suppressed the I/R-induced increases in lung injury scores, inflammatory cell infiltration, lung wet/dry ratio, MPO activity, MDA level, inflammatory cytokines, and caspase-3 expression while augmenting SOD activity and Bcl-2 expression, indicating attenuation of lung injury. Dexmedetomidine treatment also increased the expression of Akt. The protective effects of dexmedetomidine treatment were reversed by the CB₂ receptor antagonist AM630 or the PI3K inhibitor wortmannin. And the CB₂ receptor antagonist AM630 also downregulated the expression of Akt. Thus, our findings suggest that treatment with dexmedetomidine provides a protective role against lung injury caused by intestinal I/R in rats, possibly due to the upregulation of the CB₂ receptor, followed by the activation of the PI3K/Akt pathway.

1. Introduction

Intestinal ischemia/reperfusion (I/R) is a clinical emergency frequently occurring in multiple clinical conditions, including acute mesenteric ischemia, abdominal aortic aneurysm surgery, small bowel transplantation, shock, and cardiopulmonary bypass [1]. In addition to causing local intestinal damage, I/R is often followed by distant organ injury, especially lung injury, associated with high morbidity and mortality [2]. Although the exact mechanism is poorly understood, some factors, such as oxidative stress, activated neutrophils, complement components, released inflammatory cytokines, and cell apoptosis, are believed to be involved in the development of I/R-induced lung injury [3–5].

Dexmedetomidine (DEX), a highly selective alpha-2 adrenoceptor (α_2 AR) agonist, exhibits anesthetic-sparing, analgesia, and sympatholytic properties and is widely used as a sedative agent in clinical anesthesia and ICU management [6]. Previous studies have identified DEX as having protective effects in some models of I/R injury, such as in the liver [7, 8], lung [9], heart [10], kidney [11], and intestine [12] because of its antioxidant, anti-inflammatory, and anti-apoptotic properties. Further research has shown that some molecular mechanisms, such as α_2 AR/phosphatidylinositol 3-kinase (PI3K)/Akt [13], HMGB1-TLR₄-MyD88-NF- κ B [14], and JAK/STAT [15], are involved in the process of protection of DEX against some organ I/R injuries. It has also been demonstrated that treatment with DEX mitigated lung

injury caused by various factors, including intestinal I/R [16]. Although the protective effect of DEX treatment on intestinal I/R-induced lung injury has been investigated, the potential molecular mechanism by which DEX ameliorates lung injury remains unclear.

Recently, the role of cannabinoid (CB) receptors, especially the CB₂ receptor, has attracted much attention in health and disease. Although the CB₂ receptor was first identified in the peripheral immune system, it is now expressed in most organ systems, including in the cells of the brain, heart, liver, and cardiovascular and gastrointestinal (GI) systems [17]. Early studies focused mainly on the role of the CB₂ receptor in fundamental physiological processes. However, accumulating evidence supports that the CB₂ receptor has a critical role in regulating many disease processes, including inflammation [18], cancer [19], pain [20], and I/R injury [21], with it shown that the CB₂ agonist, HU-910, protected against hepatic I/R injury by attenuating oxidative stress, inflammatory response, and apoptosis [22]. Using the selective CB₂ agonist, JWH-133, and CB₂ gene-deficient mice, Defer et al. [23] also revealed that activating the CB₂ receptor promoted the survival of cardiac myocytes and protected against I/R-induced myocardial infarction through the direct inhibition of myocyte and fibroblast death and the prevention of myofibroblast activation. The role of the CB₂ receptor in the GI tract has been investigated, including in regulating abnormal motility, modulating intestinal inflammation, and limiting visceral sensitivity and pain [18, 24]. However, it remains unclear whether the CB₂ receptor is involved in the intestinal I/R-induced lung injury.

Thus, we hypothesized that DEX might improve intestinal I/R-induced lung injury by activating the CB₂ receptor pathway. In this study, we established a rat model of lung injury induced by intestinal I/R and investigated the effect of DEX on intestinal I/R-induced lung injury and its potential mechanisms.

2. Materials and Methods

2.1. Animals. Male Sprague-Dawley rats weighing 220-270 g were obtained from the Department of Laboratory Animal Center of the Wuhan University and housed under standardized conditions of food, water, light, and temperature. All animals were subjected to fasting for 12 h before experiments, but they were allowed free access to tap water throughout the experimental procedure. All procedures were approved by the Research Committee on Ethics of the Zhongnan Hospital of Wuhan University.

2.2. Drugs. DEX was acquired from Jiangsu Nhwa Pharmaceutical Corporation Ltd. (Jiangsu, China). The CB₂R antagonist AM630 was obtained from Tocris (Baldwin, MO, USA). The PI3K inhibitor wortmannin was purchased from Sigma-Aldrich (St. Louis, MO, USA). AM630 and wortmannin were dissolved in DMSO. DMSO alone was used in control experiments.

2.3. Experimental Protocol. Fifty-six male Sprague-Dawley rats were randomly assigned to the following seven groups

($n = 8$): sham operation (Sham) group, intestinal I/R (I/R) group, dexmedetomidine-treated I/R (DEX) group, dexmedetomidine- and AM630-treated I/R (DA) group, AM630-treated I/R (AI) group, dexmedetomidine- and wortmannin-treated I/R (DW) group, and wortmannin-treated I/R (WI) group. Animals in the DEX, DA, and DW groups were infused continuously with dexmedetomidine (i.v.) at $5 \mu\text{g kg}^{-1} \text{h}^{-1}$ for 1 h before ischemia. This dose was chosen based on the results from a previous study [12]. Animals in the DA, AI, DW, and WI groups were given the CB₂ receptor antagonist, AM630 (3 mg/kg, i.p.), or the PI3K inhibitor, wortmannin (15 $\mu\text{g/kg}$, i.v.), before the injection of dexmedetomidine. Animals in the Sham or I/R groups were given an equal volume of the vehicle at the same time point.

2.4. Surgical Procedure. The model of intestinal I/R injury was established as we previously described [25]. Each animal was anesthetized with an intraperitoneal injection of sodium pentobarbital (50 mg/kg). An upper midline laparotomy was performed to expose the abdomen and the superior mesenteric artery (SMA). An atraumatic microvascular clamp was applied to the SMA for 1 h of ischemia induction, after which the occluding clamp was removed for 2 h of reperfusion. Sham-operated animals underwent the same surgical procedure as the experimental rats, except for the induction of I/R injury. The animals were sacrificed with pentobarbital overdose, and lung samples were harvested after reperfusion and used to assess biochemical parameters or fixed in buffered formalin for histopathological evaluation.

2.5. Histological Assessment. Lung samples were immersed in 10% formalin and then embedded in paraffin. Tissue blocks were cut into 5 μm sections and stained with hematoxylin and eosin (HE). The morphologic examination of lung tissues was carried out under a light microscope by two pathologists blinded to the experiment. The histological injury was graded using our previously described method [26]: grade 0, no diagnostic change; grade 1, mild neutrophil infiltration and mild to moderate interstitial congestion; grade 2, moderate neutrophil infiltration, perivascular edema formation, and partial destruction of the pulmonary architecture; and grade 3, dense neutrophil infiltration and the complete destruction of the pulmonary architecture.

2.6. Assessment of Pulmonary Edema. The left lower lung lobe was removed at the end of reperfusion, weighed, and then dried in an oven at 80°C for 24 h. The wet weight to dry weight (W/D) ratio of the lung tissue was calculated and used as an indicator for estimating pulmonary edema.

2.7. Assay of Myeloperoxidase Activity. Frozen lung tissues were homogenized on ice using a homogenizer. The myeloperoxidase (MPO) activity was measured according to the manufacturer's instructions (Jiancheng Biologic Project Company, Nanjing, China). One MPO activity unit was defined as the amount of lung tissue that converted 1 μmol of hydrogen peroxide to water per minute at 37°C. The MPO activity was expressed in units per gram (U/g) of wet weight.

2.8. Assay of Lipid Peroxidation and Superoxide Dismutase Activity. Frozen lung tissues were homogenized on ice using a homogenizer and centrifuged at 4000 g for 10 min at 4°C. Malondialdehyde (MDA) level and superoxide dismutase (SOD) activity in the supernatant were determined according to the manufacturer's instructions using commercial kits (Jiancheng Bioengineering Institute, Nanjing, China). The SOD activity was expressed in U/mg protein, and the MDA level was expressed in nmol/mg protein.

2.9. Assay of Lung Tissue Cytokines. Frozen lung tissues were homogenized on ice using a homogenizer and centrifuged at 4000 g for 10 min at 4°C. Levels of tumor necrosis factor alpha (TNF- α) and interleukin 6 (IL-6) in the supernatant were assayed according to the manufacturer's instructions using ELISA kits (R&D Systems, Minneapolis, MN, USA). The concentrations of TNF- α and IL-6 were expressed in pg/mg protein.

2.10. Immunohistochemistry. Immunohistochemistry was performed to detect macrophage infiltration and phosphorylated Akt (p-Akt) expression in the lung tissues. F4/80 is a marker of macrophages, and its expression is used to detect macrophage infiltration. Sections were incubated with 5% bovine serum albumin and then with primary antibodies: F4/80 (Thermo Fisher Scientific, USA) and p-Akt (Cell Signaling Technology, USA). The sections were incubated in species-specific secondary antibodies labeled with horseradish peroxidase and then visualized by incubating the sections with DAB (Boster Bioengineering, Wuhan, China). Expressions of F4/80 and p-Akt were quantified by measuring the integrated optical density (IOD) of the positive staining area.

2.11. Real-Time Quantitative Reverse Transcription-PCR. The total RNA of rat lung tissues was extracted using TRIzol reagent according to the manufacturer's instructions (Takara, Japan). A real-time quantitative reverse transcription-PCR (RT-PCR) analysis was performed by using a SYBR Premix Ex Taq™ Kit (Takara, Japan), and the reactions were conducted on a StepOne™ Real-Time PCR instrument (Life Technologies, Grand Island, NY). The primers used for PCR were as follows: caspase-3 forward 5'-actactgcccggagtctgact-3'; reverse 5'-taaccgggtgctgtagagta-3'; Bax forward 5'-gaaccatcatgggctggaca-3'; reverse 5'-gtgagtgaggcagtgaggac-3'; Bcl-2 forward 5'-cttctctctgctaccgtc-3'; reverse 5'-ggggtgacatctccctgttg-3'; Akt forward 5'-gagaaccgtgctctcgagaa-3'; reverse 5'-gttctccagcttgaggtccc-3'; and GAPDH forward 5'-tgatgggtggaaccacgag-3'; reverse 5'-agtgatggcatgagctgtgg-3'. PCR conditions were as follows: 95°C for 5 min; 35 cycles at 95°C for 20s, 60°C for 20s, and 72°C for 45 s. GAPDH was selected as an internal control, and the target gene expression was normalized to GAPDH expression and calculated using the $2^{-\Delta\Delta C_t}$ method.

2.12. Western Blot Analysis. Frozen lung samples were homogenized and centrifuged at 12,000 g for 10 min at 4°C. The protein concentrations in the supernatant were measured using a BCA protein assay kit (Beyotime Institute of Biotechnology, Shanghai, China). Equal amounts of lysate were sub-

jected to 10% sodium dodecyl sulfate-polyacrylamide gel electrophoresis, then transferred to polyvinylidene fluoride membranes (Millipore, Bedford, MA, USA) that were incubated with primary antibodies against cleaved caspase-3, Bax, Bcl-2 (Santa Cruz Biotechnology, USA), and p-Akt (Cell Signaling Technology, USA) overnight at 4°C. The membranes were washed with PBS-0.05% Tween-20 the next day and incubated for 1 h in horseradish peroxidase-conjugated secondary antibody (Jackson ImmunoResearch). Another wash of the membranes with PBS-0.05% Tween 20 followed the 1 h incubation period, at the end of which protein bands were visualized using an enhanced chemiluminescence kit (Amersham, Piscataway, NJ, USA). All band densities were quantified by densitometry using the Quantity One software (BioRad, Hercules, CA, USA).

2.13. Statistical Analysis. All data are expressed as mean values \pm SEM. Differences among the groups were analyzed using the one-way analysis of variance (ANOVA), followed by the Student-Newman-Keul (SNK) test for multiple comparisons. Differences were considered significant at $P < 0.05$.

3. Results

3.1. The Effects of Dexmedetomidine Treatment on the Histological Injury. Lung histological injury was evaluated and scored by two pathologists to investigate the role of DEX treatment against lung injury caused by intestinal I/R; representative morphological changes are presented in Figure 1. No significant morphological changes were observed in the Sham group (Figure 1(a)). I/R induced obvious lung tissue injury, manifested by the apparent destruction of the pulmonary architecture, interstitial edema, hemorrhage, and massive neutrophil infiltration (Figure 1(b)). The use of DEX attenuated lung injury significantly, with mild neutrophil infiltration and interstitial congestion (Figure 1(c)). Significant morphological changes were observed in the other four groups (Figures 1(d)–1(g)). The average scores were used for analysis (Figure 1(h)). These data showed that the lung injury scores in the I/R group were higher than those in the Sham group ($P < 0.05$) and were attenuated by DEX treatment in the DEX group ($P < 0.05$) but not in the other four groups ($P > 0.05$).

3.2. The Effects of Dexmedetomidine Treatment on Lung Tissue W/D Weight Ratio. The W/D weight ratio is used as an important indicator of lung tissue damage. As presented in Figure 2(a), the lung tissue W/D weight ratio was higher in all groups that underwent intestinal I/R than in the Sham group ($P < 0.05$). DEX treatment reduced the lung tissue W/D weight ratio compared to that of the I/R rats ($P < 0.05$). However, the protective role of DEX treatment against lung injury caused by intestinal I/R was reversed by the administration of the CB₂ receptor antagonist, AM630, or the PI3K inhibitor, wortmannin ($P < 0.05$). There was no significant difference in the lung tissue W/D weight ratio in the animals treated with AM630 alone or wortmannin alone compared with animals in the I/R group ($P > 0.05$).

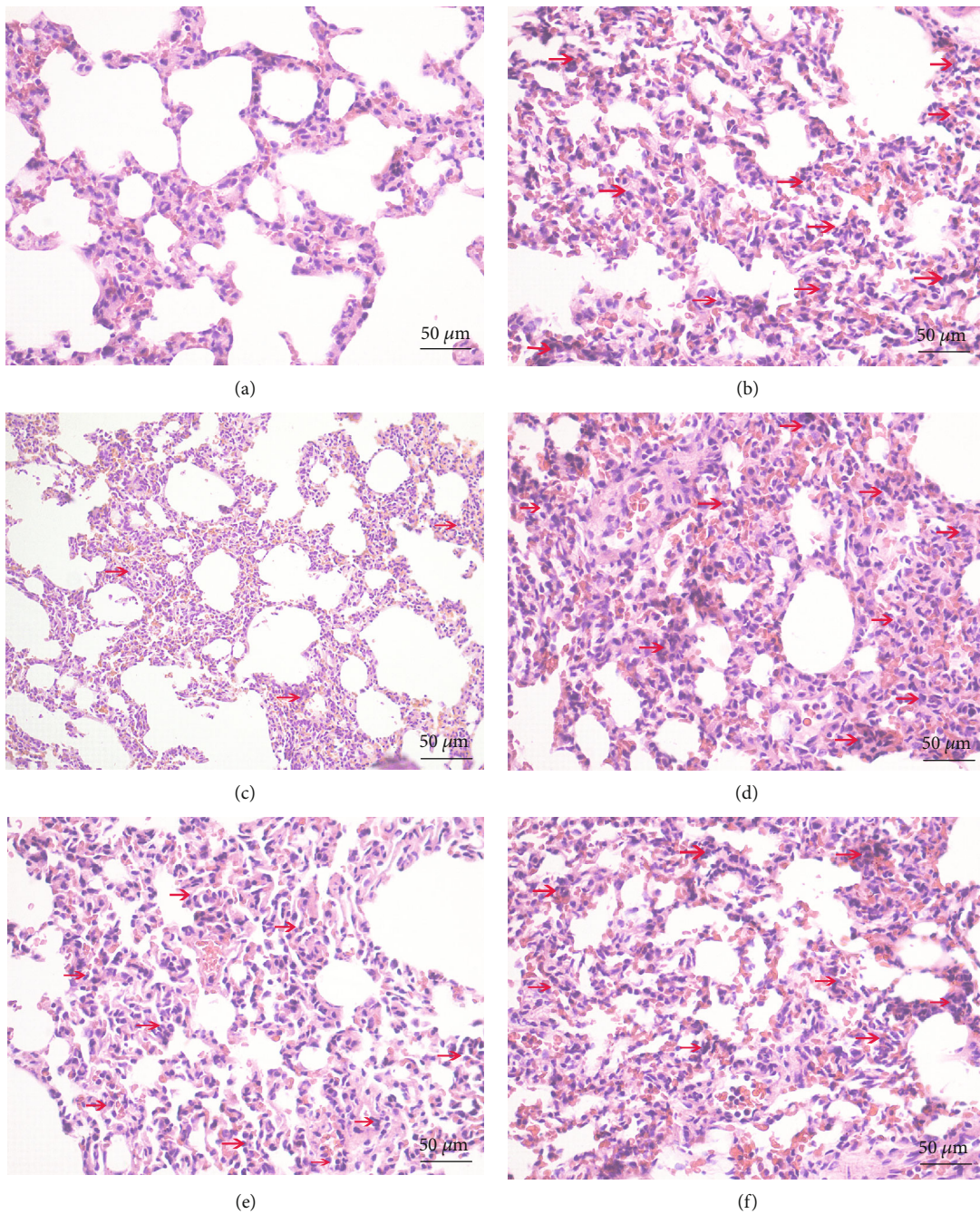


FIGURE 1: Continued.

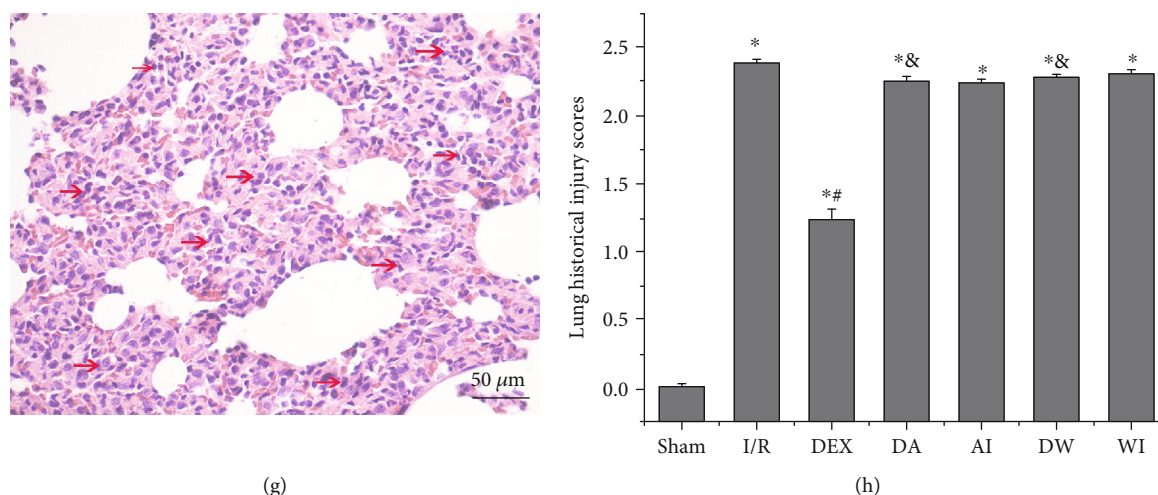


FIGURE 1: Histological changes and histological injury scores in lung tissues of all groups. (a) Sham group. (b) Intestinal ischemia/reperfusion (I/R) group. (c) Dexmedetomidine-treated I/R (DEX) group. (d) Dexmedetomidine- and AM630-treated I/R (DA) group. (e) AM630-treated I/R (AI) group. (f) Dexmedetomidine- and wortmannin-treated I/R (DW) group. (g) Wortmannin-treated I/R (WI) group. Red arrows indicate neutrophil infiltration (original magnification, $\times 200$; scale bar = $50 \mu\text{m}$). (h) Histological injury scores of the lung. Data are expressed as mean \pm SEM, $n = 8$ rats per group. * $P < 0.05$ versus the Sham group, # $P < 0.05$ versus the I/R group, & $P < 0.05$ versus the DEX group.

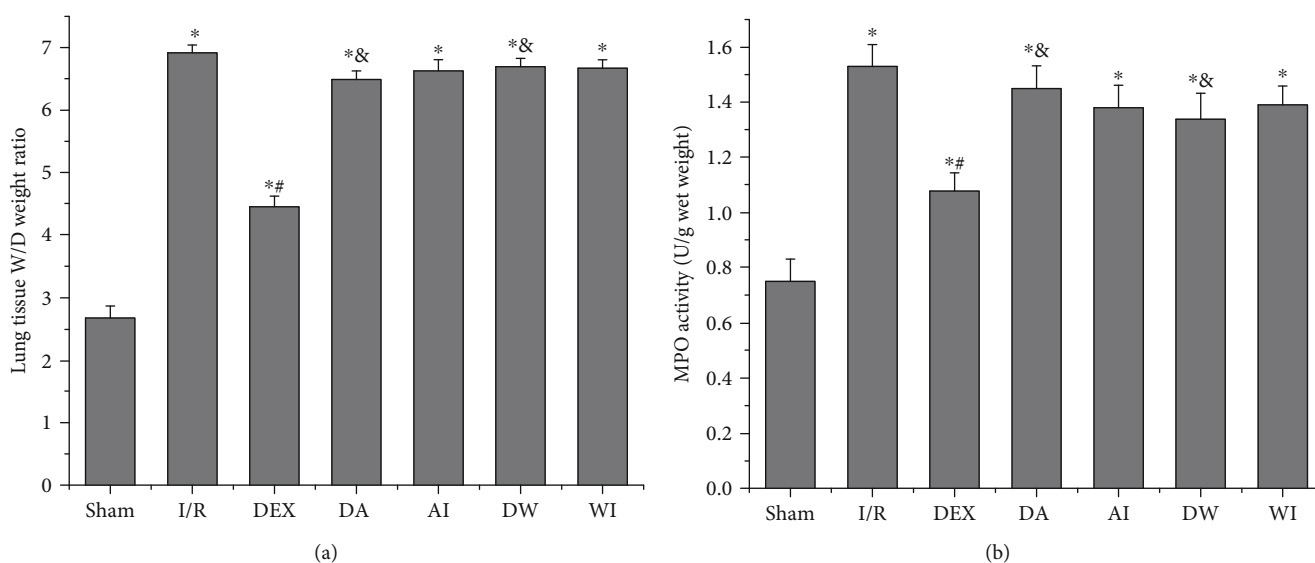


FIGURE 2: The effects of dexmedetomidine treatment on wet/dry (W/D) weight ratio and myeloperoxidase (MPO) activity in lung tissues. (a) W/D weight ratio. (b) MPO activity. Data are expressed as mean \pm SEM, $n = 8$ rats per group. * $P < 0.05$ versus the Sham group, # $P < 0.05$ versus the I/R group, & $P < 0.05$ versus the DEX group. I/R: intestinal ischemia/reperfusion; DEX: dexmedetomidine-treated I/R; DA: dexmedetomidine- and AM630-treated I/R; AI: AM630-treated I/R; DW: dexmedetomidine- and wortmannin-treated I/R; WI: wortmannin-treated I/R.

3.3. The Effects of Dexmedetomidine Treatment on MPO Activity. MPO activity is an indicator of neutrophil infiltration. We assessed the MPO activity to investigate the role of neutrophil infiltration in intestinal I/R-induced lung injury. As shown in Figure 2(b), I/R increased the MPO activity in lung tissues compared to that of the sham-operating rats ($P < 0.05$). Treatment with DEX decreased the MPO activity in lung tissues compared to that of the I/R rats ($P < 0.05$). In contrast, treatment with both AM630 and wortmannin reversed the decrease in MPO

activity compared to that of the DEX rats ($P < 0.05$). Treatment with AM630 alone or wortmannin alone had no significant effect on MPO activity compared to that of the I/R rats ($P > 0.05$).

3.4. The Effects of Dexmedetomidine Treatment on SOD Activity and MDA Level. Oxidative stress is one of the main causes of lung injury induced by intestinal I/R. We assessed the level of MDA, an indicator of lipid peroxidation damage, and the activity of SOD, an antioxidant enzyme, to examine

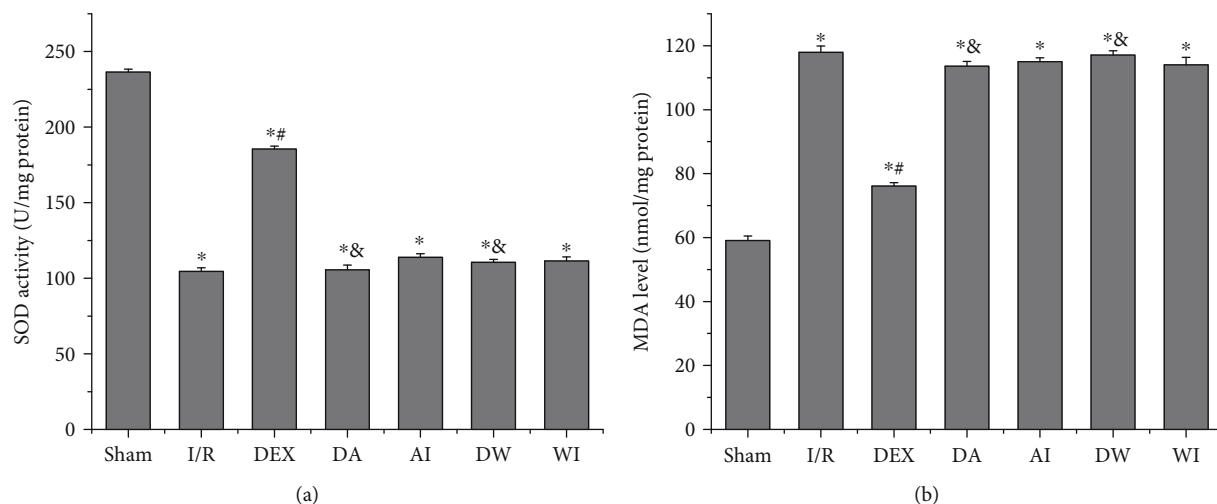


FIGURE 3: The effects of dexmedetomidine treatment on superoxide dismutase (SOD) activity and malondialdehyde (MDA) level in lung tissues. (a) SOD activity. (b) MDA level. Data are expressed as mean \pm SEM, $n = 8$ rats per group. * $P < 0.05$ versus the Sham group, # $P < 0.05$ versus I/R group, & $P < 0.05$ versus DEX group. I/R: intestinal ischemia/reperfusion; DEX: dexmedetomidine-treated I/R; DA: dexmedetomidine- and AM630-treated I/R; AI: AM630-treated I/R; DW: dexmedetomidine- and wortmannin-treated I/R; WI: wortmannin-treated I/R.

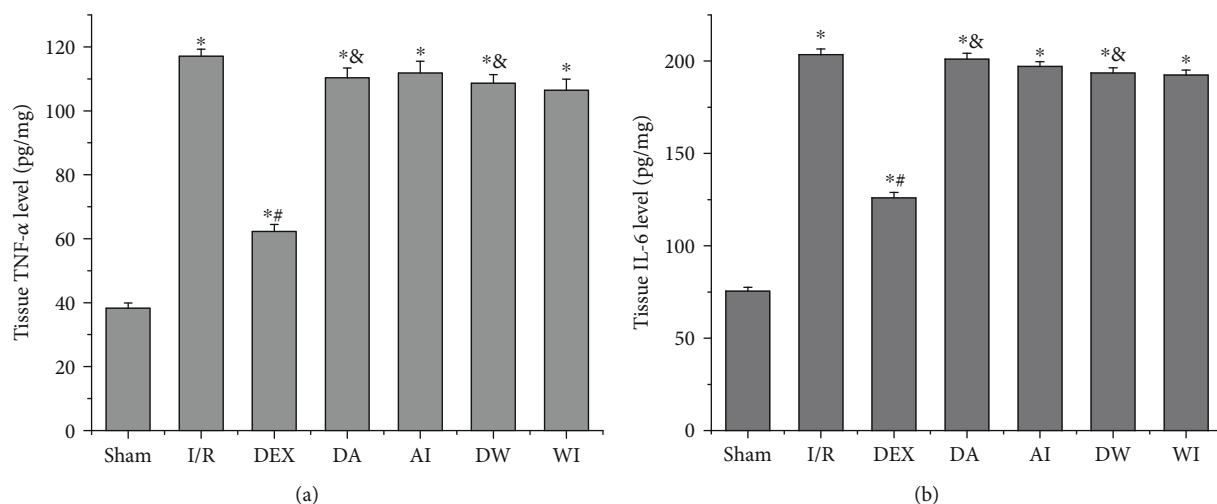


FIGURE 4: The effects of dexmedetomidine treatment on the levels of tumor necrosis factor alpha (TNF- α) and interleukin 6 (IL-6) in the lung tissues of all groups. (a) TNF- α level. (b) IL-6 level. Data are expressed as mean \pm SEM, $n = 8$ rats per group. * $P < 0.05$ versus the Sham group, # $P < 0.05$ versus the I/R group, & $P < 0.05$ versus the DEX group. I/R: intestinal ischemia/reperfusion; DEX: dexmedetomidine-treated I/R; DA: dexmedetomidine- and AM630-treated I/R; AI: AM630-treated I/R; DW: dexmedetomidine- and wortmannin-treated I/R; WI: wortmannin-treated I/R.

the role of oxidative stress in lung injury. As shown in Figure 3, I/R increased the MDA level and decreased the SOD activity compared to those of the sham-operating rats ($P < 0.05$). DEX treatment led to a decrease in MDA level and an increase in SOD activity ($P < 0.05$). However, the protective effect of DEX treatment on lung injury was reversed by the application of AM630 or wortmannin ($P < 0.05$). Treatment with AM630 alone or wortmannin alone had no significant impact on MDA level and SOD activity compared to those of the I/R rats ($P > 0.05$).

3.5. The Effects of Dexmedetomidine Treatment on the Levels of TNF- α and IL-6.

We assessed the levels of TNF- α and IL-6

in the lung to evaluate the inflammatory cytokines in the lung injury caused by intestinal I/R. As shown in Figure 4, I/R led to an increase in the levels of TNF- α and IL-6 compared to those of the sham-operating rats ($P < 0.05$). Treatment with DEX decreased the levels of TNF- α and IL-6 compared to those of the I/R rats ($P < 0.05$). In contrast, treatment with AM630 or wortmannin reversed the protective role of DEX by increasing the levels of TNF- α and IL-6 ($P < 0.05$). AM630 alone or wortmannin alone had no significant impact on the levels of TNF- α and IL-6 compared to those of the I/R rats ($P > 0.05$). These results suggest that DEX treatment has a protective role against I/R-induced lung injury by reducing cytokine production.

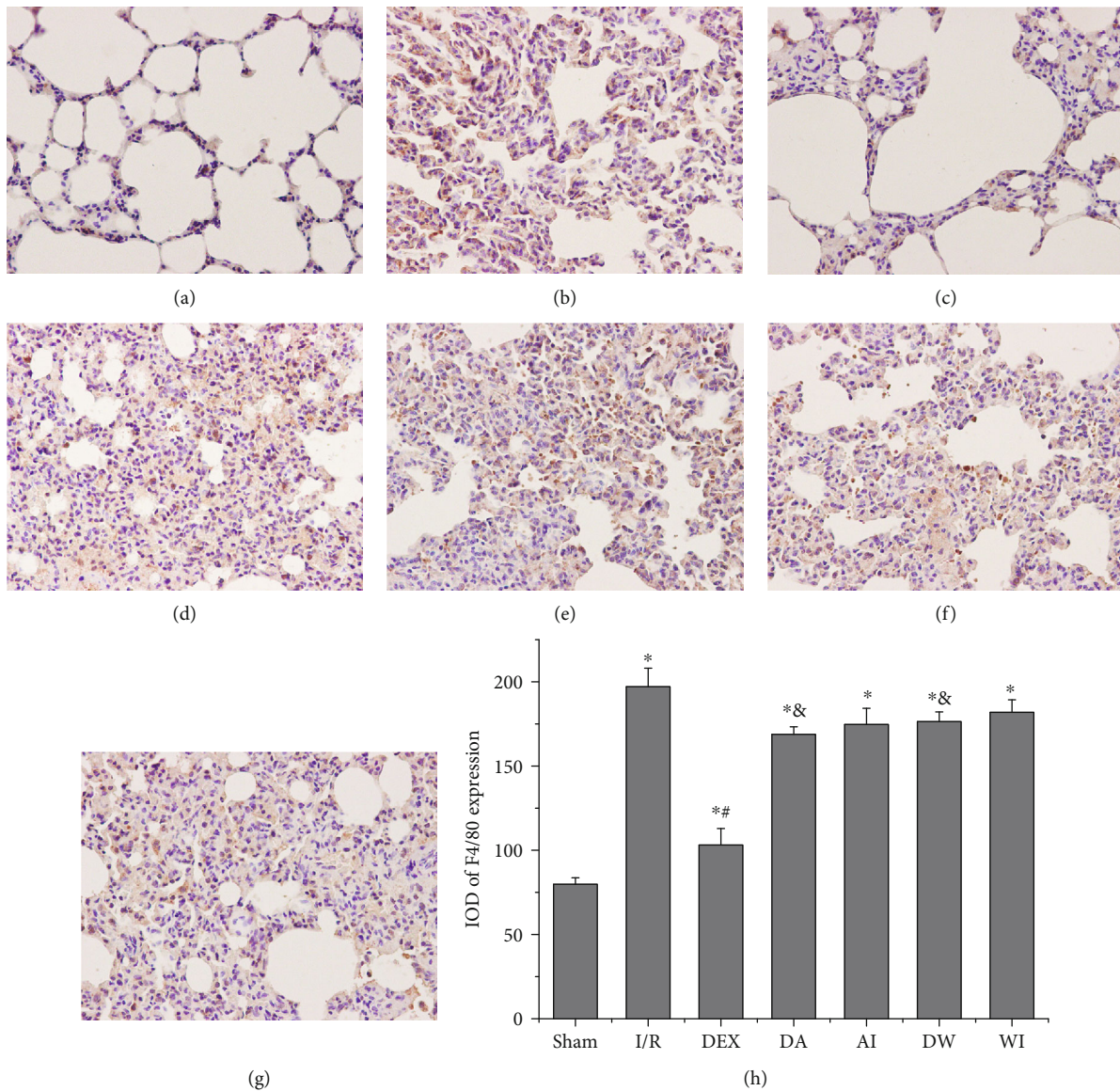


FIGURE 5: Immunohistochemical analysis of macrophage infiltration in the lung tissues of all groups. Macrophage infiltration was investigated by detecting F4/80 expression with immunohistochemistry. Dexmedetomidine treatment reduced macrophage infiltration in the lung tissues following I/R. (a) Sham group. (b) Intestinal ischemia/reperfusion (I/R) group. (c) Dexmedetomidine-treated I/R (DEX) group. (d) Dexmedetomidine- and AM630-treated I/R (DA) group. (e) AM630-treated I/R (AI) group. (f) Dexmedetomidine- and wortmannin-treated I/R (DW) group. (g) Wortmannin-treated I/R (WI) group (original magnification, $\times 400$). (h) Integrated optical density (IOD) of F4/80 expression in all groups. Data are expressed as mean \pm SEM, $n = 6$ rats per group. * $P < 0.05$ versus the Sham group, # $P < 0.05$ versus the I/R group, & $P < 0.05$ versus the DEX group.

3.6. The Effects of Dexmedetomidine Treatment on Macrophage Infiltration and p-Akt Expression in Lung Tissue by Immunohistochemical Assay. To assess macrophage infiltration in the lungs, we detected F4/80 expression by immunohistochemistry. As shown in Figure 5. In the Sham group, there were only a few positive staining in lung sections. Remarkable strong staining was observed in the rats subjected to I/R, and the expression of F4/80 in the I/R group, DEX group, DA group, AI group, DW group, and WI group was higher than that in the Sham group ($P < 0.05$). In contrast, treatment with DEX decreased the expression of F4/80 compared to that of the I/R rats ($P < 0.05$). Treatment

with AM630 or wortmannin increased the expressions of F4/80 compared to that of the DEX-treated rats ($P < 0.05$). AM630 alone or wortmannin alone had no significant impact on the expressions of F4/80 compared to that of the I/R rats ($P > 0.05$). This suggests that treatment with DEX may inhibit macrophage infiltration.

The lung tissues were obtained to measure the expression of p-Akt by immunohistochemistry, as shown in Figure 6. The results of immunohistochemistry showed that the level of p-Akt expression was low in the Sham group. I/R increased p-Akt expression, but the differences in the values between the Sham and I/R groups were not statistically significant

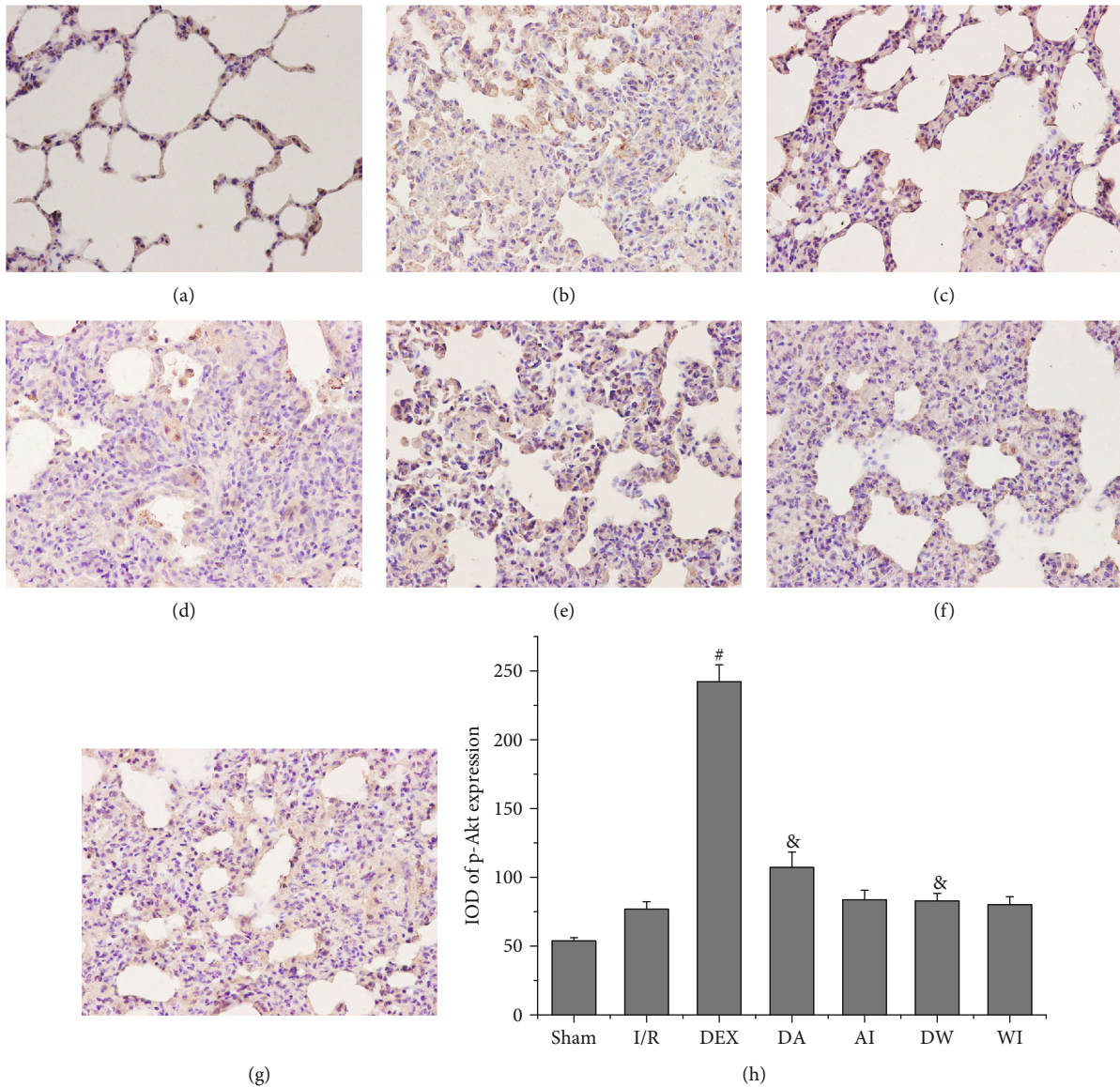


FIGURE 6: Immunohistochemical analysis of the expression of p-Akt in all groups. (a) Sham group. (b) Intestinal ischemia/reperfusion (I/R) group. (c) Dexmedetomidine-treated I/R (DEX) group. (d) Dexmedetomidine- and AM630-treated I/R (DA) group. (e) AM630-treated I/R (AI) group. (f) Dexmedetomidine- and wortmannin-treated I/R (DW) group. (g) Wortmannin-treated I/R (WI) group (original magnification, $\times 400$). (h) Integrated optical density (IOD) of p-Akt expression in all groups. Data are expressed as mean \pm SEM, $n = 6$ rats per group. * $P < 0.05$ versus the Sham group, # $P < 0.05$ versus the I/R group, & $P < 0.05$ versus the DEX group.

($P > 0.05$). Compared with the I/R group, the expression of p-Akt was enhanced in the DEX group ($P < 0.05$). The increase of p-Akt expression caused by DEX treatment was reversed by treatment with AM630 or wortmannin ($P < 0.05$). Compared with the I/R group, AM630 alone or wortmannin alone had no significant impact on p-Akt expression ($P > 0.05$).

3.7. The Effects of Dexmedetomidine Treatment on the Expressions of I/R Injury-Induced Apoptosis in Lung Tissues. Cell apoptosis is one of the main causes of lung injury caused by intestinal I/R. To investigate the role of cell apoptosis in lung injury caused by intestinal I/R, we evaluated the expressions of proapoptotic and antiapoptotic mRNA and proteins

in lung tissues using RT-PCR and Western blot analysis. As shown in Figures 7(a)–7(c) and 8(a)–8(e), I/R upregulated the expressions of caspase-3 and Bax mRNA and cleaved caspase-3 and Bax proteins but reduced the expressions of Bcl-2 mRNA and protein ($P < 0.05$). The Bcl-2/Bax ratio was decreased significantly in the I/R rats ($P < 0.05$). Compared with the I/R group, the expressions of caspase-3 and Bax mRNA and cleaved caspase-3 and Bax proteins were downregulated significantly, the expressions of Bcl-2 mRNA and protein were increased, and the Bcl-2/Bax ratio was enhanced in the DEX group ($P < 0.05$). Compared with the DEX group, the expressions of caspase-3 and Bax mRNA and cleaved caspase-3 and Bax proteins were increased significantly, the expressions of Bcl-2 mRNA and protein were

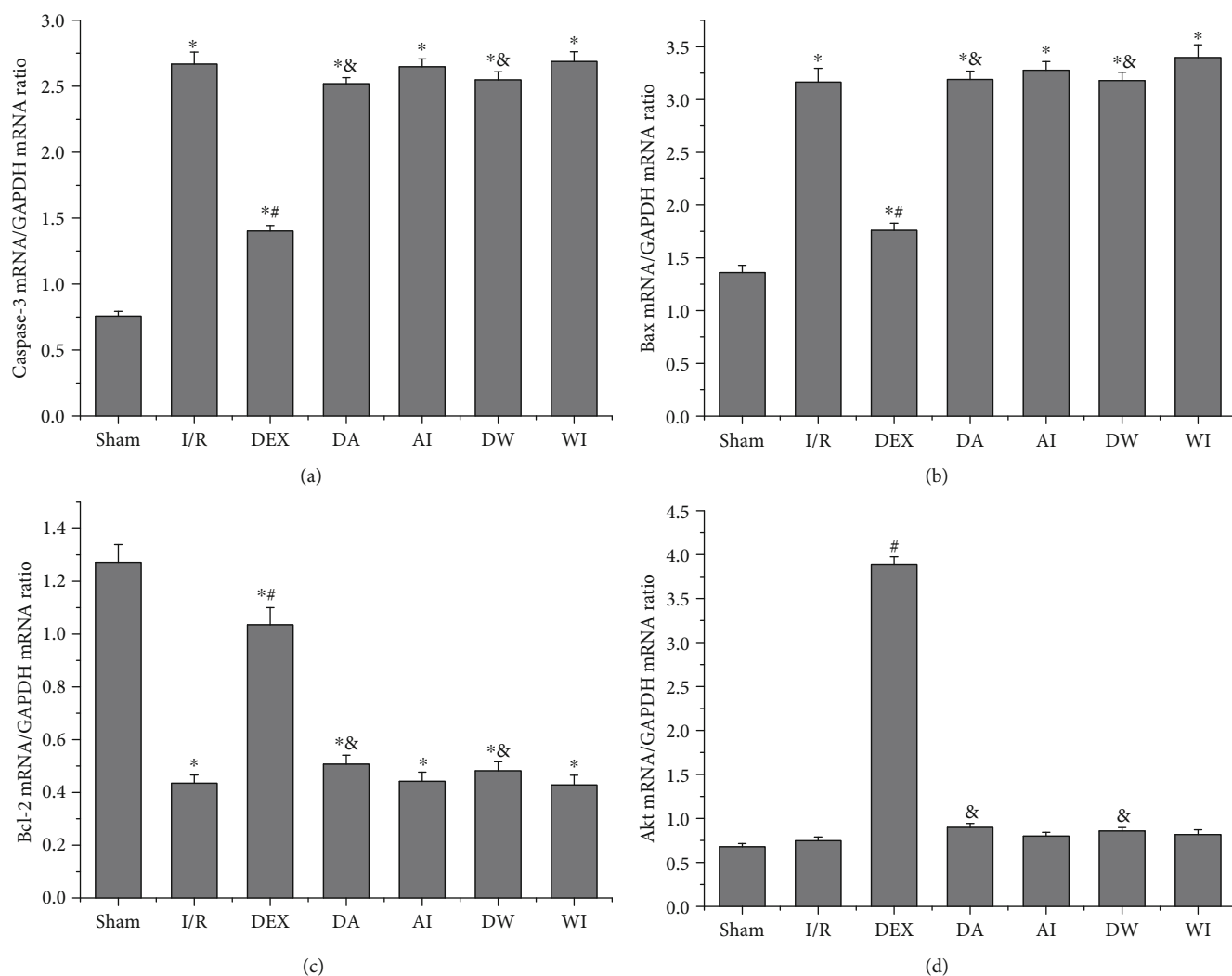


FIGURE 7: The effects of dexmedetomidine treatment on the mRNA expressions of caspase-3, Bax, Bcl-2, and Akt in all groups. (a) Caspase-3 mRNA expression. (b) Bax mRNA expression. (c) Bcl-2 mRNA expression. (d) Akt mRNA expression. Data are expressed as mean \pm SEM, $n = 6$ rats per group. * $P < 0.05$ versus the Sham group, # $P < 0.05$ versus the I/R group, & $P < 0.05$ versus the DEX group. I/R: intestinal ischemia/reperfusion; DEX: dexmedetomidine-treated I/R; DA: dexmedetomidine- and AM630-treated I/R; AI: AM630-treated I/R; DW: dexmedetomidine- and wortmannin-treated I/R; WI: wortmannin-treated I/R.

decreased, and the Bcl-2/Bax ratio was reduced in the rats given AM630 or wortmannin ($P < 0.05$). AM630 alone or wortmannin alone had no significant impact on the expressions of caspase-3 mRNA and cleaved caspase-3 protein, Bcl-2, and Bax mRNA and proteins compared to those of the I/R rats ($P > 0.05$).

3.8. The Effects of Dexmedetomidine Treatment on the Expressions of the PI3K/Akt Pathway. To investigate the protective mechanism of DEX on lung injury caused by intestinal I/R, we evaluated the expressions of Akt mRNA and proteins in lung tissues by RT-PCR and Western blot analysis. As shown in Figures 7(d), 8(a), and 8(f), I/R increased only the expressions of Akt mRNA and p-Akt protein, but there was no statistical difference, compared to those of the sham-operating rats ($P > 0.05$). Treatment with DEX increased the expressions of Akt mRNA and p-Akt protein compared to those of the I/R rats ($P < 0.05$). Treatment with

AM630 or wortmannin downregulated the expressions of Akt mRNA and p-Akt protein compared to those of the DEX-treated rats ($P < 0.05$). AM630 alone or wortmannin alone had no significant impact on the expressions of Akt mRNA and p-Akt protein compared to those of the I/R rats ($P > 0.05$). These results suggest that the PI3K/Akt pathway may be involved in the protective role of CB₂ receptor-mediated DEX treatment of I/R-induced lung injury. Collectively, our findings suggest that dexmedetomidine ameliorates lung injury induced by intestinal ischemia/reperfusion by upregulating the CB₂ receptor expression or activating the PI3K/Akt pathway or CB₂-mediated PI3K/Akt pathway (Figure 9).

4. Discussion

Intestinal I/R may not only cause local intestinal injury but also induce remote lung injury. In this study, we recognized

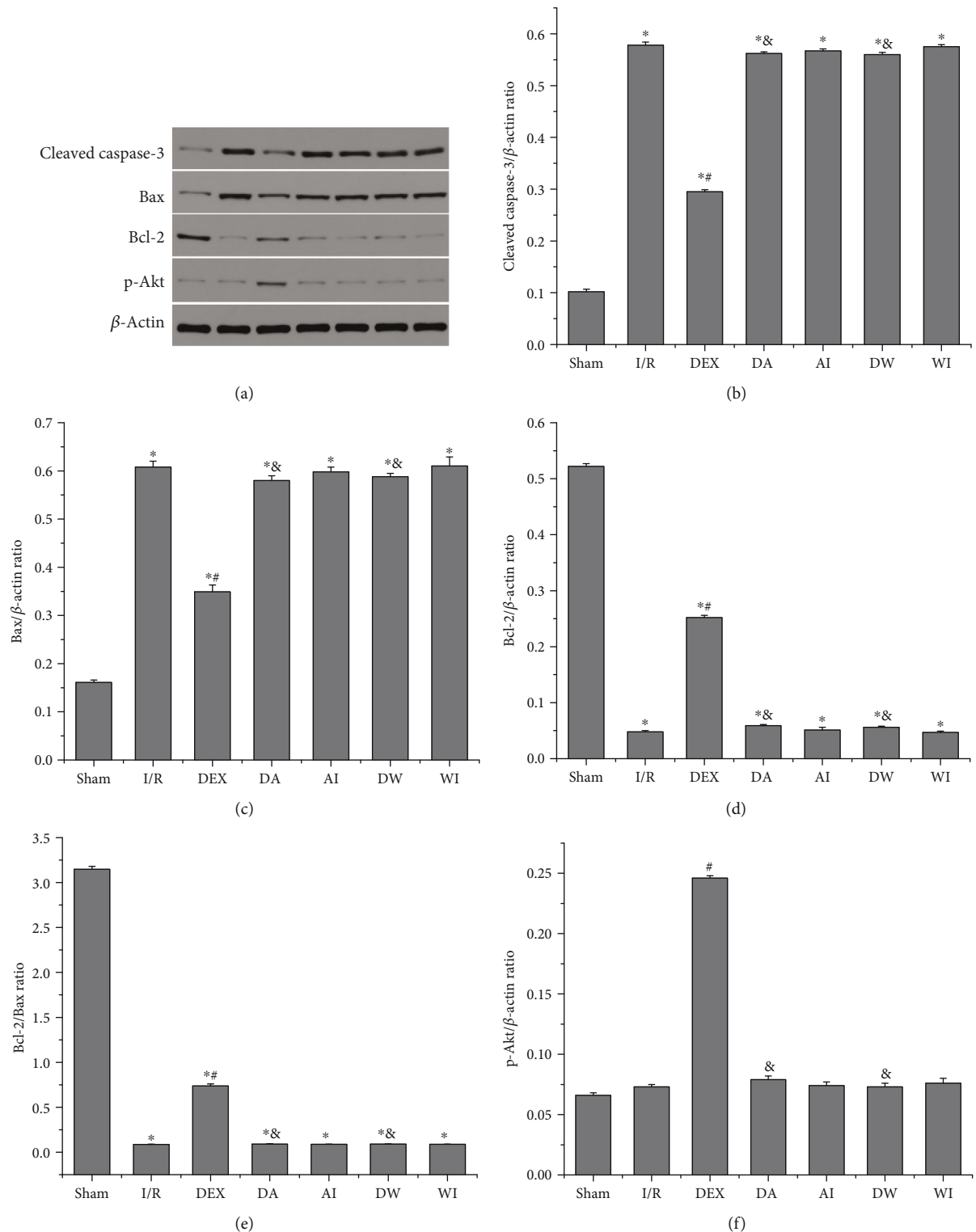


FIGURE 8: The effects of dexmedetomidine treatment on the protein expressions of cleaved caspase-3, Bax, Bcl-2, and p-Akt in all groups. (a) The expressions of cleaved caspase-3, Bax, Bcl-2, and p-Akt in lung tissues were detected using Western blot analysis. (b) Cleaved caspase-3 expression. (c) Bax expression. (d) Bcl-2 expression. (e) Bcl-2/Bax ratio. (f) p-Akt expression. Data are expressed as mean \pm SEM, $n = 6$ rats per group. * $P < 0.05$ versus the Sham group, # $P < 0.05$ versus the I/R group, & $P < 0.05$ versus the DEX group. I/R: intestinal ischemia/reperfusion; DEX: dexmedetomidine-treated I/R; DA: dexmedetomidine- and AM630-treated I/R; AI: AM630-treated I/R; DW: dexmedetomidine- and wortmannin-treated I/R; WI: wortmannin-treated I/R.

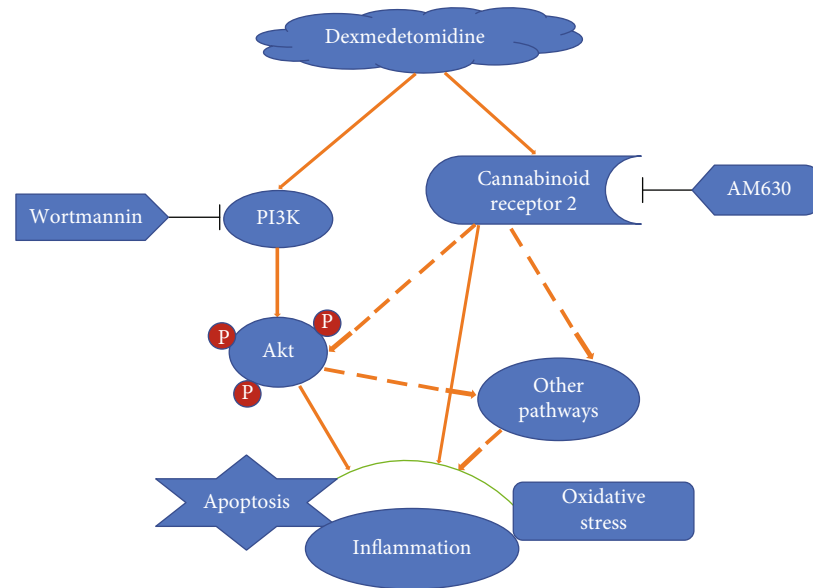


FIGURE 9: Schematic depicting model of potential molecular mechanism of protection of intestinal I/R-induced lung injury by dexmedetomidine. Dexmedetomidine may confer a protective role against intestinal I/R-induced lung injury by upregulating the CB₂ receptor expression or activating the PI3K/Akt pathway. Treatment with the CB₂ receptor antagonist, AM630, or the PI3K inhibitor, wortmannin, reverses the protective role of DEX by increasing the levels of apoptosis, inflammation, and oxidative stress (as marked by solid arrows). In addition, there may be a potential interaction between CB₂ receptor and the PI3K/Akt pathway. CB₂ receptor upregulated by dexmedetomidine may also play a protective role by activating Akt (or other pathways), because treatment with AM630 reduces Akt activation (as shown by dotted lines).

that intestinal I/R led to lung injury, manifested by an increase in lung injury scores and an increased lung wet/dry ratio. At the same time, our results showed that dexmedetomidine attenuated lung injury by upregulating the CB₂ receptor expression. However, the protective effects of dexmedetomidine treatment on lung injury induced by intestinal I/R were reversed by the CB₂ receptor antagonist AM630. We also found that the CB₂ receptor-mediated protective role of dexmedetomidine treatment of lung injury was achieved by activating the PI3K/Akt pathway.

Studies have suggested that oxidative stress is one of the major factors contributing to I/R injury [27]. In this study, we investigated and found that intestinal I/R resulted in an increase in MDA level and a decrease in SOD activity in the lung, aggravating lung tissue injury manifested by the increase in lung injury scores and lung wet/dry ratio. MDA, an end product of lipid peroxidation, is used to assess tissue peroxidative injury, while SOD, an antioxidant enzyme, is used to evaluate the antioxidant level of tissues. Several studies have indicated that I/R often increases the level of MDA and decreases the activity of SOD, leading to the aggravation of tissue damage [12, 25, 26, 28]. Our findings are consistent with those of these studies. Also, some therapeutic methods could reduce tissue damage by decreasing MDA levels and increasing SOD activity, such as antioxidant enzymes [25, 29, 30], and preconditioning [12].

Dexmedetomidine reportedly has an antioxidant effect, providing a protective role against damage in some tissues [7–12]. Here, we found that dexmedetomidine treatment alleviated lung injury caused by intestinal I/R via the inhibition of increased MDA levels and decreased SOD activity.

Our findings are consistent with previous studies suggesting that the inhibition of lipid peroxidation and enhancement of antioxidant enzyme activity in the lungs might, at least, be partially involved in the protective mechanisms of dexmedetomidine in response to lung injury caused by intestinal I/R.

Inflammation and cell apoptosis play significant roles in the progression of lung injury caused by various factors, including I/R and shock. Some studies have indicated that pretreatment with some substances, such as cyclic arginine-glycine-aspartate peptide (cRGD) [31] and anti-osteopontin Ab [32], protects lung injury caused by intestinal I/R, lowers neutrophil infiltration, suppresses inflammation, and inhibits lung apoptosis after intestinal I/R. Ben et al. [33] established that lungs from TLR4 mutant mice undergoing intestinal I/R exhibited a marked reduction in epithelial apoptosis, pulmonary MPO activity, and TNF- α and IL-6 levels and manifested a significantly smaller histological injury. In this present study, intestinal I/R increased neutrophil and macrophage infiltration, pulmonary MPO activity, the levels of TNF- α and IL-6, and cell apoptosis, manifested by the increase in the expressions of caspase-3 mRNA and cleaved caspase-3 protein and decrease in the Bcl-2/Bax ratio that aggravated intestinal I/R-induced lung injury. In contrast, dexmedetomidine treatment reversed these changes, attenuating lung injury scores and lung wet/dry ratio and alleviating lung injury caused by intestinal I/R. Our results are, hence, consistent with these previous findings.

Although dexmedetomidine treatment has a protective role against intestinal I/R-induced lung injury, the exact mechanism is not entirely clear. Recent research has revealed a critical role for the CB₂ receptor in regulating many disease

processes, including in the immune system, cardiovascular and respiratory systems, bone, gastrointestinal tract and liver, and reproductive system [17, 34]. The CB₂ receptor has also been verified to represent a very promising therapeutic target in gastrointestinal inflammatory conditions [18, 35]. Although the activation of the CB₂ receptor may have positive symptomatic effects on inflammatory bowel disease through its anti-inflammatory effects [36], it is not clear whether the CB₂ receptor is involved in the process of intestinal I/R-induced lung injury. In this study, our investigation of the role of the CB₂ receptor in the lung injury caused by intestinal I/R showed that treatment with dexmedetomidine increased the expression of the CB₂ receptor and attenuated lung injury, manifested by the decrease in lung injury scores and wet/dry ratio. Furthermore, the protective effect of dexmedetomidine treatment on lung injury caused by intestinal I/R was reversed by the CB₂ receptor antagonist, AM630. Our results suggest that dexmedetomidine treatment provided the protective role against intestinal I/R-lung injury by activating the CB₂ receptor. The role of the CB₂ receptor in the I/R injuries of some other organs has also been demonstrated, including in the myocardium [37, 38], liver [22, 39], and brain [40]. Our findings are, therefore, consistent with these studies.

The PI3K/Akt is known as an intracellular signaling pathway and has been confirmed to provide a protective role against I/R injury by regulating cell proliferation, apoptosis, and oxidative stress [41]. PI3K/Akt activation is reportedly involved in the protective effect of DEX against the I/R injuries in some organs, including the lung [42, 43], heart [44], and kidney [45]. In our study, we also found that DEX treatment increased the expressions of Akt mRNA, p-Akt protein, and Bcl-2 mRNA and protein, reduced the expressions of caspase-3 mRNA, cleaved caspase-3 protein, and levels of TNF- α , IL-6, and MDA, and attenuated lung injury scores. However, when given the PI3K inhibitor wortmannin, the above protective effects of DEX were reversed, suggesting that DEX reduced intestinal I/R-induced lung injury by activating the PI3K/Akt pathway, consistent with earlier studies.

Also, some studies have revealed that the activation of the PI3K/Akt pathway plays a part in the protective mechanism of cannabinoid receptors. Both CB₁ and CB₂ receptors stimulate the proliferation of neural stem/precursor cells through the PI3K/Akt pathway [46]. Previous research showed that the CB₂ receptor agonist, JWH133, protected the heart against I/R-induced apoptosis through the involvement of the PI3K/Akt pathway [47]. However, it is not clear whether the PI3K/Akt pathway mediates the protective effect of DEX activating the CB₂ receptor. Here, DEX upregulated the expressions of Akt mRNA and p-Akt protein, attenuated lung injury scores, and reduced intestinal I/R-induced lung injury. In contrast, the use of both the CB₂ receptor antagonist, AM630, and the PI3K inhibitor, wortmannin, reversed the protective roles of DEX against lung injury. Additionally, the CB₂ receptor antagonist AM630 downregulated the expression of Akt mRNA and p-Akt protein and increased lung injury scores. Our results indicate that DEX protected against lung injury caused by intestinal I/R via the CB₂-mediated PI3K/Akt pathway.

The present study has some limitations. Although we investigated that the protective roles of DEX against lung injury caused by intestinal I/R were reversed by both the CB₂ receptor antagonist, AM630, and the PI3K inhibitor, wortmannin, there was insufficient evidence to draw the conclusion that DEX treatment provides a protective role against intestinal I/R-induced lung injury through the activation of the CB₂-mediated PI3K/Akt pathway. Further study using deficient animals is needed.

5. Conclusions

Our data show that DEX treatment provided a protective effect on lung injury caused by intestinal I/R, with the protective effects attributed mainly to the upregulation of the CB₂ receptor and subsequent activation of the PI3K/Akt pathway. The current findings provide a basis for the development of novel strategies for the treatment of lung injury.

Data Availability

The authors have authorised me to promise that the data in our manuscript can be provided to anyone who needs it. If anyone needs these data, please contact me by the email hexh1220@aliyun.com.

Conflicts of Interest

The authors declare that there is no conflict of interests.

Authors' Contributions

Meng Chen and Xue-Tao Yan contributed equally to this work and should be considered co-first authors.

Acknowledgments

This work was supported by a grant from the National Natural Science Foundation of China (No. 81000849). This work was also supported by the Science and Technology Innovation Fostering Foundation of Zhongnan Hospital of Wuhan University (No. znp2018022).

References

- [1] I. H. Mallick, W. Yang, M. C. Winslet, and A. M. Seifalian, "Ischemia-reperfusion injury of the intestine and protective strategies against injury," *Digestive Diseases and Sciences*, vol. 49, no. 9, pp. 1359–1377, 2004.
- [2] S. An, Y. Hishikawa, J. Liu, and T. Koji, "Lung injury after ischemia-reperfusion of small intestine in rats involves apoptosis of type II alveolar epithelial cells mediated by TNF- α and activation of Bid pathway," *Apoptosis*, vol. 12, no. 11, pp. 1989–2001, 2007.
- [3] J. Hill, T. F. Lindsay, F. Ortiz, C. G. Yeh, H. B. Hechtman, and F. D. Moore Jr., "Soluble complement receptor type 1 ameliorates the local and remote organ injury after intestinal ischemia-reperfusion in the rat," *Journal of Immunology*, vol. 149, no. 5, pp. 1723–1728, 1992.
- [4] P. Sorkine, A. Setton, P. Halpern et al., "Soluble tumor necrosis factor receptors reduce bowel ischemia-induced lung

- permeability and neutrophil sequestration,” *Critical Care Medicine*, vol. 23, no. 8, pp. 1377–1381, 1995.
- [5] M. de Perrot, M. Liu, T. K. Waddell, and S. Keshavjee, “Ischemia-reperfusion-induced lung injury,” *American Journal of Respiratory and Critical Care Medicine*, vol. 167, no. 4, pp. 490–511, 2003.
 - [6] Y. Cai, H. Xu, J. Yan, L. Zhang, and Y. Lu, “Molecular targets and mechanism of action of dexmedetomidine in treatment of ischemia/reperfusion injury (Review),” *Molecular Medicine Reports*, vol. 9, no. 5, pp. 1542–1550, 2014.
 - [7] Z. Chen, T. Ding, and C. G. Ma, “Dexmedetomidine (DEX) protects against hepatic ischemia/reperfusion (I/R) injury by suppressing inflammation and oxidative stress in NLRC5 deficient mice,” *Biochemical and Biophysical Research Communications*, vol. 493, no. 2, pp. 1143–1150, 2017.
 - [8] A. Tüfek, O. Tokgöz, I. Aliosmanoglu et al., “The protective effects of dexmedetomidine on the liver and remote organs against hepatic ischemia reperfusion injury in rats,” *International Journal of Surgery*, vol. 11, no. 1, pp. 96–100, 2013.
 - [9] L. Jiang, L. Li, J. Shen, Z. Qi, and L. Guo, “Effect of dexmedetomidine on lung ischemia-reperfusion injury,” *Molecular Medicine Reports*, vol. 9, no. 2, pp. 419–426, 2014.
 - [10] Y. Yoshikawa, N. Hirata, R. Kawaguchi, Y. Tokinaga, and M. Yamakage, “Dexmedetomidine maintains its direct cardioprotective effect against ischemia/reperfusion injury in hypertensive hypertrophied myocardium,” *Anesthesia and Analgesia*, vol. 126, no. 2, pp. 443–452, 2018.
 - [11] Q. Li, C. Chen, X. Chen, M. Han, and J. Li, “Dexmedetomidine attenuates renal fibrosis via α_2 -adrenergic receptor-dependent inhibition of cellular senescence after renal ischemia/reperfusion,” *Life Sciences*, vol. 207, pp. 1–8, 2018.
 - [12] X. Y. Zhang, Z. M. Liu, S. H. Wen et al., “Dexmedetomidine administration before, but not after, ischemia attenuates intestinal injury induced by intestinal ischemia-reperfusion in rats,” *Anesthesiology*, vol. 116, no. 5, pp. 1035–1046, 2012.
 - [13] J. Li, Q. Chen, X. He et al., “Dexmedetomidine attenuates lung apoptosis induced by renal ischemia-reperfusion injury through α_2 AR/PI3K/Akt pathway,” *Journal of Translational Medicine*, vol. 16, no. 1, 2018.
 - [14] J. J. Zhang, K. Peng, J. Zhang, X. W. Meng, and F. H. Ji, “Dexmedetomidine preconditioning may attenuate myocardial ischemia/reperfusion injury by down-regulating the HMGB1-TLR4-MyD88-NF- κ B signaling pathway,” *PLoS One*, vol. 12, no. 2, article e0172006, 2017.
 - [15] Y. Si, H. Bao, L. Han et al., “Dexmedetomidine protects against renal ischemia and reperfusion injury by inhibiting the JAK/STAT signaling activation,” *Journal of Translational Medicine*, vol. 11, no. 1, 2013.
 - [16] J. Shen, G. Fu, L. Jiang, J. Xu, L. Li, and G. Fu, “Effect of dexmedetomidine pretreatment on lung injury following intestinal ischemia-reperfusion,” *Experimental and Therapeutic Medicine*, vol. 6, no. 6, pp. 1359–1364, 2013.
 - [17] K. D. Patel, J. S. Davison, Q. J. Pittman, and K. A. Sharkey, “Cannabinoid CB(2) receptors in health and disease,” *Current Medicinal Chemistry*, vol. 17, no. 14, pp. 1393–1410, 2010.
 - [18] K. L. Wright, M. Duncan, and K. A. Sharkey, “Cannabinoid CB2 receptors in the gastrointestinal tract: a regulatory system in states of inflammation,” *British Journal of Pharmacology*, vol. 153, no. 2, pp. 263–270, 2008.
 - [19] A. Alexander, P. F. Smith, and R. J. Rosengren, “Cannabinoids in the treatment of cancer,” *Cancer Letters*, vol. 285, no. 1, pp. 6–12, 2009.
 - [20] A. Dhopeshwarkar and K. Mackie, “CB2 cannabinoid receptors as a therapeutic target-what does the future hold?,” *Molecular Pharmacology*, vol. 86, no. 4, pp. 430–437, 2014.
 - [21] P. Pacher and G. Haskó, “Endocannabinoids and cannabinoid receptors in ischaemia-reperfusion injury and preconditioning,” *British Journal of Pharmacology*, vol. 153, no. 2, pp. 252–262, 2008.
 - [22] B. Horváth, L. Magid, P. Mukhopadhyay et al., “A new cannabinoid CB2 receptor agonist HU-910 attenuates oxidative stress, inflammation and cell death associated with hepatic ischaemia/reperfusion injury,” *British Journal of Pharmacology*, vol. 165, no. 8, pp. 2462–2478, 2012.
 - [23] N. Defer, J. Wan, R. Souktani et al., “The cannabinoid receptor type 2 promotes cardiac myocyte and fibroblast survival and protects against ischemia/reperfusion-induced cardiomyopathy,” *The FASEB Journal*, vol. 23, no. 7, pp. 2120–2130, 2009.
 - [24] C. Lehmann, M. Kianian, J. Zhou et al., “Cannabinoid receptor 2 activation reduces intestinal leukocyte recruitment and systemic inflammatory mediator release in acute experimental sepsis,” *Critical Care*, vol. 16, no. 2, 2012.
 - [25] X. H. He, X. T. Yan, Y. L. Wang, C. Y. Wang, Z. Z. Zhang, and J. Zhan, “Transduced PEP-1-heme oxygenase-1 fusion protein protects against intestinal ischemia/reperfusion injury,” *The Journal of Surgical Research*, vol. 187, no. 1, pp. 77–84, 2014.
 - [26] X. H. He, Q. W. Li, Y. L. Wang et al., “Transduced PEP-1-heme oxygenase-1 fusion protein reduces remote organ injury induced by intestinal ischemia/reperfusion,” *Medical Science Monitor*, vol. 21, pp. 1057–1065, 2015.
 - [27] R. S. Ferrari and C. F. Andrade, “Oxidative stress and lung ischemia-reperfusion injury,” *Oxidative Medicine and Cellular Longevity*, vol. 2015, Article ID 590987, 14 pages, 2015.
 - [28] L. G. Melo, R. Agrawal, L. Zhang et al., “Gene therapy strategy for long-term myocardial protection using adeno-associated virus-mediated delivery of heme oxygenase gene,” *Circulation*, vol. 105, no. 5, pp. 602–607, 2002.
 - [29] Y. E. Zhang, J. N. Wang, J. M. Tang et al., “In vivo protein transduction: delivery of PEP-1-SOD1 fusion protein into myocardium efficiently protects against ischemic insult,” *Molecules and Cells*, vol. 27, no. 2, pp. 159–166, 2009.
 - [30] G. Q. Huang, J. N. Wang, J. M. Tang et al., “The combined transduction of copper, zinc-superoxide dismutase and catalase mediated by cell-penetrating peptide, PEP-1, to protect myocardium from ischemia-reperfusion injury,” *Journal of Translational Medicine*, vol. 9, no. 1, p. 73, 2011.
 - [31] S. Matsuo, W. L. Yang, M. Aziz, A. Jacob, and P. Wang, “Cyclic arginine-glycine-aspartate attenuates acute lung injury in mice after intestinal ischemia/reperfusion,” *Critical Care*, vol. 17, no. 1, 2013.
 - [32] Y. Hirano, M. Aziz, W. L. Yang, M. Ochani, and P. Wang, “Neutralization of osteopontin ameliorates acute lung injury induced by intestinal ischemia-reperfusion,” *Shock*, vol. 46, no. 4, pp. 431–438, 2016.
 - [33] D. F. Ben, X. Y. Yu, G. Y. Ji et al., “TLR4 mediates lung injury and inflammation in intestinal ischemia-reperfusion,” *The Journal of Surgical Research*, vol. 174, no. 2, pp. 326–333, 2012.
 - [34] D. J. Chen, M. Gao, F. F. Gao, Q. X. Su, and J. Wu, “Brain cannabinoid receptor 2: expression, function and modulation,” *Acta Pharmacologica Sinica*, vol. 38, no. 3, pp. 312–316, 2017.

- [35] A. A. Izzo, "The cannabinoid CB (2) receptor: a good friend in the gut," *Neurogastroenterology and Motility*, vol. 19, no. 9, pp. 704–708, 2007.
- [36] K. L. Leinwand, A. A. Jones, R. H. Huang et al., "Cannabinoid receptor-2 ameliorates inflammation in murine model of Crohn's disease," *Journal of Crohn's & Colitis*, vol. 11, no. 11, pp. 1369–1380, 2017.
- [37] H. J. Sun, Y. Lu, H. W. Wang et al., "Activation of endocannabinoid receptor 2 as a mechanism of propofol pretreatment-induced cardioprotection against ischemia-reperfusion injury in rats," *Oxidative Medicine and Cellular Longevity*, vol. 2017, Article ID 2186383, 18 pages, 2017.
- [38] P. F. Wang, L. S. Jiang, J. Bu et al., "Cannabinoid-2 receptor activation protects against infarct and ischemia-reperfusion heart injury," *Journal of Cardiovascular Pharmacology*, vol. 59, no. 4, pp. 301–307, 2012.
- [39] M. Rajesh, H. Pan, P. Mukhopadhyay et al., "Cannabinoid-2 receptor agonist HU-308 protects against hepatic ischemia/reperfusion injury by attenuating oxidative stress, inflammatory response, and apoptosis," *Journal of Leukocyte Biology*, vol. 82, no. 6, pp. 1382–1389, 2007.
- [40] M. Zhang, M. W. Adler, M. E. Abood, D. Ganea, J. Jallo, and R. F. Tuma, "CB2 receptor activation attenuates microcirculatory dysfunction during cerebral ischemic/reperfusion injury," *Microvascular Research*, vol. 78, no. 1, pp. 86–94, 2009.
- [41] D. L. Williams, T. Ozment-Skelton, and C. Li, "Modulation of the phosphoinositide 3-kinase signaling pathway alters host response to sepsis, inflammation, and ischemia/reperfusion injury," *Shock*, vol. 25, no. 5, pp. 432–439, 2006.
- [42] S. Liang, Y. Wang, and Y. Liu, "Dexmedetomidine alleviates lung ischemia-reperfusion injury in rats by activating PI3K/Akt pathway," *European Review for Medical and Pharmacological Sciences*, vol. 23, no. 1, pp. 370–377, 2019.
- [43] W. Zhang, J. Q. Zhang, F. M. Meng, and F. S. Xue, "Dexmedetomidine protects against lung ischemia-reperfusion injury by the PI3K/Akt/HIF-1 α signaling pathway," *Journal of Anesthesia*, vol. 30, no. 5, pp. 826–833, 2016.
- [44] X. Cheng, J. Hu, Y. Wang et al., "Effects of dexmedetomidine postconditioning on myocardial ischemia/reperfusion injury in diabetic rats: role of the PI3K/Akt-dependent signaling pathway," *Journal Diabetes Research*, vol. 2018, article 3071959, pp. 1–10, 2018.
- [45] J. Gu, P. Sun, H. Zhao et al., "Dexmedetomidine provides renoprotection against ischemia-reperfusion injury in mice," *Critical Care*, vol. 15, no. 3, 2011.
- [46] F. Molina-Holgado, A. Rubio-Araiz, D. García-Ovejero et al., "CB2 cannabinoid receptors promote mouse neural stem cell proliferation," *The European Journal of Neuroscience*, vol. 25, no. 3, pp. 629–634, 2007.
- [47] Q. Li, F. Wang, Y. M. Zhang, J. J. Zhou, and Y. Zhang, "Activation of cannabinoid type 2 receptor by JWH133 protects heart against ischemia/reperfusion-induced apoptosis," *Cellular Physiology and Biochemistry*, vol. 31, no. 4-5, pp. 693–702, 2013.

Research Article

Combination of Dichloroacetate and Atorvastatin Regulates Excessive Proliferation and Oxidative Stress in Pulmonary Arterial Hypertension Development via p38 Signaling

Tangzhiming Li ^{1,2}, Suqi Li,³ Yilu Feng,^{2,4} Xiaofang Zeng,^{2,4} Shaohong Dong,¹ Jianguhua Li,¹ Lihuang Zha,^{2,4} Hui Luo,² Lin Zhao,⁵ Bin Liu,² Ziwei Ou,^{2,4} Wenchao Lin,^{2,4} Mengqiu Zhang,^{2,4} Sheng Li,^{2,4} Qiuqiong Jiang,¹ Qiangqiang Qi,² Qingyao Xu,² and Zaixin Yu ^{2,4}

¹Department of Cardiology, Shenzhen People's Hospital, The First Affiliated Hospital of Southern University of Science and Technology, The Second Clinical Medical College of Jinan University, Guangdong, China

²Department of Cardiology, Xiangya Hospital, Central South University, Changsha, China

³State Key Laboratory of Cardiovascular Disease, Fu Wai Hospital, National Center for Cardiovascular Diseases, Chinese Academy of Medical Sciences and Peking Union Medical College, Beijing, China

⁴National Clinical Research Center for Geriatric Disorders, Xiangya Hospital, Central South University, 87 Xiangya Road, Changsha, Hunan, China

⁵Centre for Pharmacology and Therapeutics, Division of Experimental Medicine, Imperial College London, Hammersmith Hospital, London W12 0NN, UK

Correspondence should be addressed to Zaixin Yu; yuzaxin@csu.edu.cn

Received 19 February 2020; Accepted 19 May 2020; Published 12 June 2020

Guest Editor: Bhagavatula Moorthy

Copyright © 2020 Tangzhiming Li et al. This is an open access article distributed under the Creative Commons Attribution License, which permits unrestricted use, distribution, and reproduction in any medium, provided the original work is properly cited.

Pulmonary arterial hypertension (PAH) is a lethal disease generally characterized by pulmonary artery remodeling. Mitochondrial metabolic disorders have been implicated as a critical regulator of excessively proliferative- and apoptosis-resistant phenotypes in pulmonary artery smooth muscle cells (PASMCs). Dichloroacetate (DCA) is an emerging drug that targets aerobic glycolysis in tumor cells. Atorvastatin (ATO) is widely used for hyperlipemia in various cardiovascular diseases. Considering that DCA and ATO regulate glucose and lipid metabolism, respectively, we hypothesized that the combination of DCA and ATO could be a potential treatment for PAH. A notable decrease in the right ventricular systolic pressure accompanied by reduced right heart hypertrophy was observed in the DCA/ATO combination treatment group compared with the monocrotaline treatment group. The DCA/ATO combination treatment alleviated vascular remodeling, thereby suppressing excessive PASMC proliferation and macrophage infiltration. In vitro, both DCA and ATO alone reduced PASMC viability by upregulating oxidative stress and lowering mitochondrial membrane potential. Surprisingly, when combined, DCA/ATO was able to decrease the levels of reactive oxygen species and cell apoptosis without compromising PASMC proliferation. Furthermore, suppression of the p38 pathway through the specific inhibitor SB203580 attenuated cell death and oxidative stress at a level consistent with that of DCA/ATO combination treatment. These observations suggested a complementary effect of DCA and ATO on rescuing PASMCs from a PAH phenotype through p38 activation via the regulation of mitochondrial-related cell death and oxidative stress. DCA in combination with ATO may represent a novel therapeutic strategy for PAH treatment.

1. Introduction

Pulmonary arterial hypertension (PAH) is characterized by the remodeling of precapillary pulmonary arteries, leading

to the increase in pulmonary vascular resistance and eventually right heart failure if left untreated [1]. Excessive proliferation of pulmonary artery smooth muscle cells (PASMCs) has been identified as the hallmark of promoting this pulmonary

vascular change [2]. However, no specific therapeutic approach to date has been successfully translated into clinical practice in PAH. Vasodilators remains the mainstay of currently licensed PAH treatments [3, 4], although they have been proved inadequate in reversing PASM proliferation while also being prohibitively expensive [5]. Therefore, discovering novel pathobiology mechanisms is crucial in developing new drugs or repurposing existing drugs for successful PAH treatment.

Mitochondrion dysfunction has been theorized as a crucial player in PAH development by increasing the production of reactive oxygen species (ROS) through the activity of the mitochondrial electron transport chain [6]. The metabolic shift of mitochondria, known as “Warburg effect,” is related to the hyperpolarization of the mitochondrial membrane [7] and accompanied by resistance to apoptosis [8]. Compelling evidence supports the hypothesis that correction of metabolic abnormalities could suppress PAH development [9–11].

Dichloroacetate (DCA) is an analog of pyruvate that inhibits mitochondrial pyruvate dehydrogenase kinase [12] and enhances oxidative phosphorylation [13]. DCA is used to treat several types of solid tumors [14–16] and PAH [7, 9–11, 17–19] owing to its ability to restore aerobic glycolysis. DCA is speculated to prevent or reverse established monocrotaline- (MCT-) induced PAH in rats [17]. However, DCA only has a moderate inhibition effect on PAH development, implying that it may not be sufficient to suppress PAH pathologies. Statins are a class of drugs that inhibit 3-hydroxy-3-methylglutaryl Co-A reductase. Several experiments have demonstrated that statins attenuate the development of PAH models [20, 21]. The effect of reducing hypercholesterolemia may help in metabolic regulation; moreover, statin therapy for PAH has been evaluated in randomized controlled trials for simvastatin [22, 23] and atorvastatin (ATO) [5]. However, none of these clinical studies provided evidence of an improvement in patients’ long-term prognoses.

DCA has been shown to reverse resistance to the antiapoptotic and hyperproliferative susceptibility of PSMCs by suppressing the Warburg effect, resulting in the reversal of PAH vascular remodeling. ATO has been approved for the treatment of cardiovascular diseases that have the potential for rapid translation to PAH. Given that DCA and ATO have potent inhibition effects on PAH development by metabolic regulation, we hypothesized that combined therapy with DCA and ATO would reverse MCT-induced pulmonary vascular remodeling by attenuating the hyperproliferative and antiapoptotic phenotypes of PSMCs.

2. Materials and Methods

2.1. Animal Experiments. All experiments were approved by the Institutional Animal Care and Use Committee of Central South University. Adult male Sprague–Dawley (SD) rats (8–10 weeks old) were matched according to weight (200–250 g). The rats were randomly assigned to one of the five groups ($n = 5$ for each group): (1) control group, saline injection with normal drinking and food; (2) MCT group, MCT injection with normal drinking and food; (3) MCT+DCA group,

MCT injection with DCA treatment (drinking water, 70 mg/kg per day, Sigma-Aldrich, USA); (4) MCT+ATO group, MCT injection with ATO treatment (oral gavage, 10 mg/kg per day, Pfizer, USA); and (5) MCT+DCA+ATO group, MCT injection with DCA and ATO treatment. Saline was given to the control group as placebo. For the other four groups, MCT (60 mg/kg) [24, 25] was injected into the subcutaneous tissue to induce progressive pulmonary arterial hypertension at the end of 21 days.

2.2. Hemodynamic Measurements and Tissue Collection. At the end of the experiment, the rats were deeply anesthetized with a lethal dose of sodium pentobarbital (50 mg/kg i.p). Right ventricular systolic pressure (RVSP) was measured through the right jugular vein by a precurved catheter. Hemodynamic data were recorded and analyzed with a PowerLab Data Acquisition system (AD Instruments) [24]. The right lung and heart tissues were flushed with saline to clear blood and snap frozen in liquid nitrogen and stored at -80°C in preparation for Western blot analysis. Hearts were dissected and weighed; the ratio of the right ventricle to the left ventricle plus the septum ($\text{RV}/[\text{LV}+\text{S}]$) was used as an index of RV hypertrophy. The left lung was fixed in 4% paraformaldehyde solution and embedded in paraffin for histological examination.

2.3. Morphometry Analysis, Immunohistochemistry, and Immunofluorescence. Formaldehyde-fixed and paraffin-embedded lung tissue sections were stained with hematoxylin and eosin (H&E staining). Morphometric analyses were performed on pulmonary arteries with an external diameter between 50 and 100 μm . Medial thickness was calculated using the following formula: medial thickness (%) = medial wall thickness/external diameter $\times 100$ [24, 26]. For quantitative analyses, 30 small pulmonary vessels from each animal that were less than 50 μm in external diameter were evaluated for muscularization [24]. Elastic staining was conducted according to the manufacturer’s protocol (Sigma-Aldrich® Elastic Stain Procedure No. HT25). For immunohistochemistry examination, lung sections were stained for anti-Ki67 and anti-CD68 to evaluate proliferation and inflammation in each group.

2.4. PSMC Isolation and Culture. Segments of pulmonary artery of the SD rats were cut to expose the luminal surface. The endothelium was removed by gentle scraping, and the media were peeled away from the underlying adventitial layer. After isolation, a modified collagenase digestion protocol was employed. PSMCs were incubated in a medium containing 0.5 mg/ml collagenase type I (Worthington Biochemical Corporation). The explants were incubated in DMEM supplemented with 20% FBS until the cells formed confluent monolayers [2, 27]. After reaching confluency, the cells were passaged in 0.25% trypsin, maintained in culture in DMEM supplemented with 10% FBS, and maintained at 37°C in 5% CO_2 . The cells up to passage five were used for experiments. The cells were stained for α -smooth muscle actin by immunocytochemistry. PA smooth muscle cells were placed in a serum-free medium for 24 h and then

exposed to dichloroacetate (DCA, 5 mM, dissolved in PBS) (Sigma-Aldrich, Lyon, France) and ATO (1 or 10 mM, dissolved in DMSO) (R&D Systems, Lille, France) for 24 h.

2.5. Cell Viability Assay. Cell viability was detected using a CCK-8 Kit (Dojindo, Japan) according to the manufacturer's instructions. The absorbance was measured at 450 nm.

2.6. Mitochondrial Membrane Potential, Mitochondrial Reactive Oxygen Species, and Intracellular Reactive Oxygen Species Detection. Mitochondrial membrane potential (MMP) was assessed using the fluorescent probe JC-1 (C2006, Beyotime Biotech, China). PSMCs of each group were incubated with 5 μ mol/l MitoSOX Red (407778ES50, Yeasen Biotech, China) in HBSS to measure mitochondrial ROS. Superoxide ($O_2^{\cdot-}$) production was measured with dihydroethidium (DHE, S0063, Beyotime Biotech, China) as previously described [28]. The cultured PSMCs of each group were enriched by $O_2^{\cdot-}$ and stained by DHE (2 mM).

The samples were left in the fluorescent probe for 30 min at 37°C and then washed to remove unbound dye. The samples were immediately monitored under a fluorescence microscope (Nikon, Tokyo, Japan) in a dark room. Mean JC-1, MitoSOX, and DHE fluorescence intensity was captured by dividing individual object fluorescence intensities and is expressed in arbitrary fluorescence units (A. U.). The experiments were performed in triplicate.

2.7. Western Blotting and Quantification. After the indicated duration of treatment, lung tissue samples and cells were homogenized in lysis buffer containing Roche complete protease inhibitor cocktail (Roche, Basel, Switzerland). Concentration-normalized protein samples were prepared with SDS loading buffer. About 20–30 μ g of total protein was separated on 12% polyacrylamide gels and transferred onto polyvinylidene fluoride membranes [29]. The membranes were then blocked and probed with one of the following primary antibodies: anti-GRP78 (1:1,000, #ab108613, Abcam, USA), anti-CHOP (1:1,000, #ab11419, Abcam, USA), anti-Bax (1:1,000, 50599-2-Ig, Proteintech, USA), and anti-Bcl2 (1:1,000, 12789-1-AP, Proteintech, USA). As a loading control, all blots were reprobed with an antibody toward anti-beta actin (1:1,000, #ab8827, Abcam, USA). Densitometry analysis was performed using ImageJ software.

2.8. Flow Cytometry Analysis of Cell Cycle. Cell cycle distribution was determined by staining DNA with propidium iodide (PI). The cells were collected, washed with ice-cold PBS (pH 7.4) buffer twice, fixed with 70% alcohol at 4°C overnight, and then stained with PI (20x) in the presence of RNase A (50x) for 30 min at least. The percentages of cells in different cell cycle phases were measured using a flow cytometer (Beckman Coulter Epics), and the percentages of cells in the G0/G1, S, and G2/M phases were analyzed with the Modifit LT 5.0 software.

2.9. Flow Cytometry Analysis of Apoptosis. Flow cytometry analysis of PSMC apoptosis was conducted using annexin V/PI staining. The extent of apoptosis was measured with the annexin V-FITC apoptosis detection kit (Beyotime,

China) as described by the manufacturer's instruction. The samples were then analyzed with FlowJo software.

2.10. Statistical Analysis. Student's *t*-tests were used for comparisons between two groups. Multiple comparisons were assessed by one-way ANOVA, followed by the appropriate post hoc test for significance. All statistical tests used two-sided tests of significance. All data are reported as mean \pm SD. $P < 0.05$ was considered statistically significant. Data analysis was performed using SPSS 20 (IBM SPSS Inc., Chicago, USA), and figures were prepared using GraphPad Prism 6.0 software.

3. Results

3.1. Combination of DCA and ATO Attenuated PAH Hemodynamic Disorder and Right Heart Hypertrophy. DCA or ATO was given separately and in combination to MCT-treated rats to assess their effects in a PAH model. The DCA and ATO combination treatment significantly restored the right ventricular systolic pressure and right heart remodeling in MCT rats while monotherapy of DCA or ATO only presented a marginal reversal of hemodynamic change or right ventricular hypertrophy (Figures 1(a) and 1(b)).

We then determined vascular remodeling by Elastic Van Gieson staining and H.E. staining. Thickened intima and medium layers of pulmonary vessels were noted in MCT-induced PAH rats, which was moderately modified by separate treatments of DCA or ATO but significantly ameliorated in the combination group (Figures 1(c)–1(e)). Quantification of vascular muscularization revealed MCT increased the ratio of partially and fully muscularized vessels and reduction of peripheral arterial volume was restored by DCA or ATO at different levels. By contrast, the DCA/ATO combination treatment induced a remarkable increase in normal vascular ratio and a decrease in partially occluded vessels (Figure 1(g)).

Collectively, these results demonstrated that DCA and ATO play different roles in regulating disordered hemodynamics, and combining both of them can lead to histological improvement in PAH.

3.2. Combination of DCA and ATO Was Superior in Proliferation and Inflammatory Suppression. Pulmonary vascular proliferation and inflammation infiltration in each group of rats were investigated. The DCA/ATO combination treatment elicited a better effect in suppressing the Ki67 expression (Figures 2(a) and 2(c)) and CD68 infiltration (Figures 2(b) and 2(d)) in peripheral vessels than the control group. This result was consistent with that described in Figure 1. DCA and ATO exhibited a complementary effect on PAH pathology suppression.

3.3. DCA Reduced PSMC Viability and Enhanced Viability when Combined with ATO without Stimulating Further Cell Damage. Primary cultures were isolated from the pulmonary arteries to determine the inhibitory effects of DCA and ATO on PSMC proliferation (Supplementary Figure 1). PSMCs were exposed to 30 μ g/ml PDGF-BB for further experiments (Supplementary Figure 2).

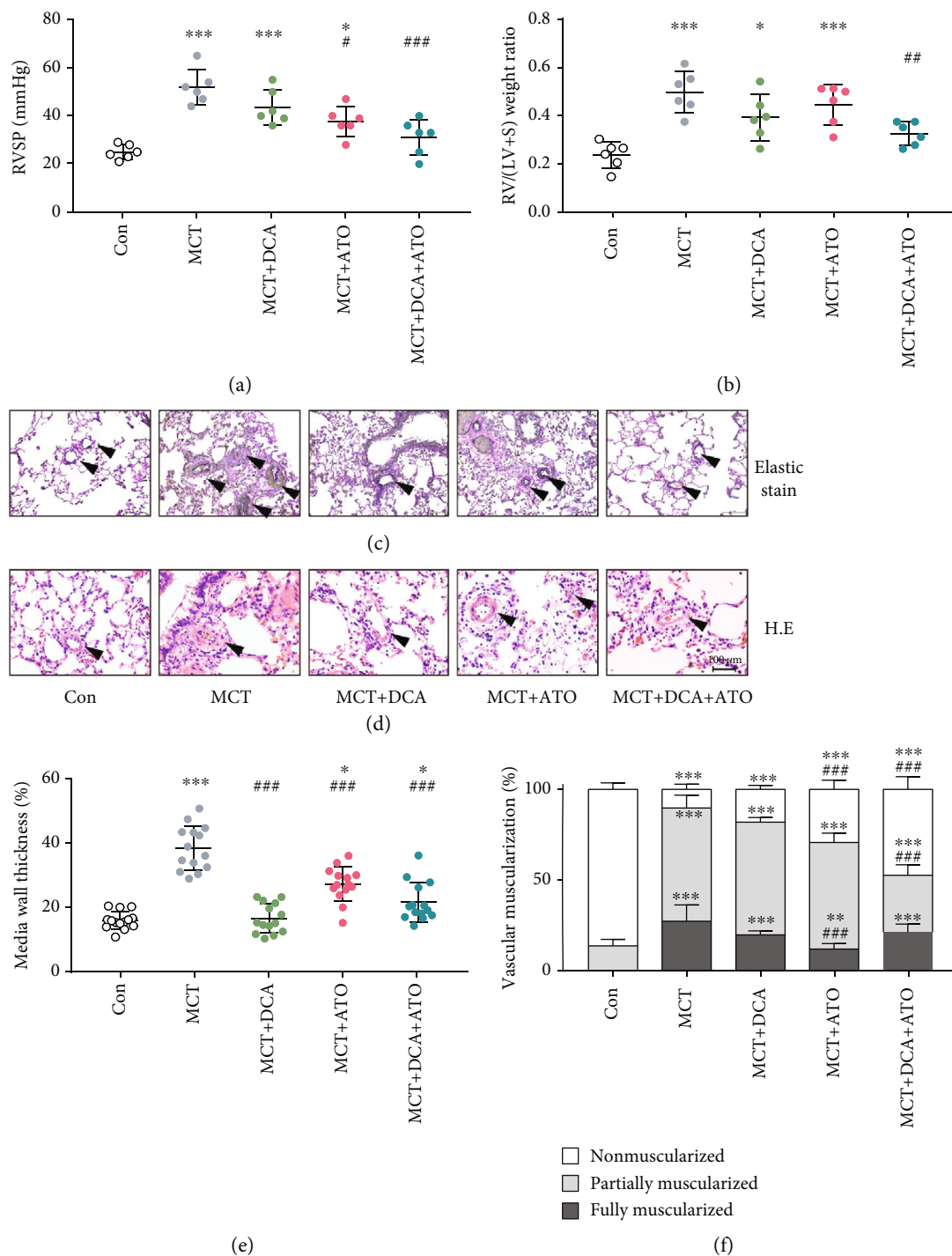


FIGURE 1: Pulmonary arterial hypertension induced by MCT is inhibited by dichloroacetate and atorvastatin combination therapy. (a, b) Measurement of RVSP and right ventricular hypertrophy in each treatment group ($n=6$). (c, d) Representative images of pulmonary artery remodeling in each group; arrows indicate representative vessels. (c) Elastic Van Gieson staining and (d) Hematoxylin and eosin staining. Scale bars, $100\ \mu\text{m}$. (e, f) Quantification of remodeled vessels. (e) Medial wall thickness ($n=15$) and (f) percentage of nonmuscularized or partially muscularized or fully muscularized arteries at alveolar and duct levels ($n=30$). * and *** indicate $P < 0.05$ and $P < 0.001$, respectively, comparing the control group; #, ##, and ### indicate $P < 0.05$, $P < 0.01$, and $P < 0.001$, respectively, comparing the MCT group. MCT: monocrotaline; RVSP: right ventricular systolic pressure; RV/(LV+S): right ventricular/(left ventricular + septum); H&E: hematoxylin and eosin staining. Bars represent mean \pm SEM.

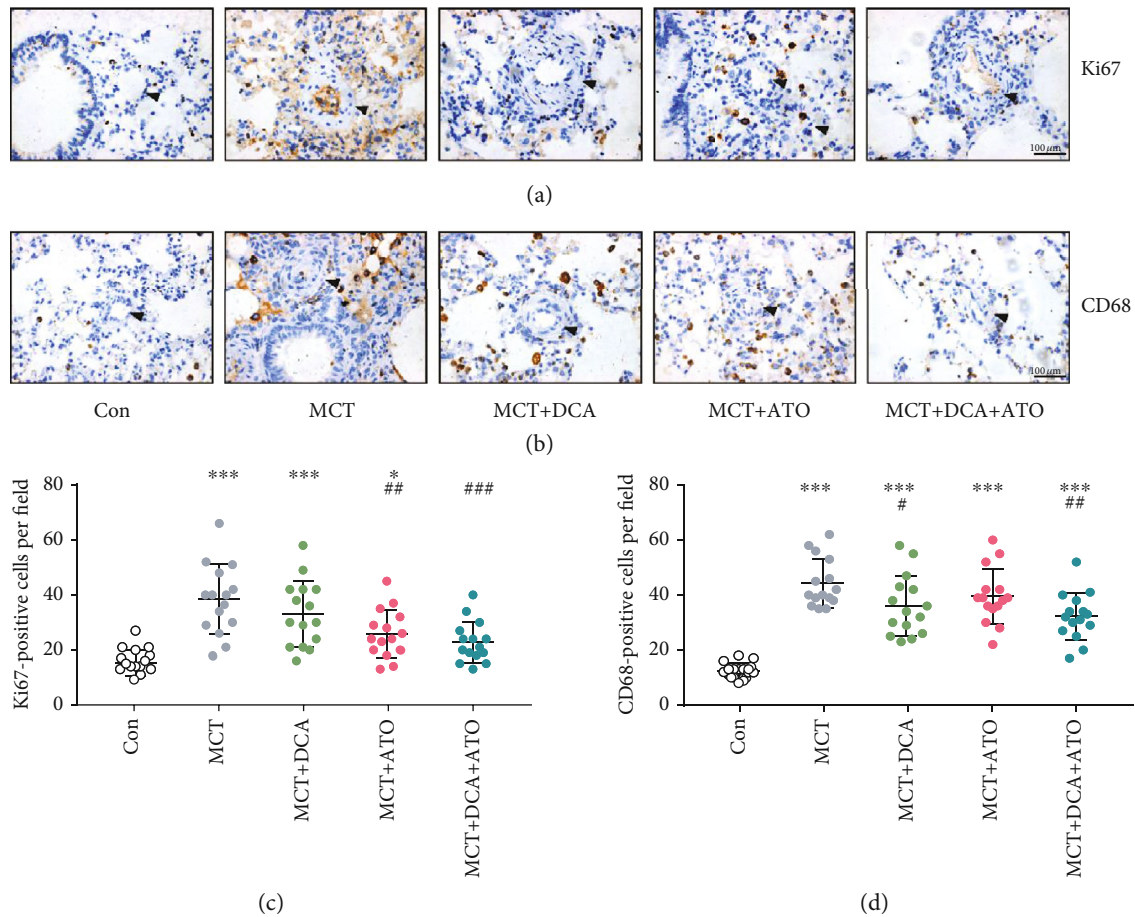


FIGURE 2: Cell proliferation and macrophage infiltration in PAH were reduced by dichloroacetate and atorvastatin combination treatment. (a, b) Representative immunohistochemistry images of proliferation and inflammation status of each group. Arrows indicate morphological structures of pulmonary arteries after indicated treatment. Scale bars, 100 μm . (c, d) Semiquantitative (c) Ki67- and (d) CD68-positive cells in high-resolution fields of view ($n = 15$). * and *** indicate $P < 0.05$ and $P < 0.001$, respectively, comparing the control group; #, ##, and ### indicate $P < 0.05$, $P < 0.01$, and $P < 0.001$, respectively, comparing the MCT group.

When PSMCs were treated with DCA and ATO separately, cell viability decreased in a concentration-dependent manner (Figures 3(a) and 3(b)). Therefore, CCK-8 assay was performed on PDGF-stimulated PSMCs treated with DCA with or without ATO. Compared with DCA monotherapy, the combination treatment induced a marked decrease in cell proliferation (Figure 3(c)). According to the morphological appearance of the PSMCs (Figure 3(d)), the single DCA treatment motivated a moderate proapoptotic effect. Conversely, ATO-exposed cells typically became rounded and isolated from their neighbors. These changes were restored by DCA cotreatment, which preserved the morphological structures of the cells, i.e., dual combination may result in cell death through a more controlled manner (Figure 3 (d)).

3.4. DCA and ATO Combination Treatment Modified Mitochondrion-Related Oxidative Stress in Proliferative PSMCs. To determine the underlying cytotoxicity mechanisms of DCA and ATO, we analyzed mitochondrion-associated cell death by using the redox-sensitive probe JC-1. Separate DCA and ATO treatments decreased MMP, imply-

ing that these two drugs are capable of leading to proliferative SMC apoptosis. However, when DCA and ATO were combined, MMP increased compared with either treatment alone (Figures 4(a) and 4(d)).

Cytosolic ROS and mitochondrial superoxide production were measured by DHE and MitoSOX, respectively (Figures 4(b) and 4(c)). Consistent with JC-1 detection, DCA only slightly upregulated mitochondrial superoxide production compared with ATO, indicating that severe mitochondrion-associated cell damage was caused by ATO exposure. The substantial increases in cytosolic ROS caused by ATO were prevented in the DCA/ATO combination treatment group. A similar trend was observed in mitochondrial ROS detection, where DCA attenuated ATO-induced mitochondrial superoxide production (although the effect was not statistically significant) (Figures 4(e) and 4(f)).

3.5. DCA and ATO Combination Treatment Balanced Apoptosis Proliferation and Endoplasmic Reticulum Stress Disorder in PSMCs. We further determined the role of DCA and ATO in proliferation and apoptosis balance. Established proliferative PSMCs were harvested to measure Bax,

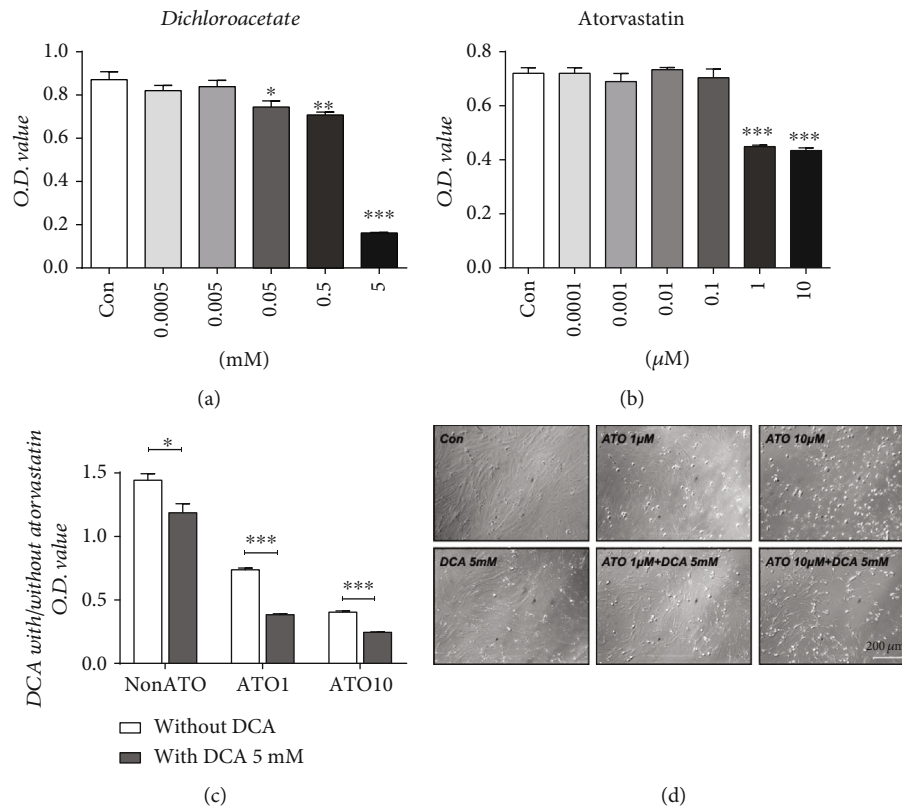


FIGURE 3: PASMOC proliferation in response to prohypertensive growth factor was inhibited by dichloroacetate and atorvastatin exposure. (a, b) Cell viability assay in PSMCs exposed to (a) dichloroacetate ($n = 7$) and (b) atorvastatin ($n = 7$). *, **, and *** indicate $P < 0.05$, $P < 0.01$, and $P < 0.001$, respectively, comparing the control group. (c) Cell viability assay in PSMCs treated with different concentrations of atorvastatin with or without 5 mM dichloroacetate ($n = 5$). * and *** indicate $P < 0.05$ and $P < 0.001$, respectively, comparing the non-DCA group. (f) White field of PSMCs showed characteristic morphological changes. Scale bar: 100 μ m.

Bcl2, and PCNA expression. DCA increased apoptosis, whereas ATO upregulated Bax and Bcl2 expression. However, the net effect on Bax/Bcl2 increase was not different from that of the control group (Figures 5(a)–5(d)). DCA did not attenuate cytotoxicity when the combination treatment was applied (Figure 5(d)). In addition, both DCA and ATO inhibited cell proliferation, and the combination treatment led to a considerable reduction in PCNA expression (Figures 5(a) and 5(e)). Additionally, we compared the effects of ATO monotherapy and DCA/ATO combination treatment on Bax, Bcl2, and PCNA expression. We found that the combination treatment further attenuated antiapoptosis and proliferation compared with ATO monotherapy.

We analyzed the effects of DCA and ATO on oxidative stress by using a fluorescence probe and cytosolic stress (endoplasmic reticulum stress, ERS) biomarker. DCA and ATO exhibited the capacity to activate the ERS of PSMCs, especially ATO. DCA prevented ATO-induced ERS-related cellular damage (Figures 5(a), 5(g), and 5(h)), implying that DCA relieved ATO's prooxidative effect. Similar results were observed in p38 signaling. DCA ameliorated ATO-induced p38 activation in PDGF-BB-pretreated PSMCs. DCA also partly (but not significantly) restored ATO-related p38 upregulation in MCT rats.

Collectively, these results provided evidence that DCA prevented ATO-induced overoxidative stress in which p38

may participate. DCA plus ATO effectively reduced PSMC proliferation and enhanced apoptosis.

3.6. p38 Activation Was Involved in DCA- and ATO-Related Apoptosis and Proliferation in PSMCs. To gain additional perspective on p38 in DCA and ATO treatments, we sought to target this pathway by using the p38-specific inhibitor. DCA and ATO monotherapy and DCA/ATO combination therapy of PSMCs were treated with SB203580. These therapies inhibited p38 phosphorylation (Figures 6(a) and 6(g)), resulting in the reduction of endoplasmic reticulum stress (Figures 6(a)–6(c)). As expected, SB203580 downregulated Bcl2 and Bax expression, suggesting that ATO-mediated antiapoptosis and apoptosis balance was p38 dependent, at least partially. Simultaneously, PCNA expression was found to be also related to p38 inhibition, and SB203580 reduced the effects of DCA on cell growth inhibition.

We investigated the effects of DCA and ATO with or without SB203580 on cell cycle regulation (Figure 6(h)). Cell cycle distribution in the PSMCs was considerably modified by PDGF pretreatment, advancing the cells from the G1 and S phases to G2/M phase. DCA and ATO abolished the effects of PDGF on proliferation enhancement. DCA and ATO treatment in conjunction with SB203580 resulted in a greater percentage of the cell population in the S phase compared with that in single drug delivery, suggesting that p38

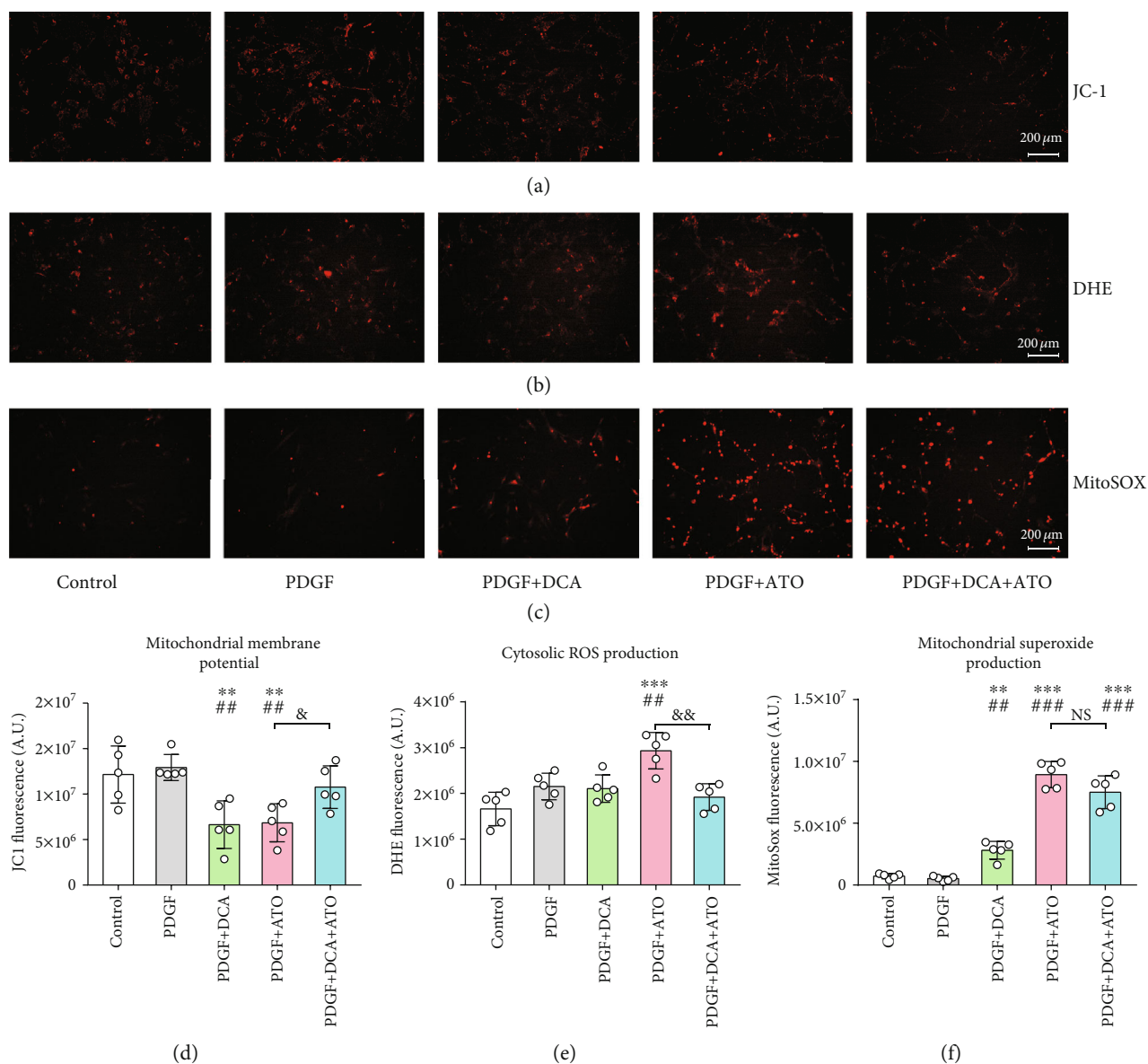


FIGURE 4: Dichloroacetate and atorvastatin regulated mitochondrial alterations in PSMCs. (a) Mitochondrial membrane potential (MMP) evaluated using the JC-1 probe. (b) Cytosolic ROS production detected using the DHE fluorescence probe. (c) Mitochondrial superoxide expressed by MitoSOX fluorescence probe. (d–f) Semiquantitation of MMP (d), cytosolic reactive oxygen species (e), and mitochondrial superoxide (f) ($n = 5$). ** and *** indicate $P < 0.01$ and $P < 0.001$, respectively, comparing the control group; ## and ### indicate $P < 0.01$ and $P < 0.001$, respectively, comparing the PDGF group. & and && indicate $P < 0.05$ and $P < 0.01$, PDGF+ATO compared with PDGF +DCA+ATO. Scale bars: 200 μm .

inhibition led to greater cell proliferation and reversed DCA/ATO cell growth inhibition. Cell growth and apoptosis are accompanied by ROS and ERS conditions in proliferative PSMCs, as we demonstrated above. Herein, we exposed PDGF-pretreated PSMCs to DCA and ATO with or without SB203580 for MMP and oxidative stress evaluation. P38 inhibition did not affect MMP when DCA and ATO were given separately, but the combination treatment restored MMP (Figures 7(a) and 7(b)). Moreover, SB203580 substantially reduced cytosolic ROS and mitochondrial superoxide production caused by DCA and ATO (Figures 7(c)–7(f)).

Hence, regulation of growth and apoptosis was closely related to p38 activation and its resulting oxidative stress.

Lastly, annexin V-FITC and a PI staining flow cytometry apoptosis detection kit were utilized to examine the influence of the two drugs on PSMC cytotoxicity. As shown in Figure 7, apoptotic PSMCs greatly increased in the DCA, ATO, and DCA+ATO groups. When SB203580 was added to the drug treatment groups, only ATO and DCA+ATO showed a reduction in apoptotic cell population, although SB203580 mediated a moderate apoptosis decrease. These results also supported our previous findings discussed above.

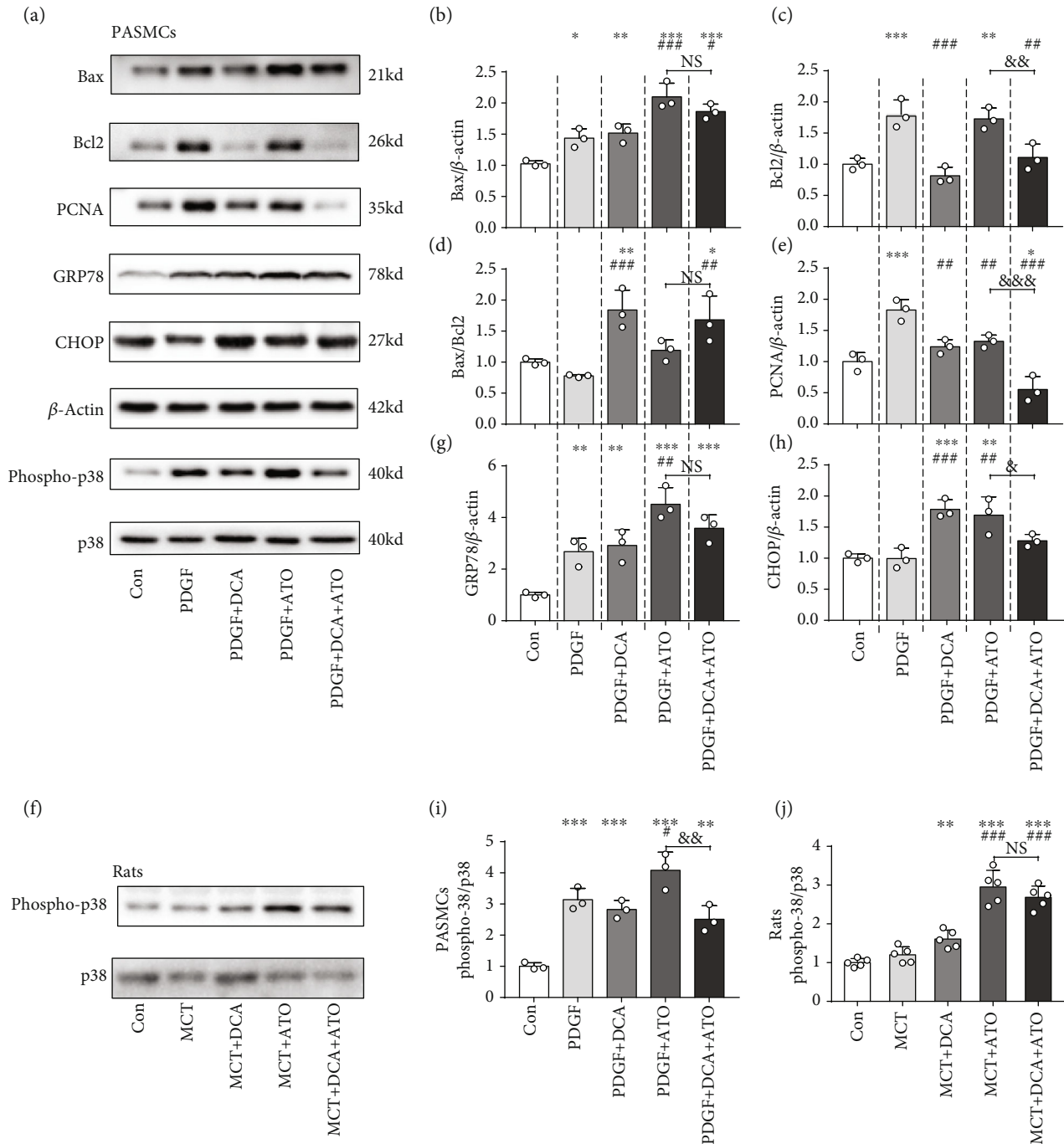


FIGURE 5: Dichloroacetate and atorvastatin regulated the balance of proliferation and apoptosis and endoplasmic reticulum stress accompanied by p38 activation. Representative immunoblots and relative densitometric analysis of proliferation, apoptosis marker, and endoplasmic reticulum stress-associated marker. (a) PASMCS exposed to PDGF, DCA, or ATO as indicated above compared with the controls ($n = 3$). (b–e, g–i) Immunoblot quantifications of Bax, Bcl2, Bax/Bcl2, PCNA, GRP78, CHOP, and phospho-p38/total p38 of each group ($n = 3$). (f, j) Immunoblot phospho-p38 and total p38 quantification in the PASMCS ($n = 3$) and rat model ($n = 5$). β -Actin was used as a loading control. *, **, and *** indicate $P < 0.05$, $P < 0.01$, and $P < 0.001$, respectively, compared with the control group; #, ##, and ### denote $P < 0.05$, $P < 0.01$, and $P < 0.001$, respectively, comparing the PDGF group. &, &&, and &&& represent $P < 0.05$, $P < 0.01$, and $P < 0.001$, the PDGF+ATO group compared with the PDGF+DCA+ATO group.

4. Discussion

In the present study, we demonstrated that the DCA/ATO combination therapy was more efficient in inhibiting PSMC proliferation, correcting apoptosis resistance, and reducing an

overwhelmed oxidative stress phenotype than monotherapy. This concept (Figure 8) was based on the findings that (1) DCA and ATO positively altered the phenotype of the PAH rat model, (2) DCA and ATO worked collaboratively in inhibiting PSMC viability, (3) DCA- and ATO-induced cell

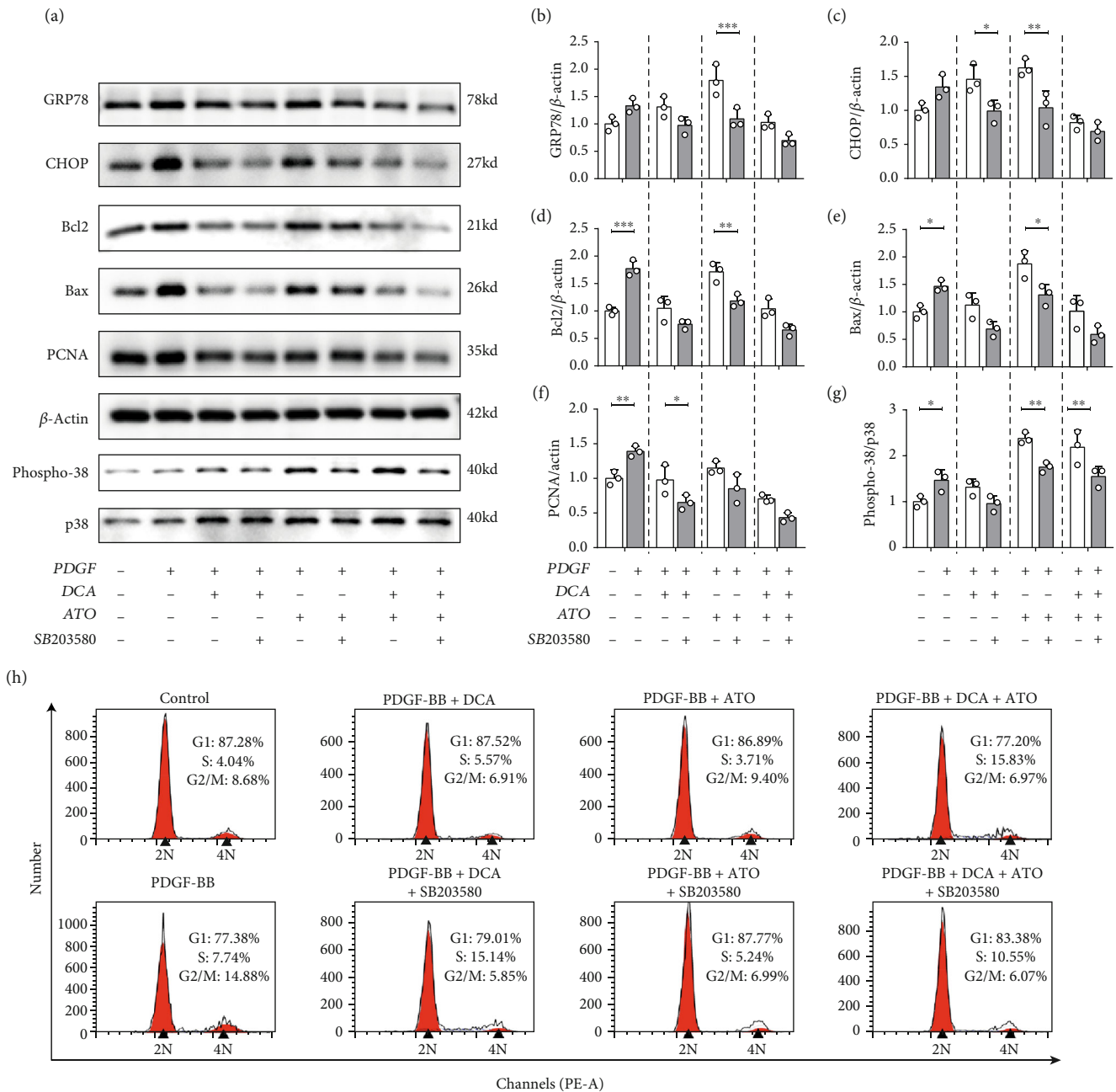


FIGURE 6: p38 inhibition alleviated dichloroacetate- and atorvastatin-related endoplasmic reticulum stress and apoptosis/antiapoptosis and proliferation disorders. Representative immunoblots and relative densitometric analysis of proliferation, apoptosis marker, and endoplasmic reticulum stress-associated marker. (a) PSMCs exposed to PDGF, DCA, and ATO with or without p38 inhibitor as indicated above ($n = 3$). (b–g) Immunoblot quantifications of related markers ($n = 3$). (H) Flow cytometry analysis of indicated exposure to PSMCs on cell cycle distribution. $P < 0.05$, $P < 0.01$, and $P < 0.001$. SB203580: p38-specific inhibitor.

death was accompanied by p38-dependent ROS production, and (4) DCA alone was capable of suppressing cell proliferation; however, when ROS and cell apoptosis was great, DCA prevented excessive oxidative stress and cell injury.

These experiments are our first attempt to combine glucose- and cholesterol-modulating drugs in treating PAH. DCA and ATO combination treatment prevented vascular cell hyperproliferation and macrophage infiltration (Figure 2),

which are the hallmarks of PAH pathogenesis. Consequently, we demonstrated that DCA or ATO monotherapy exhibited a dose-dependent cytotoxic manner, whereas the combination treatment conferred greater and more substantial suppression of cell viability than monotherapy, indicating that these drugs have a reciprocal effect on proliferation inhibition. In a PAH rat model, ATO administration is associated with protective effects, including a reduction in pulmonary

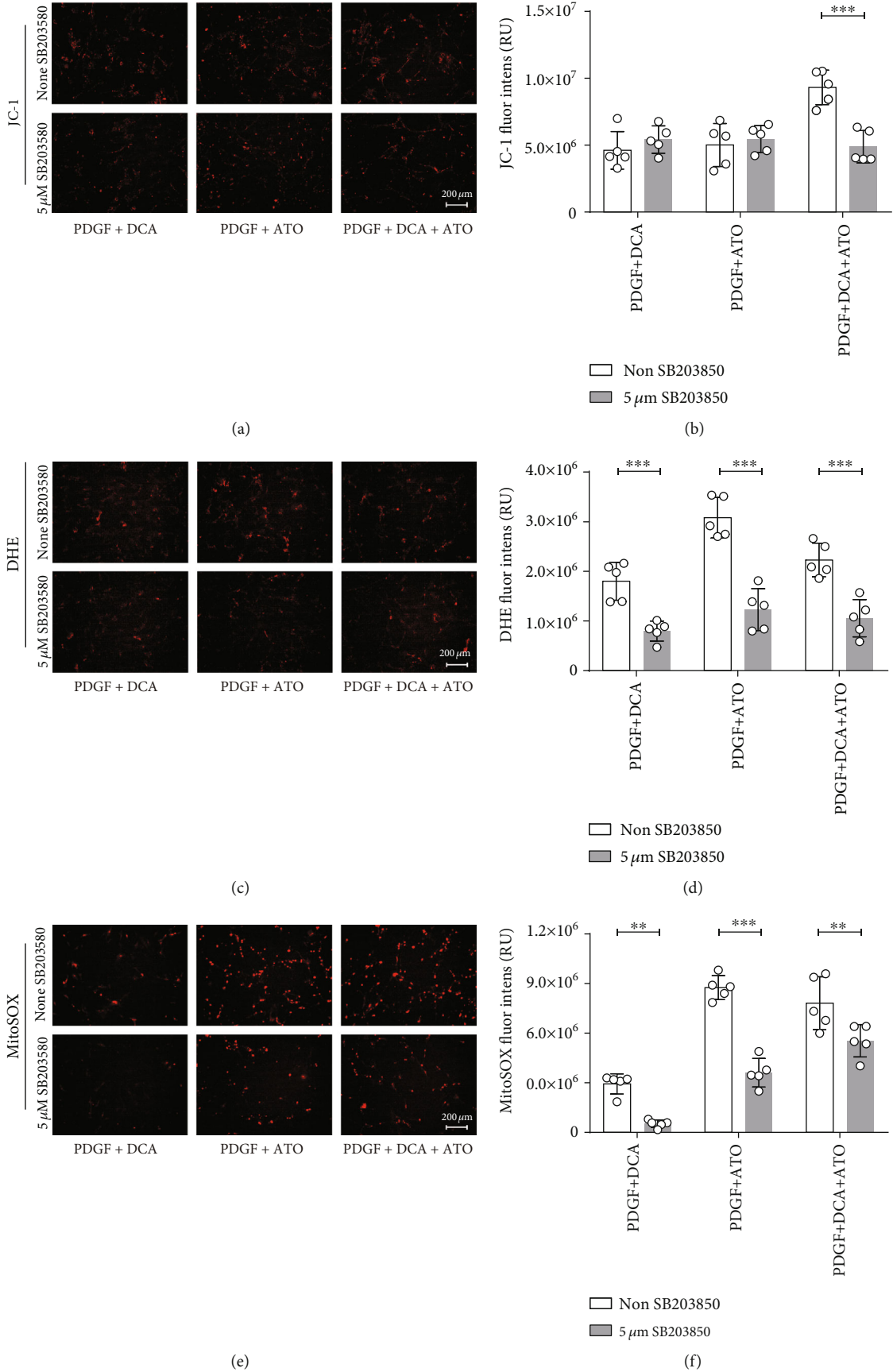


FIGURE 7: Continued.

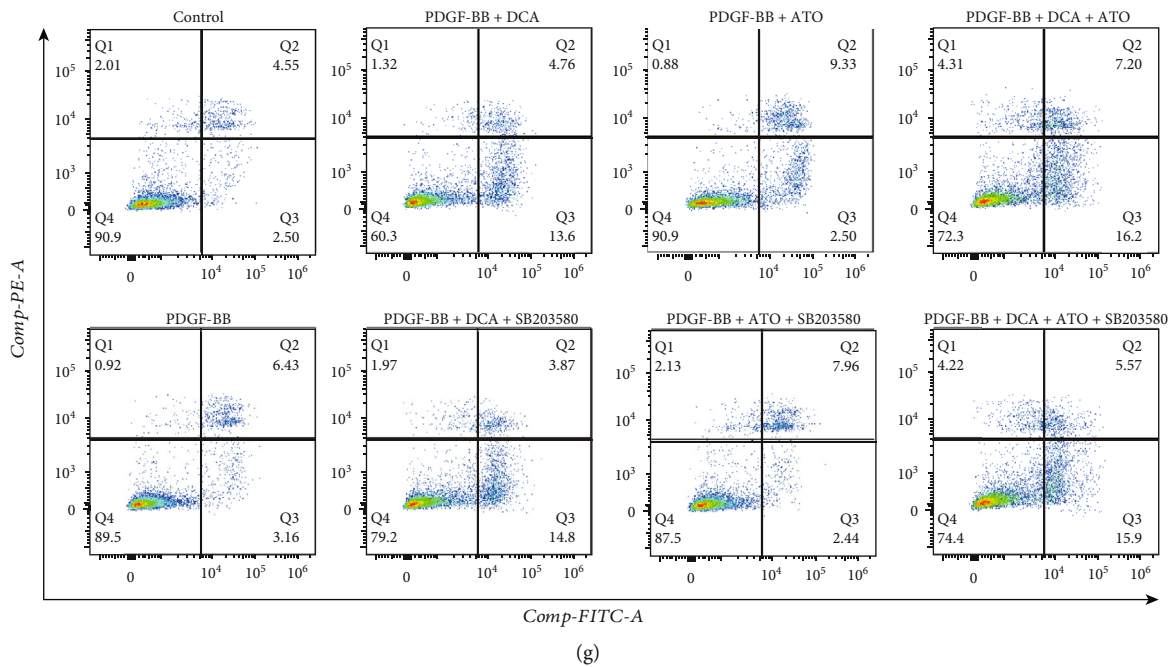


FIGURE 7: p38 inhibitor reduced dichloroacetate- and atorvastatin-related cytosolic and mitochondrial reactive oxidative stress accompanied by apoptosis suppression. (a, b) Mitochondrial membrane potential evaluated using a JC-1 probe and its semiquantitation. (c, d) Cytosolic ROS production detected using the DHE fluorescence probe and its measurement. (e, f) Mitochondrial superoxide expressed by MitoSOX fluorescence probe and its assessment. Scale bars: 200 μm ($n = 5$). ** and *** indicate $P < 0.01$ and $P < 0.001$, respectively. Analyses performed by unpaired Student's t -test. Bars represent mean \pm SEM. (g) Flow cytometry analysis of PASM C apoptosis induced by indicated treatment using annexin V/PI staining. SB203580: p38-specific inhibitor.

thickness [30–32] and right heart hypertrophy [33]. We also found that ATO administration resulted in the apoptosis of PASM Cs, as their morphology became round and isolated from their neighbors. Intriguingly, DCA in combination with ATO resulted in a remarkable decrease in viability while relatively preserving cell morphology, implying that coadministration of both drugs could prevent cell proliferation in a comparably controlled manner (Figure 3(d)). This observation was consistent with that of a recent study that showed that DCA and cisplatin combination treatment retained their anticancer properties while inducing better effects on preventing cisplatin-induced nephrotoxicity [34].

Thus, we clarified the underlying mechanism by which DCA and ATO reduce proliferation and revealed their reciprocal effects on reducing cellular toxicity. ATO led to greater cytosolic ROS and mitochondrial superoxide production than DCA, whereas DHE and MitoSOX fluorescence density was relatively restored in the combination treatment group. DCA was previously reported to contribute to cell protection by attenuating oxidative stress [34]. In the present study, DCA either alone or in combination with ATO presented a bidirectional role in maintaining the balance of cell proliferation and apoptosis, making it a potential approach in PAH treatment.

p38 activation has a potent role in PAH pathobiology [31, 35, 36]. p38 signaling plays a crucial role in the production of proinflammatory cytokines [37]. p38 inhibition by SB203580 can prevent PAH development by reversing RVSP and right heart hypertrophy [36]. p38 is a well-known redox-sensitive kinase involved in vascular diseases [35]. As a regulator of

apoptosis, p38 is activated upon phosphorylation often in response to cell stress and ROS. Multiple studies have implicated oxidative stress in PAH development [38, 39]. ROS modulates vascular force and tone, thereby regulating cellular proliferation and apoptosis and PAH pathological processes. Suppression of mitochondrial activities, such as glucose oxidation, which results in metabolic switch to glycolysis, contributes to an antiapoptotic phenotype [40]. Therefore, maintaining oxidative stress at a proper level is essential for PAH treatment. The mitochondria are the key source of vascular oxidative stress in vessel dysfunction [41]. Therefore, we investigated p38-dependent cell death and ROS production following DCA and ATO treatment. In the present study, we demonstrated that DCA and ATO exerted their PASM C inhibition effect in a p38-dependent manner (Figures 5 and 6). In DCA- and ATO-treated PASM Cs, p38 activation was associated with different treatment strategies (Figures 5(a) and 5(i)). Coadministration of these drugs resulted in a notable reduction in p38 phosphorylation compared with the ATO-treated group. A similar trend was observed *in vivo*. However, p38 phosphorylation moderately decreased in the DCA/ATO combination treatment group compared with ATO-treated group (Figures 5(f) and 5(j)). Nevertheless, we recognize that numerous factors were at play in the animal experiments. We believe that amplification of the rat samples would be helpful in achieving a statistical difference.

DCA has the ability to reverse pulmonary artery remodeling and improve right heart function and survival by reversing aerobic glycolysis [7, 42]. Mitochondrial abnormalities are

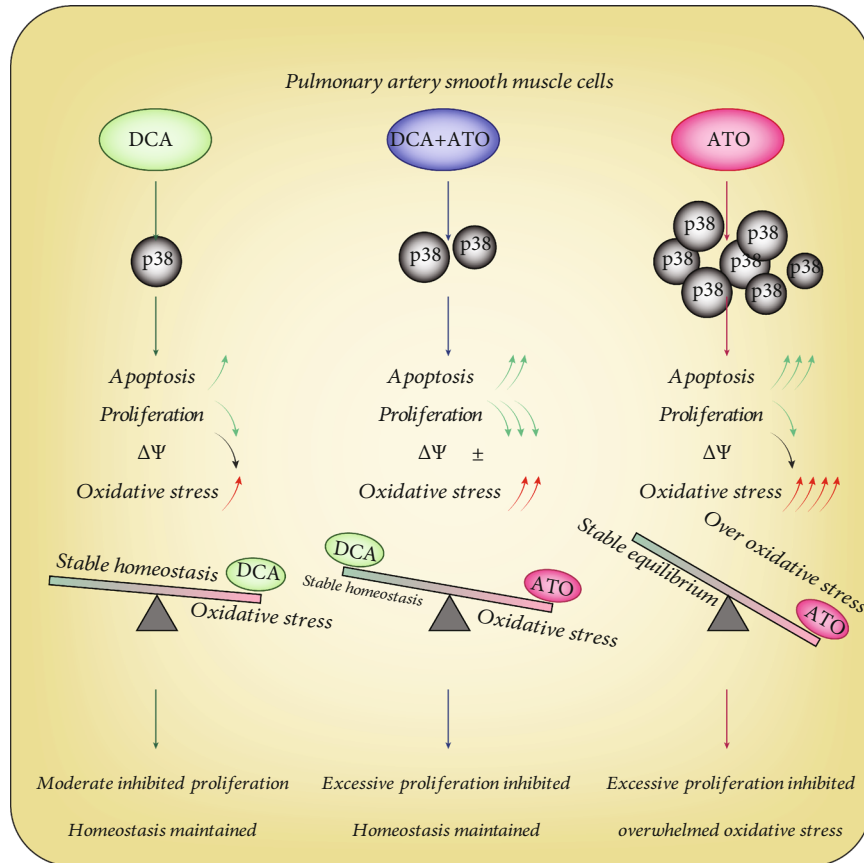


FIGURE 8: A schematic showing the proposed mechanism of dichloroacetate- and atorvastatin-related phenotype regulation. DCA inconsiderably increased apoptosis and oxidative stress and decreased proliferation and $\Delta\Psi_m$ (MMP) in a p38 activation-dependent manner. By contrast, ATO markedly upregulated the p38 signal pathway and oxidative stress, resulting in profound apoptosis. Slightly reduced proliferation and MMP when DCA and ATO combination treatment could achieve more therapeutic targets and only cause moderate ROS damage.

attracting increased attention in the PAH treatment. In the present study, we demonstrated that DCA could reduce MMP and alleviate oxidative stress induced by ATO. This result was consistent with that of our previous studies. Statins can reportedly induce apoptosis of neointimal smooth muscle cells [43], reduce MCT-induced PAH [44] and chronic hypoxia PAH [45], and prevent pulmonary artery muscularization [21]. We found that ATO had a better effect in preventing RVSP elevation and Ki67 upregulation than DCA. However, we believe that PASMCM apoptosis caused by statin administration, through oxidative stress buildup both *in vivo* and *in vitro*, could abolish its protective effects.

In the present study, we reviewed previous studies and presented a potential strategy for the combination therapy of PAH. Markedly reduced right ventricular systolic pressure and right heart hypertrophy were observed in the DCA and ATO combination treatment group, and this result may correspond to reduced vascular remodeling. DCA and ATO exhibited complementary effects on rescuing from a PAH phenotype.

However, several limitations of the current study should be mentioned. First, although the p38-specific inhibitor SB203580 would reportedly not affect oxidative stress or proliferation by itself [46, 47], whether SB203580 could induce

ROS without DCA or ATO delivery should be investigated. In addition, we did not conduct p38 genetic depletion in the animal experiments. A previous study reported that p38 inhibition alleviates PAH development [36]. The present results were consistent with this conclusion. Finally, further studies should evaluate the safety of DCA/ATO combination treatment. Several previous works stated that DCA and ATO are relatively safe for patients. ATO dosages ranging from 10 mg to 40 mg daily rarely result in adverse events [5]. DCA dosages of 3–12.5 mg/kg are approved for PAH treatment (ClinicalTrials.gov NCT01083524) [11], with no clinically significant change in QT intervals of electrocardiogram, cardiac rhythm, and liver, bone marrow, and renal functions.

Accumulating evidence indicates that appropriate combinations of multiple classes of drugs that target different pathogenic pathways may improve clinical outcomes [48–51]. The use of applicable combination therapies is not well documented, but it is a promising prospect for broadening PAH treatment strategies. We based our hypotheses on observations that metabolic disorders are a crucial underlying mechanism in PAH development. We then focused on the properties of DCA and ATO in regulating glucose and cholesterol separately. We found that the combination of these drugs had a superior effect in inhibiting PAH

phenotypes. The novel combination is a clinically relevant finding that may provide new insights for PAH treatment.

5. Conclusions

The combination of DCA and ATO reduced excessive proliferation and promoted apoptosis and reduced oxidative stress in a controlled manner that is dependent on p38 activation.

Data Availability

The data that support the findings of this study are openly available.

Conflicts of Interest

The authors declare that they have no conflicts of interest.

Acknowledgments

We acknowledge the contributions of all site investigators and clinical coordinators. This study was supported by the National Natural Science Foundation of China (grant Nos. 81873416, 81770496, and 81570050) and the National Science and Technology Plan of China (Grant 2017ZX0930401405).

Supplementary Materials

Supplementary Figure 1: PASMIC isolation and identification. Supplementary Figure 2: PASMICs were starved for 24h following indicated stimulation methods. (*Supplementary Materials*)

References

- [1] G. E. D'Alonzo, R. J. Barst, S. M. Ayres et al., "Survival in patients with primary pulmonary hypertension. Results from a national prospective registry," *Annals of Internal Medicine*, vol. 115, no. 5, pp. 343–349, 1991.
- [2] R. Savai, H. M. Al-Tamari, D. Sedding et al., "Pro-proliferative and inflammatory signaling converge on FoxO1 transcription factor in pulmonary hypertension," *Nature Medicine*, vol. 20, no. 11, pp. 1289–1300, 2014.
- [3] M. Humbert, O. Sitbon, and G. Simonneau, "Treatment of pulmonary arterial hypertension," *The New England Journal of Medicine*, vol. 351, no. 14, pp. 1425–1436, 2004.
- [4] N. Galie, W. Seeger, R. Naeije, G. Simonneau, and L. J. Rubin, "Comparative analysis of clinical trials and evidence-based treatment algorithm in pulmonary arterial hypertension," *Journal of the American College of Cardiology*, vol. 43, no. 12, Supplement, pp. S81–S88, 2004.
- [5] W. J. Zeng, C. M. Xiong, L. Zhao et al., "Atorvastatin in pulmonary arterial hypertension (APATH) study," *The European Respiratory Journal*, vol. 40, no. 1, pp. 67–74, 2012.
- [6] E. D. Michelakis, B. Thebaud, E. K. Weir, and S. L. Archer, "Hypoxic pulmonary vasoconstriction: redox regulation of O₂-sensitive K⁺ channels by a mitochondrial O₂-sensor in resistance artery smooth muscle cells," *Journal of Molecular and Cellular Cardiology*, vol. 37, no. 6, pp. 1119–1136, 2004.
- [7] M. S. McMurtry, S. Bonnet, X. Wu et al., "Dichloroacetate prevents and reverses pulmonary hypertension by inducing pulmonary artery smooth muscle cell apoptosis," *Circulation Research*, vol. 95, no. 8, pp. 830–840, 2004.
- [8] S. Krick, O. Platoshyn, S. S. McDaniel, L. J. Rubin, and J. X. J. Yuan, "Augmented K⁺ currents and mitochondrial membrane depolarization in pulmonary artery myocyte apoptosis," *American Journal of Physiology-Lung Cellular and Molecular Physiology*, vol. 281, no. 4, pp. L887–L894, 2001.
- [9] L. Piao, V. K. Sidhu, Y. H. Fang et al., "FOXO1-mediated upregulation of pyruvate dehydrogenase kinase-4 (PDK4) decreases glucose oxidation and impairs right ventricular function in pulmonary hypertension: therapeutic benefits of dichloroacetate," *Journal of Molecular Medicine*, vol. 91, no. 3, pp. 333–346, 2013.
- [10] G. Sutendra, S. Bonnet, G. Rochefort et al., "Fatty acid oxidation and malonyl-CoA decarboxylase in the vascular remodeling of pulmonary hypertension," *Science Translational Medicine*, vol. 2, no. 44, article 44ra58, 2010.
- [11] E. D. Michelakis, V. Gurtu, L. Webster et al., "Inhibition of pyruvate dehydrogenase kinase improves pulmonary arterial hypertension in genetically susceptible patients," *Science Translational Medicine*, vol. 9, no. 413, article eaao4583, 2017.
- [12] M. M. Bowker-Kinley, I. W. Davis, P. Wu, A. R. Harris, and M. K. Popov, "Evidence for existence of tissue-specific regulation of the mammalian pyruvate dehydrogenase complex," *Biochemical Journal*, vol. 329, no. 1, pp. 191–196, 1998.
- [13] M. Kato, J. Li, J. L. Chuang, and D. T. Chuang, "Distinct structural mechanisms for inhibition of pyruvate dehydrogenase kinase isoforms by AZD7545, dichloroacetate, and radicicol," *Structure*, vol. 15, no. 8, pp. 992–1004, 2007.
- [14] E. B. Garon, H. R. Christofk, W. Hosmer et al., "Dichloroacetate should be considered with platinum-based chemotherapy in hypoxic tumors rather than as a single agent in advanced non-small cell lung cancer," *Journal of Cancer Research and Clinical Oncology*, vol. 140, no. 3, pp. 443–452, 2014.
- [15] Q. S.-C. Chu, R. Sangha, J. Spratlin et al., "A phase I open-labeled, single-arm, dose-escalation, study of dichloroacetate (DCA) in patients with advanced solid tumors," *Investigational New Drugs*, vol. 33, no. 3, pp. 603–610, 2015.
- [16] E. M. Dunbar, B. S. Coats, A. L. Shroads et al., "Phase 1 trial of dichloroacetate (DCA) in adults with recurrent malignant brain tumors," *Investigational New Drugs*, vol. 32, no. 3, pp. 452–464, 2014.
- [17] S. Bonnet, E. D. Michelakis, C. J. Porter et al., "An abnormal mitochondrial-hypoxia inducible factor-1 α -Kv channel pathway disrupts oxygen sensing and triggers pulmonary arterial hypertension in fawn hooded rats," *Circulation*, vol. 113, no. 22, pp. 2630–2641, 2006.
- [18] E. D. Michelakis, M. S. McMurtry, X. C. Wu et al., "Dichloroacetate, a metabolic modulator, prevents and reverses chronic hypoxic pulmonary hypertension in rats: role of increased expression and activity of voltage-gated potassium channels," *Circulation*, vol. 105, no. 2, pp. 244–250, 2002.
- [19] C. Guignabert, L. Tu, M. Izikki et al., "Dichloroacetate treatment partially regresses established pulmonary hypertension in mice with SM22 α -targeted overexpression of the serotonin transporter," *The FASEB Journal*, vol. 23, no. 12, pp. 4135–4147, 2009.
- [20] H. Hu, A. Sung, G. Zhao et al., "Simvastatin enhances bone morphogenetic protein receptor type II expression," *Biochemical and Biophysical Research Communications*, vol. 339, no. 1, pp. 59–64, 2006.

- [21] T. Murata, K. Kinoshita, M. Hori et al., "Statin protects endothelial nitric oxide synthase activity in hypoxia-induced pulmonary hypertension," *Arteriosclerosis, Thrombosis, and Vascular Biology*, vol. 25, no. 11, pp. 2335–2342, 2005.
- [22] M. R. Wilkins, O. Ali, W. Bradlow et al., "Simvastatin as a treatment for pulmonary hypertension trial," *American Journal of Respiratory and Critical Care Medicine*, vol. 181, no. 10, pp. 1106–1113, 2010.
- [23] S. M. Kawut, E. Bagiella, D. J. Lederer et al., "Randomized clinical trial of aspirin and simvastatin for pulmonary arterial hypertension," *Circulation*, vol. 123, no. 25, pp. 2985–2993, 2011.
- [24] T. Li, L. Zha, H. Luo et al., "Galectin-3 mediates endothelial-to-mesenchymal transition in pulmonary arterial hypertension," *Aging and Disease*, vol. 10, no. 4, pp. 731–745, 2019.
- [25] L.-H. Zha, J. Zhou, T. Z. Li et al., "NLRC3 inhibits MCT-induced pulmonary hypertension in rats via attenuating PI3K activation," *Journal of Cellular Physiology*, vol. 234, no. 9, pp. 15963–15976, 2019.
- [26] P. Yuan, W. H. Wu, L. Gao et al., "Oestradiol ameliorates monocrotaline pulmonary hypertension via NO, prostacyclin and endothelin-1 pathways," *The European Respiratory Journal*, vol. 41, no. 5, pp. 1116–1125, 2013.
- [27] G. Marsboom, P. T. Toth, J. J. Ryan et al., "Dynamin-related protein 1-mediated mitochondrial mitotic fission permits hyperproliferation of vascular smooth muscle cells and offers a novel therapeutic target in pulmonary hypertension," *Circulation Research*, vol. 110, no. 11, pp. 1484–1497, 2012.
- [28] J. He, X. Li, H. Luo et al., "Galectin-3 mediates the pulmonary arterial hypertension-induced right ventricular remodeling through interacting with NADPH oxidase 4," *Journal of the American Society of Hypertension*, vol. 11, no. 5, pp. 275–289.e2, 2017.
- [29] H. Luo, X. Li, T. Li et al., "microRNA-423-3p exosomes derived from cardiac fibroblasts mediates the cardioprotective effects of ischaemic post-conditioning," *Cardiovascular Research*, vol. 115, no. 7, pp. 1189–1204, 2019.
- [30] L. Xie, P. Lin, H. Xie, and C. Xu, "Effects of atorvastatin and losartan on monocrotaline-induced pulmonary artery remodeling in rats," *Clinical and Experimental Hypertension*, vol. 32, no. 8, pp. 547–554, 2010.
- [31] Y. F. Gao, X. D. Zhu, D. M. Shi et al., "The effects of atorvastatin on pulmonary arterial hypertension and expression of p38, p27, and Jab1 in rats," *International Journal of Molecular Medicine*, vol. 26, no. 4, pp. 541–547, 2010.
- [32] D. C. Souza-Costa, L. Figueiredo-Lopes, J. C. Alves-Filho et al., "Protective effects of atorvastatin in rat models of acute pulmonary embolism: involvement of matrix metalloproteinase-9," *Critical Care Medicine*, vol. 35, no. 1, pp. 239–245, 2007.
- [33] K. Satoh, Y. Fukumoto, M. Nakano et al., "Statin ameliorates hypoxia-induced pulmonary hypertension associated with down-regulated stromal cell-derived factor-1," *Cardiovascular Research*, vol. 81, no. 1, pp. 226–234, 2008.
- [34] R. Galgamuwa, K. Hardy, J. E. Dahlstrom et al., "Dichloroacetate prevents cisplatin-induced nephrotoxicity without compromising cisplatin anticancer properties," *Journal of the American Society of Nephrology*, vol. 27, no. 11, pp. 3331–3344, 2016.
- [35] J. Wu, S. R. Thabet, A. Kirabo et al., "Inflammation and mechanical stretch promote aortic stiffening in hypertension through activation of p38 mitogen-activated protein kinase," *Circulation Research*, vol. 114, no. 4, pp. 616–625, 2014.
- [36] A. C. Church, D. H. Martin, R. Wadsworth et al., "The reversal of pulmonary vascular remodeling through inhibition of p38 MAPK- α : a potential novel anti-inflammatory strategy in pulmonary hypertension," *American Journal of Physiology-Lung Cellular and Molecular Physiology*, vol. 309, no. 4, pp. L333–L347, 2015.
- [37] Z. Guan, S. Y. Buckman, A. P. Pentland, D. J. Templeton, and A. R. Morrison, "Induction of cyclooxygenase-2 by the activated MEK1 \rightarrow SEK1/MKK4 \rightarrow p38 mitogen-activated protein kinase pathway," *The Journal of Biological Chemistry*, vol. 273, no. 21, pp. 12901–12908, 1998.
- [38] A. Smukowska-Gorynia, P. Rzymiski, J. Marcinkowska et al., "Prognostic value of oxidative stress markers in patients with pulmonary arterial or chronic thromboembolic pulmonary hypertension," *Oxidative Medicine and Cellular Longevity*, vol. 2019, Article ID 3795320, 10 pages, 2019.
- [39] Y. Ban, Y. Liu, Y. Li et al., "S-nitrosation impairs KLF4 activity and instigates endothelial dysfunction in pulmonary arterial hypertension," *Redox Biology*, vol. 21, article 101099, 2019.
- [40] M. S. McMurtry, S. L. Archer, D. C. Altieri et al., "Gene therapy targeting *survivin* selectively induces pulmonary vascular apoptosis and reverses pulmonary arterial hypertension," *Journal of Clinical Investigation*, vol. 115, no. 6, pp. 1479–1491, 2005.
- [41] S. I. Dikalov and R. R. Nazarewicz, "Angiotensin II-induced production of mitochondrial reactive oxygen species: potential mechanisms and relevance for cardiovascular disease," *Antioxidants & Redox Signaling*, vol. 19, no. 10, pp. 1085–1094, 2013.
- [42] S. Bonnet, S. L. Archer, J. Allalunis-Turner et al., "A mitochondria-K⁺ channel axis is suppressed in cancer and its normalization promotes apoptosis and inhibits cancer growth," *Cancer Cell*, vol. 11, no. 1, pp. 37–51, 2007.
- [43] T. Nishimura, L. T. Vaszar, J. L. Faul et al., "Simvastatin rescues rats from fatal pulmonary hypertension by inducing apoptosis of neointimal smooth muscle cells," *Circulation*, vol. 108, no. 13, pp. 1640–1645, 2003.
- [44] T. Nishimura, J. L. Faul, G. J. Berry et al., "Simvastatin attenuates smooth muscle neointimal proliferation and pulmonary hypertension in rats," *American Journal of Respiratory and Critical Care Medicine*, vol. 166, no. 10, pp. 1403–1408, 2002.
- [45] R. E. Girgis, D. Li, X. Zhan et al., "Attenuation of chronic hypoxic pulmonary hypertension by simvastatin," *American Journal of Physiology-Heart and Circulatory Physiology*, vol. 285, no. 3, pp. H938–H945, 2003.
- [46] A. M. Allawzi, A. Vang, R. T. Clements et al., "Activation of anoctamin-1 limits pulmonary endothelial cell proliferation via p38-mitogen-activated protein kinase-dependent apoptosis," *American Journal of Respiratory Cell and Molecular Biology*, vol. 58, no. 5, pp. 658–667, 2018.
- [47] D. Jia, Y. He, Q. Zhu et al., "RAGE-mediated extracellular matrix proteins accumulation exacerbates HySu-induced pulmonary hypertension," *Cardiovascular Research*, vol. 113, no. 6, pp. 586–597, 2017.
- [48] V. F. Tapson, Z. C. Jing, K. F. Xu et al., "Oral treprostinil for the treatment of pulmonary arterial hypertension in patients receiving background endothelin receptor antagonist and phosphodiesterase type 5 inhibitor therapy (the FREEDOM-C2 study): a randomized controlled trial," *Chest*, vol. 144, no. 3, pp. 952–958, 2013.

- [49] T. Pulido, I. Adzerikho, R. N. Channick et al., “Macitentan and morbidity and mortality in pulmonary arterial hypertension,” *The New England Journal of Medicine*, vol. 369, no. 9, pp. 809–818, 2013.
- [50] N. Galiè, B. H. Brundage, H. A. Ghofrani et al., “Tadalafil therapy for pulmonary arterial hypertension,” *Circulation*, vol. 119, no. 22, pp. 2894–2903, 2009.
- [51] H. A. Ghofrani, N. Galiè, F. Grimminger et al., “Riociguat for the treatment of pulmonary arterial hypertension,” *The New England Journal of Medicine*, vol. 369, no. 4, pp. 330–340, 2013.

Review Article

The Research Progress of Vascular Macrophages and Atherosclerosis

Yeqing Tong ¹, Li Cai,^{2,3} Shiyu Yang,³ Shuang Liu,¹ Zhihong Wang ⁴,
and Jinquan Cheng ⁵

¹Hubei Center for Disease Control and Prevention, 430079, China

²Wuhan Center for Disease Control and Prevention, Wuhan 430015, China

³School of Health Sciences, Wuhan University, Wuhan 430071, China

⁴Department of Neurology, Shenzhen No. 2 People's Hospital, The First Affiliated Hospital of Shenzhen University, Shenzhen 518035, China

⁵Key Laboratory of Molecular Biology of Guangdong Province, Center for Disease Control and Prevention, Shenzhen 518055, China

Correspondence should be addressed to Zhihong Wang; w_zhihong01@163.com and Jinquan Cheng; c_jinquan@163.com

Received 9 December 2019; Revised 9 March 2020; Accepted 25 March 2020; Published 25 May 2020

Guest Editor: Bhagavatula Moorthy

Copyright © 2020 Yeqing Tong et al. This is an open access article distributed under the Creative Commons Attribution License, which permits unrestricted use, distribution, and reproduction in any medium, provided the original work is properly cited.

Background/Aims. Vascular macrophages may affect the immune regulation of atherosclerosis (AS). In recent years, there are lots of researches on the association of vascular macrophages and AS which has attracted increasing attention, and the in-depth study of its mechanism is gradually clear. **Materials.** We made a minireview on the association of vascular macrophages with AS based on recent research studies systematically, from the mechanisms of macrophages accumulating in the walls of blood vessels, and the role of macrophages in AS as well as microenvironmental determinants of macrophage function in AS. The discovery of these mechanisms could reveal the pathogenesis of AS comprehensively and is crucial to provide scientific evidence for formulating the related measures of prevention and treatment for AS. **Discussion.** Vascular macrophages play important roles in the development of AS, and the vascular macrophages may become new targets for the prevention and treatment of AS. Effective regulation of host genes may help prevent or even treat AS. **Conclusion.** This minireview focuses on the association of vascular macrophages with the development of AS, which may supply some clues for future therapies and novel drug targets for AS.

1. Introduction

Atherosclerosis (AS) is a chronic inflammatory vascular wall disease. Its complications, especially myocardial infarction and stroke, are the most common cause of death worldwide. Macrophages are the most abundant type of immune cells in atherosclerotic lesions and play important roles in all stages of disease, from atherosclerotic lesion formation to plaque rupture [1, 2].

The role of macrophages in AS can be briefly described as follows: when the local blood flow is nonlaminar, vascular endothelial dysfunction causes circulating low-density lipoprotein (LDL) to penetrate into the lining of blood vessels, especially in hyperlipidemia. In vascular walls, LDL undergo

oxidative modifications, activating endothelial cells and resident immune cells, leading to the upregulation of chemokines and adhesion molecule expression that attract circulating monocytes to vascular walls, allowing them to adhere and roll, and transendothelial migration, resulting in intimal infiltration of monocytes. After monocytes enter the intima of blood vessels, they differentiate into macrophages and take in modified lipoproteins to further become foam cells. The accumulated foam cell apoptosis in the endothelium is not cleared in time, which gradually leads to the formation of thrombus and inflammatory necrosis core [3]. Macrophages further aggravate pathological inflammation by secreting cytokines and proteolytic enzymes, leading to decreased plaque stability and rupture, forming atherosclerotic thrombosis.

1.1. The Mechanisms of How Macrophages Were Accumulated in the Walls of Blood Vessels. For a long time, bone marrow hematopoiesis has been considered the main source of monocytes in the development of AS, hyperlipidemia, hyperglycemia, and other AS-associated diseases [1–4]. More than 20 years ago, the proliferation of macrophages in atherosclerotic plaques was observed in human and animal models, but the quantitative contribution of macrophage accumulation to the development of lesions has not yet been clearly studied [5]. Through the distinction between sources of tissue cells, either they are tissue circulating monocyte or local expansion of the cells, macrophage proliferation was considered to account for about 87% of macrophage accumulation in established lesions, while the circulating monocytes added only works in the early stages of the disease [6]. However, data from the same study using the long-term chimeric model showed that all established macrophages in lesions ultimately came from circulating precursors and that monocytes increased with the addition proportion in the progression of lesions [7]. A recent report showed that compared to previous studies, the proliferative activity of macrophages was higher in early rather than late lesions [8]. However, it has recently been found that a large proportion of macrophages in identified lesions are senescent [9], so macrophages cannot proliferate according to the definition of cell proliferation. Moreover, studies have shown that highly proliferative and plastic vascular smooth muscle cells can present a macrophage-like phenotype and express classic macrophage markers in lesions, such as MAC 3 or MAC 2, which could further complicate the interpretation of studies on macrophage proliferation in AS [10].

In the past 20 years, markers coexpressed by macrophages and vascular smooth muscle cells (VSMC) were found in AS. A recent study showed that up to 50% of cells identified as macrophage foam cells coexpressed smooth muscle cell markers [11]. However, these studies based on immunohistological analysis were unable to determine whether the cells were derived from macrophages with upregulated VSMCs or were transformed into macrophage foam cells. In the study of pedigree fate of VSMC in a mouse model with AS, the transformation of VSMC into macrophage-like cells in lesions was confirmed [12]. In *in vivo* studies, VSMC-derived macrophages can form foam cells, but these cells are different from real macrophages in function [13].

Macrophages are widely expressed in humans, so healthy arteries already contain resident macrophages and dendritic cells that may self-renew after infection-induced failure. The role of macrophages, which are present in the arteries by themselves, remains to be determined in AS, but some studies have suggested that a group of epigastric macrophage progenitors exist in the aorta of adult mice and may locally differentiate to promote the accumulation of macrophages [14].

Atherosclerotic plaque and its macrophage content can be decreased, which has been shown in a hypercholesterolemia reversal mouse model [15]. However, the exact potential mechanism is still controversial, and some studies have suggested that macrophage autophagy may be the cause of this phenomenon [16]. Some reports of atherosclerotic aortic transplantation models have found that pathological changes

in mature macrophages during migration will lead to the formation of plaques [17]. Another study showed that the reduced load of macrophages is not related to macrophage migration but depends on the inhibition of monocyte accumulation and the apoptosis of plaque macrophages [15]; the mechanisms of how macrophages were accumulated in the walls of blood vessels are described in Figure 1.

1.2. The Role of Macrophages in AS. After entering into the lesion site, macrophages actively participate in vascular inflammation by secreting proinflammatory cytokines and producing chemokines, further promoting absorption of immune cells. Plaque macrophages express proinflammatory cytokines, such as tumor necrosis factor alpha (TNF alpha), interleukin-18 (IL-18), and interleukin-12 (IL-12) [4]. CCL2 overexpression in bone marrow cells increases macrophages' absorption of lesions, suggesting that leukocyte derived from chemokines can fuel plaque inflammation [18]. Meanwhile, macrophages were known to have a strong proteolysis activity and were considered to be related to the instability and rupture of plaques [19].

The formation of macrophage-derived foam cells in the intima of blood vessels is a hallmark of AS. Macrophages ingest modified LDL through a variety of scavenger receptors, such as CD36, scavenger receptor A1 (sr-a1, also known as MSR-1) [20], scavenger receptor B1, LDL receptor-related protein 1 (LRP-1), and lectin-like receptor 1 (LOX-1) [21, 22]. Several studies have shown that foam cell formation reduced in mice lacking specificity in MSR-1 [23]. In addition to its role in lipid uptake, MSR-1 was also found to play a key role in the proliferation of macrophages in advanced lesions [6].

Given the importance of macrophage proliferation in macrophage infiltration, the proliferative ability can also be considered an important functional feature of disease-associated macrophages. Since macrophage proliferation is preferentially activated in advanced lesions [10]. Deciphering the mechanism of transition from a nonproliferative state to a proliferative state is worth studying. Compared to proliferating macrophages, the lesion also contains senescent cells that have lost their ability to proliferate. Although the pathogenic role of senescent cells in AS has been suspected [23], a recent report pointed out that foam cells of senescent macrophages in the intima of blood vessels were pathogenic in the whole process of AS [24]. In conclusion, the increase of macrophage survival or apoptosis ultimately determines the progression and regression of plaque, which is likely to depend on the stability of plaque macrophages and aggregation of monocytes [16].

1.3. Microenvironmental Determinants of Macrophage Function in AS. The effective cellular function of apoptotic cells can also promote the accumulation of intracellular lipids in macrophages, and how this affects the macrophage phenotype remains unclear [18]. Cholesterol crystals can form both intracellular and extracellular lesions, and cholesterol crystal deposits can be detected even in the early stage of atherosclerotic lesions. It is worth noting that cholesterol crystals activate NLRP-3 inflammasome which further transforms proinflammatory cytokines IL-1 beta and IL-18 into mature

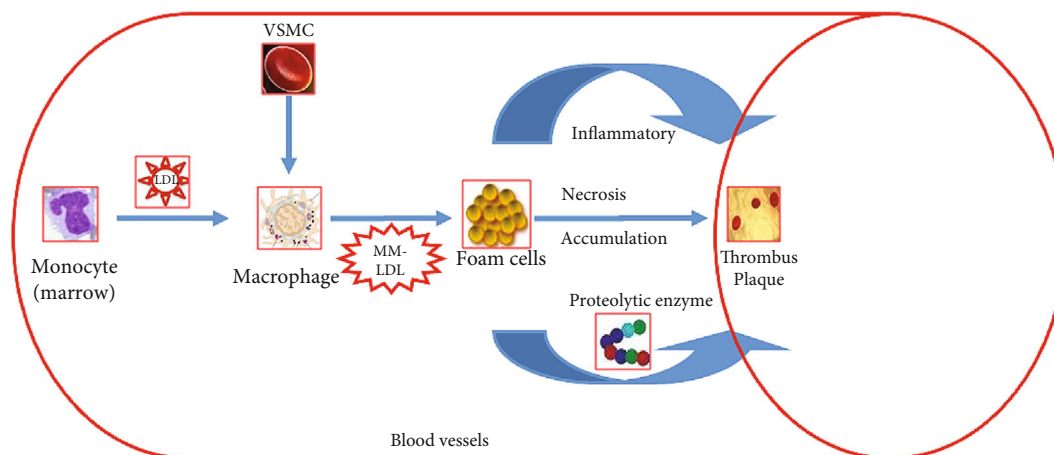


FIGURE 1: The mechanisms of how macrophages were accumulated in the walls of blood vessels; VSMC: vascular smooth muscle cell; MM-LDL: minimally modified low-density lipoprotein.

and secretory forms and converts them into cholesterol crystal mediators. Activation of NLRP-3 inflammasome has been considered essential in the development of AS [25].

In the late stage of AS, the increased distance from the vascular lumen to the plaque core increases the metabolic demands, leading to hypoxic areas. Hypoxia induces the expression of oxygen-sensitive transcription factor-1 alpha (HIF1 alpha), a process that can be further demonstrated by inflammatory signaling pathways such as NF-kappa B [26]. Therefore, hypoxia may be involved in the development of AS.

Macrophages are also activated by growth factors, such as granulocyte-macrophage colony-stimulating factor (CSF-2) or CSF-1, which control macrophage survival and proliferation. CSF-2 also indirectly induces apoptosis of plaque macrophages by upregulating the expression of IL-9 [27]. The plaque microenvironment also contains a large number of proinflammatory and anti-inflammatory cytokines that affect the macrophage phenotype. Cytokines such as IL-1 beta, TNF alpha, or IFN-gamma promote the formation of proatherogenic macrophage phenotype and increase the expression of proinflammatory cytokines, chemokines, and proteases [28, 29].

2. Conclusions

Taken together, these studies supported that vascular macrophages play important roles in mediating the regulation of AS infection. The development of AS is correlated with vascular macrophages, and vascular macrophage plays a unique role in the development of AS. But most effects in different subjects are inconsistent, which may be influenced by a variety of factors. Therefore, it is necessary to conduct repetitive, multicenter, and large-sample researches in order to draw more scientific conclusions, to further confirm the relationship between vascular macrophages and AS, and to better clarify the immunopathological mechanisms of AS for a theoretical basis for prevention and treatment as well as to provide clues for finding new drug targets for AS-associated diseases.

Conflicts of Interest

The authors declare no conflicts of interest.

Authors' Contributions

Yeqing Tong, Li Cai, Shiyu Yang, and Shuang Liu contributed equally to this work.

Acknowledgments

This study was supported by funds of Hubei Province's young medical talent program (20191229), Hubei Province's young talent program (20171102), China Postdoctoral Scientific Foundation (Nos. 2014M550394 and 2015T80807), and Hubei Natural Science Foundation (Nos. 2013CFB056, 2016CFB403 and 2017ADC061).

References

- [1] W. Chenyang, Z. Fuliang, L. Wei, and J. Minghong, "Research progress on immune mechanism of atherosclerosis," *Chinese journal of evidence-based cardiovascular medicine*, vol. 10, pp. 1431–1433, 2018.
- [2] O. Soehnlein and F. K. Swirski, "Hypercholesterolemia links hematopoiesis with atherosclerosis," *Trends in Endocrinology & Metabolism*, vol. 24, no. 3, pp. 129–136, 2013.
- [3] S. Ke, L. Hanning, S. Cheng, Y. Shaojun, and Z. Zhe, "Role and mechanism of macrophages in coronary atherosclerosis," *Chinese Journal of Molecular Cardiology*, vol. 18, pp. 2704–2707, 2018.
- [4] D. Junjun, H. Jiakai, and Y. Na, "Role of macrophage autophagy in the pathogenesis of atherosclerosis," *Journal of Integrated Traditional Chinese and Western Medicine*, vol. 28, pp. 1136–1140, 2019.
- [5] M. E. Rosenfeld and R. Ross, "Macrophage and smooth muscle cell proliferation in atherosclerotic lesions of WHHL and comparably hypercholesterolemic fat-fed rabbits," *Arteriosclerosis*, vol. 10, no. 5, pp. 680–687, 1990.
- [6] C. S. Robbins, I. Hilgendorf, G. F. Weber et al., "Local proliferation dominates lesional macrophage accumulation in

- atherosclerosis," *Nature Medicine*, vol. 19, no. 9, pp. 1166–1172, 2013.
- [7] F. K. Swirski, M. J. Pittet, M. F. Kircher et al., "Monocyte accumulation in mouse atherogenesis is progressive and proportional to extent of disease," *Proceedings of the National Academy of Sciences of the United States of America*, vol. 103, no. 27, pp. 10340–10345, 2006.
- [8] Š. Lhoták, G. Gyulay, J. C. Cutz et al., "Characterization of proliferating lesion-resident cells during all stages of atherosclerotic growth," *J Am Heart Assoc*, vol. 5, no. 8, 2016.
- [9] B. G. Childs, D. J. Baker, T. Wijshake, C. A. Conover, J. Campisi, and J. M. van Deursen, "Senescent intimal foam cells are deleterious at all stages of atherosclerosis," *Science*, vol. 354, no. 6311, pp. 472–477, 2016.
- [10] S. M. Chaudhari, J. C. Sluimer, M. Koch et al., "Deficiency of HIF1 α in Antigen-Presenting cells aggravates atherosclerosis and type 1 T-helper cell responses in mice," *Arteriosclerosis, Thrombosis, and Vascular Biology*, vol. 35, no. 11, pp. 2316–2325, 2015.
- [11] S. Allahverdian, A. C. Chehroudi, B. M. McManus, T. Abraham, and G. A. Francis, "Contribution of intimal smooth muscle cells to cholesterol accumulation and macrophage-like cells in human atherosclerosis," *Circulation*, vol. 129, no. 15, pp. 1551–1559, 2014.
- [12] S. Liufang, J. Xijuan, Y. Lin, W. Liping, and Q. Xin, "Research progress on the effect of phenotypic transformation of vascular smooth muscle cells on atherosclerosis," *Chinese Journal of Arteriosclerosis*, vol. 26, pp. 99–102, 2018.
- [13] L. S. Shankman, D. Gomez, O. A. Cherepanova et al., "KLF4-dependent phenotypic modulation of smooth muscle cells has a key role in atherosclerotic plaque pathogenesis," *Nature Medicine*, vol. 21, no. 6, pp. 628–637, 2015.
- [14] S. Ensan, A. Li, R. Besla et al., "Self-renewing resident arterial macrophages arise from embryonic CX3CR1⁺ precursors and circulating monocytes immediately after birth," *Nature Immunology*, vol. 17, no. 2, pp. 159–168, 2016.
- [15] S. Potteaux, E. L. Gautier, S. B. Hutchison et al., "Suppressed monocyte recruitment drives macrophage removal from atherosclerotic plaques of Apoe^{-/-} mice during disease regression," *The Journal of Clinical Investigation*, vol. 121, no. 5, pp. 2025–2036, 2011.
- [16] W. Binyi, L. Feifei, W. Dongfang, and Y. Hong, "Research progress on the role of macrophage autophagy in atherosclerosis," *Chinese Journal of Atherosclerosis*, vol. 27, pp. 439–444, 2019.
- [17] J. E. Feig, I. Pineda-Torra, M. Sanson et al., "LXR promotes the maximal egress of monocyte-derived cells from mouse aortic plaques during atherosclerosis regression," *The Journal of Clinical Investigation*, vol. 120, no. 12, pp. 4415–4424, 2010.
- [18] R. J. Aiello, P. A. K. Bourassa, S. Lindsey et al., "Monocyte chemoattractant protein-1 accelerates atherosclerosis in apolipoprotein E-deficient mice," *Arteriosclerosis, Thrombosis, and Vascular Biology*, vol. 19, no. 6, pp. 1518–1525, 1999.
- [19] T. Quillard, K. Croce, F. A. Jaffer, R. Weissleder, and P. Libby, "Molecular imaging of macrophage protease activity in cardiovascular inflammation in vivo," *Thrombosis and Haemostasis*, vol. 105, no. 5, pp. 828–836, 2011.
- [20] L. Jing, G. Sen, and Z. Juan, "Mechanism of type A scavenger receptor involved in atherosclerosis," *Progress in Cardiology*, vol. 39, pp. 456–459, 2018.
- [21] I. Tabas and K. E. Bornfeldt, "Macrophage phenotype and function in different stages of atherosclerosis," *Circulation Research*, vol. 118, no. 4, pp. 653–667, 2016.
- [22] V. R. Babaev, L. A. Gleaves, K. J. Carter et al., "Reduced atherosclerotic lesions in mice deficient for total or macrophage-specific expression of scavenger receptor-a," *Arteriosclerosis, Thrombosis, and Vascular Biology*, vol. 20, no. 12, pp. 2593–2599, 2000.
- [23] B. G. Childs, M. Durik, D. J. Baker, and J. M. van Deursen, "Cellular senescence in aging and age-related disease: from mechanisms to therapy," *Nature Medicine*, vol. 21, no. 12, pp. 1424–1435, 2015.
- [24] M. H. Askenase, S. J. Han, A. L. Byrd et al., "Bone-marrow-resident NK cells prime monocytes for regulatory function during infection," *Immunity*, vol. 42, no. 6, pp. 1130–1142, 2015.
- [25] P. Duewell, H. Kono, K. J. Rayner et al., "NLRP3 inflammasomes are required for atherogenesis and activated by cholesterol crystals," *Nature*, vol. 464, no. 7293, pp. 1357–1361, 2010.
- [26] L. R. Oslin, "Research progress of NF-kappa B in atherosclerosis," *Chinese journal of immunology*, vol. 34, pp. 1095–1101, 2018.
- [27] M. Subramanian, E. Thorp, and I. Tabas, "Identification of a non-growth factor role for GM-CSF in advanced atherosclerosis: promotion of macrophage apoptosis and plaque necrosis through IL-23 signaling," *Circulation Research*, vol. 116, no. 2, pp. e13–e24, 2015.
- [28] D. P. Ramji and T. S. Davies, "Cytokines in atherosclerosis: key players in all stages of disease and promising therapeutic targets," *Cytokine & Growth Factor Reviews*, vol. 26, no. 6, pp. 673–685, 2015.
- [29] C. Cochain and A. Zerneck, "Macrophages in vascular inflammation and atherosclerosis," *Pflugers Arch - Eur J Physiol*, vol. 469, no. 3-4, pp. 485–499, 2017.

Research Article

Asiatic Acid Protects against Doxorubicin-Induced Cardiotoxicity in Mice

Xiaoping Hu,¹ Baijun Li¹,² Luocheng Li,¹ Bowen Li,¹ Jinlong Luo¹,² and Bin Shen²

¹Department of Cardiovascular Surgery, Renmin Hospital of Wuhan University, Wuhan, Hubei 430060, China

²Department of Thoracic Cardiovascular Surgery, The People's Hospital of Guangxi Zhuang Autonomous Region, Nanning, Guangxi Zhuang Autonomous Region, China

Correspondence should be addressed to Baijun Li; libaijun1979@126.com

Received 26 November 2019; Accepted 28 January 2020; Published 16 May 2020

Guest Editor: Lynette K. Rogers

Copyright © 2020 Xiaoping Hu et al. This is an open access article distributed under the Creative Commons Attribution License, which permits unrestricted use, distribution, and reproduction in any medium, provided the original work is properly cited.

The use of doxorubicin (DOX) can result in depression of cardiac function and refractory cardiomyopathy. Currently, there are no effective approaches to prevent DOX-related cardiac complications. Asiatic acid (AA) has been reported to provide cardioprotection against several cardiovascular diseases. However, whether AA could attenuate DOX-related cardiac injury remains unclear. DOX (15 mg/kg) was injected intraperitoneally into the mice to mimic acute cardiac injury, and the mice were given AA (10 mg/kg or 30 mg/kg) for 2 weeks for protection. The data in our study found that AA-treated mice exhibited attenuated cardiac injury and improved cardiac function in response to DOX injection. AA also suppressed myocardial oxidative damage and apoptosis without affecting cardiac inflammation in DOX-treated mice. AA also provided protection in DOX-challenged cardiomyocytes, improved cell viability, and suppressed intracellular reactive oxygen species (ROS) in vitro. Detection of signaling pathways showed that AA activated protein kinase B (AKT) signaling pathway in vivo and in vitro. Furthermore, we found that AA lost its protective effects in the heart with AKT inactivation. In conclusion, our results found that AA could attenuate DOX-induced myocardial oxidative stress and apoptosis via activation of the AKT signaling pathway.

1. Introduction

Anthracyclines are the primary choice particularly in patients with severe leukemias, lymphomas, and solid tumors [1]. Cardiotoxicity is a fatal side effect of doxorubicin (DOX), which largely limits its clinical use. The use of DOX can also trigger cardiac arrhythmia, pericarditis, depression of cardiac function, and refractory cardiomyopathy in a dose-dependent manner [2, 3]. Moreover, previous studies demonstrated that cardiac dysfunction even occurs at a very low therapeutic dose of DOX [4, 5]. DOX-related cardiac injury is irreversible, and currently, there are no effective approaches to prevent DOX-related cardiac complications in cancer patients with chemotherapy. Therefore, it is of great importance to find drugs that could protect against DOX-induced cardiac injury.

DOX-induced cardiotoxicity involves in multiple biological processes including increased reactive oxygen species (ROS) production and lipid peroxidation, which eventually

lead to the death of cardiomyocytes. DOX treatment resulted in massive production of superoxide anion free radicals (O₂⁻) and ROS and thereafter caused DNA damage and apoptosis [6, 7]. A previous study found that oxidative stress and subsequent lipid peroxidation could be detected in DOX-treated hearts even at three hours after DOX administration [8]. Therefore, prevention of oxidative stress may be a promising method against DOX-induced cell loss and cardiac dysfunction.

Asiatic acid (AA) is a pentacyclic triterpene in *Centella asiatica*, which has been widely used in China and in India [9]. Previous studies indicated that AA possessed a wide variety of pharmacological effects. AA has been reported to attenuate hepatic ischemia/reperfusion injury, protect against pressure overload-induced cardiac hypertrophy, and reduce cardiovascular remodeling in rats with L-NAME-induced hypertension [10–12]. AA has been reported to activate the cellular antioxidant system to protect rat hepatocyte against carbon tetrachloride-induced injury [13]. Moreover, in vitro

data suggested that AA could enhance the nuclear factor erythroid 2-related factor 2 (Nrf2) signal [14], which plays a key role against oxidative injury. However, the effects of AA on DOX-induced cardiotoxicity and the precise mechanisms still remain unclear. In this study, we determined the effect of AA on DOX-induced cardiotoxicity and investigate the underlying mechanisms. Results of our study indicate that DOX-induced cardiac injury can be reduced by AA administration with concomitant activation of protein kinase B (AKT).

2. Materials and Methods

2.1. Animals and Treatment. All animal studies followed the protocols approved by the Animal Care and Use Committee of Renmin Hospital of Wuhan University (Wuhan, China). All male C57BL/6 mice (male, age: 10 weeks, body weight: 24–26 g) were purchased from HFK Bioscience (Beijing, China). All the mice were housed in a specific pathogen-free facility. DOX (purity $\geq 98.5\%$ as determined by high-performance liquid chromatography) was purchased from Sigma-Aldrich (St. Louis, MO, USA). DOX (15 mg/kg) dissolved into 200 μl isotonic phosphate-buffered saline was injected intraperitoneally into the animals. And the mice in the control group received the same volume of vehicle as a control. The dose of DOX was determined according to a previous study [15]. One week before DOX injection, mice were orally given AA (10 mg/kg or 30 mg/kg) or the same volume vehicle for 2 weeks; this regimen provided one week of AA pretreatment prior to DOX exposure. The dose of AA used in this study was determined according to a previous study [10]. Alteration in body weight was recorded daily during the whole experimental period. Adenovirus vectors carrying dominant-negative AKT (Ad-dnAKT) and GFP (Ad-GFP) were generated by Vigene Biosciences (Rockville, MD, USA). To confirm whether AKT activation was involved in the protective effect of AA, the animals were intramyocardially injected with 1×10^9 viral genome particles (Ad-dnAKT or Ad-GFP) in the left ventricle at one week before DOX injection.

2.2. Echocardiography and Hemodynamics. Mice were anesthetized with 1.5% isoflurane, and cardiac function of mice after DOX injection was monitored by the Vevo 770 high-resolution microimaging system (VisualSonics, Toronto, Canada) with an RMV 707-B Scanhead (frequency 30 MHz, focal length 12.7 mm) as previously described [16, 17]. To detect hemodynamics, we used a microtip catheter transducer (Millar, SPR-1000) to insert into the right carotid artery and advanced into the left ventricle, and the obtained data were analyzed by the PowerLab software (ADInstruments, LabChart 5) [15].

2.3. Cardiac Injury Detection. Blood was collected from the retroorbital plexus after the mice were anesthetized at three days after DOX injection. After that, plasma samples were isolated via centrifuging whole blood at 1000 g for 15 min. Mouse cardiac troponin I (cTnI) was detected using an ELISA kit from Life Diagnostics, Inc. (PA, USA) according to the manufacturer's protocol. Creatine kinase (CK) and

lactate dehydrogenase (LDH) detection kits were purchased from Nanjing Jiancheng Institute of Biotechnology (Nanjing, China). Plasma CK and LDH detection were performed according to the manufacturer's protocol.

2.4. Determination of Lipid Peroxidation Levels. The hearts in the indicated groups were excised and homogenized in PBS containing 1% protease inhibitor and 1% phosphatase inhibitor (Thermo Scientific). The level of 4-hydroxynonenal (4-HNE) adduct was determined using a 4-HNE assay kit (Abcam, ab238538, Cambridge, UK). The level of 3-nitrotyrosine (3-NT) was detected using a 3-NT ELISA kit (Abcam, ab116691). For each determination, 100 mg of protein was used.

2.5. Detection of Cellular Antioxidant System. The activity of superoxide dismutase (SOD) and the levels of malondialdehyde (MDA) and glutathione (GSH) in the hearts were detected according to the manufacturer's instructions using kits obtained from Nanjing Jiancheng Institute of Biotechnology.

We detected intracellular ROS and superoxide using spectrophotometry with 2',7'-dichlorodihydrofluorescein diacetate (DCFH-DA) and dihydroethidium (DHE), respectively. In brief, the cells were reacted with 5 $\mu\text{mol/l}$ dyes for 25 mins at 37°C in the dark. After that, the fluorescence intensity of cells was determined using a microplate reader (BioTek Instruments, Inc., VT, USA).

2.6. Western Blot. Protein lysates were extracted from frozen heart samples using RIPA buffer supplemented with 1% protease inhibitor and 1% phosphatase inhibitor (Thermo Scientific). A BCA Protein Assay Kit was used to determine the protein concentrations of the heart samples. Thereafter, the proteins were electrophoresed by SDS-PAGE and then transferred to PVDF membranes [18]. After being blocked with 5% nonfat milk for 2 h at room temperature, these proteins were blotted with the following primary antibodies: rabbit anti-Nrf2 (Abcam, ab62352, 1:1000), rabbit anti-GAPDH (Abcam, ab181602, 1:5000), rabbit anti-Bax (Abcam, ab32503, 1:1000), rabbit anti-Bcl-2 (Abcam, ab185002, 1:500), rabbit anti-AKT (Abcam, ab8805, 1:1000), rabbit anti-p-AKT (Abcam, ab8933, 1:1000), rabbit anti-glycogen synthase kinase-3 (GSK-3) β (Abcam, ab32391, 1:1000), and rabbit anti-p-GSK3 β (Abcam, ab75814, 1:1000). After being incubated with a peroxidase-coupled secondary antibody, these bands were scanned with a BioSpectrum Gel Imaging System, respectively (UVP, California, USA).

2.7. Quantitative Real-Time PCR Analysis. We used TRIzol to extract total RNA from left ventricles. We used the PrimeScript RT Reagent Kit (#RR036B, TaKaRa, Otsu, Japan) to perform reverse transcriptional reactions. Quantitative real-time PCR was performed using the SYBR® Premix Ex Taq™ II Kit (#RR820DS, TaKaRa). GAPDH was used for normalization [19].

2.8. TUNEL and Caspase 3 Activity Assay. To detect cell apoptosis after DOX treatment, terminal deoxynucleotidyl transferase-mediated dUTP nick-end labeling (TUNEL)

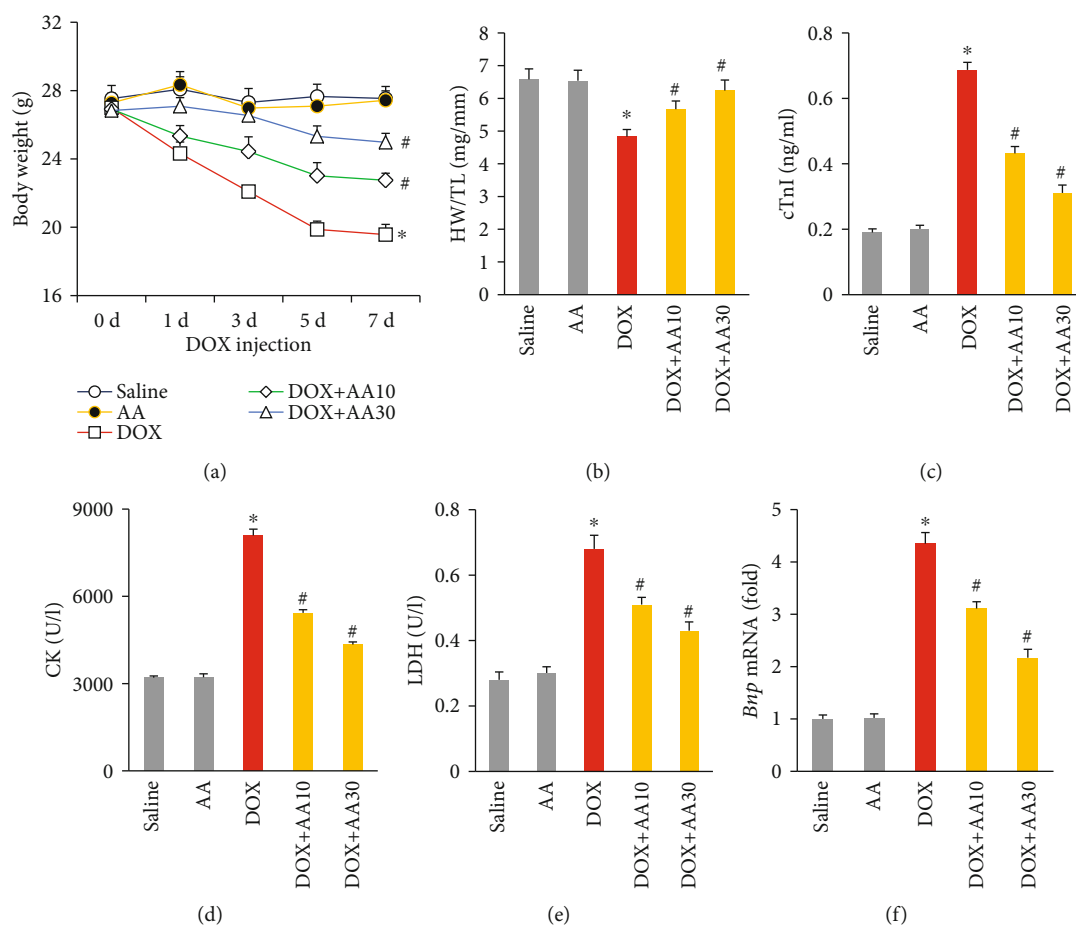


FIGURE 1: AA attenuated DOX-related cardiac injury in mice. (a) Body weight in the indicated groups ($n = 12$). (b) The ratio of heart weight to tibia length ($n = 12$). (c) The level of cTnI among groups ($n = 6$). (d, e) The plasma CK and LDH in the indicated groups ($n = 6$). (f) The mRNA level of *Bnp* in the hearts ($n = 6$). * $P < 0.05$ vs. saline group; # $P < 0.05$ vs. DOX group.

staining was performed using the In Situ Cell Death Detection Kit (Roche Applied Science) according to the manufacturer's instructions [20]. The activity of caspase 3 was assayed using the Caspase 3 Activity Assay Kit obtained from Beyotime Biotechnology (Beijing, China).

2.9. Cell Culture and Treatment. H9c2 cells were obtained from ATCC (CRL-1446) and cultured in DMEM supplemented with 10% FBS and 0.5% penicillin/streptomycin in a humidified atmosphere of 5% CO₂ and 95% O₂ at 37°C. To detect DOX-induced cell injury, H9c2 cells were seeded in 96-well plates (density: 1×10^5 cells/ml). After 48 hours, these cells were pretreated with series doses of AA for 4 hours, which were dissolved into 0.1% DMSO. After that, 0.1% DMSO- or AA-pretreated H9c2 cells were subsequently treated with DOX (5 μ g/ml) or PBS for 24 hours to detect cell viability using the CCK-8 kit (Dojindo, Rockville, MD). To detect alteration in oxidative markers, H9c2 cells were treated with DOX (5 μ g/ml) for 12 hours. To verify the hypothesis that the protection provided by AA was mediated by the activation of AKT, we used adenoviruses carrying sequences encoding a dominant-negative AKT. Briefly, at 48 hours after plating, H9c2 were infected with Ad-dnAKT or Ad-GFP at

50 MOI for 4 hours. After that, H9c2 cells were treated with AA (20 μ mol/l) or 0.1% DMSO in the presence of DOX or PBS treatment.

2.10. Data Analysis. All data are expressed as the mean \pm standard deviation (SD) and were analyzed by SPSS 22.0 software. We used unpaired Student's *t*-test to compare the differences between two groups. In our study, we used one-way analysis of variance (ANOVA) followed by the Tukey post hoc test for multiple group comparisons. A repeated-measures ANOVA was used to examine the alteration in body weight. $P < 0.05$ was considered statistically significant.

3. Result

3.1. AA Treatment Attenuated DOX-Induced Cardiac Injury. Exposure to DOX for 7 days significantly decreased body weight; however, AA-treated mice exhibited more body weight than vehicle-treated mice (Figure 1(a)). DOX treatment resulted in a decreased in the ratio of heart weight to tibia length (HW/TL), and this pathological change was attenuated by AA treatment in a dose-dependent manner (Figure 1(b)). Elevation of plasma cTnI after DOX injection

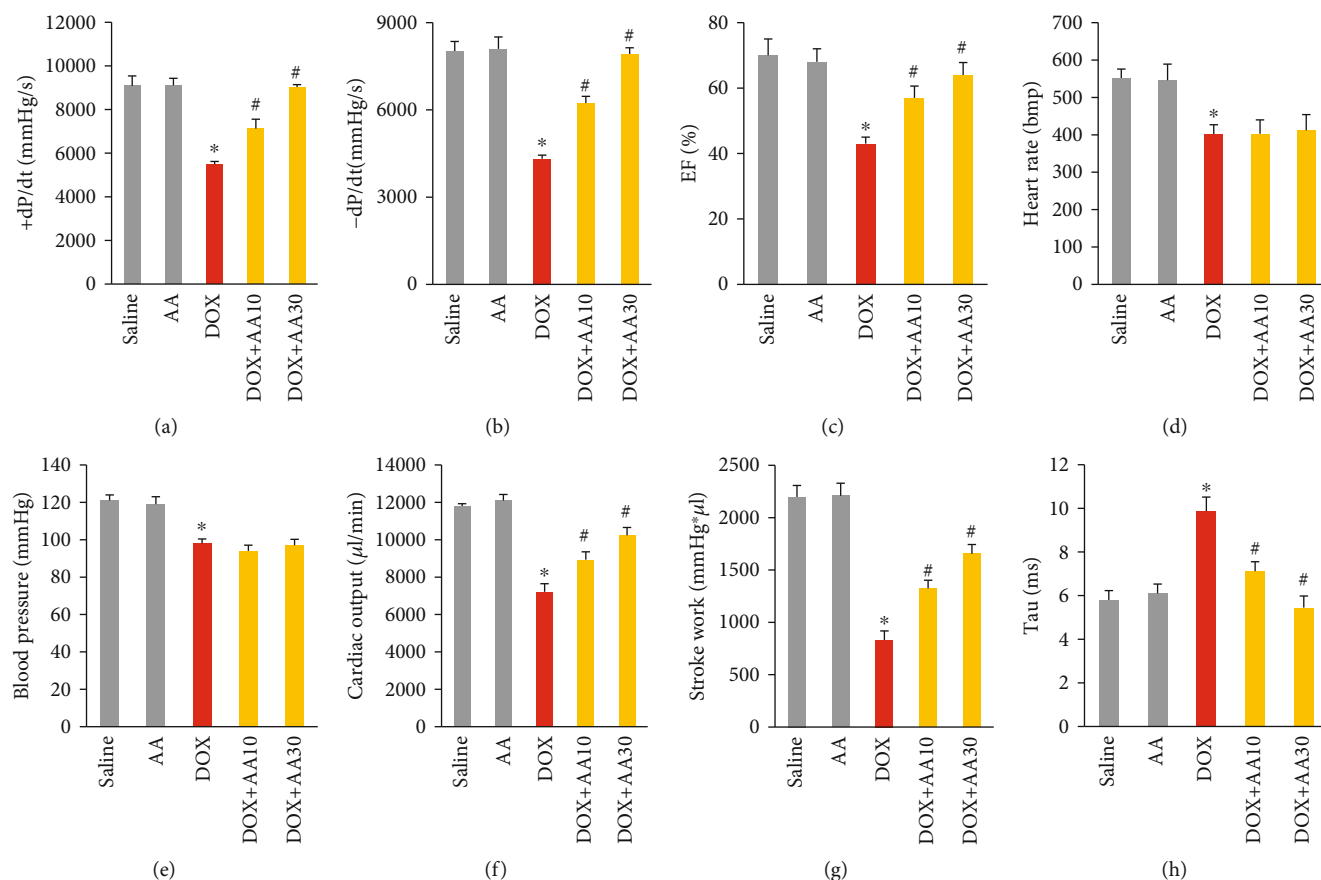


FIGURE 2: AA treatment improved cardiac function in mice. (a, b) $\pm dP/dt$ in the mice ($n = 8$). (c) EF in the indicated groups ($n = 8$). (d, e) Heart rate and blood pressure in the mice ($n = 8$). (f, g) Cardiac output and stroke work ($n = 8$). (h) Tau in the mice ($n = 8$). * $P < 0.05$ vs. saline group; # $P < 0.05$ vs. DOX group.

reflects cardiac injury and indicates irreversible cell loss. To evaluate the effect of AA on DOX-induced cardiotoxicity, we detected cTnI levels at three days after DOX injection and found that the release of cTnI induced by DOX injection was largely prevented by oral treatment of AA (Figure 1(c)). The plasma CK and LDH levels in DOX-treated mice were significantly increased compared with those in control groups, and these pathological upregulation could be attenuated by AA in a dose-dependent manner (Figures 1(d) and 1(e)). Further detection of BNP mRNA level suggested that AA also decreased the mRNA level of *Bnp* in DOX-treated mice (Figure 1(f)).

3.2. AA Treatment Improved Cardiac Function in Mice with DOX Treatment. Treatment of mice with DOX, 15 mg/kg intraperitoneally, led to a significant decrease in maximum first derivative of ventricular pressure with respect to time (+dP/dt), -dP/dt, and ejection fraction (EF). Oral treatment with AA (10 mg/kg or 30 mg/kg) daily significantly attenuated the DOX-induced changes in ventricular function (Figures 2(a)–2(c)). DOX induced the decrease in heart rate and blood pressure, and there was no difference between DOX and DOX+AA groups in the two parameters (Figures 2(d) and 2(e)). DOX injection induced reductions

in cardiac output, stroke work, and prolongation of relaxation time constants (Tau), and these effects were significantly attenuated after AA treatment (Figures 2(f)–2(h)).

3.3. AA Treatment Inhibited DOX-Induced Oxidative Injury in the Hearts. DOX treatment increased production of 4-HNE in the hearts, which is a highly reactive lipid peroxidation product. To determine the effect of AA on the oxidative injury in the heart after DOX injection, we detected 4-HNE level in the cardiac tissues. ELISA detection revealed that the levels of 4-HNE-adducts were significantly higher in the hearts of DOX-only-treated animals. AA treatment dose-dependently reduced the 4-HNE level in the hearts of DOX-treated animals (Figure 3(a)). AA treatment also decreased the level of 3-NT in the hearts of DOX-treated mice (Figure 3(b)). To further evaluate the lipid peroxidation, we detected the level of MDA and found that AA treatment could significantly decrease the level of MDA in a dose-dependent manner (Figure 3(c)). Of note, we found that AA (30 mg/kg)-treated mice had similar level of MDA as those treated with saline only (Figure 3(c)). DOX injection decreased SOD activity and GSH content; however, these pathological alterations were largely attenuated after AA treatment (Figures 3(d) and 3(e)). As shown in Figure 3(f),

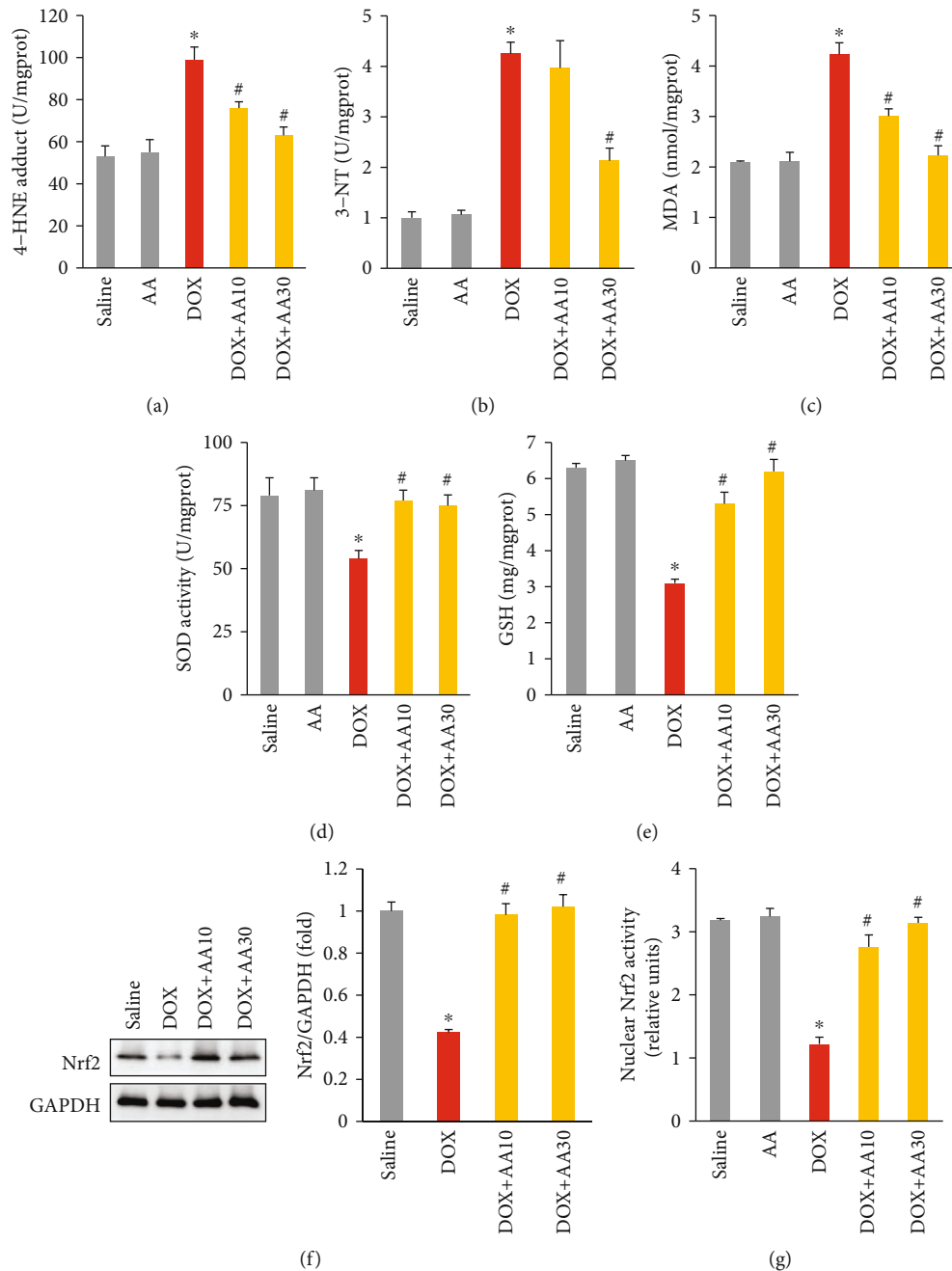


FIGURE 3: AA inhibited DOX-induced oxidative damage in mice. (a–c) The level of 4-HNE, 3-NT, and MDA in the mice ($n = 6$). (d) The activity of SOD ($n = 6$). (e) The GSH content ($n = 6$). (f, g) The Nrf2 protein expression and activity ($n = 6$). * $P < 0.05$ vs. saline group; # $P < 0.05$ vs. DOX group.

the expression levels of cardiac Nrf2 were obviously decreased in DOX groups compared with those in control groups. And AA treatment could restore cardiac Nrf2 to the normal level (Figure 3(f)). DOX treatment significantly lowered cardiac Nrf2 activity, and AA treatment almost increased active Nrf2 in nuclear extracts to the level of those in the hearts of mice with saline only (Figure 3(g)). Next, we examined a number of genes that are known to be regulated by Nrf2. Without DOX injection, AA increased the mRNA levels of *Sod2* and *Gpx4* at basal condition (Table 1). All the

examined transcript levels, including *Cat*, *Sod1*, *Sod2*, *Gpx1*, *Gpx4*, *Ho-1*, *Nqo-1*, *Gsta3*, and *Gsta4*, were decreased in the DOX-treated group. The reductions in these genes were largely reversed after AA treatment (Table 1).

3.4. AA Treatment Prevented DOX-Induced Cardiac Apoptosis In Vivo. As inflammation also plays a key role in DOX-mediated cardiac injury, next we detected cardiac inflammatory factors and found that there was no difference in the mRNA levels of *Tnf- α* and *Mcp-1* between DOX

TABLE 1: The genes that regulated by Nrf2.

Gene name	Control	AA30	DOX	DOX+AA30
<i>Cat</i>	0.88 ± 0.12	0.93 ± 0.09	0.32 ± 0.07*	0.73 ± 0.05 [#]
<i>Sod1</i>	2.16 ± 0.22	2.15 ± 0.34	0.64 ± 0.12*	1.89 ± 0.18 [#]
<i>Sod2</i>	3.17 ± 0.23	4.76 ± 0.21*	1.14 ± 0.11*	2.67 ± 0.24 [#]
<i>Gpx1</i>	0.94 ± 0.09	0.89 ± 0.07	0.45 ± 0.04*	0.78 ± 0.08 [#]
<i>Gpx4</i>	3.58 ± 0.22	4.54 ± 0.13*	2.14 ± 0.34*	3.13 ± 0.46 [#]
<i>HO-1</i>	0.25 ± 0.04	0.27 ± 0.05	0.09 ± 0.01*	0.18 ± 0.02 [#]
<i>NQO1</i>	0.58 ± 0.03	0.55 ± 0.05	0.32 ± 0.04*	0.43 ± 0.05 [#]
<i>Gsta3</i>	0.09 ± 0.01	0.08 ± 0.02	0.04 ± 0.01*	0.07 ± 0.01 [#]
<i>Gsta4</i>	2.44 ± 0.21	2.54 ± 0.43	1.02 ± 0.11*	2.54 ± 0.12 [#]

* $P < 0.05$ vs. control group; [#] $P < 0.05$ vs. DOX group.

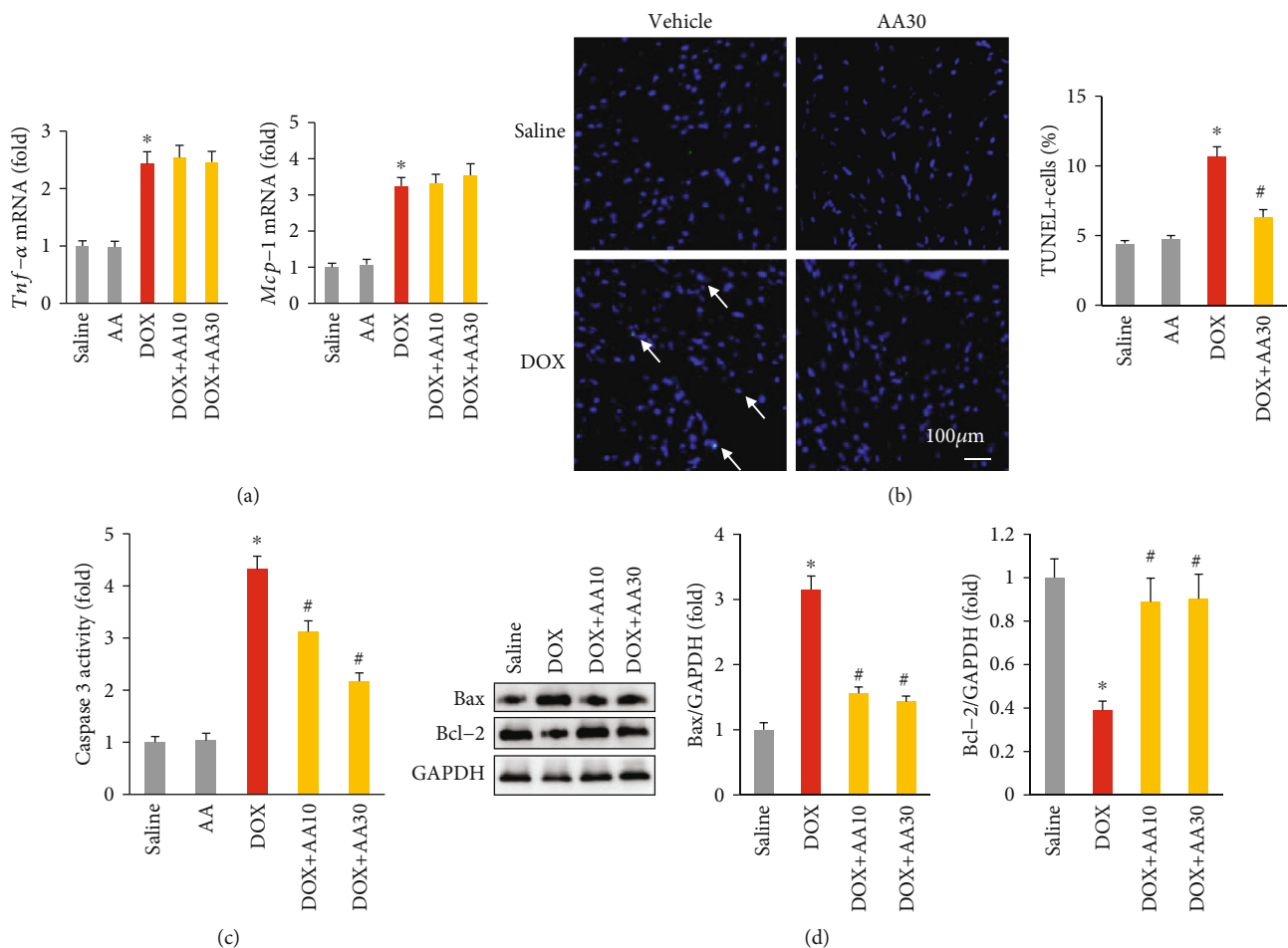


FIGURE 4: AA reduced cardiac apoptosis in DOX-treated mice. (a) The mRNA levels of inflammatory factors in the hearts ($n = 6$). (b) TUNEL staining ($n = 6$). (c) Caspase 3 activity in the hearts ($n = 6$). (d) The expression of Bax and Bcl-2 in the hearts ($n = 6$). * $P < 0.05$ vs. saline group; [#] $P < 0.05$ vs. DOX group.

and DOX+AA groups (Figure 4(a)). A DOX injection induced an increase in the number of TUNEL-positive cells in mice, and AA treatment could significantly decrease the number of TUNEL-positive cells (Figure 4(b)). Further detection of caspase 3 activity revealed that AA treatment

decreased the elevation of caspase 3 activity in DOX-treated mice (Figure 4(c)). Furthermore, AA treatment also significantly attenuated DOX-induced upregulation of Bax, as well as downregulation of Bcl-2, in the hearts (Figure 4(d)).

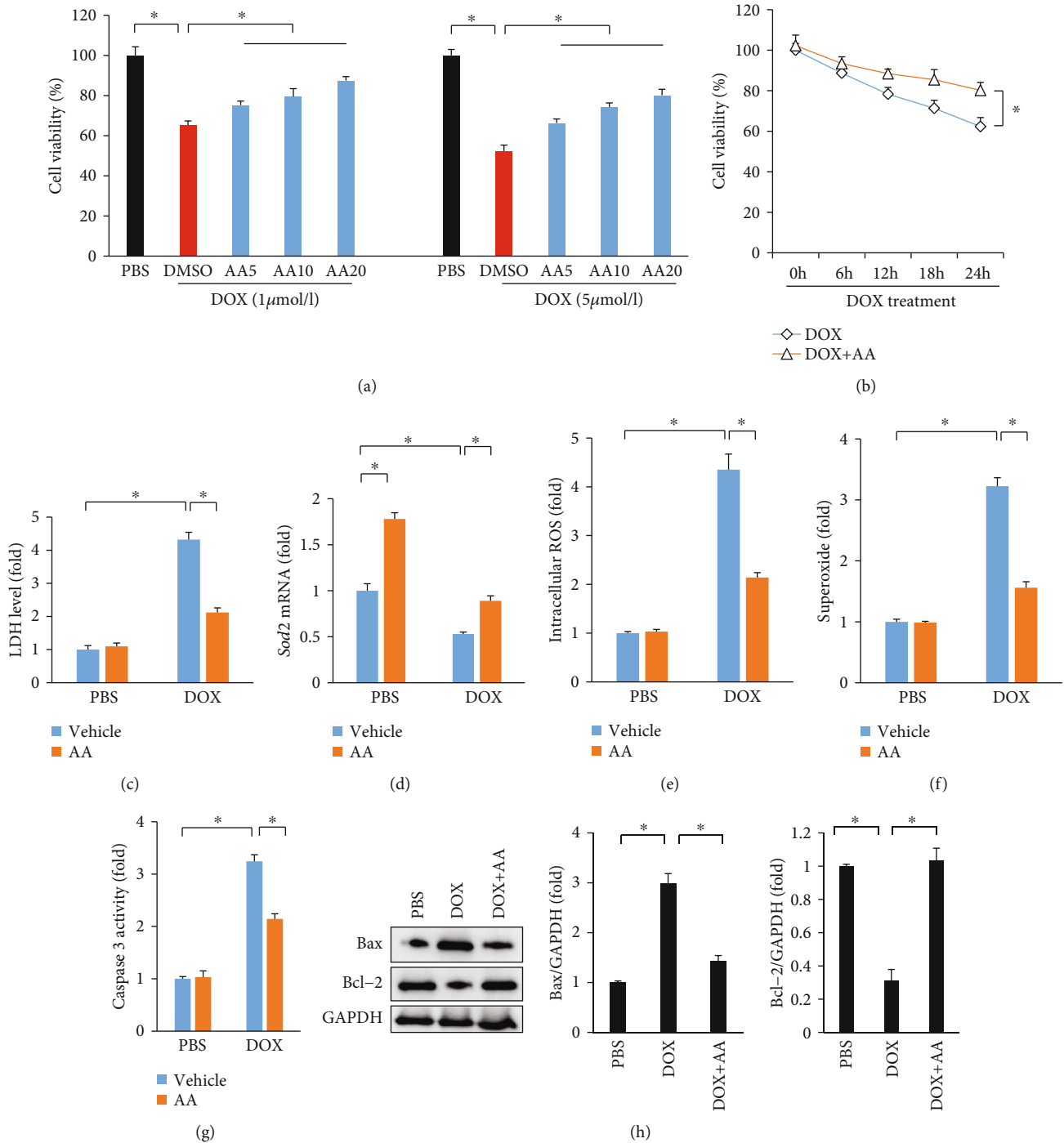


FIGURE 5: AA improved cell viability and reduced cell injury in vitro. (a, b) Cell viability after DOX treatment ($n = 6$). (c) LDH release after DOX ($n = 6$). (d) The mRNA level of *Sod2* ($n = 6$). (e, f) ROS and superoxide levels ($n = 6$). (g) Caspase 3 activity in the cells ($n = 6$). (h) The protein expression of Bax and Bcl-2. * $P < 0.05$ compared with the matched control.

3.5. AA Treatment Attenuated DOX-Induced Oxidative Stress and Cell Death in Cardiomyocytes. To further confirm the role of AA in DOX-mediated cardiomyocytes injury, we used H9c2 cardiomyocytes. Incubation of H9c2 cells with 1 or 5 μmol/l DOX for 24 hours resulted in significant decreases in cell viability, as measured by CCK-8 assay to $65.3 \pm 2.1\%$ or $52.3 \pm 2.8\%$, respectively. DOX-induced cell death was

prevented by 4 h of pretreatment (followed by constant incubation during the 24 hours of DOX exposure) with AA treatment (DOX 1 μmol/l+AA 20 μmol/l: $87.4 \pm 1.9\%$; DOX 5 μmol/l+AA 20 μmol/l: $80.1 \pm 2.0\%$) (Figure 5(a)). This result was further confirmed by the following finding that AA (20 μmol/l) improved cell viability in DOX-treated cardiomyocytes at different time points (Figure 5(b)). The

increased LDH levels in DOX-treated H9c2 cells were suppressed by AA treatment (Figure 5(c)). AA treatment also increased the mRNA level of *Sod2* in cells with DOX administration (Figure 5(d)). Compared with the PBS group, the intracellular ROS level and superoxide in cardiomyocytes in the DOX group was remarkably increased. However, AA treatment markedly decreased the ROS level in DOX-treated H9c2 cells (Figures 5(e) and 5(f)). Next, we detected the alteration in caspase 3 activity and found that AA treatment significantly suppressed the upregulation of caspase 3 activity (Figure 5(g)). AA treatment also suppressed upregulation of Bax and downregulation of Bcl-2 in H9c2 cardiomyocytes with DOX treatment (Figure 5(h)).

3.6. AA Exerted Protection against Cardiac Injury via Activation of AKT Signaling Pathway. Previous study demonstrated that AA protected against diabetes-related injury via activation of the AKT signaling pathway [21]. Next, we detected the alteration in the AKT signaling pathway. DOX significantly decreased the phosphorylation of AKT, and AA completely restored this to the normal level (Figure 6(a)). Further detection of downstream target also suggested that AA could promote the activation of the GSK3 β signaling pathway (Figure 6(a)). To further confirm this, we detected this signaling pathway in vitro and found that AA activated the AKT-GSK3 β pathway even without any stimuli (Figure 6(b)). To verify the protection of AA against cell injury which was mediated by activation of the AKT signaling pathway, we used adenoviruses to overexpress a plasmid carrying sequences encoding a dominant-negative AKT. AA treatment-induced Nrf2 upregulation was blocked by dominant-negative AKT infection (Figure 6(c)). As shown in Figures 6(d) and 6(e), AA lost its protection in cells infected with Ad-dnAKT, as indicated by cell viability and LDH level. Ad-dnAKT infection also completely abolishes the effect of AA on SOD activity and intracellular ROS by AA administration in vitro (Figures 6(e)–6(g)). AA treatment decreased caspase 3 activity, and this effect was reversed by a dominant-negative AKT (Figure 6(h)).

3.7. AA Had No Cardiac Protection in Mice Infected with Ad-dnAKT. To further confirm the role of AKT in AA-mediated protection, mice were subjected to intramyocardial injection of Ad-dnAKT. DOX-treated mice infected with Ad-dnAKT showed reversal of the inverse morphological changes during AA treatment, as reflected by HW/TL, cTnI level, *Bnp* mRNA level, EF, 4-HNE content, and caspase 3 activity (Figures 7(a)–7(f)).

4. Discussion

In the present study, we investigated the effect of AA on DOX-induced cardiotoxicity. Our results showed that AA treatment protected against DOX-induced cardiac injury, oxidative stress, and cell death without affecting inflammation. AA treatment activated the AKT signaling pathway in vivo and in vitro. AA lost its protection against oxidative stress and cell apoptosis after AKT inhibition. Thus, our

study indicated that AA activated the AKT signaling pathway to suppress DOX-related cardiac injury.

Currently, there were no specific strategies to prevent DOX-induced cardiotoxicity. Moreover, heart failure caused by DOX is standardly treated to alleviate symptoms and improve life quality. Finding a drug would be of great clinical significance. Indeed, several chemicals have been evaluated for their ability to attenuate DOX-related cardiac injury, but with little success [22, 23]. Lack of benefit of these drugs was largely attributed to low bioavailability of drugs or secondary reactions with other molecules [24]. Here, we tested AA and found AA obviously prevented DOX-induced cardiac injury, as reflected by increased body weight and HW/TL, and decreased levels of cardiac injury markers, including cTnI, CK, and LDH. Moreover, AA existed in a number of edible vegetables (including brown mustard and spinach) and dietary intake of AA increased their bioavailability in the heart [10, 25]. Additionally, in our study, we did not observe any adverse events in mice with AA (30 mg/kg) daily. Taken together, these data suggested that AA has the potential for the clinical use.

There were a lot of mitochondria which could produce ROS and relatively lower levels of oxidative enzymes, making the hearts more susceptible to oxidative stress. Previous studies have reported that DOX resulted in accumulation of ROS, which stimulated lipid peroxidation and formed highly reactive electrophile 4-HNE [26]. DOX treatment also depleted cardiac GSH levels [27]. In agreement with these studies, we also found that the levels of 4-HNE, 3-NT, and MDA in the hearts were increased. AA inhibited the pathological accumulation of these products. AA also improved SOD activity and increased cardiac GSH content. In vitro, we found that AA decreased the production of ROS and superoxide. Nrf2 is a transcription factor that regulates the expression of antioxidant and detoxification genes [28]. Next, we also found that AA treatment upregulated Nrf2 protein expression and activity in vivo. The reduced oxidative damage caused by AA treatment might partly explain the improved cardiac function in AA-treated mice.

Unexpectedly, we found that AA treatment unaffected the mRNA levels of inflammatory factors, which is inconsistent with a previous study that AA attenuated lipopolysaccharide-induced acute lung injury in mice by inhibiting inflammatory factor production [29]. This discrepancy might be explained by different disease models. Cell loss is one of the main reasons of the impaired cardiac function in DOX-treated mice. The data in our study indicated that AA treatment reduced cardiac apoptosis in mice and improved cardiomyocyte viability in vitro, which was in line with the previous study [11]. The protection provided by AA against DOX-related cardiac injury was also partly attributed to the prosurvival effect of AA.

Previous study has found that the AKT phosphorylation facilitated the translocation of Nrf2 [30]. It has been found that AA enhanced Nrf2 to protect HepG2 cells from oxidative damage through AKT activation [14]. Here, we found that AA increased phosphorylation of AKT in vivo and in vitro. Using dominant-negative AKT, we found that the activation of Nrf2 by AA was blocked. In line with this

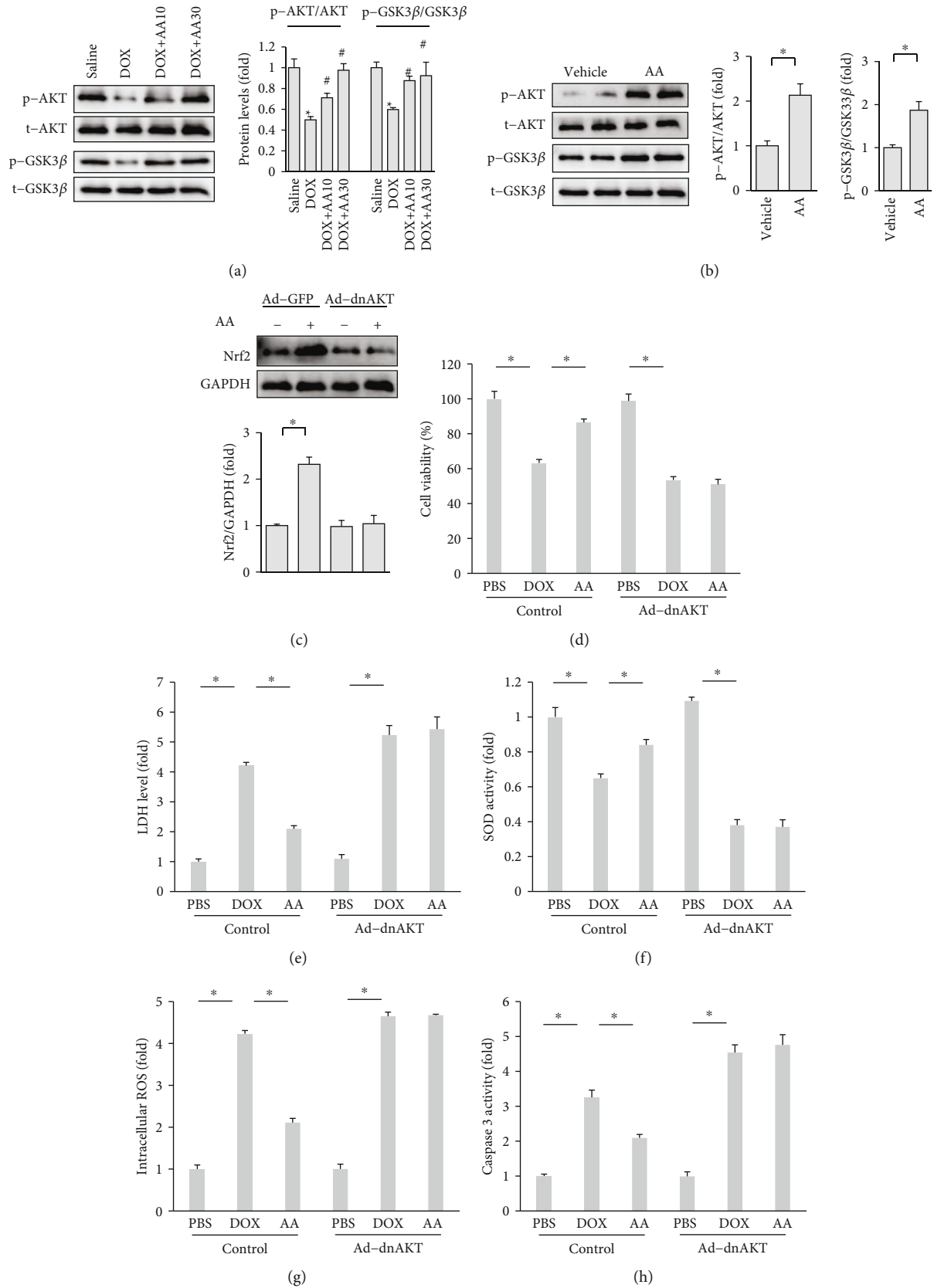


FIGURE 6: AA provided cardioprotection via the activation of AKT signaling pathway. (a, b) AKT and GSK3 β in the H9c2 cells ($n = 6$). (c) The protein expression of Nrf2 ($n = 6$). (d) Cell viability in the cells ($n = 6$). (e) LDH release in vitro ($n = 6$). (f) SOD activity after DOX treatment ($n = 6$). (g) ROS production in the cells ($n = 6$). (h) Caspase 3 activity ($n = 6$). * $P < 0.05$ compared with the matched control.

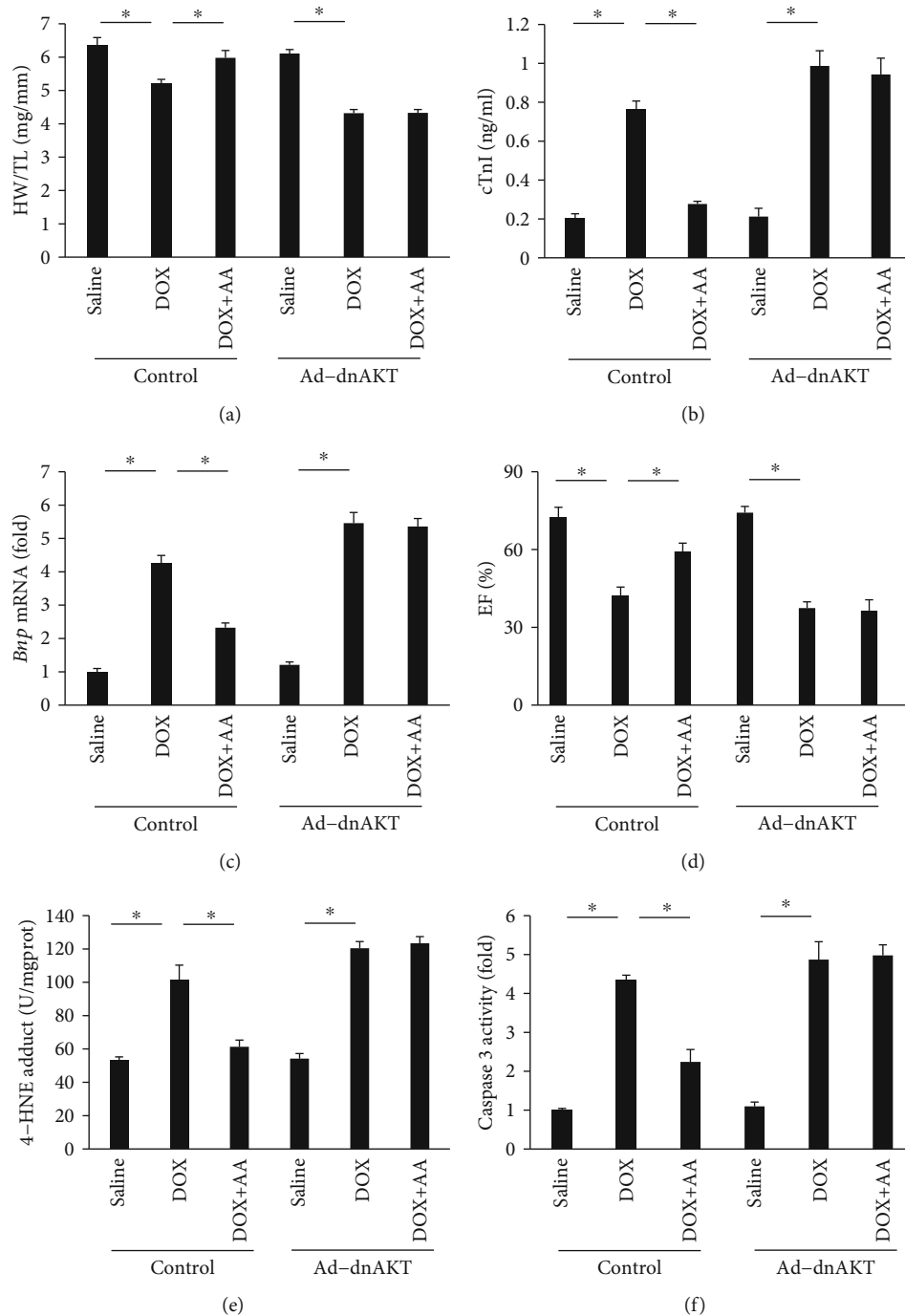


FIGURE 7: AA lost cardiac protection in the hearts after AKT inactivation. (a) The ratio of heart weight to tibia length ($n = 10$). (b) The level of cTnI among groups ($n = 6$). (c) The mRNA level of *Bnp* in the hearts ($n = 6$). (d) EF ($n = 8$). (e, f) The levels of 4-HNE and caspase 3 activity in the hearts ($n = 6$). * $P < 0.05$ compared with the matched control.

finding, we found that the inhibitory effects of AA on oxidative damage and cardiac apoptosis were offset by the infection of Ad-dnAKT. The improvement of cardiac function after AA treatment in DOX-treated animals was also lost after AKT inactivation. These data indicated that the protective effects of AA were mediated by AKT activation. However, there sounds a quite different voice that AA exerted anticancer effect in human ovarian cancer cells via suppres-

sion of AKT signaling [31]. This discrepancy could be explained by the different roles of AKT in different models.

In conclusion, we found that our results demonstrated that AA protected against DOX-induced cardiomyopathy via activating AKT signaling, which restored Nrf2 activation and suppressed oxidative damage to improve cardiac function. Our study may offer a new perspective on the treatment of DOX cardiac toxicity.

Data Availability

The data that support the findings of this study are available from the corresponding author upon reasonable request.

Conflicts of Interest

The authors declare that they have no conflicts of interest.

Acknowledgments

This work was supported by grants from the National Natural Science Foundation of China (No. 81700414).

References

- [1] C. Carvalho, R. Santos, S. Cardoso et al., "Doxorubicin: the good, the bad and the ugly effect," *Current Medicinal Chemistry*, vol. 16, no. 25, pp. 3267–3285, 2009.
- [2] C. E. Myers, W. P. McGuire, R. H. Liss, I. Ifrim, K. Grotzinger, and R. C. Young, "Adriamycin: the role of lipid peroxidation in cardiac toxicity and tumor response," *Science*, vol. 197, no. 4299, pp. 165–167, 1977.
- [3] T. Force and Y. Wang, "Mechanism-based engineering against anthracycline cardiotoxicity," *Circulation*, vol. 128, no. 2, pp. 98–100, 2013.
- [4] J. D. Groarke and A. Nohria, "Anthracycline cardiotoxicity: a new paradigm for an old classic," *Circulation*, vol. 131, no. 22, pp. 1946–1949, 2015.
- [5] L. C. M. Kremer, H. J. H. van der Pal, M. Offringa, E. C. van Dalen, and P. A. Voûte, "Frequency and risk factors of subclinical cardiotoxicity after anthracycline therapy in children: a systematic review," *Annals of Oncology*, vol. 13, no. 6, pp. 819–829, 2002.
- [6] L. Rochette, C. Guenancia, A. Gudjoncik et al., "Anthracyclines/trastuzumab: new aspects of cardiotoxicity and molecular mechanisms," *Trends in Pharmacological Sciences*, vol. 36, no. 6, pp. 326–348, 2015.
- [7] R. M. Damiani, D. J. Moura, C. M. Viau, R. A. Caceres, J. A. P. Henriques, and J. Saffi, "Pathways of cardiac toxicity: comparison between chemotherapeutic drugs doxorubicin and mitoxantrone," *Archives of Toxicology*, vol. 90, no. 9, pp. 2063–2076, 2016.
- [8] L. Chaiswing, M. P. Cole, D. K. St. Clair, W. Ittarat, L. I. Szveda, and T. D. Oberley, "Oxidative damage precedes nitrate damage in adriamycin-induced cardiac mitochondrial injury," *Toxicologic Pathology*, vol. 32, no. 5, pp. 536–547, 2004.
- [9] S. M. Kamble and C. R. Patil, "Asiatic acid ameliorates doxorubicin-induced cardiac and hepato-renal toxicities with Nrf2 transcriptional factor activation in rats," *Cardiovascular Toxicology*, vol. 18, no. 2, pp. 131–141, 2018.
- [10] Z. G. Ma, J. Dai, W. Y. Wei et al., "Asiatic acid protects against cardiac hypertrophy through activating AMPK α signalling pathway," *Cardiovascular Toxicology*, vol. 12, no. 7, pp. 861–871, 2016.
- [11] Y. Lu, H. Kan, Y. Wang et al., "Asiatic acid ameliorates hepatic ischemia/reperfusion injury in rats via mitochondria-targeted protective mechanism," *Toxicology and Applied Pharmacology*, vol. 338, pp. 214–223, 2018.
- [12] S. Bunbupha, P. Prachaney, U. Kukongviriyapan, V. Kukongviriyapan, J. U. Welbat, and P. Pakdeechote, "Asiatic acid alleviates cardiovascular remodelling in rats with L-NAME-induced hypertension," *Clinical and Experimental Pharmacology and Physiology*, vol. 42, no. 11, pp. 1189–1197, 2015.
- [13] M. K. Lee, S. H. Kim, H. Yang et al., "Asiatic acid derivatives protect primary cultures of rat hepatocytes against carbon tetrachloride-induced injury via the cellular antioxidant system," *Natural Product Communications*, vol. 4, no. 6, pp. 765–768, 2009.
- [14] Z. Qi, X. Ci, J. Huang et al., "Asiatic acid enhances Nrf2 signaling to protect HepG2 cells from oxidative damage through Akt and ERK activation," *Biomedicine & Pharmacotherapy*, vol. 88, pp. 252–259, 2017.
- [15] Y. P. Yuan, Z. G. Ma, X. Zhang et al., "CTRP3 protected against doxorubicin-induced cardiac dysfunction, inflammation and cell death via activation of Sirt1," *Journal of Molecular and Cellular Cardiology*, vol. 114, pp. 38–47, 2018.
- [16] C. Ni, P. Ma, R. Wang et al., "Doxorubicin-induced cardiotoxicity involves IFN γ -mediated metabolic reprogramming in cardiomyocytes," *The Journal of Pathology*, vol. 247, no. 3, pp. 320–332, 2019.
- [17] Z. G. Ma, J. Dai, Y. P. Yuan et al., "T-bet deficiency attenuates cardiac remodelling in rats," *Basic Research in Cardiology*, vol. 113, no. 3, p. 19, 2018.
- [18] Z. G. Ma, Y. P. Yuan, X. Zhang et al., "C1q-tumour necrosis factor-related protein-3 exacerbates cardiac hypertrophy in mice," *Cardiovascular Research*, vol. 115, no. 6, pp. 1067–1077, 2019.
- [19] Z. G. Ma, Y. P. Yuan, S. C. Xu et al., "CTRP3 attenuates cardiac dysfunction, inflammation, oxidative stress and cell death in diabetic cardiomyopathy in rats," *Diabetologia*, vol. 60, no. 6, pp. 1126–1137, 2017.
- [20] X. Zhang, C. Hu, C. Y. Kong et al., "FNDC5 alleviates oxidative stress and cardiomyocyte apoptosis in doxorubicin-induced cardiotoxicity via activating AKT," *Cell Death & Differentiation*, vol. 27, no. 2, pp. 540–555, 2020.
- [21] V. Ramachandran and R. Saravanan, "Glucose uptake through translocation and activation of GLUT4 in PI3K/Akt signaling pathway by asiatic acid in diabetic rats," *Human & Experimental Toxicology*, vol. 34, no. 9, pp. 884–893, 2015.
- [22] M. Štěrba, O. Popelová, A. Vávrová et al., "Oxidative stress, redox signaling, and metal chelation in anthracycline cardiotoxicity and pharmacological cardioprotection," *Antioxidants & Redox Signaling*, vol. 18, no. 8, pp. 899–929, 2013.
- [23] P. Singh, R. Sharma, K. McElhanon et al., "Sulforaphane protects the heart from doxorubicin-induced toxicity," *Free Radical Biology and Medicine*, vol. 86, pp. 90–101, 2015.
- [24] H. J. Forman, K. J. A. Davies, and F. Ursini, "How do nutritional antioxidants really work: Nucleophilic tone and parhormesis versus free radical scavenging in vivo," *Free Radical Biology and Medicine*, vol. 66, pp. 24–35, 2014.
- [25] M. C. Yin, M. C. Lin, M. C. Mong, and C. Y. Lin, "Bioavailability, distribution, and antioxidative effects of selected triterpenes in mice," *Journal of Agricultural and Food Chemistry*, vol. 60, no. 31, pp. 7697–7701, 2012.
- [26] Y. Zhao, S. Miriyala, L. Miao et al., "Redox proteomic identification of HNE-bound mitochondrial proteins in cardiac tissues reveals a systemic effect on energy metabolism after doxorubicin treatment," *Free Radical Biology and Medicine*, vol. 72, pp. 55–65, 2014.

- [27] S. E. al-Harhi, O. M. Alarabi, W. S. Ramadan et al., "Amelioration of doxorubicin-induced cardiotoxicity by resveratrol," *Molecular Medicine Reports*, vol. 10, no. 3, pp. 1455–1460, 2014.
- [28] J. Li, T. Ichikawa, L. Villacorta et al., "Nrf2 protects against maladaptive cardiac responses to hemodynamic stress," *Arteriosclerosis, Thrombosis, and Vascular Biology*, vol. 29, no. 11, pp. 1843–1850, 2009.
- [29] Z. Li, X. Xiao, and M. Yang, "Asiatic acid inhibits lipopolysaccharide-induced acute lung injury in mice," *Inflammation*, vol. 39, no. 5, pp. 1642–1648, 2016.
- [30] A. M. Benson, M. J. Hunkeler, and P. Talalay, "Increase of NAD(P)H:quinone reductase by dietary antioxidants: possible role in protection against carcinogenesis and toxicity," *Proceedings of the National Academy of Sciences of the United States of America*, vol. 77, no. 9, pp. 5216–5220, 1980.
- [31] L. Ren, Q. X. Cao, F. R. Zhai, S. Q. Yang, and H. X. Zhang, "Asiatic acid exerts anticancer potential in human ovarian cancer cells via suppression of PI3K/Akt/mTOR signalling," *Pharmaceutical Biology*, vol. 54, no. 11, pp. 2377–2382, 2016.

Research Article

DHA Supplementation Attenuates MI-Induced LV Matrix Remodeling and Dysfunction in Mice

I. Habicht,¹ G. Mohsen,² L. Eichhorn,² S. Frede,² C. Weisheit,² T. Hilbert ,² H. Treede,³ E. Güresir,⁴ O. Dewald,⁵ G. D. Duerr ,³ and M. Velten ²

¹Department of Orthopaedics and Trauma Surgery, University Hospital Bonn, Germany

²Department of Anesthesiology and Intensive Care Medicine, University Hospital Bonn, Germany

³Department of Cardiac Surgery, University Hospital Bonn, Germany

⁴Department of Neurosurgery, University Hospital Bonn, Germany

⁵Department of Cardiac Surgery, University Medical Center Oldenburg, Germany

Correspondence should be addressed to G. D. Duerr; dduerr@uni-bonn.de and M. Velten; markus.velten@ukbonn.de

Received 2 February 2020; Revised 24 March 2020; Accepted 7 April 2020; Published 14 May 2020

Guest Editor: Lynette K. Rogers

Copyright © 2020 I. Habicht et al. This is an open access article distributed under the Creative Commons Attribution License, which permits unrestricted use, distribution, and reproduction in any medium, provided the original work is properly cited.

Objective. Myocardial ischemia and reperfusion (I/R) injury is associated with oxidative stress and inflammation, leading to scar development and malfunction. The marine omega-3 fatty acids (ω -3 FA), eicosapentaenoic acid (EPA), and docosahexaenoic acid (DHA) are mediating cardioprotection and improving clinical outcomes in patients with heart disease. Therefore, we tested the hypothesis that docosahexaenoic acid (DHA) supplementation prior to LAD occlusion-induced myocardial injury (MI) confers cardioprotection in mice. **Methods.** C57BL/6N mice were placed on DHA or control diets (CD) beginning 7 d prior to 60 min LAD occlusion-induced MI or sham surgery. The expression of inflammatory mediators was measured via RT-qPCR. Besides FACS analysis for macrophage quantification and subtype evaluation, macrophage accumulation as well as collagen deposition was quantified in histological sections. Cardiac function was assessed using a pressure-volume catheter for up to 14 d. **Results.** DHA supplementation significantly attenuated the induction of peroxisome proliferator-activated receptor- α (PPAR- α) (2.3 ± 0.4 CD vs. 1.4 ± 0.3 DHA) after LAD occlusion. Furthermore, TNF- α (4.0 ± 0.6 CD vs. 1.5 ± 0.2 DHA), IL-1 β (60.7 ± 7.0 CD vs. 11.6 ± 1.9 DHA), and IL-10 (223.8 ± 62.1 CD vs. 135.5 ± 38.5 DHA) mRNA expression increase was diminished in DHA-supplemented mice after 72 h reperfusion. These changes were accompanied by a less prominent switch in α/β myosin heavy chain isoforms. Chemokine mRNA expression was stronger initiated (CCL2 6 h: 32.8 ± 11.5 CD vs. 78.8 ± 13.6 DHA) but terminated earlier (CCL2 72 h: 39.5 ± 7.8 CD vs. 8.2 ± 1.9 DHA; CCL3 72 h: 794.3 ± 270.9 CD vs. 258.2 ± 57.8 DHA) in DHA supplementation compared to CD mice after LAD occlusion. Correspondingly, DHA supplementation was associated with a stronger increase of predominantly alternatively activated Ly6C-positive macrophage phenotype, being associated with less collagen deposition and better LV function (EF 14 d: 17.6 ± 2.6 CD vs. 31.4 ± 1.5 DHA). **Conclusion.** Our data indicate that DHA supplementation mediates cardioprotection from MI via modulation of the inflammatory response with timely and attenuated remodeling. DHA seems to attenuate MI-induced cardiomyocyte injury partly by transient PPAR- α downregulation, diminishing the need for antioxidant mechanisms including mitochondrial function, or α - to β -MHC isoform switch.

1. Introduction

Coronary heart disease (CHD) is a significant health concern in the western world with increasing prevalence and the leading cause of death in Europe, accounting for €60 billion in health care costs annually [1]. Timely coronary reperfusion

using either percutaneous coronary intervention (PCI) or thrombolytic therapy is the most effective strategy for limiting infarct size, preserving left-ventricular (LV) function, and therefore preventing myocardial injury and the development of heart failure [2]. Despite early onset therapies, in hospital mortality has risen up to 14% and productivity loss

accounts for 38% of CHD-related health care costs [1]. Therefore, novel therapeutic approaches are required to reduce MI size, preserve LV function, and improve clinical outcomes after MI.

Although an early intervention reestablishing coronary perfusion is essential for myocardial salvage after MI, reperfusion itself triggers a further injury [3]. This so-called ischemia/reperfusion (I/R) injury is an inherent response to the restoration of blood flow involving numerous mechanisms including the increased generation of reactive oxygen species (ROS), acute calcium overload of cardiomyocytes, and opening of the mitochondrial permeability transition pore (MPTP), leading to uncoupled oxidative phosphorylation and thus contractile dysfunction. These insults further aggravate myocardial remodeling after MI, through increased generation of proinflammatory and proapoptotic molecules resulting in myocyte death, collagen deposition, and scar formation, exacerbating the development of heart failure [4, 5]. In summary, reperfusion itself induces additional cardiac damage that is responsible for up to 50% of infarct size, making this cascade of events a viable target for therapeutic interventions [3]. Currently, there is no effective clinical therapy preventing the deleterious consequences of myocardial I/R injury. Therefore, attenuating I/R injury is an important target for cardioprotection and a promising therapeutic approach to improve clinical outcomes after an acute MI.

Inflammation is pivotal for the development of heart failure, and an unrestricted inflammatory response is associated with worse prognosis after MI [6, 7]. Furthermore, excessive increases in inflammatory mediators, e.g., cytokines, have been shown to induce myocardial injury, including impaired cardiomyocyte contractility and excessive myocardial remodeling [8–11]. Myocardial reperfusion after ischemia generates an imbalance between reactive oxygen species (ROS) and the capacity of cells to defend against them, leading to increased ROS generation. The inducible transcription factor peroxisome proliferator-activated receptor- γ (PPAR- γ) regulates various cardiovascular processes and reduces I/R injury-induced cardiac inflammation and ROS generation [12]. Elevated ROS levels consume and surpass the antioxidant capacity of the injured myocardium, significantly contributing to oxidative stress generation and affecting protein function, resulting in myocardial damage with morphological and functional abnormalities [13]. In cardiac I/R injury, significant sources of ROS are inflammation-induced phagocyte-type NAD (P) H oxidase and mitochondrial metabolism-associated fatty acid oxidation [14, 15]. Excessive ROS generation opens the mitochondrial permeability transition pore (MPTP) further contributing to myocardial injury and contractile dysfunction. Mitochondrial uncoupling proteins (UCP) have been shown to protect cardiomyocytes from ROS-induced cell death and heart failure. Furthermore, UCP overexpression has been reported as an adaptive mechanism against oxidative stress in various cardiac pathologies. ROS overproduction and oxidative stress play key roles for the development of cardiac injury, promoting complications of cardiac reperfusion [16]. Thus, preventing I/R injury-induced ROS generation is an important target

for the development of novel strategies to preserve cardiac function after MI.

Polyunsaturated fatty acids (PUFAs) are a group of metabolic active lipid molecules. The marine omega-3 fatty acids (ω -3 FA), eicosapentaenoic acid (EPA), and docosahexaenoic acid (DHA) are beneficial for health outcomes [17], mediating cardiovascular benefits in preclinical studies and improve clinical outcomes in patients with MI, potentially through modulation of inflammation and antioxidant effects [18, 19]. Long-lasting ω -3 FA intake is reported to reduce mortality up to 45% and morbidity (myocardial infarction, arrhythmia) in adult patients with cardiovascular disease [20]. Consequently, supplementation is recommended for patients with prevalent CHD such as a recent MI [21, 22]. DHA is either obtained from diet but can also be synthesized from EPA [23, 24]. Thus, various investigations used combinations of DHA and EPA to investigate ω -3 FA effects on cardiac health. The OMEGA-REMODEL trial proved that high-dose DHA/EPA supplementation beginning at the onset of MI improved LV function after 6 months [18]. However, underlying mechanisms, signaling pathways, and effectors of DHA/EPA-mediated prevention of I/R injury-induced cardiac dysfunction in acute MI remain to be revealed [24, 25]. DHA/EPA modulate numerous receptors and decrease the generation of intracellular reactive oxygen species with a subsequent diminished activation of redox-sensitive transcription factors through its incorporation into cellular membranes. In addition to inflammatory resolution, DHA has numerous effects that include oxygen consumption, mitochondrial energy metabolism, contractile function, calcium signaling, and ROS generation, potentially protecting the cardiovascular system [26–28].

Previous attempts to translate cardioprotective strategies for I/R injury from the experimental into the clinical setting have not been successful, potentially due to an incomplete understanding of the underlying molecular mechanisms including inflammation, oxidative stress, calcium overload, mitochondrial dysfunction, and different cell types affected [29]. However, most approaches targeted just one mechanism, but several of these mechanisms interact. Therefore, understanding these interactions and targeting multiple mechanisms are essential to prevent I/R injury-induced cardiac dysfunction. DHA and EPA interact with many mechanisms that are associated with the development of I/R injury-induced cardiac dysfunction including inflammation, ROS generation, matrix remodeling, and mitochondrial metabolism [26]. Therefore, ω -3 FA are promising therapeutics and understanding its interactions in myocardial I/R injury may help to reduce infarct size, prevent the development of LV dysfunction, and improve clinical outcomes after MI.

2. Materials and Methods

2.1. Animal Protocol. All animals were handled according to the animal protocol and to the EU Directive 2010/63/EU for animal research. Experimental procedures have been approved by the government animal care and use committee “Landesamt für Natur, Umwelt und Verbraucherschutz NRW” (50.203.2-BN 43, 28/01). 20–25 g and 10–12 weeks

old male C57BL/6 mice were purchased from Charles River (Sulzfeld, Germany). To limit transportation and social stress, mice were housed at our facility for at least 7 days prior to the experiments. Animals were placed in plastic cages filled with autoclaved bedding in a filtered flow cage rack on a 12-hour light/dark cycle with free access to water and standard rodent chow. All mice were sacrificed by cervical dislocation at the end of the experiment.

2.2. Closed Chest Mouse Model of LAD Occlusion. Before surgery perioperative analgesia was performed using carprofen 5 mg/kg s.c. and Temgesic 0.1 mg/kg s.c. Anesthesia was then induced with 3% isoflurane (Forene®, Abbott) and maintained with 0.8% isoflurane in 100% O₂. Left parasternal thoracotomy was performed for implantation of the ligature (8-0 Prolene suture, Ethicon, Norderstedt, Germany) around the left descending coronary artery (LAD). The suture ends were threaded through a sterile PE10 tube (Becton Dickinson, Franklin Lakes, NJ, USA), exteriorized through the thoracic wall, and stored subcutaneously [30]. After chest closure, cefuroxime suspension was injected i.p. (50 mg/kg, Zinacef; Bristol-Myers Squibb, Munich, Germany) for antibiotic prophylaxis. Mice were allowed to recover for 7–10 days from initial surgery intervention.

2.3. Induction of Myocardial Ischemia and Reperfusion (I/R). Myocardial ischemia was induced under the same analgesic and anesthetic measures as described above. The LAD ligature ends were connected to heavy metal picks, and LAD occlusion for 60 min was achieved by pulling the picks apart as described previously [30]. Myocardial ischemia was confirmed by visualization of ST segment elevation in EKG lead II of Einthoven. The hearts were reperfused after removal of the LAD ligature. Persistence of ST-segment elevation confirmed myocardial infarction. After reperfusion, the hearts were excised at different time points, dissected free from the atria and great vessels, and rinsed in ice-cold cardioplegic solution.

2.4. Experimental Groups and Protocols. To evaluate whether ω -3 FA pretreatment associated mechanisms mediating cardioprotection for I/R injury-induced LV dysfunction, after implantation of the LAD ligature, C57BL/6N mice were randomly distributed to receive either DHA or control diet (CD) beginning 7 days prior to I/R and for the duration of the experiment. DHA and control diets were identical with the exception of the composition of the ω -3 FA, and 7 days of diet supplementation has shown to increase DHA concentrations and attenuate inflammation and oxidation in other pathologies [31–33]. Linoleic acid was used as a source for ω -6 FA, and amounts were similar in CD and DHA diets. However, total ω -3 FA contents were similar in control and DHA diets, but 37% ω -3 FA content in the DHA diet was DHA and the remaining half was linolenic acid from flaxseed oil, while in the control diet, the entire amount of ω -3 FA was linolenic acid (Table 1).

A purified diet with higher linolenic acid concentrations that is metabolized to arachidonic acid was chosen to isolate

TABLE 1: Diet composition.

PUFA	Control diet	DHA diet
Linoleic (18 : 2)	3.00 g/kg	2.9 g/kg
Linolenic (18 : 3)	0.7 g/kg	0.43 g/kg
DHA (22 : 6)	0.0 g/kg	0.26 g/kg

the effects of preformed DHA supplementation from those of the precursor α -linolenic acid and to avoid variability in standard chows [34].

2.4.1. In Vivo Functional Analysis Using Millar® Pressure-Volume Left Heart Catheter. Anesthetized mice (0.8% isoflurane) were ventilated, and the jugular vein was cannulated with microenathane-033 tubing for hypertonic saline administration. After warming, the conductance catheter probe was advanced into the LV through the right carotid artery. Data collection was initiated after baseline stabilization. The Millar catheter uses conductance to determine relative volume units or “RVU.” Once RVU’s are measured, we then use a known volume of blood from the individual mouse using mock-up cylinders with known volumes to convert to a known volume [35]. Furthermore, inferior vena cava occlusion was used to measure the end-systolic pressure-volume relationship (ESPVR) and end-diastolic pressure-volume relationship (EDPVR), which are the index of ventricular filling pressures.

2.4.2. Immunohistochemistry. For immunohistochemistry, Vectastain Elite ABC kits and diaminobenzidine (AXXORA, Lörrach, Germany) were used. Cell density was described as cells/mm², as previously reported and evaluated by a histological technician blinded for group assignment [31–33]. For mouse-derived antibodies, the mouse-on-mouse (M.O.M) immunodetection kit (AXXORA) was used. MAC-2 rat anti-mouse antibody (clone 3/38) was used for macrophages (Cedarlane, Ontario, Canada).

2.4.3. Collagen Content. Excised hearts were fixated in 10% buffered zinc-formalin followed by paraffin embedding. 5 μ m sections from the level of the papillary muscle insertion were stained with hematoxylin and eosin (HE) or picosirius red (SR), as previously described [36]. Quantitative analysis was accomplished by light microscopy with a video-image analyzer. Planimetric evaluation of collagen was performed on one section, including all four sites of the left ventricular myocardium, each at 100x magnification. Data was given as a percentage of the total left ventricular area. Collagen-stained vessels and pericardium were excluded.

2.4.4. Flow Cytometry Analyses (FACS). LV tissue was homogenized, inflammatory cells were labeled with fluorescence AB, and single-cell suspensions from the heart were generated as previously described [37]. The following antibodies from Thermo Fisher and BioLegend (San Diego, CA, USA) were used: CD45 (AFS98), F4/80 (BM-8), Gr1 (RB6-8C5), CD11c (N418), CD4 (RM4-5), CD8 (53-6.4), and B220 (RA3-6B2). In addition, the Annexin V-FITC Apoptosis Detection Kit (Thermo Fisher) was used according to the manufacturer’s protocol. We performed flow cytometry on a

FACS-Canto II, LSR II, and Fortessa (BD Biosciences, Heidelberg, D), and data was analyzed with FlowJo software (TreeStar, Ashland, OR, USA).

2.4.5. Gene Expression Analysis. Gene expression was measured on a transcriptional level using Taqman® real-time quantitative RT-qPCR. FAM-TAMRA-linked customized primers were used in an ABI Prism 7900HT Sequence Detection System and SDS2.4 software (Applied Biosystems/Life Technologies, Karlsruhe, Germany). The mRNA expression was related to shams and GAPDH using the comparative $\Delta\Delta C_t$ -method [38].

2.4.6. Statistical Analysis. Normal distribution was tested, and data was presented as mean \pm SEM. Statistical analysis was performed by two-way ANOVA and Bonferroni post hoc testing (PRISM 5.1; GraphPad, La Jolla, CA, USA). $P < 0.05$ was considered statistically significant.

3. Results

3.1. DHA Supplementation Attenuates MI-Induced Systolic and Diastolic Dysfunction. To evaluate whether DHA pretreatment attenuates the development of MI-induced LV dysfunction, we examined the pressure-volume parameters of LV function in CD- and DHA-pretreated mice 14 days after 60 min of LAD occlusion-induced myocardial infarction (MI). Left ventricular end-systolic pressure (LVESP) was not different between sham or MI groups, regardless of DHA or CD pretreatment (Figure 1(a)). However, left ventricular end-diastolic pressure (LVEDP) significantly increased in CD mice 14 days after MI, compared to respective sham. Nevertheless, LVEDP remained at sham levels in DHA-supplemented mice and was significantly lower compared to CD mice 14 days after MI (Figure 1(b)). Mice with surgical MI had poorer ejection fraction (EF), but DHA pretreatment improved EF in the MI group compared to CD (Figure 1(c)). Peak pressure decline (dP/dt_{\min}) was reduced in CD-fed mice compared to sham 14 days after MI. However, dP/dt_{\min} was sustained at sham levels in DHA-supplemented mice 14 days after MI and was significantly higher compared to CD mice at the same time point (Figure 1(d)). No differences were observed in peak pressure rise (dP/dt_{\max}) 14 days after MI in CD- or DHA-supplemented mice compared to respective sham (Figure 1(e)). Isovolumic relaxation constant (Tau) increased in CD mice compared to sham 14 days after MI. However, Tau remained at sham levels in DHA-supplemented mice and was significantly lower compared to CD mice 14 days after MI (Figure 1(f)). Two-way ANOVA indicated effects of DHA supplementation, MI, and an interaction between EF and Tau. Furthermore, statistical analyses indicated independent effects of DHA supplementation and MI on LVEDP and dP/dt_{\min} .

3.2. DHA Supplementation Modulates Cytokine Expression after MI. Sham procedure did not induce a sustained cytokine expression 7 days after LAD ligation implantation compared to native animals. However, the murine myocardium exhibited a marked mRNA upregulation of inflammatory

cytokines after 60 min LAD occlusion compared to sham mice. TNF- α mRNA expression was increased in CD mice 6 h and 24 h after MI, while DHA-supplemented mice exhibited just a brief induction 6 h after MI compared to respective sham. Furthermore, MI-induced TNF- α mRNA expression increase was significantly lower in DHA-supplemented mice 6 h and 72 h after MI compared to CD groups (Figure 2(a)). Furthermore, IL-1 β mRNA expression was increased in CD mice 24 h and 72 h after MI compared to respective sham, while MI-induced IL-1 β mRNA expression occurred in DHA-supplemented mice already at 6 h and was terminated after 24 h. Furthermore, IL-1 β mRNA expression was significantly greater in CD mice 72 h after MI compared to DHA-supplemented mice (Figure 2(b)). IL-10 mRNA was upregulated 72 h after MI in both CD- and DHA-supplemented mice. However, in mice with surgical MI, the DHA pretreatment was associated with a lower IL-10 expression than CD 72 h after MI (Figure 2(c)). MI-induced cytokine mRNA expression demonstrated a similar pattern in DHA-supplemented mice; however, induction occurred earlier, levels were lower, and increase was terminated sooner compared to respective CD mice (Figures 2(a)–2(c)). Two-way ANOVA indicated independent effects of DHA supplementation and MI on TNF- α mRNA expression and an effect of MI on IL-1 β and IL-10 expressions.

3.3. DHA Supplementation Modifies Inflammatory Response after MI. Data shown in Figure 3 demonstrate an effect of DHA supplementation on MI-induced inflammation. CCL2 chemokine expression was increased in CD mice 6 h, 24 h, and 72 h after MI, while DHA-supplemented mice only exhibited CCL2 mRNA increases at 6 h and 24 h after MI compared to respective sham. However, CCL2 mRNA induction was significantly greater in DHA-supplemented mice 6 h after MI but terminated earlier compared to CD animals (Figure 3(a)). Furthermore, CCL3 mRNA expression was increased in CD mice compared to respective sham and DHA-supplemented mice 72 h after MI, while remained unchanged in DHA-supplemented mice compared to sham (Figure 3(b)). Fluorescence-activated cell sorting (FACS) analysis revealed greater increases in cardiac neutrophil and macrophage populations in DHA-supplemented mice compared to the CD group 3 d after MI (Figures 3(c) and 3(d)). Most importantly, cardiac macrophage population shifted from a more proinflammatory Ly6C⁺ to a more anti-inflammatory and pr remodeling Ly6C⁻ phenotype in DHA supplemented compared to the CD group (Figures 3(e) and 3(f)).

In accordance with FACS analyses, MAC-2-stained histological sections revealed a large macrophage accumulation 7 days after I/R injury in both CD- and DHA-supplemented groups. However, DHA-supplemented mice showed a significantly greater infiltration of MAC-2-positive cells compared to CD-fed mice 7 days after I/R injury (Figures 3(g)–3(i)). Two-way ANOVA revealed effects of MI and an interaction between DHA supplementation and LAD occlusion on CCL2 and CCL3 mRNA expressions.

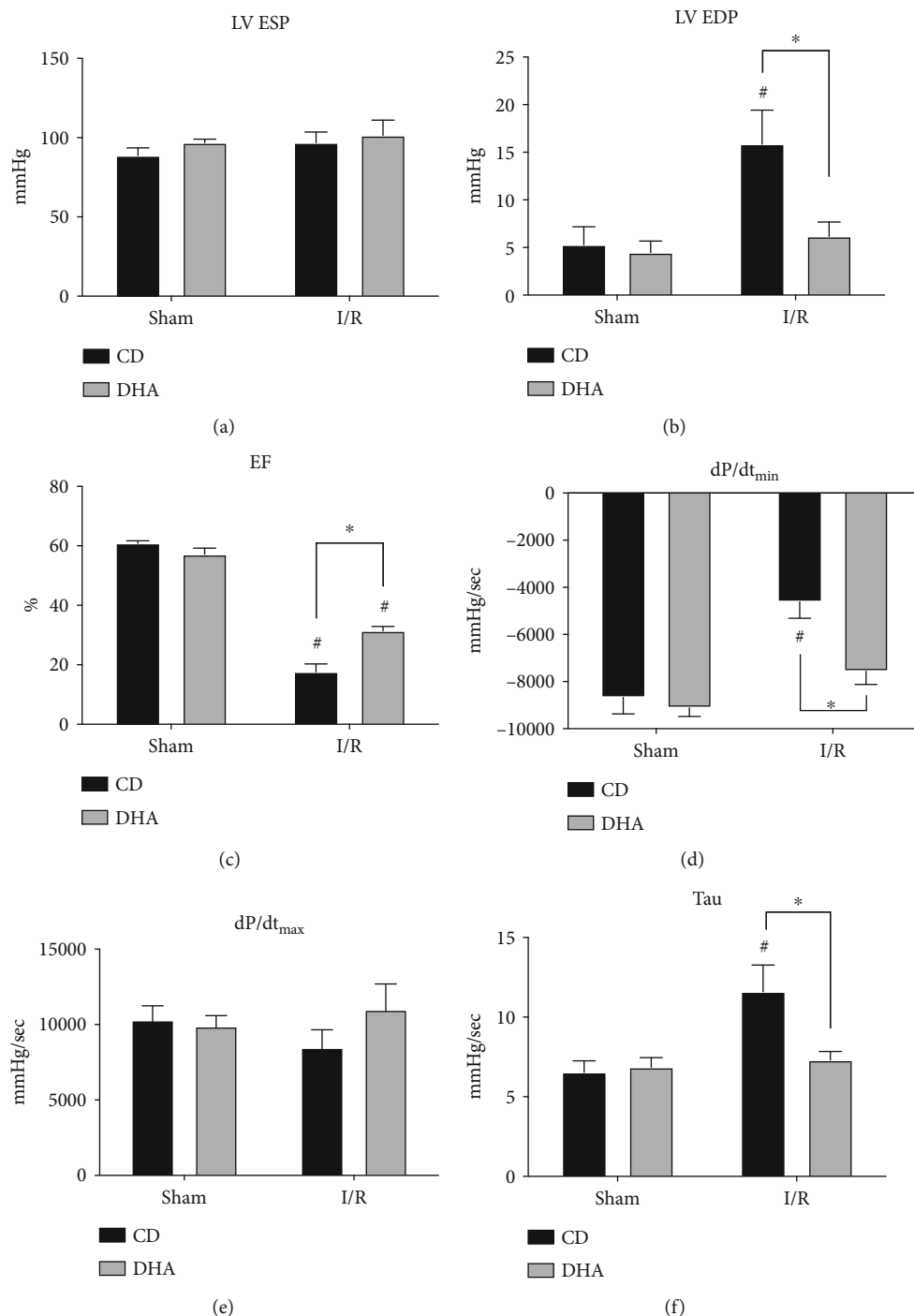


FIGURE 1: Improved cardiac function in DHA-supplemented mice after MI: functional parameters of (a) left ventricular end-systolic pressure (LVESP), (b) left ventricular end-diastolic pressure (LVEDP), (c) ejection fraction (EF), (d) peak pressure decline (dp/dt_{\min}), (e) peak pressure rise (dp/dt_{\max}), and (f) isovolumic relaxation constant (Tau), were analyzed 14 d after sham or MI in CD- or DHA-supplemented mice. $n = 8$ mice per group * $P < 0.05$.

3.4. DHA Supplementation Modifies Collagen Expression and Reduces LV Scar Formation after MI. TGF- β mRNA was increased in both CD- and DHA-supplemented groups 24 h and 72 h after MI (Figure 4(a)). Collagen I and III mRNA expressions were also increased in both groups 72 h after MI compared to respective sham. However, collagen I

mRNA expression was significantly lower in DHA-supplemented mice compared to the CD group (Figures 4(b) and 4(c)). Furthermore, analyses of picrosirius red-stained histological sections revealed less collagen deposition in DHA supplemented compared to CD mice 14 d after MI (Figures 4(d) and 4(e)). Two-way ANOVA indicated the

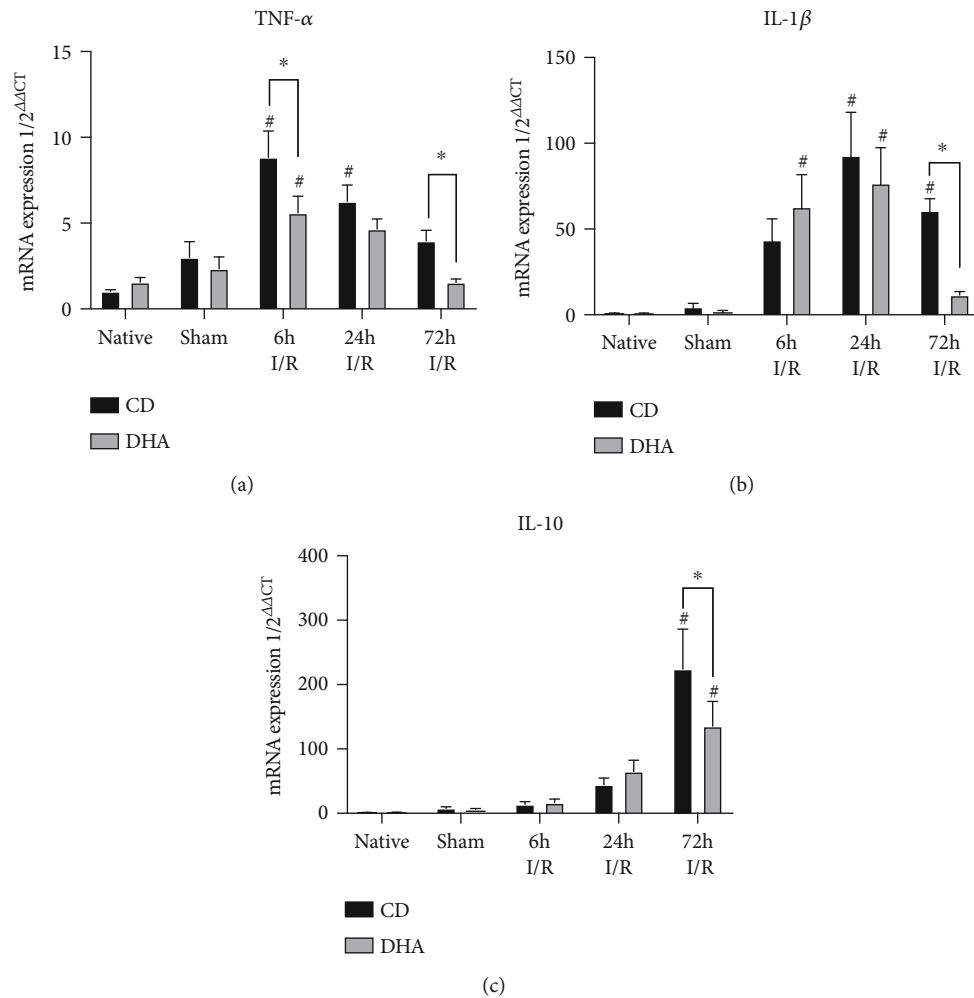


FIGURE 2: mRNA expression profile of inflammatory mediators. (a) TNF- α , (b) IL-1 β , and (c) IL-10 mRNA expressions were analyzed in the murine myocardium of native, sham, and MI-exposed mice that were CD or DHA supplemented. $n = 7$ mice per group, $*P < 0.05$.

effects of MI on TGF- β , collagen I, and collagen III mRNA expressions and an interaction of MI with DHA supplementation on collagen I expression.

3.5. Myocardial Adaptation Mechanisms toward Ischemic Injury in DHA-Supplemented Mice. α -Myosin heavy chain (MHC) mRNA expressions were decreased in both CD- and DHA-supplemented mice 6h after MI. However, α -MHC mRNA expression returned to sham levels in DHA-supplemented mice, while remained lower in CD mice compared to DHA supplemented and respective sham 72h after MI (Figure 5(a)). Furthermore, β -MHC expression was significantly increased in CD mice 24h and 72h after I/R injury, while DHA-supplemented mice only exhibited a transient increase in β -MHC expression 24h after MI compared to respective sham. Most notably, β -MHC expression was significantly greater in CD compared to DHA-supplemented mice 24h after MI (Figure 5(b)). Glutathione peroxidase 1 (GPx1) mRNA expressions were increased in both CD- and DHA-supplemented mice 24h and 72h after MI. However, GPx1 mRNA induction was also significantly greater in CD compared to DHA-supplemented mice 72h after MI

(Figure 5(c)). Heme oxygenase 1 (HOX-1) mRNA expression increased in CD mice 72h after MI compared to DHA supplemented and respective sham. Furthermore, HOX-1 remained at sham levels in DHA-supplemented mice. Two-way ANOVA indicated the effects of MI on α -MHC, β -MHC, GPx1, and HMOX-1 mRNA expressions. However, there were independent effects of DHA supplementation on β -MHC and HMOX-1 and also an interaction of MI and DHA supplementation on β -MHC, GPx1, and HMOX-1 mRNA expressions.

3.6. DHA Preconditioning Impacts mRNA Expression of Enzymes Involved in Fatty Acid Metabolism. Peroxisome proliferator-activated receptor alpha (PPAR- α) mRNA expression was lower in DHA-supplemented mice 6h after MI compared to respective sham. In opposition, PPAR- α mRNA expression increased in CD mice 72h after MI compared to DHA-supplemented and respective sham mice (Figure 6(a)). Mitochondrial uncoupling protein 3 (UCP 3) mRNA expression was increased in DHA-supplemented native and sham compared to CD mice. However, UCP 3 mRNA expression decreased in DHA supplemented, while

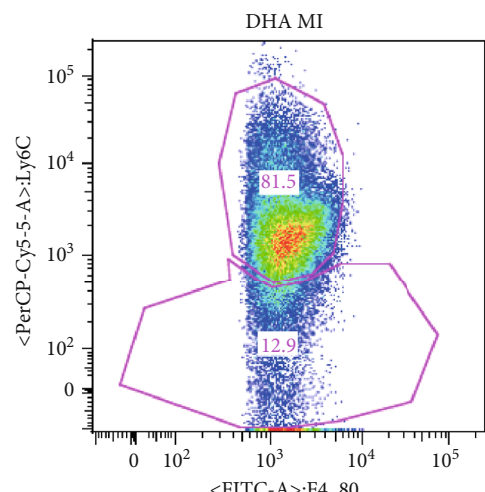
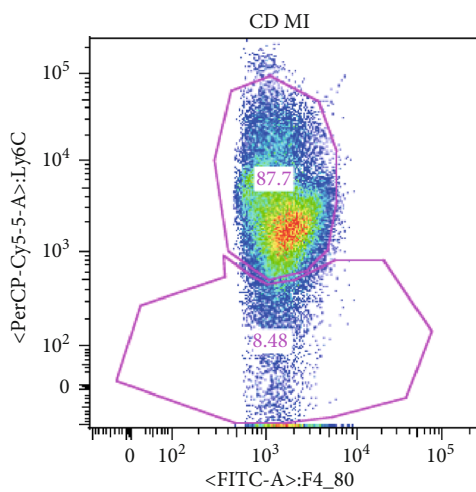
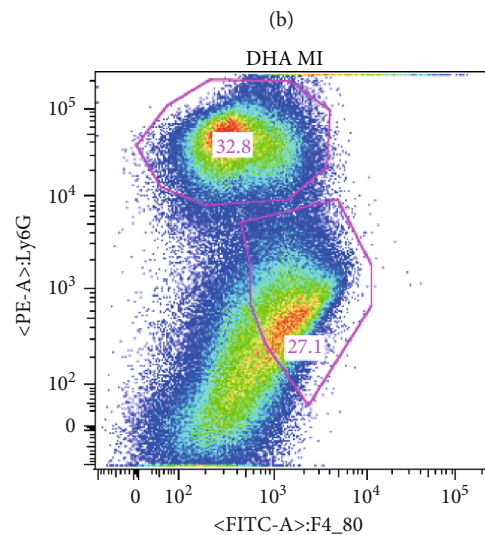
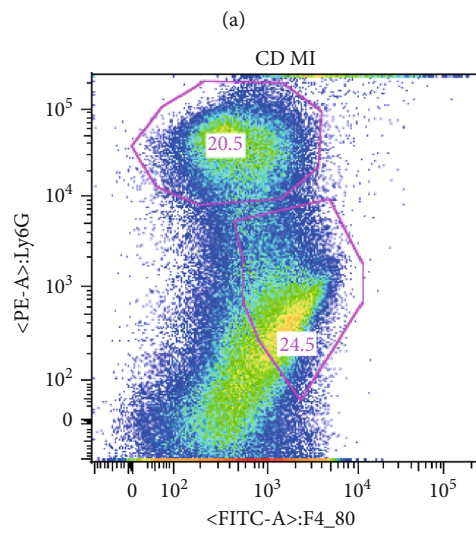
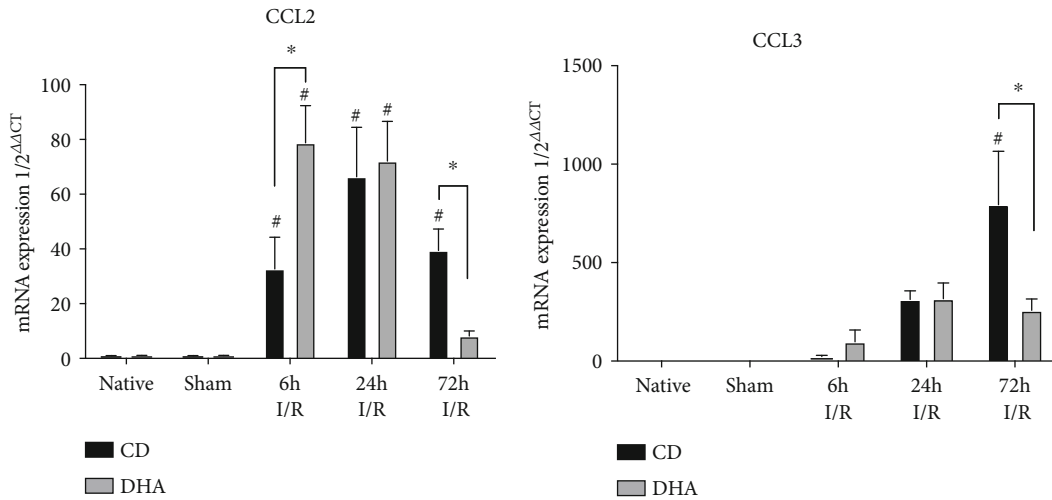


FIGURE 3: Continued.

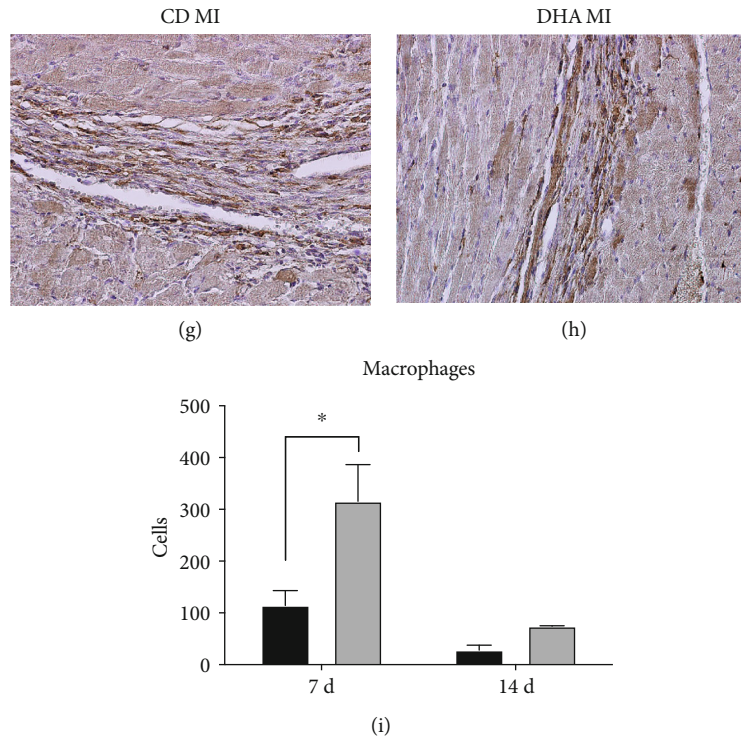


FIGURE 3: In mice with surgical MI, the DHA pretreatment was associated with a different inflammation pattern compared to the CD group. Cardiac (a) CCL2 and (b) CCL3 chemokine mRNA expressions were analyzed in the murine myocardium of native, sham, and MI-exposed mice that were CD or DHA supplemented. FACS analyses of cardiac neutrophil and macrophage populations in (c) CD or (d) DHA and phenotyping of macrophages in (e) CD- or (f) DHA-supplemented mice 3 d after MI. MAC-2 staining of representative histological left ventricular sections of cardiac macrophages in (g) CD- or (h) DHA-supplemented mice 7 d after MI and quantification (i) $n = 7$ mice per group, * $P < 0.05$.

increased in CD mice 6 h after MI compared to respective sham and DHA-supplemented mice. 24 h after MI UCP 3 mRNA expression was still reduced in DHA-supplemented mice, while returned to sham in CD groups with no difference between CD- and DHA-supplemented mice at this time point. However, UCP 3 mRNA expression increased in DHA-supplemented mice, while remained decreased in CD with a similar expression pattern compared to respective sham 72 h after MI (Figure 6(b)).

4. Discussion

The present study shows for the first time that modulation of the inflammatory response and adapted energy metabolism may play a role in the beneficial effect of DHA pretreatment on reperfused MI. Various studies investigating ω -3 FA effects on cardiac health report positive effects using either DHA, EPA, or combinations since DHA is retroconverted to EPA, especially at higher concentrations as used in our investigation [22, 24, 39, 40]. The present study used diets with similar omega-6 FA content and higher preformed DHA, but not EPA in DHA diet, in order to decrease confounding by individual and rate-limiting differences in long-chain polyunsaturated fatty acid metabolism [41]. Furthermore, the herein used concentration has been shown to increase DHA serum and tissue concentrations [31, 42], which was beneficial in pulmonary and neurological diseases

in rodents [32, 33]. Male mice were chosen to eliminate the complex cardioprotective effects that have been reported for all estrogen receptor subtypes against I/R injury, and a purified diet was chosen as the basis for both diets to avoid variability in standard chows [43].

The observed LV dysfunction in CD mice after reperfused MI is in accordance with previous studies from our groups and others [44–48]. However, in the present study, DHA supplementation beginning 7 days prior to MI resulted in sustained systolic and diastolic LV function that was characterized by lower end-diastolic pressure (EDP), greater ejection fraction (EF), and reduced isovolumetric relaxation (Tau) 14 d after 60 min LAD occlusion compared to CD-fed mice, with no difference in end-systolic blood pressures. These data suggest that DHA pretreatment has physiological consequences on the development of MI-induced LV dysfunction, preserving cardiac function in mice. The observed DHA-induced attenuation of MI-induced LV dysfunction adds to cardioprotective effects of other omega-3 FA in a Langendorff perfusion model reporting that an intravenous bolus of EPA: DHA 6: 1 protects against myocardial ischemia-reperfusion-induced injury [23]. Furthermore, preserved LV function in DHA-pretreated mice 14 days after MI is in line with the clinical data from the OMEGA-REMODEL trial, demonstrating that in humans, the combination of DHA and EPA ω -3 FA ethyl ester supplementation beginning after the onset

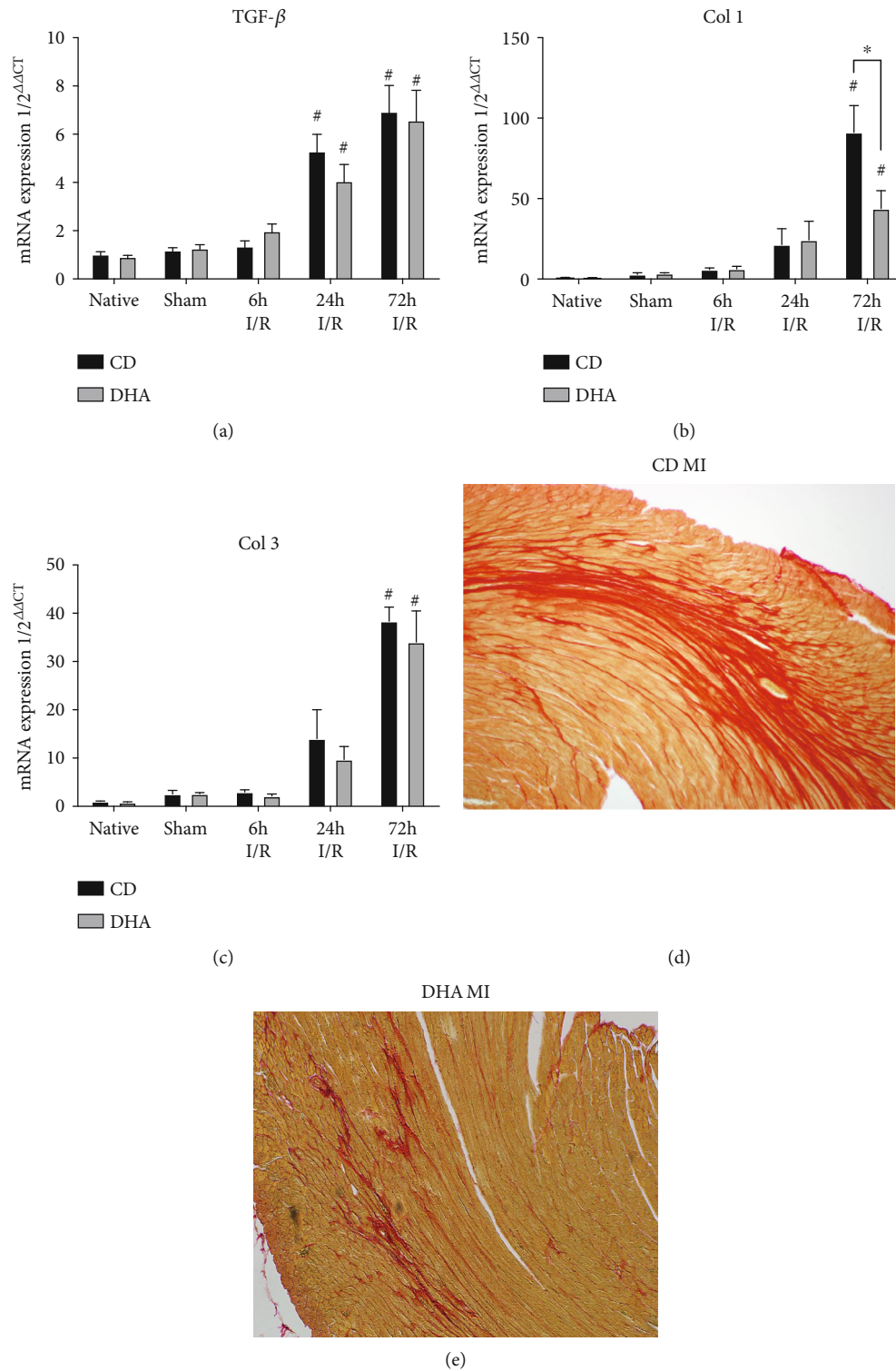


FIGURE 4: DHA supplementation modifies MI-induced myocardial remodeling: (a) TGF- β , (b) collagen I, and (c) collagen III mRNA expressions were analyzed in the murine myocardium of native, sham, and MI-exposed mice that were CD or DHA supplemented. $n = 7$ mice per group, $*P < 0.05$. Representative picosirius red-stained histological sections from (d) CD- and (e) DHA-supplemented mice 14 d after I/R.

of STEMI improved LV function after 6 months. In summary, the preserved LV function in DHA-pretreated mice after reperfused MI is corroborated by the current clinical and experimental literature and suggests that DHA pre-

treatment attenuates I/R injury-induced cardiac dysfunction in mice. Our study goes beyond this to investigate molecular mechanisms of omega-3 FA-induced cardioprotection following ischemia/reperfusion injury.

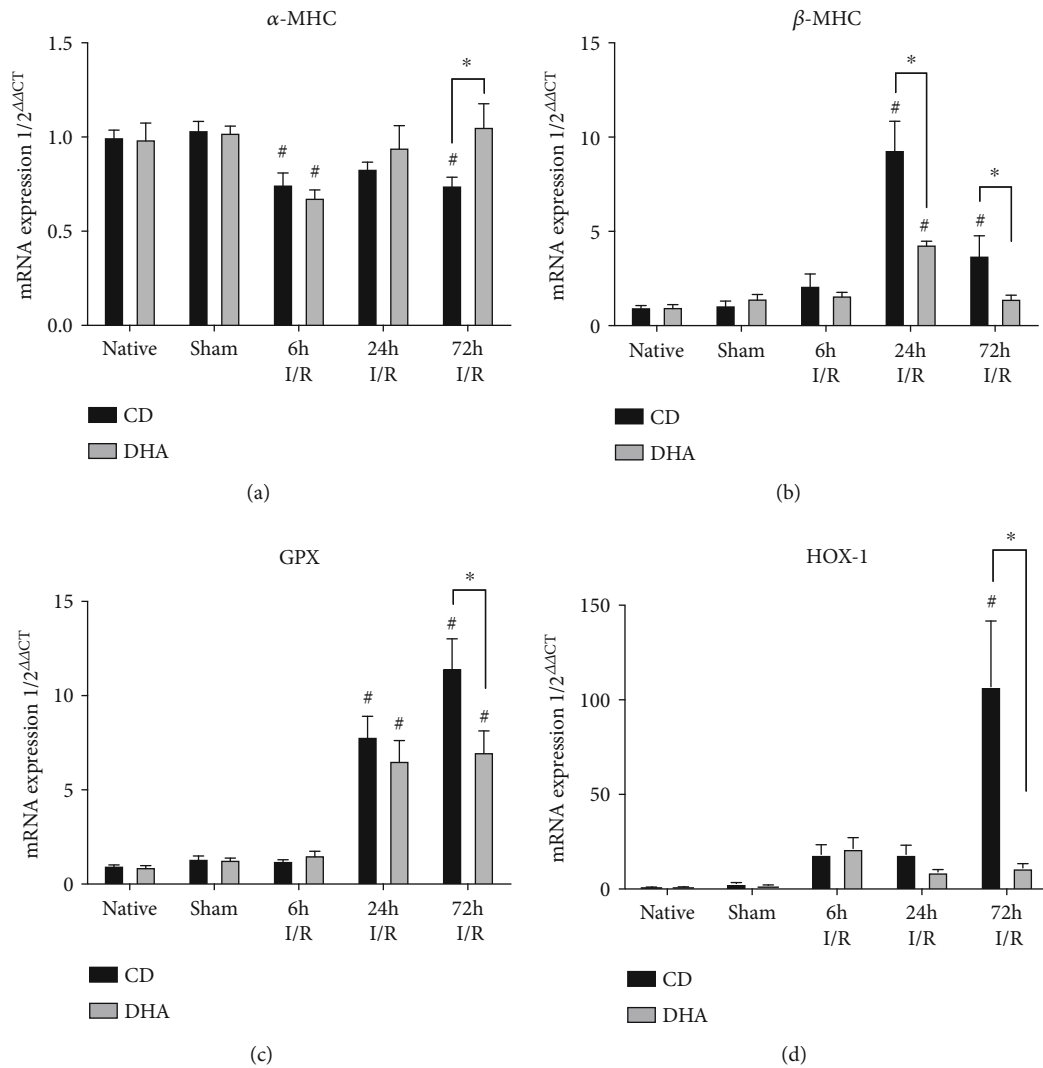


FIGURE 5: DHA-related cardiomyocyte adaptation after MI. MHC switch and induction of oxidative enzymes: myocardial (a) α -MHC, (b) β -MHC, (c) GPX, and (d) HOX mRNA expressions were analyzed in the murine myocardium of native, sham, and MI-exposed mice that were CD or DHA supplemented. $n = 7$ mice per group, $*P < 0.05$.

Even though ω -3 FA effects have been heavily studied in the context of MI, little is known about the beneficial metabolic and anti-inflammatory mechanisms that decrease the risk of heart failure associated with worse prognosis after MI if unrestricted. Various studies show the therapeutic potential of attenuating cardiac disease development via modulating the inflammatory response to various insults [8, 11, 48–50].

In our study, DHA pretreatment was associated with an attenuation of cytokine expression. Furthermore, DHA leads to earlier and stronger initiation, but prompt termination of macrophage chemoattractant CCL2 expression. This data suggests that DHA treatment results in restricted inflammation, potentially attenuating remodeling in reperfused MI.

This inflammatory stimulus is also followed by an increased macrophage infiltration in DHA-treated mice 7 d after MI, returning to baseline levels after 14 d. This strong but timely restricted inflammation in DHA-treated mice corroborates our hypothesis of timely and therefore attenuated

remodeling. Accordingly, DHA treatment leads to less collagen deposition, resulting in smaller infarct sizes after reperfused MI. In this regard, we found that the peak of macrophages in DHA mice after 7 d consisted mainly of alternatively activated Ly6C-positive macrophage phenotype, being accompanied by less collagen deposition and better LV function in DHA-pretreated mice after 14 d. In summary, this data suggests that a stronger remodeling stimulus leads to a more rapid and compacted scar formation and thus smaller infarct size in DHA-supplemented mice. Therefore, the beneficial effect of DHA may depend on modulation of the inflammatory response initiated by MI.

The expression of the myosin heavy chain (MHC) subunits is developmentally regulated and inappropriate expression associated with cardiomyopathies [51, 52]. Furthermore, heart failure is characterized by numerous molecular changes in contractile pathways including a switch from α - to β -MHC isoform [52–54]. β -MHC is characterized by lower ATP consumption and therefore higher efficiency,

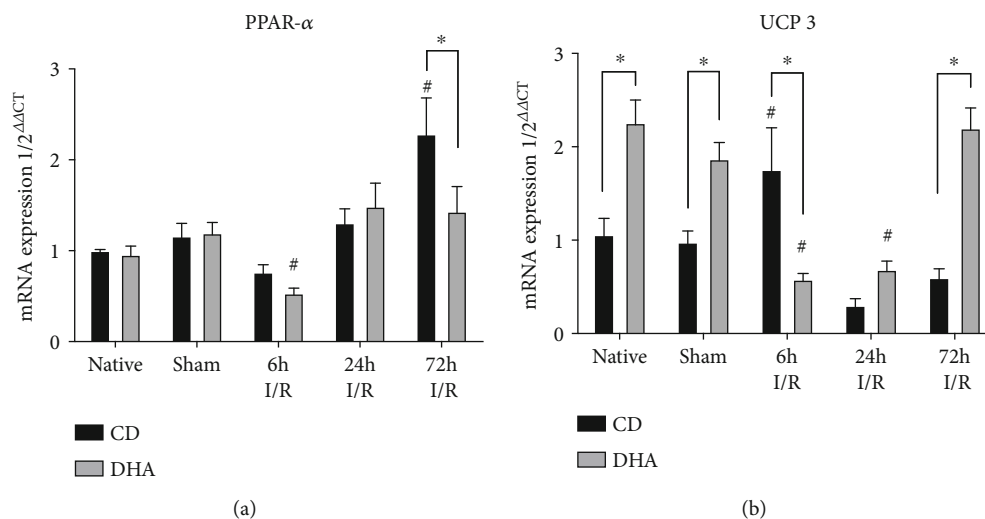


FIGURE 6: DHA pretreatment attenuates PPAR expression and enhances uncoupling protein expression post-MI; both are cardioprotective. (a) Peroxisome proliferator-activated receptor alpha (PPAR- α) and (b) mitochondrial uncoupling protein 3 (UCP 3) mRNA expressions were analyzed in the murine myocardium of native, sham, and MI-exposed mice that were CD or DHA supplemented. $n = 7$ mice per group, $*P < 0.05$.

potentially being advantageous and implying that the α - to β -MHC shift may be an adaptive response to myocardial injury [44, 48].

In our study, α -MHC mRNA expression showed a transient decrease after MI in both CD- and DHA-pretreated mice, indicative of favorable molecular changes in both groups (Figure 5(a)). Further, a significant increase in β -MHC expression was seen in both CD- and DHA-supplemented mice after 24 h. Interestingly, β -MHC expression was significantly greater in CD compared to DHA-pretreated mice 24 h after MI, indicative of a lesser need for cardiomyocyte adaptation after DHA treatment (Figure 5(b)). Thus, the lower β -MHC mRNA upregulation in DHA-pretreated mice may be indicative of a cardioprotective mechanism possibly mediated through improved energy supply or altered metabolism.

Another important mechanism protecting cardiomyocyte adaption against myocardial injury consists of the reduction of oxidative stress, which modulates inflammatory response [55, 56]. Glutathione peroxidase (GPx) reduces peroxides to nonreactive products and decreases function that induces cardiac matrix remodeling [57]. Also, HOX-1 induction is absent in mice supplemented with DHA in strong contrast to CD; here, significant induction of HOX-1 72 hrs after MI strongly indicates antioxidative mechanisms playing a key role in DHA-mediated cardioprotection, as reported by others [44]. Therefore, our data show that DHA pretreatment reduced MI-induced GPx1- and HOX-1 expressions (Figures 5(c) and 5(d)), suggesting that DHA pretreatment induces other antioxidative mechanism potentially protecting the heart from I/R injury-induced LV remodeling.

As to this, cardiomyocytes also protect themselves against oxidative stress via mitochondrial uncoupling protein (UCP) 3, separating oxidative phosphorylation from ATP synthesis and protecting mitochondria from ROS generation

[58]. Supplementation of omega-3 fatty acids specifically induces cardiac UCP 3 expression, and overexpression protects cardiomyocytes through reduced ROS generation and apoptosis from I/R injury cardiomyocyte dysfunction and preventing cardiomyocyte death, all involved in the development of LV dysfunction [59–62]. The induced UCP 3 mRNA expression seen in the myocardium of DHA supplementation sham mice is congruent with *in vitro* and *in vivo* studies potentially preventing MI-induced oxidative stress [63–65]. The fact that UCP 3 expression decreases after I/R injury in DHA-pretreated mice is surprising, but downregulation of UCP 3 has been reported after I/R injury through the nuclear transcription factor peroxisome proliferator-activated receptor- (PPAR-) α [66, 67]. We have previously shown that pressure overload-induced hypertrophy as well as repetitive I/R is associated with a transient downregulation of PPAR- α and that pharmacological reactivation of PPAR- α as well as MHC-specific PPAR- α overexpression worsens contractile function, suggesting that substrate switching from fatty acid to glucose utilization in the stressed heart may preserve contractile function [58, 68, 69]. Accordingly, we show here a transient reduction of PPAR- α expression in both CD and DHA mice after 6 h, but only being significant in DHA-supplemented mice compared to respective sham. This data is in accordance with previous results from the above-mentioned studies but also suggests a cardioprotective effect of DHA via reduced fatty acid uptake and oxidation. We hypothesize that significant I/R injury-induced PPAR- α downregulation in DHA-supplemented mice results in reduced fatty acid uptake and oxidation. We further speculate that reduced β -oxidation in DHA-supplemented mice may not act as an adequate trigger for early UCP 3 upregulation at this time point. Also, within time, UCP 3 induction normalizes to sham levels in DHA-supplemented mice, potentially interconnecting transient UCP 3 downregulation to PPAR- α expression.

In summary, our data suggest that DHA supplementation induces cardioprotection from myocardial ischemia and reperfusion injury through modulation of inflammatory response with early macrophage attraction but timely and attenuated remodeling. DHA seems to induce cardiomyocyte protection at least in part by transient PPAR- α downregulation with subsequently reduced UCP 3 expression and oxidation, diminishing the need for antioxidant mechanisms including mitochondrial function, or switch of MHC-isoforms from high ATP consuming α - to energetically more efficient β -isoforms.

5. Conclusions

Cardiac dysfunction and detrimental myocardial remodeling after MI are consequences of ROS generation, inflammation, and altered energy metabolism. Various promising experimental cardioprotective interventions have targeted individual contributors of I/R injury in animal models but have failed after translating into the clinical setting. However, MI is multifaceted and includes inflammation, ROS generation, and altered energy metabolism. Our study shows for the first time that DHA interacts with inflammation, ROS generation, LV matrix remodeling, cardiomyocyte metabolism, and contractile elements and is therefore targeting multiple mechanisms involved in cardiac I/R injury, attenuating MI-induced development of cardiac dysfunction.

Data Availability

Data will be made available upon request.

Conflicts of Interest

The authors declare that there is no conflict of interest regarding the publication of this paper.

Authors' Contributions

Habicht I. and Mohsen G. contributed equally to this work. G. D. Duerr and M. Velten contributed equally to this work.

References

- [1] M. Nichols, N. Townsend, R. Luengo-Fernandez et al., *Statistics ECD*, European Cardiovascular Disease Statistics, 2012.
- [2] G. N. Levine, E. R. Bates, J. C. Blankenship et al., "2015 ACC/AHA/SCAI focused update on primary percutaneous coronary intervention for patients with ST-elevation myocardial infarction: an update of the 2011 ACCF/AHA/SCAI guideline for percutaneous coronary intervention and the 2013 ACCF/AHA guideline for the management of ST-elevation myocardial infarction: a report of the American College of Cardiology/American Heart Association Task Force on Clinical Practice Guidelines and the Society for Cardiovascular Angiography and Interventions," *Circulation*, vol. 133, no. 11, pp. 1135–1147, 2016.
- [3] R. A. Kloner, S. L. Hale, W. Dai, and J. Shi, "Cardioprotection: where to from here?," *Cardiovascular Drugs and Therapy*, vol. 31, no. 1, pp. 53–61, 2017.
- [4] R. A. Kloner, S. L. Hale, W. Dai et al., "Reduction of ischemia/reperfusion injury with bendavia, a mitochondria-targeting cytoprotective peptide," *Journal of the American Heart Association*, vol. 1, no. 3, article e001644, 2012.
- [5] M. L. Lindsey, R. P. Iyer, M. Jung, K. Y. DeLeon-Pennell, and Y. Ma, "Matrix metalloproteinases as input and output signals for post-myocardial infarction remodeling," *Journal of Molecular and Cellular Cardiology*, vol. 91, pp. 134–140, 2016.
- [6] L. F. Shirazi, J. Bissett, F. Romeo, and J. L. Mehta, "Role of inflammation in heart failure," *Current Atherosclerosis Reports*, vol. 19, no. 6, p. 27, 2017.
- [7] M. Reindl, S. J. Reinstadler, H.-J. Feistritzer et al., "Relation of inflammatory markers with myocardial and microvascular injury in patients with reperfused ST-elevation myocardial infarction," *European Heart Journal Acute Cardiovascular Care*, vol. 6, no. 7, pp. 640–649, 2015.
- [8] M. Velten, M. W. Gorr, D. J. Youtz, C. Velten, L. K. Rogers, and L. E. Wold, "Adverse perinatal environment contributes to altered cardiac development and function," *American Journal of Physiology Heart and Circulatory Physiology*, vol. 306, no. 9, pp. H1334–H1340, 2014.
- [9] R. D. Devine, S. Bicer, P. J. Reiser, M. Velten, and L. E. Wold, "Metalloproteinase expression is altered in cardiac and skeletal muscle in cancer cachexia," *American Journal of Physiology Heart and Circulatory Physiology*, vol. 309, no. 4, pp. H685–H691, 2015.
- [10] O. Boehm, P. Knuefermann, J. Plueck et al., "TLR2 stimulation induces cardiac inflammation but not cardiac depression in vivo," *Journal of Inflammation*, vol. 10, no. 1, p. 33, 2013.
- [11] P. Knuefermann, M. Schwederski, M. Velten et al., "Bacterial DNA induces myocardial inflammation and reduces cardiomyocyte contractility: role of toll-like receptor 9," *Cardiovascular Research*, vol. 78, no. 1, pp. 26–35, 2008.
- [12] T. Ma, Z.-Q. Ma, X.-H. Du, Q.-S. Yu, R. Wang, and L. Liu, "Effect of valsartan on ACAT-1 and PPAR- γ expression in intima with carotid artery endothelial balloon injury in rabbit," *International Journal of Clinical and Experimental Medicine*, vol. 8, no. 4, pp. 5527–5533, 2015.
- [13] L. E. Wold, A. F. Ceylan-Isik, and J. Ren, "Oxidative stress and stress signaling: menace of diabetic cardiomyopathy," *Acta Pharmacologica Sinica*, vol. 26, no. 8, pp. 908–917, 2005.
- [14] E. L. Mills and L. A. O'Neill, "Reprogramming mitochondrial metabolism in macrophages as an anti-inflammatory signal," *European Journal of Immunology*, vol. 46, no. 1, pp. 13–21, 2016.
- [15] Y. Liu, D. Neumann, J. F. C. Glatz, and J. J. F. P. Luiken, "Molecular mechanism of lipid-induced cardiac insulin resistance and contractile dysfunction," *Prostaglandins, Leukotrienes, and Essential Fatty Acids*, vol. 136, pp. 131–141, 2018.
- [16] D. A. Brown, S. L. Hale, C. P. Baines et al., "Reduction of early reperfusion injury with the mitochondria-targeting peptide bendavia," *Journal of Cardiovascular Pharmacology and Therapeutics*, vol. 19, no. 1, pp. 121–132, 2014.
- [17] D. Mozaffarian and E. B. Rimm, "Fish intake, contaminants, and human health: evaluating the risks and the benefits," *Journal of the American Medical Association*, vol. 296, no. 15, pp. 1885–1899, 2006.
- [18] B. Heydari, S. Abdullah, J. V. Pottala et al., "Effect of omega-3 acid ethyl esters on left ventricular remodeling after acute myocardial infarction: the OMEGA-REMODEL randomized clinical trial," *Circulation*, vol. 134, no. 5, pp. 378–391, 2016.

- [19] X. Fang, W. Cai, Q. Cheng et al., "Omega-3 PUFA attenuate mice myocardial infarction injury by emerging a protective eicosanoid pattern," *Prostaglandins & Other Lipid Mediators*, vol. 139, pp. 1–9, 2018.
- [20] R. Marchioli and G. Levantesi, "n-3 PUFAs in cardiovascular disease," *International Journal of Cardiology*, vol. 170, no. 2, Supplement 1, pp. S33–S38, 2013.
- [21] D. Mozaffarian and S. Capewell, "United Nations' dietary policies to prevent cardiovascular disease," *BMJ*, vol. 343, article d5747, 2011.
- [22] D. S. Siscovick, T. A. Barringer, A. M. Fretts et al., "Omega-3 polyunsaturated fatty acid (fish oil) supplementation and the prevention of clinical cardiovascular disease: a science advisory from the American Heart Association," *Circulation*, vol. 135, no. 15, pp. e867–e884, 2017.
- [23] M. Burbán, G. Meyer, A. Olland et al., "An intravenous bolus of Epa: Dha 6: 1 protects against myocardial ischemia-reperfusion-induced shock," *Shock*, vol. 46, no. 5, pp. 549–556, 2016.
- [24] N. Madingou, K. Gilbert, L. Tomaro et al., "Comparison of the effects of EPA and DHA alone or in combination in a murine model of myocardial infarction," *Prostaglandins, Leukotrienes, and Essential Fatty Acids*, vol. 111, pp. 11–16, 2016.
- [25] R. Wang, Q. Chai, T. Lu, and H.-C. Lee, "Activation of vascular BK channels by docosahexaenoic acid is dependent on cytochrome P450 epoxygenase activity," *Cardiovascular Research*, vol. 90, no. 2, pp. 344–352, 2011.
- [26] G. G. Abdukeyum, A. J. Owen, T. A. Larkin, and P. L. McLennan, "Up-regulation of mitochondrial antioxidant superoxide dismutase underpins persistent cardiac nutritional preconditioning by long chain n-3 polyunsaturated fatty acids in the rat," *Journal of Clinical Medicine*, vol. 5, no. 3, p. 32, 2016.
- [27] S. Zeghichi-Hamri, M. de Lorgeril, P. Salen et al., "Protective effect of dietary n-3 polyunsaturated fatty acids on myocardial resistance to ischemia-reperfusion injury in rats," *Nutrition Research*, vol. 30, no. 12, pp. 849–857, 2010.
- [28] S. Pepe and P. L. McLennan, "Cardiac membrane fatty acid composition modulates myocardial oxygen consumption and postischemic recovery of contractile function," *Circulation*, vol. 105, no. 19, pp. 2303–2308, 2002.
- [29] D. J. Hausenloy and D. M. Yellon, "Myocardial ischemia-reperfusion injury: a neglected therapeutic target," *The Journal of Clinical Investigation*, vol. 123, no. 1, pp. 92–100, 2013.
- [30] T. O. Nossuli, V. Lakshminarayanan, G. Baumgarten et al., "A chronic mouse model of myocardial ischemia-reperfusion: essential in cytokine studies," *American Journal of Physiology Heart and Circulatory Physiology*, vol. 278, no. 4, pp. H1049–H1055, 2000.
- [31] L. K. Rogers, C. J. Valentine, M. Pennell et al., "Maternal docosahexaenoic acid supplementation decreases lung inflammation in hyperoxia-exposed newborn mice," *The Journal of Nutrition*, vol. 141, no. 2, pp. 214–222, 2011.
- [32] M. Velten, R. D. Britt, K. M. Heyob, T. E. Tipple, and L. K. Rogers, "Maternal dietary docosahexaenoic acid supplementation attenuates fetal growth restriction and enhances pulmonary function in a newborn mouse model of perinatal inflammation," *The Journal of Nutrition*, vol. 144, no. 3, pp. 258–266, 2014.
- [33] M. Ali, K. M. Heyob, M. Velten, T. E. Tipple, and L. K. Rogers, "DHA suppresses chronic apoptosis in the lung caused by perinatal inflammation," *American Journal of Physiology Lung Cellular and Molecular Physiology*, vol. 309, no. 5, pp. L441–L448, 2015.
- [34] B. M. Anderson and D. W. L. Ma, "Are all n-3 polyunsaturated fatty acids created equal?," *Lipids in Health and Disease*, vol. 8, no. 1, article 33, 2009.
- [35] P. Pacher, T. Nagayama, P. Mukhopadhyay, S. Bátkai, and D. A. Kass, "Measurement of cardiac function using pressure-volume conductance catheter technique in mice and rats," *Nature Protocols*, vol. 3, no. 9, pp. 1422–1434, 2008.
- [36] N. G. Frangogiannis, J. L. Perrard, L. H. Mendoza et al., "Stem cell factor induction is associated with mast cell accumulation after canine myocardial ischemia and reperfusion," *Circulation*, vol. 98, no. 7, pp. 687–698, 1998.
- [37] C. Weisheit, Y. Zhang, A. Faron et al., "Ly6C(low) and not Ly6C(high) macrophages accumulate first in the heart in a model of murine pressure-overload," *PLoS One*, vol. 9, no. 11, article e112710, 2014.
- [38] S. A. Bustin, V. Benes, J. A. Garson et al., "The MIQE guidelines: minimum information for publication of quantitative real-time PCR experiments," *Clinical Chemistry*, vol. 55, no. 4, pp. 611–622, 2009.
- [39] T. A. Mori, "Marine OMEGA-3 fatty acids in the prevention of cardiovascular disease," *Fitoterapia*, vol. 123, pp. 51–58, 2017.
- [40] D. D. Alexander, P. E. Miller, M. E. Van Elswyk, C. N. Kuratko, and L. C. Bylsma, "A meta-analysis of randomized controlled trials and prospective cohort studies of eicosapentaenoic and docosahexaenoic long-chain omega-3 fatty acids and coronary heart disease risk," *Mayo Clinic Proceedings*, vol. 92, no. 1, pp. 15–29, 2017.
- [41] S. Khadge, J. G. Sharp, G. M. Thiele et al., "Dietary omega-3 and omega-6 polyunsaturated fatty acids modulate hepatic pathology," *The Journal of Nutritional Biochemistry*, vol. 52, pp. 92–102, 2018.
- [42] L. Liu, Q. Hu, H. Wu et al., "Dietary DHA/EPA Ratio Changes Fatty Acid Composition and Attenuates Diet- Induced Accumulation of Lipid in the Liver of ApoE^{-/-} Mice," *Oxidative Medicine and Cellular Longevity*, vol. 2018, Article ID 6256802, 12 pages, 2018.
- [43] A. M. Deschamps, E. Murphy, and J. Sun, "Estrogen receptor activation and cardioprotection in ischemia reperfusion injury," *Trends in Cardiovascular Medicine*, vol. 20, no. 3, pp. 73–78, 2010.
- [44] G. D. Duerr, J. C. Heinemann, C. Gestrich et al., "Impaired border zone formation and adverse remodeling after reperfused myocardial infarction in cannabinoid CB2 receptor deficient mice," *Life Sciences*, vol. 138, pp. 8–17, 2015.
- [45] T. Hilbert, P. Markowski, S. Frede et al., "Synthetic CpG oligonucleotides induce a genetic profile ameliorating murine myocardial I/R injury," *Journal of Cellular and Molecular Medicine*, vol. 22, no. 7, pp. 3397–3407, 2018.
- [46] S.-C. Kim, S. Wu, X. Fang et al., "Postconditioning with a CpG containing oligodeoxynucleotide ameliorates myocardial infarction in a murine closed-chest model," *Life Sciences*, vol. 119, no. 1–2, pp. 1–8, 2014.
- [47] G. D. Duerr, D. Dewald, E. J. Schmitz et al., "Metallothioneins 1 and 2 modulate inflammation and support remodeling in ischemic cardiomyopathy in mice," *Mediators of Inflammation*, vol. 2016, Article ID 7174127, 13 pages, 2016.
- [48] G. D. Duerr, J. C. Heinemann, G. Suchan et al., "The endocannabinoid-CB2 receptor axis protects the ischemic

- heart at the early stage of cardiomyopathy," *Basic Research in Cardiology*, vol. 109, no. 4, p. 425, 2014.
- [49] M. Velten, K. M. Heyob, L. E. Wold, and L. K. Rogers, "Perinatal inflammation induces sex-related differences in cardiovascular morbidities in mice," *American Journal of Physiology-Heart and Circulatory Physiology*, vol. 314, no. 3, pp. H573–H579, 2018.
- [50] M. Velten, G. D. Duerr, T. Pessies et al., "Priming with synthetic oligonucleotides attenuates pressure overload-induced inflammation and cardiac hypertrophy in mice," *Cardiovascular Research*, vol. 96, no. 3, pp. 422–432, 2012.
- [51] E. Carniel, M. R. G. Taylor, G. Sinagra et al., "Alpha-myosin heavy chain: a sarcomeric gene associated with dilated and hypertrophic phenotypes of cardiomyopathy," *Circulation*, vol. 112, no. 1, pp. 54–59, 2005.
- [52] M. Kamisago, J. P. Schmitt, D. McNamara, C. Seidman, and J. G. Seidman, "Sarcomere protein gene mutations and inherited heart disease: a β -cardiac myosin heavy chain mutation causing endocardial fibroelastosis and heart failure," *Novartis Foundation Symposia*, vol. 274, pp. 176–189, 2006.
- [53] J. Fang, Y. Li, K. Zhou, Y. Hua, C. Wang, and D. Mu, "Anti-thetical regulation of α -myosin heavy chain between fetal and adult heart failure through shuttling of HDAC5 regulating YY-1 function," *Cardiovascular Toxicology*, vol. 15, no. 2, pp. 147–156, 2015.
- [54] L. E. Wold, Z. Ying, K. R. Hutchinson et al., "Cardiovascular remodeling in response to long-term exposure to fine particulate matter air pollution," *Circulation Heart Failure*, vol. 5, no. 4, pp. 452–461, 2012.
- [55] D. Moris, M. Spartalis, E. Spartalis et al., "The role of reactive oxygen species in the pathophysiology of cardiovascular diseases and the clinical significance of myocardial redox," *Annals of Translational Medicine*, vol. 5, no. 16, p. 326, 2017.
- [56] D. M. Muntean, A. Sturza, M. D. Dănilă, C. Borza, O. M. Duicu, and C. Mornoș, "The role of mitochondrial reactive oxygen species in cardiovascular injury and protective strategies," *Oxidative Medicine and Cellular Longevity*, vol. 2016, Article ID 8254942, 19 pages, 2016.
- [57] M. A. Forgione, A. Cap, R. Liao et al., "Heterozygous cellular glutathione peroxidase deficiency in the mouse: abnormalities in vascular and cardiac function and structure," *Circulation*, vol. 106, no. 9, pp. 1154–1158, 2002.
- [58] O. Dewald, S. Sharma, J. Adroque et al., "Downregulation of peroxisome proliferator-activated receptor- α gene expression in a mouse model of ischemic cardiomyopathy is dependent on reactive oxygen species and prevents lipotoxicity," *Circulation*, vol. 112, no. 3, pp. 407–415, 2005.
- [59] J. P. Brennan, R. Southworth, R. A. Medina, S. M. Davidson, M. R. Duchon, and M. J. Shattock, "Mitochondrial uncoupling, with low concentration FCCP, induces ROS-dependent cardioprotection independent of KATP channel activation," *Cardiovascular Research*, vol. 72, no. 2, pp. 313–321, 2006.
- [60] S. M. Nadtochiy, A. J. Tompkins, and P. S. Brookes, "Different mechanisms of mitochondrial proton leak in ischaemia/reperfusion injury and preconditioning: implications for pathology and cardioprotection," *The Biochemical Journal*, vol. 395, no. 3, pp. 611–618, 2006.
- [61] K. S. Edwards, S. Ashraf, T. M. Lomax et al., "Uncoupling protein 3 deficiency impairs myocardial fatty acid oxidation and contractile recovery following ischemia/reperfusion," *Basic Research in Cardiology*, vol. 113, no. 6, p. 47, 2018.
- [62] M. E. Young, S. Patil, J. Ying et al., "Uncoupling protein 3 transcription is regulated by peroxisome proliferator-activated receptor (α) in the adult rodent heart," *The FASEB Journal*, vol. 15, no. 3, pp. 833–845, 2001.
- [63] T. Leger, K. Azarnoush, A. Traoré et al., "Antioxidant and cardioprotective effects of EPA on early low-severity sepsis through UCP3 and SIRT3 upholding of the mitochondrial redox potential," *Oxidative Medicine and Cellular Longevity*, vol. 2019, Article ID 9710352, 21 pages, 2019.
- [64] M.-S. Lee, I.-H. Kim, and Y. Kim, "Effects of eicosapentaenoic acid and docosahexaenoic acid on uncoupling protein 3 gene expression in C(2)C(12) muscle cells," *Nutrients*, vol. 5, no. 5, pp. 1660–1671, 2013.
- [65] J. Himms-Hagen and M. E. Harper, "Physiological role of UCP3 may be export of fatty acids from mitochondria when fatty acid oxidation predominates: an hypothesis," *Experimental Biology and Medicine*, vol. 226, no. 2, pp. 78–84, 2016.
- [66] P. M. Barger and D. P. Kelly, "PPAR signaling in the control of cardiac energy metabolism," *Trends in Cardiovascular Medicine*, vol. 10, no. 6, pp. 238–245, 2000.
- [67] A. K. Rines, H.-C. Chang, R. Wu et al., "Snf1-related kinase improves cardiac mitochondrial efficiency and decreases mitochondrial uncoupling," *Nature Communications*, vol. 8, no. 1, article 14095, 2017.
- [68] G. D. Duerr, J. C. Heinemann, V. Arnoldi et al., "Cardiomyocyte specific peroxisome proliferator-activated receptor- α overexpression leads to irreversible damage in ischemic murine heart," *Life Sciences*, vol. 102, no. 2, pp. 88–97, 2014.
- [69] M. E. Young, F. A. Laws, G. W. Goodwin, and H. Taegtmeier, "Reactivation of peroxisome proliferator-activated receptor α is associated with contractile dysfunction in hypertrophied rat heart," *Journal of Biological Chemistry*, vol. 276, no. 48, pp. 44390–44395, 2001.

Research Article

The Role of DNMT and HDACs in the Fetal Programming of Hypertension by Glucocorticoids

J. Lamothe,¹ S. Khurana ,² S. Tharmalingam,² C. Williamson,³ C. J. Byrne,³ N. Khaper ,⁴ S. Mercier,⁵ and T. C. Tai ^{1,2,3}

¹Biomolecular Sciences, Laurentian University, Sudbury, ON, Canada

²Medical Science Division, Northern Ontario School of Medicine Sudbury, ON, Canada

³Biology, Laurentian University, Sudbury, ON, Canada

⁴Medical Science Division, Northern Ontario School of Medicine Thunder Bay, ON, Canada

⁵School of Human Kinetics, Laurentian University, Sudbury, ON, Canada

Correspondence should be addressed to T. C. Tai; tc.tai@nosm.ca

Received 13 September 2019; Accepted 7 March 2020; Published 30 March 2020

Guest Editor: Bhagavatula Moorthy

Copyright © 2020 J. Lamothe et al. This is an open access article distributed under the Creative Commons Attribution License, which permits unrestricted use, distribution, and reproduction in any medium, provided the original work is properly cited.

The causes of hypertension are complex and involve both genetic and environmental factors. Environment changes during fetal development have been linked to adult diseases including hypertension. Studies show that timed in utero exposure to the synthetic glucocorticoid (GC) dexamethasone (Dex) results in the development of hypertension in adult rats. Evidence suggests that *in utero* stress can alter patterns of gene expression, possibly a result of alterations in the topology of the genome by epigenetic markers such as DNA methyltransferases (DNMTs) and histone deacetylases (HDACs). The objective of this study was to determine the effects of epigenetic regulators in the fetal programming and the development of adult hypertension. Specifically, this research examined the effects of the HDAC inhibitor valproic acid (VPA) and the DNMT inhibitor 5-aza-2'-deoxycytidine (5aza2DC) on blood pressure (BP) and gene expression in prenatal Dex-programmed rats. Data suggest that both VPA and 5aza2DC attenuated the Dex-mediated development of hypertension and restored BP to control levels. Epigenetic DNMT inhibition (DNMTi) or HDAC inhibition (HDACi) also successfully attenuated elevations in the majority of altered catecholamine (CA) enzyme expression, phenylethanolamine *N*-methyltransferase (PNMT) protein, and elevated epinephrine (Epi) levels in males. Although females responded to HDACi similar to males, DNMTi drove increased glucocorticoid receptor (GR) and PNMT expression and elevations in circulating Epi in females despite showing normotensive BP.

1. Introduction

Despite many advances in hypertension research, factors contributing to the development of the disease continue to emerge. Increasing significance has been placed on the fetal environment in the pathophysiology of the disease. Of particular interest is the role of GCs in fetal development and programming [1]. GCs can stimulate tissue maturation and fetal development; however, in times of stress, excess production of maternal GCs can negatively impact the fetus, promoting premature tissue development and programming for disease [1]. As outlined in our previous paper, understanding how these changes in the fetal environment affect adult gene expression has been the key to unravelling the mechanisms

involved in the fetal programming of hypertension [2]. Previous research has highlighted a role for ROS in programming; however, epigenetic modifications such as DNA methylation and histone acetylation are suspected to propagate these fetal insults to postnatal health. Increased fetal GC exposure may mediate programming through alteration of gene DNA methylation status; studies show increased global DNA methylation status in specific tissues, including the adrenal glands following betamethasone administration in guinea pigs [3]. The adrenal gland is the downstream regulator of the HPA axis, responsible for the production of CAs including Epi and norepinephrine (NE). Many genes suspected to be implicated in the development of hypertension are regulated via promoter methylation by DNMTs and are present

in the adrenal gland [4, 5]. Given that GCs mediate large changes in the adrenal methylation status, it is likely a result of altered DNMT abundance or activity. DNMTi has been shown to prevent NE-induced cardiac hypertrophy in rats [6], which may provide evidence for DNMT propagating fetal insults via GCs to gene expression changes in adulthood. DNMTs have also been implicated in a pulmonary model of hypertension, where DNMTi was shown to restore SOD2 expression and attenuate disease [7]. DNMTs have also been shown to mediate changes in mitochondrial function in times of stress, leading to altered ROS production [8]. As a result, not only are DNMTs implicated in hypertensive gene expression changes, DNMTs may also mediate ROS through changes in antioxidant enzyme expression patterns and mitochondrial ROS production.

HDACs are also involved in the development of hypertension. HDACi via VPA has been shown to be effective in attenuating inflammation, hypertrophic, and hypertensive responses in a spontaneously hypertensive rat (SHR) model of hypertension [9]. Interestingly, HDACi has proven to be effective in remediating hypertension in a rat model of Cushing's syndrome, characterized by excess GC cortisol [10]. HDACs have also been linked to pulmonary [11], high-fat diet-induced [12], and angiotensin II-induced [13] hypertension, and HDACi has been proven effective in treatment of hypertension. HDACi via trichostatin A administration has also been proven effective in attenuating neonatal Dex programming [14]. However, the role of HDACs in GC-mediated fetal programming of the HPA axis remains unknown. Similar to DNMTs, there is much overlap between HDACs and ROS, as HDACs have been shown to promote NADPH oxidase (Nox) expression and increase ROS production [15].

This study aims to investigate the role of DNMT or HDAC inhibition in GC-mediated fetal programming of hypertension. Specifically, the DNMT inhibitor 5aza2DC and the HDAC inhibitor VPA will be employed in GC-programmed adults, to determine if epigenetic inhibition can reverse hypertensive programming of CA biosynthesis and overall phenotype.

2. Methods

2.1. Animals. Male ($n = 6$) and female ($n = 18$) Wistar-Kyoto rats were purchased from Charles River Laboratories (Montreal, QC, Canada) at 6 weeks of age. Upon arrival, rats were housed in groups of 2-3 and allowed to acclimate to their new environment until 10 weeks of age. All animals were provided with food and water *ad libitum*. Procedures were followed as per Canadian Council on Animal Care guidelines and were approved by Laurentian University Animal Care Committee.

2.2. Breeding and Experimental Design. At 10 weeks of age, a male was housed with a group of three females until vaginal plugs were observed (gestational day 0 (GD 0)). Pregnant females were separated and housed individually. They then received a subcutaneous injection of Dex ($100 \mu\text{g}/\text{kg}/\text{day}$ in 4% ethanol/0.9% saline) or saline injection

(4% ethanol/0.9% saline) from GD -15-21 [2]. Following birth, offspring were weaned at 3 weeks of age and split into male and female groups.

2.3. Blood Pressure Measurements. The CODA-8 (Kent Scientific) noninvasive volume pressure recording tail-cuff BP system was employed to record BP measurements as performed previously [2]. Offspring were acclimated to the machine beginning at week 3 and measurements began at week 4 and ran until sacrifice at the end of week 14. Animals were also acclimated to the machine for 10 minutes prior to measurements. A total of 25 readings were taken per day over the course of 25 minutes, and three days of each week were recorded to form an average measurement per week. Measurements were recorded prior to any husbandry duties and within the hours of 9 am to 6 pm to avoid diurnal variation in BP.

2.4. Injections. In this study, offspring from saline- and Dex-injected dams received injections of VPA or 5Aza2DC and were categorized into 6 groups (Saline-Control, Dex-Control, Saline-5aza2DC, Dex-5aza2DC, Saline-VPA, and Dex-VPA); $n = 6$ animals per sex per group. Beginning at week 12 (day 78), once Dex-exposed animals displayed elevated BP relative to controls, animals received daily injections of saline (0.9%), 5aza2DC (1 mg/kg/day; LC Labs), or VPA (250 mg/kg/day; Cayman Labs) I.P. (Figure 1) for a total of 20 injections by the end of week 14.

2.5. Tissue Collection and Extraction. Animals were sacrificed upon the completion of week 14 epigenetic inhibitor injections. Animals were anesthetized via an injection of 75 mg/kg Ketalean (Ketalean; Bimeda, Cambridge, ON) and 5 mg/kg xylazine (Rompun; Bayer, Etobicoke, ON) I.P. and sacrificed using decapitation [16]. Following decapitation, trunk blood was collected into EDTA-coated (10.8 mg) Vacutainer blood collection vials (Becton Dickinson, Franklin Lakes, NJ, USA), and tissues including adrenal glands were harvested and flash frozen on dry ice for future analysis [2].

2.6. Adrenal mRNA Expression. Adrenals were homogenized using stainless steel beads and run in the TissueLyser (Qiagen) with TRIzol Reagent (Sigma-Aldrich) [2]. Following RNA extraction, RNA pellets were resuspended in DEPC-treated nuclease-free water. Quantification of RNA samples was assessed via a Nanodrop 1000 spectrophotometer (260 nm). Of the RNA samples, $2 \mu\text{g}$ were then treated with DNase I (Sigma) and converted to DNA using M-MLV reverse transcriptase (Promega) [2]. Gene expression was assessed using qPCR with Bioline SensiFast Sybr Lo-Rox mix (FroggaBio) and run on a Chromo4 qPCR system (BioRad). Table 1 highlights the primers used in qPCR analysis. A custom RT² profiler array (Qiagen) was employed to assess the expression of epigenetic regulations and additional antioxidant pathway targets. Total volume of $15 \mu\text{L}$ for qPCR reactions with 7.5 ng input cDNA. Primers for PNMT, TH, DBH, GR, EGR-1 SP1, RPL29, and B-actin were obtained from Sigma-Aldrich. Fold change was determined using the Ct value for each sample via the Pfaffl method

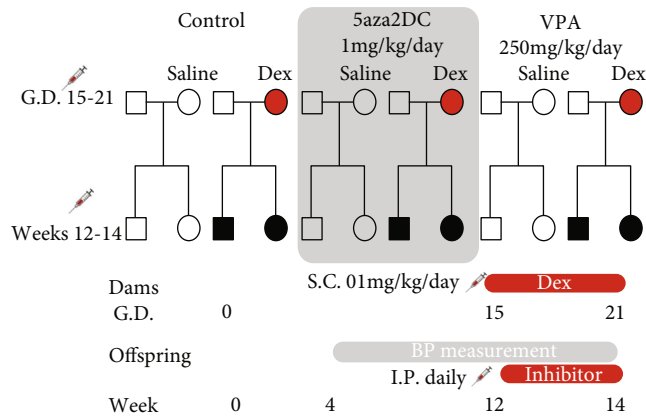


FIGURE 1: Schematic of fetal programming and epigenetic inhibitor administration. Pregnant WKY dams received 100 µg/kg/day dexamethasone S.C. from gestational days 15–21. Pups exposed to Dex *in utero* are shown in black. Weekly BP measurements were taken from weeks 4 to 14. Injections with the DNMT inhibitor 5aza2DC or VPA began at week 12 until sacrifice at the end of week 14. Adrenal glands were collected for protein and gene expression analysis, and plasma was collected for catecholamine analysis.

ratio = $(E_{\text{target}})^{\Delta C_{\text{target}}(\text{control-sample})} / (E_{\text{ref}})^{\Delta C_{\text{ref}}(\text{control-sample})}$ [17]. qPCR experiments were run in duplicate, with a biological replicate of $N = 6$ animals unless stated otherwise.

2.7. Western Blot. The All-Prep kit from Qiagen was employed to isolate protein from half of the remaining adrenal gland. Again, homogenization was performed with the TissueLyser (Qiagen). The protein-solubilizing buffer was supplemented with DTT to a total concentration of 8 mg DTT/1 mL ALO buffer to optimize pellet solubilization. ALO (300 µL) was then added to protein pellets, and samples were sonicated for 10 s at 100% amplitude (Sonic Dismembrator 500, Fisher Scientific). Following resuspension, samples were stored at -80°C until western blot analysis could be performed. A total of 5 µL of each sample was used for western blot, and gels were run as performed previously [2]. Gels were transferred to nitrocellulose membranes. Blots probing for DBH were blocked with 2% BSA. Primary antibodies used include TH (Novus Biologicals), DBH (Abcam), PNMT (Abcam), SP1 (Santa-Cruz), GR (Abcam), and GAPDH (Abcam). Based on primary antibody origin, secondaries conjugated to HRP-IgG were used. Blots were incubated for 2 minutes with ECL and exposed to a film for band visualization as described by Haan and Behrmann [18]. Quantification was performed using ImageJ (U.S. National Institutes of Health, Bethesda, MD, USA), and gels were normalized to GAPDH control. PAH and EGR1 were not quantified as antibodies suitable for western blot were not readily available.

2.8. Corticosterone and Catecholamine Levels. Following short-term storage on ice, plasma was separated from blood samples via centrifugation at 1500 g for 20 min and stored at -80°C [2]. Plasma (50 µL) was then run through the 2-CAT ELISA from LDN (Rocky Mountain Diagnostic,

Colorado Springs, CO, USA) to quantify plasma Epi and NE levels as per manufacturer's instructions. The parameter corticosterone ELISA from R&D systems (Minneapolis, MN, USA) was employed to assess plasma corticosterone levels.

2.9. Quantification and Statistical Analysis. Statistical computation was performed via the use of GraphPad PRISM software (La Jolla, CA, USA). Data is represented as mean ± SEM, and significance is indicated as * $P \leq 0.05$, ** $P \leq 0.01$, *** $P \leq 0.001$, **** $P \leq 0.0001$. * is relative to Control-Saline group, and † is relative to the Dex-Control group.

3. Results

As expected, Dex-programmed males (25.3 g) showed reduced body weight shortly after birth compared to Saline-Control (30.3 g) at weeks 3 of age, with females displaying similar trends (Figure 2(a)) [16]. Dex-programmed males and females continue to display reduced body weight compared to controls at week 11, until week 14 when significance is lost, yet the trend remains the same (Figures 2(b)–2(c)). By week 11, prenatally Dex-exposed male and female offspring display significantly increased BP compared to Saline-Control (Figures 3(a) and 3(b)). The epigenetic inhibitors 5aza2DC and VPA were effective in attenuating elevated BP induced by prenatal Dex exposure in adult offspring for both sexes (Figures 3(a) and 3(b)). 5aza2DC administration in Dex-programmed male offspring decreased mean arterial pressure (MAP) from 155 mmHg at week 11 to 117 mmHg by week 14 compared to Dex-Control animals which displayed a MAP of 140 mmHg by the end of week 14 (Figure 3(a)). 5aza2DC alone did not affect BP compared to Saline-Control (Figure 3(a)). Similarly, females administered 5aza2DC in the Dex-programmed group decreased MAP from 131 mmHg at week 11 to 117 mmHg at week 14 compared to Dex-Control animals which were at 134 mmHg at the end of week 14 (Figure 3(b)).

VPA administration in programmed male offspring decreased MAP from 140 mmHg to 109 mmHg by week 14, while Dex-Control animals maintained elevated MAP of 140 mmHg by week 14 (Figure 3(a)). Similarly, administration of VPA in Dex-exposed females decreased MAP from 133 mmHg to 112 mmHg by week 14 compared to Dex-Control females which displayed a MAP of 134 mmHg at week 14 (Figure 3(b)).

3.1. Gene Expression Analysis. The expression of CA biosynthetic enzymes and related regulatory transcription factors are shown in Figures 4(a)–4(f) and 5(a)–5(f), respectively. Prenatal Dex exposure has been shown to increase the expression of CA biosynthetic enzymes including TH, DBH, and PNMT, particularly in males [2]. Administration of the DNMT inhibitor 5aza2DC was effective in attenuating some of the increased CA enzymes due to Dex exposure for males only (Figures 4(a), 4(c), and 4(e)). Male offspring within the Dex-5aza2DC group displayed a reduction in the expression of TH (2.3-fold) and PNMT (1.0-fold), compared to Dex-Control (3.6-fold and 4.1-fold, respectively)

TABLE 1: Primer specification and qPCR parameters.

Gene target	Primer sequences	Amplicon size (bp)	Amplification conditions	cDNA input (ng)	Primer input (nM)
PAH NM_012619.2	F: GCTGCTAAGCTAGACACCTCA R: CTTGTTTCTGCCCAAAGTCT	105	1. 95°C, 2 min 2. 95°C, 1 min 3. 60°C, 1 min 4. 72°C, 1 min 5. Plate read 6. Go to line 2, 39 more times 7. Melting curve from 55-95°C, read every 1°C, hold 10 sec	7.5	600
TH L22651	F: GCGACAGAGTCTCATCGAGGAT R: AGAGCAGGTTGAGAACAGCATT	150	1. 95°C, 2 min 2. 95°C, 1 min 3. 58°C, 1 min 4. 72°C, 1 min 5. Plate read 6. Go to line 2, 29 more times 7. Melting curve from 55-95°C, read every 1°C, hold 10 sec	7.5	600
DBH NM_013158	F: TTCCCCATGTTCAACGGACC R: GCTGTGTAGTGTAGACGGATGC	240	1. 95°C, 2 min 2. 95°C, 1 min 3. 58°C, 1 min 4. 72°C, 1 min 5. Plate read 6. Go to line 2, 29 more times 7. Melting curve from 55-95°C, read every 1°C, hold 10 sec	7.5	600
PNMT X75333	F: CATCGAGGACAAGGGAGAGTC R: GCAGCGTCGTGATATGATAC	219	1. 95°C, 2 min 2. 95°C, 1 min 3. 60°C, 1 min 4. 72°C, 1 min 5. Plate read 6. Go to line 2, 39 more times 7. Melting curve from 55-95°C, read every 1°C, hold 10 sec	7.5	300
SP1 D12768.1	F: CAGACTAGCAGCAGCAATACCA R: TGAAGGCCAAGTTGAGCTCCAT	224	1. 95°C, 2 min 2. 95°C, 1 min 3. 58°C, 1 min 4. 72°C, 1 min 5. Plate read 6. Go to line 2, 29 more times 7. Melting curve from 55-95°C, read every 1°C, hold 10 sec	7.5	600
EGR1 AY551092.1	F: TTCCACAACAACAGGGAGAC R: CTCAACAGGGCAAGCATACG	261	1. 95°C, 2 min 2. 95°C, 1 min 3. 58°C, 1 min 4. 72°C, 1 min 5. Plate read 6. Go to line 2, 29 more times 7. Melting curve from 55-95°C, read every 1°C, hold 10 sec	7.5	600
GR NM_012576.2	F: TGCTGGAGGTGATTGAACCC R: TCACTTGACGCCACCTAAC	111	1. 95°C, 2 min 2. 95°C, 1 min 3. 58°C, 1 min 4. 72°C, 1 min 5. Plate read 6. Go to line 2, 29 more times 7. Melting curve from 55-95°C, read every 1°C, hold 10 sec	7.5	600

TABLE 1: Continued.

Gene target	Primer sequences	Amplicon size (bp)	Amplification conditions	cDNA input (ng)	Primer input (nM)
Beta actin NM_031144	F: TCTGTGTGGATTGGTGGCTCT R: GACTCATCGTACTCCTGCTG	83	1. 95°C, 2 min 2. 95°C, 1 min 3. 58°C, 1 min 4. 72°C, 1 min 5. Plate read 6. Go to line 2, 29 more times 7. Melting curve from 55-95°C, read every 1°C, hold 10 sec	7.5	600
RPL29 NM_017150	F: TGAGAGGTAGGGTCCCGTTT R: TCAGTTCTGGGACCTGACCA	144	1. 95°C, 2 min 2. 95°C, 1 min 3. 58°C, 1 min 4. 72°C, 1 min 5. Plate read 6. Go to line 2, 29 more times 7. Melting curve from 55-95°C, read every 1°C, hold 10 sec	7.5	600

(Figures 4(a) and 4(e)). DBH remained elevated similar to Dex-Control levels. Interestingly, 5aza2DC affected female offspring differently than males, as Dex-exposed females maintained elevated expression of TH (2.2-fold), PNMT (1.8-fold), and DBH (3.0-fold) expression as compared to the untreated Dex-exposed females (Figures 4(b), 4(d), and 4(f)).

In contrast to DNMT inhibition, Dex-exposed animals given VPA shows a drastic reduction in CA enzyme expression for both sexes (Figures 4(a)–4(f)). In males, VPA reduced the expression of TH (1.2-fold), DBH (1.2-fold), and PNMT (1.4-fold) compared to Dex-Control groups (3.6-fold, 2.7-fold, and 4.1-fold, respectively) (Figures 4(a)–4(c)). Mirroring male offspring, female offspring in the Dex-VPA group shows a significant reduction in TH (2.2-fold) and PNMT (1.1-fold) compared to Dex-Control (3.2-fold and 2.1-fold, respectively) (Figures 4(a) and 4(e)). Interestingly, for male and female offspring, animals in the Saline-VPA group displayed significantly elevated levels of TH, DBH, and PNMT similar to that of Dex-Control animals (Figures 4(a)–4(f)).

Dex-exposed animals also display significantly increased gene expression levels of transcription factors SP1, EGR1, and GR predominantly in males as shown previously [2]. Both VPA and 5aza2DC were largely effective in reducing transcription factor expression levels in males. Dex-exposed females do show a trend towards increased SP1 and GR expression although not statistically significant (Figures 5(b) and 5(f)).

Treatment with 5aza2DC in prenatally Dex-exposed male offspring decreased the expression of SP1 (1.3-fold), EGR1 (1.0-fold), and GR (1.1-fold) to levels comparable to Saline-Control (Figures 5(a), 5(c), and 5(e)). In response to 5aza2DC, Dex-exposed female offspring did not show significant changes in transcription factor expression with the exception of elevated GR (2.1-fold) although the result is not significantly different than the Dex-Control group (1.4-fold) (Figure 5(f)).

VPA reduced the expression of SP1 (0.9-fold), EGR1 (0.5-fold), and GR (1.3-fold) in males as compared to Dex-Control levels and are comparable to Saline-Control (Figures 5(a), 5(c), and 5(e)). Interestingly, female offspring in the VPA-Dex (3.6-fold) group display elevated EGR1 compared to Saline-Control and Dex-Control (1.1-fold) groups (Figure 5(d)).

3.2. Protein Expression. Prenatal Dex exposure increased protein levels for CA biosynthetic enzymes TH (2.4-fold), DBH (2.0-fold), and PNMT (2.0-fold) in males, but not females (Figures 6(a), 6(c), and 6(e)). Control-Dex females do display an increasing trend in PNMT though not significant (Figure 6(f)). Administration of 5aza2DC did not attenuate TH (2.8-fold) or DBH (2.2-fold) protein levels; however, it was effective in reducing PNMT (1.3-fold) (Figures 6(a), 6(c), and 6(e)). 5aza2DC did not display a significant effect on protein levels in programmed and unprogrammed female offspring (Figures 6(b), 6(d), and 6(f)).

Similar to the DNMT inhibitor, VPA was largely effective at reducing PNMT protein levels in males (1.1-fold) compared to Dex-Control group (2.0-fold) (Figure 6(e)). Both TH (2.4-fold) and DBH (1.8-fold) remained elevated and were comparable to Dex-Controls (2.2-fold and 2.0-fold, respectively) (Figures 6(a) and 6(c)). Interestingly, elevated mRNA expression of CA genes in unprogrammed males administered VPA matched elevated protein levels: TH (2.3-fold) and DBH (2.3-fold), with PNMT displaying a similar trend although it did not reach statistical significance (Figures 6(a), 6(c), and 6(e)).

Contrary to gene expression results, prenatal Dex exposure did not program for increased protein levels of SP1 in adult males or females (Figures 7(a) and 7(b)). Males exposed to Dex do show a trend for elevated GR levels (1.7-fold) but not females (Figure 7(c)). Administration of the DNMT inhibitor 5aza2DC reduced GR protein levels (1.0-fold) in programmed males compared to Dex-Control (1.9-fold)

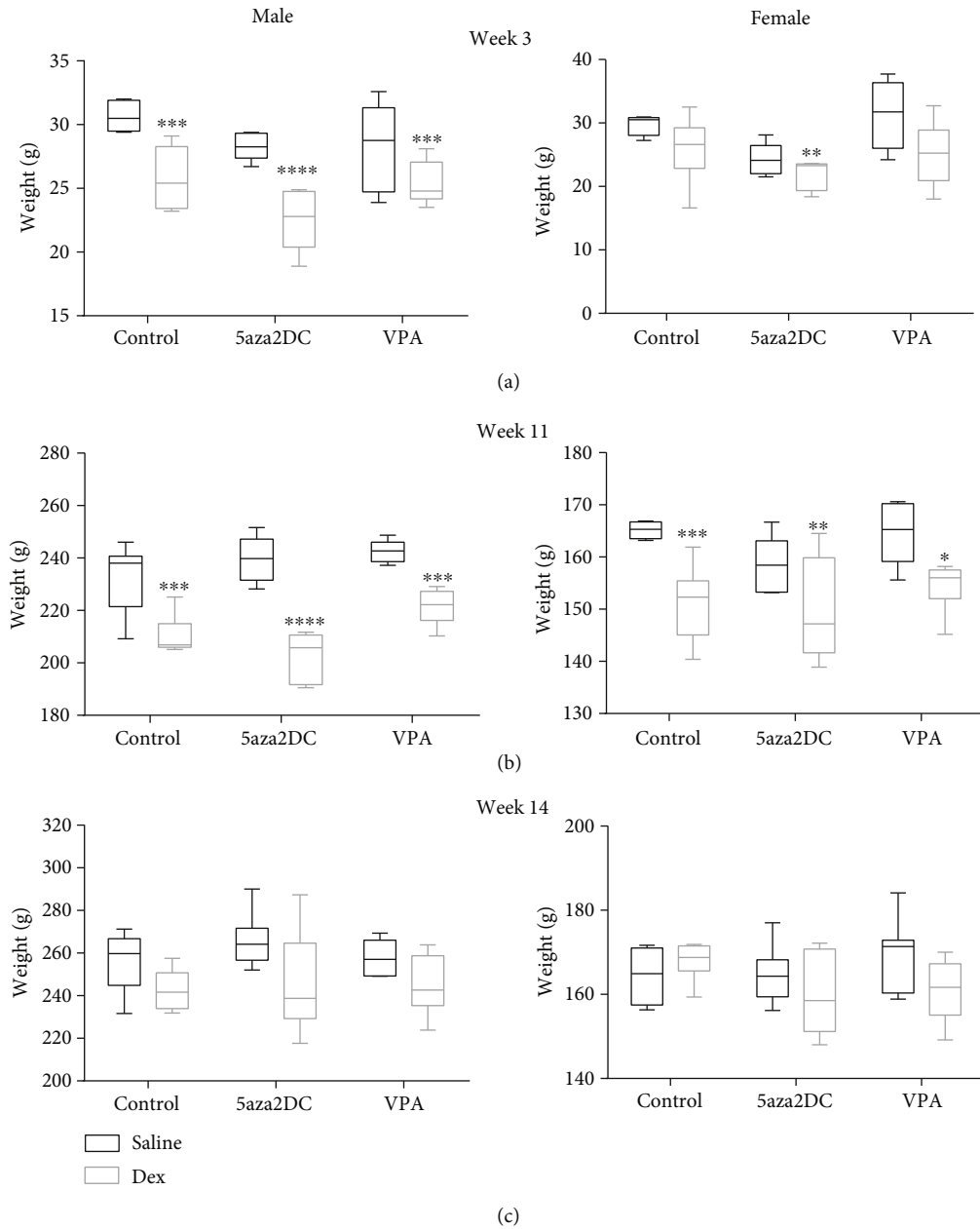


FIGURE 2: Animal body weights. Male and female body weights of Dex-programmed offspring at (a) week 3 after birth, (b) before administering drugs week 11, (c) and after receiving 5aza2DC or VPA via daily injections (I.P.) from weeks 12 to 14 at week 14. $N = 6$. Two-way ANOVA (Fisher LSD test): statistical significance is represented as * $P = 0.05$, ** $P = 0.01$, *** $P = 0.001$, and **** $P = 0.0001$. The symbol (*) indicates significance relative to Saline-Control. Plot wings represent min and max values within each group. $N = 6$ per group.

(Figure 7(c)). 5aza2DC administration in females however did not significantly alter GR protein levels (Figure 7(d)).

VPA was effective in reducing Dex-driven increases in GR protein levels (0.7-fold) compared to Dex-Control (1.9-fold) in males (Figure 7(c)). VPA did not have an impact on prenatally Dex-exposed female offspring transcription factor expression (Figure 7(d)). Moreover, VPA-Saline male offspring shows significantly increased SP1 levels (1.7-fold) and a trend towards elevated levels of GR (Figures 7(a) and 7(c)) with females displaying a similar trend in SP1 expression (Figure 7(b)).

3.3. *Plasma Catecholamines*. There was no significant change in corticosterone levels between treatment groups detectable with ELIS; however, changes in CA levels were detected following treatment with inhibitors of DNMT and HDAC. 5aza2DC was effective in reducing male Epi levels (from 7.1 ng/mL to 5.0 ng/mL) to that of Saline-Control (4.8 ng/mL) (Figure 8(a)); however, in females, 5aza2DC administration increased Epi levels (9.2 ng/mL) above Dex-Control animals (6.7 ng/mL) (Figure 8(b)). VPA was particularly effective in reducing Epi levels for both males (from 7.1 ng/mL to 4.1 ng/mL) and females (from 6.7 ng/mL to

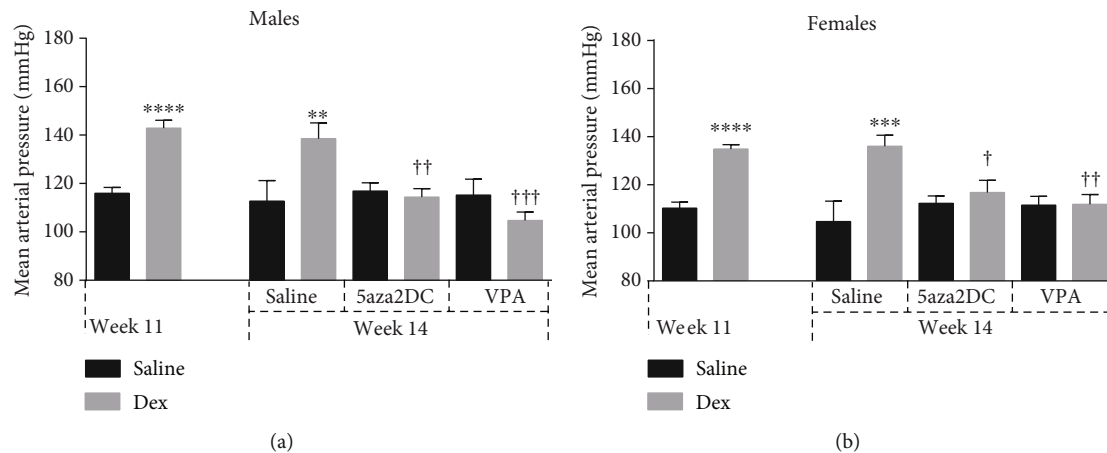


FIGURE 3: Mean arterial pressure of Dex-programmed offspring exposed to epigenetic inhibitors in adulthood. Mean arterial pressure of Dex-programmed offspring given 5aza2DC or VPA in (a) males or (b) females via daily injections (I.P.) from weeks 12 to 14. Measured using the CODA8 BP monitor from Kent Scientific. $N = 6$. Two-way ANOVA (Fisher LSD test): statistical significance is represented as $^{*/†}P \leq 0.05$, $^{**/††}P \leq 0.01$, $^{***/†††}P \leq 0.001$, and $^{****/††††}P \leq 0.0001$. Saline-Control and Dex-Control are shown here for reference, and results have been described previously. * indicates significance relative to Saline-Control, and † indicates significance relative to Dex-Control. Data are presented as mean \pm SEM. $N = 6$ per group.

3.7 ng/mL) as compared to Dex-Control groups (Figures 8(a) and 8(b)).

Interestingly, Dex-exposed offspring displayed a reduction in plasma NE levels: male (3.5 ng/mL) and female (5.2 ng/mL) compared to Saline-Control (6.5 ng/mL and 8.3 ng/mL, respectively) (Figures 8(c) and 8(d)). 5aza2DC increased NE levels above Saline-Control for males (10.2 ng/mL) and females (10.8 ng/mL), and as a result, the levels are significantly different than Dex-Control animals (Figures 8(c) and 8(d)).

VPA administration resulted in NE levels comparable to Saline-Control for unprogrammed and programmed male offspring (5.4 ng/mL and 5.3 ng/mL, respectively) (Figure 8(c)). Females however maintain a decrease in NE in the VPA-Dex group (3.5 ng/mL), significantly decreased from Saline-Control (8.3 ng/mL) and comparable to that of Dex-Control (5.2 ng/mL) (Figure 8(d)).

3.4. Additional Mechanisms in GC-Mediated Fetal Programming of Hypertension. The results from the RT² profiler array suggest distinct differences in oxidative stress markers between Control-Dex and Control-Saline groups predominantly in male offspring. Prenatal Dex exposure increased the expression of catalase (CAT) (1.7-fold), Noxa1 (5.2-fold), and SOD1 (2.1-fold) in males and not females (Figures 9(a)–9(h)).

5aza2DC was effective in reducing altered ROS-related genes in Dex-exposed offspring as CAT (1.1-fold), Noxa1 (1.7-fold), and SOD1 (1.5-fold) to expression levels comparable to Saline-Control (Figures 9(a), 9(e), and 9(g)), with the exception of GPx1 which remained unchanged (Figure 9(c)). Programmed females in the 5aza2DC-Dex group display different trends than males. No change was seen with CAT and Noxa1; however, GPx1 (4.5-fold) and SOD1 (3.2-fold) were increased compared to Saline-Control and Dex-Control (Figures 9(d) and 9(h)). SOD1 was also significantly

increased in unprogrammed 5aza2DC-Saline females (2.2-fold) compared to Dex-Control but not significantly different than Saline-Control (Figure 9(h)).

VPA was effective in reducing altered expression of CAT (1.1), Noxa1 (1.3), and SOD1 (1.1) in Dex-exposed offspring (Figures 9(a), 9(e), and 9(g)). Again, GPx1 expression was not recovered in this group with VPA (0.5) and remained reduced compared to Saline-Control (Figure 9(c)). In unprogrammed males that received VPA injections, a significant increase in CAT expression (1.6) was found as compared to Saline-Control (Figure 9(a)). VPA-Saline males show a similar trend for increased Noxa1 expression (3.2); however, the results did not reach significance (Figure 9(e)).

Programmed females that received VPA injections did not display significant changes in the expression of CAT, GPx1, or Noxa1 compared to the Dex-programmed group (Figures 9(b), 9(d), and 9(f)). Interestingly, unprogrammed females that received VPA displayed elevated SOD1 expression levels (2.6-fold) compared to Saline-Control and Dex-Control (0.6-fold) (Figures 9(h)).

Dex exposure resulted in significant changes in HDAC expression levels in male offspring including HDAC1 (1.8-fold), HDAC5 (1.5-fold), HDAC6 (1.6-fold), HDAC7 (1.8-fold), and HDAC11 (1.9-fold) (Figures 10(a), 10(c), 10(e), 10(g), and 10(i)). Dex-programmed females displayed similar trends as males in HDAC6 and HDAC7, with HDAC7 (2.1-fold) reaching significance (Figures 10(f) and 10(h)).

Interestingly, 5aza2DC was effective in reducing Dex-mediated altered HDAC expression (Figures 10(a)–10(j)) with the exception of HDAC7 for males and females (Figures 10(g) and 10(h)).

Similar to 5aza2DC, Dex-programmed male offspring that received VPA injections displays significantly reduced expression of HDAC1, HDAC5, and HDAC11 and also reducing HDAC7 compared to Dex-Control (Figures 10(a), 10(c), 10(e), 10(g), and 10(i)). Females also show a similar

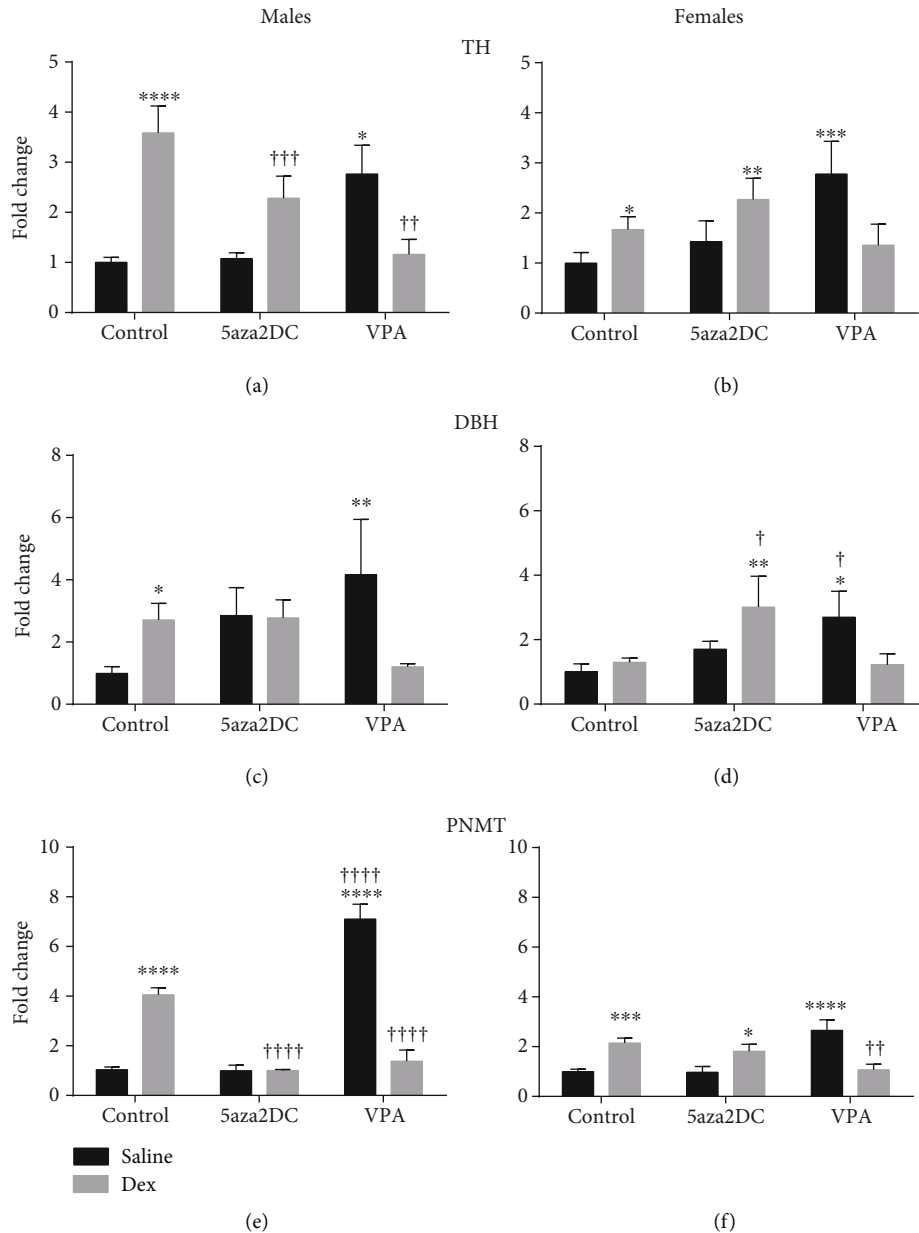


FIGURE 4: Relative mRNA expression of catecholamine biosynthetic enzyme expression ($2^{-\Delta\Delta C_t}$). qPCR gene expression of catecholamine biosynthetic enzymes including (a, b) tyrosine hydroxylase (TH), (c, d) dopamine beta-hydroxylase (DBH), and (e, f) phenylethanolamine *N*-methyltransferase (PNMT) for males and females. Two-way ANOVA (Fisher LSD test): statistical significance is represented as $^{*/\dagger}P \leq 0.05$, $^{**/\dagger\dagger}P \leq 0.01$, $^{***/\dagger\dagger\dagger}P \leq 0.001$, and $^{****/\dagger\dagger\dagger\dagger}P \leq 0.0001$. Saline-Control and Dex-Control are shown here for reference, and results have been described previously. Data are presented as mean \pm SEM. * indicates significance relative to Saline-Control, and † indicates significance relative to (c). $N = 4-6$ per group.

trend as males as both HDAC6 and HDAC7 were reduced to control (Figures 10(f) and 10(h)). VPA-Saline males did not show any significant changes in HDAC gene expression compared to Saline-Control animals.

4. Discussion

Epigenetic inhibition through DNMTi via 5aza2DC or through HDACi via VPA attenuated the GC-mediated fetal programming (FP) of the HPA axis particularly in male

offspring. Male offspring showed a significant reduction in majority of the CA enzyme and transcription factor mRNA gene expression, a reduction in PNMT protein levels, and a reduction in circulating Epi and BP. Females also display similar trends in response to VPA; however, 5aza2DC actually increased expression of CA enzymes and increased plasma Epi, suggesting sex-specific responses to epigenetic inhibitors; however, BP remained at control levels, indicating it was effective in attenuating hypertension to some extent, potentially through alternate mechanisms.

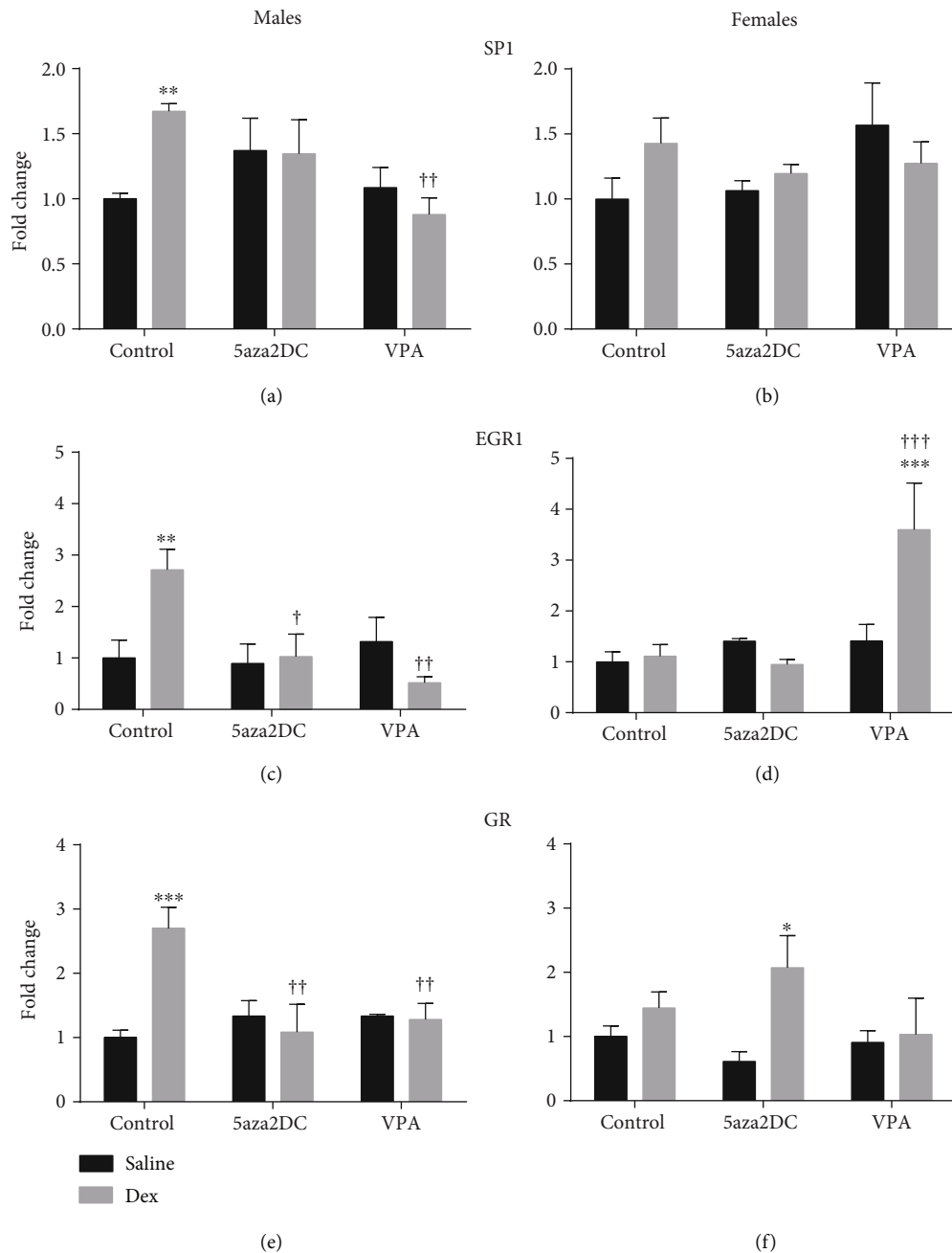


FIGURE 5: Relative mRNA expression of catecholamine biosynthetic enzyme transcription factor expression ($2^{-\Delta\Delta C_t}$). qPCR gene expression of catecholamine biosynthetic enzymes transcription factor including (a, b) specificity protein 1 (SP1), (c, d) early growth response 1 (EGR1), and (e, f) glucocorticoid receptor (GR) for males and females. Two-way ANOVA (Fisher LSD test): statistical significance is represented as $^*/\dagger P \leq 0.05$, $^{**}/\dagger\dagger P \leq 0.01$, and $^{***}/\dagger\dagger\dagger P \leq 0.001$. Saline-Control and Dex-Control are shown here for reference, and results have been described previously. Data are presented as mean \pm SEM. * indicates significance relative to Saline-Control, and † indicates significance relative to Dex-Control. $N = 3-6$ per group.

4.1. Epigenetic Inhibitors Attenuate GC-Mediated Fetal Programming of Blood Pressure and Impact on Body Weight. There is evidence that epigenetics is implicated in hypertension and is suspected to be involved in GC-mediated FP of hypertension. Epigenetic inhibitors were employed to investigate the link between epigenetics and GC-mediated programming of the HPA. Histone acetylation generally promotes euchromatin conformation promoting

gene transcription by allowing access to the gene for transcription machinery. As a result, histone deacetylation via HDACs canonically leads to heterochromatin formation and gene silencing; however, HDACs have also been shown to promote gene expression in some cases [19, 20]. VPA mediates HDACi and thus gene activation by reducing protein activity, potentially via binding to the catalytic centre [21]. VPA exhibits HDACi across several classes of HDACs

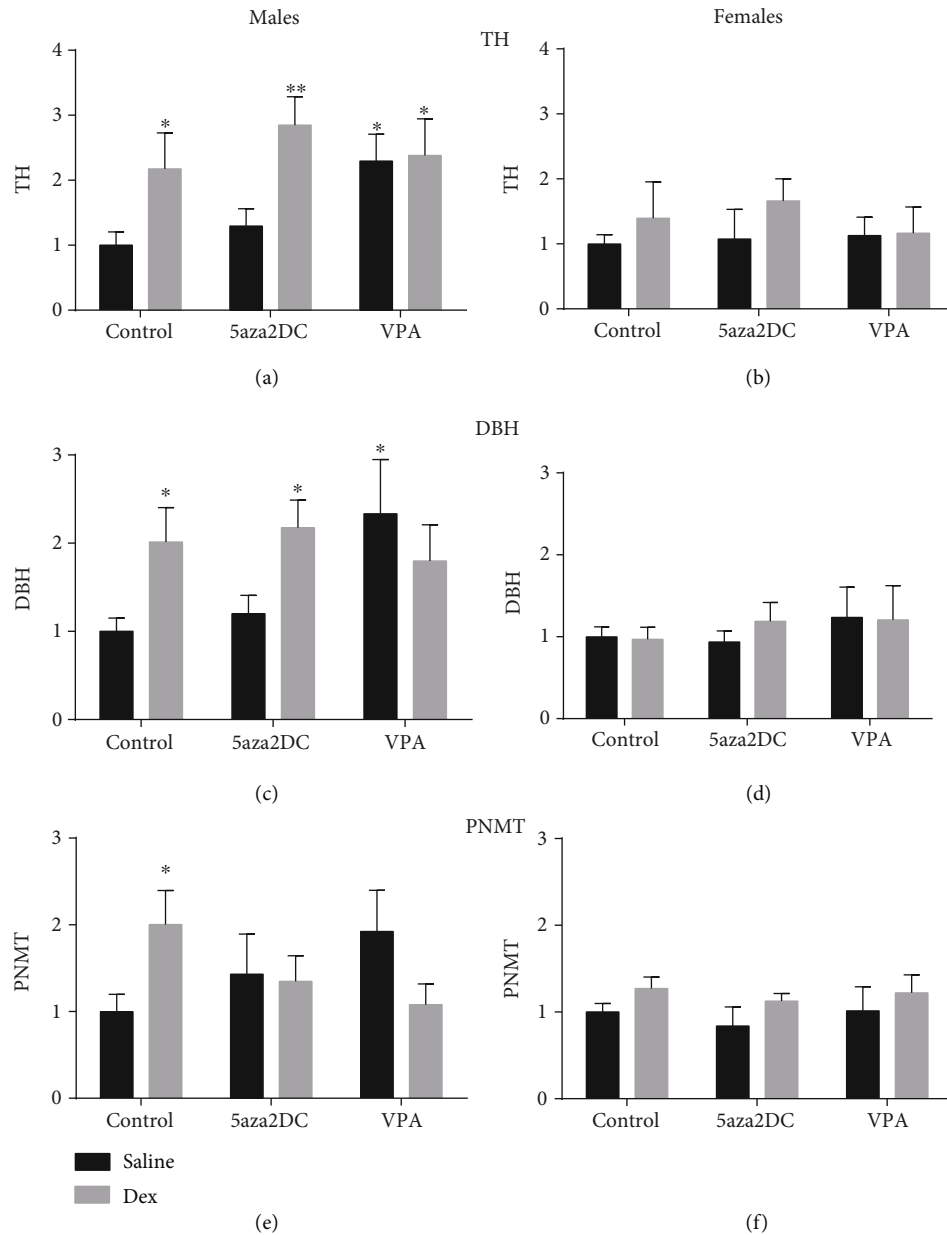


FIGURE 6: Quantification of catecholamine biosynthetic enzyme protein levels. Western blot analysis of (a, b) tyrosine hydroxylase (TH), (c, d) dopamine beta-hydroxylase (DBH), and (e, f) phenylethanolamine *N*-methyltransferase (PNMT) for males and females. Two-way ANOVA (Fisher LSD test): statistical significance is represented as * $P = 0.05$ and ** $P = 0.01$. Saline-Control and Dex-Control are shown here for reference, and results have been described previously. Data are presented as mean \pm SEM. * indicates significance relative to Saline-Control, and † indicates significance relative to Dex-Control. $N = 3-6$ per group.

including class 1 and some class 2 HDACs [1–5, 7] and is a more potent inhibitor of class IIb HDACs [6, 10] [22]. VPA also displays some activity outside of HDACi, and HDACs can deacetylate proteins other than histones to alter activity.

DNMTi via 5aza2DC is a result of the cytidine analogue replacing native cytosine residues during replication. DNMT then binds these altered bases resulting in covalent bond, decreasing soluble DNMT concentrations [23]. Furthermore, there is evidence that azacitidines increase proteasomal degradation of DNMTs, as a result multiple mechanisms are likely involved [23, 24]. The reduction in soluble DNMT is

thought to lead to hypomethylation and gene activation. Consequently, DNMTi should promote gene activation, although this is not always the case. There is evidence that 5aza2DC can induce chromatin remodeling and promote gene activation by altering histone methylation status [25]. Antithetically, DNMTi may also reduce gene expression when reduced promoter methylation allows increased repressor protein binding [26].

Previous studies have shown that GC exposure during the third trimester of pregnancy leads to the development of hypertension in adulthood [1, 2]. Indicative of *in utero*

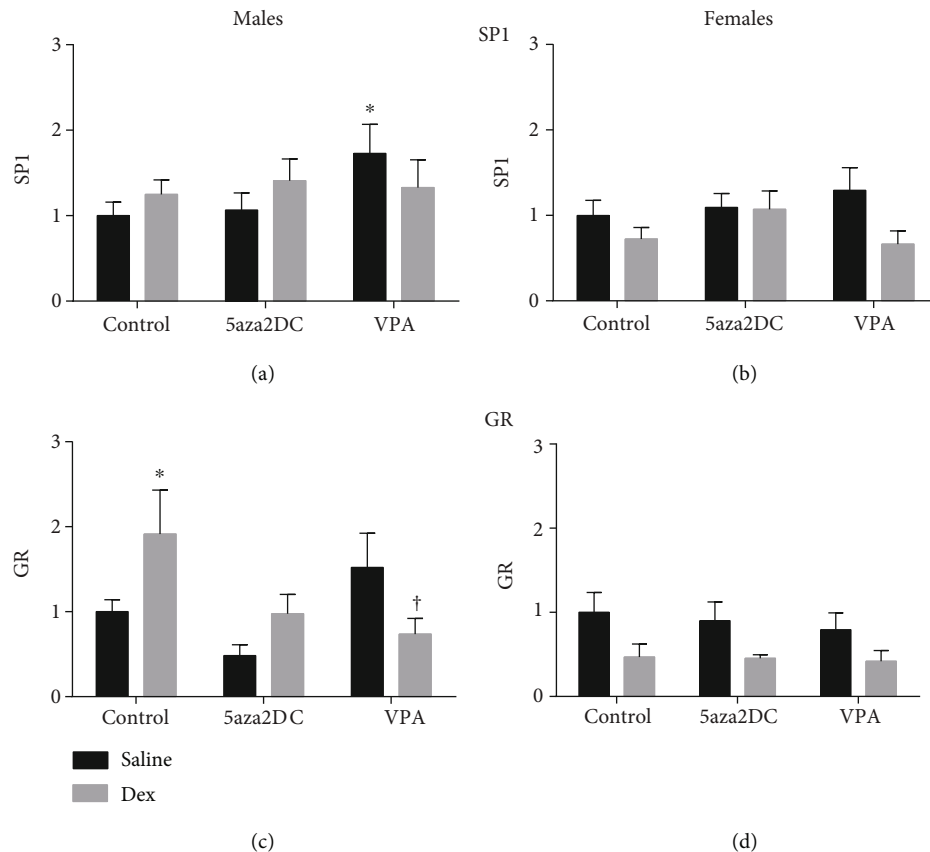


FIGURE 7: Quantification of catecholamine biosynthetic enzyme transcription factor protein levels from offspring adrenal gland. Western blot analysis of (a, b) specificity protein (SP1) and (c, d) glucocorticoid receptor (GR) for males and females. Two-way ANOVA (Fisher LSD test): statistical significance is represented as $^{*/†}P \leq 0.05$. Saline-Control and Dex-Control are shown here for reference, and results have been described previously. Data are presented as mean \pm SEM. * indicates significance relative to Saline-Control, and † indicates significance relative to Dex-Control. $N = 3-6$ per group.

Dex exposure, programmed animals display decreased birth weight [27]. In our current study, as expected, Dex programming has reduced male and female offspring body weight up until week 11, before epigenetic inhibitor administration (Figures 2(a) and 2(b)). Animals at week 14 did not display significant differences in body weight; however, this is likely not due to epigenetic inhibitor administration as treatment groups remain similar to Control-Dex animals (Figure 2(c)). However, interestingly, epigenetic inhibition successfully attenuated GC-mediated changes in BP. Following epigenetic inhibitor administration at the end of week 14, both 5aza2DC and VPA reduced BP down to control levels in males and females (Figures 3(a)–3(d)), attenuating the hypertensive phenotype and confirming a role for epigenetics in GC-programmed hypertension. Previous evidence has highlighted a role for epigenetics in the development of hypertension in SHR [9]. Additionally, evidence has linked prenatal GC exposure to altered methylation that is tissue specific in guinea pigs [3]. This study describes a novel method of attenuating postnatal increases in BP as a result of GC-mediated FP in rats via HDACi or DNMTi.

4.2. The Role of Epigenetics in CA Biosynthesis in GC-Programmed Offspring (mRNA and Protein). Methylation of

CA enzyme promoter regions is suspected to alter gene expression and binding of transcription factors. In a human cell line, TH has been shown to contain a CpG site which can be methylated, altering Sp1 binding, and DNMTi via 5aza2DC increased TH expression [28]. DBH promoter methylation has also been suggested to modulate expression and affect behaviour [29]. PNMT may be regulated by promoter methylation; however, this has yet to be investigated.

Interestingly, inhibition of methylation via 5aza2DC or HDACi via VPA significantly attenuated the majority of programmed elevations in CA enzymes in males including TH, DBH, PNMT, SP1, EGR1, and GR (Figures 4(a), 4(c), 4(e), 5(a), 5(c), and 5(e)). In females, DNMTi did not attenuate CA enzyme programming; however, HDACi was effective (Figures 5(b), 5(d), and 5(f)). Interestingly, in both sexes, the administration of VPA without prior prenatal Dex exposure significantly increased CA enzyme expression, in many instances above that of Dex alone (Figures 4(a)–4(f)). HDAC6 has been shown to bind GR forming a repressor complex which has the potential to inhibit CA enzyme expression as they are regulated by GR [30]. As a result, inhibition of HDACs via VPA may serve to increase active GR by preventing formation of the repressor complex, although this remains unknown. Furthermore, Dex has been shown to

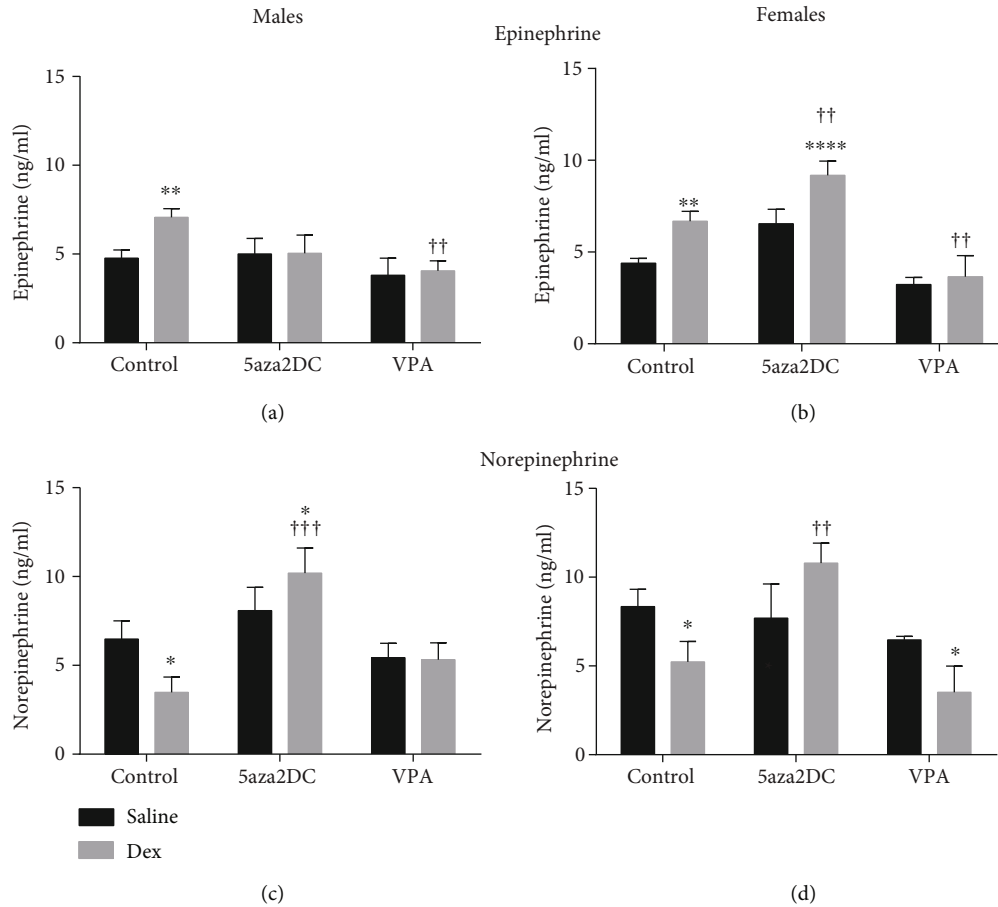


FIGURE 8: Plasma catecholamine levels. Results from plasma catecholamine ELISA for (a, b) epinephrine and (c, d) norepinephrine for males and females. Two-way ANOVA (Fisher LSD test): statistical significance is represented as $*/†P \leq 0.05$, $*/††P \leq 0.01$, $****/†††P \leq 0.001$, and $****/††††P \leq 0.0001$. Saline-Control and Dex-Control are shown here for reference, and results have been described previously. Data are presented as mean \pm SEM. * indicates significance relative to Saline-Control, and † indicates significance relative to Dex-Control. $N = 4-6$ per group.

increase this association between HDAC6 and GR increasing repression of GR target genes; however, the impact of Dex on this association has not been studied from a FP perspective [30]. HDACs also catalyze deacetylation of proteins outside of histones and can contribute significantly to cell signalling mechanisms [31]. GR is one such protein and can be deacetylated directly by HDACs (1, 2, and 3), altering how GR impacts transcription [10, 32]. Studies in a rat model of Cushing's syndrome show HDACi abolished hypertension potentially via inhibition of GR activity by increasing its acetylation directly [10]. As a result, it is difficult to determine whether HDACi impacts CA enzymes and transcription factor expression, or transcription factor binding activity through direct association and repression, or by catalyzing acetylation and activity. Elucidating the mechanisms leading to altered CA enzyme expression is difficult; however, evidence suggests a potential role for Dex-HDAC-GR interactions.

Interestingly, changes in CA enzyme expression due to either epigenetic inhibitor only resulted in reduced PNMT and GR protein levels as TH and DBH remained elevated (Figures 6(a)–6(f)). Altered expression of miRNA may explain differences in gene and protein levels; indeed,

miRNA have been shown to alter CA synthesis and secretion, and additional regulatory mechanisms are likely involved [33]. miRNA have also been shown to regulate corticosteroidogenesis [34] and dopamine synthesis [35] and transport [36] TH [37], SP1 [33], and GR levels [38].

Importantly, the reduction in PNMT protein resulted in reduced plasma Epi levels for males given VPA or 5aza2DC. VPA also mirrored these results in females. Interestingly, 5aza2DC increased plasma Epi for Dex-exposed females. This was unexpected as PNMT mRNA, and overall, BP is comparable to control animals. The protective role of estrogen in GC-mediated FP is complex. Estrogen has been shown to alter the expression of epigenetic regulators including HDACs and DNMTs, and the presence of ER on a gene promoter has been correlated with its methylation status [39]. Estrogen has also been implicated in complex cycling of gene methylation/demethylation via DNMTs and inhibition of this cycling resulted in transcriptional activation [40]. This type of complex transcriptional regulation may account for estrogen's protective effects on programming. Furthermore, if the protective effects of estrogen, specifically with respect to Epi synthesis or degradation, involve DNMT-mediated

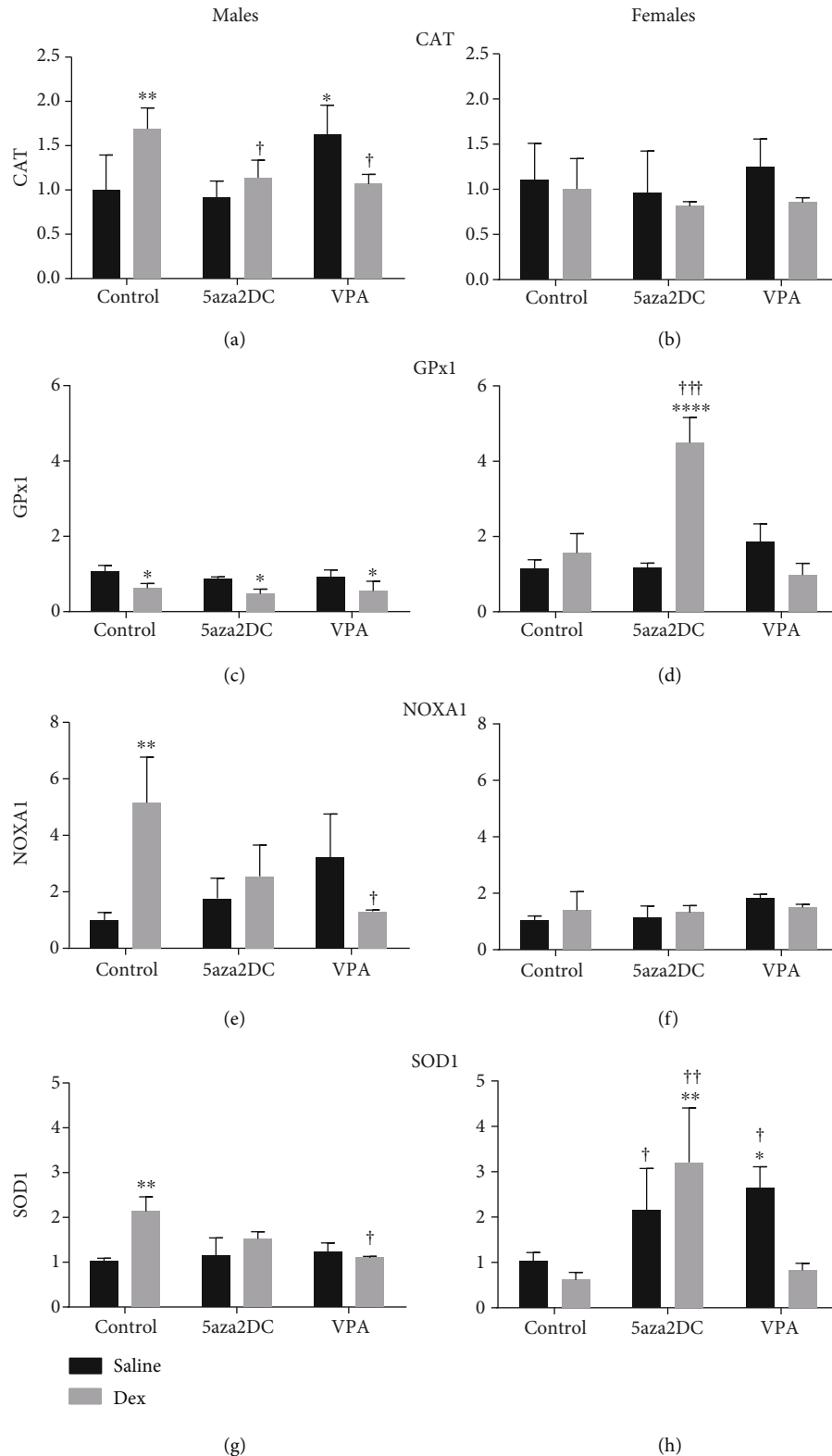


FIGURE 9: Antioxidant and ROS-related gene expression results from the RT² profiler array (Qiagen). Quantification of qPCR gene expression which showed significance from the RT² profiler array including (a) catalase (CAT), (b) glutathione peroxidase 1 (GPx1), (c) NADPH oxidase activator 1 (Noxa1), and (d) superoxide dismutase 1 (SOD1). Two-way ANOVA (Fisher LSD test): statistical significance is represented as */† $P \leq 0.05$, **/†† $P \leq 0.01$, ***/††† $P \leq 0.001$, and ****/†††† $P \leq 0.0001$. Saline-Control and Dex-Control are shown here for reference, and results have been described previously. Data are presented as mean \pm SEM. * indicates significance relative to Saline-Control, and † indicates significance relative to Dex-Control. $N = 3-5$ per group.

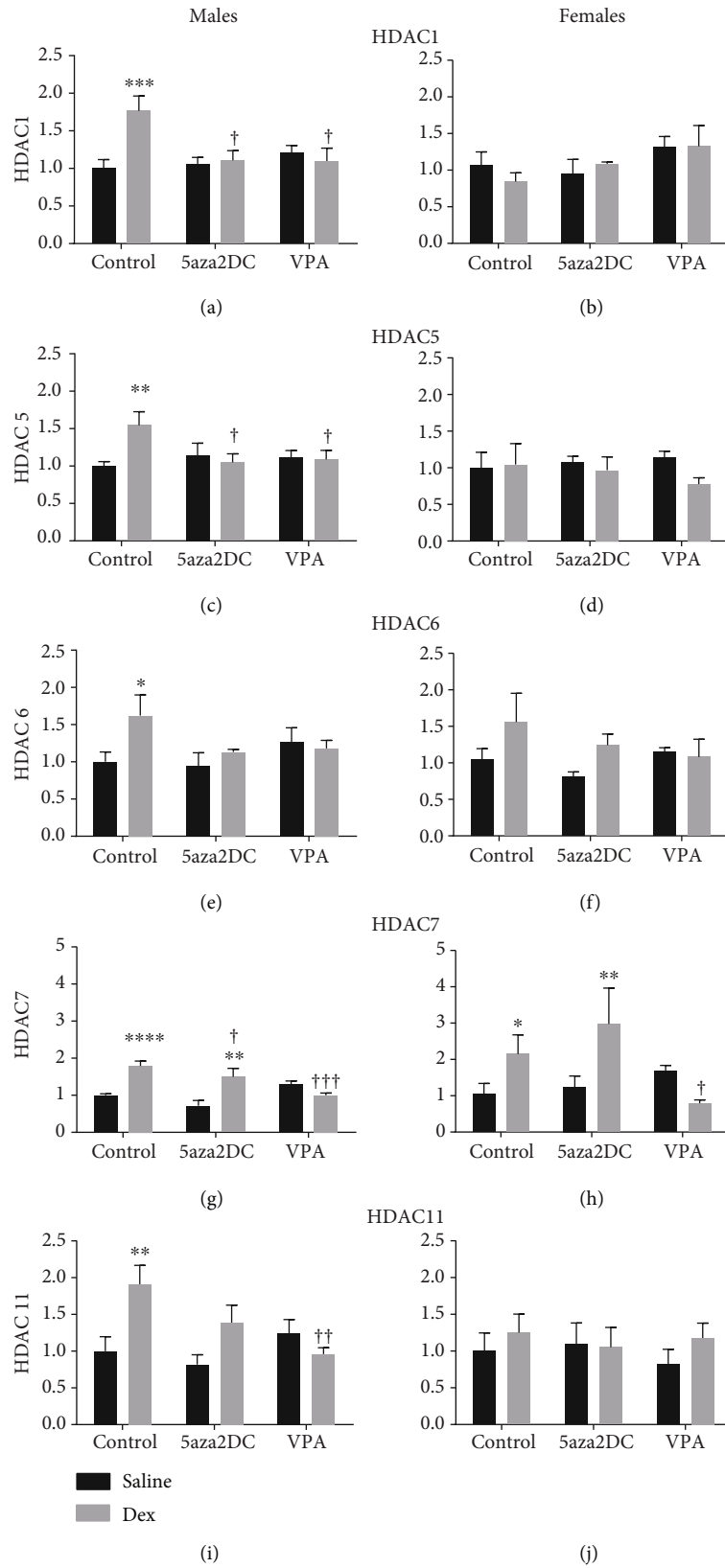


FIGURE 10: HDAC gene expression results from the RT² profiler array (Qiagen). (a) Histone deacetylase (HDAC) 1, (b) HDAC5, (c) HDAC6, (d) HDAC7, and (e) HDAC11 for males and females. Two-way ANOVA (Fisher LSD test): statistical significance is represented as ^{*/†} $P \leq 0.05$, ^{**/††} $P \leq 0.01$, ^{***/†††} $P \leq 0.001$, and ^{****/††††} $P \leq 0.0001$. Saline-Control and Dex-Control are shown here for reference, and results have been described previously. Data are presented as mean \pm SEM. * indicates significance relative to Saline-Control, and † indicates significance relative to Dex-Control. $N = 3-5$ per group.

changes in gene expression, it is plausible that this may explain the effects of 5aza2DC on Epi in Dex programming. Furthermore, estrogen plays a protective role on the cardiovascular system via its ability to reduce ROS production and increase antioxidant enzyme levels [41]. ROS levels impact gene expression and have been shown to alter the expression of PNMT [42].

Dex exposure results in reduced NE levels (Figures 8(a) and 8(b)), potentially a result of increased PNMT to mediate conversion of NE to Epi. When given 5aza2DC, both sexes display increased NE above that of control, indicating a potential build-up of substrate for Epi synthesis. Conversely, VPA decreased NE levels, comparable to control in males, and NE remained reduced and comparable to Dex alone in females (Figure 8(b)). Again, it is not surprising that NE levels differ between sexes in Dex-exposed animal given VPA, since as mentioned previously, estrogen can alter HDAC expression among others [39].

4.3. The Relationship between ROS and Epigenetics in the Fetal Programming of Hypertension. Increased GCs drive increased metabolic activity and thus mitochondrial ROS production [43], and these changes in ROS may mediate FP via GC; however, the mechanism remains undetermined. Evidence for both ROS and epigenetic dysregulation has been described in hypertensive models [3, 7, 9, 44, 45]. There is significant overlap between ROS and epigenetic gene regulation in hypertensive programming as either pathway can alter the other. For example, ROS produced via NADPH oxidases (Nox) increase DNMT and HDAC activity, which in turn can silence or upregulate Nox depending on the protein [46]. HDACi has proven to reduce Nox expression and ROS production in a rat model of pulmonary hypertension [47]. Expression of antioxidant enzymes also impact the expression of epigenetic machinery. Increased expression of SOD1 and GPx1 alters histone acetylation and methylation differentially; however, if it occurs through histone acetyltransferase or HDAC or another mechanism, regulation is unknown [26]. This study shows that Dex exposure resulted in significant changes in antioxidant and prooxidant enzyme expression as well as altered HDAC expression. Interestingly, 5aza2DC attenuated dysregulation of antioxidant/oxidant enzyme expression in males including CAT, Noxa1, and SOD1 but not GPx1 (Figure 9), indicating that altered expression of these enzymes due to GC programming involves DNMTs. Interestingly, females which generally do not display dysregulation of ROS pathways in response to Dex show that 5aza2DC in combination with Dex exposure significantly increases antioxidant enzymes Gpx1 and SOD1 (Figures 9(b) and 9(d)). Taken together, these results indicate a potential link between antioxidant response to Dex exposure and DNMTs, with sex-specific responses. It is possible that elevated SOD1 and reduced GPx1 act together in association with increased Noxa1 in Dex-programmed males to drive altered HDAC expression as seen (Figures 10(a), 10(c), 10(e), 10(g), and 10(i)) and thus impacting gene expression within the CA biosynthesis pathway. How DNMTs are implicated in this pathway and whether ROS is upstream of epigenetic regulation remains

to be determined. Inhibition of either epigenetic machinery or ROS has proven effective in remediating programming effects in previous studies. HDACi via VPA has been shown to decrease ROS and the Nox catalytic subunit gp91phox in SHR [9] and to reduce programmed ROS production due to low protein maternal diet [48]. Furthermore, maternal antioxidant administration has been shown to prevent GC-related programming in mice [45].

5. Conclusion

The fetal programming of hypertension via GCs involves both ROS and epigenetics in the pathology of adult disease. Specifically, GC FP results in dysregulation of ROS through altered expression of CAT, Gpx1, SOD1, and Noxa1 and implicating epigenetic regulators including HDACs and DNMTs. HDACi and DNMTi are effective in attenuating HPA axis programming of CA biosynthetic enzymes including PNMT, the production of CAs including Epi, and attenuating the hypertensive phenotype particularly in male offspring. It is clear that both epigenetics and ROS are connected and drive expression of each other. This feed forward loop appears to be implicated in the pathogenesis of Dex-mediated hypertension. When combined with previous studies, targeting this mechanism at the level of ROS or epigenetics are effective in remediating altered expression of key regulators in both pathways and preventing or attenuating GC-mediated FP of hypertension.

Data Availability

All relevant data are within the manuscript files.

Conflicts of Interest

The authors declare that they have no conflicts of interest.

Acknowledgments

This work was supported by the funding from the Canadian Institutes for Health Research (Grant IHD98766) and the NOSMFA Research Development Fund. Preliminary data from this manuscript was presented at the 2nd Canadian National Perinatal Research Meeting (2015).

References

- [1] N. S. Levitt, R. S. Lindsay, M. C. Holmes, and J. R. Seckl, "Dexamethasone in the last week of pregnancy attenuates hippocampal glucocorticoid receptor gene expression and elevates blood pressure in the adult offspring in the rat," *Neuroendocrinology*, vol. 64, no. 6, pp. 412–418, 1996.
- [2] P. Nguyen, S. Khurana, H. Peltsch et al., "Prenatal glucocorticoid exposure programs adrenal PNMT expression and adult hypertension," *The Journal of Endocrinology*, vol. 227, no. 2, pp. 117–127, 2015.
- [3] A. Crudo, S. Petropoulos, V. G. Moisiadis et al., "Prenatal synthetic glucocorticoid treatment changes DNA methylation states in male organ systems: multigenerational effects," *Endocrinology*, vol. 153, no. 7, pp. 3269–3283, 2012.

- [4] I. Bogdarina, S. Welham, P. J. King, S. P. Burns, and A. J. L. Clark, "Epigenetic modification of the renin-angiotensin system in the fetal programming of hypertension," *Circulation Research*, vol. 100, no. 4, pp. 520–526, 2007.
- [5] S. Stoll, C. Wang, and H. Qiu, "DNA methylation and histone modification in hypertension," *International Journal of Molecular Sciences*, vol. 19, no. 4, p. 1174, 2018.
- [6] D. Xiao, C. Dasgupta, M. Chen et al., "Inhibition of DNA methylation reverses norepinephrine-induced cardiac hypertrophy in rats," *Cardiovascular Research*, vol. 101, no. 3, pp. 373–382, 2014.
- [7] S. L. Archer, G. Marsboom, G. H. Kim et al., "Epigenetic attenuation of mitochondrial superoxide dismutase 2 in pulmonary arterial hypertension: a basis for excessive cell proliferation and a new therapeutic target," *Circulation*, vol. 121, no. 24, pp. 2661–2671, 2010.
- [8] S. K. Saini, K. C. Mangalharra, G. Prakasam, and R. N. K. Bamezai, "DNA methyltransferase1 (DNMT1) isoform3 methylates mitochondrial genome and modulates its biology," *Scientific Reports*, vol. 7, no. 1, p. 1525, 2017.
- [9] J. P. Cardinale, S. Sriramula, R. Pariaut et al., "HDAC inhibition attenuates inflammatory, hypertrophic, and hypertensive responses in spontaneously hypertensive rats," *Hypertension*, vol. 56, no. 3, pp. 437–444, 2010.
- [10] H.-A. Lee, S. H. Kang, M. Kim et al., "Histone deacetylase inhibition ameliorates hypertension and hyperglycemia in a model of Cushing's syndrome," *American Journal of Physiology-Endocrinology and Metabolism*, vol. 314, no. 1, pp. E39–E52, 2018.
- [11] L. Zhao, C. N. Chen, N. Hajji et al., "Histone deacetylation inhibition in pulmonary hypertension: therapeutic potential of valproic acid and suberoylanilide hydroxamic acid," *Circulation*, vol. 126, no. 4, pp. 455–467, 2012.
- [12] J. Choi, S. Park, T. K. Kwon, S. I. Sohn, K. M. Park, and J. I. Kim, "Role of the histone deacetylase inhibitor valproic acid in high-fat diet-induced hypertension via inhibition of HDA-C1/angiotensin II axis," *International Journal of Obesity*, vol. 41, no. 11, pp. 1702–1709, 2017.
- [13] Y. Ryu, H. J. Kee, S. Sun et al., "Class I histone deacetylase inhibitor MS-275 attenuates vasoconstriction and inflammation in angiotensin II-induced hypertension," *PLoS One*, vol. 14, no. 3, article e0213186, 2019.
- [14] T.-H. Wu, H. C. Kuo, I. C. Lin, S. J. Chien, L. T. Huang, and Y. L. Tain, "Melatonin prevents neonatal dexamethasone induced programmed hypertension: histone deacetylase inhibition," *The Journal of Steroid Biochemistry and Molecular Biology*, vol. 144, no. Part B, pp. 253–259, 2014.
- [15] S.-A. Manea, M. L. Antonescu, I. M. Fenyó, M. Raicu, M. Simionescu, and A. Manea, "Epigenetic regulation of vascular NADPH oxidase expression and reactive oxygen species production by histone deacetylase-dependent mechanisms in experimental diabetes," *Redox Biology*, vol. 16, pp. 332–343, 2018.
- [16] P. Nguyen, H. Peltsch, J. de Wit et al., "Regulation of the phenylethanolamine N-methyltransferase gene in the adrenal gland of the spontaneous hypertensive rat," *Neuroscience Letters*, vol. 461, no. 3, pp. 280–284, 2009.
- [17] M. W. Pfaffl, "A new mathematical model for relative quantification in real-time RT-PCR," *Nucleic Acids Research*, vol. 29, no. 9, pp. 45e–445, 2001.
- [18] C. Haan and I. Behrmann, "A cost effective non-commercial ECL-solution for Western blot detections yielding strong signals and low background," *Journal of Immunological Methods*, vol. 318, no. 1-2, pp. 11–19, 2007.
- [19] M. Haberland, R. L. Montgomery, and E. N. Olson, "The many roles of histone deacetylases in development and physiology: implications for disease and therapy," *Nature Reviews Genetics*, vol. 10, no. 1, pp. 32–42, 2009.
- [20] A. Wang, S. K. Kurdastani, and M. Grunstein, "Requirement of Hos2 histone deacetylase for gene activity in yeast," *Science*, vol. 298, no. 5597, pp. 1412–1414, 2002.
- [21] M. Göttlicher, S. Minucci, P. Zhu et al., "Valproic acid defines a novel class of HDAC inhibitors inducing differentiation of transformed cells," *The EMBO Journal*, vol. 20, no. 24, pp. 6969–6978, 2001.
- [22] A. V. Bieliauskas and M. K. H. Pflum, "Isoform-selective histone deacetylase inhibitors," *Chemical Society Reviews*, vol. 37, no. 7, pp. 1402–1413, 2008.
- [23] C. Stresemann and F. Lyko, "Modes of action of the DNA methyltransferase inhibitors azacytidine and decitabine," *International Journal of Cancer*, vol. 123, no. 1, pp. 8–13, 2008.
- [24] K. Patel, J. Dickson, S. Din, K. Macleod, D. Jodrell, and B. Ramsahoye, "Targeting of 5-aza-2'-deoxycytidine residues by chromatin-associated DNMT1 induces proteasomal degradation of the free enzyme," *Nucleic Acids Research*, vol. 38, no. 13, pp. 4313–4324, 2010.
- [25] C. T. Nguyen, D. J. Weisenberger, M. Velicescu et al., "Histone H3-lysine 9 methylation is associated with aberrant gene silencing in cancer cells and is rapidly reversed by 5-aza-2'-deoxycytidine," *Cancer Research*, vol. 62, no. 22, pp. 6456–6461, 2002.
- [26] K. Bahar Halpern, T. Vana, and M. D. Walker, "Paradoxical role of DNA methylation in activation of FoxA2 gene expression during endoderm development," *The Journal of Biological Chemistry*, vol. 289, no. 34, pp. 23882–23892, 2014.
- [27] E. C. Cottrell and J. R. Seckl, "Prenatal stress, glucocorticoids and the programming of adult disease," *Frontiers in Behavioral Neuroscience*, vol. 3, p. 19, 2009.
- [28] T. Aranyi, B. A. Faucheux, O. Khalfallah et al., "The tissue-specific methylation of the human tyrosine hydroxylase gene reveals new regulatory elements in the first exon," *Journal of Neurochemistry*, vol. 94, no. 1, pp. 129–139, 2005.
- [29] J. Schmitz, R. Kumsta, D. Moser, O. Güntürkün, and S. Ocklenburg, "DNA methylation of dopamine-related gene promoters is associated with line bisection deviation in healthy adults," *Scientific Reports*, vol. 9, no. 1, p. 5902, 2019.
- [30] M. G. Rimando, H. H. Wu, Y. A. Liu et al., "Glucocorticoid receptor and histone deacetylase 6 mediate the differential effect of dexamethasone during osteogenesis of mesenchymal stromal cells (MSCs)," *Scientific Reports*, vol. 6, no. 1, p. 37371, 2016.
- [31] S. Spange, T. Wagner, T. Heinzel, and O. H. Krämer, "Acetylation of non-histone proteins modulates cellular signalling at multiple levels," *The International Journal of Biochemistry & Cell Biology*, vol. 41, no. 1, pp. 185–198, 2009.
- [32] K. Ito, S. Yamamura, S. Essilfie-Quaye et al., "Histone deacetylase 2-mediated deacetylation of the glucocorticoid receptor enables NF-kappaB suppression," *The Journal of Experimental Medicine*, vol. 203, no. 1, pp. 7–13, 2006.
- [33] Y. Gai, J. Zhang, C. Wei, W. Cao, Y. Cui, and S. Cui, "miR-375 negatively regulates the synthesis and secretion of catecholamines by targeting Sp1 in rat adrenal medulla," *American Journal of Physiology-Cell Physiology*, vol. 312, no. 5, pp. C663–C672, 2017.

- [34] S. Robertson, L. A. Diver, S. Alvarez-Madrazo et al., "Regulation of corticosteroidogenic genes by microRNAs," *International Journal of Endocrinology*, vol. 2017, Article ID 2021903, 11 pages, 2017.
- [35] M. Yang, Y. Wei, F. Jiang et al., "MicroRNA-133 inhibits behavioral aggregation by controlling dopamine synthesis in locusts," *PLoS Genetics*, vol. 10, no. 2, p. e1004206, 2014.
- [36] X. Jia, F. Wang, Y. Han et al., "miR-137 and miR-491 negatively regulate dopamine transporter expression and function in neural cells," *Neuroscience Bulletin*, vol. 32, no. 6, pp. 512–522, 2016.
- [37] J. Kim, K. Inoue, J. Ishii et al., "A microRNA feedback circuit in midbrain dopamine neurons," *Science*, vol. 317, no. 5842, pp. 1220–1224, 2007.
- [38] A. Riester, O. Issler, A. Spyroglou, S. H. Rodrig, A. Chen, and F. Beuschlein, "ACTH-dependent regulation of microRNA as endogenous modulators of glucocorticoid receptor expression in the adrenal gland," *Endocrinology*, vol. 153, no. 1, pp. 212–222, 2012.
- [39] K. M. Frick, Z. Zhao, and L. Fan, "The epigenetics of estrogen: epigenetic regulation of hormone-induced memory enhancement," *Epigenetics*, vol. 6, no. 6, pp. 675–680, 2011.
- [40] R. Métivier, R. Gallais, C. Tiffoche et al., "Cyclical DNA methylation of a transcriptionally active promoter," *Nature*, vol. 452, no. 7183, pp. 45–50, 2008.
- [41] A. Iorga, C. M. Cunningham, S. Moazeni, G. Ruffenach, S. Umar, and M. Eghbali, "The protective role of estrogen and estrogen receptors in cardiovascular disease and the controversial use of estrogen therapy," *Biology of Sex Differences*, vol. 8, no. 1, p. 33, 2017.
- [42] J. A. G. Crispo, D. R. Ansell, G. Ubriaco, and T. C. Tai, "Role of reactive oxygen species in the neural and hormonal regulation of the PNMT gene in PC12 cells," *Oxidative Medicine and Cellular Longevity*, vol. 2011, Article ID 756938, 10 pages, 2011.
- [43] R. L. Flaherty, M. Owen, A. Fagan-Murphy et al., "Glucocorticoids induce production of reactive oxygen species/reactive nitrogen species and DNA damage through an iNOS mediated pathway in breast cancer," *Breast Cancer Research*, vol. 19, no. 1, p. 35, 2017.
- [44] N. H. von Bergen, S. L. Koppenhafer, D. R. Spitz et al., "Fetal programming alters reactive oxygen species production in sheep cardiac mitochondria," *Clinical Science*, vol. 116, no. 8, pp. 659–668, 2009.
- [45] R. D. Roghair, J. A. Wemmie, K. A. Volk, T. D. Scholz, F. S. Lamb, and J. L. Segar, "Maternal antioxidant blocks programmed cardiovascular and behavioural stress responses in adult mice," *Clinical Science*, vol. 121, no. 10, pp. 427–436, 2011.
- [46] Y. Mikhed, A. Görlach, U. G. Knaus, and A. Daiber, "Redox regulation of genome stability by effects on gene expression, epigenetic pathways and DNA damage/repair," *Redox Biology*, vol. 5, pp. 275–289, 2015.
- [47] F. Chen, X. Li, E. Aquadro et al., "Inhibition of histone deacetylase reduces transcription of NADPH oxidases and ROS production and ameliorates pulmonary arterial hypertension," *Free Radical Biology & Medicine*, vol. 99, pp. 167–178, 2016.
- [48] C. C. Vega, L. A. Reyes-Castro, G. L. Rodríguez-González et al., "Resveratrol partially prevents oxidative stress and metabolic dysfunction in pregnant rats fed a low protein diet and their offspring," *The Journal of Physiology*, vol. 594, no. 5, pp. 1483–1499, 2016.

Review Article

Potential Role of Antioxidants as Adjunctive Therapy in Chagas Disease

Juana P. Sánchez-Villamil ^{1,2}, Paula K. Bautista-Niño ¹, Norma C. Serrano,¹
Melvin Y. Rincon,¹ and Nisha J. Garg ³

¹Translational Biomedical Research Group, Centro de Investigaciones, Fundación Cardiovascular de Colombia, Santander, Colombia

²Faculty of Basic Sciences, Universidad Antonio Nariño, Santander, Colombia

³Department of Microbiology and Immunology, Institute for Human Infections and Immunity, University of Texas Medical Branch, Galveston, Texas, USA

Correspondence should be addressed to Juana P. Sánchez-Villamil; juanipsan3@gmail.com and Nisha J. Garg; nigarg@utmb.edu

Received 19 December 2019; Revised 2 March 2020; Accepted 7 March 2020; Published 26 March 2020

Guest Editor: Lynette K. Rogers

Copyright © 2020 Juana P. Sánchez-Villamil et al. This is an open access article distributed under the Creative Commons Attribution License, which permits unrestricted use, distribution, and reproduction in any medium, provided the original work is properly cited.

Chagas disease (CD) is one of the most important neglected tropical diseases in the American continent. Host-derived nitroxidative stress in response to *Trypanosoma cruzi* infection can induce tissue damage contributing to the progression of Chagas disease. Antioxidant supplementation has been suggested as adjuvant therapy to current treatment. In this article, we synthesize and discuss the current evidence regarding the use of antioxidants as adjunctive compounds to fight harmful reactive oxygen species and lower the tissue oxidative damage during progression of chronic Chagas disease. Several antioxidants evaluated in recent studies have shown potential benefits for the control of oxidative stress in the host's tissues. Melatonin, resveratrol, the combination of vitamin C/vitamin E (vitC/vitE) or curcumin/benznidazole, and mitochondria-targeted antioxidants seem to be beneficial in reducing plasma and cardiac levels of lipid peroxidation products. Nevertheless, further research is needed to validate beneficial effects of antioxidant therapies in Chagas disease.

1. Introduction

Chagas disease (CD), caused by *Trypanosoma cruzi*, belongs to the group of neglected tropical diseases that affects more than 1 billion of the poorest and most marginalized people in the world [1]. It is estimated that 6-7 million people are infected with *T. cruzi*, ~30,000 new cases of *T. cruzi* infection emerge each year, and CD accounts for >12,000 deaths per year (World Health Organization (WHO) Epidemiology, <http://www.who.int/chagas/epidemiology/en/>). *T. cruzi* infection and CD are endemic in South America, Central America, and Mexico. The natural cycle of *T. cruzi* transmission evidenced with the detection of a high rate of infection in dogs [2, 3] and autochthonous cases of CD in humans [4] is also documented in the Southern USA. Since 1980s, due to the migration of infected woman of childbearing age to nonendemic regions of the world who transmit the infection

to their babies, the incidences of CD have increased, transforming it into a new worldwide public health challenge [5].

Upon infection, acute blood parasitemia can be detected for approximately 60 days by various diagnostic methods (discussed in [6]). Most infected individuals develop potent immune response to control *T. cruzi* infection; however, the parasite persists at low levels in the host, and a vast majority of infected individuals develop no organ dysfunction during their life. However, up to 1/3rd of the infection cases progress into the clinical form of the disease that mainly develops with the pathological involvement of the heart, though the megaesophagus and megacolon may also be noted [7, 8]. Chagas cardiomyopathy is presented with a wide variety of manifestations including arrhythmias, apical aneurysm, left ventricular systolic dysfunction, thrombotic events, dilated cardiomyopathy, and terminal heart failure leading to patients' death [9].

Two drugs, benznidazole and nifurtimox, are currently available for the treatment of patients diagnosed early after *T. cruzi* infection. International guidelines recommend that acute infection cases (all ages) and children up to 14 years old should be treated with antiparasitic drug therapies [10]. In the US, the Food and Drug Administration agency has approved benznidazole for use in children 2–12 years of age [11]. Though the mechanism of action is not completely understood, it is suggested that the activated benznidazole and nifurtimox (and their metabolites) bind to and block the parasites' antioxidant availability [12, 13] and generate DNA-toxic glyoxal adducts [14] causing oxidative damage to the parasite [15, 16]. It is important to note that benznidazole and nifurtimox have limited efficacy in the chronic disease phase [17] when adult patients exhibit several significant side effects [17], and these drugs are not recommended for pregnant women (reviewed in [18, 19]). Thus, there is an urgent need for new drugs to control pathogen and pathogen-induced pathological events in CD [20].

The pathology of Chagas disease is complex, with several parasitic and host determinants having critical and major roles. Parasite virulence and genetic susceptibility of the host result in varying disease outcomes. In general, it is believed that the low-grade parasites contribute to heart damage through inducing inflammation, fibrosis, and oxidative injuries, leading to disruption of myofibrils, myocyte necrosis, microvascular and autonomic dysfunction, and cardiac hypertrophy and fibrosis. Depending on the extent of these processes, varied outcomes of infection ranging from no disease to cardiac damage, remodeling, and heart failure and related clinical sequelae, such as stroke, may culminate in the patient. Readers are directed to an excellent recent review for additional details on the pathology and pathogenesis of Chagas heart disease [9].

2. Antioxidant/Oxidant Imbalance in Chagas Disease

Antioxidant/oxidant imbalance is considered a main factor associated with CD progression. With regard to elicitation of oxidative stress, two major sources are identified. Studies in mice and humans show that innate and adaptive immune responses should control the parasite through the production of reactive oxygen species (ROS)/reactive nitrogen species (RNS), proinflammatory T_H1 cytokines, trypanolytic antibodies, and cytotoxic T lymphocytes' activity (reviewed in [6, 9]). Macrophages and other innate immune cells that offer the first line of defense respond to *T. cruzi* infection through an immediate increase in the expression of proinflammatory cytokines followed by subpar production of superoxide ($O_2^{\cdot-}$) and nitric oxide (NO) by NADPH oxidase (NOX2) and inducible nitric oxide synthase (iNOS), respectively [21–23]. The reaction of $O_2^{\cdot-}$ with NO produces a strong cytotoxic oxidant peroxynitrite ($ONOO^-$). While some studies have indicated that peroxynitrite and other powerful cytotoxic effectors produced by macrophages are essential for killing parasites [24], others have indicated that the macrophage oxidative environment acts as an enhancer of infection [25]. Regardless, parasites are able to persist in this oxidative

environment and the $ONOO^-$ radical can exert cytotoxic effects on the host cells [24].

Nonimmune cells, e.g., cardiac myocytes, have also been shown to respond to *T. cruzi* infection through ROS production. Indeed, several studies have identified mitochondria as the main source of the ROS in *T. cruzi*-infected cardiomyocytes [26, 27]. Typically, perturbation of membrane potential or loss of structural integrity of the mitochondrial membranes [26] adversely affects the activity of the electron transport chain and results in increased mitochondrial ROS (mtROS) production [28, 29]. Specifically, activities of the respiratory complex I and complex III were compromised, and electron leakage to O_2 and $O_2^{\cdot-}$ production occurred at the Q1 semiubiquinone of complex III in infected cardiomyocytes and CD hearts [26, 30]. Mitochondrial dysfunction has been well documented by us and other researchers in cardiomyocytes infected by *T. cruzi* and in the myocardium of chronically infected animals [31, 32] and clinically symptomatic CD patients [28, 33–35]. *In vivo* studies in rodents also showed that mitochondrial defects and high mtROS levels persist in the chronic phase of infection [36, 37].

A network of enzymatic and nonenzymatic antioxidants control oxidative stress. However, several studies have indicated that the increase in mtROS production correlated with a decline in the expression and activity of the mitochondrial antioxidant enzyme Mn⁺² superoxide dismutase (MnSOD) and a decline in the cytosolic glutathione peroxidase (GPx) activity and GSH content in the myocardium of chronically infected animals and in Chagas patients [28, 34, 35, 38, 39]. NFE2L2 (also called Nrf2) is a transcription factor that regulates the expression of antioxidant proteins. A recent study showed that NFE2L2 expression, nuclear translocation, and binding to cis-acting DNA regulatory antioxidant response elements (ARE) were significantly decreased and associated with a decline in antioxidant levels (e.g., γ GCS, HO1, GCLM) in cardiac myocytes and the myocardium of mice infected with *T. cruzi*. Overexpression of MnSOD in cardiac myocytes preserved the NFE2L2 transcriptional activity and antioxidant/oxidant balance, and MnSOD^{tg} mice also preserved the cardiac structure and function [40]. This study provides evidence that mtROS inhibition of the NFE2L2/ARE pathway constitutes a key mechanism in signaling the fibrotic gene expression and evolution of chronic Chagas cardiomyopathy.

In summary, a balance between the levels of ROS that are capable of inducing parasite damage and the antioxidant machinery that the host requires to detoxify and keep a safe environment for cells exposed to infection is fundamental. However, the host antioxidant response is exhausted during progression of Chagas disease [36, 38, 40, 41] and a lack of appropriate antioxidant and repair response results in self-perpetuating mitochondrial dysfunction and ROS production in the heart (reviewed in [9, 42]). The increased and sustained ROS production can signal the fibrotic gene expression and contribute to evolution of chronic cardiomyopathy [40, 43]. ROS can also elicit a consequent antioxidant depletion and immunological response that causes persistent inflammation and oxidative damage of proteins, lipids, and DNA leading to the pathological tissue manifestations in CD [28, 35, 44].

In these circumstances, it is necessary to review the current and new emerging evidence about antioxidant administration in CD. Several antioxidants have been studied as therapeutics for diverse pathologies in preclinical models [45]. Accordingly, we proceeded to (i) synthesize the published evidence on the use of antioxidants in CD, including experimental and preclinical research, (ii) describe the main characteristics of the published studies to shape the directions for future research, and (iii) discuss the potential usefulness of antioxidants as complementary or adjunct therapy with antiparasitic drugs for control of oxidative tissue damage and Chagas cardiomyopathy.

3. Antioxidant Effects in Experimental Models of Chagas Disease

Several antioxidant compounds have been examined as an option for multiple diseases. Their therapeutic goal is to prevent, attenuate, or block the oxidative damage of the host cells [46, 47]. In the context of CD, novel approaches are envisioned to reduce the oxidative damage in the host while maintaining the effectiveness of the antitrypanosomal agents. We appraised the published literature focusing on evaluation of the markers of oxidative stress and benefits of antioxidant treatment in CD. Except for some studies testing vitamin C/vitamin E, all other studies have not evaluated the effect of antioxidants' treatment on parasite levels or parasite persistence. Instead, most of the studies (fifteen total) were conducted in experimental animal models and primarily focused on measuring the oxidative stress levels (Table 1). The major characteristics of these studies are as follows: The potential effect of the antioxidants in terms of control of oxidative stress has been assessed *in vivo* using murine models infected with *T. cruzi*, in both acute and chronic infection. Swiss outbred mice were used in 53.3% of the studies. The animal's age for experiments ranged between 3 and 12 weeks old. Only one study by Novaes et al. [48] used 12-month-old mice. In 82% of the studies, male animals were used without a clear reference to gender exclusion parameter. However, some researchers have reported an association between males, ROS levels, and increased severity of myocardial fibrosis associated with CD [49], thus justifying the use of males for a majority of published studies examining the antioxidants' efficacy in Chagas disease. Challenge infection was performed in all the studies by intraperitoneal inoculation of *T. cruzi*. Infection was defined as acute up to 60 days after inoculation and as chronic from day 120 after inoculation. The most frequently used parasite strain was *T. cruzi* Y strain ($n = 5$ studies; 33.3%). Others used strains included *QM1*, *QM2*, *Sylvio X10/4*, *Brazil*, *Colombian*, and *Ninoa*. The number of parasites used for challenge infection was variable, ranging from 1×10^1 to 1×10^5 blood trypomastigotes, that was mostly related to virulence of the parasite isolates but unrelated to the development of the acute or chronic phase.

The antioxidant compounds used in these studies included phenyl- α -tert-butyl nitron (PBN) [50, 51], carvedilol, vitamin E (vitE) and/or vitamin C (vitC) [52, 53], melatonin [54], curcumin [55], resveratrol, and astaxanthin [56]. Vitamin C was the most commonly used antioxidant, evalu-

ated in five of the published studies. Three of the antioxidant compounds, vitC, curcumin, and PBN, were also evaluated in combination with benznidazole. Only astaxanthin was evaluated in combination with nifurtimox [56] (Table 1). The oral route of administration of the antioxidant compounds was used in >80% the studies. The oxidative stress markers commonly measured as an indicator of tissue injury included MDA, protein carbonyls (PCN), lipid hydroperoxides (LPO), and nitrites. The response of the endogenous antioxidant system was determined by evaluating the concentration of glutathione, and activities of catalase, SOD, GPx, and other antioxidant enzymes in the blood or cardiac tissues. We discuss in detail the effect of the different antioxidant treatment strategies in CD below.

3.1. Vitamins C and E. Ascorbic acid or vitC is one of the most potent antioxidant agents, but at the same time, it acts as a prooxidant [57]. VitC is also the most frequently studied antioxidant in CD (Table 1). Most studies used male Swiss mice, but they differed in experimental conditions like *T. cruzi* strain, parasitic or antioxidant dose, or the treatment time period. Two studies evaluated the effects of vitC and vitE during the acute phase, two during the chronic phase, and one study in both phases of experimental CD. When used in the acute parasitemia phase, vitC treatment was given during 15 to 60 days postinfection (Table 1).

Providello et al. tested vitC with or without benznidazole in acutely infected rodents [58]. The authors showed that treatment with vitC in combination with benznidazole rather than alone resulted in a significant decline in thiobarbituric acid reactive substances (TBARS) in the cardiac tissue of infected mice and decreased ROS generation by host macrophages [58]. Likewise, Puente et al. [59] reported that vitC exerts a prooxidant effect on the parasite, while it had an antioxidant effect on the host [59]. These authors noted that treatment with vitC did not affect the antiparasitic activity of benznidazole; however, vitC decreased the cytotoxicity of benznidazole on host cells and vitC-treated mice exhibited no weight loss and no mortality in response to acute *T. cruzi* infection [59].

Tieghi et al. evaluated the effect of vitC and vitE (individually and in combination) in acutely and chronically infected Swiss mice [53]. The authors noted that supplementation with vitC, vitE, or both had no effect on parasitemia levels. VitC treatment improved the plasma antioxidant capacity and glutathione levels in acutely infected mice, and the lipid peroxidation levels in the plasma and heart tissue of chronically infected mice. Further, vitE showed a synergistic effect with vitC in increasing GSH levels in the acute phase and reducing the plasmatic lipoperoxidation during the chronic phase. In contrast, treatment with vitE only had a prooxidant effect evidenced by an increase in lipid peroxidation in the skeletal muscle of acutely infected mice and no antioxidant effect in chronic Chagas mice. In another study, Novaes et al. [48] used a similar vitE dose as reported by Tieghi et al. [53] and showed reduction in lipid peroxidation in the cardiac muscle of vitE-treated infected mice, though these authors also noted no increase in the antioxidant enzyme activities. Others showed that vitC had a prooxidant effect

TABLE 1: Evidence supporting antioxidant use in Chagas disease as revealed by research in animal models.

Reference #	Author, year	Experimental model	Age in weeks	<i>T. cruzi</i> strain (trypomastigotes challenge dose)	Treatment	Antioxidant/oxidative stress markers	Tissue samples
[94]	Horta et al., 2018	C57BL/6 male mice	8-10	Colombian (50)	25 mg/kg/day carvedilol ± 100 mg/kg/day benznidazole for 23 days by gavage	SOD and CAT activity, TBARS, protein carbonyls	Heart
[52]	Castanheira et al., 2018	Swiss SWR/J male mice	3.5	QM2 (5×10^4)	500 mg/day vitamin C for 60 days in drinking water	FRAP, GSH, GST, plasma sulphydryl (SH) group, nitrate/nitrite	Plasma, heart, colon, skeletal muscle
[58]	Providello et al., 2018	Swiss SWR/J male mice	6	Y (1×10^4)	7.14 mg/kg/day vitamin C ± 100 mg/kg benznidazole for 15 days by gavage	TBARS ROS	Heart, macrophages
[56]	Contreras-Ortiz et al., 2017	BALB/c female mice	4-6	Ninoa (10)	10 mg/kg/day astaxanthin ± 100 mg/kg/day nifurtimox for 60 days orally	MDA	Heart, spleen, blood
[90]	Montenote et al., 2017	Swiss SWR/J male mice	3	QM2 (5×10^4)	20% blackberry plant extract (25-75 µl/day) 180 days orally	TBARS, FRAP, GSH, and sulphydryl groups	Plasma
[53]	Tieghi et al., 2017	Swiss SWR/J male mice	3	QM2 (5×10^4)	500 mg/day vitamin C and 800 IU/day vitamin E (individually and in combination) for 60 days or 120 days	FRAP, GSH, TBARS	Plasma, heart, colon, and skeletal muscle
[48]	Novaes et al., 2017	Swiss SWR/J male mice	52	Y (2×10^3)	500 mg/day vitamin C/800 UI/day vitamin E for 15 days orally	TBARS, PCN, catalase, GST and SOD activities, nitrite/nitrate, 8-OHdG	Heart
[69]	Vilar-Pereira et al., 2016	BALB/c male & female mice	5-7	Colombian (2×10^2)	15 mg/kg <i>trans</i> -resveratrol (i.p.) or 40 mg/kg resveratrol, 500 mg/kg metformin, 100 mg/kg/Tempol, or 25 mg/kg benznidazole for 30 days (per orally)	TBARS	Heart
[55]	Novaes et al., 2016	SWR/J female mice	8-12	Y (2×10^3)	Curcumin (C) ± benznidazole (B) for 20 days by gavage, C100 (±B50-B100), B50-B100 only (mg/kg/day)	MDA and PCN	Heart, liver
[54]	Brazao et al., 2015	Wistar male rats	NR	Y (1×10^5)	5 mg/kg melatonin/day for 60 days orally	Nitrite production in macrophages; TBARS in plasma	Plasma, spleen
[60]	Marim et al., 2015	SWR/J male mice	3	QM1 (5×10^4)	10 µl vitamin C (D60 mg or D500 mg) per day for 60 days or 180 days orally	TBARS, total peroxide, GSH	Plasma, heart, colon, skeletal muscle
[84]	Nagajyothi et al., 2012	CD1 mice	6-8	Brazil (5×10^4)	100 mg/kg/day curcumin for 35 days orally	mRNA levels of enzymes/proteins	Heart
[64]	Wen and Garg, 2012	Sprague Dawley rats	4-5	Sylvio ×10 (5×10^4)	1.3 mM PBN and/or 0.7 mM benznidazole for three weeks in drinking water	PCN	Heart, heart mitochondria
[51]	Wen et al., 2010	Sprague Dawley rats	4-5	Sylvio ×10 (5×10^4)	1.3 mM PBN and/or 0.7 mM benznidazole for three weeks in drinking water	ROS, TBARS	Heart, heart mitochondria

TABLE 1: Continued.

Reference #	Author, year	Experimental model	Age in weeks	<i>T. cruzi</i> strain (trypomastigotes challenge dose)	Treatment	Antioxidant/oxidative stress markers	Tissue samples
[89]	Francisco et al., 2010	SWR/J male mice	4	Y (5×10^2)	5 mg/50 μ l/day desferrioxamine (i.p.) 14 days prior to infection and for 21 days i.p.	GSH, TBARS, PCN, nitrate/nitrite	Serum, liver
[50]	Wen et al., 2006	C57BL/6 mice	6-8	Sylvio $\times 10$ (1×10^4)	50 mg/kg PBN (i.p.) on alternate days for three weeks	Respiratory complex activities, MDA, GSH, ATP, H ₂ O ₂	Heart, heart mitochondria

Cv: carvedilol; SOD: superoxide dismutase; CAT: catalase; MDA: malondialdehyde; GSH: glutathione; GST: glutathione S-transferase; FRAP: plasma antioxidant capacity; TBARS: thiobarbituric acid reactive substances; PCN: protein carbonyl levels; PBN: phenyl- α -tert-butyl nitrene; B100: 100 mg/kg of body weight benzimidazole; B50: 50 mg/kg benzimidazole; C100: 100 mg/kg curcumin; dpi: days postinfection.

in Chagas mice, though this seemed to be a dose-dependent effect; treatment with 60 mg vitC was not oxidative, while treatment with 500 mg of vitC per day led to increased total peroxide and TBARS at 60 and 180 days [52, 60].

In summary, therapeutic administration of vitC or vitE alone was unable to protect against oxidative stress in both acute and chronic phases of CD. Interestingly, vitC and vitE have a prooxidant effect by increasing ROS production, which can be harmful to the host due to the increased severity of tissue lesions but beneficial when used in cases of low parasitemia. A reduction in the parasitic burden occurs because vitC also stimulates NO production [52], which has been associated with a trypanocidal effect [61, 62]. VitC, in combination with vitE, exerted slight advantages in controlling oxidative damage in Chagas mice.

3.2. Phenyl- α -tert-butyl Nitron (PBN). PBN is a nitron-based antioxidant that scavenges free radical species and inhibits free radical generation [63]. The effects of PBN in CD have been reported in rats during the acute and chronic phases of infection using an oral administration of 1.3 mM of PBN for three weeks [51, 64] and in mice during the acute phase with injection delivery of 50 mg/kg of PBN [50]. Treatment with PBN controlled the pathologic oxidative tissue injury and preserved mitochondrial respiratory chain function in both acutely and chronically infected rodents. Wen and Garg [64] also showed that PBN restored the differential expression of 65% of the disease-associated proteins to the normal level and prevented the development of oxidative adducts on plasma proteins in chronically infected rats [51, 64]. Importantly, PBN alone or in combination with benznidazole (but not benznidazole alone) preserved the left ventricular function that otherwise was significantly compromised in chronically infected Chagas rats [51, 64].

3.3. Mitochondria-Targeted Antioxidants. Currently, the application of mitochondria-targeted therapies for parasitic diseases has focused on studying the mitochondrial function in *Leishmania* and other trypanosome parasites [65], owing to the fact that their mitochondria are different from human mitochondria. However, mitochondria-based therapies designed to improve mitochondrial health of the patients are also needed. This is because mitochondrial dysfunction contributes to the pathology of Chagas cardiomyopathy in the same way as many other disorders like neurodegeneration, metabolic disease, heart failure, and ischemia-reperfusion injury, for which several therapeutic strategies to restore mitochondrial function are emerging in recent years [66]. Encouraging results have been obtained from treatments targeting mitochondrial bioenergetics for the improvement of heart function in animal models of heart failure [67]. These same therapies can be promising alternatives to preserve mitochondrial bioenergetics and as a consequent oxidant/antioxidant balance in Chagas cardiomyopathy.

There are several mitochondria-targeted antioxidants, and the more notable among them are mitoquinone (MitoQ), MitoTEMPO, Tempol, and Mn-porphyrin. Only one mitochondria-targeted antioxidant has been studied

focusing on the control of mitochondrial dysfunction and oxidative pathology in CD and it is described below:

3.3.1. Tempol (SOD-Mimetic). Tempol is a superoxide mimetic agent that has been evaluated for treatment of many diseases related to mitochondrial dysfunction and oxidative stress [68]. Vilar-Pereira et al. have evaluated the protective action of Tempol in CD, although this was used to validate findings with resveratrol treatment [69]. Chagas mice chronically infected with the Colombian strain of *T. cruzi* were mice treated with 100 mg/kg of Tempol (SOD2 mimetic) or 500 mg/kg of metformin that were administered daily by gavage for 30 days, beginning 60 days postinfection. The authors showed that Tempol decreased lipid peroxidation and improved heart function in Chagas mice. Likewise, metformin (agonist of AMP-activated protein kinase, AMPK) that is used for the treatment of type 2 diabetes and is shown to inhibit mitochondrial complex I, reduce ROS, and modulate other cellular mechanisms associated with extension of lifespan [70] also reduced lipid peroxidation in Chagas mice [69].

3.4. Resveratrol. Resveratrol is a phenol found in many plants and fruits with a demonstrated role in the control of tissue damage in degenerative diseases and cancer. However, its major therapeutic role as a cardiovascular protector is documented in the heart failure of different etiologies [71]. Resveratrol is shown to have anti-inflammatory, antimicrobial, and antioxidant properties [72] and had inducing effects on endothelial NO synthase (eNOS) [73] and various antioxidant enzymes [74], while increased scavenging of superoxide, hydroxyl, and peroxy radicals was also noted [74].

Vilar-Pereira et al. [69] showed that treatment of chronically infected mice with resveratrol for 30 days normalized the Mn-superoxide (SOD2) levels and significantly decreased the lipid peroxidation in the hearts of Chagas mice. Reducing ROS-induced oxidative adducts was enough to improve the heart function, although histological structure of the heart showed little-to-no improvement and there was no correlation with changes in PGC1- α expression or ATP levels that are the molecular regulators of oxidative metabolism. Authors noted that Chagas mice treated with resveratrol exhibited increase in the activation of the AMPK pathway required for maintaining the cellular energy homeostasis [75].

3.5. Melatonin. Melatonin is a potent antioxidant known to neutralize hydroxyl and peroxy radicals [76]. Melatonin is shown to be effective in reducing oxidative stress in many pathological conditions [77]. Brazao et al. [54] showed that the oral administration of melatonin (5 mg/kg of body weight) for 60 days during chronic *T. cruzi* infection arrested the plasmatic lipid peroxidation. Authors showed lower levels of NO production in melatonin-treated animals and proposed that melatonin controlled the NO-dependent formation of cytotoxic ONOO⁻ in Chagas mice [54]. Because NO has a trypanocidal effect [61], it is possible that melatonin may also control the parasite burden; however, this was not examined in detail in this study [54].

3.6. Curcumin. Curcumin is a natural phenolic antioxidant and free radical scavenger that reduces the release of superoxide radicals, hydrogen peroxide, and nitric oxide in immune cells [78] and inhibits lipid peroxidation [79]. Published literature suggests that curcumin modulates multiple signaling molecules, transcription factors, and protein kinases and protein reductases linked to cardiovascular, metabolic, and other chronic diseases. [80]. Curcumin is suggested to confer therapeutic benefits, either alone or in combination with other agents, through intrinsic antioxidant, anti-inflammatory, anticancer, antiatherosclerotic, and antiaging properties [81, 82]. Curcumin has been studied in CD as well as in other parasitic diseases, focused mainly on its immunomodulatory and antiparasitic action because of its diphasic effect as a scavenger of ROS in low doses (1-15 μM) and as an inducer of ROS in high doses (20-50 μM) [83].

Novaes et al. [55] reported positive effects of treatment with curcumin alone as well as in combination with benzimidazole in controlling oxidative stress. Mice infected with *T. cruzi* Y strain and treated with curcumin for 20 days showed reduced MDA and PCN levels in cardiac and liver tissues compared to that noted in infected/untreated controls. When used in combination with benzimidazole, curcumin offered a greater reduction in MDA and PCN levels in cardiac tissue [55]. Contrarily, Nagajyothi et al. [84] showed in mice infected with the Brazil strain of *T. cruzi* that curcumin treatment for 35 days during the acute phase resulted in a decline in the expression levels of antioxidants including SOD, CAT, and peroxidases, though curcumin was beneficial in controlling the parasite burden.

3.7. Astaxanthin (ASTX). ASTX (3,3'-dihydroxy- β,β' -carotene-4,4'-dione) is a carotenoid found in plants, microorganisms, and sea creatures. Its benefits as an antioxidant include scavenging of radicals, protection of antioxidant enzymes activities, and inhibition of lipid peroxidation [85]. There was only one study examining the effects of ASTX in Chagas disease. Contreras-Ortiz et al. evaluated *in vitro* and *in vivo* effects of ASTX supplementation with or without the antiparasitic drug nifurtimox. Mice treated with ASTX (10 mg/kg/day, orally) for 60 days showed no benefits in controlling MDA levels, irrespective of whether ASTX was given alone or in combination with nifurtimox. The use of ASTX was not even recommended due to an observed increase in MDA levels during the acute phase of *T. cruzi* infection.

3.8. Desferrioxamine (DFX). DFX is an iron chelating agent that has been reported to reduce the formation of free hydroxyl radicals [86], increase the levels of antioxidant enzymes like GPx and SOD [87], and prevent lipid peroxidation with enhanced efficacy when used in combination with other antioxidants (e.g., melatonin) [88]. Francisco et al. [89] have assessed the antioxidant effects of DFX in an experimental model of acute CD. Surprisingly, the authors noted the hepatic and serum levels of thiobarbituric acid reactive species (TBARS) and nitrate/nitrite were increased in infected mice after 21 days of treatment with DFX. This was despite the finding that SOD activity was enhanced throughout the acute phase in DFX-treated infected mice.

We must note that SOD activity is increased in the heart and liver of mice acutely infected with *T. cruzi* (i.e., during 8-21 dpi) after which the antioxidant capacity is diminished [32]. Thus, the observed increase in SOD activity in acutely infected mice may not be DFX-dependent [89]. Thus, it might be of interest to evaluate DFX effects during the chronic Chagas disease phase when antioxidant status is usually compromised.

3.9. Phytotherapy Compounds. The antioxidant potential of phenolic compounds (flavonoids) in the chronic phase was evaluated using the *Morus nigra* plant extract [90]. Unlike the other studies discussed above, the plant extract was not composed of a specific purified phenolic compound. Nevertheless, the authors determined that the total flavonoid concentration was 361.83 $\mu\text{g/ml}$ of the plant extract. Mice were treated daily with 25 μl , 50 μl , or 75 μl of *M. nigra* extract corresponding to 9 μg , 18 μg , and 27 μg , respectively, of flavonoids for 180 days. However, authors noted no benefits of either of the concentrations of *M. nigra* extracts in enhancing the antioxidant ability or reducing the lipid peroxidation products in infected or uninfected animals.

3.10. Carvedilol (Cv). Cv is a nonselective third-generation β -blocker. Although Cv is not an antioxidant, it has been shown to possess both ROS-scavenging and ROS-suppressive effects [91] and offer protection against lipid and protein oxidation mediated by the binding to Fe (III) and Cu (II) transition metals [92]. Further, Cv has been found to decrease serum lipid peroxidation and, thus, exert antioxidant effects [93]. Horta et al. [94] treated the acutely infected mice with 25 mg/kg/day carvedilol for 23 days and showed that in spite of lowered TBARS content in treated mice, Cv was not efficacious in decreasing the protein carbonylation or in enhancing the expression or activities of the SOD and CAT antioxidant enzymes. Codelivery of Cv with benzimidazole also showed no benefits compared to what was noted in infected mice treated with benzimidazole alone. Authors concluded that Cv is not useful in CD, and it might cause higher inflammation and lower survival rate in infected host.

4. Therapeutic Antioxidant Effects in Human Chagas Patients

Chagas cardiomyopathy is the most common and overwhelming manifestation in the chronic phase of *T. cruzi* infection. It is suggested that heart disease occurs by irreversible tissue damage associated with oxidative stress rather than a direct continued action of the parasite [95]. Oxidative stress triggers the immunological responses related to the physiological disturbance and progression of chronic Chagas cardiomyopathy [39]. Thus, antioxidants have emerged as a potential therapeutic option for arresting the tissue injuries in the chronic phase of Chagas disease. Typically, serum and red blood oxidative stress markers are evaluated as an evidence of antioxidant effects. The studies focused on testing the antioxidants' efficacy in Chagas patients are summarized in Table 2 and discussed below.

TABLE 2: Evidence supporting antioxidant use in Chagas disease as revealed by research in humans.

Ref.	Author	Patients with chronic Chagas heart disease (ChD)	Antioxidant	Treatment	Oxidative stress markers examined
[96]	Macao et al., 2007	$n = 41$	Vitamin E (800 UI/day) and vitamin C (500 mg/day)	Benznidazole (5 mg/kg) for 2 months, vitamins for 6 months	SOD, CAT, GPx, GST, GR, GSH, TBARS, PCN, NO, MPO, GGT
[98]	Barbosa et al., 2014	$n = 41$, 41% males, 31-67 years old	Vitamin E (800 UI/day) and vitamin C (500 mg/day)	Benznidazole (5 mg/kg/day) for 2 months, vitamins for 6 months	SOD, CAT, GPx, GST, GR, GSH, TBARS, PCN
[97]	Ribeiro et al., 2010	$n = 41$	Vitamin E (800 UI/d) and vitamin C (500 mg/d)	Benznidazole (5 mg/kg) for 2 months, vitamins for 6 months	SOD, CAT, GPx, GST, GR, GSH, TBARS, PCN, NO, MPO, ADA
[99]	Budni et al., 2012	$n = 42$, 21-70 years old	Carvedilol (37.5 mg/day)	6 months	SOD, CAT, GPx, GST, GR, GSH, TBARS, PCN, NO, MPO, ADA
[100]	Budni et al., 2013	$n = 42$, 21-70 years old	Carvedilol (37.5 mg/day) and vitamin E as above	6 months	SOD, CAT, GPx, GST, GR, GSH, TBARS, PCN, NO, MPO, ADA

Abbreviations: SOD: superoxide dismutase; CAT: catalase; MDA: malondialdehyde; GSH: glutathione; GST: glutathione S-transferase; GR: glutathione reductase; GPx: glutathione peroxidase; TBARS: thiobarbituric acid reactive substances; PCN: protein carbonyl levels; NO: nitric oxide; MPO: myeloperoxidase; GGT: gamma-glutamyl transferase; ADA: adenosine deaminase.

A research group at the Universidade Federal de Santa Catarina, Brazil, first reported in year 2007 their data obtained from Chagas patients with different stages of chronic heart disease, classified according to modified Los Andes clinical-hemodynamic classification in groups IA, IB, II, and III ($n = 10$ per group) [39]. Several antioxidant and oxidant biomarkers were measured, and the authors noted that the intraerythrocytic GSH concentrations were decreased in correlation with progression of the disease. This study was followed up by treatment of the same patients' cohort with vitE (800 UI/day) and vitC (500 mg/day) for six months. Macao et al. [96] noted that the vitE/vitC supplementation decreased plasma levels of TBARS and PCN and increased red cell levels of GSH content and GPx and CAT activities in early-stage patients, but this treatment was not sufficient to attenuate oxidative insult in late stage patients.

In another study, Ribeiro et al. [97] measured biomarkers of oxidative stress in Chagas patients (classified as above) before and after two-month treatment with benznidazole and subsequent supplementation with vitE/vitC for six months. Authors noted that BZN treatment enhanced the antioxidants (SOD, CAT, GPx, and GST) as well as protein carbonyls in all groups except group III, and after antioxidant supplementation, the activities of antioxidants as well as biomarkers of oxidative insult (PCN, TBARS, NO, GSH, etc.) were decreased. The authors concluded that BZN treatment promoted an oxidative insult while the antioxidant supplementation was able to attenuate this effect by increasing vitamin E levels, decreasing PCN and TBARS levels and inhibiting SOD, GPx, and glutathione reductase (GR) activities as well as inflammatory markers, mainly in patients with the less severe form of cardiac involvement. Further, Barbosa et al. [98] noted that patients with advanced heart disease exhibited a decline in premature ventricular contraction after BZN and vitE/vitC treatment.

A similar patient cohort as discussed above was treated with carvedilol and vitE/vitC supplements for six months and followed to determine if concomitant use of carvedilol will enhance the antioxidant effects of vitE and vitC [99, 100]. Budni et al. [99, 100] noted significant decline in oxidative stress levels in patients that received carvedilol alone or in combination with vitE/vitC, the maximal benefits being noted in patients that received Cv and vitE/vitC together, thus suggesting the possibility of synergism between these compounds. Again, maximal benefits of Cv and vitE/vitC in attenuating the systemic oxidative stress were noted in patients with the less severe form of heart Chagas disease.

Other elements with antioxidant properties such as selenium have also been investigated as an adjuvant therapy in CD [101]. Nonetheless, these studies were focused on controlling the heart dysfunction and none evaluated the effects of the treatment on oxidative stress markers.

5. Outlook and Future Perspectives

The antioxidant adjuvant therapy is anticipated to decrease ROS in the host tissues; however, we have also shown here that vitC and vitE in the Chagasic host exert a synergistic trypanocidal effect as they cause an increase in reactive species that trigger redox imbalance and parasite death [102]. New studies, however, are needed to determine if vitC/vitE treatments eventually result in improved heart function in Chagas disease.

Our review highlights the reduction of plasmatic and tissue-lipid peroxidation levels as a major benefit provided by antioxidant therapies (Table 3). Curcumin, resveratrol, and Cv as well as metformin and Tempol showed this benefit in preclinical studies, although only Cv has been evaluated in Chagasic patients. Other antioxidants showed detrimental or no positive effects in Chagas disease. However, we must note

TABLE 3: Summarized presentation of oxidative stress markers and effects of antioxidant supplements evaluated in *T. cruzi* infection and Chagas disease.

Antioxidant	Oxidative stress marker						
	Mitochondrial function	NO production	Lipid peroxidation	PCN	Glutathione	SOD	CAT
PBN	+						
Melatonin		X	+				
Curcumin			+	+		D	D
Resveratrol			+			D	
ASTX			X				
DFX		X	X			I	
Flavonoids (<i>Morus nigra</i>)			X				
Vitamins C or vitamin E			X			X	X
Vitamins C/vitamin E			=		+		
Carvedilol			=	X		X _A , D _H	X

+: studies show statistically significant changes of diminishing oxidative stress markers; X: studies show statistically significant detrimental results in oxidative stress markers; =: no changes in measurements in oxidative stress markers; I or D: studies show increase or decrease in antioxidant enzyme levels after antioxidant exposure, respectively; A: animal models; H: human patients; NO: nitric oxide; PCN: protein carbonylation; glutathione: GSH, GPx, or GST; SOD: superoxide dismutase; CAT: catalase. PBN: phenyl- α -tert-butyl nitron.

that many of the antioxidant therapies have only been evaluated once and others have not reproduced the published studies. Thus, the evidence on whether antioxidant supplementation can reduce oxidative stress in Chagasic patients is insufficient right now and further studies are necessary to confirm the initial results.

The benefits of antioxidants seem greater when they are used in combination with or after antiparasitic drug administration, causing a reduction in plasmatic and cardiac lipid peroxidation. Some of the antioxidants enhanced parasite clearance as well. Thus, it is recommended that future studies should focus on evaluating antioxidant compounds in conjunction with antiparasitic therapies.

There are multiple antioxidants evaluated in CD, and some of them have shown promising results and potential benefits in the improvement of oxidative stress parameters in affected tissues. Studies on changes in oxidative stress parameters after antioxidant supplementation, alone or in combination with antiparasitic drugs, offer new hope for halting the progression of cardiac dysfunction in Chagas heart disease. This possibility must be investigated both in the acute phase and later during the chronic phase and focused on the oxidative stress imbalance. While evidence supports the association of oxidative stress with the development of cardiac alterations and that adjuvant therapy with some antioxidants modifies tissue oxidative stress parameters, the relation between antioxidants and the development or progression of tissue damage in the main organs affected by CD still needs to be further investigated. In the same way, there are no previous studies or comprehensive assessment of the signaling pathways involved in oxidative stress reduction related to antioxidant supplementation in CD. It is also necessary to explore a specific and appropriate supplementation time or dose-dependent effects that show an advantage to control oxidative stress and consequent cardiac damage and left ventricular dysfunction in Chagas disease.

Abbreviations

CD:	Chagas disease
Cv:	Carvedilol
DFX:	Desferrioxamine
eNOS:	Endothelial nitric oxide synthase
4-HNE:	4-Hydroxynonenal
iNOS:	Inducible nitric oxide synthase
MDA:	Malondialdehyde
mtROS:	Mitochondrial ROS
NO:	Nitric oxide
NOX2:	NADPH oxidase 2
PBN:	Phenyl- α -tert-butyl nitron
PCN:	Protein carbonyl
RNS:	Reactive nitrogen species
ROS:	Reactive oxygen species
SOD:	Superoxide dismutase
TBARS:	Thiobarbituric acid reactive species
<i>T. cruzi</i> :	<i>Trypanosoma cruzi</i> .

Additional Points

Highlights. *Trypanosoma cruzi* infection leads to chronic Chagas cardiomyopathy. A positive correlation between peripheral and cardiac levels of oxidative and nitrosative stress and the severity of heart disease is reported in experimental models and human patients of Chagas disease. A compromised antioxidant defense of the host contributed to myocardial oxidative damage presented by increased lipid peroxidation, protein carbonyls, and DNA adducts. The drugs used to treat *T. cruzi* infection, nifurtimox and benznidazole, induce increased ROS and DNA damage in host tissues. Combinatorial antiparasitic therapies with antioxidants have potential clinical relevance in arresting oxidative injuries. It is necessary to assess the effects of antioxidant supplementation in various disease phases to offer a unifying treatment recommendation.

Conflicts of Interest

All authors declare that they have no financial or other competing interests.

Acknowledgments

We would like to thank the research staff of Fundación Cardiovascular de Colombia, for the initial extraction of data and helpful comments provided for this paper. This work was supported by the National Financing Fund for Science, Technology and Innovation of Colombia, “Francisco José de Caldas”-COLCIENCIAS Grant: CT-649-2014, Project Code: 656671240824. This work was developed within the framework of postdoctoral research training No.784-2017, Grant: FP44842-152-2018. NJG has been supported by grants from of the National Institutes of Health and National Institute of Allergy and Infectious Diseases (R01AI054578, R01AI136031).

References

- [1] C. Fitzpatrick, U. Nwankwo, E. Lenk, S. J. de Vlas, and D. A. P. Bundy, “An investment case for ending neglected tropical diseases,” *Major Infectious Diseases*, Washington (DC), 2017.
- [2] R. Curtis-Robles, A. C. Meyers, L. D. Auckland, I. B. Zecca, R. Skiles, and S. A. Hamer, “Parasitic interactions among *Trypanosoma cruzi*, triatomine vectors, domestic animals, and wildlife in Big Bend National Park along the Texas-Mexico border,” *Acta Tropica*, vol. 188, pp. 225–233, 2018.
- [3] R. Curtis-Robles, K. F. Snowden, B. Dominguez et al., “Epidemiology and molecular typing of *Trypanosoma cruzi* in naturally-infected hound dogs and associated triatomine vectors in Texas, USA,” *PLoS Neglected Tropical Diseases*, vol. 11, no. 1, article e0005298, 2017.
- [4] M. N. Garcia, H. Burroughs, R. Gorchakov et al., “Molecular identification and genotyping of *Trypanosoma cruzi* DNA in autochthonous Chagas disease patients from Texas, USA,” *Infection, Genetics and Evolution*, vol. 49, pp. 151–156, 2017.
- [5] J. R. Coura and P. A. Vinas, “Chagas disease: a new worldwide challenge,” *Nature*, vol. 465, no. 7301, pp. S6–S7, 2010.
- [6] L. E. Rios, J. C. Vazquez-Chagoyan, A. O. Pacheco, M. P. Zago, and N. J. Garg, “Immunity and vaccine development efforts against *Trypanosoma cruzi*,” *Acta Tropica*, vol. 200, p. 105168, 2019.
- [7] L. H. Malik, G. D. Singh, and E. A. Amsterdam, “The epidemiology, clinical Manifestations, and management of Chagas heart disease,” *Clinical Cardiology*, vol. 38, no. 9, pp. 565–569, 2015.
- [8] A. Rassi Jr., A. Rassi, and J. A. Marin-Neto, “Chagas disease,” *Lancet*, vol. 375, no. 9723, pp. 1388–1402, 2010.
- [9] K. M. Bonney, D. J. Luthringer, S. A. Kim, N. J. Garg, and D. M. Engman, “Pathology and pathogenesis of Chagas heart disease,” *Annual Review of Pathology: Mechanisms of Disease*, vol. 14, no. 1, pp. 421–447, 2019.
- [10] P. A. Sales Junior, I. Molina, S. M. Fonseca Murta et al., “Experimental and clinical treatment of Chagas disease: a review,” *The American Journal of Tropical Medicine and Hygiene*, vol. 97, no. 5, pp. 1289–1303, 2017.
- [11] Centers for Disease Control and Prevention C, *Antiparasitic treatment*, 2019, https://www.cdc.gov/parasites/chagas/health_professionals/tx.html.
- [12] J. D. Maya, Y. Repetto, M. Agosin et al., “Effects of nifurtimox and benznidazole upon glutathione and trypanothione content in epimastigote, trypomastigote and amastigote forms of *Trypanosoma cruzi*,” *Molecular and Biochemical Parasitology*, vol. 86, no. 1, pp. 101–106, 1997.
- [13] A. Trochine, D. J. Creek, P. Faral-Tello, M. P. Barrett, and C. Robello, “Benznidazole biotransformation and multiple targets in *Trypanosoma cruzi* revealed by metabolomics,” *PLoS Neglected Tropical Diseases*, vol. 8, no. 5, article e2844, 2014.
- [14] B. S. Hall and S. R. Wilkinson, “Activation of benznidazole by trypanosomal type I nitroreductases results in glyoxal formation,” *Antimicrobial Agents and Chemotherapy*, vol. 56, no. 1, pp. 115–123, 2012.
- [15] R. C. Pedrosa, A. F. De Bem, C. Locatelli, R. C. Pedrosa, R. Geremias, and D. Wilhelm Filho, “Time-dependent oxidative stress caused by benznidazole,” *Redox Report*, vol. 6, no. 4, pp. 265–270, 2001.
- [16] D. A. Rendon, “Alterations of mitochondria in liver but not in heart homogenates after treatment of rats with benznidazole,” *Human & Experimental Toxicology*, vol. 33, no. 10, pp. 1066–1070, 2014.
- [17] C. A. Morillo, J. A. Marin-Neto, A. Avezum et al., “Randomized trial of benznidazole for chronic Chagas' cardiomyopathy,” *The New England Journal of Medicine*, vol. 373, no. 14, pp. 1295–1306, 2015.
- [18] J. Bermudez, C. Davies, A. Simonazzi, J. P. Real, and S. Palma, “Current drug therapy and pharmaceutical challenges for Chagas disease,” *Acta Tropica*, vol. 156, pp. 1–16, 2016.
- [19] L. Rios, E. E. Campos, R. Menon, M. P. Zago, and N. J. Garg, “Epidemiology and pathogenesis of maternal-fetal transmission of *Trypanosoma cruzi* and a case for vaccine development against congenital Chagas disease,” *Biochimica et Biophysica Acta (BBA) - Molecular Basis of Disease*, vol. 1866, no. 3, p. 165591, 2019.
- [20] A. C. C. Silva, M. C. A. Brelaz-de-Castro, A. C. L. Leite, V. R. A. Pereira, and M. Z. Hernandez, “Chagas disease treatment and rational drug discovery: a challenge that remains,” *Frontiers in Pharmacology*, vol. 10, p. 873, 2019.
- [21] N. Guinazu, E. A. Carrera-Silva, M. C. Becerra, A. Pellegrini, I. Albesa, and S. Gea, “Induction of NADPH oxidase activity and reactive oxygen species production by a single *Trypanosoma cruzi* antigen,” *International Journal for Parasitology*, vol. 40, no. 13, pp. 1531–1538, 2010.
- [22] M. Dhiman and N. J. Garg, “NADPH oxidase inhibition ameliorates *Trypanosoma cruzi*-induced myocarditis during Chagas disease,” *The Journal of Pathology*, vol. 225, no. 4, pp. 583–596, 2011.
- [23] S. J. Koo, B. Szczesny, X. Wan, N. Putluri, and N. J. Garg, “Pentose phosphate shunt modulates reactive oxygen species and nitric oxide production controlling *Trypanosoma cruzi* in macrophages,” *Frontiers in Immunology*, vol. 9, p. 202, 2018.
- [24] M. N. Alvarez, G. Peluffo, L. Piacenza, and R. Radi, “Intraphagosomal peroxynitrite as a macrophage-derived cytotoxin against internalized *Trypanosoma cruzi*: consequences for oxidative killing and role of microbial peroxiredoxins in infectivity,” *The Journal of Biological Chemistry*, vol. 286, no. 8, pp. 6627–6640, 2011.

- [25] C. N. Paiva, D. F. Feijo, F. F. Dutra et al., "Oxidative stress fuels *Trypanosoma cruzi* infection in mice," *The Journal of Clinical Investigation*, vol. 122, no. 7, pp. 2531–2542, 2012.
- [26] S. Gupta, V. Bhatia, J. J. Wen, Y. Wu, M. H. Huang, and N. J. Garg, "*Trypanosoma cruzi* infection disturbs mitochondrial membrane potential and ROS production rate in cardiomyocytes," *Free Radical Biology & Medicine*, vol. 47, no. 10, pp. 1414–1421, 2009.
- [27] X. Ba, S. Gupta, M. Davidson, and N. J. Garg, "*Trypanosoma cruzi* induces the reactive oxygen species-PARP-1-RelA pathway for up-regulation of cytokine expression in cardiomyocytes," *The Journal of Biological Chemistry*, vol. 285, no. 15, pp. 11596–11606, 2010.
- [28] J. J. Wen, P. C. Yachelini, A. Sembaj, R. E. Manzur, and N. J. Garg, "Increased oxidative stress is correlated with mitochondrial dysfunction in chagasic patients," *Free Radical Biology & Medicine*, vol. 41, no. 2, pp. 270–276, 2006.
- [29] J. J. Wen and N. J. Garg, "Mitochondrial complex III defects contribute to inefficient respiration and ATP synthesis in the myocardium of *Trypanosoma cruzi*-infected mice," *Antioxidants & Redox Signaling*, vol. 12, no. 1, pp. 27–37, 2010.
- [30] G. Vyatkina, V. Bhatia, A. Gerstner, J. Papaconstantinou, and N. J. Garg, "Impaired mitochondrial respiratory chain and bioenergetics during chagasic cardiomyopathy development," *Biochimica et Biophysica Acta*, vol. 1689, no. 2, pp. 162–173, 2004.
- [31] S. Mukherjee, T. J. Belbin, D. C. Spray et al., "Microarray analysis of changes in gene expression in a murine model of chronic chagasic cardiomyopathy," *Parasitology Research*, vol. 91, no. 3, pp. 187–196, 2003.
- [32] J.-J. Wen, G. Vyatkina, and N. J. Garg, "Oxidative damage during chagasic cardiomyopathy development: role of mitochondrial oxidant release and inefficient antioxidant defense," *Free Radical Biology & Medicine*, vol. 37, no. 11, pp. 1821–1833, 2004.
- [33] E. Cunha-Neto, V. J. Dzau, P. D. Allen et al., "Cardiac gene expression profiling provides evidence for cytokinopathy as a molecular mechanism in Chagas' disease cardiomyopathy," *The American Journal of Pathology*, vol. 167, no. 2, pp. 305–313, 2005.
- [34] M. Dhiman, Y. A. Coronado, C. K. Vallejo et al., "Innate immune responses and antioxidant/oxidant imbalance are major determinants of human Chagas disease," *PLoS Neglected Tropical Diseases*, vol. 7, no. 8, article e2364, 2013.
- [35] X. Wan, S. Gupta, M. P. Zago et al., "Defects of mtDNA replication impaired mitochondrial biogenesis during *Trypanosoma cruzi* infection in human cardiomyocytes and chagasic patients: the role of Nrf1/2 and antioxidant response," *Journal of the American Heart Association*, vol. 1, no. 6, article e003855, 2012.
- [36] J. J. Wen, M. Dhiman, E. B. Whorton, and N. J. Garg, "Tissue-specific oxidative imbalance and mitochondrial dysfunction during *Trypanosoma cruzi* infection in mice," *Microbes and Infection*, vol. 10, no. 10–11, pp. 1201–1209, 2008.
- [37] X. Wan, J. J. Wen, S. J. Koo, L. Y. Liang, and N. J. Garg, "SIRT1-PGC1 α -NF κ B pathway of oxidative and inflammatory stress during *Trypanosoma cruzi* infection: benefits of SIRT1-targeted therapy in improving heart function in Chagas disease," *PLoS Pathogens*, vol. 12, no. 10, article e1005954, 2016.
- [38] R. Perez-Fuentes, J. F. Guegan, C. Barnabe et al., "Severity of chronic Chagas disease is associated with cytokine/antioxidant imbalance in chronically infected individuals," *International Journal of Parasitology*, vol. 33, no. 3, pp. 293–299, 2003.
- [39] T. B. de Oliveira, R. C. Pedrosa, and D. W. Filho, "Oxidative stress in chronic cardiopathy associated with Chagas disease," *International Journal of Cardiology*, vol. 116, no. 3, pp. 357–363, 2007.
- [40] J. J. Wen, C. Porter, and N. J. Garg, "Inhibition of NFE2L2-antioxidant response element pathway by mitochondrial reactive oxygen species contributes to development of cardiomyopathy and left ventricular dysfunction in Chagas disease," *Antioxidants & Redox Signaling*, vol. 27, no. 9, pp. 550–566, 2017.
- [41] S.-j. Koo, H. M. Spratt, K. V. Soman et al., "S-Nitrosylation proteome profile of peripheral blood mononuclear cells in human heart failure," *International Journal of Proteomics*, vol. 2016, Article ID 1384523, 19 pages, 2016.
- [42] M. Lopez, H. B. Tanowitz, and N. J. Garg, "Pathogenesis of chronic Chagas disease: macrophages, mitochondria, and oxidative stress," *Current Clinical Microbiology Reports*, vol. 5, no. 1, pp. 45–54, 2018.
- [43] J. J. Wen, X. Wan, J. Thacker, and N. J. Garg, "Chemotherapeutic efficacy of phosphodiesterase inhibitors in chagasic cardiomyopathy," *JACC: Basic to Translational Science*, vol. 1, no. 4, pp. 235–250, 2016.
- [44] S. Gupta, M. Dhiman, J. J. Wen, and N. J. Garg, "ROS signaling of inflammatory cytokines during *Trypanosoma cruzi* infection," *Advances in Parasitology*, vol. 76, pp. 153–170, 2011.
- [45] T. Iannitti and B. Palmieri, "Antioxidant therapy effectiveness: an up to date," *European Review for Medical and Pharmacological Sciences*, vol. 13, no. 4, pp. 245–278, 2009.
- [46] V. Pooja and M. Sunita, "Antioxidants and disease prevention," *International Journal of Advanced Scientific and Technical Research*, vol. 2, pp. 903–911, 2014.
- [47] H. H. Schmidt, R. Stocker, C. Vollbracht et al., "Antioxidants in translational medicine," *Antioxidants & Redox Signaling*, vol. 23, no. 14, pp. 1130–1143, 2015.
- [48] R. D. Novaes, E. C. Santos, M. Fialho et al., "Nonsteroidal anti-inflammatory is more effective than anti-oxidant therapy in counteracting oxidative/nitrosative stress and heart disease in *T. cruzi*-infected mice," *Parasitology*, vol. 144, no. 7, pp. 904–916, 2017.
- [49] A. N. Assunção Jr., M. Jerosch-Herold, R. L. Melo et al., "Chagas' heart disease: gender differences in myocardial damage assessed by cardiovascular magnetic resonance," *Journal of Cardiovascular Magnetic Resonance*, vol. 18, no. 1, p. 88, 2016.
- [50] J. J. Wen, V. Bhatia, V. L. Popov, and N. J. Garg, "Phenyl-alpha-tert-butyl nitroner reverses mitochondrial decay in acute Chagas' disease," *The American Journal of Pathology*, vol. 169, no. 6, pp. 1953–1964, 2006.
- [51] J. J. Wen, S. Gupta, Z. Guan et al., "Phenyl-alpha-tert-butyl-nitroner and benzonidazole treatment controlled the mitochondrial oxidative stress and evolution of cardiomyopathy in chronic chagasic rats," *Journal of the American College of Cardiology*, vol. 55, no. 22, pp. 2499–2508, 2010.
- [52] J. R. P. T. Castanheira, R. E. P. Castanho, H. Rocha Jr. et al., "Paradoxical effects of vitamin C in Chagas disease," *Parasitology International*, vol. 67, no. 5, pp. 547–555, 2018.
- [53] T. M. Tieghi, C. C. Manca, L. C. T. Garcia et al., "Evaluation of antioxidant therapy in experimental Chagas disease,"

- Revista da Sociedade Brasileira de Medicina Tropical*, vol. 50, no. 2, pp. 184–193, 2017.
- [54] V. Brazão, R. P. Colato, F. H. Santello et al., “Interleukin-17, oxidative stress, and inflammation: role of melatonin during *Trypanosoma cruzi* infection,” *Journal of Pineal Research*, vol. 59, no. 4, pp. 488–496, 2015.
- [55] R. D. Novaes, M. V. Sartini, J. P. Rodrigues et al., “Curcumin enhances the anti-*Trypanosoma cruzi* activity of benzimidazole-based chemotherapy in acute experimental Chagas disease,” *Antimicrobial Agents and Chemotherapy*, vol. 60, no. 6, pp. 3355–3364, 2016.
- [56] J. M. E. Contreras-Ortiz, A. Barbabosa-Pliego, R. Oros-Pantoja et al., “Effects of astaxanthin in mice acutely infected with *Trypanosoma cruzi*,” *Parasite*, vol. 24, p. 17, 2017.
- [57] A. Chakraborty, P. Ramani, H. J. Sherlin, P. Premkumar, and A. Natesan, “Antioxidant and pro-oxidant activity of vitamin C in oral environment,” *Indian Journal of Dental Research*, vol. 25, no. 4, pp. 499–504, 2014.
- [58] M. V. Providello, Z. A. Carneiro, G. B. Portapilla et al., “Benefits of ascorbic acid in association with low-dose benzimidazole in treatment of Chagas disease,” *Antimicrobial Agents and Chemotherapy*, vol. 62, no. 9, 2018.
- [59] V. Puente, A. Demaria, F. M. Frank, A. Batlle, and M. E. Lombardo, “Anti-parasitic effect of vitamin C alone and in combination with benzimidazole against *Trypanosoma cruzi*,” *PLoS Neglected Tropical Diseases*, vol. 12, no. 9, article e0006764, 2018.
- [60] R. G. Marim, A. S. de Gusmao, R. E. Castanho et al., “Effects of vitamin C supplementation on the chronic phase of Chagas disease,” *Revista do Instituto de Medicina Tropical de São Paulo*, vol. 57, no. 3, pp. 245–250, 2015.
- [61] M. Saeftel, B. Fleischer, and A. Hoerauf, “Stage-dependent role of nitric oxide in control of *Trypanosoma cruzi* infection,” *Infection and Immunity*, vol. 69, no. 4, pp. 2252–2259, 2001.
- [62] R. Sesti-Costa, Z. A. Carneiro, M. C. Silva et al., “Ruthenium complex with benzimidazole and nitric oxide as a new candidate for the treatment of Chagas disease,” *PLoS Neglected Tropical Diseases*, vol. 8, no. 10, article e3207, 2014.
- [63] E. G. Janzen, J. L. Poyer, M. S. West, C. Crossley, and P. B. McCay, “Study of reproducibility of spin trapping results in the use of C-phenyl-N-tert-butyl nitrene (PBN) for trichloromethyl radical detection in CCl₄ metabolism by rat liver microsomal dispersions Biological spin trapping I,” *Journal of Biochemical and Biophysical Methods*, vol. 29, no. 3-4, pp. 189–205, 1994.
- [64] J. J. Wen and N. J. Garg, “Proteome expression and carbonylation changes during *Trypanosoma cruzi* infection and Chagas disease in rats,” *Molecular & Cellular Proteomics*, vol. 11, no. 4, article 010918, 2012.
- [65] L. M. Fidalgo and L. Gille, “Mitochondria and trypanosomatids: targets and drugs,” *Pharmaceutical Research*, vol. 28, no. 11, pp. 2758–2770, 2011.
- [66] M. P. Murphy and R. C. Hartley, “Mitochondria as a therapeutic target for common pathologies,” *Nature Reviews Drug Discovery*, vol. 17, no. 12, pp. 865–886, 2018.
- [67] D. A. Brown, J. B. Perry, M. E. Allen et al., “Expert consensus document: mitochondrial function as a therapeutic target in heart failure,” *Nature Reviews Cardiology*, vol. 14, no. 4, pp. 238–250, 2017.
- [68] H. Jin, A. Kanthasamy, A. Ghosh, V. Anantharam, B. Kalyanaraman, and A. G. Kanthasamy, “Mitochondria-targeted antioxidants for treatment of Parkinson's disease: preclinical and clinical outcomes,” *Biochimica et Biophysica Acta*, vol. 1842, no. 8, pp. 1282–1294, 2014.
- [69] G. Vilar-Pereira, V. C. Carneiro, H. Mata-Santos et al., “Resveratrol reverses functional Chagas heart disease in mice,” *PLoS Pathogens*, vol. 12, no. 10, article e1005947, 2016.
- [70] N. Barzilai, J. P. Crandall, S. B. Kritchevsky, and M. A. Espeland, “Metformin as a tool to target aging,” *Cell Metabolism*, vol. 23, no. 6, pp. 1060–1065, 2016.
- [71] D. Bonnefont-Rousselot, “Resveratrol and cardiovascular diseases,” *Nutrients*, vol. 8, no. 5, p. 250, 2016.
- [72] L. Kursvietiene, I. Staneviciene, A. Mongirdiene, and J. Bernatoniene, “Multiplicity of effects and health benefits of resveratrol,” *Medicina*, vol. 52, no. 3, pp. 148–155, 2016.
- [73] N. Xia, U. Forstermann, and H. Li, “Resveratrol and endothelial nitric oxide,” *Molecules*, vol. 19, no. 10, pp. 16102–16121, 2014.
- [74] N. Xia, A. Daiber, U. Forstermann, and H. Li, “Antioxidant effects of resveratrol in the cardiovascular system,” *British Journal of Pharmacology*, vol. 174, no. 12, pp. 1633–1646, 2017.
- [75] M. Kim and R. Tian, “Targeting AMPK for cardiac protection: opportunities and challenges,” *Journal of Molecular and Cellular Cardiology*, vol. 51, no. 4, pp. 548–553, 2011.
- [76] R. J. Reiter, D. Melchiorri, E. Sewerynek et al., “A review of the evidence supporting melatonin's role as an antioxidant,” *Journal of Pineal Research*, vol. 18, no. 1, pp. 1–11, 1995.
- [77] D. Bonnefont-Rousselot and F. Collin, “Melatonin: action as antioxidant and potential applications in human disease and aging,” *Toxicology*, vol. 278, no. 1, pp. 55–67, 2010.
- [78] B. Joe and B. R. Lokesh, “Role of capsaicin, curcumin and dietary n-3 fatty acids in lowering the generation of reactive oxygen species in rat peritoneal macrophages,” *Biochimica et Biophysica Acta*, vol. 1224, no. 2, pp. 255–263, 1994.
- [79] A. C. P. Reddy and B. R. Lokesh, “Studies on spice principles as antioxidants in the inhibition of lipid peroxidation of rat liver microsomes,” *Molecular and Cellular Biochemistry*, vol. 111, no. 1-2, pp. 117–124, 1992.
- [80] A. B. Kunnumakkara, D. Bordoloi, G. Padmavathi et al., “Curcumin, the golden nutraceutical: multitargeting for multiple chronic diseases,” *British Journal of Pharmacology*, vol. 174, no. 11, pp. 1325–1348, 2017.
- [81] M. A. Tomeh, R. Hadianamrei, and X. Zhao, “A review of curcumin and its derivatives as anticancer agents,” *International Journal of Molecular Sciences*, vol. 20, no. 5, p. 1033, 2019.
- [82] A. Bielak-Zmijewska, W. Grabowska, A. Ciolko et al., “The role of curcumin in the modulation of ageing,” *International Journal of Molecular Sciences*, vol. 20, no. 5, p. 1239, 2019.
- [83] M. Shahiduzzaman and A. Dausgchies, “Curcumin: a natural herb extract with antiparasitic properties,” in *Nature Helps*, H. Mehlhorn, Ed., pp. 141–152, Springer, Berlin, Heidelberg, 2011.
- [84] F. Nagajyothi, D. Zhao, L. M. Weiss, and H. B. Tanowitz, “Curcumin treatment provides protection against *Trypanosoma cruzi* infection,” *Parasitology Research*, vol. 110, no. 6, pp. 2491–2499, 2012.
- [85] R. R. Ambati, S. M. Phang, S. Ravi, and R. G. Aswathanarayana, “Astaxanthin: sources, extraction, stability, biological activities and its commercial applications-a review,” *Marine Drugs*, vol. 12, no. 1, pp. 128–152, 2014.

- [86] J. M. Gutteridge, R. Richmond, and B. Halliwell, "Inhibition of the iron-catalysed formation of hydroxyl radicals from superoxide and of lipid peroxidation by desferrioxamine," *The Biochemical Journal*, vol. 184, no. 2, pp. 469–472, 1979.
- [87] U. N. Basaran, S. Ayvaz, B. Aksu et al., "Desferrioxamine reduces oxidative stress in the lung contusion," *Scientific-WorldJournal*, vol. 2013, p. 376959, 2013.
- [88] S. Ortega-Gutierrez, J. J. Garcia, E. Martinez-Ballarín et al., "Melatonin improves deferoxamine antioxidant activity in protecting against lipid peroxidation caused by hydrogen peroxide in rat brain homogenates," *Neuroscience Letters*, vol. 323, no. 1, pp. 55–59, 2002.
- [89] A. F. Francisco, P. M. de Abreu Vieira, J. M. Arantes et al., "Increase of reactive oxygen species by desferrioxamine during experimental Chagas' disease," *Redox Report*, vol. 15, no. 4, pp. 185–190, 2010.
- [90] M. C. Montenote, V. Z. Wajsman, Y. T. Konno et al., "Antioxidant effect of *Morus nigra* on Chagas disease progression," *Revista do Instituto de Medicina Tropical de São Paulo*, vol. 59, article e73, 2017.
- [91] P. Dandona, H. Ghanim, and D. P. Brooks, "Antioxidant activity of carvedilol in cardiovascular disease," *Journal of Hypertension*, vol. 25, no. 4, pp. 731–741, 2007.
- [92] K. Oettl, J. Greilberger, K. Zangger, E. Haslinger, G. Reibnegger, and G. Jurgens, "Radical-scavenging and iron-chelating properties of carvedilol, an antihypertensive drug with antioxidative activity," *Biochemical Pharmacology*, vol. 62, no. 2, pp. 241–248, 2001.
- [93] S. Ayashi, A. R. Assareh, M. T. Jalali, S. Olapour, and H. Yaghooti, "Role of antioxidant property of carvedilol in mild to moderate hypertensive patients: a prospective open-label study," *Indian Journal of Pharmacology*, vol. 48, no. 4, pp. 372–376, 2016.
- [94] A. L. Horta, V. P. Figueiredo, A. L. J. Leite et al., "The β -blocker carvedilol and the benzimidazole modulate the cardiac immune response in the acute infection induced by Colombian strain of the *Trypanosoma cruzi*," *Memórias do Instituto Oswaldo Cruz*, vol. 113, no. 11, article e180271, 2018.
- [95] Y. Tada and J. Suzuki, "Oxidative stress and myocarditis," *Current Pharmaceutical Design*, vol. 22, no. 4, pp. 450–471, 2016.
- [96] L. B. Macao, D. Wilhelm Filho, R. C. Pedrosa et al., "Antioxidant therapy attenuates oxidative stress in chronic cardiopathy associated with Chagas' disease," *International Journal of Cardiology*, vol. 123, no. 1, pp. 43–49, 2007.
- [97] C. M. Ribeiro, P. Budni, R. C. Pedrosa et al., "Antioxidant therapy attenuates oxidative insult caused by benzonidazole in chronic Chagas' heart disease," *International Journal of Cardiology*, vol. 145, no. 1, pp. 27–33, 2010.
- [98] J. L. Barbosa, C. A. Thiers, B. de Bragança Pereira et al., "Impact of the use of benzonidazole followed by antioxidant supplementation in the prevalence of ventricular arrhythmias in patients with chronic Chagas disease: pilot study," *American Journal of Therapeutics*, vol. 23, no. 6, pp. e1474–e1483, 2014.
- [99] P. Budni, R. C. Pedrosa, T. R. Garlet et al., "Carvedilol attenuates oxidative stress in chronic chagasic cardiomyopathy," *Arquivos Brasileiros de Cardiologia*, vol. 98, no. 3, pp. 218–224, 2012.
- [100] P. Budni, R. C. Pedrosa, E. M. Dalmarco, J. B. Dalmarco, T. S. Frode, and D. Wilhelm Filho, "Carvedilol enhances the anti-oxidant effect of vitamins E and C in chronic Chagas heart disease," *Arquivos Brasileiros de Cardiologia*, vol. 101, no. 4, pp. 304–310, 2013.
- [101] L. A. Jelicks, A. P. de Souza, T. C. Araujo-Jorge, and H. B. Tanowitz, "Would selenium supplementation aid in therapy for Chagas disease?," *Trends in Parasitology*, vol. 27, no. 3, pp. 102–105, 2011.
- [102] V. C. Desoti, D. Lazarin-Bidóia, F. M. Ribeiro et al., "The combination of vitamin K3 and vitamin C has synergic activity against forms of *Trypanosoma cruzi* through a redox imbalance process," *PLoS One*, vol. 10, no. 12, article e0144033, 2015.

Research Article

Norepinephrine Induces Lung Microvascular Endothelial Cell Death by NADPH Oxidase-Dependent Activation of Caspase-3

Andreia Z. Chignalia ^{1,2,3}, Guy Weinberg,¹ and Randal O. Dull ^{1,2,3}

¹College of Medicine, Department of Anesthesiology, University of Illinois at Chicago, Chicago, Illinois, USA

²College of Medicine, Department of Anesthesiology, University of Arizona, Tucson, Arizona, USA

³College of Medicine, Department of Physiology, University of Arizona, Tucson, Arizona, USA

Correspondence should be addressed to Andreia Z. Chignalia; azchignalia@email.arizona.edu

Received 16 July 2019; Revised 15 November 2019; Accepted 3 January 2020; Published 12 February 2020

Guest Editor: Lynette K. Rogers

Copyright © 2020 Andreia Z. Chignalia et al. This is an open access article distributed under the Creative Commons Attribution License, which permits unrestricted use, distribution, and reproduction in any medium, provided the original work is properly cited.

Norepinephrine (NE) is the naturally occurring adrenergic agonist that is released in response to hypotension, and it is routinely administered in clinical settings to treat moderate to severe hypotension that may occur during general anesthesia and shock states. Although NE has incontestable beneficial effects on blood pressure maintenance during hypotensive conditions, deleterious effects of NE on endothelial cell function may occur. In particular, the role of reactive oxygen species (ROS) and NADPH oxidase (Nox) on the deleterious effects of NE on endothelial cell function have not been fully elucidated. Therefore, we investigated the effects of NE on ROS production in rat lung microvascular endothelial cells (RLMEC) and its contribution to cell death. RLMEC were treated with NE (5 ng/mL) for 24 hours and ROS production was assessed by CellROX and DCFDA fluorescence. Nox activity was assessed by NADPH-stimulated ROS production in isolated membranes and phosphorylation of p47phox; cell death was assessed by flow cytometry and DNA fragmentation. Caspase activation was assessed by fluorescent microscopy. Nox1, Nox2, and Nox4 mRNA expression was assessed by real-time PCR. NE increased ROS production, Nox activity, p47phox phosphorylation, Nox2 and Nox4 mRNA content, caspase-3 activation, and RLMEC death. Phentolamine, an α_1 -adrenoreceptor antagonist, inhibited NE-induced ROS production and Nox activity and partly inhibited cell death while β -blockade had no effect. Apocynin and PEGSOD inhibited NE-induced caspase-3 activation and cell death while direct inhibition of caspase-3 abrogated NE-induced cell death. PEG-CAT inhibited NE-induced cell death but not caspase-3 activation. Collectively, these results indicate that NE induces RLMEC death via activation of Nox by α -adrenergic signaling and caspase-3-dependent pathways. NE has deleterious effects on RLMECs that may be important to its long-term therapeutic use.

1. Introduction

Norepinephrine (NE) is the endogenous catecholamine released by sympathetic nerve fibers in the vascular wall in response to acute reductions in blood pressure. Exogenous NE is commonly used to support blood pressure during shock due to its dual action on both α_1 - and β_1 -adrenoreceptors that, respectively, cause vasoconstriction and increase myocardial contractility, ultimately resulting in increased peripheral vascular resistance and cardiac output. However, studies in rats indicate that typical pressor doses of NE or epinephrine can alter pulmonary capillary integrity leading to accumulation of lung water and ultimately pulmonary

edema [1, 2]. These reports reveal an important and yet unexplored area: the potential long-term side effects of the use of catecholamines in clinical settings. Whether NE exerts deleterious effects on vascular cells is still unknown and is worth of exploration as it may have direct bearing on the clinical use of catecholamines. In particular, understanding the potential deleterious effects of pathophysiological concentrations of NE in lung endothelial cells may be critical as it has been shown that these cells develop dysfunction, and, specifically barrier failure, when acutely exposed to NE. Moreover, the lung endothelium uptakes approximately 30% of the circulating NE, making this organ an important target for NE.

The effects of NE on endothelial function have been related to increased reactive oxygen species (ROS) production. We have recently shown that, in rats, continuous infusion of NE for two hours leads to nitric oxide synthase (NOS) uncoupling in the lungs. Uncoupled NOS then drives superoxide anion generation leading to oxidative stress, endothelial dysfunction, and endothelial barrier disruption that ultimately causes pulmonary edema [2]. Additionally, it has been shown that NE increases ROS production by a NADPH oxidase1 (Nox1) dependent pathway in human peripheral mononuclear cells [3] and in rat endothelial cardiac cells [4]. Interestingly, ROS production by NE can be mediated either by α - [3] or β -adrenoceptors depending on the cell type [5].

The suprapharmacological concentrations of NE used in many studies have limited clinical significance. We therefore investigated the effects of a clinically relevant concentration of NE [6–8] on Nox activity and ROS production in endothelial cells and its contribution to endothelial cell death. Herein, we report that NE, in a concentration in the same order of magnitude as the ones found in human plasma of critically ill patients, can be toxic to rat lung microvascular endothelial cells.

2. Methods

2.1. Drugs and Reagents. Chemicals were the highest grade available. Norepinephrine bitartrate salt, apocynin, propranolol, phentolamine, superoxide dismutase-polyethylene glycol (PEG-SOD), and catalase-polyethylene glycol (PEG-CAT) were purchased from Sigma Chemicals. Phospho-p47phox (Ser370) was purchased from Invitrogen. Caspase-3 inhibitor III, was purchased from Santa Cruz Biotechnologies (Dallas, TX). FITC Annexin V/Dead Cell Apoptosis Kit[®], CellROX[®] probe, 5-(and-6)-carboxy-2',7'-dichlorodihydrofluorescein, CellEventTM[®] kit, Alexa Fluor[™] 647 goat anti-rabbit antibody, and one step Power SYBR[™] Green RNA to CT[™] RT-PCR kit were purchased from Thermo Fisher Scientific (Waltham, MA). FragEL[™] DNA Fragmentation Detection Kit Fluorescence TdT enzyme was purchased from EMD Millipore (Billerica, MA).

2.2. Cell Culture. Rat lung microvascular endothelial cells (RLMEC) were purchased from VEC Technologies (Rensselaer, NY) and cultured with EBM-2 medium (Lonza, Walkersville, MD) supplemented with 10% fetal bovine serum; cells were maintained in an incubator at 37°C, 5% CO₂. Cells from passage 4 to 10 were used in these experiments. Experiments were performed using NE 5 ng/mL (15.7 nM). The concentration of NE was chosen based on a cell viability concentration-response curve, assessed by trypan blue, as the first dose capable of decreasing lung endothelial cell viability *in vitro* after 24 h of NE exposure (data not shown). This concentration is in the ng/mL order of magnitude, which is found in critically ill patients [6–8].

2.3. Measurement of Reactive Oxygen Species

2.3.1. CellROX[®]. ROS production was assessed by fluorescence via measurement of CellROX[®] oxidation in a 96-well plate assay according to the manufacturer's instructions.

RLMEC (10³ cells/well) were serum deprived for 24 hours and stimulated with NE 5 ng/mL for 5 to 120 minutes. To assess if NE induces superoxide anion or hydrogen peroxide generation, RLMEC were preincubated with PEG-SOD (25 U/mL) or PEG-CAT (200 U/mL) for 30 minutes before RLMEC exposure to NE for 5 minutes. Concentrations of PEG-SOD and PEG-CAT were chosen based on the literature [9]. To assess the contribution of α - and β -adrenoceptors, RLMEC were incubated with phentolamine (10⁻⁸ mol/L) or propranolol (10⁻⁸ mol/L) for 30 minutes before exposure to NE for 5 minutes. The concentration on phentolamine and propranolol was chosen based on a concentration-response curve as the lowest dose capable of inhibiting NE-inducing ROS production in RLMEC.

2.3.2. DCFDA. ROS production was assessed by the detection of carboxy-2',7', dichlorofluorescein fluorescence (DCF) by epifluorescence microscopy. RLMEC were plated in glass coverslips pretreated with 0.4% gelatin. Cells were serum deprived for 24 hours and stimulated with NE 5 ng/mL for 15 minutes. To assess if NE induces superoxide anion or hydrogen peroxide generation, RLMEC were preincubated with PEG-SOD (25 U/mL) or PEG-CAT (200 U/mL) for 30 minutes before RLMEC exposure to NE for 15 minutes. Concentrations of PEG-SOD and PEG-CAT were chosen based on the literature [9]. After stimulation with NE, cells were washed with HBSS buffer and incubated with 25 μ M of carboxy-5-(and-6)-carboxy-2',7'-dichlorodihydrofluorescein (carboxy-DCFDA) for 30 minutes. Cells were fixed in 10% methanol for 5 minutes and mounted in prolong antifade mounting media. Images were acquired by Leica microscope (DMI6000) using LAS X[®] software. Images were quantified with ImageJ (NIH) software. Data is presented as relative fluorescent units (RFU, fluorescence on 488 channel normalized by the number of cells in the field (assessed by DAPI staining)).

2.3.3. Nox Activity. Nox activity was assessed in membrane fractions as previously described [10, 11]. RLMEC were stimulated with NE (5 ng/mL) for 5 up to 120 minutes. In specific studies, RLMEC were preincubated with phentolamine (10⁻⁸ mol/L) or propranolol (10⁻⁸ mol/L) before exposure to NE (5 ng/mL) for 5 minutes. Membrane fractions were isolated from RLMEC using Mem-PER[™] Plus[®] Membrane Protein Extraction Kit according to the manufactures' instructions. Nox activity in membrane fractions was assessed by the kinetics of DHE oxidation in a 96-well plate fluorimeter. One hundred microliters of the membrane extract was added to each well, along with 0.12 μ L DHE (10 mM), 25 mg/mL DNA, and 101.88 μ L phosphate buffer (50 mM, pH 7.4). Fluorescence was read for 30 min (λ_{exc} = 485 nm, λ_{em} = 595 nm). Three microliters of NADPH (2 mmol/L) was then added and a new reading was performed for 30 min. The delta for the area under the curve (Δ AUC) was calculated (Δ AUC = AUC after NADPH – AUC before NADPH). Δ AUC was normalized by protein content in the sample. The results are expressed as percentage of control.

2.4. Immunohistochemistry. RLMEC were plated in glass coverslips pretreated with 0.4% gelatin. When cells reached confluence, they were serum deprived for 24 h and incubated with PBS or NE (5 ng/mL) for 15 minutes. Cells were fixed with 4% paraformaldehyde and permeabilized with triton 0.1% in HBSS. Blocking of nonspecific binding sites was done with 5% normal goat serum. Cells were incubated with phospho-p47phox (Ser370) antibody overnight at 4°C. Cells were washed and incubated with Alexa Fluor™ 647 goat anti-rabbit antibody for 2 hours at room temperature followed up by incubation with DAPI. Slides were mounted and imaged on a Leica microscope (DMI6000) using LAS X® software. Images were quantified with ImageJ (NIH). Data is presented as relative fluorescent units (RFU, fluorescence on 647 channel normalized by the number of cells in the field (assessed by DAPI staining)).

2.5. Real-Time PCR. RNA was extracted by TRIZOL® (Invitrogen) and quantified using NanoDrop (Thermo Fisher Scientific). One-step real-time PCR was performed using Power SYBR™ Green RNA to C_T™ RT-PCR kit (Applied Biosystems by Thermo Fisher Scientific) and the QuantStudio 3 (Thermo Fisher Scientific). Primers were obtained from Integrated DNA Technologies (Coralville, IA). Data were analyzed using the comparative cycle threshold (CT) method. Relative quantification to the control sample calibrator was calculated using the formula $2^{(-\Delta\Delta CT)}$. Gene expression was normalized to the level of beta actin, which was used as an internal control. Data are presented as relative expression levels compared with the control.

2.6. Cell Viability and Cell Death. Cell viability was assessed by trypan blue staining. Results are expressed as percentage of viable cells. Cell death was assessed by annexin V and propidium iodide (PI) staining via flow cytometry using a commercially available kit (FITC Annexin V/Dead Cell Apoptosis Kit®) from Thermo Fisher Scientific. Apoptotic cells were detected by FragEL™ DNA Fragmentation Detection Kit Fluorescence TdT enzyme according to the manufacturer's instructions and DNA fragmentation was assessed by electrophoresis. For these studies, RLMEC were incubated with NE 5 ng/mL or PBS for 24 hours. When required, cells were preincubated with PEG-SOD (25 U/mL) or PEG-CAT (200 U/mL) for 30 minutes before RLMEC exposure to NE.

2.7. Caspase Activation. Caspase-3 and caspase-7 activation were assessed by fluorescence microscopy using CellEvent™ kit (Invitrogen). RLMEC were exposed to NE 5 ng/mL for 24 hours in the presence or absence of phentolamine (10^{-8} mol/L), apocynin (30 μ mol/L), PEG-SOD (25 U/mL), or PEG-CAT (200 U/mL). Images were acquired by an upright fluorescence microscope (Olympus BX51) using Olympus Screen Saver software (Olympus).

2.8. Statistical Analysis. Data are presented as mean \pm SD. Groups were compared using 1-way ANOVA or Student *t* test, as appropriate. Newman-Keuls post hoc test was used to compensate for multiple testing procedures. $p < 0.05$ was considered statistically significant.

3. Results

3.1. ROS Production. ROS production was measured in a real-time manner using CellROX® probe (Thermo Fisher Scientific) in RLMEC stimulated or not with NE. A two-fold increase in ROS production was observed as early as 5 minutes after exposure to NE (3223.8 ± 631.55 RFU in the NE group vs. 1072.9 ± 520.29 RFU in the control group); steady ROS production lasted for 2 hours (Figure 1(a)). ROS production was partly inhibited by PEG-SOD (NE + PEG-SOD = 4257 ± 800.0 RFU vs. NE = 6149 ± 626.2 RFU) (Figure 1(a)) and PEG-catalase (NE + PEG-CAT = 2330 ± 473.4 RFU vs. NE = 6149 ± 626.2 RFU) (Figure 1(b)) indicating that NE leads to the generation of both superoxide anion and hydrogen peroxide. Incubation of RLMEC with PEG-SOD or PEG-CAT only did not alter ROS production (PEG-SOD = 1204 ± 756.4 RFU and PEG-CAT = 988.7 ± 208.7 RFU) (Figures 1(a)–1(c)). To confirm the effects of NE on ROS production, we assessed ROS generation via a second methodology, oxidation of DCFDA by epifluorescence microscopy. NE increased ROS production (NE = 86350 ± 9380 RFU vs. vehicle = 24677 ± 4712 RFU) in RLMEC, an effect inhibited by both PEG-SOD and PEG-CAT (19138 ± 2531 and 25710 ± 9278 , respectively) (Figures 1(d) and 1(e)). Next, to determine the adrenoceptor involved, cells were incubated with phentolamine (10^{-8} mol/L) or propranolol (10^{-8} mol/L) for 30 minutes before stimulation with NE for 5 minutes. Incubation of RLMEC with only phentolamine (Phen = 1814 ± 285.4) or propranolol (Prop = 1332 ± 94.8) did not alter ROS levels in RLMEC. Cells were then stimulated with NE+phentolamine or NE+propranolol. Whereas phentolamine fully blocked the effects of NE on ROS production (NE + Phen = 2003 ± 290.5 vs. NE = 5832 ± 215.0), propranolol partly inhibited ROS production by NE (NE + Prop = 4815 ± 324.3 vs. NE = 5832 ± 215.0) (Figure 1(f)).

3.2. Nox Activity. NE increased Nox activity in isolated membrane fractions after 5 minutes (in % of control: NE = 140.6 ± 19.12); activity peaked at 15 minutes (NE = $195.4 \pm 54.62\%$) and decreased after 30 minutes (NE = $126.6 \pm 25.26\%$) (Figure 2(a)). Additionally, exposure of RLMEC to NE for 15 minutes increased phosphorylation of p47phox at Ser370 (Figures 2(b) and 2(c)). To assess the contribution of alpha-adrenergic receptor, Nox activity was measured in the presence of phentolamine. Phentolamine completely blocked the increase in Nox activity after exposure to NE (NE + Phen = $83.2 \pm 16.01\%$ vs. NE = $146.3 \pm 40.13\%$) (Figure 2(d)). To evaluate the role of β -adrenoceptors in NE-induced Nox activation, cells were treated with propranolol, a nonselective β -adrenoceptor antagonist. Propranolol did not inhibit the effects of NE on Nox activity (in %: NE + Prop = 127.3 ± 13.03 vs. NE = 136.3 ± 36.96) (Figure 2(e)). Incubation of RLMEC with phentolamine or propranolol only did not alter Nox activity (Phen = $100.8 \pm 4.28\%$ and Prop = $93.84 \pm 7.922\%$) (Figures 2(d) and 2(e), respectively).

3.3. Nox Expression. Incubation of RLMEC with NE increased Nox2 and Nox4 mRNA expression in RLMEC in a time-dependent manner. Nox2 was the first isoform to

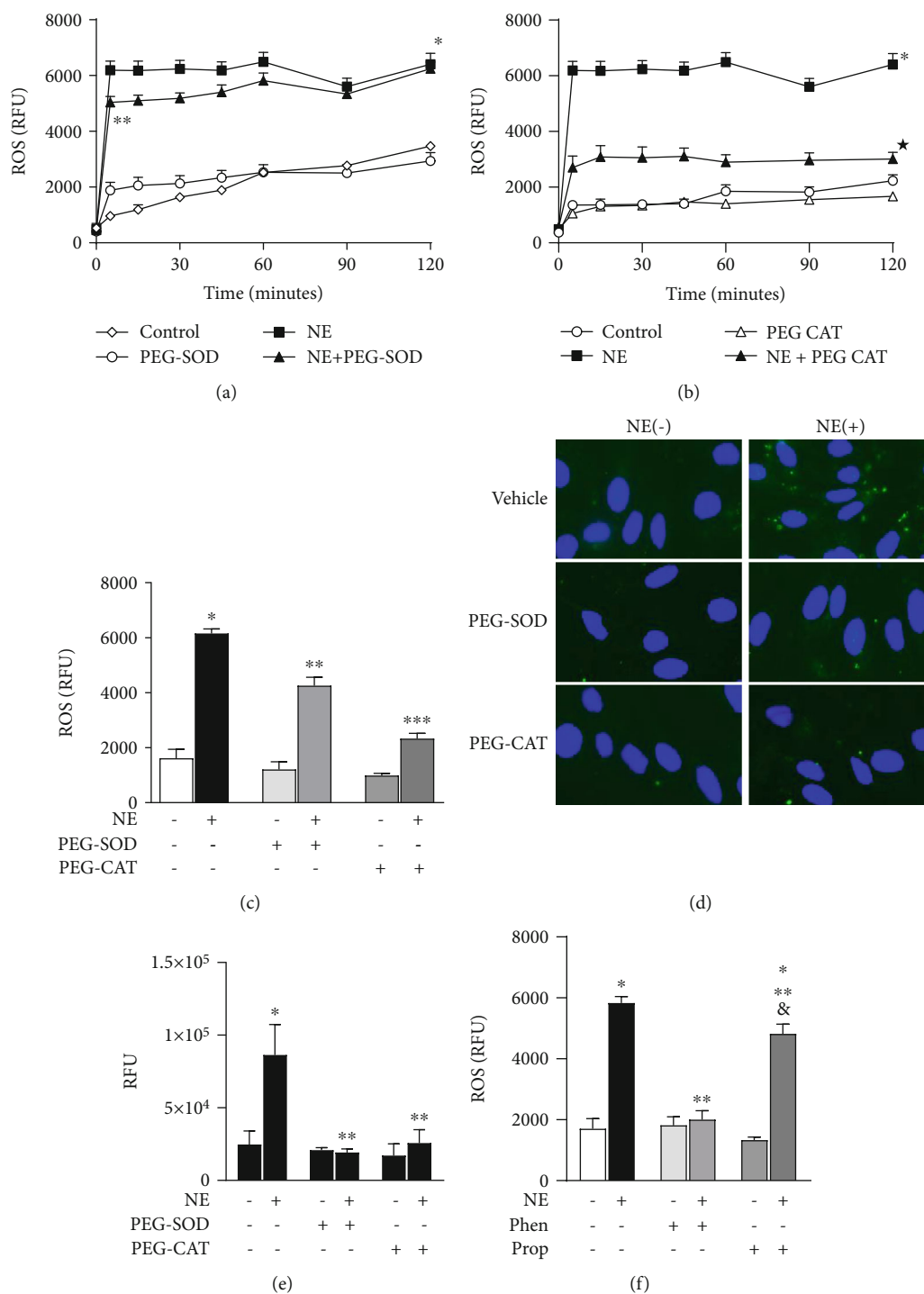


FIGURE 1: Norepinephrine induces ROS production in rat lung microvascular endothelial cells. Rat lung microvascular endothelial cells (RLMEC) were stimulated with norepinephrine (NE) 5 ng/mL for 120 minutes. (a) NE increases ROS production in RLMEC, an effect inhibited in the presence of PEG-SOD. (b) ROS levels are decreased in the presence of PEG-CAT. (c) Comparative graph illustrating the effects of PEG-SOD and PEG-CAT on ROS production stimulated by the exposure of RLMEC to NE for 5 minutes. (d) Representative images of ROS production by NE in RLMEC assessed by DCF fluorescence; effects of PEG-SOD and PEG-catalase are also shown. (e) Quantification of ROS production assessed by DCF fluorescence: RLMEC were stimulated with NE 5 ng/mL for 15 min in the presence and absence of PEG-SOD and PEG-CAT. (f) Phentolamine (Phen) and propranolol (Prop) had no effects on basal ROS production; Phen inhibited NE-induced ROS production in RLMEC and Prop partly inhibited NE-induced ROS production on RLMEC. * $p < 0.05$ vs. control, ** $p < 0.05$ vs. NE, *** $p < 0.05$ vs. NE+PEG-SOD, & $p < 0.05$ vs. propranolol. $N \geq 5$ /group.

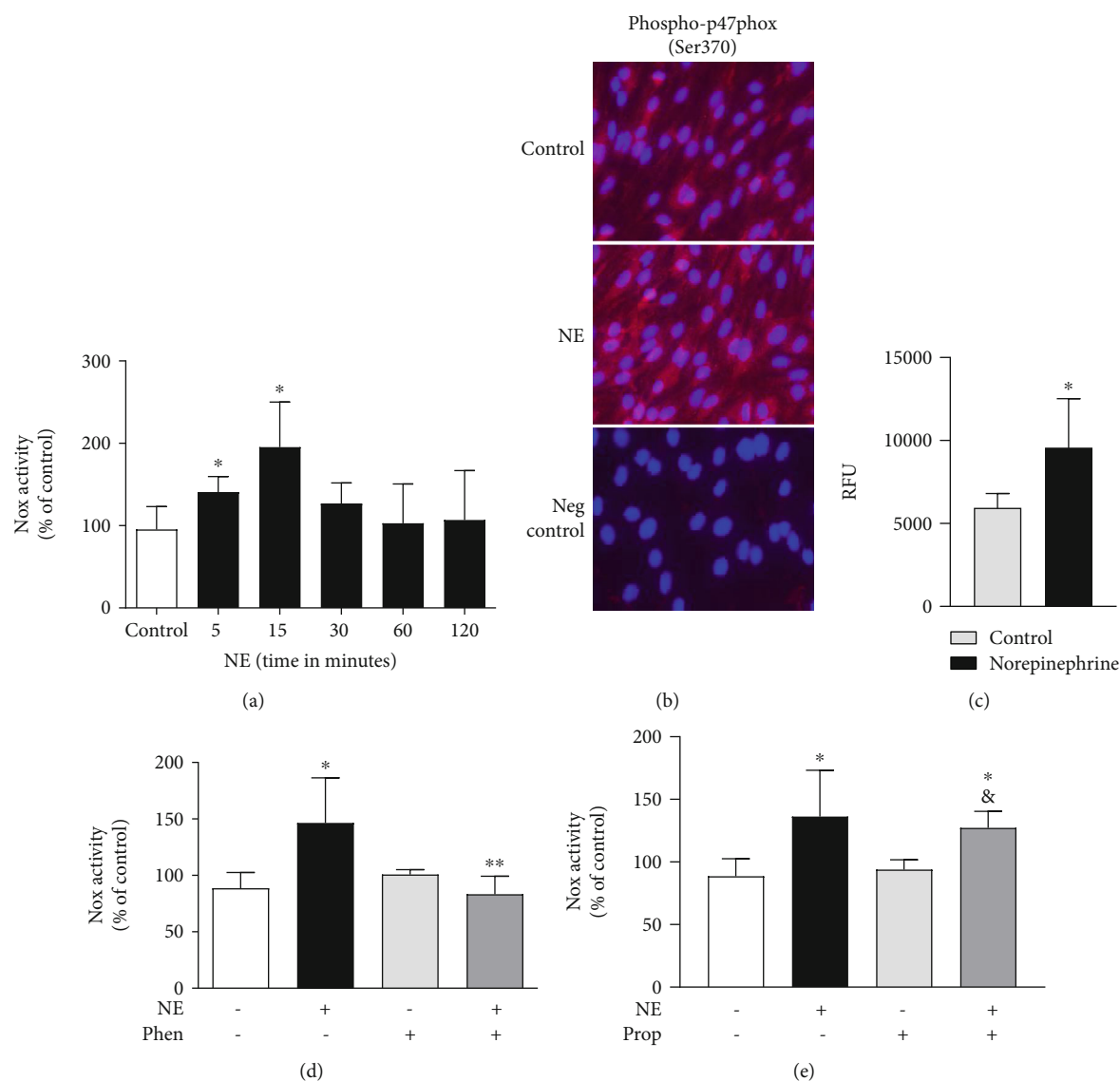


FIGURE 2: Norepinephrine activates Nox via α -adrenergic receptors. Rat lung microvascular endothelial cells (RLMEC) were stimulated with norepinephrine (NE) 5 ng/mL for 5 to 120 minutes. (a) NE increases Nox activity in RLMEC after 5 and 15 minutes of stimulation. (b) Representative images: NE increases p47phox phosphorylation at Ser370 in RLMEC after 15 minutes of incubation. (c) Quantification of p47phox phosphorylation in RLMEC stimulated or not with NE for 15 minutes: RFU (relative fluorescent units) is the ratio of fluorescence intensity/cell number of a given field in cells treated or not with NE. (d) Phentolamine (Phen), an antagonist of α_1 -adrenoceptors, inhibits NE-induced Nox activation. (e) Propranolol (Prop), a nonspecific β -adrenoceptor antagonist, do not inhibit NE-induced Nox activation. * $p < 0.05$ vs. control; ** $p < 0.05$ vs. NE; & $p < 0.05$ vs. prop. $N \geq 5$ /group.

show increased content after 4 hours (2.5 delta increase relative to control) of RLMEC incubation with NE. Importantly, a gradual increase pattern in Nox2 mRNA was observed (3.29-fold at 8 h and 3.5-fold at 24 h). Nox4 was augmented only 24 hours after cells exposure to NE (2.0-fold). Nox1 mRNA expression was not altered by NE (Figures 3(a)–3(c)).

3.4. NE Induces RLMEC Death. NE decreased the number of viable cells by 10% when compared to control (NE = $86.4 \pm 5.41\%$ vs. control = $96.5 \pm 2.13\%$) as assessed by trypan blue. In the presence of apocynin (30 $\mu\text{mol/L}$), a ROS scavenger in vascular cells, the deleterious effects of NE on cell viability were abolished (NE + APO = $93.3 \pm 1.6\%$ vs.

NE = $86.4 \pm 5.41\%$). Phentolamine inhibited the deleterious effects of NE on RLMEC viability (Phen + NE = $92.7 \pm 1.26\%$ vs. NE = $86.4 \pm 5.41\%$). Apocynin (Apo = $94.2 \pm 0.84\%$ vs. control = $96.5 \pm 2.13\%$) or phentolamine (Phen = $93.2 \pm 1.5\%$ vs. control = $96.5 \pm 2.13\%$) alone had no effects on cell viability (Figure 4(a)).

To further investigate the effects of NE on cell death, we assessed staining of RLMEC with propidium iodide and annexin V by flow cytometry. NE increased the number of annexin+/PI+ cells by 70% when compared to control (NE = 1.8 ± 0.05 vs. control = 1.1 ± 0.14). In the presence of apocynin, NE-induced cell death, as measured by the number of annexin+/PI+ cells, was inhibited by 50%

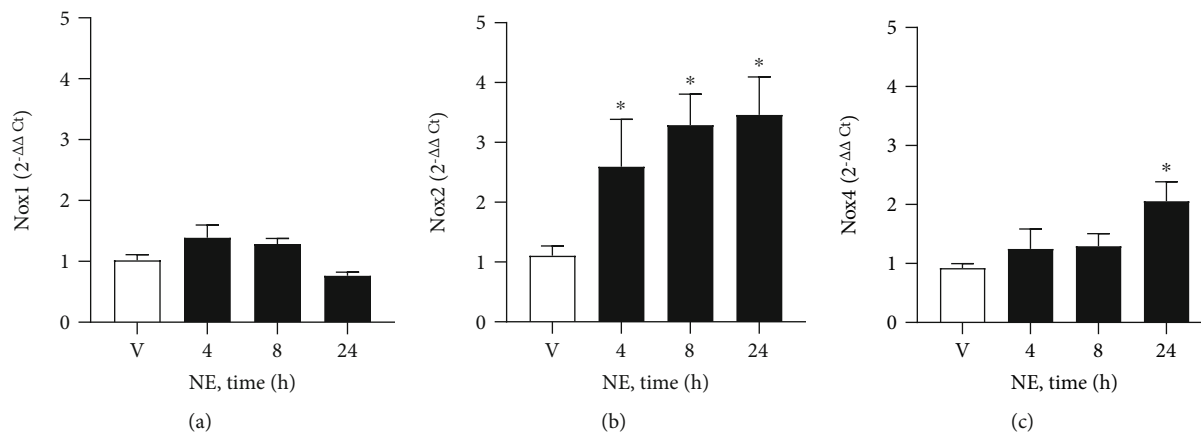


FIGURE 3: NE increases Nox2 and Nox4 mRNA expression. Rat lung microvascular endothelial cells (RLMEC) were stimulated with norepinephrine (NE, 5 ng/mL) or vehicle (V) for 4 to 24 hours (h). (a) NE does not alter mRNA expression of Nox1. (b) NE increases mRNA expression of Nox2 after 24 hours. (c) NE increased mRNA expression of Nox4 in a time-dependent manner. * $p < 0.05$ vs. vehicle (V). $N = 5$ /group.

(NE + Apo = 1.2 ± 0.02 vs. NE = 1.8 ± 0.05). Apocynin alone had no effect on RLMEC cell death (Apo = 1.1 ± 0.14 vs. control = 1.1 ± 0.14) (Figures 4(b) and 4(d)).

To confirm that NE-induced cell death was mediated by alpha-adrenergic receptor activation, we measured cell death in the presence of phentolamine. Phentolamine inhibited NE-induced cell death by approximately 25% (NE + Phen = 1.51 ± 0.01 vs. NE = 1.77 ± 0.05). Phentolamine alone had no effect on RLMEC death (Phen = 1.21 ± 0.07) (Figures 4(c) and 4(e)).

NE also increased the number of annexin+/PI- cells by 40% compared to control cells (NE = 1.4 ± 0.16 vs. control = 1.0 ± 0.18). This effect was not inhibited by either apocynin (NE + Apo = 1.3 ± 0.1) or phentolamine (NE + Phen = 1.7 ± 0.2) (Figure 4(f)). NE did not alter the number of annexin-/PI+ cells (NE = 0.8 ± 0.08 vs. control = 0.9 ± 0.10) (Figure 4(g)).

In order to pinpoint which Nox-derived reactive oxygen species mediate NE deleterious effects on RLMEC, we assessed RLMEC death in the presence of PEG-SOD and PEG-CAT by two different methodologies: the detection of apoptotic cells by the FragEL DNA fragmentation commercial kit and assessment of DNA fragmentation via electrophoresis. NE induced both DNA fragmentation and appearance of cells in the late apoptotic stage. Those effects were inhibited by PEG-SOD and PEG-CAT (Figures 5(a) and 5(b)).

3.5. Norepinephrine Regulates Caspase-3 by ROS and Alpha-Adrenoceptor-Dependent Mechanisms. To assess the role of reactive oxygen species and α_1 -adrenoceptors in norepinephrine (NE)-induced caspase-3 activation, RLMEC were treated with apocynin (Apo), phentolamine (Phen), PEG-SOD, or PEG-CAT for 30 minutes before stimulation with NE (5 ng/mL) for 24 h. NE induced the translocation of caspase-3 to the nucleus, an index of caspase-3 activity (Figure 6). Incubation with either apocynin or phentolamine (Figure 6(a)) inhibited nuclear staining of caspase-3. In the same manner, incubation of RLMEC with PEG-SOD inhibited

NE-induced caspase-3 activation. Incubation of RLMEC with PEG-CAT had no effect on caspase-3 activation by NE (Figure 6(b)).

3.6. Norepinephrine Induces Rat Lung Microvascular Endothelial Cell Death by Caspase-3-Dependent Mechanisms.

NE increased the number of annexin+/PI+ cells identified via flow cytometry when compared to untreated cells (NE = 1.48 ± 0.19 vs. control = 0.99 ± 0.01). In the presence of caspase-3 inhibitor, NE-induced cell death returned to control levels (NE + Casp 3 Inhibitor = 0.92 ± 0.04). Caspase-3 inhibitor had no effects *per se* on the number of annexin+/PI+ cells (Casp 3 inhibitor = 0.98 ± 0.21 vs. control = 0.99 ± 0.01). No changes were detected in the number of annexin+/PI- or annexin-/PI+ cells (Figures 7(a) and 7(b)).

4. Discussion

The major finding of this study was that NE, at a concentration in the order of magnitude found in plasma of critically ill patients, has deleterious effects on lung microvascular endothelial cells. NE is routinely used in the clinical settings to treat hypotension, at significant higher concentrations, and the immediate effects of NE appear beneficial insofar as NE improves blood pressure and, possibly, short-term patient survival. For example, studies in rats indicate that typical pressor doses of NE can alter pulmonary capillary integrity leading to accumulation of lung water and ultimately pulmonary edema [1, 2]. We therefore investigated the deleterious effects of a clinically relevant concentration of NE on lung endothelial cells. Our findings demonstrate that NE triggers Nox activation and ROS production via α_1 -adrenoceptors and that the onset of oxidative stress leads to caspase-3 activation, mainly by superoxide anion, which ultimately causes RLMEC death. Collectively, these data suggest that concentrations of NE typically found in critically ill patients may be deleterious to lung endothelial cells.

NE is known to produce ROS in a broad range of cell types via the activation of different adrenoceptors. Deo and

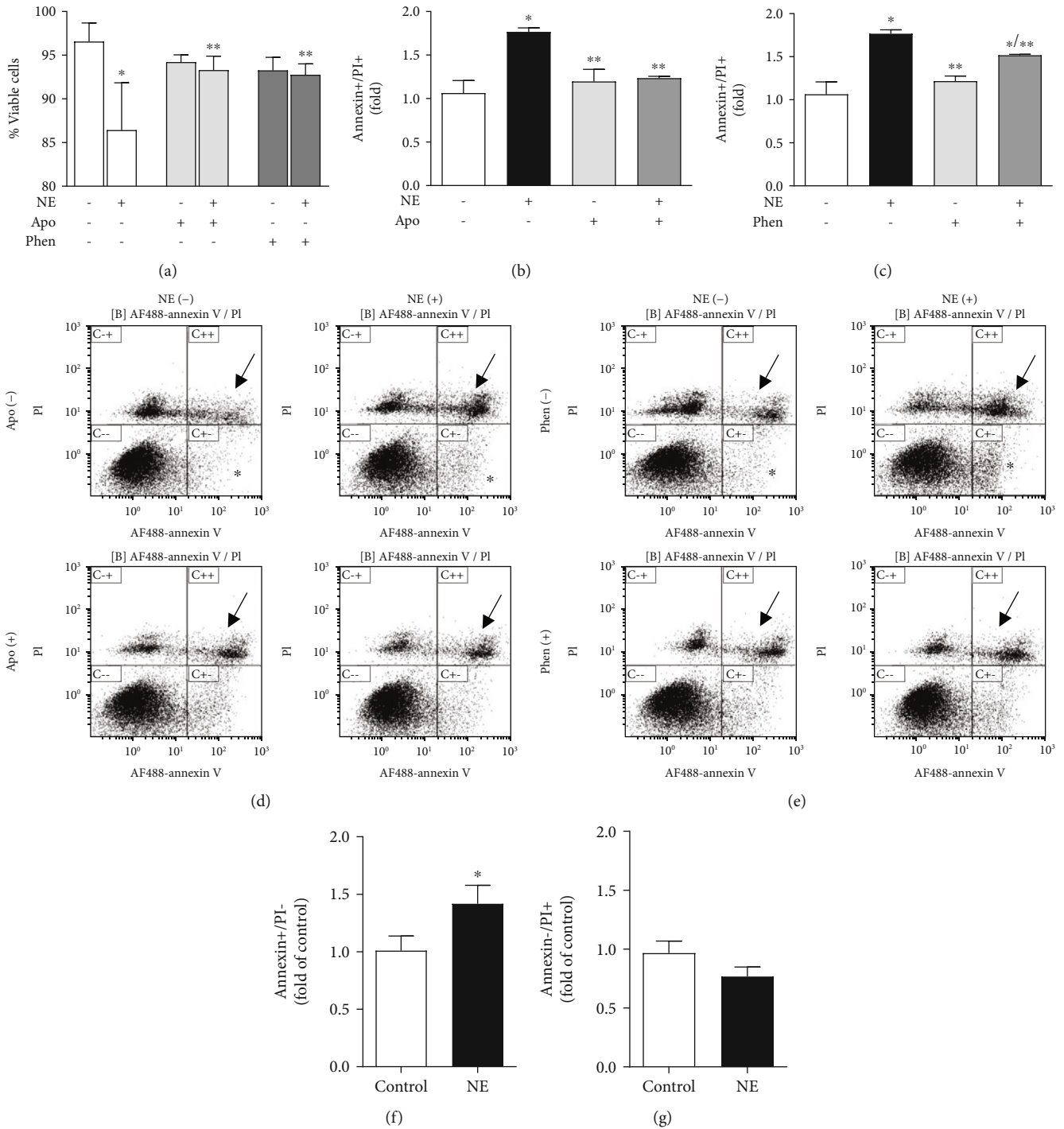


FIGURE 4: Norepinephrine induces RLMEC death via ROS production and α_1 -adrenoceptor-mediated pathways. To assess the role of reactive oxygen species and α_1 -adrenoceptors in NE-induced cells death, RLMEC were treated with apocynin (Apo) and phentolamine (Phen) for 30 minutes before stimulation with NE (5 ng/mL) for 24 h. (a) NE reduced cell viability as assessed by trypan blue, an effect inhibited by Apo and Phen. (b). NE induces cell death as it increases the amount of annexin+/PI+ cells, an effect is abolished by Apo. (c). Phen partly inhibits NE-induced cell death. (d, e) Representative flow cytometry charts evidencing that NE increases the number of annexin+/PI+ cells (arrows) and the number of annexin-positive cells (stars); apocynin reduces the number of annexin+/PI+ cells to control levels, and Phen decreased the number of annexin+/PI+ cells in 25%. (f) Bar graph indicating that NE increases the number of annexin+/PI- cells. (g) Bar graph indicating that NE does not alter the number of annexin-/PI+ cells. * $p < 0.05$ vs. control, ** $p < 0.05$ vs. NE; $N \geq 4$ /group.

collaborators showed that NE increases ROS production in human peripheral blood mononuclear cells (PBMCs) via α_2 -adrenoceptors [3]. NE also induces ROS generation in

U937 macrophages via beta-adrenergic signaling as evidenced by the reversal of ROS production to basal levels when U937 cells were pretreated with propranolol [5]. Here,

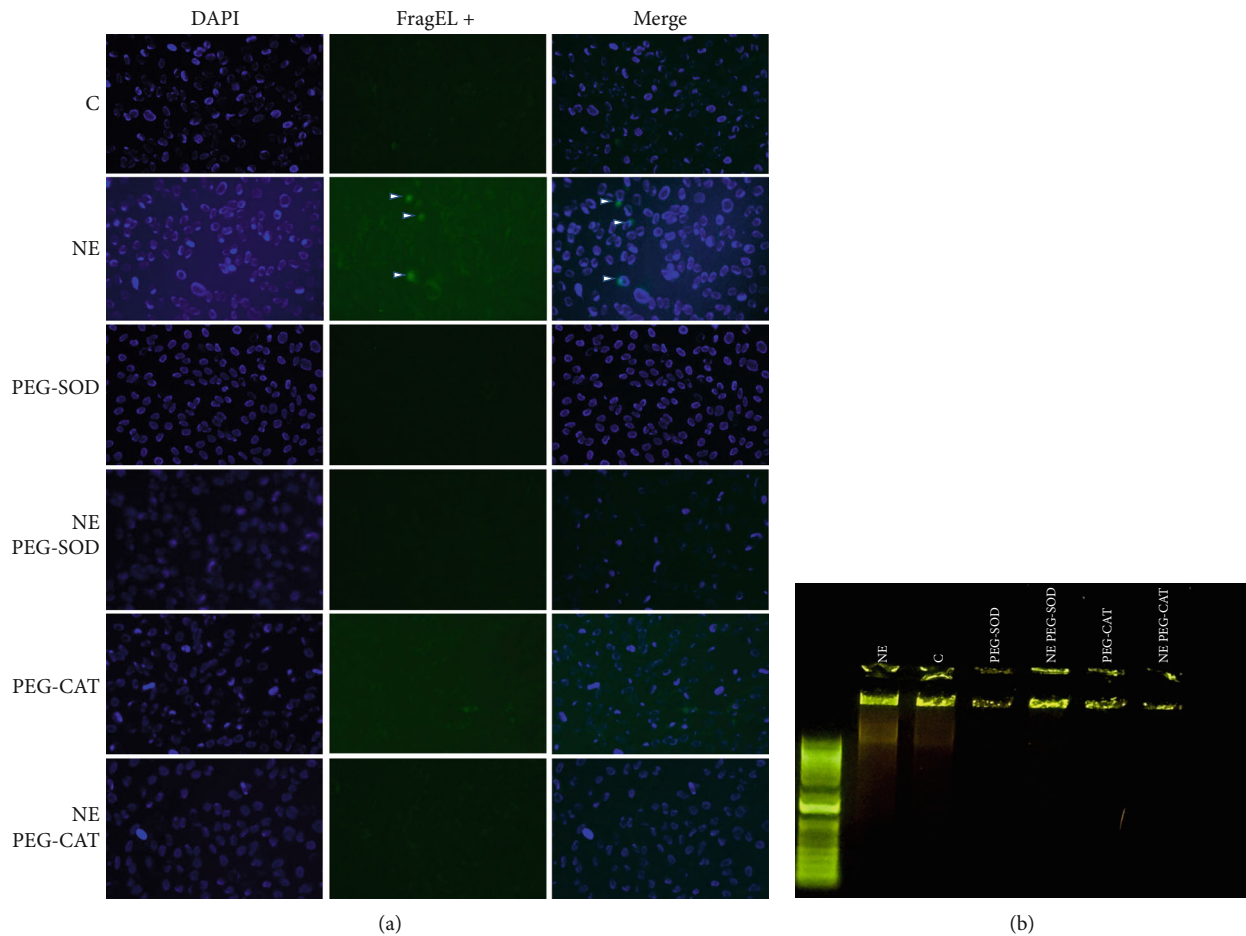


FIGURE 5: Superoxide anion and hydrogen peroxide are involved in NE-induced RLMEC death. RLMEC were stimulated with NE (5 ng/mL) for 24 h. Detection of apoptotic cells was performed using (a) FragEL kit (Millipore) and by (b) DNA fragmentation. NE induced the appearance of RLMEC in late apoptotic stages as evidenced by both the FragEL and DNA fragmentation assays. These effects were inhibited in the presence of PEG-SOD and PEG-CAT.

we show that, in RLMEC, NE induces Nox-dependent ROS production by activation of α_1 -adrenoceptors since phentolamine, a specific α_1 -adrenoceptor antagonist, abolishes NE-induced ROS production. Furthermore, incubation of RLMEC with propranolol, a nonspecific antagonist of β -adrenoceptors, did not inhibit NE-induced Nox activation. In addition, we found that incubation of RLMEC with either PEG-SOD or PEG-catalase partly inhibits NE-induced ROS production indicating NE can promote generation of both superoxide anion and hydrogen peroxide. Propranolol, a nonselective β -adrenoceptor antagonist, partly inhibited ROS production by NE but did not alter the increase in Nox activity induced by NE, suggesting that exposure to NE may result in increased ROS production by different pathways in RLMEC. Herein, we focused on investigating how Nox-driven ROS may contribute to cell death in RLMEC exposed to NE.

Nox is the main source of ROS in the vasculature. Interestingly, different Nox isoforms preferentially generate hydrogen peroxide over superoxide anion. Nox2 is the main isoform present in endothelial cells and it is known to constitutively generate superoxide anion in basal conditions. The fact that we detected increased production of both superox-

ide anion and hydrogen peroxide in cells treated with NE suggests that a different source of ROS, such as mitochondrial, may also participate in the deleterious effects of NE. Our findings show that apocynin, a ROS scavenger/antioxidant in vascular cells, decreases the number of annexin+/PI+ cells but does not change the number of annexin+/PI- cells. Moreover, incubation of RLMEC with either PEG-SOD or PEG-CAT inhibit the effects of NE on DNA fragmentation. These findings support the idea that NE may act via additional pathways that contribute to its toxic effects on endothelial cells. It is important to mention that the effects of apocynin in vascular cells is not directly related to Nox activity as vascular cells lack myeloperoxidase and are not able to dimerize apocynin [12]. Further studies are required to identify additional mechanisms of NE actions on endothelial cells. NE has been shown to increase ROS generation in cardiac endothelial cells, albeit at concentrations over 1000-fold higher than we used in this study [13]. Xiong and collaborators showed that NE augments ROS production in embryonic ventricular myocyte H9c2 cells via selective increase in Nox1 expression [4], but others found that NE-induced ROS production occurs by Nox2-dependent pathways in adult cardiac myocytes [14, 15]. In PBMCs, ROS production

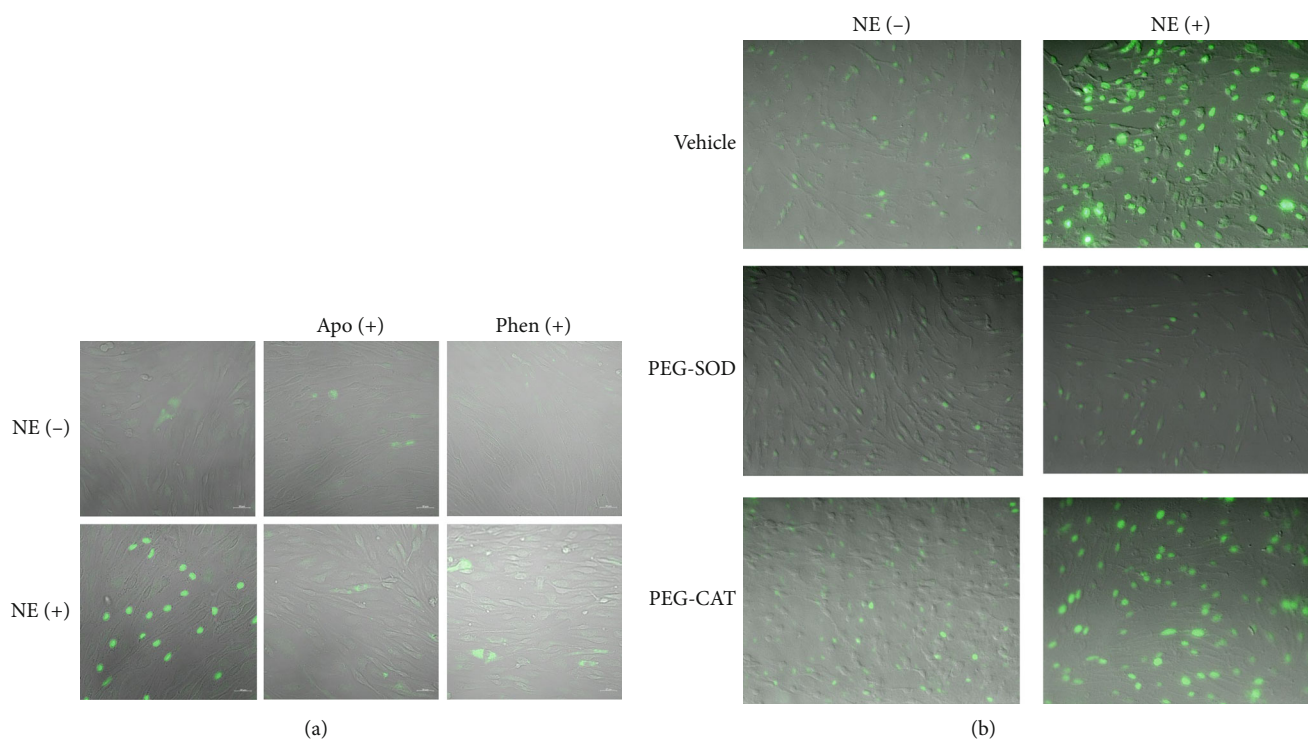


FIGURE 6: Norepinephrine activates caspase-3 via ROS production and α_1 -adrenoceptor-mediated pathways. To assess the role of reactive oxygen species and α_1 -adrenoceptors in norepinephrine- (NE-) induced caspase-3 activation, RLMEC were treated with apocynin (Apo), phentolamine (Phen), PEG-SOD, or PEG-CAT for 30 minutes before stimulation with NE (5 ng/mL) for 24 h. NE induces caspase-3 translocation to the nucleus, an effect inhibited by (a) Apo and Phen and (b) PEG-SOD. PEG-CAT did not inhibit caspase-3 activation by NE. $N = 3$ /group.

was associated with increased gp91phox, p22phox, and p67phox mRNA expressions. Collectively, these reports corroborate our findings that NE induces ROS production via Nox-dependent mechanisms. Notably, ours is the first report to highlight the effects of physiological concentrations of NE on ROS production and Nox activity.

The effects of ROS on the vasculature vary according to source and cell type. Herein, we show that NE-induced ROS results in caspase-3 activation and RLMEC death. Our data corroborate studies in the literature that report ROS activators of caspase-3-mediated apoptosis is triggered by different stimuli. Particularly in EC, ROS have been shown to mediate TNF-induced Nox4 caspase-3 activity and Bcl1 expression in HUVEC [16]. Tian and collaborators also reported a role for Nox4 in caspase-mediated endothelial cell death in inflammatory conditions [17]. Park and collaborators reported the specific role of superoxide anion in lysophosphatidylcholine-induced caspase-3 activation and apoptosis in HUVEC [18]. Likewise, Tawfik and colleagues reported that exogenous addition of hydrogen peroxide or hyperglycemia-stimulated ROS activates caspase3-induced cell death via JAK2-dependent pathways in aortic endothelial cells [19]. Our data indicate that NE induces production of both superoxide anion and hydrogen peroxide via Nox2- and Nox4-dependent mechanisms.

Fu and collaborators reported that micromolar concentrations of NE induce neonatal rat endothelial cell death by ROS-dependent activation of c-jun N-terminal

kinase (JNK) [13]. The same group also showed that this effect is mediated by caspases 2 and 3 via beta-adrenergic signaling, with no contribution of α -adrenoceptors [20, 21]. Taken together, these data support our findings of NE increasing ROS production by alpha- and beta-adrenoceptor signaling and corroborate our finding that in NE-induced caspase-3 activation. They have also reported that production of ROS by NE is a NADPH-independent mechanism. The fact that they have not found a role for alpha-adrenoceptor signaling in NE-induced apoptosis and described a different pathway for ROS formation can be potentially related to the adrenoceptor subtype in the studied cell type and or be a tissue-dependent phenomenon.

Herein, we showed that NE can result in RLMEC death by two different assessments, cell viability via trypan blue staining and cell death by annexin V and PI double positive staining. Annexin V is an early marker for apoptosis but may occur in late stages of different forms of cell death such as necrosis. In the same way, PI positive staining is usually a marker for necrosis but it may occur in the later stages of apoptosis. Further studies are necessary to clarify what type of cell death is predominant when endothelial cells are exposed to clinically found concentrations of NE.

5. Conclusion and Clinical Significance

The results presented here demonstrate a potential adverse effect of NE at concentrations expected in a clinical setting.

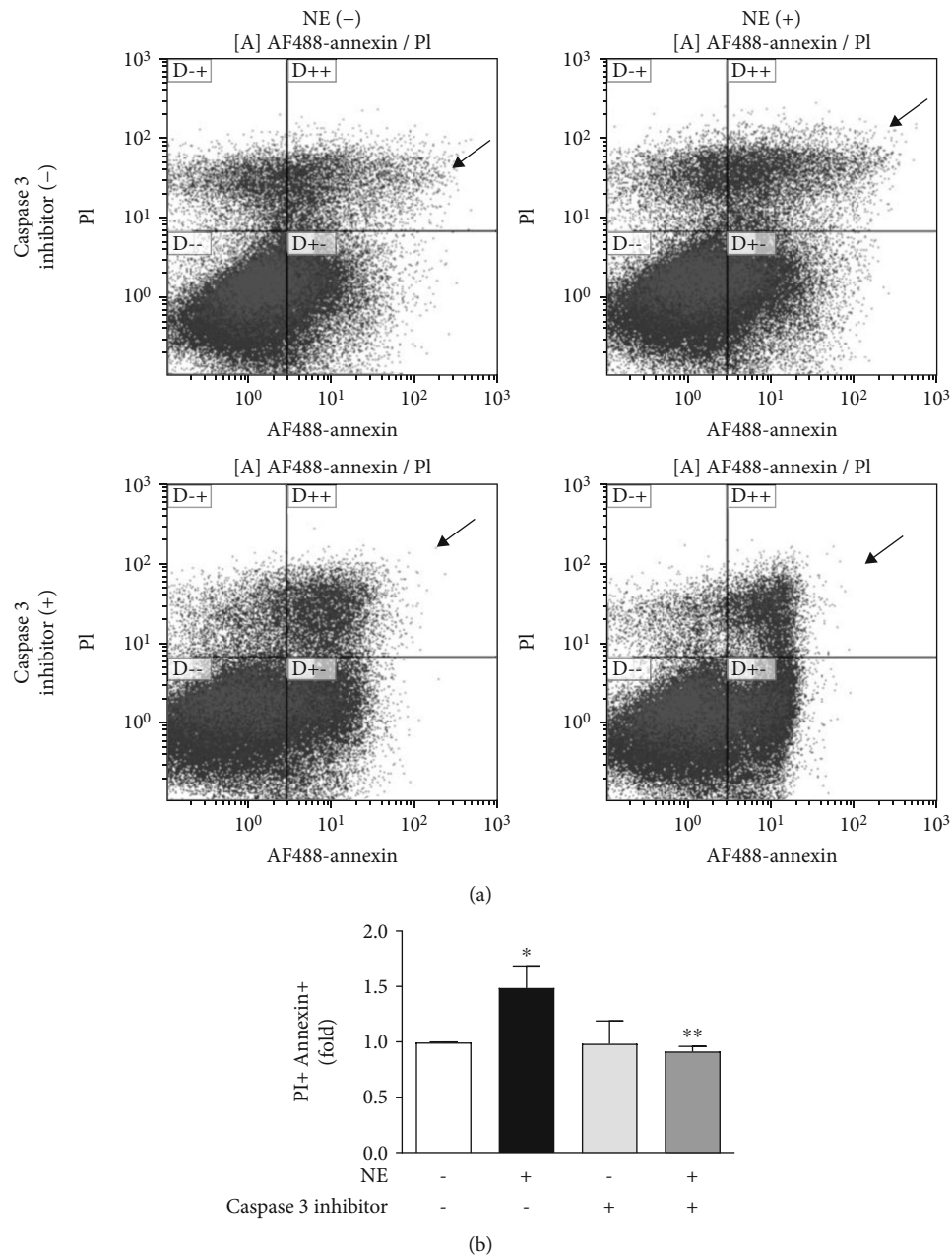


FIGURE 7: Norepinephrine induces cell death via caspase-3-dependent pathways. Rat lung microvascular endothelial cell (RLMEC) death was assessed by measurement of annexin and propidium iodide staining by flow cytometry after stimulation with norepinephrine (5 ng/mL). To assess the role of caspase-3 in NE-induced cell death, RLMEC were treated with caspase-3 inhibitor. (a) NE increases the number of annexin +/PI+ cells as indicates by arrows. (b) Bar graph corresponding to the quantification of annexin+/PI+ cells in cells treated and nontreated with NE, in the presence or absence of caspase-3 inhibitor. * $p < 0.05$ vs. control and ** $p < 0.05$ vs. NE; $N \geq 3$ /group.

These findings suggest that exposure of lung endothelial cells to supraphysiological doses of NE could be harmful to patients as it triggers lung endothelial cells death. Further studies are necessary to address the potential deleterious effects of NE in clinical settings.

Abbreviations

PEG-catalase: Catalase-polyethylene glycol
DHE: Dihydroethidium

NADPH: Dihyronicotinamide-adenine dinucleotide phosphate
RLMEC: Rat lung microvascular endothelial cells
Nox: NADPH oxidase
NE: Norepinephrine
PI: Propidium iodide
ROS: Reactive oxygen species
RIPA buffer: Radioimmunoprecipitation assay buffer
PEG-SOD: Superoxide dismutase-polyethylene glycol
TBS-T: Tris-buffered saline-Tween 20.

Data Availability

The data used to support the findings of this study are available from the corresponding author upon request

Conflicts of Interest

The authors have no conflicts of interest to declare.

Authors' Contributions

AZC contributed to the study conception and design, performed experiments, collected and interpreted data, and wrote the manuscript. RD contributed to the data interpretation and wrote the manuscript. GW contributed to the data interpretation and wrote the manuscript.

Acknowledgments

We thank the support of David E. Schwartz MD, Chairman of the Department of Anesthesiology at University of Illinois at Chicago and the support of Jerry McCoy MD, Chairman of the Department of Anesthesiology at University of Arizona for providing funds for the presented work.

References

- [1] V. Krishnamoorthy, D. B. Hiller, R. Ripper et al., "Epinephrine induces rapid deterioration in pulmonary oxygen exchange in intact, anesthetized rats: a flow and pulmonary capillary pressure-dependent phenomenon," *Anesthesiology*, vol. 117, no. 4, pp. 745–754, 2012.
- [2] A. Z. Chignalia, A. Isbatan, M. Patel et al., "Pressure-dependent NOS activation contributes to endothelial hyperpermeability in a model of acute heart failure," *Bioscience Reports*, vol. 38, no. 6, 2018.
- [3] S. H. Deo, N. T. Jenkins, J. Padilla, A. R. Parrish, and P. J. Fadel, "Norepinephrine increases NADPH oxidase-derived superoxide in human peripheral blood mononuclear cells via α -adrenergic receptors," *American Journal of Physiology Regulatory, Integrative and Comparative Physiology*, vol. 305, no. 10, pp. R1124–R1132, 2013.
- [4] F. Xiong, D. Xiao, and L. Zhang, "Norepinephrine causes epigenetic repression of PKC ϵ gene in rodent hearts by activating Nox1-dependent reactive oxygen species production," *The FASEB Journal*, vol. 26, no. 7, pp. 2753–2763, 2012.
- [5] M. Li, W. Yao, S. Li, and J. Xi, "Norepinephrine induces the expression of interleukin-6 via β -adrenoreceptor- NAD(P)H oxidase system -NF- κ B dependent signal pathway in U937 macrophages," *Biochemical and Biophysical Research Communications*, vol. 460, no. 4, pp. 1029–1034, 2015.
- [6] S. Naganathar, H. D. de'Ath, J. Wall, and K. Brohi, "Admission biomarkers of trauma-induced secondary cardiac injury predict adverse cardiac events and are associated with plasma catecholamine levels," *Journal of Trauma and Acute Care Surgery*, vol. 79, no. 1, pp. 71–77, 2015.
- [7] P. Moliner, C. Enjuanes, M. Tajés et al., "Association between norepinephrine levels and abnormal iron status in patients with chronic heart failure: is iron deficiency more than a comorbidity?," *Journal of the American Heart Association*, vol. 8, no. 4, article e010887, 2019.
- [8] S. R. Ostrowski, A. Sørensen, C. F. Larsen, and P. I. Johansson, "Thrombelastography and biomarker profiles in acute coagulopathy of trauma: a prospective study," *Scandinavian Journal of Trauma, Resuscitation and Emergency Medicine*, vol. 19, no. 1, p. 64, 2011.
- [9] D. C. Fernandes, J. Wosniak Jr., L. A. Pescatore et al., "Analysis of DHE-derived oxidation products by HPLC in the assessment of superoxide production and NADPH oxidase activity in vascular systems," *American Journal of Physiology-Cell Physiology*, vol. 292, no. 1, pp. C413–C422, 2007.
- [10] A. Z. Chignalia, M. A. Oliveira, V. Debbas et al., "Testosterone induces leucocyte migration by NADPH oxidase-driven ROS- and COX2-dependent mechanisms," *Clinical Science*, vol. 129, no. 1, pp. 39–48, 2015.
- [11] D. C. Fernandes, R. C. Goncalves, and F. R. Laurindo, "Measurement of superoxide production and NADPH oxidase activity by HPLC analysis of dihydroethidium oxidation," *Methods in Molecular Biology*, vol. 1527, pp. 233–249, 2017.
- [12] S. Heumüller, S. Wind, E. Barbosa-Sicard et al., "Apocynin is not an inhibitor of vascular NADPH oxidases but an antioxidant," *Hypertension*, vol. 51, no. 2, pp. 211–217, 2008.
- [13] Y. C. Fu, S. C. Yin, C. S. Chi, B. Hwang, and S. L. Hsu, "Norepinephrine induces apoptosis in neonatal rat endothelial cells via a ROS-dependent JNK activation pathway," *Apoptosis*, vol. 11, no. 11, pp. 2053–2063, 2006.
- [14] Y. Li, J. M. Arnold, M. Pampillo, A. V. Babwah, and T. Peng, "Taurine prevents cardiomyocyte death by inhibiting NADPH oxidase-mediated calpain activation," *Free Radical Biology and Medicine*, vol. 46, no. 1, pp. 51–61, 2009.
- [15] N. Saleem, A. Prasad, and S. K. Goswami, "Apocynin prevents isoproterenol-induced cardiac hypertrophy in rat," *Molecular and Cellular Biochemistry*, vol. 445, no. 1–2, pp. 79–88, 2018.
- [16] F. Xia, C. Wang, Y. Jin et al., "Luteolin protects HUVECs from TNF- α -induced oxidative stress and inflammation via its effects on the Nox4/ROS-NF- κ B and MAPK pathways," *Journal of Atherosclerosis and Thrombosis*, vol. 21, no. 8, pp. 768–783, 2014.
- [17] X. Y. Tian, L. H. Yung, W. T. Wong et al., "Bone morphogenic protein-4 induces endothelial cell apoptosis through oxidative stress-dependent p38MAPK and JNK pathway," *Journal of Molecular and Cellular Cardiology*, vol. 52, no. 1, pp. 237–244, 2012.
- [18] S. Park, J. A. Kim, S. Choi, and S. H. Suh, "Superoxide is a potential culprit of caspase-3 dependent endothelial cell death induced by lysophosphatidylcholine," *Journal of Physiology and Pharmacology*, vol. 61, no. 4, pp. 375–381, 2010.
- [19] A. Tawfik, L. Jin, A. K. L. Banes-Berceli et al., "Hyperglycemia and reactive oxygen species mediate apoptosis in aortic endothelial cells through Janus kinase 2," *Vascular Pharmacology*, vol. 43, no. 5, pp. 320–326, 2005.
- [20] Y. C. Fu, C. S. Chi, S. C. Yin, B. Hwang, Y. T. Chiu, and S. L. Hsu, "Norepinephrine induces apoptosis in neonatal rat endothelial cells via down-regulation of Bcl-2 and activation of β -adrenergic and caspase-2 pathways," *Cardiovascular Research*, vol. 61, no. 1, pp. 143–151, 2004.
- [21] Y. C. Fu, C. S. Chi, S. C. Yin, B. Hwang, Y. T. Chiu, and S. L. Hsu, "Norepinephrine induces apoptosis in neonatal rat cardiomyocytes through a reactive oxygen species-TNF α -caspase signaling pathway," *Cardiovascular Research*, vol. 62, no. 3, pp. 558–567, 2004.

Research Article

Resveratrol Prevents Right Ventricle Remodeling and Dysfunction in Monocrotaline-Induced Pulmonary Arterial Hypertension with a Limited Improvement in the Lung Vasculature

Eduardo Vázquez-Garza,¹ Judith Bernal-Ramírez,¹ Carlos Jerjes-Sánchez,^{1,2} Omar Lozano,^{1,2} Edgar Acuña-Morín,¹ Mariana Vanoye-Tamez,¹ Martín R. Ramos-González,¹ Héctor Chapoy-Villanueva,¹ Luis Pérez-Plata,¹ Luis Sánchez-Trujillo,^{1,3} Guillermo Torre-Amione,^{1,4} Alicia Ramírez-Rivera,⁵ and Gerardo García-Rivas^{1,2}

¹Tecnologico de Monterrey, Escuela de Medicina y Ciencias de la Salud, Ave. Morones Prieto 3000, 64710 Monterrey, N.L., Mexico

²Centro de Investigación Biomédica, Hospital Zambrano-Hellion, Tec Salud, Tecnológico de Monterrey, Batallón San Patricio 112 Col. Real de San Agustín, 66278 San Pedro Garza García, N.L., Mexico

³Unidad de Investigación Clínica en Medicina SC, 64718 Monterrey, N.L., Mexico

⁴Weill Cornell Medical College, Methodist DeBakey Heart & Vascular Center, The Methodist Hospital, Houston, 77030 TX, USA

⁵Unidad de Investigación Clínica en Medicina, 64718 Monterrey, N.L., Mexico

Correspondence should be addressed to Gerardo García-Rivas; gdejesus@itesm.mx

Received 21 September 2019; Revised 24 December 2019; Accepted 7 January 2020; Published 4 February 2020

Guest Editor: Bhagavatula Moorthy

Copyright © 2020 Eduardo Vázquez-Garza et al. This is an open access article distributed under the Creative Commons Attribution License, which permits unrestricted use, distribution, and reproduction in any medium, provided the original work is properly cited.

Pulmonary arterial hypertension (PAH) is a life-threatening disease that is characterized by an increase in pulmonary vascular pressure, leading to ventricular failure and high morbidity and mortality. Resveratrol, a phenolic compound and a sirtuin 1 pathway activator, has known dietary benefits and is used as a treatment for anti-inflammatory and cardiovascular diseases. Its therapeutic effects have been published in the scientific literature; however, its benefits in PAH are yet to be precisely elucidated. Using a murine model of PAH induced by monocrotaline, the macroscopic and microscopic effects of a daily oral dose of resveratrol in rats with PAH were evaluated by determining its impact on the lungs and the right and left ventricular function. While most literature has focused on smooth muscle cell mechanisms and lung pathology, our results highlight the relevance of therapy-mediated improvement of right ventricle and isolated cardiomyocyte physiology in both ventricles. Although significant differences in the pulmonary architecture were not identified either micro- or macroscopically, the effects of resveratrol on right ventricular function and remodeling were observed to be beneficial. The values for the volume, diameter, and contractility of the right ventricular cardiomyocytes returned to those of the control group, suggesting that resveratrol has a protective effect against ventricular dysfunction and pathological remodeling changes in PAH. The effect of resveratrol in the right ventricle delayed the progression of findings associated with right heart failure and had a limited positive effect on the architecture of the lungs. The use of resveratrol could be considered a future potential adjunct therapy, especially when the challenges to making a diagnosis and the current therapy limitations for PAH are taken into consideration.

1. Introduction

Pulmonary arterial hypertension (PAH) is a rare but progressive and often fatal pulmonary vascular disease [1]. PAH is characterized by a progressive increase in pulmonary vascular resistance and pulmonary arterial pressure, with secondary vascular and right ventricular (RV) remodeling, RV dysfunction, heart failure syndromes, and, finally, premature death [2]. Currently, approved therapies target three main pathways important in endothelial function: the prostacyclin and nitric oxide pathways, which are underexpressed, and the endothelin pathway, which is overexpressed in PAH patients [3]. PAH triggers a series of events on RV function, including activation of several signaling pathways that regulate cell growth, metabolism, extracellular matrix remodeling, and energy production [4, 5]. Right heart failure syndrome emerges in the setting of ischemia, alterations in substrate and mitochondrial energy metabolism, increased free oxygen radicals, increased cell loss, downregulation of adrenergic receptors, increased inflammation and fibrosis, and pathologic microRNA expression [4]. Current therapeutic schemes have not been able to regulate these mechanisms in the long term; therefore, there is a need for more successful strategies to manage right ventricular heart failure in the future [4].

Although the current treatment improves quality of life and survival [6, 7], a therapeutic approach to improve the RV function is lacking. Resveratrol (RES) is a phenolic compound with a known cardioprotective effect in several cardiovascular diseases [8]. However, its primary mechanisms of action have yet to be fully elucidated but include sirtuin modulation, reactive oxygen species (ROS) scavenging, and antioxidant mechanisms [9, 10]. The *in vitro* use of RES has been demonstrated to reduce oxidative stress and increase cell survival, inhibiting apoptosis and modulating the cell cycle in several cell lines [11]. RES has also been reported to have antifibrotic and anti-inflammatory effects *in vivo* [12]. This compound has been evaluated in some PAH animal models for its ability to decrease lung damage in the tissue or pulmonary trunk [13], but the molecular mechanism of cardioprotection afforded by RES remains only partially understood. Thus, in this study, the effect of RES in a PAH model on the lungs and ventricles was assessed in its ability to delay PAH progression. To achieve this, we performed an echocardiographic assessment to evaluate ventricular function, macroscopic and histologic changes, as well as contractile modifications, and biomarker expression in isolated cells. RES was demonstrated to be preferentially cardioprotective of the function and structure of the right ventricle, and it was shown to have a limited effect on the pulmonary vasculature.

2. Materials and Methods

2.1. Murine Model of Pulmonary Hypertension. All animal studies were approved by the Internal Committee for Care and Handling of Laboratory Animals of the School of Medicine of the Tecnológico de Monterrey (Protocol no. 2017-006) and were performed following the Mexican National Laboratory Animal Health Guidelines (NOM 062-ZOO

1999). Experiments were performed on adult male Sprague–Dawley rats (Bioinvert, MX), weighing >300 g. Pulmonary hypertension was induced by a single subcutaneous injection of monocrotaline (MC) (60 mg/kg body weight) diluted in dimethylsulfoxide (DMSO, Sigma-Aldrich, St. Louis, MO, USA). DMSO was used with the same volume for both groups of control rats and only RES rats. Animals were kept in a controlled temperature environment with a 12 h light cycle. Water and food were given *ad libitum*. To assess the effect of RES (Trans-isomer, RyTLabs), we divided the specimens into four groups: control rats (CTRL, $n = 12$), monocrotaline-treated rats (PAH, $n = 12$), rats treated with MC and RES (20 mg/kg per day, by gavage) (PAH+RES, $n = 11$), and only RES rats (20 mg/kg/day, by gavage) (RES, $n = 13$), from day 1 to day 42 after injection. All animals were observed for general appearance and respiratory symptomatology. Disease progression was characterized by anatomical postmortem data and echocardiography, which correlate strongly with the right heart catheterization measurements.

2.2. Echocardiographic Assessment of Cardiac Function. Noninvasive, transthoracic cardiac ultrasonography was performed 35 days after MC/DMSO injection, with a Philips EnVisor Ultrasound (Philips Healthcare, Andover, MA) equipped with a 12 MHz S-type transducer, under 1–3% sevoflurane anesthesia. After placing the animal on a thermal pad, with the chest shaved and using ultrasound transmission gel, standard views recommended by the American Society of Echocardiography were obtained. A parasternal short-axis view at the level of the great vessels was used to measure pulmonary artery flow, using pulse wave Doppler mode with a sample gate of 1.0 mm just proximal to the pulmonary valve. Here, we measured the pulmonary artery velocity time integral (VTI), pulmonary ejection time (ET), peak pulmonary flow velocity, and the pulmonary artery acceleration time (PAAT). A ratio between PAAT and ET was obtained, and the mean pulmonary artery pressure (mPAP) was estimated using the formula $mPAP = 58.7 - (1.21 \times PAAT)$. By combining pulmonary artery velocity-time integral, pulmonary artery area, and heart rate, echocardiographically derived cardiac output was determined, as previously published [14]. RV free wall thickness was measured at end-diastole from the parasternal long-axis view using M-mode. The apical four-chamber view was employed to measure the end-diastolic RV diameter and M-mode-derived tricuspid annular plane systolic excursion (TAPSE). Left ventricle (LV) diameters and fractional shortening ($FS = \text{diastolic LVID} - \text{systolic LVID} / \text{diastolic LVID} \times 100$ [LVID (LV internal diameter)]) were measured with M-mode from the short-axis view at the level of the papillary muscles. Subsequently, the echocardiographic RV/LV end-diastolic diameter ratio was calculated and used as an assessment of RV enlargement.

2.3. Histological Preparations. After 42 days of RES treatment, the specimens were euthanized. Hearts were quickly excised from the rats after being anesthetized with inhaled 5% sevoflurane and sodium heparin (1000 U/kg). The heart and lungs were dissected and weighed. The RV and LV were

identified and isolated for different preparations. The sections for histological findings were fixed in 4% (wt/vol) paraformaldehyde in PBS for at least 2 hours at room temperature, transferred to 70% ethanol, embedded in paraffin, and processed for hematoxylin/eosin (H&E) and Masson's trichrome staining. Fibrotic index assessment was performed following previously published data [15]; in brief, microphotographs were acquired using an Imager Z1 Zeiss microscope with an AxioCam HRm and microphotograph processing with the AxioVision software. To assess fibrosis, we used a semiquantitative approach; after staining with Masson's trichrome, we take microphotographs of the whole slide at 2.5x, and the image is then decomposed in at least seven fields at 5x. After the photos were taken, we quantified the number of blue and red pixels, and the results were recorded to make a ratio of blue%/red% using ImageJ software. Data correspond to the analysis of 2 blinded analysts and three different fields. Cardiomyocyte area was assessed using H&E slides. Microphotography of the papillary muscles was taken at 10x; only cells with a complete visible cytoplasm and central nuclei were considered. At least ten cells per photography were counted at two different levels. All slides were analyzed using an object carrier with a capacity for 7 slides, for their respective batches.

Regarding lung sections, the primary lung architecture was assessed for each group using the H&E-stained slides. Predominant findings included inflammatory infiltration and proliferation of the smooth muscular medial layer of the lung arterioles. We quantified the amount of these arterioles in seven random fields; vessels of an average 100 μm were selected to analyze diameter, luminal area, and occlusion. Occlusion was assessed by at least seven measurements of the medial layer thickness for the average.

2.4. Cardiomyocyte Isolation. Ventricular myocytes were isolated following previously described methods [16]. The hearts were excised and mounted on a Langendorff apparatus and perfused with Tyrode medium (TM), in mM: 128 NaCl, 0.4 NaH_2PO_4 , 6 glucose, 5.4 KCl, 0.5 $\text{MgCl}_2 \cdot 6\text{H}_2\text{O}$, 5 creatinine, 5 taurine, and 25 HEPES, pH 7.4 at 37°C, for 5 min and digested by 0.1% collagenase type II (Worthington Biochemical, Lakewood, NJ) dissolved in TM. Afterwards, the RV and LV were dissected, and their cells mechanically disaggregated. Cardiomyocytes were rinsed with TM plus 0.1% albumin solution at increasing Ca^{2+} concentrations (0.25, 0.5, and 1 mM). Only rod-shaped cells were used in the studies. All the confocal measurements were acquired using a Leica TCS SP5 confocal microscope equipped with a D-apochromatic 63x, 1.2 NA, oil objective (Leica Microsystems, Wetzlar, Germany). To assess cell volume, freshly isolated cardiomyocytes were incubated in TM with 5 μM calcein-AM (Life Technologies, Carlsbad, CA, USA) at room temperature (RT) for 30 min as previously described [17]. Then, cells were washed with a fluorophore-free and calcium-free solution and images were taken at 400 Hz, obtaining a stack of 2D images of 1 μm section thickness every 1 μm in the z -axis, covering the whole cell depth. A 488 nm wavelength was used to excite the fluorophore, and its emission was collected at 500-600 nm. Cell volume was evaluated as previ-

ously described [18]. Freshly isolated cardiomyocytes were incubated in TM (1 mM Ca^{2+}) with 10 μM Fluo-4 AM (Life Technologies, Carlsbad, CA, USA) for 45 min at RT. Afterwards, the cells were washed with a fluorophore-free solution, plated on laminin-covered glass coverslips and mounted in a superfusion chamber. Excitation and emission wavelengths were 488 nm and 500-600 nm, respectively. Cell shortening was evaluated under field stimulation (MYP100 MyoPacer Field Stimulator; IonOptix, Milton, MA). The cells were evaluated under field stimulation at 0.5, 1, and 2 Hz, and line-scan images were recorded along the longitudinal axis of the cell at 400 Hz with a one μm section thickness. Fluorescence data were normalized as $\Delta F/F_0$, where F is fluorescence intensity; all confocal microscopy images were analyzed using ImageJ.

2.5. Western Blotting. Total heart protein from right ventricles (30 μg) was resolved on SDS-PAGE gel 15% and transferred onto a PVDF membrane at 300 mA for 2 hours and incubated with anti-Acetylated-Lysine protein antibody (9441S, Cell Signaling) (1:2000). The membrane was washed three times for 10 min with PBS-0.5% Tween 20 and subsequently probed with an HRP-conjugated secondary antibody anti-rabbit IgG 1:5000 (sc-2004, Santa Cruz) for 2 hours at room temperature. After washing three times for 10 min, the blots were developed with SuperSignal West Dura Extended Duration Substrate (Thermo Fisher Scientific, USA) and quantified by using a BioSpectrum 415 Image Acquisition System (UVP, Upland, CA, USA). Anti-GAPDH antibody (1:2000) (ab9484, Abcam) was used as a loading control.

2.6. Real-Time Polymerase Chain Reaction (PCR) Analysis

2.6.1. RNA Isolation, Reverse Transcription, and Quantitative PCR (qPCR). The total RNA from the tissue of the right ventricles was isolated using a TRIzol Reagent (15596026, Invitrogen). The purity of all samples was confirmed measuring their 260/280 nm absorbance ratio using a Take3 multivolume plate in a Synergy HT microplate reader (BioTek Instruments). The cDNA was reverse-transcribed from 1 μg of total RNA using the SensiFAST cDNA Synthesis Kit (BIO-65053, Biorline). The qPCR reaction was performed using the SensiFAST SYBR Lo-ROX Kit (BIO-94020, Biorline) in a QuantStudio 3 RT PCR System (Thermo Fisher Scientific) and the data analyzed by the $2^{-\Delta\Delta\text{Ct}}$ method to estimate each gene's mRNA expression. The primers were synthesized by T4 Oligo (Mexico). All primer sequences for BNP, collagen 1, IL-1 β , IL-10, troponin C, Sirt1, and HPRT as housekeeping genes are detailed in Supplementary Table 1.

2.6.2. Reagents. All chemical reagents were purchased from Sigma-Aldrich (St. Louis, MO, USA) unless otherwise stated.

2.7. Statistical Analysis. Statistical data are presented as the mean \pm SEM. Comparisons between means were made by unpaired Student's t -test or one-way ANOVA followed by Dunnett's, Tukey's, or Bonferroni's post hoc tests when appropriate to compare experimental groups. Differences were considered significant when $p < 0.05$. Data processing,

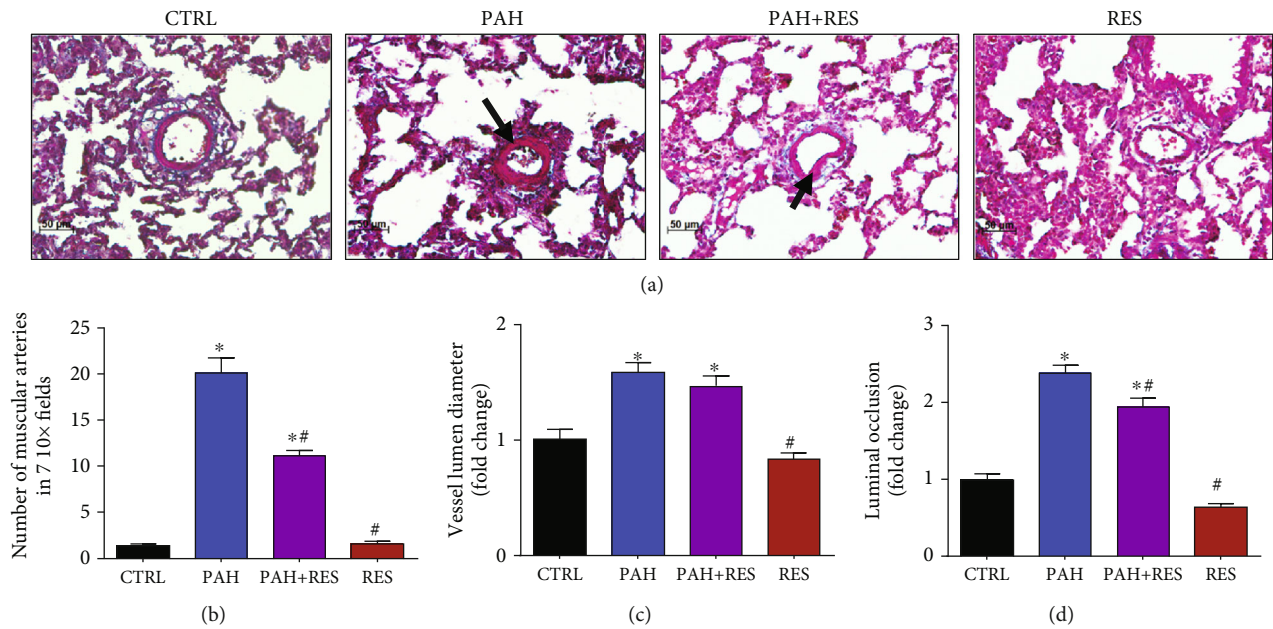


FIGURE 1: There is a limited effect of RES exerted in the lung vessel histopathology structure. (a) Representative microphotographs of pulmonary blood vessels. PAH induced hypertrophy and proliferation of the tunica media; this effect is decreased by RES. 20x magnification; H&E staining. Arrows indicate the muscularized vessel wall. (b) Amount of muscular arteries in 7 random fields in lung tissue. (c) Diameter of pulmonary blood vessels. (d) Luminal occlusion by the media layer in lung arteries. The values are given as the mean and fold change \pm SEM; * $p < 0.05$ vs. control; # $p < 0.05$ vs. PAH; $n = 15$ for CTRL, PAH, and PAH+RES; $n = 11$ for RES.

graphs, and statistical analysis were performed with GraphPad Prism (V.5.01; La Jolla, CA, USA).

3. Results

3.1. Resveratrol Had a Limited Effect on the Development of a Monocrotaline-Induced PAH Changes in the Vascular Architecture of the Lungs and the Echocardiographic Pulmonary Artery Values. The study duration for this PAH model was 42 days as this was an adequate amount of time for phenotypic changes (i.e., cyanosis in the extremities and weight loss) to take place. An increase in the weight of the heart and lungs was identified as a specific macroscopic change. Compared to the untreated control group (CTRL) (1.4 ± 0.2 g), heart weight increased by 21% in the PAH group (1.7 ± 0.2 g) and 35% with 1.7 ± 0.3 g for the PAH+RES group. Lungs weight followed the same trend: a weight increase of 2.0 ± 0.3 g was reported for the CTRL group, 45% increase was observed for the PAH group (2.9 ± 0.3 g), and a 60% increase was seen for the PAH+RES group (3.2 ± 0.4 g). Normalized organ weight and the weight of each specimen showed the same trend (data not shown). There were no statistically significant changes in these values between the PAH+RES and PAH groups and no differences between the CTRL group and the group treated only with RES. To exclude other cardiovascular pathologies, systemic, systolic, and diastolic blood pressure and heart rate values were evaluated. No differences were observed between the groups (data not shown). The pathognomonic findings for lung vasculature in the PAH model included an increase in the muscularized arteries, an increase in the lumen diameter,

and a concomitant decrease in luminal occlusion in the media layer. The changes were due to the proliferation of the smooth muscle cells and a slight increase in vessel diameter. Representative microphotographs can be seen in Figure 1(a). RES was unable to avoid the transformation of healthy vessels into muscularized arteries; however, it diminished the amount of them (i.e., an 11.2-fold increase in the PAH+RES group and a 20-fold increase in the PAH group, representing a 56% decrease mediated by RES between these two groups), when compared with its effect on the CTRL group (Figure 1(b)). There was a reduced effect of RES on the vascular lumen diameter (Figure 1(c)). Although there was a noticeable increase of the PAH group compared to the CTRL group, this value was not significantly decreased by RES, having $57.2 \pm 2.3 \mu\text{m}$ (a 1.59-fold increase in the PAH group and a 1.47-fold increase in the PAH+RES group). This represented a 4% decrease in terms of the effect of RES on the PAH phenotype (i.e., $73.5 \pm 2.4 \mu\text{m}$ vs. $70.7 \pm 2.6 \mu\text{m}$). Luminal occlusion followed a similar trend, with at least a 2.3-fold increase in the PAH group and a 1.9-fold increase in the PAH+RES group compared to CTRL; this represented a 13% decrease in occlusion due to the effect of RES when the PAH+RES and PAH groups were compared (i.e., $30.5 \pm 0.9\%$ vs. $26.6 \pm 0.9\%$, respectively) (Figure 1(d)). The rodents treated only with RES showed no differences compared to the CTRL for all the variables.

These data correlate with the echocardiographic values pertaining to the pulmonary artery. Compared with the CTRL group, the PAAT decreased significantly in the PAH and PAH+RES groups (i.e., by 40% and 43%, respectively). The PAAT/ET ratio was seen to reduce in correlation with

TABLE 1: Echocardiographic measurements of right ventricle outflow tract flow profiles.

	CTRL (<i>n</i> = 15)	PAH (<i>n</i> = 13)	PAH+RES (<i>n</i> = 13)	RES (<i>n</i> = 13)
Heart rate (bpm)	315 ± 10	328 ± 18	328 ± 7	318 ± 6.4
Pulmonary artery acceleration time (ms)	35 ± 2.2	21 ± 1.8**	20 ± 1.3*	31 ± 2.1 [#]
Ejection time (ms)	98.2 ± 5.1	82.9 ± 4.6	80.6 ± 4.6	87.5 ± 5.8
PAAT/ET ratio	0.35 ± 0.02	0.25 ± 0.02*	0.26 ± 0.02	0.35 ± 0.01 [#]
Peak gradient (mmHg)	3.1 ± 0.3	3.2 ± 0.2	3.4 ± 0.4	3.5 ± 0.2
Estimated mPAP (mmHg)	21 ± 2	36 ± 2.2*	30 ± 1.1*	21 ± 1.7 [#]

PAAT: pulmonary artery acceleration time; ET: ejection time. All data are presented as the mean ± SEM. **p* < 0.05 vs. CTRL; [#]*p* < 0.05 vs. PAH.

TABLE 2: Echocardiographic measurements of right ventricle function.

	CTRL (<i>n</i> = 15)	PAH (<i>n</i> = 13)	PAH+RES (<i>n</i> = 13)	RES (<i>n</i> = 13)
Right ventricle outflow tract (mm)	2.9 ± 0.09	3.6 ± 0.2*	3.3 ± 0.08*	3.4 ± 0.08*
Right ventricle output (L/min)	0.19 ± 0.02	0.16 ± 0.02	0.18 ± 0.01	0.24 ± 0.02
TAPSE (mm)	1.9 ± 0.1	1.3 ± 0.1*	1.9 ± 0.1 [#]	2.4 ± 0.1* [#]
RV wall thickness (mm)	1 ± 0.08	1.6 ± 0.12*	1.2 ± 0.11 [#]	1.1 ± 0.09 [#]
RV diastolic diameter (mm)	3.4 ± 0.1	4.7 ± 0.2*	3.5 ± 0.2 [#]	3.6 ± 0.2 [#]
RV systolic diameter (mm)	2.5 ± 0.2	3.1 ± 0.3	2.8 ± 0.3	2.5 ± 0.1
LV posterior wall thickness (mm)	1.7 ± 0.08	1.8 ± 0.1	1.7 ± 0.09	1.6 ± 0.1
LV diastolic diameter (mm)	5.8 ± 0.4	4.6 ± 0.1	5.5 ± 0.3	6.7 ± 0.3 [#]
LV systolic diameter (mm)	4 ± 0.6	2.7 ± 0.2	3 ± 0.2	3 ± 0.1
RV/LV diastolic diameter	0.57 ± 0.07	1.04 ± 0.06*	0.65 ± 0.05 [#]	0.53 ± 0.02 [#]

TAPSE: tricuspid annular plane systolic excursion; RV: right ventricle; LV: left ventricle. All data are presented as the mean ± SEM. **p* < 0.05 vs. CTRL; [#]*p* < 0.05 vs. PAH.

an increase in pulmonary vascular resistance in both groups, but the change was increased higher in the PAH group than in the PAH+RES group (29% and 25%, respectively). The mPAP markedly increased in the PAH and PAH+RES groups (71% and 43%, respectively) compared to the CTRL group. The mPAP for both groups was estimated to be higher than 20 mmHg, but this change was without statistical significance (Table 1).

3.2. Resveratrol Treatment Improves Right Ventricular Remodeling and Function. The values found using TAPSE, a surrogate measurement of right ventricular performance, worsened significantly by 31% in the PAH group compared to the CTRL group. In contrast with PA hemodynamics, this value improved considerably by 46% in the PAH+RES group, compared to PAH. RV free wall thickness increased markedly by 60% in the PAH group compared with the CTRL group. However, in the treated PAH+RES group, RV free wall thickness decreased significantly by 25% compared with the PAH group. The end-diastolic diameter of the RV and the ratio of the end-diastolic diameter for the RV/LV increased significantly in the PAH group compared to the CTRL group. A significant difference was not observed for both parameters in the PAH+RES group compared to the CTRL group (Table 2). The effect of RES, at the microscopic level, on the tissues and isolated cells is depicted in Figure 2(a). To assess tissue remodel-

ing, the ventricular wall sections were stained with Masson's trichrome. A multiple-fold increase in fibrosis was observed in the RV in PAH. RES treatment kept the fibrosis at CTRL levels in the PAH+RES phenotype, while the effect of RES treatment alone was the same as that of the CTRL group. The LV in all groups remained unchanged (Figure 2(d)).

3.3. Resveratrol Restored Right Ventricular Cardiomyocyte Structure and Contractile Function in Rodents with Pulmonary Arterial Hypertension. The cardiomyocyte area was analyzed using H&E-stained slides at the level of the papillary muscles. The PAH group had this parameter with at least a two-fold increase ($600 \pm 23 \mu\text{m}^2$) compared to the CTRL group ($290 \pm 11 \mu\text{m}^2$). The cardiomyocyte area decreased by 17% in the PAH+RES group ($498 \pm 17.8 \mu\text{m}^2$) compared to the PAH group (Figure 2(b)). In contrast, a difference between any of the groups was not observed in the LV myocyte area (Figure 2(d)). The cellular volume of the isolated RV cardiomyocytes in rodents with PAH assessed using confocal microscopy reflected a 1.7-fold increase compared to the CTRL group (34.8 ± 1.9 vs. 23.6 ± 1.1 fL, respectively). The PAH+RES group was seen to have a 13% decrease in volume compared to the PAH phenotype (26.8 ± 1.7 fL), and there was no statistical difference with the CTRL group (Figure 2(c)). There were no differences observed between the LV groups (Figure 2(d)). These changes could indicate

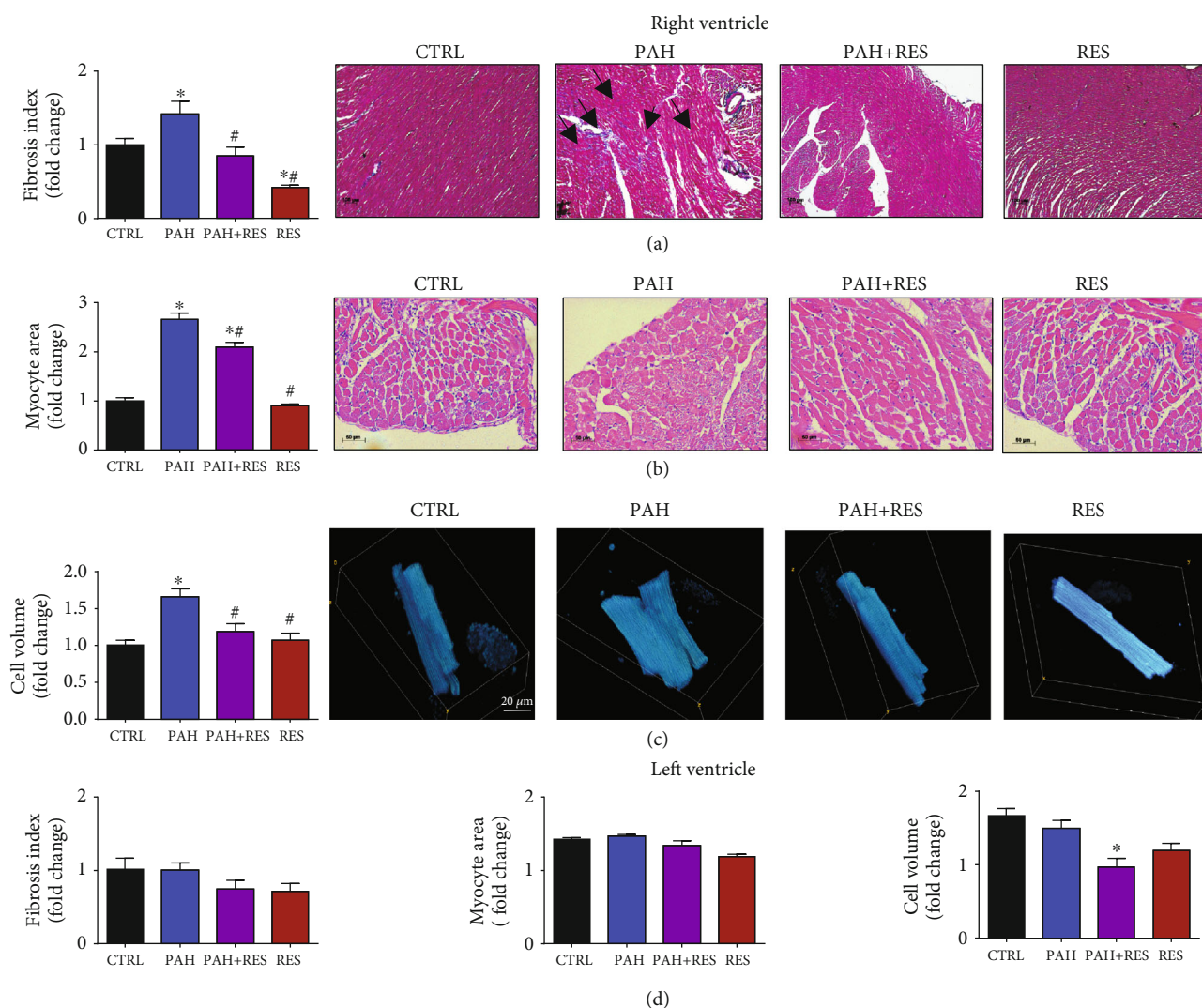


FIGURE 2: RES reduces the fibrotic index and myocyte hypertrophy in RV of PAH-treated specimens. (a) Fibrotic index. Representative right ventricles stained with Masson's trichrome of all treated groups (5x). Black arrows indicate the zones of fibrotic tissue. (b) Myocyte area. Representative cross-section cardiomyocytes from groups (H&E, 10x). (c) Cell volume analysis. Representative right ventricle cardiomyocytes stained with calcein and analyzed by confocal microscopy. (d) Unchanged LV morphological features in the PAH model and the lack of effect of RES on these features. Fibrotic index, myocyte area, and isolated cell volume. All data have been normalized to RV CTRL mean values. The values are given as the mean and fold change \pm SEM ($n = 15$ for CTRL, PAH, and PAH+RES; $n = 11$ for RES). The values are given as the mean and fold change \pm SEM; * $p < 0.05$ vs. CTRL; # $p < 0.05$ vs. PAH.

the prevention or delay of tissue remodeling exerted by RES. Taken together, these data prompted the analysis of functional cell shortening in the isolated cells. The effect of increased stimulation frequency on cell contractility in the RV and LV cells was evaluated. The cells were paced at 0.5, 1.0, and 2.0 Hz. The RV CTRL cells had respective values of $5.1 \pm 2.4\%$, $4.6 \pm 2.4\%$, and $4.1 \pm 1.7\%$. There were no changes in the RES-only group compared to the CTRL group (data not shown). In our animal model, the PAH group exhibited a contractility decrease of 8% at 0.5 Hz, 18% at 1.0 Hz, and 39% at 2.0 Hz compared to the CTRL group. Cell shortening in all paces was demonstrated to be significantly improved in the PAH+RES group compared to the other groups. Compared to PAH in this regard, there was a respective increase of 59% for 0.5 Hz, 71% for 1.0 Hz, and 148% for 2.0 Hz in the PAH+RES phenotype

(Figure 3(a)). A statistically significant difference was not seen regarding the effect of PAH or RES on the LV cells (Figure 3(b)).

3.4. Inflammatory and Remodeling Effect of RES in RV Tissue from Specimens with PAH. We performed qPCR from RV tissue to analyze the remodeling and inflammatory markers. We selected BNP, troponin C1 (Tnnc1), and collagen 1 to analyze the hypertrophy mediated by MC. For the inflammatory markers, we chose pro-inflammatory IL-1 β and anti-inflammatory IL-10. There was a significant RES-mediated decrease in the PAH+RES group of the following mRNAs compared to PAH phenotype: BNP (6.7 ± 1.02 vs. 15.7 ± 1.5), Tnnc1 (0.7 ± 0.5 vs. 5.5 ± 2.7), collagen 1 (1.7 ± 0.7 vs. 2.7 ± 0.5), IL-1 β (3.2 ± 0.7 vs. 4.6 ± 1.7), and an increase in IL-10 (8.7 ± 1.5 vs. 3.5 ± 1.6) (Figures 4(a)–4(e)).

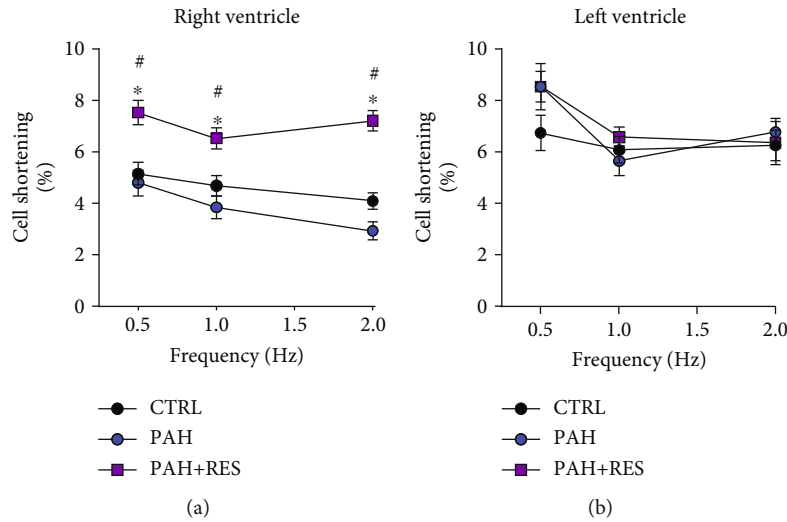


FIGURE 3: RES improves cardiomyocyte shortening isolated from RV, and had with on LV isolated cardiomyocytes. Percentage of cell shortening after 1 Hz stimulation in isolated cardiomyocyte from the (a) right ventricle and (b) left ventricle. The values are given as the mean \pm SEM (* p < 0.05 vs. control, # p < 0.05 vs. PAH; n = 26-44 cells from 2 animals for CTRL, n = 15-26 cells from 2-3 animals for PAH, and n = 19-61 cells from 2-4 animals for PAH+RES).

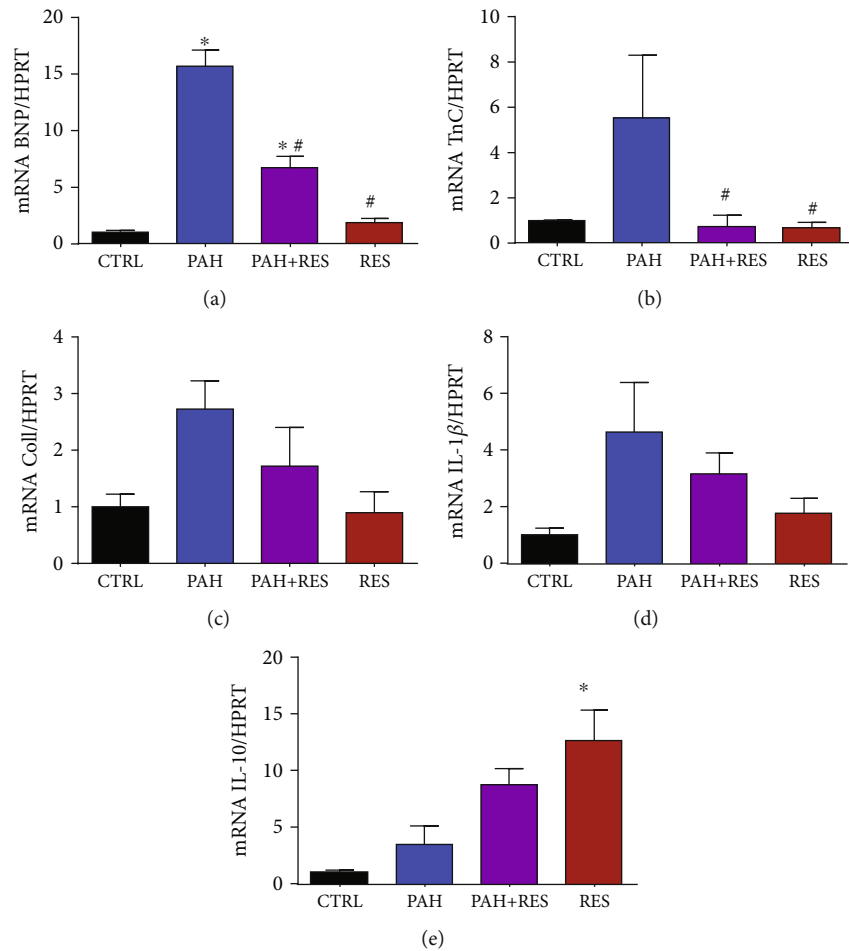


FIGURE 4: RES modulates the decrease of tissue remodeling and inflammatory mRNA on the RV of PAH-treated specimens. qPCR analysis of RV from the tissue samples show (a) BNP, (b) troponin C, (c) collagen type 1, (d) IL-1 β , and (e) IL-10. All data have been normalized to RV CTRL mean values. The values are given as the mean and fold change \pm SEM (n = 4 for CTRL, n = 3 for PAH and PAH+RES, and n = 6 for RES). The values are given as the mean and fold change \pm SEM; * p < 0.05 vs. control; # p < 0.05 vs. PAH.

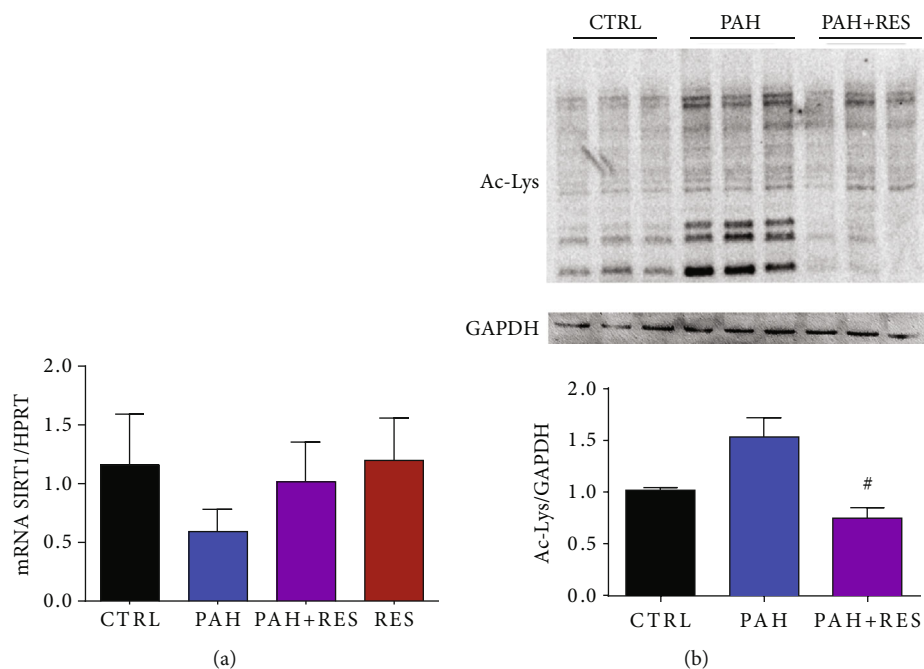


FIGURE 5: There is a decrease in the mediated SIRT1 deacetylation. (a) qPCR analysis of SIRT1 mRNA expression on heart tissue. (b) Representative western blot membrane of Ac lysine of heart tissue proteins and below the acetylation profile in heart tissue in fold change. For (a), $n = 4$ for all groups; for (a), $n = 3$ for all groups. The values are given as the mean and fold change \pm SEM; * $p < 0.05$ vs. control; # $p < 0.05$ vs PAH.

3.5. There Is a RES-Mediated Increase in SIRT1 in Treated PAH RV. We found an expected downregulation of SIRT1 mRNA in the RV of PAH phenotypic rats compared to CTRL. This decrease (0.5 ± 0.2) was abrogated by the treatment of RES in these specimens (0.8 ± 0.3) (Figure 5(a)). To evaluate the effect of the decrease in SIRT1 expression, we performed a western blot of the acetylation profile. Treatment of PAH with RES prevented the increased acetylation of the RV, remaining at the level of the CTRL group (Figure 5(b)).

4. Discussion and Conclusion

The use of animal models, like the MC-induced PAH in rats has been an alternative to characterize and explore the pathophysiology and therapeutics against PAH [19]. The majority of the literature has focused on relevant topics such as pulmonary changes in the smooth muscle of the vessels and the incidence of fibrosis [13, 20, 21]. However, it is important to highlight the lack of protocols focused on improving RV function, a critical parameter for outcome and survival [22]. An example of the clinical relevance of improving the ventricular function comes from the reversible effects after treating chronic thromboembolic pulmonary hypertension (CT-PH), where careful removal of the thrombus reverses the compromised ventricular function and its remodeling. Therefore, there is a need to continue the development of coadjuvant treatments for RHF and improve their mechanisms of delivery [10, 22, 23].

A decision was made to address these issues by studying the underlying mechanisms associated with RES treatment on the cardiovascular and pulmonary system in a valid model

of PAH. The use of RES as an adjuvant in a therapeutic setting owing to its multiple effects as a ROS scavenger, mitochondrial agent, and cell cycle modulator is ongoing and constitutes promising research [10]. Varying doses of RES [14, 24, 25] and administration routes [25–27] have been used for numerous therapeutic purposes and diseases. Several RES doses for PAH models have been described in the literature, and variable results have been reported [28]. The cause of this variation relates to the MC dosage, the initial weight of the specimen, and the duration of the study.

For the model in this study, RES at a dose of 20 mg/kg/day by gavage was used, a dose that has been used elsewhere [29]. According to the findings of the current study, heart and lung weight increased in both the PAH and PAH+RES groups. The effect of RES was not significant, and this phenomenon has been reported in other research [13] and may be associated with several factors. An explanation for this is that a higher RES dosage is required for a macroscopic impact.

Consistent and pathognomonic results were found for the vascular bed of the lungs for all groups treated with the PAH phenotype [30, 31]. RES had a minimal effect in reversing them, other authors found that RES had a limited anti-remodeling effect on the lungs, and this effect was limited to the medial layer of the pulmonary trunk and did not impact the heart wall structure [13]. In the current study, RES had a partial effect on lung histopathology in the PAH+RES-treated group. Using a higher dose and improving the administration route (i.e., using nebulization therapy) could be an effective way of improving these results.

The finding in the current study that RES had a limited effect on the lungs correlates with ultrasonographic evidence of PA. Echocardiography was chosen as it is a noninvasive

tool that can be used to assess RV function. The current study demonstrated that it was a feasible technique that could be used in rats for a PAH evaluation, and this has also been demonstrated by other groups [32]. The PAAT and PAA-T/ET ratio are PA hemodynamic parameters that are highly susceptible to changes in pulmonary vascular resistance and impedance [33], and it shortens in correlation with an increase in systolic PAP and mPAP [34]. Although RES prevented the development of specific pathognomonic PAH characteristics, it was insufficient to elicit a significant change in surrogate markers of increased mPAP. Chronic RV pressure overload has been shown to lead to a gradual change in RV phenotype, which ultimately resulted in RV-arterial uncoupling and subsequent functional deterioration [35]. A significantly low value of mPAP was found in the PAH group in the current research, and more importantly, an improvement of this parameter was reported for the PAH+RES group, suggesting that treatment with RES prevented systolic failure, commonly observed in the advanced stages of PAH. Interestingly, this value was even higher in the RES-only treatment group, which could indicate that this polyphenol not only prevents failure but is also a potential enhancer of RV function [35]. RV free wall thickness, an objective reflection of RV hypertrophy and remodeling [34], was markedly increased in rodents with PAH, which is consistent with remodeling secondary to pressure overload. Most importantly, and in contrast with the findings of the PAH group, RES treatment attenuated RV hypertrophy induced by high mPAP, and a significant difference with the CTRL group was not observed. This can be secondary to fewer fibrotic changes, which is consistent with previous *in vitro* research on the impact of RES on cardiac fibrosis [36]. An increase in the RV end-diastolic diameter was observed in the PAH model, and this increase was significant when compared to the untreated controls, reaching a ratio of ≥ 1 , which is associated with an increased risk of adverse clinical events, while being a marker for poor prognosis [37]. Dilation and the increased ratio were not present in the PAH+RES group. Therefore, even with the increased mPAP identified in the PAH+RES group, the RV was able to endure it and prevent pathologic remodeling. A further study in this direction is to investigate the effect of RES on cardiac strain because it is possible that enhancement of these variables by RES could explain the increased capacity of RV to manage elevated pulmonary pressure. The LV echocardiography findings did not show any change associated with increased mPAP with RES treatment. Even though its diameter can decrease as a consequence of RV dilatation or the presence of pericardial effusion, this effect in the PAH groups was not seen upon analysis. One explanation for the absence of these findings and for negative ventricular interaction is that the model did not allow the development of PAH that was severe enough to cause pericardial effusion or result in higher values of mPAP. More research with a focus on echocardiographic changes is warranted to clarify the changes elicited by MC PAH in LV and LHF.

Signs of increased tissue remodeling consistent with fibrotic changes were identified in the current research as previously reported [38, 39]. Interestingly, these changes

focused on the right ventricles of MC-treated rats, while the RES treatment led to a tissue structure that was almost identical to that of the untreated controls. Right heart chambers differ from those on the left side, even in terms of their embryology [40] and primary functions, both physiologically and hemodynamically [41].

RES decreased, or, at the very least, inhibited, the progression of fibrosis in the right ventricles of the PAH+RES group. This finding suggests that pressure on the heart decreased after treatment with RES, and this was the primary reason for validating it using an ultrasonographic assessment in the current research. RES-mediated molecular mechanisms involving TGF- β modulation [42, 43] and its effect on the medial vascular layer have been associated with afterload pressure changes [44]. Other pathways have been described, such as a MC-induced upregulation of SphK1-mediated NF- κ B activation, albeit not in the scope of our current study [45]. Accompanied by a decrease in tissue remodeling, changes in the myocyte area and isolated cell volume were found with RES treatment. Consistent with the lack of fibrotic changes in the LV, these effects were also absent in these chambers. The results showed that individual cell volume and the area in the left ventricular cells in all the studied groups increased in comparison with those in the healthy CTRL RV cells. Hypertrophic LV compensation has been reported in heart failure when the MC model was used and is associated with an increase in neurohumoral activation [46]. An interesting finding was that there were no differences between the LV groups (i.e., the PAH and PAH+RES groups). It could be speculated that remodeling changes in the LV could appear later. However, this study duration was twice as long as the typical duration of 21 days. Therefore, this is unlikely. Generally, PAH is characterized by an increase in pulmonary vascular resistance, which causes RV remodeling and leads to RHF. In the current PAH model, compromised RV function, myocyte hypertrophy, and isolated RV cardiomyocytes were identified. Changes in cellular contractility in the LV were not seen. Interestingly, while a decrease in RV fractional shortening by echocardiography [47] is well known, some studies reported an increase in cellular shortening after treatment with MC [48, 49], but this higher contraction force was not sustained at high-stimulation frequencies [48]; this was also observed in the current study (Figure 3). Consistent with these changes in hypertrophy in an inflammatory model like MC, we found increased levels of mRNA of the remodeling markers BNP, collagen 1, Tnn1c, the inflammatory IL-1 β , and the anti-inflammatory cytokine IL-10. These markers have been reported previously for PAH [50, 51], while the cytokine IL-10 has been linked with the increase of fibrosis and TGF- β [52]. RES treatment in PAH decreased the inflammatory markers and modulated a decrease of the remodeling effect (Figure 4). These results also correlate with the effect of RES-mediated SIRT1 upregulation, with a consequent decrease in the acetylation profile (Figure 5(b)). This has been linked to mitochondrial dysfunction concomitant with ventricular dysfunction and heart failure [53].

The increase in myocardial stiffness, as a result of the overexpression of titin, has been proposed as a possible

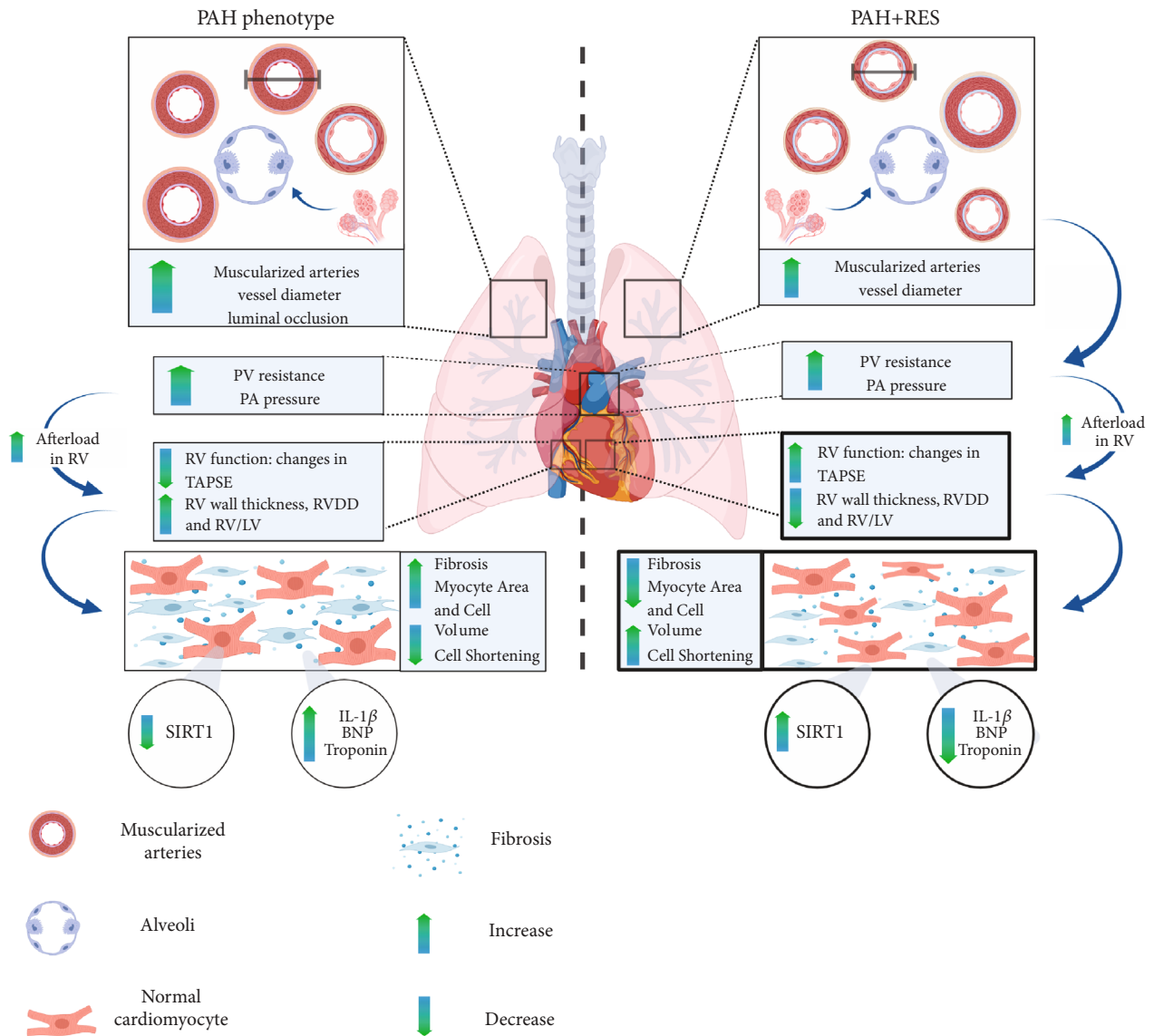


FIGURE 6: Effects of resveratrol in the PAH phenotype. Monocrotaline-induced PAH is a disease characterized by a progressive remodeling of the pulmonary vasculature, as a consequence of excessive proliferation and migration of pulmonary artery endothelial and smooth muscle cells. With the progression of the disease, the increase of the mean pulmonary artery pressure leads to a chamber pressure overload in the right ventricle (RV). When the optimal RV-arterial coupling is lost, the RV systolic function cannot remain matched to the afterload, and subsequently, dilation of the RV occurs, as well as diastolic dysfunction, secondary to myocardial fibrosis and sarcomeric stiffening. These changes ultimately lead to right heart failure and death. Even though the administration of resveratrol decreased the pathological remodeling of the pulmonary vasculature, it did not change the afterload for the RV (represented in the figure as a change in arrows' thickness). Nevertheless, resveratrol was able to protect directly the RV, improving its function, evidenced with microscopic changes: less fibrosis, decreased cardiomyocyte area and volume and better cell function, with increased cell shortening, increasing SIRT1-mediated deacetylation, and decreasing inflammatory and remodeling markers. The arrows in the PAH model indicate the changes compared to the CTRL group; the arrows in the PAH+RES model indicate the changes compared to the PAH group.

explanation for contractile dysfunction [54, 55] since this large protein is responsible for the passive elasticity of the muscle. Additionally, some changes in calcium handling could be involved. For instance, in the PAH model, faster calcium transients concomitant with increased sarcoplasmic reticulum calcium content and phosphorylation of phospholamban were demonstrated. Moreover, calcium spark frequency was higher in the RV cardiomyocytes from rodents in the PAH group. In this regard, RES has been

shown to upregulate the ratio of phosphorylated phospholamban and is accompanied by a significant improved sarcoplasmic reticulum calcium load. In the current study, the RES-treated group showed an increase in cellular shortening; this may have been due to an increase in myocyte stiffness as the RV energetic calcium handling might have been altered. Impaired mitochondrial function due to hypoxia in hypertrophy remodeling has been reported in PAH, which compromises the supply of energy to the

tissues [56]. Furthermore, creatine kinase activity and expression have been demonstrated to decrease after MC treatment [57]. This downregulation has been linked to a compromise in ATP/ADP transport between the mitochondria and the myofilaments. RES, besides being a potent antioxidant, is known for its cardioprotective action as it preserves the mitochondrial function by regulating the activity of anti-oxidant enzymes by reducing ROS [58].

PAH remains a challenging disease owing to its high morbidity, mortality, and time to diagnose. Although current therapies are improving the quality of life and survival, there is a need to identify adjunctive treatments focussing on RV function. As a result, PAH continues to be revisited, and an increasing number of therapeutic approaches are evaluated annually. However, the current guidelines for pharmacotherapy primarily focus on the vascular effects [59]. Since the disease is usually diagnosed late, a large amount of structural damage in the RV has already taken place. Contrary to some models where RES has been reported to have an effect on the pulmonary trunk [13] and although using an inflammatory model such as MC, the findings of the current study demonstrated that RES improved the RV and had a limited positive effect on the lungs (Figure 6). This finding is crucial since RV function correlates with symptomatology and the prognostic survival of the patients. Focusing on comparative ventricular assessment and isolated cell function, the current study showed how RES-mediated mechanisms might be involved using this model. Some other mechanisms include activation of specific sirtuin pathways like SIRT3, the modulation of cardiac energetics [53], and transcription factors relating to proliferation and the cell cycle [11]. Possible novel targets that focus on RV HF could become an exciting future scope for therapy. The multitargeted nature of RES, as an example of these polyphenolic compounds, holds future potential for novel approaches to this disease [60]. Ongoing research is needed to help characterize the molecular mechanisms and cell bioenergetics of these compounds in PAH and other cardiovascular conditions.

Data Availability

The data used to support the findings of this study are available from the corresponding author upon request.

Conflicts of Interest

The authors declare that there is no conflict of interest regarding the publication of this paper.

Acknowledgments

This work was partially supported by the Cardiovascular Medicine Research Group-Tecnológico de Monterrey (0020CAT131), CONACYT-México (grants 151136, 256577, and A1-S-43883 (G. García-Rivas), A1-S-23901 (Omar Lozano), 492122 (Judith Bernal)), and Fronteras de la Ciencia (Grant 0682). We thank Paulo Martinez, DVM, for his exceptional veterinarian assistance.

Supplementary Materials

Supplementary Table 1: primer sequences for real-time qPCR in heart tissue. (*Supplementary Materials*)

References





- [1] R. J. White, C. Jerjes-Sanchez, G. M. Bohns Meyer et al., "Combination therapy with oral treprostinil for pulmonary arterial hypertension: a double-blind, placebo-controlled study," *American Journal of Respiratory and Critical Care Medicine*, 2019, <https://www.atsjournals.org/doi/abs/10.1164/rccm.201908-1640OC>.
- [2] J. Sandoval Zarate, C. Jerjes-Sanchez, A. Ramirez-Rivera et al., "Mexican registry of pulmonary hypertension: REMEHIP," *Archivos de Cardiología de México*, vol. 87, no. 1, pp. 13–17, 2017.
- [3] N. Galiè, R. N. Channick, R. P. Frantz et al., "Risk stratification and medical therapy of pulmonary arterial hypertension," *The European Respiratory Journal*, vol. 53, no. 1, article 1801889, 2018.
- [4] X. Ren, R. A. Johns, and W. D. Gao, "Right heart in pulmonary hypertension: from adaptation to failure," *Pulmonary Circulation*, vol. 9, no. 3, 2019.
- [5] G. Garcia-Rivas, C. Jerjes-Sánchez, D. Rodriguez, J. Garcia-Pelaez, and V. Trevino, "A systematic review of genetic mutations in pulmonary arterial hypertension," *BMC Medical Genetics*, vol. 18, no. 1, article 82, 2017.
- [6] B. Vaidya, M. Pangallo, G. Ruffenach et al., "Advances in treatment of pulmonary arterial hypertension: patent review," *Expert Opinion on Therapeutic Patents*, vol. 27, no. 8, pp. 907–918, 2017.
- [7] S. Bruderer, N. Hurst, T. Remenova, and J. Dingemanse, "Clinical pharmacology, efficacy, and safety of selexipag for the treatment of pulmonary arterial hypertension," *Expert Opinion on Drug Safety*, vol. 16, no. 6, pp. 743–751, 2017.
- [8] Y. Liu, W. Ma, P. Zhang, S. He, and D. Huang, "Effect of resveratrol on blood pressure: a meta-analysis of randomized controlled trials," *Clinical Nutrition*, vol. 34, no. 1, pp. 27–34, 2015.
- [9] D. Xu, Y. Li, B. Zhang et al., "Resveratrol alleviate hypoxic pulmonary hypertension via anti-inflammation and anti-oxidant pathways in rats," *International Journal of Medical Sciences*, vol. 13, no. 12, pp. 942–954, 2016.
- [10] N. Treviño-Saldaña and G. García-Rivas, "Regulation of sirtuin-mediated protein deacetylation by cardioprotective phytochemicals," *Oxidative Medicine and Cellular Longevity*, vol. 2017, Article ID 1750306, 16 pages, 2017.
- [11] S. K. Singh, S. Banerjee, E. P. Acosta, J. W. Lillard, and R. Singh, "Resveratrol induces cell cycle arrest and apoptosis with docetaxel in prostate cancer cells via a p53/ p21WAF1/CIP1 and p27KIP1 pathway," *Oncotarget*, vol. 8, no. 10, pp. 17216–17228, 2017.
- [12] R. Akgedik, Ş. Akgedik, H. Karamanli et al., "Effect of resveratrol on treatment of bleomycin-induced pulmonary fibrosis in rats," *Inflammation*, vol. 35, no. 5, pp. 1732–1741, 2012.
- [13] D. N. Wilson, S. E. Schacht, L. Al-Nakkash, J. R. Babu, and T. L. Broderick, "Resveratrol prevents pulmonary trunk remodeling but not right ventricular hypertrophy in monocrotaline-induced pulmonary hypertension," *Pathophysiology*, vol. 23, no. 4, pp. 243–250, 2016.

- [14] J. W. Koskenvuo, R. Mirsky, Y. Zhang et al., "A comparison of echocardiography to invasive measurement in the evaluation of pulmonary arterial hypertension in a rat model," *The International Journal of Cardiovascular Imaging*, vol. 26, no. 5, pp. 509–518, 2010.
- [15] A. M. Cordero-Reyes, K. A. Youker, A. R. Trevino et al., "Full expression of cardiomyopathy is partly dependent on B-cells: a pathway that involves cytokine activation, immunoglobulin deposition, and activation of apoptosis," *Journal of the American Heart Association*, vol. 5, no. 1, article e002484, 2016.
- [16] C. E. Guerrero-Beltrán, J. Bernal-Ramírez, O. Lozano et al., "Silica nanoparticles induce cardiotoxicity interfering with energetic status and Ca^{2+} handling in adult rat cardiomyocytes," *American Journal of Physiology-Heart and Circulatory Physiology*, vol. 312, no. 4, pp. H645–H661, 2017.
- [17] D. Montalvo, P. Pérez-Treviño, K. Madrazo-Aguirre et al., "Underlying mechanism of the contractile dysfunction in atrophied ventricular myocytes from a murine model of hypothyroidism," *Cell Calcium*, vol. 72, pp. 26–38, 2018.
- [18] H. Satoh, L. M. Delbridge, L. A. Blatter, and D. M. Bers, "Surface:volume relationship in cardiac myocytes studied with confocal microscopy and membrane capacitance measurements: species-dependence and developmental effects," *Biophysical Journal*, vol. 70, no. 3, pp. 1494–1504, 1996.
- [19] R. Nogueira-Ferreira, R. Vitorino, R. Ferreira, and T. Henriques-Coelho, "Exploring the monocrotaline animal model for the study of pulmonary arterial hypertension: a network approach," *Pulmonary Pharmacology & Therapeutics*, vol. 35, pp. 8–16, 2015.
- [20] A. Csiszar, N. Labinsky, S. Olson et al., "Resveratrol prevents monocrotaline-induced pulmonary hypertension in rats," *Hypertension*, vol. 54, no. 3, pp. 668–675, 1979.
- [21] M. L. Paffett, S. N. Lucas, and M. J. Campen, "Resveratrol reverses monocrotaline-induced pulmonary vascular and cardiac dysfunction: a potential role for atrogen-1 in smooth muscle," *Vascular Pharmacology*, vol. 56, no. 1-2, pp. 64–73, 2012.
- [22] J. J. Ryan and S. L. Archer, "The right ventricle in pulmonary arterial hypertension," *Circulation Research*, vol. 115, no. 1, pp. 176–188, 2014.
- [23] A. E. Borrie, D. N. Ostrow, R. D. Levy, and J. R. Swiston, "Assessing response to therapy in idiopathic pulmonary arterial hypertension: a consensus survey of Canadian pulmonary hypertension physicians," *Canadian Respiratory Journal*, vol. 18, no. 4, pp. 230–234, 2011.
- [24] V. W. Dolinsky, S. Chakrabarti, T. J. Pereira et al., "Resveratrol prevents hypertension and cardiac hypertrophy in hypertensive rats and mice," *Biochimica et Biophysica Acta (BBA) - Molecular Basis of Disease*, vol. 1832, no. 10, pp. 1723–1733, 2013.
- [25] J. M. Smoliga and O. Blanchard, "Enhancing the delivery of resveratrol in humans: if low bioavailability is the problem, what is the solution?," *Molecules*, vol. 19, no. 11, pp. 17154–17172, 2014.
- [26] K. Pallauf, D. Chin, I. Günther et al., "Resveratrol, lunularin and dihydroresveratrol do not act as caloric restriction mimetics when administered intraperitoneally in mice," *Scientific Reports*, vol. 9, no. 1, pp. 1–12, 2019.
- [27] E.-J. Park and J. M. Pezzuto, "The pharmacology of resveratrol in animals and humans," *Biochimica et Biophysica Acta (BBA) - Molecular Basis of Disease*, vol. 1852, no. 6, pp. 1071–1113, 2015.
- [28] L.-X. Zou, C. Chen, X. Yan et al., "Resveratrol attenuates pressure overload-induced cardiac fibrosis and diastolic dysfunction via PTEN/AKT/Smad2/3 and NF- κ B signaling pathways," *Molecular Nutrition & Food Research*, vol. 63, no. 24, article e1900418, 2019.
- [29] R. Z. Hamza and N. S. El-Shenawy, "Anti-inflammatory and antioxidant role of resveratrol on nicotine-induced lung changes in male rats," *Toxicology Reports*, vol. 4, pp. 399–407, 2017.
- [30] L. A. Ahmed, S. M. Rizk, and S. A. El-Maraghy, "Pinocembrin ex vivo preconditioning improves the therapeutic efficacy of endothelial progenitor cells in monocrotaline-induced pulmonary hypertension in rats," *Biochemical Pharmacology*, vol. 138, pp. 193–204, 2017.
- [31] R. Xiao, Y. Su, T. Feng et al., "Monocrotaline induces endothelial injury and pulmonary hypertension by targeting the extracellular calcium-sensing receptor," *Journal of the American Heart Association*, vol. 6, no. 4, 2017.
- [32] H. B. Thibault, K. Baptiste, M. J. Raheer et al., "Noninvasive assessment of murine pulmonary arterial Pressure," *Circulation: Cardiovascular Imaging*, vol. 3, no. 2, pp. 157–163, 2010.
- [33] M. D'Alto, E. Romeo, P. Argiento et al., "Pulmonary arterial hypertension: the key role of echocardiography," *Echocardiography*, vol. 32, no. S1, pp. S23–S37, 2015.
- [34] D. Urboniene, I. Haber, Y.-H. Fang, T. Thenappan, and S. L. Archer, "Validation of high-resolution echocardiography and magnetic resonance imaging vs. high-fidelity catheterization in experimental pulmonary hypertension," *American Journal of Physiology Lung Cellular and Molecular Physiology*, vol. 299, no. 3, pp. L401–L412, 2010.
- [35] D.-L. Yang, H.-G. Zhang, Y.-L. Xu et al., "Resveratrol inhibits right ventricular hypertrophy induced by monocrotaline in rats," *Clinical and Experimental Pharmacology & Physiology*, vol. 37, no. 2, pp. 150–155, 2010.
- [36] E. R. Olson, J. E. Naugle, X. Zhang, J. A. Bomser, and J. G. Meszaros, "Inhibition of cardiac fibroblast proliferation and myofibroblast differentiation by resveratrol," *American Journal of Physiology Heart and Circulatory Physiology*, vol. 288, no. 3, pp. H1131–H1138, 2005.
- [37] P.-N. Jone, J. Hinzman, B. D. Wagner, D. D. Ivy, and A. Younoszai, "Right ventricular to left ventricular diameter ratio at end-systole in evaluating outcomes in children with pulmonary hypertension," *Journal of the American Society of Echocardiography*, vol. 27, no. 2, pp. 172–178, 2014.
- [38] L. Chen, X. T. Gan, J. V. Haist et al., "Attenuation of compensatory right ventricular hypertrophy and heart failure following monocrotaline-induced pulmonary vascular injury by the Na^+ - H^+ exchange inhibitor cariporide," *The Journal of Pharmacology and Experimental Therapeutics*, vol. 298, no. 2, pp. 469–476, 2001.
- [39] A. Behringer, M. Trappiel, E. M. Berghausen et al., "Pioglitazone alleviates cardiac and vascular remodeling and improves survival in monocrotaline induced pulmonary arterial hypertension," *Naunyn-Schmiedeberg's Archives of Pharmacology*, vol. 389, no. 4, pp. 369–379, 2016.
- [40] S. Zaffran, R. G. Kelly, S. M. Meilhac, M. E. Buckingham, and N. A. Brown, "Right ventricular myocardium derives from the anterior heart field," *Circulation Research*, vol. 95, no. 3, pp. 261–268, 2004.
- [41] C. E. Molina, J. Heijman, and D. Dobrev, "Differences in left versus right ventricular electrophysiological properties in cardiac dysfunction and arrhythmogenesis," *Arrhythmia & Electrophysiology Review*, vol. 5, no. 1, pp. 14–19, 2016.

- [42] T. Chen, J. Li, J. Liu et al., "Activation of SIRT3 by resveratrol ameliorates cardiac fibrosis and improves cardiac function via the TGF- β /Smad3 pathway," *American Journal of Physiology-Heart and Circulatory Physiology*, vol. 308, no. 5, pp. H424–H434, 2015.
- [43] H. Wu, G.-N. Li, J. Xie et al., "Resveratrol ameliorates myocardial fibrosis by inhibiting ROS/ERK/TGF- β /periostin pathway in STZ-induced diabetic mice," *BMC Cardiovascular Disorders*, vol. 16, no. 1, article 5, 2016.
- [44] B. Ha, C. L. Lucas, G. W. Henry, E. G. Frantz, J. I. Ferreiro, and B. R. Wilcox, "Effects of chronically elevated pulmonary arterial pressure and flow on right ventricular afterload," *The American Journal of Physiology*, vol. 267, no. 1, pp. H155–H165, 1994.
- [45] W. Shi, C. Zhai, W. Feng et al., "Resveratrol inhibits monocrotaline-induced pulmonary arterial remodeling by suppression of SphK1-mediated NF- κ B activation," *Life Sciences*, vol. 210, pp. 140–149, 2018.
- [46] J. Correia-Pinto, T. Henriques-Coelho, R. Roncon-Albuquerque et al., "Time course and mechanisms of left ventricular systolic and diastolic dysfunction in monocrotaline-induced pulmonary hypertension," *Basic Research in Cardiology*, vol. 104, no. 5, article 17, pp. 535–545, 2009.
- [47] Y.-P. Xie, B. Chen, P. Sanders et al., "Sildenafil prevents and reverses transverse-tubule remodeling and Ca²⁺ handling dysfunction in right ventricle failure induced by pulmonary artery hypertension," *Hypertension*, vol. 59, no. 2, pp. 355–362, 1979.
- [48] D. Benoist, R. Stones, M. J. Drinkhill et al., "Cardiac arrhythmia mechanisms in rats with heart failure induced by pulmonary hypertension," *American Journal of Physiology-Heart and Circulatory Physiology*, vol. 302, no. 11, pp. H2381–H2395, 2012.
- [49] J. Sabourin, A. Boet, C. Rucker-Martin et al., "Ca²⁺ handling remodeling and STIM1L/Orai1/TRPC1/TRPC4 upregulation in monocrotaline-induced right ventricular hypertrophy," *Journal of Molecular and Cellular Cardiology*, vol. 118, pp. 208–224, 2018.
- [50] H. K. Bae, H. Lee, K. C. Kim, and Y. M. Hong, "The effect of sildenafil on right ventricular remodeling in a rat model of monocrotaline-induced right ventricular failure," *Korean Journal of Pediatrics*, vol. 59, no. 6, pp. 262–270, 2016.
- [51] A. Groth, B. Vrugt, M. Brock, R. Speich, S. Ulrich, and L. C. Huber, "Inflammatory cytokines in pulmonary hypertension," *Respiratory Research*, vol. 15, no. 1, p. 47, 2014.
- [52] E. Sziksz, D. Pap, R. Lippai et al., "Fibrosis related inflammatory mediators: role of the IL-10 cytokine family," *Mediators of Inflammation*, vol. 2015, Article ID 764641, 15 pages, 2015.
- [53] E. C. Castillo, J. A. Morales, H. Chapoy-Villanueva et al., "Mitochondrial hyperacetylation in the failing hearts of obese patients mediated partly by a reduction in SIRT3: the involvement of the mitochondrial permeability transition pore," *Cellular Physiology & Biochemistry International Journal of Experimental Cellular Physiology, Biochemistry and Pharmacology*, vol. 53, no. 3, pp. 465–479, 2019.
- [54] S. Rain, M. L. Handoko, P. Trip et al., "Right ventricular diastolic impairment in patients with pulmonary arterial hypertension," *Circulation*, vol. 128, no. 18, pp. 2016–2025, 2013.
- [55] S. Rain, D. da Silva Goncalves Bos, M. L. Handoko et al., "Protein changes contributing to right ventricular cardiomyocyte diastolic dysfunction in pulmonary arterial hypertension," *Journal of the American Heart Association*, vol. 3, no. 3, article e000716, 2014.
- [56] E. D. Fowler, D. Hauton, J. Boyle, S. Egginton, D. S. Steele, and E. White, "Energy metabolism in the failing right ventricle: limitations of oxygen delivery and the creatine kinase system," *International Journal of Molecular Sciences*, vol. 20, no. 8, p. 1805, 2019.
- [57] E. D. Fowler, M. J. Drinkhill, R. Stones, and E. White, "Diastolic dysfunction in pulmonary artery hypertension: creatine kinase and the potential therapeutic benefit of beta-blockers," *Clinical and Experimental Pharmacology & Physiology*, vol. 45, no. 4, pp. 384–389, 2018.
- [58] E. D. B. Danz, J. Skramsted, N. Henry, J. A. Bennett, and R. S. Keller, "Resveratrol prevents doxorubicin cardiotoxicity through mitochondrial stabilization and the Sirt1 pathway," *Free Radical Biology & Medicine*, vol. 46, no. 12, pp. 1589–1597, 2009.
- [59] J. R. Klinger, C. G. Elliott, D. J. Levine et al., "Therapy for pulmonary arterial hypertension in adults: update of the CHEST guideline and expert panel report," *Chest*, vol. 155, no. 3, pp. 565–586, 2019.
- [60] B. N. M. Zordoky, I. M. Robertson, and J. R. B. Dyck, "Preclinical and clinical evidence for the role of resveratrol in the treatment of cardiovascular diseases," *Biochimica et Biophysica Acta (BBA) - Molecular Basis of Disease*, vol. 1852, no. 6, pp. 1155–1177, 2015.

Research Article

Virgin Coconut Oil Supplementation Prevents Airway Hyperreactivity of Guinea Pigs with Chronic Allergic Lung Inflammation by Antioxidant Mechanism

Luiz Henrique C. Vasconcelos ^{1,2} **Maria da Conceição C. Silva**,¹ **Alana C. Costa**,³ **Giuliana A. de Oliveira**,³ **Iara Leão Luna de Souza**,^{1,4} **Renato F. Righetti** ^{5,6}, **Fernando R. Queiroga**,^{1,7} **Glêbia A. Cardoso**,⁸ **Alexandre S. Silva**,⁸ **Patrícia M. da Silva**,⁷ **Giciane C. Vieira**,⁹ **Iolanda de F. L. C. Tibério**,⁵ **Marta S. Madruga**,¹⁰ **Fabiana de A. Cavalcante** ^{1,2} and **Bagnólia A. da Silva** ^{1,11}

¹Programa de Pós-graduação em Produtos Naturais e Sintéticos Bioativos, Centro de Ciências da Saúde, Universidade Federal da Paraíba, João Pessoa, PB, Brazil

²Departamento de Fisiologia e Patologia, Centro de Ciências da Saúde, Universidade Federal da Paraíba, João Pessoa, PB, Brazil

³Graduação em Farmácia, Departamento de Ciências Farmacêuticas, Centro de Ciências da Saúde, Universidade Federal da Paraíba, João Pessoa, PB, Brazil

⁴Departamento de Ciências Biológicas e Saúde, Universidade Estadual de Roraima, Boa Vista, RR, Brazil

⁵Faculdade de Medicina FMUSP, Universidade de São Paulo, São Paulo, SP, Brazil

⁶Hospital Sírio-Libanês, Serviço de Reabilitação, São Paulo, SP, Brazil

⁷Departamento de Biologia Molecular, Centro de Ciências da Saúde, Universidade Federal da Paraíba, João Pessoa, PB, Brazil

⁸Departamento de Educação Física, Centro de Ciências da Saúde, Universidade Federal da Paraíba, João Pessoa, PB, Brazil

⁹Departamento de Morfologia, Centro de Ciências da Saúde, Universidade Federal da Paraíba, João Pessoa, PB, Brazil

¹⁰Departamento de Engenharia de Alimentos, Centro de Tecnologia, Universidade Federal da Paraíba, João Pessoa, PB, Brazil

¹¹Departamento de Ciências Farmacêuticas, Centro de Ciências da Saúde, Universidade Federal da Paraíba, João Pessoa, PB, Brazil

Correspondence should be addressed to Bagnólia A. da Silva; bagnolia@lft.ufpb.br

Received 14 September 2019; Accepted 16 December 2019; Published 29 January 2020

Guest Editor: Bhagavatula Moorthy

Copyright © 2020 Luiz Henrique C. Vasconcelos et al. This is an open access article distributed under the Creative Commons Attribution License, which permits unrestricted use, distribution, and reproduction in any medium, provided the original work is properly cited.

Asthma is a chronic inflammatory disease of the airways characterized by immune cell infiltrates, bronchial hyperresponsiveness, and declining lung function. Thus, the possible effects of virgin coconut oil on a chronic allergic lung inflammation model were evaluated. Morphology of lung and airway tissue exhibited peribronchial inflammatory infiltrate, epithelial hyperplasia, and smooth muscle thickening in guinea pigs submitted to ovalbumin sensitization, which were prevented by virgin coconut oil supplementation. Additionally, in animals with lung inflammation, trachea contracted in response to ovalbumin administration, showed a greater contractile response to carbachol (CCh) and histamine, and these responses were prevented by the virgin coconut oil supplementation. Apocynin, a NADPH oxidase inhibitor, did not reduce the potency of CCh, whereas tempol, a superoxide dismutase mimetic, reduced potency only in nonsensitized animals. Catalase reduced the CCh potency in nonsensitized animals and animals sensitized and treated with coconut oil, indicating the participation of superoxide anion and hydrogen peroxide in the hypercontractility, which was prevented by virgin coconut oil. In the presence of L-NAME, a nitric oxide synthase (NOS) inhibitor, the CCh curve remained unchanged in nonsensitized animals but had increased efficacy and potency in sensitized animals, indicating an inhibition of endothelial NOS but ineffective in inhibiting inducible NOS. In animals sensitized and treated with coconut oil, the CCh curve was not altered, indicating a reduction in the release of NO by

inducible NOS. These data were confirmed by peribronchiolar expression analysis of iNOS. The antioxidant capacity was reduced in the lungs of animals with chronic allergic lung inflammation, which was reversed by the coconut oil, and confirmed by analysis of peribronchiolar 8-iso-PGF 2α content. Therefore, the virgin coconut oil supplementation reverses peribronchial inflammatory infiltrate, epithelial hyperplasia, smooth muscle thickening, and hypercontractility through oxidative stress and its interactions with the NO pathway.

1. Introduction

Functional foods have properties in the body, with respect to the metabolic and physiological role, which may or may not have health properties, that is, a beneficial relation between food and a certain health condition [1]. Several foods are classified within this classification, highlighting the coconut oil, which is recognized as a food for supplementation, based on safety and efficacy data [2].

The coconut oil (species: *Cocos nucifera* L., family: Areaceae) is a product obtained from the mature seed of coconut or copra (dry coconut pulp), which is mainly used to obtain the oil, being constituted between 65 and 75% of it [3], widely used in food and industry [4, 5].

This oil is rich in medium-chain saturated fatty acids, effective against the development of cardiovascular and inflammatory diseases [6], as well as antioxidant compounds (carotenoids and tocopherols) and vitamins [7]. In addition, it is described in the literature that virgin coconut oil has a composition of unsaponifiable compounds—mostly polyphenols and tocotrienols with antioxidant activity—superior to oils obtained by conventional methods such as cooling or enzymatically [4].

Among the pharmacological properties described for this oil are the anti-inflammatory [8], antihypertensive [9] to prevent coronary disease [10], and cardioprotective [11]. Thus, because of its actions on the inflammatory process, coconut oil is a potential candidate in the adjuvant therapy of several chronic inflammatory diseases, such as allergic asthma.

Asthma is a chronic inflammatory disease of the airways in which many innate and adaptive cells of the immune system act in conjunction with epithelial cells to promote bronchial hyperactivity, characterized as the tendency of smooth muscle cells to react exacerbatedly to nonspecific stimuli, such as cold air and exercise, in addition to excess production of mucus, remodeling of the airway wall and narrowing of the lumen of these conductive pathways. In susceptible patients, it leads to dyspnea and repeated periods of shortness of breath, wheezing during breathing, and chest tightness [12].

Despite the great diversity of drugs for the treatment of this disease, this is still done in a palliative and/or preventive way; therefore, new therapeutic approaches are necessary with the purpose of limiting or at least make acute crises less frequent or that potentiate the effects of drugs currently available for the treatment of asthma and, then, reducing the development of acute attacks.

In view of the above, virgin coconut oil presents potential as a functional food with health properties, emerging as a complementary therapy to prevent or reduce asthmatic crises. Therefore, the aim of this study was to evaluate a possible modulating activity of virgin coconut oil on the parameters of airway smooth muscle contraction, pulmonary inflammation, and oxidative stress, in order to characterize its effects

on the pathophysiological process of chronic allergic lung inflammation.

2. Materials and Methods

2.1. Animals. Male and female adult guinea pigs (*Cavia porcellus*), approximately 300-350 g, were obtained from the Biotherium of Research Institute in Pharmaceuticals and Medicine (IPeFarM/UFPB). The animals were maintained under controlled ventilation and temperature ($21 \pm 1^\circ\text{C}$) with water and food (Presence[®]) *ad libitum* in a 12 h light-dark cycle (lights on from 6 a.m to 18 p.m). The experimental procedures were performed following the principles of guidelines for the ethical use of animals in applied etiology studies [13] and from the Brazilian Guide for the Production, Maintenance or Use of Animals in Teaching or Scientific Research Activities, from Conselho Nacional de Controle de Experimentação Animal (CONCEA) [14] and were previously approved by the Ethics Committee on Animal Use of UFPB (protocol no 0410/13).

2.2. Drugs. Calcium chloride (CaCl_2), magnesium sulphate (MgSO_4), sodium chloride (NaCl), and potassium chloride (KCl) were purchased from Vetec Química Fina Ltda. (Brazil). Sodium bicarbonate (NaHCO_3) and glucose ($\text{C}_6\text{H}_{12}\text{O}_6$) were purchased from Dinâmica (Brazil). Potassium monobasic phosphate (KH_2PO_4), sodium hydroxide (NaOH), and hydrochloric acid (HCl) were purchased from Nuclear (Brazil). These substances, except glucose, NaHCO_3 , and NaCl , were diluted in distilled water to obtain each solution, which were maintained under refrigeration.

Catalase was purchased from Cayman Chemical (Brazil), and saline (0.9% NaCl) was purchased from Fresenius Kabi LTDA (Brazil). Carbamylcholine hydrochloride (CCh), histamine dihydrochloride, iberiotoxin (IbTX), isoproterenol, Cremophor[®], tetramethoxypropane, perchloric acid, Mayer's hematoxylin, eosin, 1,1-diphenyl-2-picrylhydrazyl (DPPH), apocynin, arachidonic acid (AA), ethylenediaminetetraacetic acid (EDTA), formaldehyde, nifedipine, ovalbumin (OVA) (grade V), and tempol were acquired from Sigma-Aldrich (Brazil). All substances were diluted in distilled water as needed for each experimental protocol. The carbogen mixture (95% O_2 and 5% CO_2) was obtained from White Martins (Brazil).

2.3. Experimental Groups. Animals were randomly divided into six groups (5-8 animals/group): guinea pigs submitted to nebulization with saline solution (Ctrl); guinea pigs with chronic allergic pulmonary inflammation, submitted to nebulization with OVA (Asth); guinea pigs with chronic allergic lung inflammation treated with dexamethasone (2 mg/kg/day) (Asth+Dexa); guinea pigs with chronic allergic

lung inflammation supplemented with virgin coconut oil (1 g/kg/day) (AstH+VCO1); guinea pigs with chronic allergic lung inflammation supplemented with virgin coconut oil (2 g/kg/day) (AstH+VCO2); and guinea pigs with chronic allergic lung inflammation supplemented with virgin coconut oil (4 g/kg/day) (AstH+VCO4).

2.4. Virgin Coconut Oil. The virgin coconut oil was purchased from a natural product store in the municipality of João Pessoa/PB, Brazil, brand Dr. Orgânica® (lot no. V15 245), extracted by cold pressing, not refined. A sample of the oil (500 mL) was used in order to determine the acidity, peroxide and saponification indexes, and the fatty acid profile.

2.5. Determination of Fatty Acid Composition of the Virgin Coconut Oil. Methyl esters of the oil sample were obtained by esterification. Identification and quantification of the fatty acid esters were performed by gas chromatography (GC), using helium as the entrainment gas (flow rate of 1 mL/min).

The GC conditions were injector temperature of 250°C, initial furnace temperature of 100°C, increasing at 2.5°C/min to 240°C, remaining for 40 min, with a total run time of 96 min. The detector temperature was 250°C, aux gas flow: helium 25 mL/min, hydrogen 30 mL/min, and synthetic air 300 mL/min. 1.0 µL aliquots of the esterified sample were injected into the injector, and the chromatograms were recorded. Fatty acids were identified by comparing the retention times of the methyl esters of the samples with Supelco ME19-Kit standards (Fatty Acid Methyl Esters C4-C24). The analyses were performed in duplicate.

2.6. Determination of the Acid Index of the Virgin Coconut Oil. Virgin coconut oil samples, completely liquid, were homogenized. Next, 2 g of the sample was added in an Erlenmeyer flask and filled with 25 mL of neutral ether-alcohol solution (2:1). Two drops of acid/basic phenolphthalein indicator were added, and titration was carried out with 0.1 M sodium hydroxide solution until the appearance of pink staining, which should persist for 30 sec.

The absolute acidity index (KOH/g oil) was calculated by the formula: $(v \times f \times 5.61)/P$, where v is the volume (mL) of NaOH solution spent in the titration of the sample, f the NaOH solution factor, and P the mass (g) of the sample [15]. The analyses were performed in triplicate.

2.7. Determination of the Peroxide Index of the Virgin Coconut Oil. Acetic acid-chloroform solution (3:2) (30 mL) was added to 5 g of the virgin coconut oil in an Erlenmeyer flask under gentle stirring, followed by the addition of 0.5 mL of saturated iodide solution of potassium. Subsequently, the mixture was left out in the light for 1 minute, and then, 30 mL of distilled water were added. This content was titrated with 0.1 N sodium thiosulphate solution under constant stirring until the yellow color disappeared. Then, 0.5 mL of 1% starch solution (indicator) was added, continuing the titration until the complete disappearance of the blue color.

The peroxide index (meq/kg sample) was calculated by the formula: $[(A - B) \times N \times f \times 1000]/P$, wherein A is the volume (mL) of sodium thiosulfate spent on titration of the

sample and B on the titration of the blank, N is the normality of the sodium thiosulphate solution, f is the factor of sodium thiosulphate solution, and P is the mass (g) of the sample. The analyses were performed in triplicate.

2.8. Determination of the Saponification Index of the Virgin Coconut Oil. The coconut oil sample was melted and filtered on filter paper to remove impurities and moisture traces. Then, 5 mL of the sample was added 50 mL of alcoholic KOH solution. A condenser was connected and allowed to boil gently until complete saponification of the sample, and then, its cooling was done. Then, 1 g of the phenolphthalein indicator was added, and the solution was titrated with 0.5 M HCl until the complete disappearance of the pink color.

The saponification index (mg KOH/g oil) was calculated by the formula: $[26.06 \times f \times (B - A)]/P$, where A is the volume (mL) of HCl spent on the titration of the sample, B is the volume spent on the blank titration, f is the 0.5 M HCl solution factor, and P is the mass (g) of the sample. The analyses were performed in triplicate.

2.9. Induction of Chronic Allergic Lung Inflammation. Animals were individually placed in a closed polyacrylic box coupled to an ultrasonic nebulizer for nebulization. Then, guinea pigs were nebulized with OVA in saline solution for a maximum of 15 min or until the onset of sneezing, coryza, coughing, and/or drawing of the thoracic wall, characterizing the respiratory distress; the Ctrl received only saline solution (NaCl 0.9%). The time that the guinea pigs remained in nebulization was defined as the inhalation time.

The protocol consisted of seven inhalations performed in four weeks, with 96 h intervals between each inhalation, with OVA concentration being increased (1-5 mg/mL) to avoid tolerance. In the first four inhalations, the guinea pigs were submitted to OVA 1 mg/mL; in the fifth and sixth inhalations, the animals received OVA 2.5 mg/mL; and at the seventh inhalation, they received OVA 5 mg/mL. After 72 h of the last inhalation, the animals were euthanized by cervical dislocation followed by sectioning of cervical vessels for experimentation. The ctrl was submitted to the same inhalation procedure but only receiving saline solution (adapted from Tibério et al. [16], Angeli et al. [17], Pigati et al. [18], Vasconcelos et al. [19]).

The groups supplemented with virgin coconut oil received orally, daily doses of 1, 2 or 4 g/kg [9, 20–22], ending the day before the euthanasia of the animal. Guinea pigs from the AstH+Dexa group were treated with the drug at 2 mg/kg/day intraperitoneally, starting 24 hours after the fourth nebulization, to ensure that the animals were sensitized (Figure 1). During this period, dexamethasone treatment was done 5 hours prior to exposure to the antigen [23].

2.10. Evaluation of Lung and Bronchial Morphology. Guinea pigs were euthanized by guillotine, the lung and the right extrapulmonary bronchus were isolated, fixed in 10% formaldehyde solution for 24 h, and subjected to standard histological procedures as follows: (1) dehydration, by increasing alcohol series of 70% for 24 h and 80, 96, and 100% (third

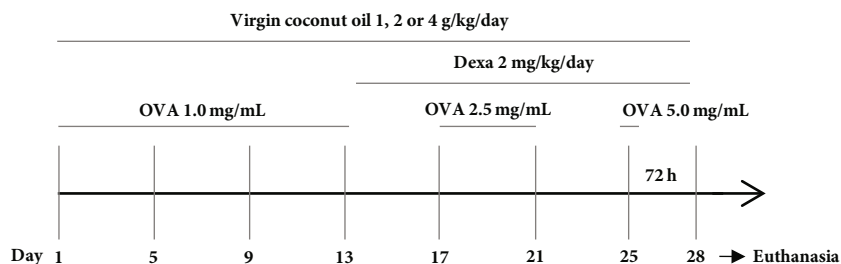


FIGURE 1: Protocol for induction of chronic allergic pulmonary inflammation in guinea pigs. OVA = ovalbumin; Dexa = dexamethasone.

bath) for 1 h each; (2) diaphanization, by bath in 100% xylene alcohol (1 : 1) for 1 h, followed by two baths in pure xylene for 1 h each; and (3) embedding in paraffin by passing the sample through two baths of liquid paraffin (heated to 50°C) for 1 h each. Next, the samples were embedded in new paraffin. The blocks obtained were cut to 5 μm thick and stained with Mayer's hematoxylin/eosin. For a panoramic analysis of the histological section, the slides were analyzed in the increase lens (I.L.) of $\times 40$ (1500 μm) and $\times 100$ (600 μm).

For bronchial analysis, the evaluated aspects were wall structure, tissue integrity, and cellular migration. In these experiments, 5 slides of 5 different animals were analysed for each group. The photomicrographs of the slides were made with a camera coupled to an optical microscope. The images were calibrated through the Motic Plus program according to the objectives used: 4x and 10x. The histological analysis of the slides was performed by a trained operator who qualitatively analyzed the histological parameters and then quantified statistically by score (below).

- (1) Preserved histoarchitecture of the airways with the absence of perivascular and peribronchiolar cellular infiltrate
- (2) Mild degree: an increase of less than 25% in relation to the control
- (3) Moderate degree: an increase of 25 to 49% in relation to the control
- (4) Accentuated degree: an increase of 50 to 75% in relation to the control
- (5) Very pronounced degree: an increase of more than 75% in relation to the control.

2.11. Trachea Preparation. Guinea pigs were euthanized by guillotine. The trachea was removed, cleaned of fat and connective tissue, immersed in Krebs solutions, and bubbled with carbogen mixture (95% O_2 and 5% CO_2). The Krebs solution composition was (mM): NaCl (118.0), KCl (4.55), MgSO_4 (5.7), KH_2PO_4 (1.1), CaCl_2 (2.52), NaHCO_3 (25.0), and glucose (11.0), with pH adjusted to 7.4. To register isometric contractions, tracheal rings (2-3 cm) were suspended in steel rods in organ baths (6 mL), connected to a force transducer (TIM 05), attached to an amplifier (AECAD04F), and connected to an A/D converter into a PC running AQCAD® software (São Paulo, Brazil). The system contained a thermostatic pump model BT 60 that controlled the organ

bath's temperature. The trachea resting time was 60 min in a preload tension of 1 g (baseline). During the organ-resting phase, the solution was changed every 15 min to avoid metabolite accumulation [24].

After the stabilization period, the tracheal segments were contracted with CCh 1 μM , and the isometric tension was recorded. The arachidonic acid 0.1 mM was added to the organ bath, when a stable contraction was attained, in order to confirm the presence of epithelium by the presence of arachidonic acid-induced relaxation equal or higher than 50% of maximal tension. In some tracheal rings, the luminal surface was gently rubbed with Krebs wet cotton to remove the epithelial layer. The absence of epithelium was confirmed when arachidonic acid-induced relaxation was absent or lower than 10% of maximal tension [24].

2.12. Reactivity Measurement. The trachea was assembled as described previously. After the stabilization period, when the baseline remained constant, the intact epithelium tracheal rings were stimulated with OVA 10 $\mu\text{g}/\text{mL}$ [25–28], and the contraction amplitude was compared between all groups.

In another experiments, after the evaluation of epithelium integrity, a cumulative concentration-response curve was obtained to CCh (10 nM to 0.1 mM), an agonist of muscarinic receptors [29], or histamine (10 nM to 3 mM), an agonist of histaminergic receptors [29]. The contractile reactivity was evaluated based on the values of the maximum effect (E_{max}) and the negative logarithm of the molar concentration of a substance that produced 50% of its maximal effect (pEC_{50}) of the contractile agent, calculated from the concentration-response curves obtained. The maximum amplitude obtained from the control concentration-response curve was elected as 100% of contraction, and the other percentages of contraction were calculated related to this value.

2.13. Role of ROS and NO Pathways in the Reactivity Measurement. The trachea was assembled as described previously. After checking for the presence of epithelium, the curves to CCh were obtained either in the absence or presence of apocynin 10 μM , an inhibitor of NADPH oxidase [30], and tempol 1 mM, a superoxide dismutase mimetic [31], after 30 min of incubation; or catalase 100 IU/mL, after 10 min incubation for ROS pathway investigation. In other experiments, the curves to CCh were obtained either in the absence or presence of L-NAME 10^{-4} M, an inhibitor of NOS [31], after 45 min incubation for NO pathway investigation.

2.14. Antioxidant Activity Assay. In order to obtain the plasma, after euthanasia of the animals, 10 mL of blood was collected through cervical vessel sections, placed immediately in anticoagulant (EDTA) containing test tubes and centrifuged at $1,198 \times g$ for 10 min. The supernatant was then transferred to Eppendorf® tubes and refrigerated at 20°C until analysis [32, 33]. Additionally, to obtain the lung tissue homogenate, the lungs were isolated and frozen at 20°C until preparation of the homogenate. For this, the tissue was weighed, macerated, and homogenized with 10% KCl (1:1). Then, the samples were centrifuged ($1,198 \times g/10$ min), and the supernatant was separated for further analysis.

For total antioxidant capacity analysis, an aliquot of 1.25 mg of DPPH was diluted in ethanol (100 mL), kept under refrigeration, and protected from light. In proper centrifuge tubes, 3.9 mL of DPPH solution was added with 100 μ L of the samples. These tubes were vortexed and left to stand during 30 min, centrifuged at $7,489 \times g$ at 20°C during 15 min. Then, the samples were read in a spectrophotometer at a wavelength of 515 nm (Biospectro, SP-220 model, Brazil). Results were expressed as percentage of the antioxidant capacity: $AOA = 100 - ((DPPH \cdot R)S / (DPPH \cdot R)W \cdot 100)$, where (DPPH · R)S and (DPPH · R)W corresponding to the concentration of DPPH • remaining after 30 min, measured in the sample (S) and white (W) prepared with distilled water.

2.15. Immunohistochemistry for Peribronchiolar iNOS and 8-Iso-PGF2 α Measurement. The slices obtained as described previously were deparaffinized and rehydrated for immunohistochemistry, treated with Proteinase K (20 min at 37°C followed by 20 min at room temperature), and washed with PBS. Blocking of endogenous peroxidases was performed by incubation with 3% hydrogen peroxide (H₂O₂) 10 V (3 \times 10 min), and sections of experimental and control (positive and negative) tissue slides were incubated overnight with the anti-iNOS, dilution 1:1600 (IS-20 Goat Polyclonal; Oxford Biomed, Resear, MI, USA) or anti-8-iso-PGF2 α , dilution 1:1500 (N-32020 Mouse Monoclonal; BD transduction Lab., CA, USA). The following day, the slides were washed in PBS and incubated with a secondary antibody using ABCKit by Vectastain (Vector Elite-PK-6105 anti-goat) or PK-6102 (anti-mouse). For visualization of positive cells, the slides were washed in PBS, and proteins were visualized using 3,3'-diaminobenzidine chromosom (DAB) (Sigma Chemical Co., St. Louis, MO, USA). Slide sections were contrasted with Harris hematoxylin (Merck, Darmstadt, Germany) and assembled using Entellan microscopy resin (Merck).

The optical density was used to evaluate the expression of iNOS and isoprostane PGF2 α . Images were captured using a Leica DM2500 microscope (Leica Microsystems, Wetzlar, Germany) and a digital camera (Leica DFC420 Leica Microsystems, Wetzlar, Germany). The images were acquired and processed using Optimas v.4.10 software. We analyzed 10 fields per lamina and one lamina per animal. The images were analyzed using Image-Proplus 4.5 software (NIH, MD, USA). This software allowed a thresholding of the color shades to be developed. These shades represent the positive areas quantified in the previously determined area. The volume fractions of these markers are expressed as percentages of the area.

2.16. Statistical Analysis. Data were expressed as the mean and standard error of the mean (S.E.M.), the normality of the variance was verified by the Shapiro Wilk test, and results were statistically analyzed using Student's *t*-test to intergroup comparison or analysis of variance (ANOVA) one-way, followed by Tukey's post-test, for multiple comparisons between experimental groups. Cumulative concentration-response curves were fitted, and pEC₅₀ values were obtained by nonlinear regression [34]. Values were significantly different when $p < 0.05$. All data were analyzed by GraphPad Prism® version 5.01 (GraphPad Software Inc., USA).

3. Results

3.1. Evaluation of Pulmonary and Bronchial Morphology. The analysis of histological sections of the lungs in A.T. $\times 40$ demonstrated that the Ctrl group presented normal histological appearance and preserved pulmonary histoarchitecture (Figures 2(a) and 3(a)), whereas the lungs of the Asth group showed large infiltration of inflammatory cells in the peribronchiolar and perivascular and absence of pulmonary alveoli infiltrates (Figures 2(b) and 3(a)). The treatment with dexamethasone (Figures 2(c) and 3(a)) or virgin coconut oil supplementation at doses of 1, 2, and 4 g/kg (Figures 2(d)–2(f) and 3(a)), decreases the migration from cells to the lung.

The analysis of histological sections of the lungs in A.T. $\times 100$ showed epithelial hyperplasia in the animals of the Asth group (Figures 4(b) and 3(b)) compared to the Ctrl group (Figures 4(a) and 3(b)). Treatment with dexamethasone (Figures 4(c) and 3(b)) or supplementation with virgin coconut oil at 1, 2, and 4 g/kg (Figures 4(d)–4(f) and 3(b)) reduced epithelial hyperplasia. In addition, compared to the Ctrl group (Figures 4(a) and 3(c)), the animals of the Asth group presented a greater thickness of intrapulmonary bronchial smooth muscle due to hypertrophy and/or hyperplasia (Figures 4(b) and 3(c)). Treatment with dexamethasone (Figures 4(c) and 3(c)) or with virgin coconut oil at doses of 1, 2, and 4 g/kg (Figures 4(d)–4(f) and 3(c)) reduced this thickening.

The analysis of histological sections of extrapulmonary bronchus in A.T. $\times 40$ demonstrated that compared to the Ctrl group (Figures 5(a) and 3(c)), the Asth group showed bronchial smooth muscle development due to hypertrophy and/or hyperplasia (Figures 5(b) and 3(c)). Treatment with dexamethasone (Figures 5(c) and 3(c)) or supplementation with virgin coconut oil at 1, 2, and 4 g/kg (Figures 5(d)–5(f) and 3(c)) decreased the smooth muscle thickness.

3.2. Reactivity Measurement

3.2.1. Contractile Response to Ovalbumin. The guinea pig trachea of the Ctrl group did not show contractile reactivity to OVA stimulation ($E_{max} = 1.8 \pm 0.8\%$, $n = 5$), differently, in the Asth group, OVA promoted contractile reactivity ($E_{max} = 100\%$, $n = 5$). Neither treatment with dexamethasone ($E_{max} = 89.1 \pm 10.5\%$, $n = 5$) nor supplementation with virgin coconut oil at doses of 1 ($E_{max} = 65.4 \pm 8.3\%$, $n = 5$) and 2 g/kg ($E_{max} = 81.6 \pm 13.3\%$, $n = 5$) reduced the contractile

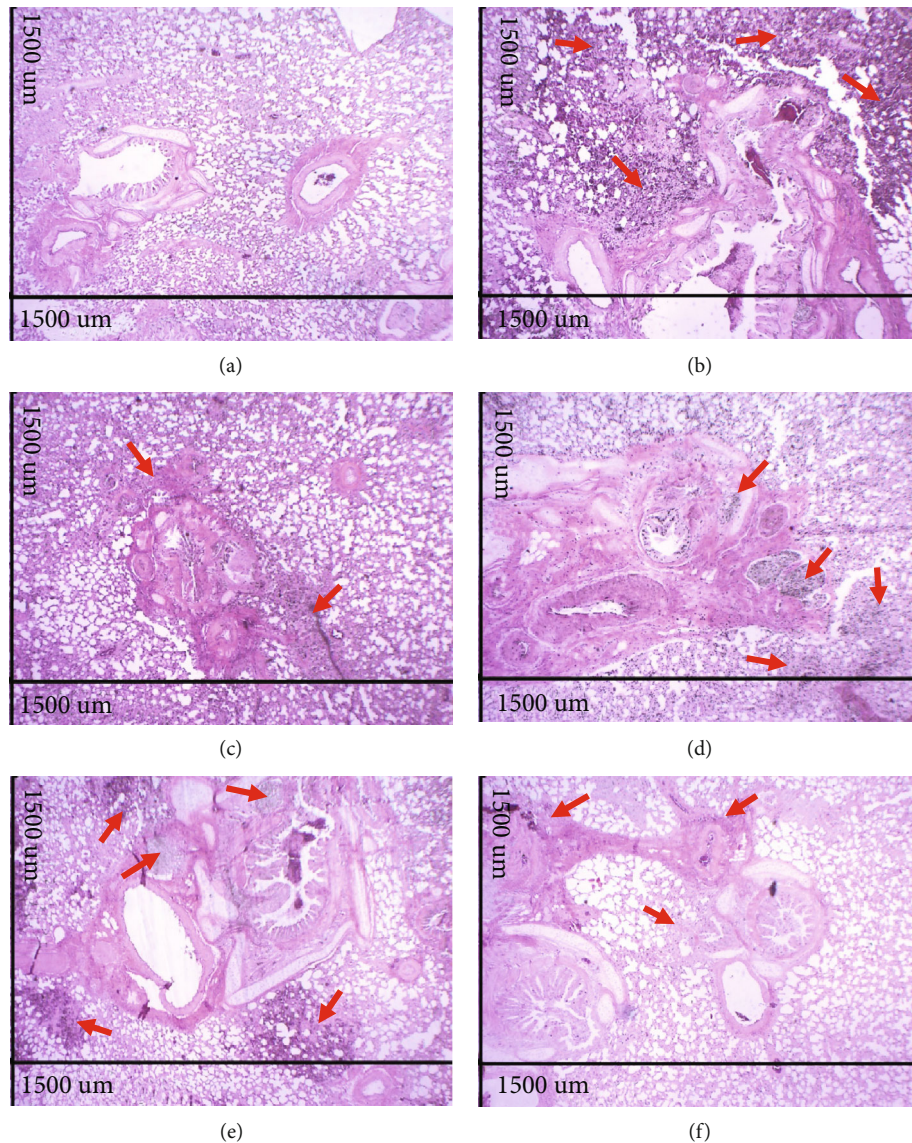


FIGURE 2: Photomicrographs of lungs of guinea pigs from Ctrl (a), Asth (b), Asth+Dexa (c), Asth+VCO1 (d), Asth+VCO2 (e), and Asth+VCO4 groups (f) showing the inflammatory infiltrate. Cellular infiltrate (red arrows). HE, A.T. $\times 40$, 1500 μm .

reactivity of the trachea, not differing from the Asth group. Differently, supplementation with virgin coconut oil at the dose of 4 g/kg reduced the amplitude of the contraction of the trachea ($E_{\text{max}} = 40.3 \pm 2.1\%$, $n = 5$) in relation to the Asth group, not differing from the Ctrl group.

3.2.2. Contractile Response to CCh in the Presence of Functional Epithelium. In Ctrl, the trachea contracted in response to cumulative concentrations of CCh ($E_{\text{max}} = 100\%$, $\text{pEC}_{50} = 6.63 \pm 0.10$). Pulmonary inflammation, in Asth group, increased the contractile efficacy of CCh ($E_{\text{max}} = 185.3 \pm 16.1\%$) but did not alter its potency ($\text{pEC}_{50} = 6.74 \pm 0.03$) compared to the Ctrl group (Figure 6(a), $n = 5$).

Treatment with dexamethasone partially prevented the increase in the contractile efficacy of CCh ($E_{\text{max}} = 133.4 \pm 4.9\%$) but did not change its potency

($\text{pEC}_{50} = 6.59 \pm 0.11$), in relation to both Ctrl and Asth groups (Figure 6(a), $n = 5$).

Supplementation with virgin coconut oil at a dose of 1 g/kg did not prevent increased efficacy or potency of CCh ($E_{\text{max}} = 153.2 \pm 9.3\%$; $\text{pEC}_{50} = 6.61 \pm 0.08$), compared to both Ctrl and Asth groups. However, in both Asth+VCO2 and Asth+VCO4, the increase in the contractile efficacy of CCh was completely prevented ($E_{\text{max}} = 108.6 \pm 13.7$ and $98.3 \pm 18.5\%$, respectively), with no change in potency ($\text{pEC}_{50} = 6.60 \pm 0.07$ and 6.49 ± 0.09 , respectively), in both Ctrl and Asth groups (Figures 6(a), $n = 5$).

3.2.3. Contractile Response to Histamine in the Presence of Functional Epithelium. The trachea of guinea pigs from the Ctrl group contracted in response to the addition of histamine ($E_{\text{max}} = 100\%$; $\text{pEC}_{50} = 5.05 \pm 0.04$). Pulmonary inflammation, in the Asth group, increased the contractile

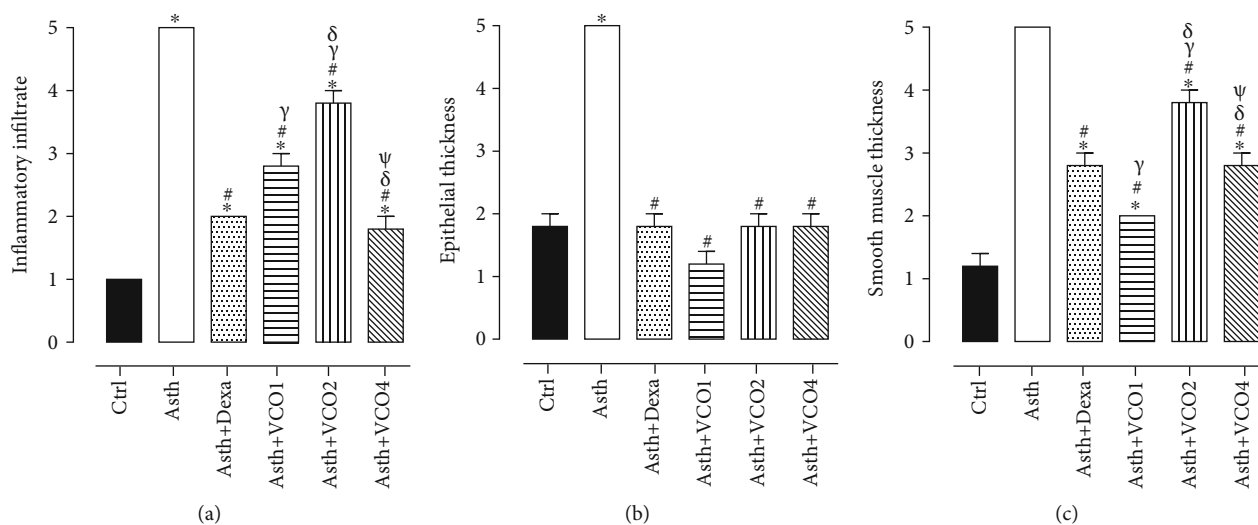


FIGURE 3: Inflammatory cell infiltrate in lung (a), epithelial hyperplasia (b), and thickness of airway smooth muscle layer (c) of guinea pigs of Ctrl, Asth, Asth+Dexa, Asth+VCO1, Asth+VCO2, and Asth+VCO4 groups. The columns and vertical bars represent the mean and S.E.M., respectively ($n = 5$). One-way ANOVA followed by Tukey's post-test: * $p < 0.05$ (Ctrl vs. other groups); # $p < 0.05$ (Asth vs. other groups); $\gamma p < 0.05$ (Asth+Dexa vs. Asth+VCO1 or Asth+VCO2); $\delta p < 0.05$ (Asth+VCO1 vs. Asth+VCO2 or Asth+VCO4) and $\psi p < 0.05$ (Asth+VCO2 vs. Asth+VCO4).

efficacy of histamine ($E_{\max} = 132.6 \pm 5.9\%$) but did not change its potency ($pEC_{50} = 5.11 \pm 0.12$) (Figure 6(b), $n = 5$).

Treatment with dexamethasone completely prevented the increased contractile efficacy of histamine ($E_{\max} = 89.5 \pm 9.2\%$) but did not change its potency ($pEC_{50} = 5.21 \pm 0.15$), compared to both Ctrl and Asth groups (Figure 6(b), $n = 5$).

Supplementation with virgin coconut oil at doses of 1 and 2 g/kg did not prevent an increase in the contractile efficacy of histamine ($E_{\max} = 158.8 \pm 16.4$ and $101.5 \pm 5.8\%$, respectively) and did not alter its potency ($pEC_{50} = 5.23 \pm 0.05$ and 4.99 ± 0.13 , respectively), compared to both Ctrl and Asth groups. In contrast, in the Asth+VCO4 group, the increased contractile efficacy of histamine was completely prevented ($E_{\max} = 87.6 \pm 8.0\%$), but there was no change in potency ($pEC_{50} = 4.99 \pm 0.16$), in relation to both Ctrl and Asth groups (Figure 6(b), $n = 5$).

3.2.4. Role of ROS and NO Pathways in the Reactivity Measurement

(1) *Cumulative Concentration-Response Curves to CCh, in the Absence and Presence of Apocynin, Tempol, or Catalase.* The cumulative concentration-response curve to CCh of the Ctrl group ($E_{\max} = 100\%$; $pEC_{50} = 6.82 \pm 0.06$) was not altered in the presence of NADPH oxidase, an inhibitor of apocynin ($E_{\max} = 115.6 \pm 9.4\%$; $pEC_{50} = 6.52 \pm 0.13$). Differently, in the presence of tempol, a SOD mimetic, the CCh contraction curve was shifted to the right 3.2-fold ($pEC_{50} = 6.30 \pm 0.07$), without altering the contractile efficacy of the agonist ($E_{\max} = 99.4 \pm 12.3\%$). Similarly, in the presence of catalase, which converts H_2O_2 to H_2O and O_2 , the contractile potency of CCh was reduced by 4-fold ($pEC_{50} = 6.23 \pm 0.09$), with no change in its efficacy ($E_{\max} = 116.6 \pm 11.9\%$) (Figure 7(a), $n = 5$).

In the guinea pigs of the Asth group with lung inflammation, the cumulative curve to CCh ($E_{\max} = 100\%$; $pEC_{50} = 6.35 \pm 0.11$) was not modified by apocynin ($E_{\max} = 105.6 \pm 11.7\%$; $pEC_{50} = 6.54 \pm 0.11$). Likewise, in the presence of tempol, the CCh curve was not modified ($E_{\max} = 101.0 \pm 11.7\%$; $pEC_{50} = 6.62 \pm 0.27$), as well as in the presence of catalase ($E_{\max} = 102.4 \pm 9.1\%$; $pEC_{50} = 5.99 \pm 0.06$) (Figure 7(b), $n = 5$).

In the supplementation with virgin coconut oil at the dose of 4 g/kg, it was observed that in the presence of apocynin, the CCh curve ($E_{\max} = 100\%$; $pEC_{50} = 6.88 \pm 0.07$) was not altered ($E_{\max} = 102.3 \pm 4.3\%$; $pEC_{50} = 6.81 \pm 0.14$). In the presence of tempol, the same was observed in the Asth group, in which the potency ($pEC_{50} = 6.44 \pm 0.12$) and the contractile efficacy of CCh ($E_{\max} = 91.9 \pm 13.0\%$) were not altered. Differently, in the presence of catalase, the contractile potency of CCh was reduced by 6.6-fold ($pEC_{50} = 6.07 \pm 0.08$), without the agonist's contractile efficacy being altered ($E_{\max} = 111.4 \pm 8.8\%$) (Figure 7(c), $n = 5$).

(2) *Cumulative Concentration-Response Curves to CCh, in the Absence and Presence of L-NAME.* The cumulative concentration-response curve to CCh of the Ctrl group ($E_{\max} = 100\%$; $pEC_{50} = 6.82 \pm 0.06$) was not altered by the NOS inhibitor L-NAME, both with respect to efficacy ($E_{\max} = 109.5 \pm 10.4\%$) and contractile potency ($pEC_{50} = 6.54 \pm 0.11$) (Figure 8(a), $n = 5$).

In guinea pigs of the Asth group with lung inflammation, both efficacy ($E_{\max} = 100\%$) and the contractile potency ($pEC_{50} = 6.35 \pm 0.11$) of CCh were increased by L-NAME ($E_{\max} = 144.4 \pm 16.0\%$; $pEC_{50} = 6.74 \pm 0.03$), about 1.4- and 2.2-fold, respectively (Figure 8(b), $n = 5$).

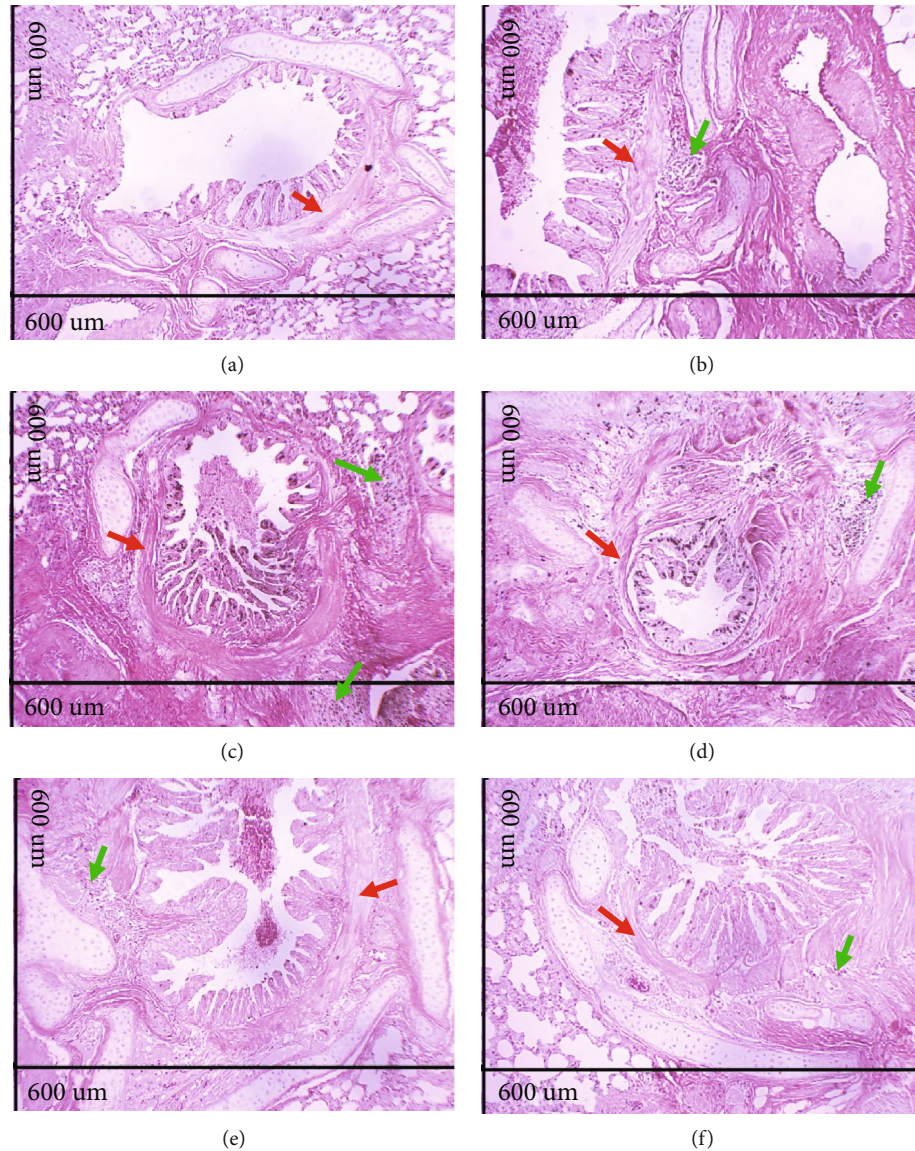


FIGURE 4: Photomicrographs of lungs of guinea pigs from Ctrl (a), Asth (b), Asth+Dexa (c), Asth+VCO1 (d), Asth+VCO2 (e), and Asth+VCO4 groups (f) showing the smooth muscle of the intrapulmonary bronchi. Intrapulmonary bronchial smooth muscle (red arrows), inflammatory infiltrate (green arrows). HE, A.T. $\times 100$, 600 μm .

Supplementation with virgin coconut oil at the dose of 4 g/kg promoted a similar response to that observed in the Ctrl group, and the contraction curve to CCh ($E_{\text{max}} = 100\%$; $\text{pEC}_{50} = 6.88 \pm 0.07$) was not altered by L-NAME ($E_{\text{max}} = 87.4 \pm 7.9\%$; $\text{pEC}_{50} = 6.98 \pm 0.19$) (Figure 8(c), $n = 5$).

(3) *Measurement of Total Antioxidant Capacity in Plasma and Lung Tissue.* In the plasma, the animals of the Ctrl group had an antioxidant capacity value of $23.6 \pm 3.6\%$, which did not differ from the Asth group ($19.8 \pm 3.2\%$). Dexamethasone treatment or supplementation with virgin coconut oil at all doses did not alter the plasma antioxidant capacity of guinea pigs (16.8 ± 3.0 ; 21.2 ± 1.5 ; 16.2 ± 3.4 , and $17.4 \pm 4.5\%$, respectively). In the lungs, the Ctrl group had an antioxidant capacity value of $83.0 \pm 4.2\%$, while pulmonary inflammation of the Asth group reduced the antioxidant

capacity to $59.8 \pm 6.6\%$. Dexamethasone treatment did not alter the lung antioxidant capacity of guinea pigs with pulmonary inflammation ($74.6 \pm 5.0\%$), as well as supplementation with virgin coconut oil at the dose of 1 g/kg ($77.2 \pm 2.8\%$). However, virgin coconut oil at 2 and 4 g/kg increased the antioxidant lung capacity to 82.6 ± 5.0 and $87.8 \pm 1.4\%$, respectively, in relation to both Ctrl and Asth groups.

(4) *Measurement of Peribronchiolar iNOS and 8-Iso-PGF $_{2\alpha}$ Expression.* The numbers of peribronchiolar cells positive for iNOS and the volume fractions of PGF- 2α isoprostane are shown in Figures 9(a) and 9(b) ($n = 5$). Both markers in the Asth group were increased compared to the Ctrl group. Treatment with dexamethasone attenuated these markers, as well as the supplementation with virgin coconut oil 4 g/kg.

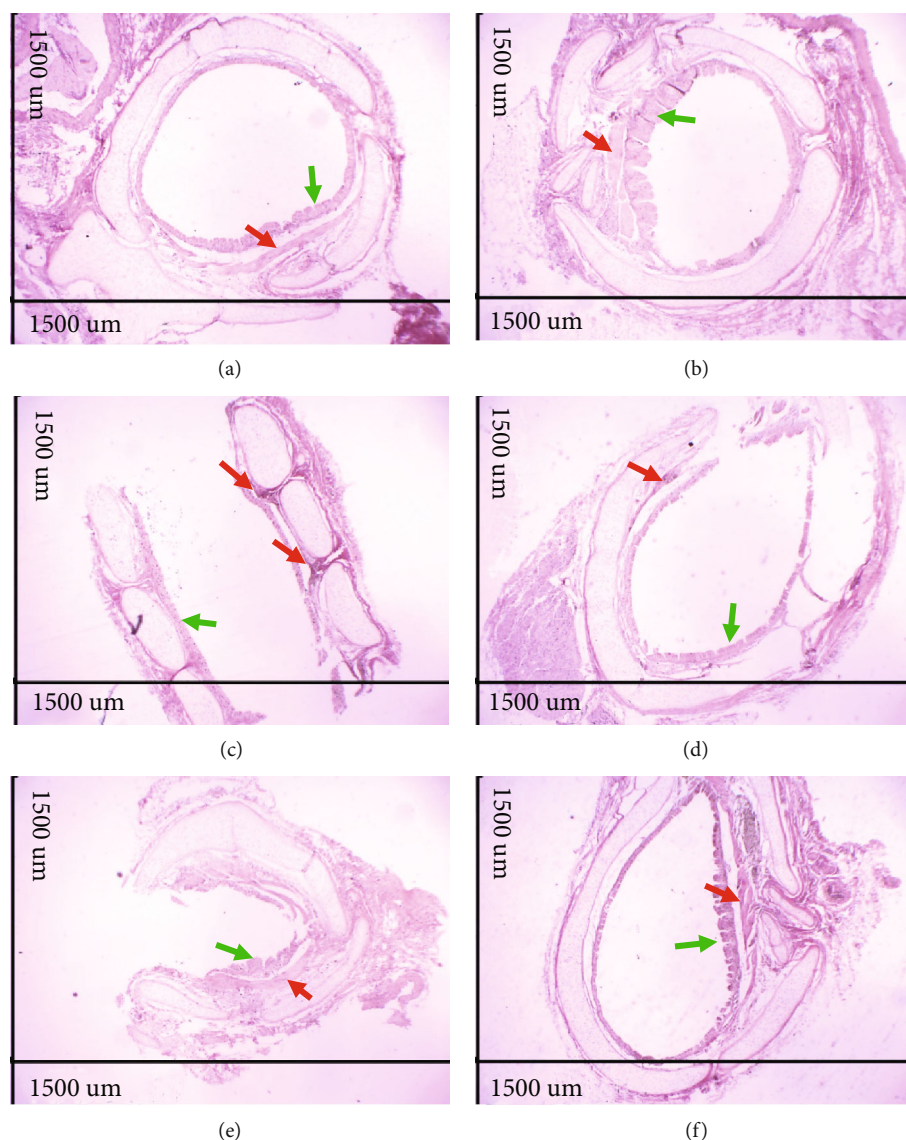


FIGURE 5: Photomicrographs of extrapulmonary bronchi of guinea pigs from Ctrl (a), Asth (b), Asth+Dexa (c), Asth+VCO1 (d), Asth+VCO2 (e), and Asth+VCO4 groups (f) showing the epithelium and smooth muscle. Smooth bronchial muscle (red arrows), epithelium and hyperplasia (green arrows). HE, A.T. $\times 40$, 1500 μm .

4. Discussion

In this study, we have demonstrated for the first time a preventive effect of virgin coconut oil supplementation on the airway hyperactivity and oxidative damage promoted by chronic allergic lung inflammation, a model that mimics the pathologic alterations of asthma. It was shown that this prevention was obtained by increasing the pulmonary antioxidant defenses and impairing the nitric oxide-peroxynitrite-isoprostanes pathway.

Despite the large number of animal models that reproduce the characteristics of allergic asthma described in the literature, these studies have not led to new therapies for the growing number of asthmatic patients [35]. In view of this scenario, new therapeutic approaches are necessary that limit or at least make the acute attacks of asthmatic patients less frequent. In this context, it inserts virgin coconut oil, a

product that has been widely used in food and industry and whose consumption has been growing mainly due to its beneficial activity on the lipid profile [36, 37] and the reduction of body fat [38, 39].

In this study, the characterization of the fatty acid profile and the chemical characterization of the virgin coconut oil were carried out in order to attest its quality. In the characterization of the fatty acid profile by gas chromatography (Supplementary data (available here)), the total fatty acids of the oil is mostly saturated (94.27%), followed by monounsaturated (3.99%) and polyunsaturated (1.68%). The major fatty acid in the sample was the lauric acid (66.96%), followed by myristic acid (18.90%), both medium chain, according to literature data, which point to virgin coconut oil as a “lauric oil”, due to its high content of this fatty acid [40].

In the chemical analysis, the acidity index of virgin coconut oil was relatively low, indicating the good quality

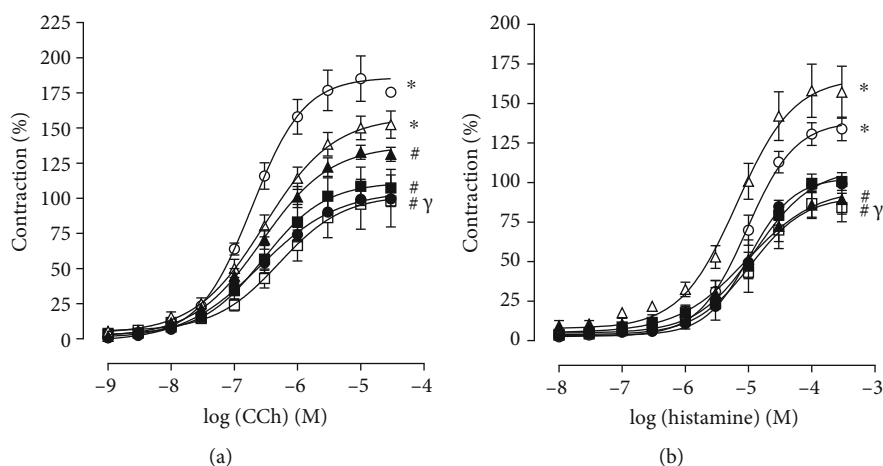


FIGURE 6: Cumulative concentration-response curves to CCh (a) and histamine (b) in guinea pigs trachea from Ctrl (black circle), Asth (white circle), Asth + Dexa (black triangle), Asth + VCO1 (white triangle), Asth + VCO2 (black square) and Asth + VCO4 groups (white square). The symbols and vertical bars represent the mean and S.E.M., respectively ($n = 5$). One-way ANOVA followed by Tukey's post-test: * $p < 0.05$ (Ctrl vs. other groups), # $p < 0.05$ (Asth vs. other groups), and $\gamma p < 0.05$ (Asth+VCO4 vs. Asth+VCO1).

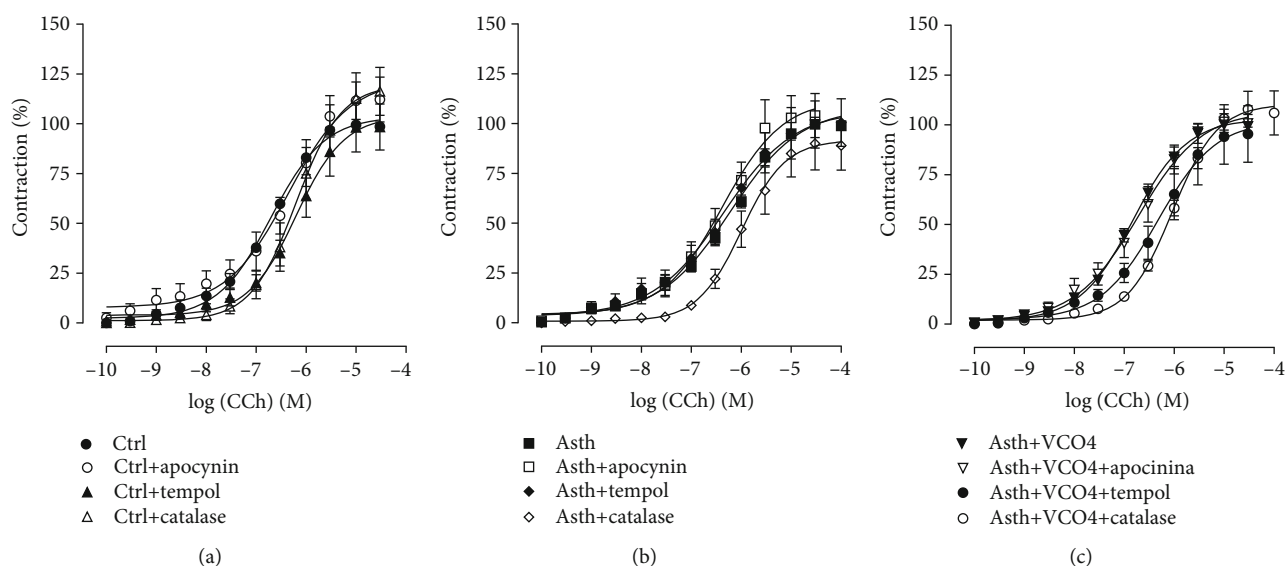


FIGURE 7: Cumulative concentration-response curves to CCh in guinea pigs' trachea from Ctrl (a), Asth (b), and Asth+VCO4 groups (c), in the absence and presence of apocynin, tempol, or catalase. The symbols and vertical bars represent the mean and S.E.M., respectively (s).

of the oil, in agreement with the established by the Technical Regulation for vegetable oils and fats [41] and by the Standard for Named Vegetable Oils of FAO/UN, which establish a maximum absolute value of 4.0 mg KOH/g oil for cold pressed oils and [41] or virgin oils [42]. The peroxide index showed that the levels of peroxides in the sample of virgin coconut oil are in accordance with ANVISA [41] and FAO/UN standards [42], which determine maximum levels of 15 meq/kg of oil, for cold pressed and unrefined (or virgin) oils. Additionally, the saponification index was slightly below the range determined by the international regulatory agency [42] which establishes a value between 248 and 265 mg KOH/g oil. This can be explained by the high content of lauric acid, higher than that established by international standards, since this fatty

acid is medium chain, which contributes to reduce the saponification index [42].

Virgin coconut oil has higher amounts of minor constituents like polyphenols and tocotrienols than coconut oil obtained by other methods. Additionally, it is described as antioxidant activity for these nutraceuticals from unsaponifiable fractions of the coconut oil [4, 40]. So, it is reasonable to suppose that these compounds also play a role as anti-inflammatory.

After characterization of the virgin coconut oil, we proceeded with the evaluation of its effect by food supplementation in a model of chronic allergic lung inflammation [19], based on prolonged exposure of guinea pigs to ovalbumin at increasing inhaled concentrations for four weeks at short intervals, in order to evaluate a possible modulating effect

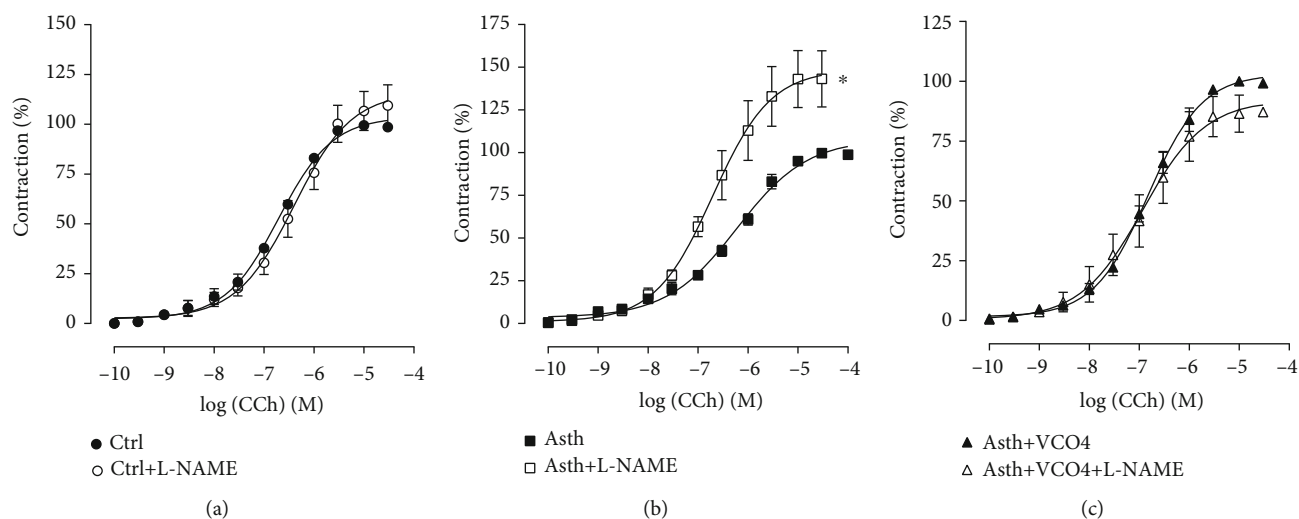


FIGURE 8: Cumulative concentration-response curves to CCh in guinea pigs' trachea from Ctrl (a), Asth (b), and Asth+VCO4 groups (c), in the absence and presence of L-NAME. The symbols and vertical bars represent the mean and S.E.M., respectively ($n = 5$). Student's *t*-test: * $p < 0.05$ (Asth+L-NAME vs. Asth).

of virgin coconut oil on the pathophysiological mechanisms of asthma, both in the light of the chronic inflammatory process and bronchial hyperactivity.

Through the morphological analysis (Figures 2–3), the chronic allergic lung inflammation promotes a peribronchial infiltrate of inflammatory cells, in addition to some characteristics of the tissue remodeling, namely, hyperplasia of airway epithelial cells and thickening of the bronchial smooth muscle layer by a process of hyperplasia and/or hypertrophy. These findings are in agreement with what occurs in allergic asthma in humans, in which the remodeling process promotes the changes observed in the lungs of the guinea pigs [43–45].

Treatment with dexamethasone, as well as the supplementation with the virgin coconut oil (especially at 4 g/kg dose), reduced the migration of inflammatory cells to the pulmonary interstitium and to the peribronchial region. In addition, there was a reduction of epithelial hyperplasia, in the same proportion for both dexamethasone and three doses of the oil, and a prevention of smooth muscle thickening, being the dose of 1 g/kg more effective for this parameter (Figures 2–3). Thus, it is suggested that the effect of the oil is mainly due to an attenuation of the inflammatory process, rather than its own action on the bronchial smooth muscle and epithelial hyperplasia, which act through the release of cytokines, growth factors, and contractile mediators to promote the smooth muscle contractility characteristic of asthmatic crisis [46–48].

The effectiveness of induction of pulmonary inflammation was observed *in vitro* by the Schultz-Dale reaction, in which the smooth muscle of an antigenically sensitized animal contracted after reexposure to this antigen by the release of contractile mediators by the cells of the microenvironment [24; 25]. The fact that guinea pigs with pulmonary inflammation, the Asth group, presented a significant contractile response to OVA, unlike the Ctrl group, confirmed the sensitization process. This data is supported by previous

studies, which showed that the trachea of asthmatic guinea pigs contracts in response to antigenic stimulation *in vitro* [49–51].

Dexamethasone-treated guinea pigs responded similarly to those with pulmonary inflammation upon stimulation with OVA. Although controversial, data in the literature show that corticosteroids play an important role in containing the inflammatory process, while its role on smooth muscle is still uncertain [23]. In animals supplemented with the virgin coconut oil, it was observed that, at doses of 1 and 2 g/kg, there was no change in the contractile response of the trachea, while the dose of 4 g/kg reduced the contraction by about 60% in relation to the animals with pulmonary inflammation. These data indicate that the coconut oil may partially inhibit the release of contractile factors by OVA-stimulated immune cells or negatively modulate smooth muscle contractility to reduce the bronchoconstriction observed in asthma.

In view of the primary role of smooth muscle in bronchial hyperresponsiveness, this study investigated the reactivity of guinea pig trachea in response to contractile and relaxing stimuli. An increase in the contractile reactivity of the trachea of guinea pigs with pulmonary inflammation, the Asth group, was observed in relation to nonsensitized animals, compared to CCh (Figure 6(a)) and histamine (Figure 6(b)), indicating a participation of the mechanical drug component in hypercontractility of the guinea pig trachea in pulmonary inflammation. However, it was observed that dexamethasone reversed the contractile response of the trachea to both CCh (Figure 6(a)) and histamine (Figure 6(b)), as observed by the reduction of the efficacy of these two agonists.

Supplementation with the virgin coconut oil at 1 g/kg did not prevent contractile hyperactivity of the guinea pig trachea with pulmonary inflammation against CCh (Figure 7(a)) or histamine (Figure 6(a)) but prevented CCh at doses of 2 and 4 g/kg and histamine at only the highest dose tested (Figures 6(a) and 6(b)). These results correlate with that observed for OVA stimulation, whose contraction

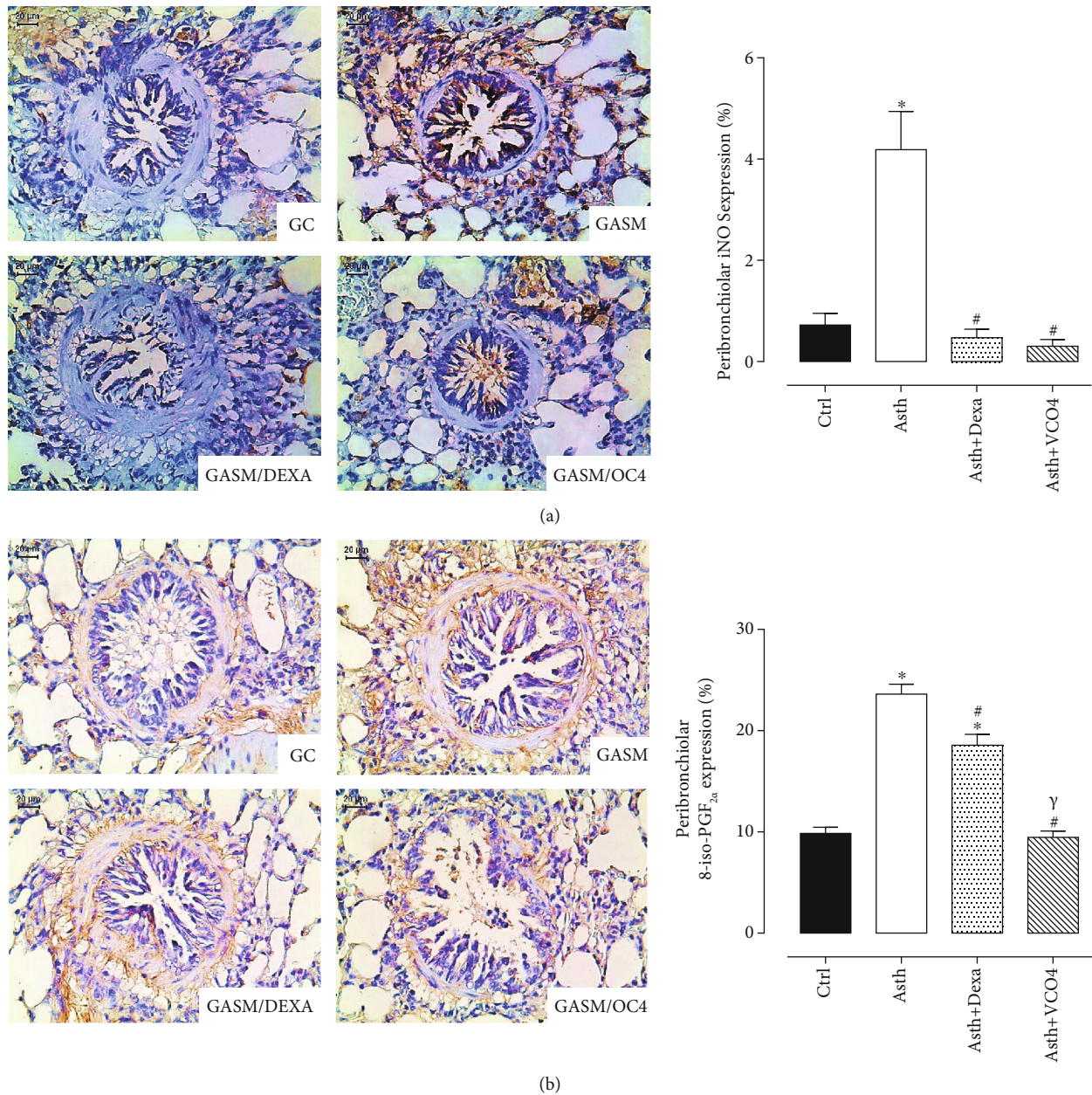


FIGURE 9: Representative photomicrographs of airway stained with immunohistochemistry to detect iNOS (a) and isoprostane (b) in Ctrl, Asth, Asth+Dexa, and Asth+VCO4 experimental groups, and the graphs representing the mean and S.E.M. of each group for iNOS and isoprostane expression in the peribronchiolar wall. ANOVA followed by Tukey post-test: * $p < 0.05$ (Ctrl vs. all groups), # $p < 0.05$ (Asth vs. all groups), § (Asth+Dexa vs. Asth+VCO4).

amplitude was reduced by the dose of 4 g/kg of virgin coconut oil. These data point to a possible negative modulatory effect on the contractile mechanisms that have been altered by pulmonary inflammation, especially the expression of muscarinic and histaminergic receptors, as well as the proteins of its downstream pathways of intracellular signaling.

Asthma is characterized by an overload of reactive oxygen species, which causes oxidative stress and changes in the functions of various components of the respiratory system [52, 53]. Several works have reported the effects of ROS on the smooth muscle functioning of the airways. Hydrogen peroxide and increased oxygen levels induce contraction in the guinea pig

trachea [54]. In addition to their direct effects, ROS also influence airway reactivity to contractile and relaxing agonists, highlighting the increase in the contractile response to acetylcholine and methacholine [55] and to histamine [56].

In view of this, it was investigated the contribution of ROS in CCh-mediated contraction in trachea of guinea pigs with and without pulmonary inflammation. It was observed that apocynin, a NADPH oxidase inhibitor, did not alter the cumulative curve to CCh, in guinea pig trachea preparations of Ctrl, Asth, and Asth+VCO4 (Figures 7(a)–7(c)). This data indicates that superoxide anion from NADPH oxidase plays no important role in the modulation of

contractile tone of the guinea pig trachea regardless of whether or not there is a picture of allergic pulmonary inflammation and that coconut oil also does not alter this ROS formation pathway.

Differently, SOD mimetic tempol reduced the contractile potency of CCh in animals without pulmonary inflammation, but not in animals with inflamed lungs of the Asth group (Figures 7(a) and 7(b)). Similar to the Asth group, in the Asth+VCO4 group, the potency of CCh was not reduced by tempol (Figure 7(c)), therefore indicating that the superoxide anion is increased in asthmatic animals once the tempol was unable to prevent the action of this anion in the tracheal smooth muscle, but that this increase would occur through pathways independent of NADPH oxidase, such as xanthine oxidase and decoupled eNOS, also responsible for the formation of superoxide anion.

Catalase, an enzyme that converts hydrogen peroxide into water and molecular oxygen [54], reduced the contractile potency of CCh by about 4-fold in the Ctrl group; in the Asth group, the potency of CCh was not altered (Figures 8(a) and 8(b)), indicating an increase in H₂O₂ production triggered by the inflammatory process, reflecting the inability of catalase to reduce the levels of ROS. Interestingly, in animals with lung inflammation supplemented with the virgin coconut oil, there was a strong prevention of the formation of this free radical, since the contractile potency of CCh was reduced by 6.6-fold in the presence of catalase (Figure 7(c)). Thus, it is suggested that the coconut oil promotes its antioxidant effect in the lungs of guinea pigs with lung inflammation by reducing not the formation or clearance of superoxide anion, but the damaging effects of hydrogen peroxide on smooth muscle contractility.

Another important mediator of the contractile and relaxing reactivity of smooth muscle, in general, is NO, also produced by the tracheal and bronchial epithelium, as well as other sources such as nitrergic neurons, inflammatory cells, and smooth muscle itself [57].

The respiratory system presents the constitutive isoforms of NOS both in neurons iNANC (nNOS) and endothelium of pulmonary vessels and tracheobronchial epithelium (eNOS), involved in the regulation of airway tonus [58]. High concentrations of NO produced from iNOS have been considered to be damaging to the airways [58], since their effects are associated with the formation of the peroxynitrite free radical [56], having a strong correlation between NO levels, eosinophilia, and airway hyperresponsiveness [59, 60].

In view of this premise, it was evidenced that, while the pretreatment with the NOS inhibitor (L-NAME) did not alter the curve to CCh in the animals of the Ctrl group (Figure 8(a)), in the Asth group, both efficacy and potency of CCh were increased (Figure 8(b)). Therefore, it is assumed that, in nonasthmatic animals, there is no tonic action of NO on airway contractility, different from that observed in animals with pulmonary inflammation. It is assumed that L-NAME blocks mostly to eNOS, and little to iNOS, through which NO is predominantly formed in the Asth group, and in which eNOS is deficient.

Interestingly, in the Asth+VCO4, L-NAME did not alter the CCh contraction curve (Figure 8(c)), similar to that

observed in the Ctrl group, indicating a reversibility in NO signaling promoted by the virgin coconut oil. Since the oil also had a beneficial effect on oxidative stress, it is possible to suggest a cascade effect promoted by this supplementation as the reduction in ROS and NO formation, via iNOS, with a consequent decrease lipid peroxidation.

These assumptions were confirmed by immunohistochemical data, which demonstrated that pulmonary inflammation promoted an increase in iNOS peribronchiolar expression, while dexamethasone treatment or supplementation with virgin coconut oil reduced its levels (Figure 9(a)), confirming its antioxidant protective effect for airways during asthma.

In view of the probable role of oxidative stress as a trigger for the alterations triggered by pulmonary inflammation, it was decided to evaluate the antioxidant defense in the pulmonary tissue and plasma of the guinea pigs, in order to corroborate the observed functional data. Therefore, while plasma antioxidant capacity remained unchanged in all groups, in the lung tissue, the antioxidant capacity was reduced in the Asth group, and supplementation with virgin coconut oil at doses of 2 and 4/kg increased the antioxidant capacity. However, 1 g/kg of this oil or dexamethasone treatment did not prevent this reduction.

In addition, in animals with lung inflammation, immunohistochemical staining demonstrated an increase in the levels of the 8-iso-PGF2 α , a pro-contractile and marker of lipid peroxidation, generated as a result of nonenzymatic peroxidation of arachidonic acid in membrane phospholipids by ROS [61], followed by its reduction by dexamethasone treatment or supplementation with VCO (Figure 9(b)).

The reduction in antioxidant capacity is corroborated by studies that show similar results with other animal models of allergic asthma [62–64]. In addition, the effect observed for the coconut oil is in agreement with data from the literature, which point out its antioxidant effect as one of the benefits promoted by its supplementation [9, 40, 65–68].

In conclusion, we have shown for the first time that supplementation with virgin coconut oil emerges as promising, in light of its potential role as a functional food, in the adjuvant therapy of chronic allergic lung inflammation, especially by its actions on the inflammatory and oxidative processes of the airways that characterize asthma.

Data Availability

No data were used to support this study.

Conflicts of Interest

The authors declare that there is no conflict of interest regarding the publication of this paper.

Acknowledgments

The authors thank José Crispim Duarte and Luís C. Silva for providing technical assistance. The authors thank Coordenação de Aperfeiçoamento de Pessoal de Nível Superior

(CAPES) and Conselho Nacional de Desenvolvimento Científico e Tecnológico (CNPq) for financial support.

Supplementary Materials

Supplementary material contains representative figure of the gas chromatography of virgin coconut oil. Also includes the tables of the fatty acid content (Table 1) and the chemical index of acidity, peroxide, and saponification (Table 2) of the virgin coconut oil. (*Supplementary Materials*)

References

- [1] Brazil Ministério da Saúde and Agência Nacional de Vigilância Sanitária, *Resolução n° 18, de 30 de abril de 1999. Aprova o Regulamento Técnico que estabelece as diretrizes básicas para análise e comprovação de propriedades funcionais e ou de saúde alegadas em rotulagem de alimentos, constante do anexo desta portaria*, Diário Oficial da União, Brasília, DF, 1999.
- [2] Brazil Ministério da Saúde and Agência Nacional de Vigilância Sanitária, *Suplementos alimentares: Documento de base para discussão regulatória*, Ministério da Saúde, Brasília-DF, Brazil, 2017.
- [3] NMCE, *Report on copra*, National multi-commodity Exchange of India Limited, 2007.
- [4] V. P. Dia, V. V. Garcia, R. C. Mabesa, and E. M. Tecson-Mendoza, “Comparative Physicochemical Characteristics of Virgin Coconut Oil Produced by Different Methods,” *The Philippine Agricultural Scientist*, vol. 88, pp. 462–475, 2005.
- [5] M. Debmandal and S. Mandal, “Coconut (*Cocos nucifera* L.: Arecaceae): in health promotion and disease prevention,” *Asian Pacific Journal of Tropical Medicine*, vol. 4, no. 3, pp. 241–247, 2011.
- [6] P. Chandrashekar, B. R. Lokesh, and A. G. G. Krishna, “Hypolipidemic effect of blends of coconut oil with soybean oil or sunflower oil in experimental rats,” *Food Chemistry*, vol. 123, no. 3, pp. 728–733, 2010.
- [7] M. Yousefi, L. Nateghi, and K. Rezaee, “Investigation of physiochemical properties, fatty acids profile and sterol content in Malaysian coconut and palm oil,” *Annals of Biological Research*, vol. 4, pp. 214–219, 2013.
- [8] Z. A. Zakaria, M. N. Somchit, A. M. Mat Jais, L. K. Teh, M. Z. Salleh, and K. Long, “*In vivo* antinociceptive and anti-inflammatory activities of dried and fermented processed virgin coconut oil,” *Medical Principles and Practice*, vol. 20, no. 3, pp. 231–236, 2011.
- [9] N. F. B. Alves, S. K. P. Porpino, M. M. O. Monteiro, E. R. M. Gomes, and V. A. Braga, “Coconut oil supplementation and physical exercise improves baroreflex sensitivity and oxidative stress in hypertensive rats,” *Applied Physiology, Nutrition, and Metabolism*, vol. 40, no. 4, pp. 393–400, 2015.
- [10] A. Inayat, S. A. Baig, and T. Baqai, “Does coconut oil reduce the risk of coronary artery diseases?,” *Journal of the Pakistan Medical Association*, vol. 63, no. 6, p. 797, 2013.
- [11] Y. Kamisah, V. Periyah, K. T. Lee et al., “Cardioprotective effect of virgin coconut oil in heated palm oil diet-induced hypertensive rats,” *Pharmaceutical Biology*, vol. 53, no. 9, pp. 1243–1249, 2015.
- [12] B. N. Lambrecht and H. Hammad, “The immunology of asthma,” *Nature Immunology*, vol. 16, no. 1, pp. 45–56, 2015.
- [13] C. M. Sherwin, S. B. Christiansen, I. J. Duncan et al., “Guidelines for the ethical use of animals in applied ethology studies,” *Applied Animal Behaviour Science*, vol. 81, no. 3, pp. 291–305, 2003.
- [14] Brazil Ministério da Ciência, Tecnologia e Inovação, *Conselho Nacional de Controle de Experimentação Animal. Guia Brasileiro de Produção, Manutenção ou Utilização de Animais em Atividades de Ensino ou Pesquisa Científica: fascículo 1: introdução geral*, Ministério da Ciência, Tecnologia e Inovação, Brasília-DF, Brazil, 2016.
- [15] O. Zenebon, N. S. Pascuet, and P. Tiglea, *Métodos Físico-Químicos para Análise de Alimentos*, Instituto Adolfo Lutz, São Paulo, 2008.
- [16] I. F. Tibério, G. M. Turco, E. A. Leick-Maldonado et al., “Effects of neurokinin depletion on airway inflammation induced by chronic antigen exposure,” *American Journal of Respiratory and Critical Care Medicine*, vol. 155, no. 5, pp. 1739–1747, 1997.
- [17] P. Angeli, C. M. Prado, D. G. Xisto et al., “Effects of chronic-NAME treatment lung tissue mechanics, eosinophilic and extracellular matrix responses induced by chronic pulmonary inflammation,” *American Journal of Physiology-Lung Cellular and Molecular Physiology*, vol. 294, no. 6, pp. L1197–L1205, 2008.
- [18] P. A. Pigati, R. F. Righetti, S. S. Poessa et al., “Y-27632 is associated with corticosteroid-potentiated control of pulmonary remodeling and inflammation in Guinea pigs with chronic allergic inflammation,” *BMC Pulmonary Medicine*, vol. 15, no. 1, pp. 85–100, 2015.
- [19] L. H. C. Vasconcelos, M. C. C. Silva, A. C. Costa et al., “A Guinea pig model of airway smooth muscle hyperreactivity induced by chronic allergic lung inflammation: contribution of epithelium and oxidative stress,” *Frontiers in Pharmacology*, vol. 9, pp. 1–15, 2019.
- [20] S. Intahphuak, P. Khonsung, and A. Panthong, “Anti-inflammatory, analgesic, and antipyretic activities of virgin coconut oil,” *Pharmaceutical Biology*, vol. 48, no. 2, pp. 151–157, 2010.
- [21] M. Nandakumaran, E. Angelaki, N. Al-Azemi, H. Al-Sarraf, and E. Al-Saleh, “Influence of coconut oil administration on some hematologic and metabolic parameters in pregnant rats,” *The Journal of Maternal-Fetal & Neonatal Medicine*, vol. 24, no. 10, pp. 1254–1258, 2011.
- [22] M. H. A. Vasconcelos, *Avaliação da qualidade física e química de óleo de coco (Cocos nucifera L.) e seus efeitos sobre os parâmetros lipídicos e oxidativos em ratos dislipidêmicos sedentários e exercitados*, 141 f. Pós-graduação em Ciência e Tecnologia de Alimentos (Dissertação) – Centro de Tecnologia, Universidade Federal da Paraíba – UFPB, 2015.
- [23] E. A. Leick-Maldonado, F. U. Kay, M. C. Leonhardt et al., “Comparison of glucocorticoid and cysteinyl leukotriene receptor antagonist treatments in an experimental model of chronic airway inflammation in Guinea-pigs,” *Clinical and Experimental Allergy*, vol. 34, no. 1, pp. 145–152, 2004.
- [24] E. Tschirhart, N. Frossard, C. Bertrand, and Y. Landry, “Arachidonic acid metabolites and airway epithelium-dependent relaxant factor,” *Journal of Pharmacology and Experimental Therapeutics*, vol. 243, no. 1, pp. 310–316, 1987.
- [25] W. H. Schultz, “Physiological studies in anaphylaxis 1. The reaction of smooth muscle of the guineapig sensitized with horse serum,” *The Journal of Pharmacology and Experimental Therapeutics*, vol. 1, pp. 549–567, 1910.

- [26] H. H. Dale, "The anaphylactic reaction of plain muscle in the Guinea-pig," *Journal of Pharmacology and Experimental Therapeutics*, vol. 4, pp. 167–223, 1913.
- [27] N. Chand and P. Eyre, "The Schultz-Dale reaction: a review," *Agents & Actions*, vol. 8, no. 3, pp. 171–184, 1978.
- [28] T. R. Jones, L. Charette, and D. Denis, "Antigen-induced contraction of guinea-pig isolated trachea: studies with novel inhibitors and antagonists of arachidonic acid metabolites," *British Journal of Pharmacology*, vol. 95, no. 1, pp. 309–321, 1988.
- [29] N. Ouedraogo and E. Roux, "Physiology of airway smooth muscle contraction: an overview," *Journal of Pulmonary & Respiratory Medicine*, vol. 4, no. 6, p. 2, 2014.
- [30] A. Sutcliffe, F. Hollins, E. Gomez et al., "Increased nicotinamide adenine dinucleotide phosphate oxidase 4 expression mediates intrinsic airway smooth muscle hypercontractility in asthma," *American Journal of Respiratory and Critical Care Medicine*, vol. 185, no. 3, pp. 267–274, 2012.
- [31] J. de Boer, H. Meurs, L. Flendrig, M. Koopal, and J. Zaagsma, "Role of nitric oxide and superoxide in allergen-induced airway hyperreactivity after the late asthmatic reaction in guinea-pigs," *British Journal of Pharmacology*, vol. 133, no. 8, pp. 1235–1242, 2001.
- [32] O. Y. Okafor, O. L. Erukainure, J. A. Ajiboye, R. O. Adejobi, F. O. Owolabi, and S. B. Kosoko, "Modulatory effect of pineapple peel extract on lipid peroxidation, catalase activity and hepatic biomarker levels in blood plasma of alcohol-induced oxidative stressed rats," *Asian Pacific Journal of Tropical Biomedicine*, vol. 1, no. 1, pp. 12–14, 2011.
- [33] A. S. da Silva, F. C. Paim, R. C. V. Santos et al., "Nitric oxide level, protein oxidation and antioxidant enzymes in rats infected by *Trypanosoma evansi*," *Experimental Parasitology*, vol. 132, no. 2, pp. 166–170, 2012.
- [34] R. R. Neubig, M. Spedding, T. Kenakin, A. Christopoulos, and International Union of Pharmacology Committee on Receptor Nomenclature and Drug Classification, "International Union of Pharmacology Committee on Receptor Nomenclature and Drug Classification. XXXVIII. Update on terms and symbols in quantitative pharmacology," *Pharmacological Reviews*, vol. 55, no. 4, pp. 597–606, 2003.
- [35] C. M. Lloyd and E. M. Hessel, "Functions of T cells in asthma: more than just T_H2 cells," *Nature Reviews Immunology*, vol. 10, no. 12, pp. 838–848, 2010.
- [36] K. G. Nevin and T. Rajamohan, "Beneficial effects of virgin coconut oil on lipid parameters and *in vitro* LDL oxidation," *Clinical Biochemistry*, vol. 37, no. 9, pp. 830–835, 2004.
- [37] A. B. Feranil, P. L. Duazo, C. W. Kuzawa, and L. S. Adair, "Coconut oil is associated with a beneficial lipid profile in pre-menopausal women in the Philippines," *Asia Pacific Journal of Clinical Nutrition*, vol. 20, no. 2, pp. 190–195, 2011.
- [38] M. Kasai, N. Nosaka, H. Maki et al., "Effect of dietary medium- and long-chain triacylglycerols (MLCT) on accumulation of body fat in healthy humans," *Asia Pacific Journal of Clinical Nutrition*, vol. 12, no. 2, pp. 151–160, 2003.
- [39] M. L. Assunção, H. S. Ferreira, A. F. dos Santos, C. R. Cabral, and T. M. M. T. Florêncio, "Effects of dietary coconut oil on the biochemical and anthropometric profiles of women presenting abdominal obesity," *Lipids*, vol. 44, no. 7, pp. 593–601, 2009.
- [40] A. M. Marina, Y. B. Che Man, S. A. H. Nazimah, and I. Amin, "Antioxidant capacity and phenolic acids of virgin coconut oil," *International Journal of Food Sciences and Nutrition*, vol. 60, pp. 114–123, 2009.
- [41] Brazil Ministério da Saúde and Agência Nacional de Vigilância Sanitária, *Resolução de Diretoria Colegiada (RDC) no. 270 de 22 de setembro de 2005. Regulamento técnico para óleos vegetais, gorduras e creme vegetal*, Diário Oficial da República Federativa do Brasil, Brasília – DF, Brazil, 2005.
- [42] Codex Alimentarius Commission, *Guidelines for vitamin and mineral food supplements (CAC/GL 55 - 2005)*, Food and Agricultural Organization of the United Nations and the World Health Organization, 2005.
- [43] T. Aikawa, S. Shimura, H. Sasaki, M. Ebina, and T. Takishima, "Marked goblet cell hyperplasia with mucus accumulation in the airways of patients who died of severe acute asthma attack," *Chest*, vol. 101, no. 4, pp. 916–921, 1992.
- [44] N. Carroll, J. Elliot, A. Morton, and A. James, "The structure of large and small airways in nonfatal and fatal asthma," *American Review of Respiratory Disease*, vol. 147, no. 2, pp. 405–410, 1993.
- [45] L. Cohen, X. E. J. Tarsi et al., "Epithelial cell proliferation contributes to airway remodeling in severe asthma," *American Journal of Respiratory and Critical Care Medicine*, vol. 176, no. 2, pp. 138–145, 2007.
- [46] D. D. Metcalfe, D. Baram, and Y. A. Mekori, "Mast cells," *Physiological Reviews*, vol. 77, no. 4, pp. 1033–1079, 1997.
- [47] F. Galli, A. Battistoni, R. Gambari et al., "Oxidative stress and antioxidant therapy in cystic fibrosis," *Biochimica et Biophysica Acta (BBA) - Molecular Basis of Disease*, vol. 1822, no. 5, pp. 690–713, 2012.
- [48] N. A. Barrett and K. F. Austen, "Innate cells and T helper 2 cell immunity in airway inflammation," *Immunity*, vol. 31, no. 3, pp. 425–437, 2009.
- [49] J. F. Souhrada and D. W. Dickey, "Effect of antigen challenge on sensitized guinea pig trachea," *Respiration Physiology*, vol. 27, no. 2, pp. 241–251, 1976.
- [50] A. Shaukat, S. Tariq, M. Sharif, and M. H. Najmi, "Effect of nebulolol on tone of tracheal muscle of guinea pig," *Journal of Ayub Medical College Abbottabad*, vol. 27, no. 3, pp. 527–529, 2015.
- [51] I. R. R. Martins, *A ação relaxante de novos derivados N-sulfonilidrazônicos do LASSBio-448, inibidores de PDE4, em um modelo de asma alérgica em cobaias: caracterização funcional do mecanismo relaxante do LASSBio-1847*, vol. 2016, Tese (doutorado em Produtos Naturais e Sintéticos Bioativos) – Centro de Ciências da Saúde, Universidade Federal da Paraíba, João Pessoa, 2016.
- [52] K. Morwood, D. Gillis, W. Smith, and F. Kette, "Aspirin-sensitive asthma," *Internal Medicine Journal*, vol. 35, no. 4, pp. 240–246, 2005.
- [53] A. Bishopp, R. Sathyamurthy, S. Manney, C. Webster, M. T. Krishna, and A. H. Mansur, "Biomarkers of oxidative stress and antioxidants in severe asthma: a prospective case-control study," *Annals of Allergy, Asthma & Immunology*, vol. 118, no. 4, pp. 445–451, 2017.
- [54] K. J. Rhoden and P. J. Barnes, "Effect of hydrogen peroxide on guinea-pig tracheal smooth muscle *in vitro*: role of cyclooxygenase and airway epithelium," *British Journal of Pharmacology*, vol. 98, no. 1, pp. 325–330, 1989.
- [55] P. A. J. Henricks and F. P. Nijkamp, "Reactive oxygen species as mediators in asthma," *Pulmonary Pharmacology & Therapeutics*, vol. 14, no. 6, pp. 409–421, 2001.

- [56] Sadeghi-Hashjin, Folkerts, Henricks, Muijsers, and Nijkamp, "Peroxyne nitrite in airway diseases," *Clinical and Experimental Allergy*, vol. 28, no. 12, pp. 1464–1473, 1998.
- [57] F. L. M. Ricciardolo, "Multiple roles of nitric oxide in the airways," *Thorax*, vol. 58, no. 2, pp. 175–182, 2003.
- [58] F. L. M. Ricciardolo, P. J. Sterk, B. Gaston, and G. Folkerts, "Nitric oxide in health and disease of the respiratory system," *Physiological Reviews*, vol. 84, no. 3, pp. 731–765, 2004.
- [59] L. J. Dupont, F. Rochette, M. G. Demedts, and G. M. Verleden, "Exhaled nitric oxide correlates with airway hyperresponsiveness in steroid-naïve patients with mild asthma," *American Journal of Respiratory and Critical Care Medicine*, vol. 157, no. 3, pp. 894–898, 1998.
- [60] A. Jatakanon, S. Lim, S. A. Kharitonov, K. F. Chung, and P. J. Barnes, "Correlation between exhaled nitric oxide, sputum eosinophils, and methacholine responsiveness in patients with mild asthma," *Thorax*, vol. 53, no. 2, pp. 91–95, 1998.
- [61] Y. Bossé, "Endocrine regulation of airway contractility is overlooked," *Journal of Endocrinology*, vol. 222, no. 2, pp. R61–R73, 2014.
- [62] H. R. Bao, X. J. Liu, Y. L. Li, X. Men, and X. L. Zeng, "Sinomenine attenuates airway inflammation and remodeling in a mouse model of asthma," *Molecular Medicine Reports*, vol. 13, no. 3, pp. 2415–2422, 2016.
- [63] N. Chekchaki, T. Khaldi, Z. Rouibah et al., "Anti-inflammatory and antioxidant effects of two extracts from *Pistacia lentiscus* in liver and erythrocytes, in an experimental model of asthma," *Methods*, vol. 18, p. 19, 2017.
- [64] R. T. Nesi, E. Kennedy-Feitosa, M. Lanzetti et al., "Inflammatory and Oxidative Stress Markers in Experimental Allergic Asthma," *Inflammation*, vol. 40, no. 4, pp. 1166–1176, 2017.
- [65] K. G. Nevin and T. Rajamohan, "Virgin coconut oil supplemented diet increases the antioxidant status in rats," *Food Chemistry*, vol. 99, no. 2, pp. 260–266, 2006.
- [66] M. A. Abujazia, N. Muhammad, A. N. Shuid, and I. N. Soelaiman, "The effects of virgin coconut oil on bone oxidative status in ovariectomised rat," *Evidence-based Complementary and Alternative Medicine*, vol. 2012, 6 pages, 2012.
- [67] S. Arunima and T. Rajamohan, "Effect of virgin coconut oil enriched diet on the antioxidant status and paraoxonase 1 activity in ameliorating the oxidative stress in rats – a comparative study," *Food & Function*, vol. 4, no. 9, pp. 1402–1409, 2013.
- [68] A. Vysakh, M. Ratheesh, T. P. Rajmohanan et al., "Polyphenolics isolated from virgin coconut oil inhibits adjuvant induced arthritis in rats through antioxidant and anti-inflammatory action," *International Immunopharmacology*, vol. 20, no. 1, pp. 124–130, 2014.

Research Article

Melatonin Ameliorates MI-Induced Cardiac Remodeling and Apoptosis through a JNK/p53-Dependent Mechanism in Diabetes Mellitus

Linhe Lu ¹, Jipeng Ma,¹ Mingming Sun,² Xiaowu Wang,¹ Erhe Gao,³ Lintao Lu ⁴,
Jun Ren ², Lifang Yang ⁵, and Jian Yang ¹

¹Department of Cardiovascular Surgery, Xijing Hospital, The Air Force Medical University, 710032, China

²Center for Cardiovascular Research and Alternative Medicine, University of Wyoming, Laramie, WY 82071, USA

³Center for Translational Medicine, Lewis Katz School of Medicine at Temple University, Philadelphia, PA 19140, USA

⁴Department of Cardiology, Xijing Hospital, Air Force Medical University, Xi'an, China

⁵Department of Anesthesiology, Xi'an Children's Hospital, Xi'an 710003, China

Correspondence should be addressed to Jun Ren; jren@uwyo.edu, Lifang Yang; yanglf@fmmu.edu.cn, and Jian Yang; yangjian1212@hotmail.com

Received 29 August 2019; Revised 25 November 2019; Accepted 16 December 2019; Published 9 January 2020

Guest Editor: Bhagavatula Moorthy

Copyright © 2020 Linhe Lu et al. This is an open access article distributed under the Creative Commons Attribution License, which permits unrestricted use, distribution, and reproduction in any medium, provided the original work is properly cited.

Diabetes mellitus, a worldwide health threat, is considered an independent risk factor for cardiovascular diseases. The overall cardiovascular risk of diabetes is similar to the one having one myocardial infarction (MI) attack although the precise impact of diabetes on MI-induced myocardial anomalies remains elusive. Given that mortality following MI is much greater in diabetic patients compared to nondiabetic patients, this study was designed to examine the effect of melatonin on MI injury-induced myocardial dysfunction in diabetes. Adult mice were made diabetic using high-fat feeding and streptozotocin (100 mg/kg body weight) prior to MI and were treated with melatonin (50 mg/kg/d, p.o.) for 4 weeks prior to assessment of cardiac geometry and function. The MI procedure in diabetes displayed overt changes in cardiac geometry (chamber dilation and interstitial fibrosis) and functional anomalies (reduced fractional shortening and cardiomyocyte contractile capacity) in association with elevated c-Jun N-terminal kinase (JNK) phosphorylation and p53 level. Melatonin treatment markedly attenuated cardiac dysfunction and myocardial fibrosis in post-MI diabetic mice. Furthermore, melatonin decreased JNK phosphorylation, reduced p53 levels, and suppressed apoptosis in hearts from the post-MI diabetic group. *In vitro* findings revealed that melatonin effectively counteracted high-glucose/high fat-hypoxia-induced cardiomyocyte apoptosis and contractile dysfunction through a JNK-mediated mechanism, the effects of which were impaired by the JNK activator anisomycin. In summary, our study suggests that melatonin protects against myocardial injury in post-MI mice with diabetes, which offers a new therapeutic strategy for the management of MI-induced cardiac injury in diabetes.

1. Introduction

Type 2 diabetes mellitus (T2DM) is a major public health threat worldwide and triggers severe clinical complications such as diabetic cardiomyopathy, retinopathy, nephropathy, and neuropathy [1–4]. Importantly, it is well recognized that T2DM is an independent risk factor for coronary heart diseases [5]. Ample clinical studies have provided compelling

evidence that diabetic patients suffer from an unfavorable prognosis following myocardial infarction (MI) [6]. In particular, the 28-day mortality after MI nearly doubles in diabetic patients compared with nondiabetic patients [7]. However, despite its clinical importance, the impact of MI on myocardial geometry and function remains somewhat obscure in diabetes. Thus, it is pertinent to elucidating the underlying molecular mechanisms behind MI-induced

cardiac geometric and contractile anomalies in diabetes mellitus, in an effort to explore novel and better therapeutic options against this devastating comorbidity.

Melatonin is a hormone secreted from the pineal gland found in nearly all organisms. In addition to its well-known roles in the circadian rhythm of sleep and antioxidant regulation [8, 9], melatonin was reported to preserve liver function from streptozotocin-induced diabetes [10–12] as well as to alleviate left ventricular remodeling and cardiac dysfunction after MI through apoptosis inhibition [13–15]. Importantly, it was shown that the low level of nocturnal serum melatonin was associated with not only acute myocardial infarction but also left ventricular remodeling in patients following acute MI [16, 17]. Moreover, recent evidence suggested that melatonin dramatically attenuated post-MI injury through regulating the Notch1/Mfn2 pathway and reducing ROS generation [18–20]. Nonetheless, the possible impact of melatonin on post-MI-induced cardiac injury has not been carefully delineated in diabetes. To this end, the effect of melatonin on post-MI-induced cardiac anomalies was examined in diabetes.

Activation of the mitogen-activated protein kinase (MAPK) stress signaling has been well documented in both ischemic and diabetic heart diseases [21, 22]. MAPKs mainly are composed of three well-defined protein kinases including the extracellular signal-regulated kinases (ERKs), the c-Jun NH₂-terminal kinases (JNKs), and the p38 enzymes (p38 MAPKs), to regulate a wide array of cellular activities including mitosis, metabolism, and programmed cell death [23]. Importantly, inhibition of JNK using the JNK inhibitor SP600125 or endogenous macrophage migration inhibitory factor significantly reduced cardiac ischemia-reperfusion injury [24, 25]. Furthermore, doxorubicin-induced JNK activation provoked cardiac apoptosis and functional abnormalities [26]. A novel curcumin derivative, namely, C66, was found to attenuate diabetic cardiomyopathy through inhibition of JNK phosphorylation [27, 28]. Although JNK serves as a key player in multiple pathological settings of the heart, the function of JNK in post-MI injury with diabetes needs further elucidation.

2. Materials and Methods

2.1. Animals and Experimental Protocol. This study was performed according to the National Institutes of Health Guidelines on the Use of Laboratory Animals (National Institutes of Health Publication No. 8523, revised 1996), and experimental protocol herein was approved by the Air Force Medical University Institutional Committee on Animal Care. In brief, male C57BL/6J mice (18–22 g) at the age of 8–10 weeks were purchased from the Experimental Animal Center of the Air Force Medical University. Mice were housed with access to normal diet and water *ad libitum* at 23–25°C and were acclimatized for 1 week under a 12 hr/12 hr light/dark cycle. Mice were then randomly divided into the following groups: (I) The normal control group (CON) was fed standard chow *ad libitum* for 4 weeks. Mice were fasted overnight before they were injected intraperitoneally with an equal volume (100 μ L) of 0.1 M citrate buffer for two consecutive days.

Mice were raised for another 6 weeks after sham operation. (II) The type 2 diabetes group (T2DM) was fed high-fat diet (D12451, 45% kcal from fat, Research Diets, New Brunswick, NJ, USA) for 4 weeks prior to overnight fasting. Mice were then given 100 μ L solution of streptozotocin (S0130, Sigma-Aldrich, MO, USA, 50 mg/kg body weight/d, dissolved in 0.1 M citrate buffer, pH 4.5, i.p.) for two consecutive days. Mice were deemed diabetic with fasting plasma glucose (FPG) of >11.1 mmol/L 3 days after injection. After that, mice were randomly assigned into the following three groups: (IIa) type 2 diabetes mellitus (diabetic cardiomyopathy, DCM group) with sham operation, (IIb) type 2 diabetes mellitus with myocardial infarction surgery (diabetes with MI, DMI group), and (IIc) type 2 diabetes mellitus with myocardial infarction supplemented with melatonin (DMI supplemented with melatonin, DMI-MEL group). Melatonin (Sigma, St. Louis, MO, USA) was dissolved in absolute ethanol and then diluted in tap water (at a dose of 50 mg/kg body weight/day) [29]. Mice were given melatonin daily immediately following the myocardial infarction procedure till the end of the study. All mice in these three groups were fed high-fat diet for 2 weeks after induction of diabetes prior to the MI or sham procedure. Then, mice were continuously fed with high-fat diet for 4 weeks before sacrifice after the MI surgery or sham operation.

2.2. Determination of Blood Glucose Levels. Fasting plasma glucose levels were measured with a blood glucometer (Accu-Chek® Active, Roche Diagnostics, Mannheim, Germany) according to the manufacturer's instruction. Mouse blood was obtained from the tail vein 3 days after STZ injection. According to the previous study [30], mice with FPG > 11.1 mmol/L were confirmed for type 2 diabetes mellitus.

2.3. Myocardial Infarction Model. For the myocardial infarction model, the procedure was followed as previously described [31, 32]. In brief, male mice were anesthetized with 1.5% isoflurane by an isoflurane delivery system in the surgical plane. The whole procedure was performed in aseptic conditions, and mice were placed on a heating pad to maintain the body temperature. After a small cut on the left chest, a tiny hole was made in the fourth intercostal space. Then, the heart was squeezed out of the thoracic cavity, and the left coronary artery was ligated using a 6-0 silk suture. The heart was placed back into the intrathoracic space once the ligation was completed. The exposure time for hearts being out of the thoracic cavity was between 30 sec and 1 min. Air was evacuated out of the thoracic cavity prior to the stature of muscles and the skin. The recovery process was under 37°C in an incubator until mice were fully ambulatory. A similar procedure was repeated for the sham-operated group without ligation of the left coronary artery.

2.4. Echocardiography. Mice were anesthetized with 1–1.5% isoflurane in oxygen for two-dimensional and motion- (M-) mode echocardiographic measurements at 1 week and 4 weeks, respectively, after surgery, which was performed using the Vevo 2100 high-resolution *in vivo* imaging system

(Visual Sonics, Toronto, ON, Canada). The procedure to evaluate cardiac function was executed blindly. Left ventricular ejection fraction (LVEF) and left ventricular fractional shortening (LVFS) were measured, which were carried out from three consecutive cardiac cycles. Data was calculated on an accompanying workstation with VevoStrain software [33]. Following completion of echocardiography, mice were sacrificed before collection of hearts for further analysis.

2.5. Histopathology. Mice were anesthetized and sacrificed. Hearts were obtained and rinsed with an ice-cold PBS and were immediately fixed in 4% polyformaldehyde for 3 days. After that, tissues were immersed in ethanol solutions with various concentrations from 70% to absolute ethanol for dehydration. Then, ethanol in the tissue was displaced by xylene. Then, cardiac tissue was embedded in paraffin and cut in 3 μm sections for histopathological examination. To assess morphological changes, sections were stained with hematoxylin and eosin (H&E). Similarly, sections were stained with Masson's trichrome staining and imaged under the light microscope to evaluate the degree of myocardial interstitial fibrosis. For further analysis, 5 random fields at 200x magnification were chosen for cardiac fibrosis quantification using Image-Pro Plus software. Results were presented using the blue-stained area normalized to the total area excluding endocardial and epicardial regions or perivascular fibrosis [33].

2.6. Cell Viability Determination. The Cell Count Kit-8 (CCK-8, Dojindo, Japan) assay was used to determine the effect of melatonin (Tiancheng Biotechnology, Shanghai, China) on H9c2 cell viability and was performed according to the manufacturer's instruction. In brief, H9c2 cells were seeded into 96-well culture plates and were cultured at a density of 4×10^3 cells/well in 200 μL complete medium. Melatonin was dissolved in absolute ethanol at various levels (50 μM , 100 μM , 200 μM , and 300 μM). Vehicle control cells were cultured in DMEM supplemented with 0.1% ethanol. Each treatment group consisted of 5 parallel wells. Then, the medium was replaced after drug treatment, and 10 μL of CCK-8 solution was added to each well and incubated for 2 hr at 37°C. Subsequently, optical density (OD) was measured at a wavelength of 450 nm using a SpectraMax M5 plate reader (Molecular Devices, Sunnyvale, California, USA). Cell viability was calculated as the percentage of the absorbance of the melatonin treated/vehicle control $\times 100\%$.

2.7. Cell Culture and Treatment. H9c2 cells were cultured in Dulbecco's modified Eagle's medium (DMEM; HyClone, Logan, UT, USA) supplemented with 10% fetal bovine serum (Gibco, Carlsbad, CA, USA) with 100 U/mL streptomycin and 100 U/mL penicillin in an incubator at 95% humidity (37°C with 5% CO_2). Melatonin (Sigma-Aldrich, Merck Millipore, Darmstadt, Germany) was dissolved in ethanol first and was then diluted in DMEM (5 mM glucose). H9c2 cells were divided into five groups. Cells were cultured in normal DMEM including two groups (groups 1 and 2). In group 1 (control group, CON), cells were cultured in normal DMEM with 0.1% ethanol. In group 2 (ANI), cells were

supplemented with 5 μM anisomycin for 2 hr followed by replacement of normal DMEM and were cultured for 14 hr. To examine the effect in diabetic condition, we mimicked the pathological condition with high glucose and high fat (HG/HF, 33 mM glucose and saturated FFA palmitate (16:0, 500 μM)) [34]. In group 3 (HG/HF-hypoxia group), cells were cultured in HG/HF medium for 12 hr followed by hypoxia (5% CO_2 , 95% N_2 humidified atmosphere, yielding less than 1% O_2 concentrations) for 2 hr. In group 4 (HG/HF-hypoxia-MEL group), cells were cultured in HG/HF medium for 12 hr followed by hypoxia for 2 hr with the addition of melatonin (100 μM) at the second hour. In group 5 (HG/HF-hypoxia-MEL-ANI group), cells were cultured in HG/HF medium under hypoxia and were supplemented with 5 μM anisomycin for 2 hr prior to incubation in HG/HF medium. Following replacement with the HG/HF medium, cells were cultured for 12 hr and were subjected to hypoxic condition for 2 hr along with 100 μM melatonin. Each group consisted of 5 replicates.

2.8. TUNEL Staining. The degree of myocardial and cellular apoptosis was measured by TUNEL analysis using an *in situ* cell death detection kit (Roche Molecular Biochemicals, Mannheim, Germany) following the manufacturer's instructions. Nuclei were visualized by DAPI staining. The samples were examined under an Olympus Fluoview FV100 microscope (Olympus, Tokyo, Japan), and the results are presented as an apoptotic index ($\times 100\%$).

2.9. Assessment of Mechanical Properties of Adult Cardiomyocytes. Mice were sacrificed and the hearts were harvested and digested by Liberase Blendzyme (Roche Molecular Biochemicals, Indianapolis, IN, USA). The collected cardiomyocytes were divided into five groups. The cells in the high-glucose/high-fat-hypoxia (HG/HF-hypoxia) group were treated with 33 mM glucose and 500 μM palmitate under hypoxia for 2 hr. To evaluate the role of melatonin, cells in the melatonin (HG/HF-hypoxia-MEL) group were pretreated with 100 μM melatonin for 2 hr before high-glucose/high-fat and hypoxia treatment. The JNK activator anisomycin was used to evaluate the role of JNK in the mechanical properties of adult cardiomyocytes (HG/HF-hypoxia-MEL-ANI). Anisomycin (2 μM) was added to cardiomyocytes for 30 min prior to melatonin treatment.

Following respective drug treatment, only rod-shape cardiomyocytes were used for mechanical assessment. Cardiomyocytes were visualized using an inverted microscope (IX-70, Olympus, Tokyo, Japan), and mechanical properties of cardiomyocytes were assessed by using a Soft-Edge MyoCam system (IonOptix Corporation, Milton, MA, USA). The indices of peak shortening, maximal velocity of shortening and relengthening ($\pm\text{dL}/\text{dt}$), time-to-peak shortening (TPS), and time-to-90% relengthening (TR_{90}) were measured to evaluate the mechanical properties of adult cardiomyocytes [33].

2.10. Western Blot. Lysis buffer was prepared with protease inhibitors and phosphatase inhibitor cocktail (Roche, Shanghai, China) after cardiac tissues and H9c2

cardiomyocytes were collected. After homogenizing the samples, the lysates were centrifuged at 12,000 rpm for 15 min at 4°C. Protein concentration was quantified by a BCA protein assay kit, and then, the protein sample was separated by SDS-PAGE. Proteins were transferred to a polyvinylidene difluoride (PVDF) membrane (Merck Millipore, Darmstadt, Germany). After blocking the PVDF membrane with 5% non-fat milk for 2 hr at room temperature (RT), the membranes were incubated with primary antibodies against p-JNK, JNK, p53, Bcl-2, Bax, caspase-3, and GAPDH (Cell Signaling Technology, Beverly, MA, USA) at 4°C overnight. After washing with TBS containing 0.1% Tween 20 (TBST) five times for 10 min each, the membranes were incubated with secondary antibodies in TBST buffer for 2 hours at RT and washed with TBST as previously described. The bands were visualized by adding the chemiluminescent HRP substrate (Merck Millipore, MA, USA) to the membrane, and the signals were detected by a ChemiDoc system (Bio-Rad, Richmond, USA) and quantified by using Image Lab software (Bio-Rad, Richmond, USA) [33].

2.11. Statistical Analysis. All data were presented as means \pm standard error of the mean (SEM). Differences were compared using a one-way ANOVA followed by the Bonferroni correction for *post hoc* analysis. A *p* value < 0.05 was considered to be statistically significant. All statistical analyses were performed using GraphPad Prism software (GraphPad Software, San Diego, CA, USA).

3. Results

3.1. Echocardiogram of Diabetic Mice following MI with or without Melatonin Treatment. Cardiac function and geometry were evaluated in post-MI diabetic mice with ejection fraction (EF) and fractional shortening (FS) assessed using echocardiography at the first and fourth weeks. Results shown in Figures 1(a)–1(e) demonstrated the minimal effects of diabetes on cardiac geometry and function compared to the control group although post-MI imposed overt functional and geometric alterations in the diabetic state (manifested by reduced ejection fraction, fractional shortening, and enlarged LVIDs and LVIDd at both 1- and 4-week time points) compared to mice in the DCM group, the effect of which was significantly attenuated or negated by melatonin treatment (except for the elevated LV geometry at 1-week post-MI). These data indicated that melatonin treatment improved cardiac geometry and contractile function at various time points (with a more pronounced effect with longer duration) post-MI in diabetic condition. In addition, results in Figures 1(f)–1(h) depicted that body weight was overtly elevated in the diabetic group, the effect of which was spared by the MI procedure and melatonin treatment. Although diabetes failed to significantly alter heart weight or heart size (heart-to-body weight ratio), the MI procedure overly elevated heart weight and heart size in the diabetic model, the effect of which was significantly attenuated by melatonin treatment in the diabetic state.

3.2. Melatonin Reduced Cardiac Fibrosis in the Border Zone of the Infarcted Area Post-MI in Diabetic Mice. To determine whether melatonin administration alleviated cardiac fibrosis post-MI in diabetic mice, cardiac tissue was examined using H&E staining and Masson's trichrome staining. Results shown in Figures 2(a)–2(c) suggested that diabetes alone failed to significantly affect the cross-sectional area of cardiomyocytes compared with the control group. However, the cross-sectional area of cardiomyocytes was overtly elevated following MI in diabetes compared to the diabetic-alone group, the effect of which was alleviated by melatonin treatment in the diabetic state. Besides, the cardiac interstitial fibrotic area in the infarct border zone evaluated by Masson's trichrome staining depicted a significant rise in the post-MI diabetes group compared to the diabetic-alone group although diabetes alone did not significantly increase myocardial fibrosis compared with the control group as shown in Figures 2(a)–2(c). Compared to the DMI group, melatonin administration markedly attenuated cardiac interstitial fibrosis in the diabetic state. These results collectively demonstrated that melatonin mitigated MI-induced rises in the cardiomyocyte cross-sectional area and cardiac interstitial fibrotic area in diabetes.

3.3. Melatonin Treatment Preserved Heart Function by Reducing Apoptosis Post-MI in Diabetic Mice. Myocardial apoptosis was assessed using TUNEL staining to demonstrate the protective effects of melatonin in post-MI diabetic mice. Results in Figures 3(a) and 3(b) showed that MI greatly enhanced myocardial apoptosis compared with the diabetic group although diabetes alone did not significantly increase cellular apoptosis compared with the control group. However, apoptotic cells were significantly decreased following melatonin treatment in the diabetic state, demonstrating an inhibitory effect of melatonin on cardiomyocyte apoptosis post-MI in diabetic hearts *in vivo*.

3.4. Melatonin Reduced Cardiac Apoptosis via Inhibiting the JNK Pathway Post-MI in Diabetic Mice. Levels of JNK and apoptotic proteins were further examined in post-MI diabetic mice with or without melatonin treatment. Results shown in Figures 4(a)–4(f) revealed that the post-MI procedure markedly promoted JNK phosphorylation in the diabetic group compared with the diabetic-only group although diabetes alone failed to notably alter levels of JNK phosphorylation compared with the control group. Furthermore, rises in p53, caspase-3, and Bax levels along with a drop in Bcl-2 level were observed in the diabetic group following MI compared with the diabetic-only or control group. However, these changes were reversed by melatonin treatment in the diabetic state. These data collectively demonstrated that melatonin could alleviate cardiac injury in post-MI diabetic mice through inhibition of the JNK/p53-mediated apoptotic pathway.

3.5. Melatonin Decreased JNK Phosphorylation to Inhibit Cardiomyocyte Apoptosis In Vitro under Hypoxia with High-Glucose/High-Fat Insult. To verify the role of the JNK pathway in the pathological progress of diabetic post-MI

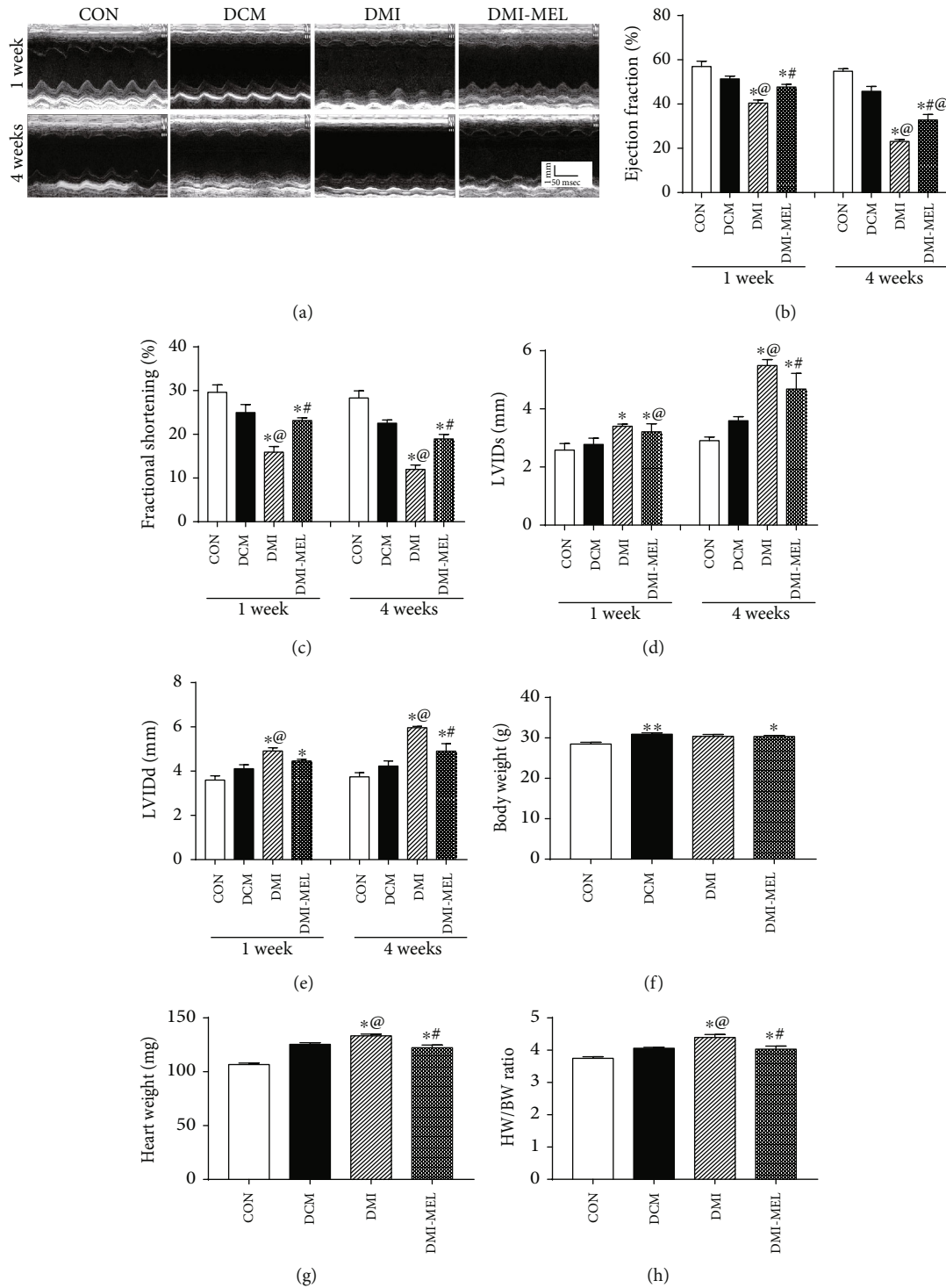


FIGURE 1: Effect of melatonin treatment on cardiac contractile function in post-MI diabetic mice. (a) Representative M-mode echocardiographic images from four respective mouse groups. Cardiac function was assessed using echocardiography at the first and fourth weeks post-MI. (b) Ejection fraction. (c) Fractional shortening. (d) LVIDs: left ventricular internal dimension during systole (end-systolic diameter). (e) LVIDd: left ventricular internal dimension during diastole (end-diastolic diameter). (f) Body weight. (g) Heart weight. (h) Heart weight-to-body weight (HW/BW) ratio. CON: normal control; DCM: diabetic cardiomyopathy; DMI: diabetes mellitus with MI; DMI-MEL: diabetes mellitus with MI treated with melatonin. Mean \pm SEM, $n = 4-6$. * $p < 0.05$ vs. CON group, # $p < 0.05$ vs. DMI group, and @ $p < 0.05$ vs. DCM group.

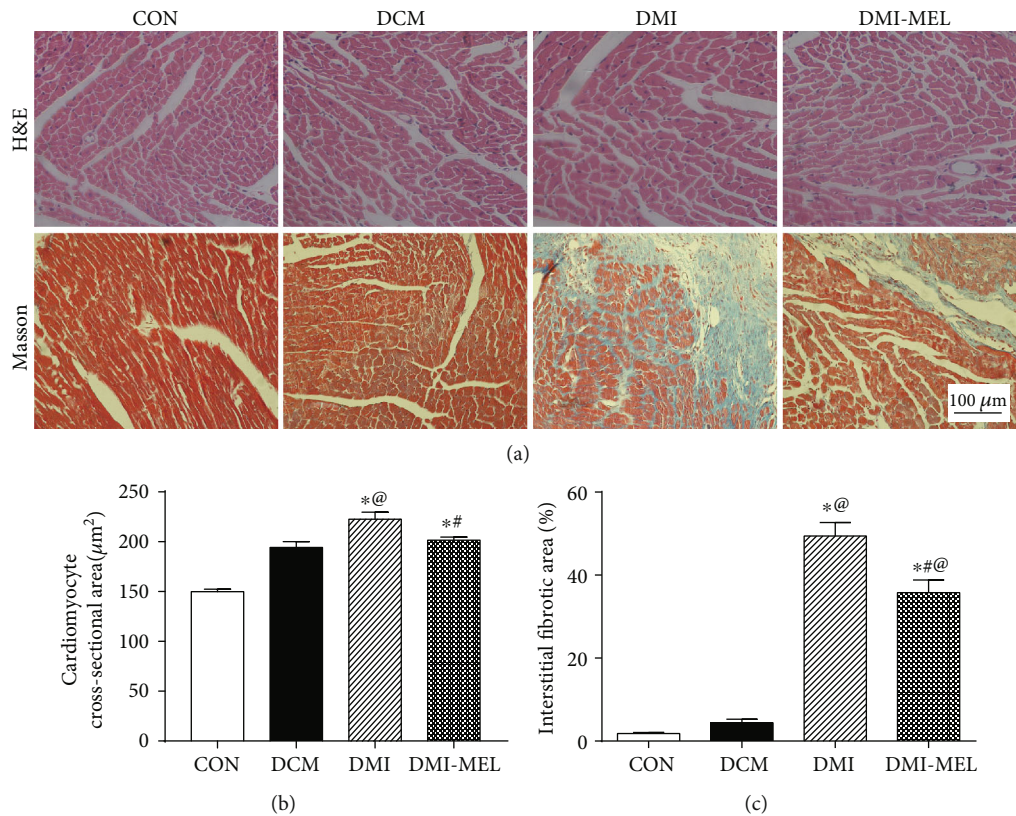


FIGURE 2: Effect of melatonin on the cardiomyocyte cross-sectional area and cardiac fibrosis with high-fat diet and/or myocardial infarction. (a) H&E staining and Masson's trichrome staining. The upper panel exhibits representative images of H&E staining of cardiac tissues. The lower panel depicts representative images of cardiac interstitial fibrosis with Masson's trichrome staining. (b) Pooled data of the cardiomyocyte cross-sectional area ($n = 20$ –25 cells per group). (c) Pooled data of the interstitial fibrotic area of myocardial tissues. CON: normal control; DCM: diabetic cardiomyopathy; DMI: diabetes mellitus with MI; DMI-MEL: diabetes mellitus with MI treated with melatonin. Mean \pm SEM, $n = 3$ –4 per group. * $p < 0.05$ vs. CON group, # $p < 0.05$ vs. DMI group, and @ $p < 0.05$ vs. DCM group. Scale bar = 100 μm .

hearts, we further tested the effects of JNK activation on cellular apoptosis *in vitro* in H9c2 myocytes under hypoxia combined with high-glucose/high-fat treatment. Our results in Figures 5(a) and 5(b) showed that high-glucose/high-fat insult combined with hypoxia significantly triggered cellular apoptosis compared with the control group. However, melatonin treatment greatly reduced cellular apoptosis compared with the HF/HG-hypoxia group. Interestingly, the protective role of melatonin was negated in the presence of the JNK activator anisomycin in high-glucose/high-fat treatment under hypoxia. These data consolidated that melatonin overtly reduced cell apoptosis at least in part via JNK inhibition in the face of high-glucose/high-fat and hypoxia insult.

3.6. Melatonin Protects Cardiomyocytes from Apoptosis Induced by Hypoxia and High-Glucose/High-Fat Treatment via the JNK-Mediated Apoptosis Pathway. We further examined levels of JNK and related apoptotic proteins in H9c2 cells treated with the JNK activator anisomycin under hypoxia in conjunction with high-glucose/high-fat insult. In line with our results of TUNEL staining, results in Figures 6(a)–6(f) showed that high glucose/high fat in combination with hypoxia significantly increased JNK phosphorylation and levels of p53, Bax, and caspase-3 and reduced the

expression of Bcl-2, the effects of which were reversed by the addition of melatonin. However, anisomycin treatment partially attenuated the protective effects of melatonin and reversed the changes of protein levels, confirming an obligatory role of the JNK pathway in melatonin-produced protection against apoptosis in the face of high-glucose/high-fat and hypoxia insult.

3.7. Melatonin Improved Contractile Properties of Adult Cardiomyocytes Insulted by Hypoxia and High-Glucose/High-Fat Treatment. To clarify the role of the JNK pathway in melatonin-mediated protection of cardiomyocytes, isolated adult murine cardiomyocytes were treated with high glucose/high fat and hypoxia in the presence or the absence of melatonin and JNK activator anisomycin. Results shown in Figures 7(a)–7(f) displayed that high-glucose/high-fat and hypoxia treatment markedly decreased peak shortening, maximal velocity of shortening/relengthening, and prolonged relengthening time without affecting resting cell length and time-to-peak shortening. Furthermore, melatonin overtly improved cardiomyocyte contractile properties under HF/HG-hypoxia challenge. Although anisomycin alone did not exhibit any effect on these mechanical indices, it nullified melatonin-offered protection against

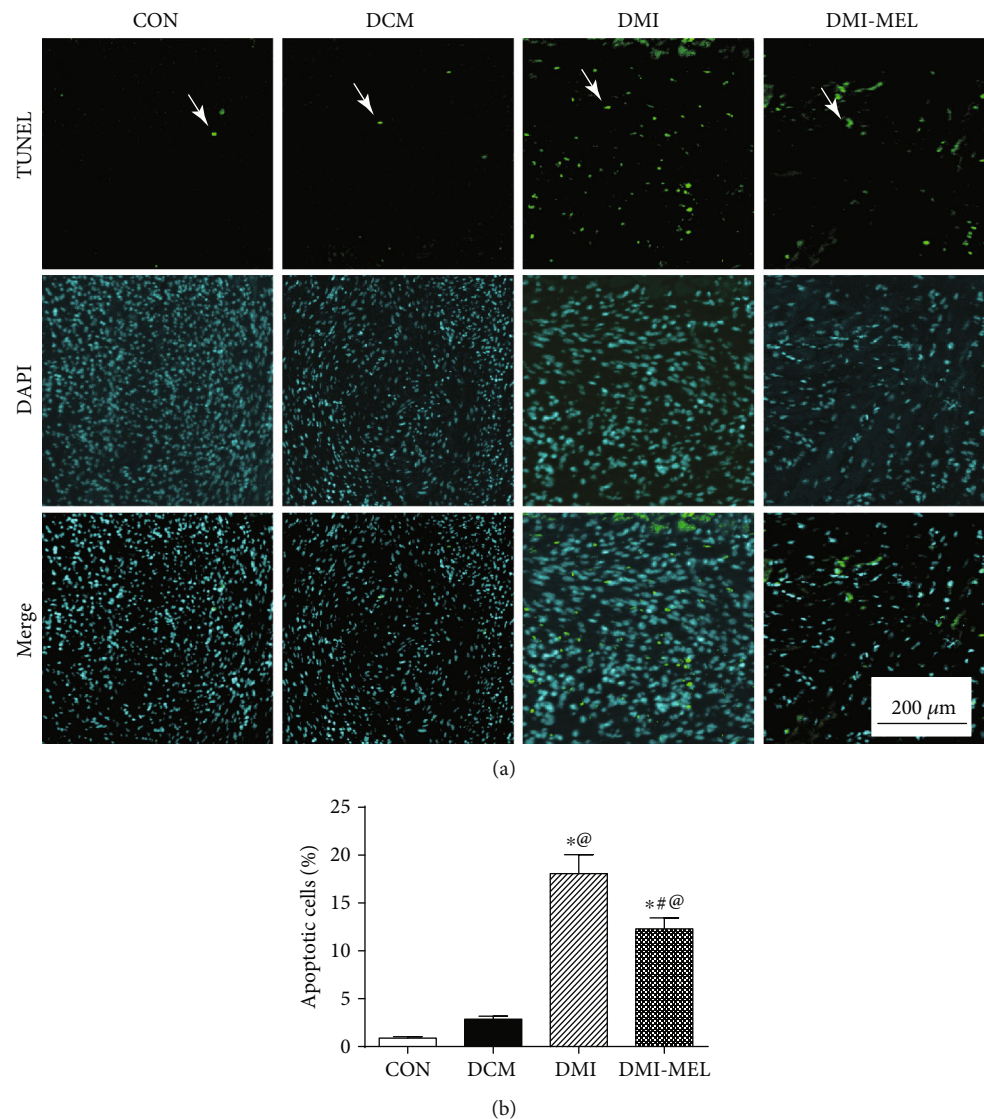


FIGURE 3: Effect of melatonin treatment on myocardial TUNEL apoptosis in post-MI diabetic mice. (a) Representative images of TUNEL staining 4 weeks post-MI in diabetic mice. Representative TUNEL staining images are displayed in the upper panel while the images with DAPI staining are displayed in the middle panel demonstrating nuclei of cells. The lower panel exhibits the overlay images to illustrate apoptotic cells. (b) Pooled data displaying the percentage of apoptotic cells. Mean \pm SEM, $n = 3-5$ per group. * $p < 0.05$ vs. CON group, # $p < 0.05$ vs. DMI group, and @ $p < 0.05$ vs. DCM group. Scale bar = 200 μm .

HF/HG-hypoxia-induced cardiomyocyte anomalies. Our data revealed the involvement of the JNK pathway in melatonin-offered protection against HG/HF-hypoxia-elicited contractile anomalies.

4. Discussion

The salient findings from our present study revealed that administration of melatonin ameliorated post-MI-induced cardiac dysfunction and interstitial fibrosis in the diabetic state. Post-MI diabetes elicited decreased ejection performance of the left ventricle, increased LV dilation, worsened cardiac fibrosis of the border zone, and exacerbated apoptosis in the heart. Further scrutiny depicted that melatonin-offered benefits were accompanied by alterations in the levels

of phosphorylated JNK, p53, Bcl-2, Bax, and caspase-3. These findings along with the *in vitro* findings convincingly indicated that the JNK activator anisomycin nullified melatonin-induced cardioprotection against high-glucose/high-fat-hypoxia-induced cardiac biochemical and functional deficits, validating the role for the JNK pathway in melatonin-offered benefit against post-MI in diabetes.

Over the past decades, the prevalence of type 2 diabetes is dramatically increasing globally in both developed and developing countries [1, 35]. In Asia, type 2 diabetes occurs at a much younger age with lower degree of obesity and has a higher mortality rate compared with that in other regions [36–38]. While diabetes is considered a substantial risk of cardiovascular disease [38], evidence has shown that the risk of developing cardiovascular diseases in patients with type 2

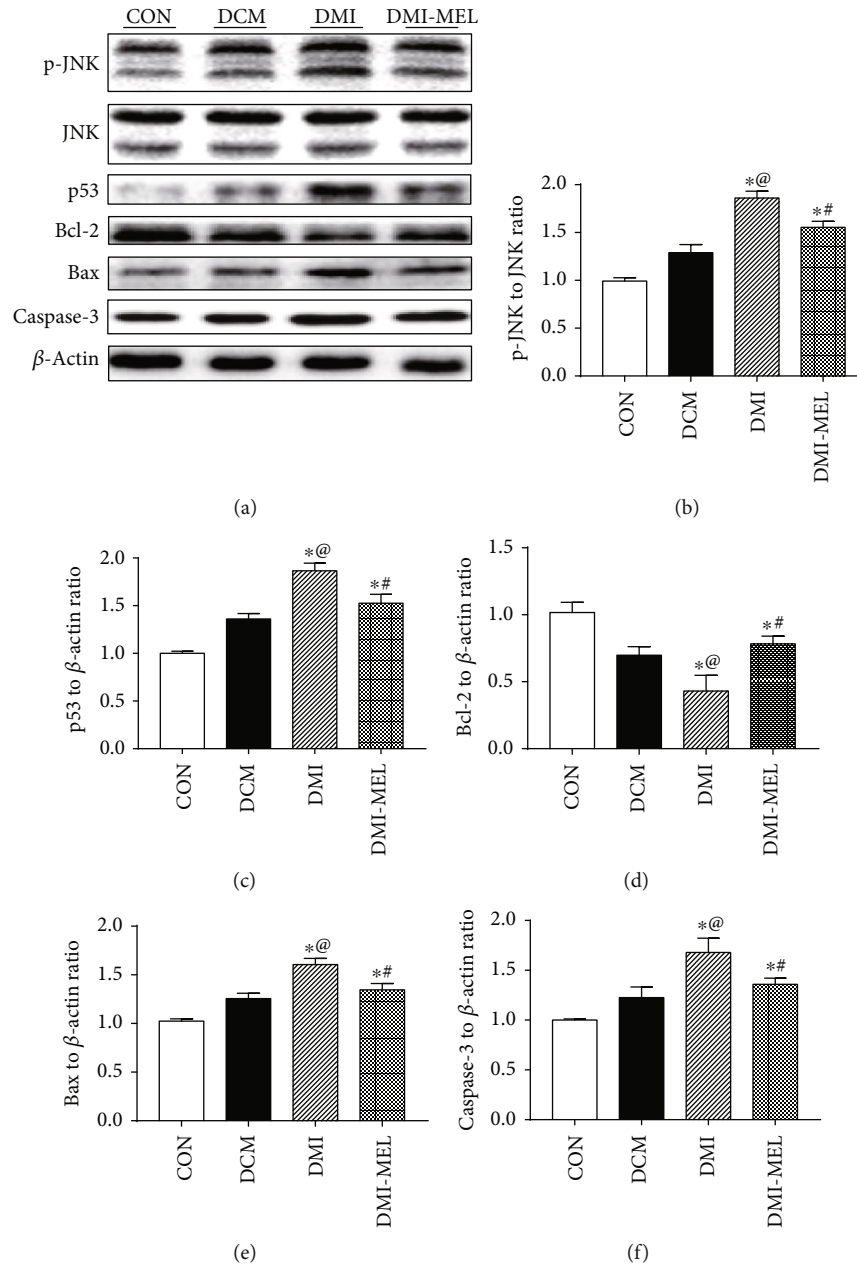


FIGURE 4: Effect of melatonin on JNK and apoptotic-related protein expressions with or without melatonin treatment in diabetic MI hearts. (a) Representative images of western blot 4 weeks post-MI in diabetic mice. (b) p-JNK to total JNK ratio. (c) p53 level. (d) Bcl-2 level. (e) Bax level. (f) Caspase-3 level. Mean \pm SEM, $n = 3-5$ per group. * $p < 0.05$ vs. CON group, # $p < 0.05$ vs. DMI group, and @ $p < 0.05$ vs. DCM group.

diabetes was twice higher than the risk in those without type 2 diabetes [39]. Despite the fact that ample studies clarified the potential molecular mechanisms of MI, the unique features of the pathogenesis of MI in diabetic hearts remain elusive. Findings from earlier studies revealed that diabetes may downregulate the expression of Sirt3 and disrupt the Ang-1/Tie-2 signaling cascade to enhance myocardial infarction injury via regulation of myocardial vascular maturation and angiogenesis [40, 41]. Importantly, enhanced apoptosis of cardiomyocytes contributed to the exacerbation of cardiac function and fibrosis in diabetic MI compared to nondiabetic MI settings in rats [42]. Involvement of JNK stress signaling has been considered over the past decades.

As a well-characterized member of the MAPK superfamily, JNK participates in the pathogenesis of cardiovascular diseases such as myocardial infarction, heart failure, myocardial ischemia-reperfusion (MI/R) injury, diabetic cardiomyopathy, dilated cardiomyopathy, and cardiac hypertrophy [43–47]. In particular, overactivation of JNK *in vivo* can cause restrictive cardiomyopathy and cardiac fibrosis, as well as leading to conduction defects and heart failure [48–50]. JNK is also considered an essential modulator for mitochondrial homeostasis and apoptosis in the onset and progression of heart failure [47, 51, 52]. Activation of JNK/p38 cascades has been demonstrated to aggravate the development of MI/R injury [53]. However, the roles of JNK in diabetic MI

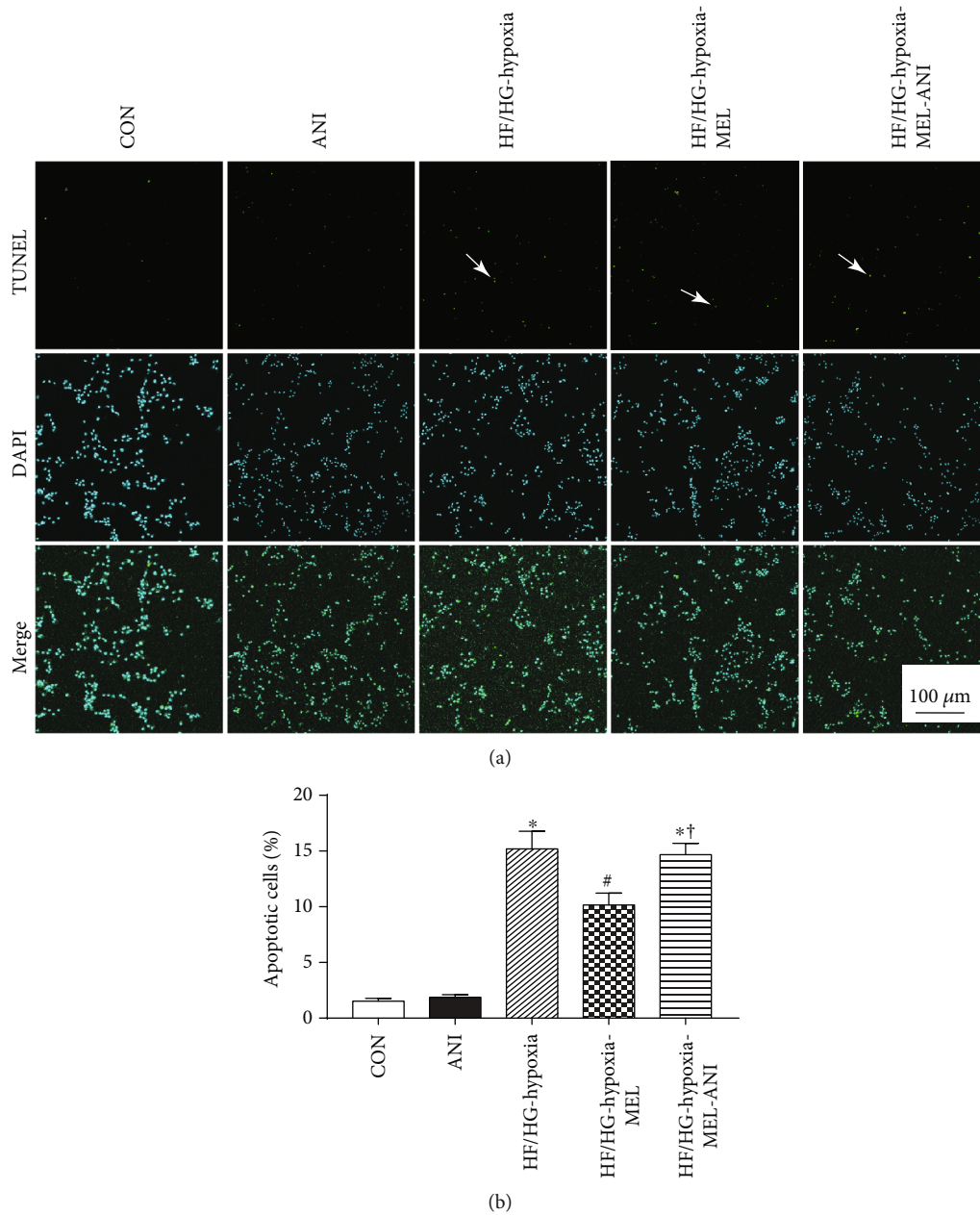


FIGURE 5: The effect of melatonin treatment on cellular apoptosis in H9c2 myocytes challenged by high glucose/high fat under hypoxia. (a) Representative images of TUNEL staining of H9c2 cells with or without melatonin and anisomycin treatment. The images with TUNEL staining are displayed in the upper panel. Images with DAPI staining are displayed in the middle panel depicting nuclei of cells. Lower panel indicates the overlay images to illustrate the apoptotic cells. (b) Pooled data depicting the percentage of apoptotic cells. Mean \pm SEM, $n = 3$ per group. * $p < 0.05$ vs. CON group, # $p < 0.05$ vs. HF/HG-hypoxia group, † $p < 0.05$ vs. HF/HG-hypoxia-MEL group. Scale bar = 100 μ m.

hearts were not fully examined with recent findings favoring the role of JNKs in I/R injury of the heart in diabetes mellitus [54]. Nonetheless, clinical application of JNK inhibitors for target therapy has been dismal due to family subtype specificity and toxicity [54]. In our hands, the MI procedure greatly increased phosphorylation of JNK in diabetes compared with the diabetes-alone group (which exerts no significant effect on JNK phosphorylation). Our data also revealed prominent apoptosis in conjunction with JNK activation in the diabetic MI group. Levels of antiapoptotic

protein Bcl-2 were decreased while those of p53, Bax, and caspase-3 were elevated in post-MI diabetic hearts compared to control or diabetic-alone group. Our TUNEL staining result also showed that the apoptosis is markedly increased in diabetic post-MI hearts. We further demonstrated the enhanced cell apoptosis through JNK activation in H9c2 cells with HG/HF and hypoxia treatment. These data together illustrated that apoptosis activated by the JNK pathway is important in the pathogenesis of MI of diabetic hearts.

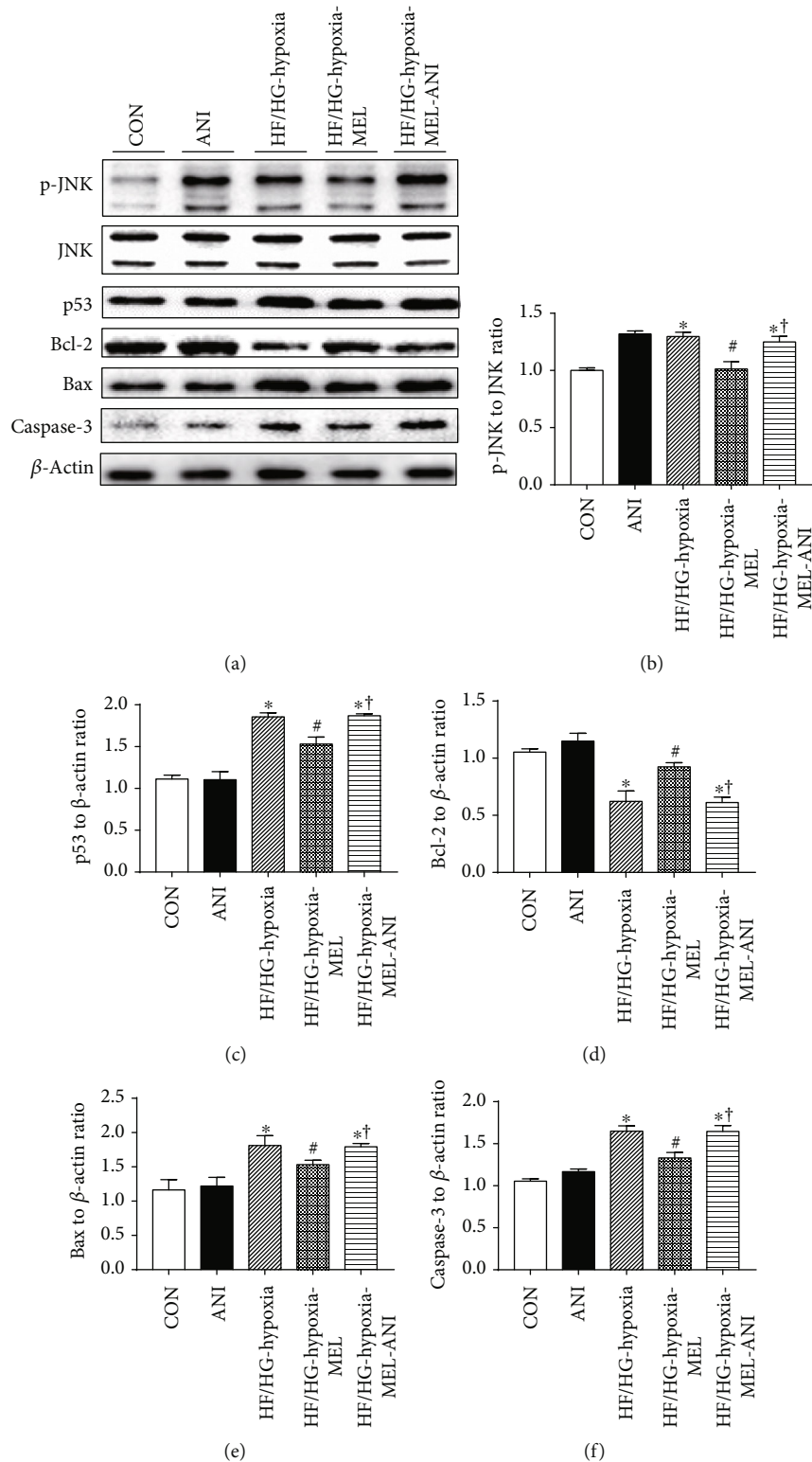


FIGURE 6: Effect of melatonin and the JNK activator anisomycin on protein levels of apoptotic-related proteins in H9c2 cells challenged by high glucose/high fat under hypoxia. (a) Representative images of western blot of H9c2 cells with or without melatonin and anisomycin treatment. (b) p-JNK to total JNK ratio. (c) p53 level. (d) Bcl-2 level. (e) Bax level. (f) Caspase-3 level. Mean \pm SEM, $n = 3$. * $p < 0.05$ vs. CON group, # $p < 0.05$ vs. high-glucose/high-fat treatment under hypoxia, and † $p < 0.05$ vs. HF/HG-hypoxia-MEL group.

As a hormone secreted by the pineal gland, poor secretion of melatonin was associated with a high risk of type 2 diabetes, implying the potential benefits of melatonin in met-

abolic diseases [55]. Besides, melatonin significantly alleviated metabolic disorder and oxidative stress in the diabetic state [56, 57]. Furthermore, 6melatonin was shown to protect

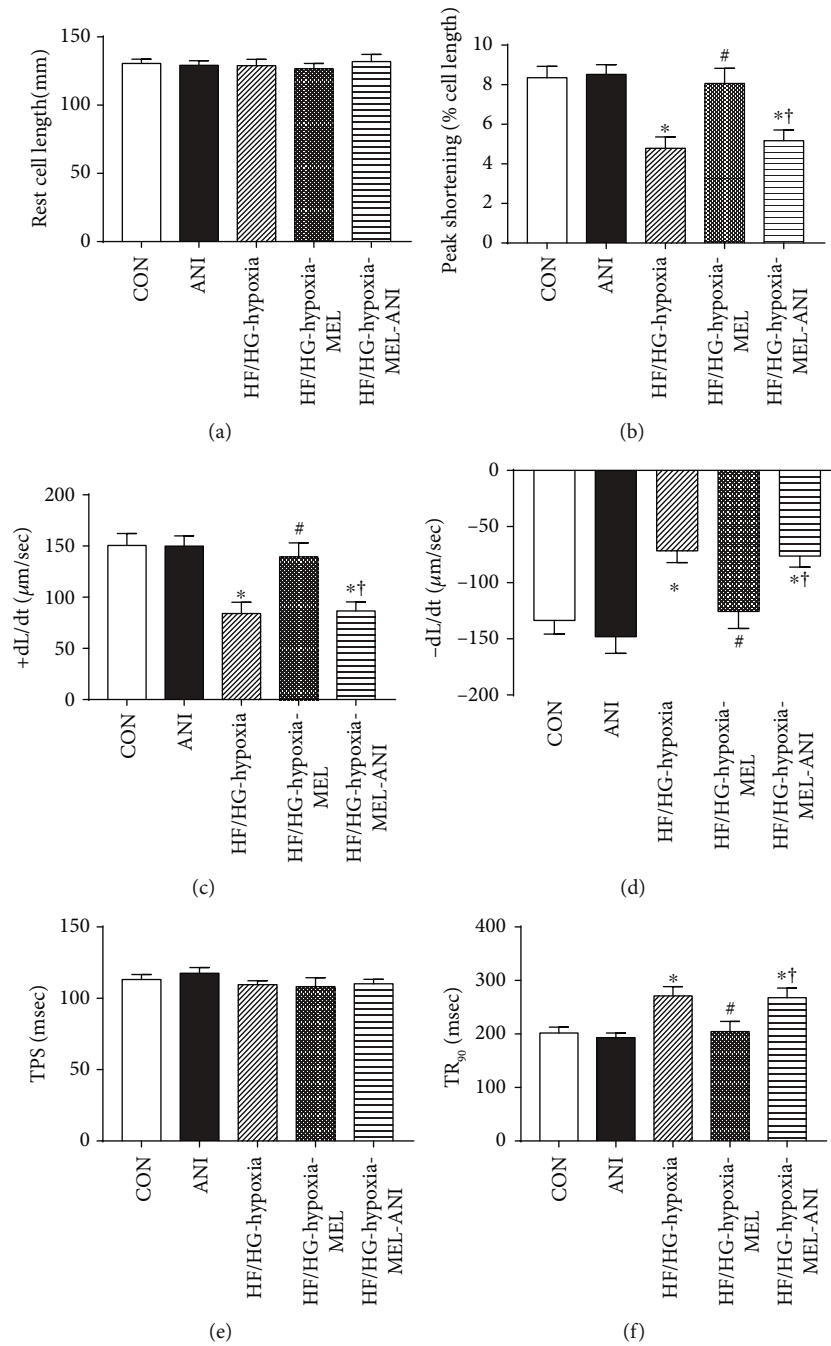


FIGURE 7: Effect of melatonin and the JNK activator anisomycin on contractile function of isolated cardiomyocytes. (a) Resting cell length. (b) Peak shortening (PS, normalized to resting cell length). (c) Maximal velocity of shortening (+dL/dt). (d) Maximal velocity of relengthening (-dL/dt). (e) Time-to-peak shortening (TPS). (f) Time-to-90% relengthening (TR₉₀). Mean \pm SEM, $n = 39$ cells per group. * $p < 0.05$ vs. CON group, # $p < 0.05$ vs. HF/HG-hypoxia group, and † $p < 0.05$ vs. HF/HG-hypoxia-MEL group.

diabetic hearts via an apoptosis- and Mst1/Sirt3-dependent mechanism [58, 59]. In our hands, blood glucose level of the DMI-MEL group was comparable between diabetic and diabetic MI groups (data not shown), suggesting a lack of effect for melatonin on blood glucose in the diabetic state. It was noticed that the heart weight in the DMI-MEL group dropped although body weight in the DMI-MEL group did not significantly change compared to that in the DMI group. Although LVEF and LVFS values were overtly lowered in the

diabetic MI group compared with the diabetic group, melatonin treatment restored LVEF and LVFS values in the diabetic MI group. Compared with the diabetic MI group, melatonin significantly reduced myocardial fibrosis of the infarct border zone and cross-sectional area of cardiomyocytes. These results favored that administration of melatonin significantly decreased phosphorylation of JNK and apoptosis (manifested by apoptotic proteins such as Bax and caspase-3 and TUNEL staining), in line with the previous study [60]. We

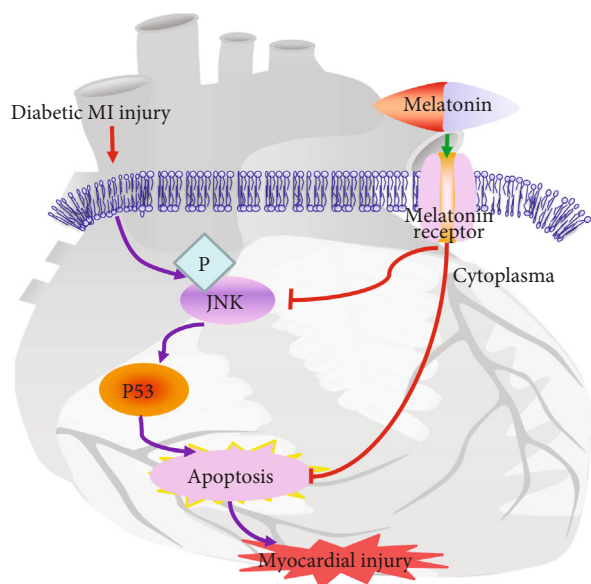


FIGURE 8: Schematic diagram depicting the proposed signaling pathways involving JNK, p53, and apoptosis behind the melatonin-offered protective effect against post-MI injury in diabetes.

further validated the obligatory role of JNK in melatonin-offered cardioprotection using anisomycin to nullify the protective effect of melatonin. Although high glucose/high fat in combination with hypoxia greatly impaired the mechanical properties of cardiomyocytes, melatonin overtly improved the contractile function of murine cardiomyocytes, the effects of which were nullified by anisomycin. These data collectively demonstrated that melatonin treatment effectively protected the hearts from MI injury in diabetic mice possibly through a JNK-mediated mechanism as depicted in Figure 8.

In summary, findings from our present study demonstrate that JNK signaling is turned on in post-MI diabetic hearts. Administration of melatonin is capable of improving post-MI diabetes-induced cardiac dysfunction and myocardial fibrosis of the infarct border zone in the diabetic state, possibly through a mechanism associated with JNK-mediated apoptosis. Our data should shed some lights on a better exploration of novel therapeutic targets and development of the potential clinical use of melatonin on ischemic cardiovascular diseases with diabetes.

Data Availability

The data used to support the findings of this study are available from the corresponding authors upon request.

Conflicts of Interest

The authors confirm that this article content has no conflict of interest.

Authors' Contributions

Linhe Lu, Jipeng Ma, and Mingming Sun contributed equally to this work.

Acknowledgments

This study was supported by grants from the National Natural Science Foundation of China (Nos. 81470500, 81500319, 81774415, 81600295, and 81600240), the Distinguished Young Scholar Foundation of Shaanxi Province (2018JC-015), the Key Science and Technology Innovation Team in Shaanxi Province (No. 2014KCT-19), and the Subject Boosting Project of Xijing Hospital (XJZT18MJ14).

References


- [1] Y. Zheng, S. H. Ley, and F. B. Hu, "Global aetiology and epidemiology of type 2 diabetes mellitus and its complications," *Nature Reviews Endocrinology*, vol. 14, no. 2, pp. 88–98, 2018.
- [2] L. Chen, D. J. Magliano, and P. Z. Zimmet, "The worldwide epidemiology of type 2 diabetes mellitus—present and future perspectives," *Nature Reviews Endocrinology*, vol. 8, no. 4, pp. 228–236, 2011.
- [3] E. L. Feldman, B. C. Callaghan, R. Pop-Busui et al., "Diabetic neuropathy," *Nature Reviews Disease Primers*, vol. 5, no. 1, p. 41, 2019.
- [4] J. Ren and A. F. Ceylan-Isik, "Diabetic cardiomyopathy: do women differ from men?," *Endocrine*, vol. 25, no. 2, pp. 073–084, 2004.
- [5] T. Almdal, H. Scharling, J. S. Jensen, and H. Vestergaard, "The independent effect of type 2 diabetes mellitus on ischemic heart disease, stroke, and death: a population-based study of 13,000 men and women with 20 years of follow-up," *Archives of Internal Medicine*, vol. 164, no. 13, pp. 1422–1426, 2004.
- [6] S. M. Haffner, S. Lehto, T. Ronnema, K. Pyorala, and M. Laakso, "Mortality from coronary heart disease in subjects with type 2 diabetes and in nondiabetic subjects with and without prior myocardial infarction," *The New England Journal of Medicine*, vol. 339, no. 4, pp. 229–234, 1998.
- [7] H. Miettinen, S. Lehto, V. Salomaa et al., "Impact of diabetes on mortality after the first myocardial Infarction," *Diabetes Care*, vol. 21, no. 1, pp. 69–75, 1998.
- [8] L. C. Manchester, A. Coto-Montes, J. A. Boga et al., "Melatonin: an ancient molecule that makes oxygen metabolically tolerable," *Journal of Pineal Research*, vol. 59, no. 4, pp. 403–419, 2015.
- [9] V. M. Cassone, "Effects of melatonin on vertebrate circadian systems," *Trends in Neurosciences*, vol. 13, no. 11, pp. 457–464, 1990.
- [10] A. A. Alqasim, E. E. M. Noureldin, S. H. Hammad, and G. E. Esheba, "Effect of melatonin versus vitamin D as antioxidant and hepatoprotective agents in STZ-induced diabetic rats," *Journal of Diabetes & Metabolic Disorders*, vol. 16, no. 1, p. 41, 2017.
- [11] I. Herichová, M. Zeman, K. Stebelová, and T. Ravingerová, "Effect of streptozotocin-induced diabetes on daily expression of per 2 and dbp in the heart and liver and melatonin rhythm in the pineal gland of Wistar rat," *Mol Cell Biochem*, vol. 270, no. 1-2, pp. 223–229, 2005.
- [12] I. Grigorov, D. Bogojević, S. Jovanović et al., "Hepatoprotective effects of melatonin against pronecrotic cellular events in streptozotocin-induced diabetic rats," *Journal of Physiology and Biochemistry*, vol. 70, no. 2, pp. 441–450, 2014.
- [13] S. Xie, Y. Deng, Y. Y. Pan et al., "Melatonin protects against chronic intermittent hypoxia-induced cardiac hypertrophy

- by modulating autophagy through the 5' adenosine monophosphate-activated protein kinase pathway," *Biochem Biophys Res Commun*, vol. 464, no. 4, pp. 975–981, 2015.
- [14] S. I. Choi, K. S. Kim, J. Y. Oh, J. Y. Jin, G. H. Lee, and E. K. Kim, "Melatonin induces autophagy via an mTOR-dependent pathway and enhances clearance of mutant-TGFB1p," *Journal of Pineal Research*, vol. 54, no. 4, pp. 361–372, 2013.
- [15] C. Aktas, M. Kanter, M. Erboğa, R. Mete, and M. Oran, "Melatonin attenuates oxidative stress, liver damage and hepatocyte apoptosis after bile-duct ligation in rats," *Toxicology and Industrial Health*, vol. 30, no. 9, pp. 835–844, 2014.
- [16] A. Domínguez-Rodríguez, P. Abreu-González, M. J. García, J. Sanchez, F. Marrero, and D. Armas-Trujillo, "Decreased nocturnal melatonin levels during acute myocardial infarction," *Journal of Pineal Research*, vol. 33, no. 4, pp. 248–252, 2002.
- [17] A. Domínguez-Rodríguez, P. Abreu-Gonzalez, E. Arroyo-Ucar, and R. J. Reiter, "Decreased level of melatonin in serum predicts left ventricular remodelling after acute myocardial infarction," *Journal of Pineal Research*, vol. 53, no. 3, pp. 319–323, 2012.
- [18] H. Pei, J. du, X. Song et al., "Melatonin prevents adverse myocardial infarction remodeling via Notch1/Mfn2 pathway," *Free Radical Biology & Medicine*, vol. 97, pp. 408–417, 2016.
- [19] H. F. Pei, J. N. Hou, F. P. Wei et al., "Melatonin attenuates postmyocardial infarction injury via increasing Tom70 expression," *Journal of Pineal Research*, vol. 62, no. 1, article e12371, 2017.
- [20] H. Zhou, Q. Ma, P. Zhu, J. Ren, R. J. Reiter, and Y. Chen, "Protective role of melatonin in cardiac ischemia-reperfusion injury: from pathogenesis to targeted therapy," *Journal of Pineal Research*, vol. 64, no. 3, article e12471, 2018.
- [21] L. E. Wold, A. F. Ceylan-Isik, and J. Ren, "Oxidative stress and stress signaling: menace of diabetic cardiomyopathy," *Acta Pharmacologica Sinica*, vol. 26, no. 8, pp. 908–917, 2005.
- [22] Q. Zhang, L. Lu, T. Liang, M. Liu, Z. L. Wang, and P. Y. Zhang, "MAPK pathway regulated the cardiomyocyte apoptosis in mice with post-infarction heart failure," *Bratislava Medical Journal*, vol. 118, no. 6, pp. 339–346, 2017.
- [23] G. L. Johnson and R. Lapadat, "Mitogen-activated protein kinase pathways mediated by ERK, JNK, and p38 protein kinases," *Science*, vol. 298, no. 5600, pp. 1911–1912, 2002.
- [24] Z. F. Song, X. P. Ji, X. X. Li, S. J. Wang, S. H. Wang, and Y. Zhang, "Inhibition of the activity of poly (ADP-ribose) polymerase reduces heart ischaemia/reperfusion injury via suppressing JNK-mediated AIF translocation," *Journal of Cellular and Molecular Medicine*, vol. 12, no. 4, pp. 1220–1228, 2008.
- [25] D. Qi, X. Hu, X. Wu et al., "Cardiac macrophage migration inhibitory factor inhibits JNK pathway activation and injury during ischemia/reperfusion," *Journal of Clinical Investigation*, vol. 119, no. 12, pp. 3807–3816, 2009.
- [26] J. Ghosh, J. Das, P. Manna, and P. C. Sil, "The protective role of arjunolic acid against doxorubicin induced intracellular ROS dependent JNK-p38 and p53-mediated cardiac apoptosis," *Biomaterials*, vol. 32, no. 21, pp. 4857–4866, 2011.
- [27] Y. Pan, Y. Wang, Y. Zhao et al., "Inhibition of JNK phosphorylation by a novel curcumin analog prevents high glucose-induced inflammation and apoptosis in cardiomyocytes and the development of diabetic cardiomyopathy," *Diabetes*, vol. 63, no. 10, pp. 3497–3511, 2014.
- [28] J. Ren and J. R. Sowers, "Application of a novel curcumin analog in the management of diabetic cardiomyopathy," *Diabetes*, vol. 63, no. 10, pp. 3166–3168, 2014.
- [29] L. G. R. Oliveira, C. C. Kuehn, C. D. dos Santos et al., "Protective actions of melatonin against heart damage during chronic Chagas disease," *Acta Tropica*, vol. 128, no. 3, pp. 652–658, 2013.
- [30] Y. Yao, X. Zhao, J. Xin, Y. Wu, and H. Li, "Coumarins improved type 2 diabetes induced by high-fat diet and streptozotocin in mice via antioxidation," *Canadian Journal of Physiology and Pharmacology*, vol. 96, no. 8, pp. 765–771, 2018.
- [31] E. Gao and W. J. Koch, "A novel and efficient model of coronary artery ligation in the mouse," *Methods Molecular Biology*, vol. 1037, pp. 299–311, 2013.
- [32] L. Tao, E. Gao, X. Jiao et al., "Adiponectin cardioprotection after myocardial ischemia/reperfusion involves the reduction of oxidative/nitrate stress," *Circulation*, vol. 115, no. 11, pp. 1408–1416, 2007.
- [33] L. Yang, S. Wang, J. Ma et al., "CD74 knockout attenuates alcohol intake-induced cardiac dysfunction through AMPK-Skp2-mediated regulation of autophagy," *Biochimica et Biophysica Acta (BBA) - Molecular Basis of Disease*, vol. 1865, no. 9, pp. 2368–2378, 2019.
- [34] D. Dytar, M. Eppenberger-Eberhardt, K. Maedler et al., "Glucose and palmitic acid induce degeneration of myofibrils and modulate apoptosis in rat adult cardiomyocytes," *Diabetes*, vol. 50, no. 9, pp. 2105–2113, 2001.
- [35] S. Chatterjee, K. Khunti, and M. J. Davies, "Type 2 diabetes," *The Lancet*, vol. 389, no. 10085, pp. 2239–2251, 2017.
- [36] J. C. N. Chan, V. Malik, W. Jia et al., "Diabetes in Asia: epidemiology, risk factors, and pathophysiology," *JAMA*, vol. 301, no. 20, pp. 2129–2140, 2009.
- [37] K. H. Yoon, J. H. Lee, J. W. Kim et al., "Epidemic obesity and type 2 diabetes in Asia," *The Lancet*, vol. 368, no. 9548, pp. 1681–1688, 2006.
- [38] Y. Zhang, A. T. Whaley-Connell, J. R. Sowers, and J. Ren, "Autophagy as an emerging target in cardiorenal metabolic disease: from pathophysiology to management," *Pharmacology & Therapeutics*, vol. 191, pp. 1–22, 2018.
- [39] The Emerging Risk Factors Collaboration, "Diabetes mellitus, fasting blood glucose concentration, and risk of vascular disease: a collaborative meta-analysis of 102 prospective studies," *The Lancet*, vol. 375, no. 9733, pp. 2215–2222, 2010.
- [40] X. Hou, H. Zeng, X. He, and J. X. Chen, "Sirt3 is essential for apelin-induced angiogenesis in post-myocardial infarction of diabetes," *Journal of Cellular and Molecular Medicine*, vol. 19, no. 1, pp. 53–61, 2015.
- [41] J. X. Chen and A. Stinnett, "Disruption of Ang-1/Tie-2 signaling contributes to the impaired myocardial vascular maturation and angiogenesis in type II diabetic mice," *Arteriosclerosis, Thrombosis, and Vascular Biology*, vol. 28, no. 9, pp. 1606–1613, 2008.
- [42] T. Bäcklund, E. Palojoki, A. Saraste et al., "Sustained cardiomyocyte apoptosis and left ventricular remodelling after myocardial infarction in experimental diabetes," *Diabetologia*, vol. 47, no. 2, pp. 325–330, 2004.
- [43] C. Li, X. Miao, Y. Lou et al., "Cardioprotective effects of the novel curcumin analogue C66 in diabetic mice is dependent on JNK2 inactivation," *Journal of Cellular and Molecular Medicine*, vol. 22, no. 12, pp. 6314–6326, 2018.

- [44] Q. Jin, R. Li, N. Hu et al., "DUSP1 alleviates cardiac ischemia/reperfusion injury by suppressing the Mff- required mitochondrial fission and Bnip3-related mitophagy via the JNK pathways," *Redox Biology*, vol. 14, pp. 576–587, 2018.
- [45] X. Jiang, Y. Liu, X. Liu et al., "Over-expression of a cardiac-specific human dopamine D5 receptor mutation in mice causes a dilated cardiomyopathy through ROS over-generation by NADPH oxidase activation and Nrf2 degradation," *Redox Biology*, vol. 19, pp. 134–146, 2018.
- [46] C. Li, J. Li, K. Xue et al., "MicroRNA-143-3p promotes human cardiac fibrosis via targeting sprouty3 after myocardial infarction," *Journal of Molecular and Cellular Cardiology*, vol. 129, pp. 281–292, 2019.
- [47] C. Y. Huang, W. W. Kuo, Y. L. Yeh et al., "ANG II promotes IGF-IIR expression and cardiomyocyte apoptosis by inhibiting HSF1 via JNK activation and SIRT1 degradation," *Cell Death & Differentiation*, vol. 21, no. 8, pp. 1262–1274, 2014.
- [48] B. G. Petrich, B. C. Eloff, D. L. Lerner et al., "Targeted activation of c-Jun N-terminal kinase in vivo induces restrictive cardiomyopathy and conduction defects," *Journal of Biological Chemistry*, vol. 279, no. 15, pp. 15330–15338, 2004.
- [49] S. Kyoj, H. Otani, S. Matsuhisa et al., "Opposing effect of p38 MAP kinase and JNK inhibitors on the development of heart failure in the cardiomyopathic hamster," *Cardiovascular Research*, vol. 69, no. 4, pp. 888–898, 2006.
- [50] D. M. Abraham, T. E. Lee, L. J. Watson et al., "The two-pore domain potassium channel TREK-1 mediates cardiac fibrosis and diastolic dysfunction," *Journal of Clinical Investigation*, vol. 128, no. 11, pp. 4843–4855, 2018.
- [51] A. H. Chaanine, D. Jeong, L. Liang et al., "JNK modulates FOXO3a for the expression of the mitochondrial death and mitophagy marker BNIP3 in pathological hypertrophy and in heart failure," *Cell Death & Disease*, vol. 3, no. 2, article e265, 2012.
- [52] C. Y. Huang, C. H. Lai, C. H. Kuo et al., "Inhibition of ERK-Drp1 signaling and mitochondria fragmentation alleviates IGF-IIR-induced mitochondria dysfunction during heart failure," *Journal of Molecular and Cellular Cardiology*, vol. 122, pp. 58–68, 2018.
- [53] W. Xu, L. Zhang, Y. Zhang, K. Zhang, Y. Wu, and D. Jin, "TRAF1 exacerbates myocardial ischemia reperfusion injury via ASK1-JNK/p38 signaling," *Journal of the American Heart Association*, vol. 8, no. 21, article e012575, 2019.
- [54] M. Shvedova, Y. Anfinogenova, E. N. Atochina-Vasserman, I. A. Schepetkin, and D. N. Atochin, "c-Jun N-terminal kinases (JNKs) in myocardial and cerebral ischemia/reperfusion injury," *Frontiers in Pharmacology*, vol. 9, p. 715, 2018.
- [55] C. J. McMullan, E. S. Schernhammer, E. B. Rimm, F. B. Hu, and J. P. Forman, "Melatonin secretion and the incidence of type 2 diabetes," *JAMA*, vol. 309, no. 13, pp. 1388–1396, 2013.
- [56] K. Winiarska, T. Fraczyk, D. Malinska, J. Drozak, and J. Bryla, "Melatonin attenuates diabetes-induced oxidative stress in rabbits," *Journal of Pineal Research*, vol. 40, no. 2, pp. 168–176, 2006.
- [57] E. J. Sudnikovich, Y. Z. Maksimchik, S. V. Zabrodskaia et al., "Melatonin attenuates metabolic disorders due to streptozotocin-induced diabetes in rats," *European Journal of Pharmacology*, vol. 569, no. 3, pp. 180–187, 2007.
- [58] A. H. Amin, M. A. El-Missiry, and A. I. Othman, "Melatonin ameliorates metabolic risk factors, modulates apoptotic proteins, and protects the rat heart against diabetes-induced apoptosis," *European Journal of Pharmacology*, vol. 747, pp. 166–173, 2015.
- [59] M. Zhang, J. Lin, S. Wang et al., "Melatonin protects against diabetic cardiomyopathy through Mst1/Sirt3 signaling," *Journal of Pineal Research*, vol. 63, no. 2, article e12418, 2017.
- [60] T. Ali, H. Badshah, T. H. Kim, and M. O. Kim, "Melatonin attenuates D-galactose-induced memory impairment, neuro-inflammation and neurodegeneration via RAGE/NF-KB/JNK signaling pathway in aging mouse model," *Journal of Pineal Research*, vol. 58, no. 1, pp. 71–85, 2015.

Research Article

Toxic Acetaminophen Exposure Induces Distal Lung ER Stress, Proinflammatory Signaling, and Emphysematous Changes in the Adult Murine Lung

Jeryl Sandoval,¹ David J. Orlicky,² Ayed Allawzi,³ Brittany Butler,¹ Cynthia Ju,⁴ Caroline T. Phan,¹ Roy Toston,¹ Robyn De Dios,¹ Leanna Nguyen,¹ Sarah McKenna,¹ Eva Nozik-Grayck,³ and Clyde J. Wright ¹

¹Section of Neonatology, Department of Pediatrics, University of Colorado School of Medicine, Aurora, CO, USA

²Department of Pathology, University of Colorado School of Medicine, Aurora, CO, USA

³Developmental Lung Biology and Cardiovascular Pulmonary Research Laboratories, Departments of Pediatrics and Medicine, University of Colorado, Anschutz Medical Campus, Aurora, CO, USA

⁴Department of Anesthesiology, The University of Texas Health Science Center at Houston, McGovern Medical School, Houston, TX, USA

Correspondence should be addressed to Clyde J. Wright; clyde.wright@cuanschutz.edu

Received 17 August 2019; Revised 21 October 2019; Accepted 4 November 2019; Published 28 November 2019

Guest Editor: Bhagavatula Moorthy

Copyright © 2019 Jeryl Sandoval et al. This is an open access article distributed under the Creative Commons Attribution License, which permits unrestricted use, distribution, and reproduction in any medium, provided the original work is properly cited.

Clinical studies have demonstrated a strong association between both acute toxic exposure and the repetitive, chronic exposure to acetaminophen (APAP) with pulmonary dysfunction. However, the mechanisms underlying this association are unknown. Preclinical reports have demonstrated that significant bronchiolar injury occurs with toxic APAP exposure, but very little information exists on how the distal lung is affected. However, cells in the alveolar space, including the pulmonary epithelium and resident macrophages, express the APAP-metabolizing enzyme CYP2E1 and are a potential source of toxic metabolites and subsequent distal lung injury. Thus, we hypothesized that distal lung injury would occur in a murine model of toxic APAP exposure. Following exposure of APAP (280 mg/kg, IP), adult male mice were found to have significant proximal lung histopathology as well as distal lung inflammation and emphysematous changes. Toxic APAP exposure was associated with increased CYP2E1 expression in the distal lung and accumulation of APAP-protein adducts. This injury was associated with distal lung activation of oxidant stress, endoplasmic reticulum stress, and inflammatory stress response pathways. Our findings confirm that following toxic APAP exposure, distal lung CYP2E1 expression is associated with APAP metabolism, tissue injury, and oxidant, inflammatory, and endoplasmic reticulum signaling. This previously unrecognized injury may help improve our understanding of the relationship between APAP and pulmonary-related morbidity.

1. Introduction

Acetaminophen (*N*-acetyl-*p*-aminophenol, APAP) is the most commonly used analgesic and antipyretic around the world [1, 2]. APAP is perceived to be safe and effective, leading to human exposures that begin in utero with maternal use and continue throughout lifetime. However, this perception is challenged by the fact that acute overdose of APAP is highly toxic and is the leading cause of acute liver failure in the USA and Europe [1, 2]. Additionally, it is increasingly

recognized that chronic APAP use is associated with various morbidities affecting multiple-organ systems [3, 4].

One consistent observation has been the association between APAP exposure and pulmonary dysfunction. Both prenatal and early-life APAP exposures have been linked to an increased risk of developing asthma [3, 5–7]. Furthermore, acute overdose has been associated with pulmonary injury [8, 9]. Preclinical studies have also linked APAP exposure to lung injury. Rats and mice exposed to APAP develop bronchiolar injury that occurs within 4 hours of initial

exposure [10–14]. When looked for, pulmonary injury induced by toxic APAP exposure occurs as consistently and with similar severity as hepatic injury [13, 15]. Despite this consistent and reliable observation, the mechanisms underlying APAP-induced pulmonary injury are unknown [4].

In contrast, the mechanisms underlying APAP-induced liver injury have been well studied. In response to toxic APAP exposure, the hepatic cytochrome P450 2E1 (CYP2E1) enzyme converts APAP to its toxic metabolite N-acetyl-para-benzo-quinone imine (NAPQI). Accumulation of this toxin leads to multiple deleterious effects, including glutathione (GSH) depletion, oxidative damage, APAP-protein adducts, mitochondrial dysfunction, and hepatocyte death [2, 16, 17]. A growing body of literature supports the hypothesis that these same mechanisms are also active in the lung, making it susceptible to the toxic effects of APAP. Direct intratracheal administration of the toxic APAP metabolite NAPQI injures the trachea and bronchial epithelium [18]. Importantly, like the liver, the lung expresses the APAP-metabolizing enzyme CYP2E1. Previous studies have demonstrated that the bronchial and bronchiolar epithelia [19–22], as well as the club cell within the bronchioles [11], express CYP2E1. Accordingly, following APAP exposure, APAP-protein adducts can be detected in the areas of the lung that express CYP2E1 [11, 15, 18, 23, 24]. These data support the hypothesis that pulmonary metabolism of APAP results in localized GSH depletion and accumulation of toxic metabolites resulting in injury to the large conducting airways.

Importantly, expression of the APAP-metabolizing enzyme CYP2E1 is not limited to the proximal lung and larger conducting airways. Specifically, CYP2E1 is also expressed in the peripheral lung [25], including the alveolar epithelium and alveolar macrophages [26, 27]. Furthermore, APAP exposure is toxic to isolated type II pulmonary epithelial cells and alveolar macrophages and associated with GSH depletion [9, 28]. However, the mechanism by which this injury occurs and whether APAP exposure damages the distal lung *in vivo* is unknown. Understanding whether the distal lung is susceptible to the toxic effects of APAP would improve our understanding of the mechanisms underlying APAP exposure and long-term pulmonary dysfunction.

Therefore, we hypothesized that distal lung injury would occur in a murine model of toxic APAP exposure. In this study, we exposed adult male mice to APAP (280 mg/kg, IP) and performed robust and blinded histopathologic assessments of pulmonary injury. We found that in addition to significant proximal lung injury with epithelial cell death, toxic APAP exposure induced distal lung inflammation and emphysematous changes. Concurrently, we observed activation of proinflammatory and endoplasmic reticulum (ER) stress response signaling. Immunofluorescent staining confirmed CYP2E1 expression in the distal lung, and the presence of CYP2E1 in the distal lung was confirmed via Western blot of isolated microsomes. Importantly, following toxic APAP exposure, APAP adducts were present in the areas of distal lung injury. This injury was associated with GSH depletion and activation of proinflammatory NF κ B signaling and target gene expression. Our findings confirm that

following toxic APAP exposure, distal lung CYP2E1 expression is associated with APAP metabolism and tissue injury as well as inflammatory and ER signaling. This previously unrecognized injury may help explain the association between APAP exposure and pulmonary morbidity and suggest the importance of further studies. These results also urge cautious use of APAP in settings where the effect on the lung is unknown and understudied.

2. Methods

2.1. Murine Model of Toxic Acetaminophen (APAP) Exposure. Adult (6–8-week old) male ICR mice were exposed to APAP (280 mg/kg, intraperitoneal (IP); dissolved in phosphate-buffered saline). Mice were fasted overnight (~16 hours) prior to the day of exposure. Following exposure, the mice were sacrificed, blood was collected by cardiac puncture after which normal saline was perfused through the right ventricle, and tissue samples were collected and processed as described below. All procedures were approved by the IACUC at the University of Colorado (Aurora, CO), and care and handling of the animals was in accord with the National Institutes of Health guidelines for ethical animal treatment.

2.2. Histologic Evaluation of APAP-Induced Hepatic Injury. Liver tissue was fixed with 4% paraformaldehyde, paraffin embedded, and sections were cut (5 μ m) and stained with hematoxylin and eosin at the University of Colorado Denver Morphology and Phenotyping Core. Histopathological scoring of the liver tissue was performed by a trained histologist blinded to the treatments or grouping of animals. Briefly, the acetaminophen-induced liver injury system relied on 3 semiquantitative and 1 quantitative criteria. These criteria included (1) the extent and locale of necrosis, (2) the extent of inflammatory cell infiltration, (3) the extent of centrilobular sinusoidal dilatation, and (4) measurement of the serum alanine transaminase (ALT) all as indicated in Martin-Murphy et al. [29].

2.3. Serum Alanine Aminotransferase (ALT) and HMGB1 Measurements. Serum ALT was quantitatively determined using the ALT (SGPT) reagent and the colorimetric, end-point method according to the manufacturer's instructions (Teco Diagnostics). Serum HMGB1 was measured using HMGB1 ELISA according to the manufacturer's protocol (MyBioSource).

2.4. Histologic Evaluation of APAP-Induced Pulmonary Injury. Following perfusion of the lungs through the right ventricle as described above, the trachea was cannulated with a 24 G angiocatheter. The lungs were inflation-fixed at 20 cm H₂O pressure for 20 minutes with 4% paraformaldehyde and stored. The lungs were paraffin-embedded, and sections were cut (5 μ m) and stained with hematoxylin and eosin at the University of Colorado Denver Morphology and Phenotyping Core. Measurements of mean linear intercept (MLI), a measurement of the mean distance in the air spaces, and airspace area (ASA) and surface area (SA) were performed using the computer-assisted image-analysis program

MetaMorph Basic (Molecular Devices, Sunnyvale, CA) with custom-designed macros (subroutines) on images captured on an Olympus IX83 microscope (10x, 20x, and 40x objective lenses). Ten randomly selected nonoverlapping sections per mouse at 40x magnification were assessed.

Histopathological scoring of the lungs was performed by a trained histologist blinded to the treatments or grouping of animals. Briefly, 4 semiquantitative criteria were used for this scoring: (1) the integrity of the respiratory and terminal bronchiole epithelium (0-3, normal to severe, as well as the presence or absence of the apoptotic epithelium in the airway lumen); (2) the relative quantity of bronchus-associated lymphoid tissue (BALT; 0-2, none to lots); (3) the quantity of macrophages found in the peripheral airway (0-3, none to lots with clumps); and (4) the presence of peripheral lung emphysema with alveolar wall clubbing (0-2, none to lots). The relative quantity of neutrophils in the tissue was also noted. Scores were tallied, grouped, and finally unblinded by the individual with knowledge of the groupings. Histological images were captured on an Olympus BX51 microscope equipped with a 17 MP Olympus DP73 high-definition, color, digital camera using the Olympus cellSens software (Olympus, Waltham, MA, USA). All composite images were cropped and assembled using Adobe Photoshop.

2.5. Bronchoalveolar Lavage Fluid Analysis. After exposure to APAP, adult mice were sacrificed and bronchoalveolar lavage fluid (BALF) was obtained and analyzed [30]. Total protein content was determined by the Bradford method with bovine serum albumin as a standard. BALF total cell count and cell differentials were assessed for characteristics of pulmonary injury.

2.6. Isolation of mRNA, cDNA Synthesis, and Analysis of Relative mRNA Levels by RT-qPCR. At the time of tissue collection, both the right and left lungs were dissected into “proximal” and “distal” sections. The “proximal” section was demarcated by where the conducting airway was no longer visualized without assistance. The “distal” lung was the remainder of the available section. Frozen tissue was placed in RLT buffer (Qiagen), and tissue was homogenized using the Bullet Blender (Next Advance). Pulmonary mRNA was collected from homogenized tissue using the RNeasy Mini Kit (Qiagen) according to the manufacturer’s instructions. Initially, tissue RNA was assessed for purity and concentration using the NanoDrop (Thermo Fisher Scientific), and cDNA was synthesized using the Verso cDNA Synthesis Kit (Thermo Fisher Scientific). Relative mRNA levels were evaluated by quantitative real-time PCR using exon spanning primers (Table 1), TaqMan gene expression, and the StepOnePlus Real-Time PCR System (Applied Biosystems). Relative quantitation was determined via normalization to the endogenous control 18S using the cycle threshold ($\Delta\Delta Ct$) method.

2.7. Preparation of Whole Lung Lysate and Cytosolic/Nuclear Extracts and Western Blot. Frozen distal pulmonary tissue was homogenized using the Bullet Blender (Next Advance). Pulmonary whole cell lysates were collected in T-PER

TABLE 1: List of genes and primers used for qPCR analysis.

Target	Assay ID
<i>Cyp2e1</i>	Mm00491127_m1
<i>Il1b</i>	Mm01336189_m1
<i>Nfkbia</i>	Mm00477798_m1
<i>Gclc</i>	Mm00802655_m1
<i>Ptgs2</i>	Mm00478374_m1
<i>Ddit3</i>	Mm01135937_g1
<i>Hspa5</i>	Mm00517691_m1
<i>18S</i>	Mm03928990_g1
<i>Mmp9</i>	Mm00442991_m1
<i>Ccl2</i>	Mm00441242_m1

TABLE 2: List of antibodies used for Western blot analysis.

Antibody	Vendor	Catalog number
Anti-CYP2E1	Abcam	ab28146
Anti-GAPDH	Cell Signaling Technology	5174
Anti-APAP	Bio-Rad	0016-0104
Anti-p105	Cell Signaling Technology	4717
Anti-I κ B β	R&D Systems	AF5225
Anti-I κ B α	Cell Signaling Technology	4814
Anti-p65	Cell Signaling Technology	8242
Anti-p50	Abcam	ab32360
Anti-HDAC1	Cell Signaling Technology	5356
Anti-CHOP	Cell Signaling Technology	2895

(Thermo Fisher Scientific), and cytosolic and nuclear extracts were collected in NE-PER (Thermo Fisher Scientific). Lysates and cytosolic and nuclear extracts were electrophoresed on a 4-12% polyacrylamide gel (Invitrogen), and proteins were transferred to an Immobilon Membrane (Millipore) and blotted with antibodies (Table 2). Blots were imaged using the LI-COR Odyssey Imaging System, and densitometric analysis was performed using Image Studio (LI-COR). In the figures, cropped images grouped together are from the same gel. No images have been spliced together and no images from separate blots have been grouped together.

2.8. Isolation of Microsomes from Pulmonary Tissue. Microsomes were isolated from distal pulmonary tissue using a microsome isolation kit (Abcam, 206995) according to the manufacturer’s instructions.

2.9. Immunohistochemical Staining of CYP2E1 and APAP Adducts. For immunofluorescence, tissues were deparaffinized by heating and rehydrated with xylene and ethanol. Antigen retrieval was performed with citrate antigen retrieval buffer, pH 6.0, and tissues were permeabilized with 0.5% triton, quenched with glycine, and blocked with 5% donkey serum. Sections were then incubated with anti-acetaminophen (Bio-Rad, 0016-0104) and anti-CYP2E1 (Abcam, ab28146) primary antibodies overnight followed by incubation with secondary antibodies (Alexa Fluor Anti-Rabbit Donkey 594

and Alexa Fluor Anti-Sheep 647) for 1 hour. Finally, nuclear counterstaining was performed by incubating slides with DAPI (Sigma-Aldrich, D8417). Staining was visualized using the Olympus IX83 microscope and Olympus DP80 camera using Olympus cellSens software.

2.10. Pulmonary and Hepatic Glutathione Fluorescent Detection. Pulmonary and hepatic whole cell lysates were collected in T-PER (Thermo Fisher Scientific). Lysate extracts were serially diluted, and glutathione (GSH) and oxidized glutathione (GSSG) contents were quantified using the Glutathione Fluorescent Detection Kit (Thermo Fisher Scientific).

2.11. Flow Sorting. Lungs were digested as previously described [31]. In brief, lungs were first inflated with CD45-APC (Clone # 30-F11) at a concentration of 1/500 to label alveolar leukocytes for 3 minutes. Lungs were then flushed and digested with Liberase™ (0.4 mg/ml) and DNase I (100 U/ml) by mincing in a gentleMACS C tube using program m_lung_01_02 for a full cycle, incubated for 20 minutes at 37°C, then agitated again using program m_lung_02 for 5 seconds of the cycle. Cell suspension was then washed through a 70 and 40 µm cell strainer and red blood cell (RBC) lysis was performed using 1x RBC Lysis Buffer (eBioscience). Cell surface staining was then performed using the following antibodies: Ly6G-BV421 (Clone # 1A8), CD3-BV421 (Clone # 17A2), Ly6C-BV421 (Clone # AL-21), CD31-BV421 (Clone # MEC13.3), CD326-BV510 (Clone # G8.8), CD64-PE (Clone # X54-5/7.1), CD11b-PE/Cy7 (Clone # M1/70), and SigF-APC/R700 (Clone # E50-2440). All antibodies were used at a concentration of 1/200 and stained on ice for 15 minutes. Cells were then washed using 1 ml of cell staining buffer and centrifuged at 300 rcf for 5 minutes. Cell pellets were then resuspended with 500 µl of 1x Cytofix buffer (Biolegend) and incubated in the dark at room temperature for 30 minutes. Cells were then washed with 1 ml of Cytoperm wash buffer and centrifuged at 300 rcf for 5 minutes then resuspended in 100 µl of Cytoperm wash buffer and stained with CYP2E1-AF488 antibody overnight at 4°C. Cells were washed using 1 ml of cell staining buffer and then analyzed on a ZE5 Cell Analyzer (Propel Labs). Single cells were identified using forward and side scatter followed by forward scatter area and height. Using a dump gate, monocytes, neutrophils, B-cells, and T-cells were excluded and macrophages were identified using CD45 and CD64. Resident and recruited macrophages were differentiated using positive selection for SigF and CD11b, respectively. Epithelial cells were gated on using positive staining for CD326 and negative staining for CD45. CYP2E1 expression was performed by assessing geometric mean fluorescence (MFI) for resident macrophages (Dump⁻, CD45⁺CD64⁺SigF⁺CD11b⁻), recruited macrophages (Dump⁻, CD45⁺CD64⁺CD11b⁺SigF⁺), and epithelial cells (Dump⁻, CD45⁺CD326⁺).

2.12. Statistical Analysis. For comparison between treatment groups, the null hypothesis that no difference existed between treatment means was tested by Student's *t*-test for two groups and two-way ANOVA for multiple groups with potentially

interacting variables (time, APAP exposure), with statistical significance between and within groups determined by means of the Bonferroni method of multiple comparisons (Prism, GraphPad Software, Inc.). Statistical significance was defined as $p < 0.05$.

3. Results

3.1. Time Course of APAP-Induced Hepatic Injury in ICR Mice. First, we sought to confirm the time course of APAP-induced liver injury in adult male ICR mice. Histologic analysis demonstrated necrotic and inflammatory injury as soon as 2 hours after APAP exposure (Figure 1(a)). Blinded histopathologic analysis revealed early and significant increases in objective scoring of necrosis (Figure 1(b)) and inflammation (Figure 1(c)) that were sustained from 2 hours through 24 hours post APAP exposure, while sinusoidal dilatation was significantly increased at 8 and 24 hours of exposure (Figure 1(d)). Concurrent with histologic evidence of injury, hepatic total glutathione decreased (Figure 1(e)) and GSSG/GSH ratio increased (Figure 1(f)). Finally, there was a significant increase in circulating markers of injury, including serum ALT (Figure 1(g)) and serum HMGB1 (Figure 1(h)). These data reliably demonstrate that significant hepatic injury occurs early and is sustained during the first 24 hours following an IP exposure to APAP.

3.2. Toxic APAP Exposure Induces Proximal and Distal Lung Injury. Next, we performed histopathologic evaluation of the lungs of APAP-exposed mice. Consistent with previous reports, APAP exposure induced significant injury to the proximal airway including death and shedding of some of the injured pseudostratified columnar epithelium into the airway lumen (Figure 2(a) B, red arrows). Objective scoring showed a significant increase in respiratory and terminal bronchial epithelial injury (Figure 2(c)) and bronchus-associated lymphoid tissue (BALT, Figure 2(d)) at 24 hours of APAP exposure. In addition to this bronchiolar injury, we observed significant changes in the alveolar lung structure that included the emphysematous-like changes of breakdown of alveolar walls and “clubbing” of the broken alveolar wall tops (Figure 2(b) D, yellow circles). Additionally, the lumenally located alveolar macrophage load increased (Figure 2(b) D, yellow arrows). Objectively, this manifested as an increase in the peripheral lung emphysema score (Figure 2(e)) and the peripheral lung airway macrophage load (Figure 2(f)). Objective morphometric analysis revealed that APAP exposure resulted in decreased surface area (Figure 2(g)), increased mean linear intercept length (Figure 2(h)), and increased airspace area (Figure 2(i)), with all markers being consistent with a destructive type of alveolar injury.

Having observed this injury, we next evaluated the bronchial-alveolar lavage fluid for evidence of injury. Analysis of BALF fluid obtained from mice exposed to APAP revealed additional markers of injury. The total cellular content of BALF significantly increased in a time-dependent manner following APAP exposure (Figure 3(a)), with an initial increase in neutrophils (Figure 3(b)) followed by macrophages (Figure 3(c)). The total protein content of BALF fluid

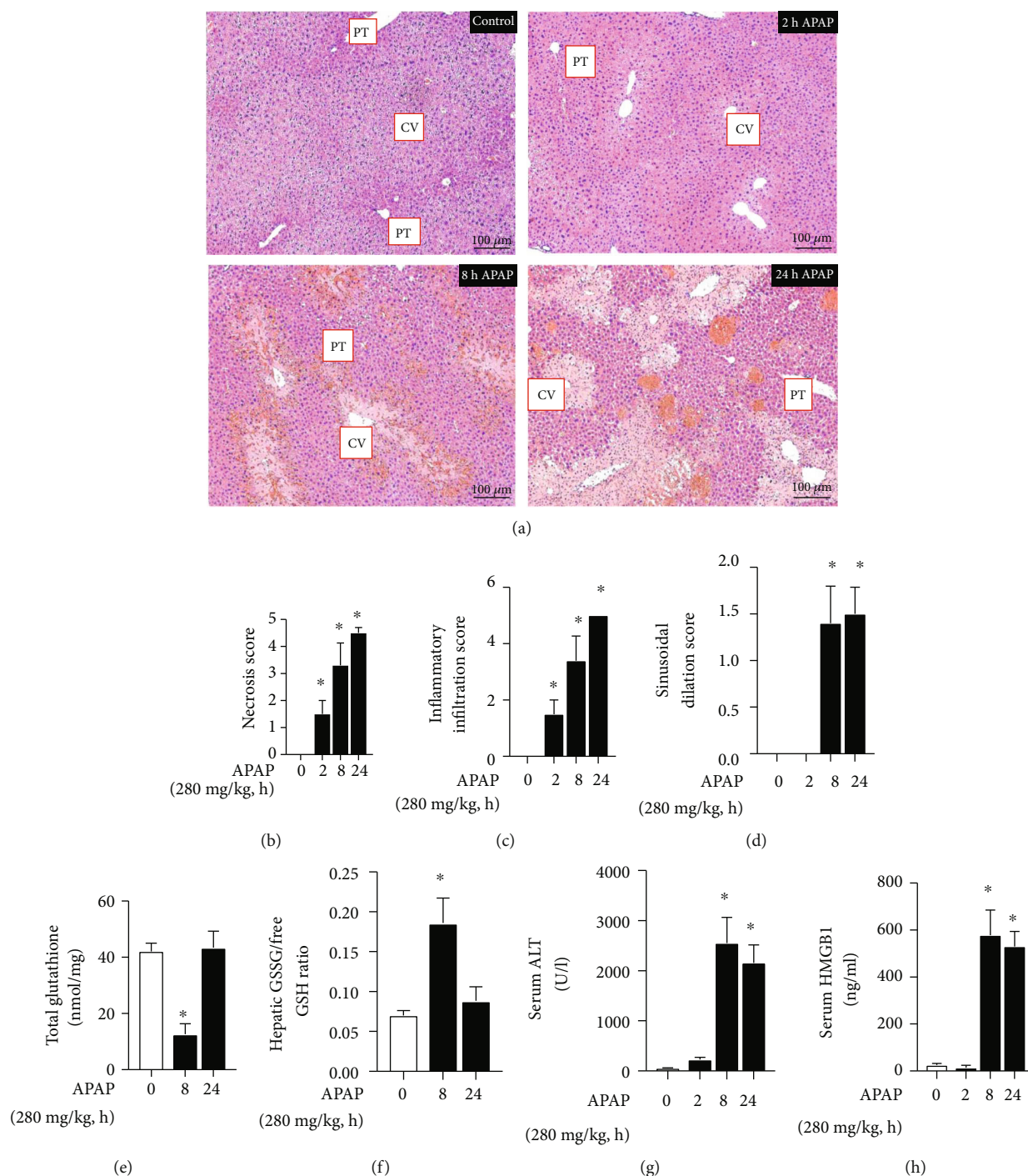


FIGURE 1: Time course of APAP-induced hepatic injury in ICR mice. (a) Representative H&E-stained hepatic sections from control and APAP-exposed (2, 8, and 24 hours; 280 mg/kg, IP) adult male ICR mice. Examples of portal triad (PT) and central vein (CV) have been added. Internal scale bar: 100 μm . (b–d) Blind histopathologic evaluation of H&E-stained hepatic sections scored for (b) necrosis, (c) inflammatory infiltration, and (d) sinusoidal dilatation. $N = 6-8$ per time point. Data are expressed as mean \pm SEM; * $p < 0.05$ vs. unexposed control. (e) Total hepatic glutathione, (f) ratio of oxidized (GSSG) vs. reduced free glutathione (GSH), and change in serum (g) ALT and (h) HMGB1 protein following APAP exposure (280 mg/kg, IP). $N = 6-8$ per time point. Data are expressed as mean \pm SEM; * $p < 0.05$ vs. unexposed control.

significantly increased at 4 hours of exposure and remained at this elevated level throughout 24 hours of exposure (Figure 3(d)). Concurrent with histologic and BALF evidence of injury, the lungs of APAP-exposed mice demonstrated evidence of oxidant stress and glutathione depletion

consistent with toxic APAP exposure. Specifically, pulmonary total glutathione remained significantly decreased (Figure 3(e)) and GSSG/GSH ratio remained significantly increased (Figure 3(f)) through the duration of exposure. Together, these data demonstrate that alveolar injury occurs

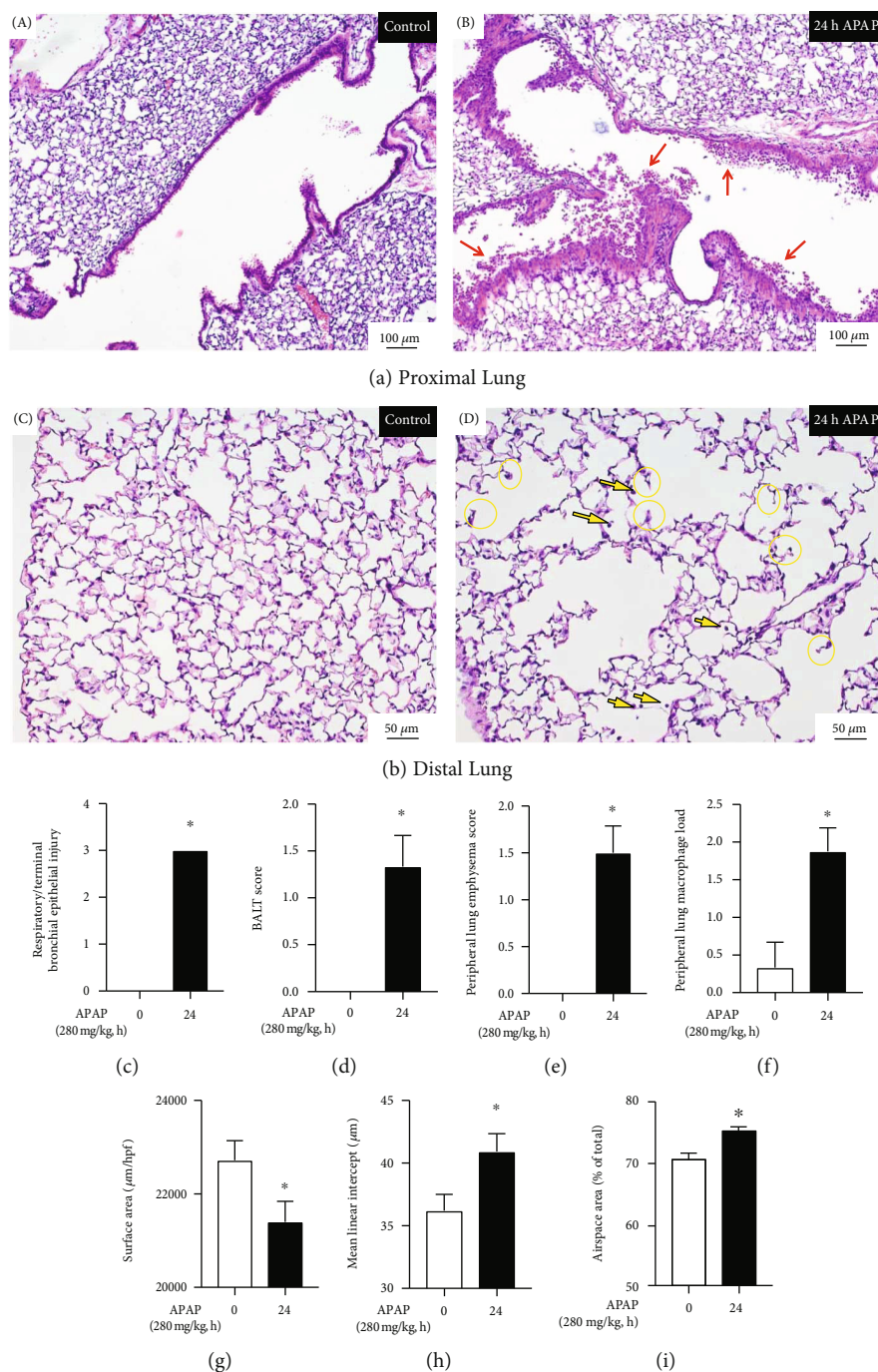


FIGURE 2: Toxic APAP exposure induces proximal and distal lung injury. Representative H&E-stained (a) proximal control (A) and APAP-exposed (B) (24 hours, 280 mg/kg, IP) adult male ICR mice and (b) distal control (C) and APAP-exposed (D) (24 hours, 280 mg/kg, IP) adult male ICR mice. Red arrows indicate epithelial cells in the airway lumen. Yellow arrows indicate distal lung macrophages. Yellow circles indicate emphysematous-like changes of the breakdown of alveolar walls and the “clubbing” of the broken wall tops. (c) Respiratory/terminal bronchiole epithelial injury, (d) bronchus-associated lymphoid tissue (BALT), (e) peripheral lung emphysema score, (f) peripheral lung macrophage load, (g) surface area, (h) mean linear intercept, and (i) airspace area in control vs. APAP-exposed (280 mg/kg, IP) adult male ICR mouse lung. $N = 3-4$ per time point. Data are expressed as mean \pm SEM; * $p < 0.05$ vs. unexposed control.

along with the injury previously described in the larger conducting airways.

3.3. The Distal Lung Expresses CYP2E1. Next, we sought to answer whether the APAP-metabolizing enzyme CYP2E1 was expressed in the distal lung. While the expression of

CYP2E1 in the alveolar space of humans has been described, expression in the murine lung is less well characterized [25–27]. At baseline, and prior to any APAP exposure, we found that the distal lung expressed *Cyp2e1* mRNA, albeit at a level significantly lower than the proximal lung (Figure 4(a)). Protein expression in whole lung

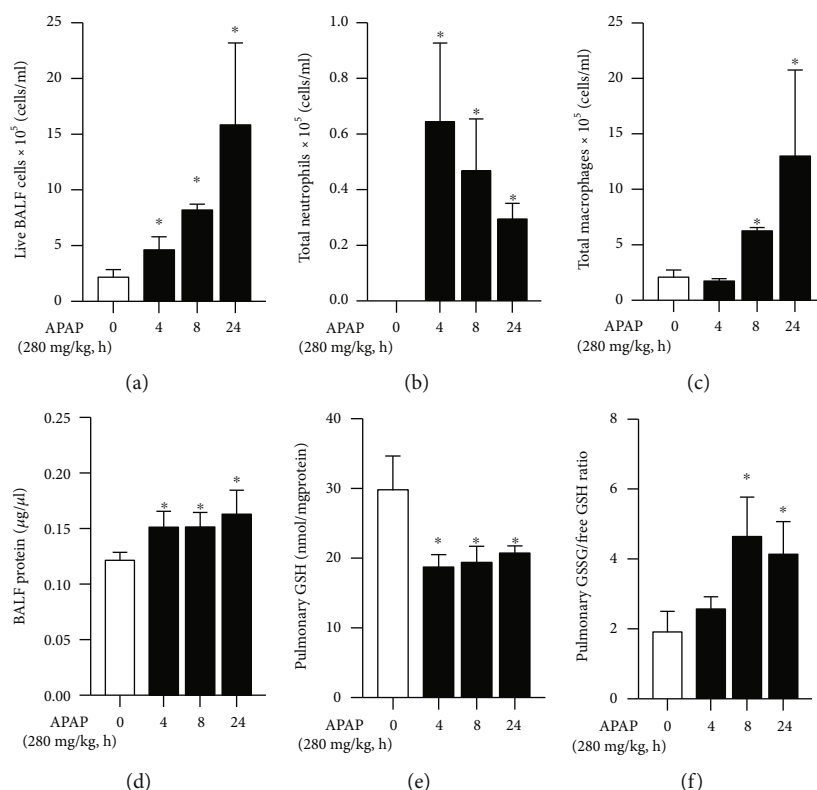


FIGURE 3: Toxic APAP exposure induces pulmonary inflammation and oxidant stress. Bronchial-alveolar fluid lavage (BALF) analysis of (a) live BALF cells, (b) total neutrophils, (c) total macrophages, and (d) BALF protein. (e) Total pulmonary glutathione and (f) ratio of oxidized (GSSG) vs. reduced free glutathione (GSH) following APAP exposure (4, 8, and 24 hours; 280 mg/kg, IP) in adult male ICR mice. $N = 6-8$ per time point. Data are expressed as mean \pm SEM; * $p < 0.05$ vs. unexposed control.

homogenate isolated from proximal and distal lung mirrored mRNA expression, with CYP2E1 being more highly expressed in the proximal lung (Figure 4(b)). Comparatively, there is a higher expression in the trachea, and expression in the liver far exceeds that of the distal and proximal lung (Figure 4(b)). The antibody for CYP2E1 used for these experiments performed as expected with negative controls (RAW 264.7) and positive controls (liver homogenate) (Figure 4(c)). Furthermore, the antibody detects higher expression of CYP2E1 in liver microsomes compared to liver homogenate, higher expression in the liver compared to that in the lungs, higher expression in lung microsomes compared to that in lung homogenate, expression in the kidney, and no cross reactivity with serum proteins (Figure 4(d)). Importantly, following APAP exposure, significant increases in distal lung *Cyp2E1* mRNA expression were observed (Figure 4(e)). Additionally, whole lung CYP2E1 content increased following APAP exposure (Figure 4(f)). These data confirm that at the location of injury—specifically the alveolar space—the APAP-metabolizing enzyme CYP2E1 is expressed and that this expression increases in the lung following toxic APAP exposure.

3.4. Toxic APAP Metabolites and CYP2E1 Expression Localizes to the Distal Lung. Having determined that the distal lung expresses CYP2E1, we assessed the presence of APAP-protein adducts using fluorescent immunostaining. Consistent with our results from qPCR and Western

blot, the distal lung demonstrated CYP2E1 staining that was present prior to (Figure 5(a) A) and after (Figure 5(b) A) APAP exposure. Of note, at 24 h post APAP exposure, alveolar staining was diffused and punctuated with positive staining in larger cells in the lumen of the alveoli and the alveoli show the emphysematous changes described above. Importantly, APAP-protein adduct staining that was absent in the unexposed lung (Figure 5(a) B) appeared in the distal lung following APAP exposure (Figures 5(b) B and 5 (c)). To further determine the cellular expression of CYP2E1, we used intracellular flow cytometry to assess CYP2E1 expression in epithelial cells and macrophages in the lungs of control and APAP-exposed mice. The flow gating strategy is provided (Figures 5(f)–5(k)). In line with our fluorescent immunostaining, CYP2E1 fluorescence is increased in both epithelial (Dump⁻, CD45⁻CD326⁺) (Figure 5(d)) and resident alveolar macrophages (Dump⁻, CD45⁺CD64⁺SigF⁺CD11b⁻) (Figure 5(e)). Intriguingly, there was no presence of a distinct recruited alveolar macrophage population (CD45⁺CD64⁺CD11b⁺SigF⁻) in the lungs of either control or APAP-exposed mice 24 hours post exposure. While histopathologic evaluation of the lung demonstrated an increase in peripheral lung macrophage load at 24 hours of APAP exposure (Figure 2(f)), this increase was not detectable by flow cytometry as an increase in recruited alveolar macrophages. A review of the histology demonstrates a visible increase in the number of peripheral lung macrophages; however, the number of recruited cells appears

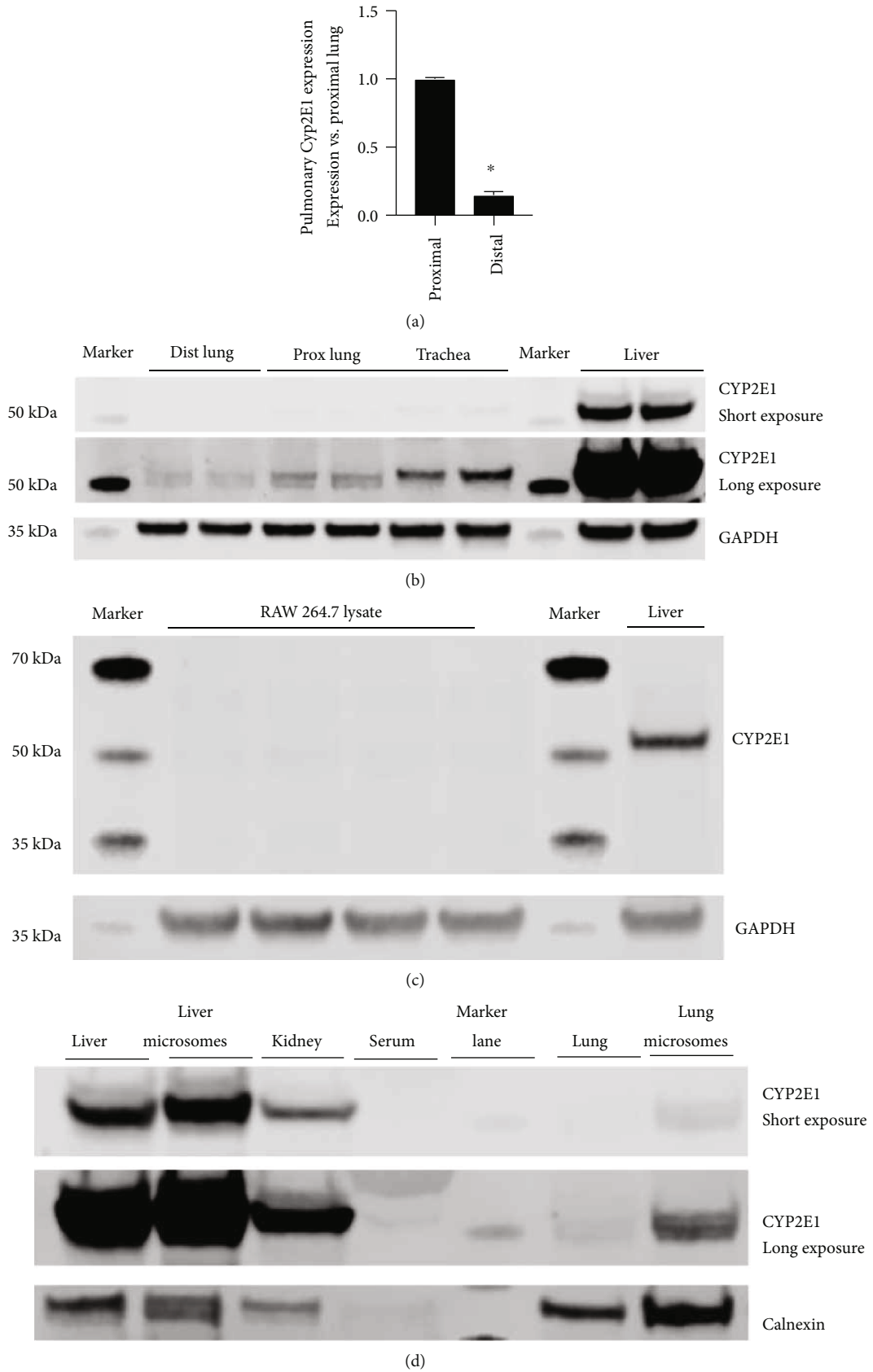


FIGURE 4: Continued.

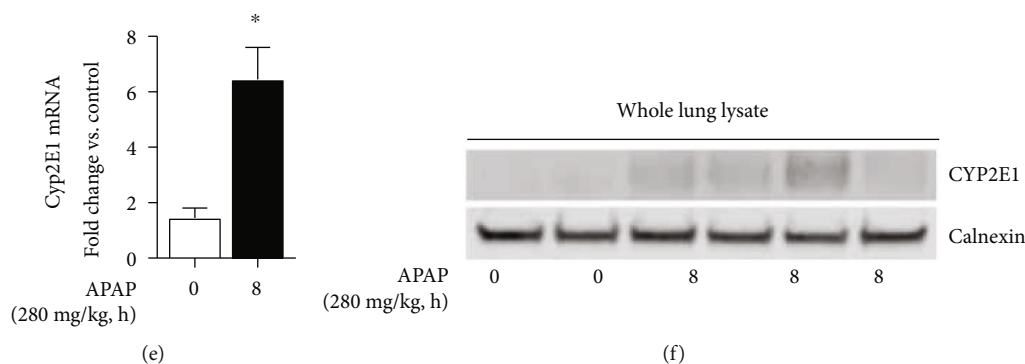


FIGURE 4: The distal lung expresses CYP2E1. (a) Fold difference in CYP2E1 mRNA expression in the distal compared to the proximal lung. Data are expressed as mean \pm SEM; * $p < 0.05$ vs. proximal lung. $N = 6-8$ mice. (b) Representative Western blot of CYP2E1 in the distal and proximal lung, as well as the trachea and liver. A “short exposure” is provided to demonstrate CYP2E1 expression in the liver without overexposing the blot. The “long exposure” is provided to allow comparisons between the distal lung, proximal lung, and trachea. GAPDH as loading control. (c) Representative Western blot of CYP2E1 in the RAW 264.7 whole cell lysate and liver homogenate. GAPDH as loading control. (d) Representative Western blot of CYP2E1 in the liver, liver microsomes, kidney, serum, lung, and lung microsomes. For each sample, 40 μ g of protein was evaluated. Calnexin as loading control, to demonstrate enrichment of the microsomal fraction. (e) Fold change in CYP2E1 mRNA expression in the distal lung following APAP exposure (8 hours; 280 mg/kg, IP). Data are expressed as mean \pm SEM; * $p < 0.05$ vs. control. $N = 4-6$ per time point. (f) Representative Western blot of whole lung lysate following APAP exposure (8 hours; 280 mg/kg, IP). Calnexin shown as loading control.

less than would be present with other types of inflammatory injury (e.g., pneumonia). We speculate this visible increase was not large enough to provide an adequate number of cells to make any conclusions using flow cytometry. These results demonstrate that the APAP-metabolizing enzyme CYP2E1 is expressed and is active in the distal lung and that toxic APAP metabolites accumulate in the distal lung where injury is observed.

3.5. Toxic APAP Exposure Induces Proinflammatory NF κ B Signaling in the Distal Lung. Toxic APAP exposure is associated with multiple cellular insults that can lead to downstream proinflammatory signaling. These include, but are not limited to ROS production, inflammasome activation and IL1 β secretion, HMGB1 release, and TLR4/TLR9 signaling [16, 32, 33]. Of note, the transcription factor NF κ B is activated downstream of these pathways and is known to control the expression of multiple genes previously identified to be involved in APAP-induced hepatic injury. Thus, we interrogated APAP-induced pulmonary NF κ B activation and downstream gene expression.

First, we assessed pulmonary cytosolic extracts from APAP-exposed adult mice for evidence of degradation of the NF κ B inhibitory proteins p105, I κ B α , and I κ B β . In APAP-exposed adult mice, p105, I κ B α , and I κ B β had all degraded by 8 hours of exposure (Figure 6(a)). We next sought to confirm that cytosolic NF κ B inhibitory protein degradation was associated with pulmonary nuclear translocation of the NF κ B subunits p65 and p50. In APAP-exposed mice, there was robust nuclear accumulation of p50 while levels of p65 decreased and were nearly absent by 8 hours (Figure 6(b)). Interestingly, this pattern of NF κ B subunit nuclear translocation mirrors what is seen in the lungs of adult mice exposed to endotoxemia by intraperitoneal injection of LPS [34]. Next, we assessed the distal lung expression

of NF κ B target genes previously associated with APAP-induced hepatic injury (*Mmp9*, *Ccl2*, *Il1b*, *Nfkbia*, *Gclc*, and *Ptgs2*). Consistent with pulmonary NF κ B activation, by 8 hours of APAP exposure, the expression of all genes was significantly increased compared to baseline (Figure 6(c)).

3.6. Toxic APAP Exposure Induces Endoplasmic Reticulum Stress in the Distal Lung. Following APAP administration, the liver demonstrates evidence of endoplasmic reticulum (ER) stress [35, 36]. Interrupting this process attenuates APAP-induced liver injury [37]. While we could find reports that other tissues demonstrate evidence of ER stress following APAP exposure, we could find no such report for the lung [38]. Having demonstrated that the distal lung expresses CYP2E1 and accumulates APAP adducts, we specifically interrogated this tissue for evidence of endoplasmic reticulum stress following toxic APAP exposure. Following APAP exposure, distal lung expression of the ER-stress-related markers *Ddit3* (CHOP) and *Hspa5* (BiP0 increased (Figure 7(a))). Furthermore, we found significant nuclear accumulation of CHOP in the distal lung following exposure to APAP (Figures 7(b) and 7(c)). These data demonstrate initiation of ER stress signaling in the distal murine lung following toxic exposure to APAP. This conformation suggests a means to pharmaceutically treat APAP-induced lung injury.

4. Discussion

We found that the lung is susceptible to APAP-induced injury. Similar to previous reports, we found that toxic APAP exposure induced significant injury in the large, conducting airways. Here, we report that the peripheral lung is also subject to the injurious effects of APAP. Histologically, there is evidence of macrophage infiltration and alveolar injury

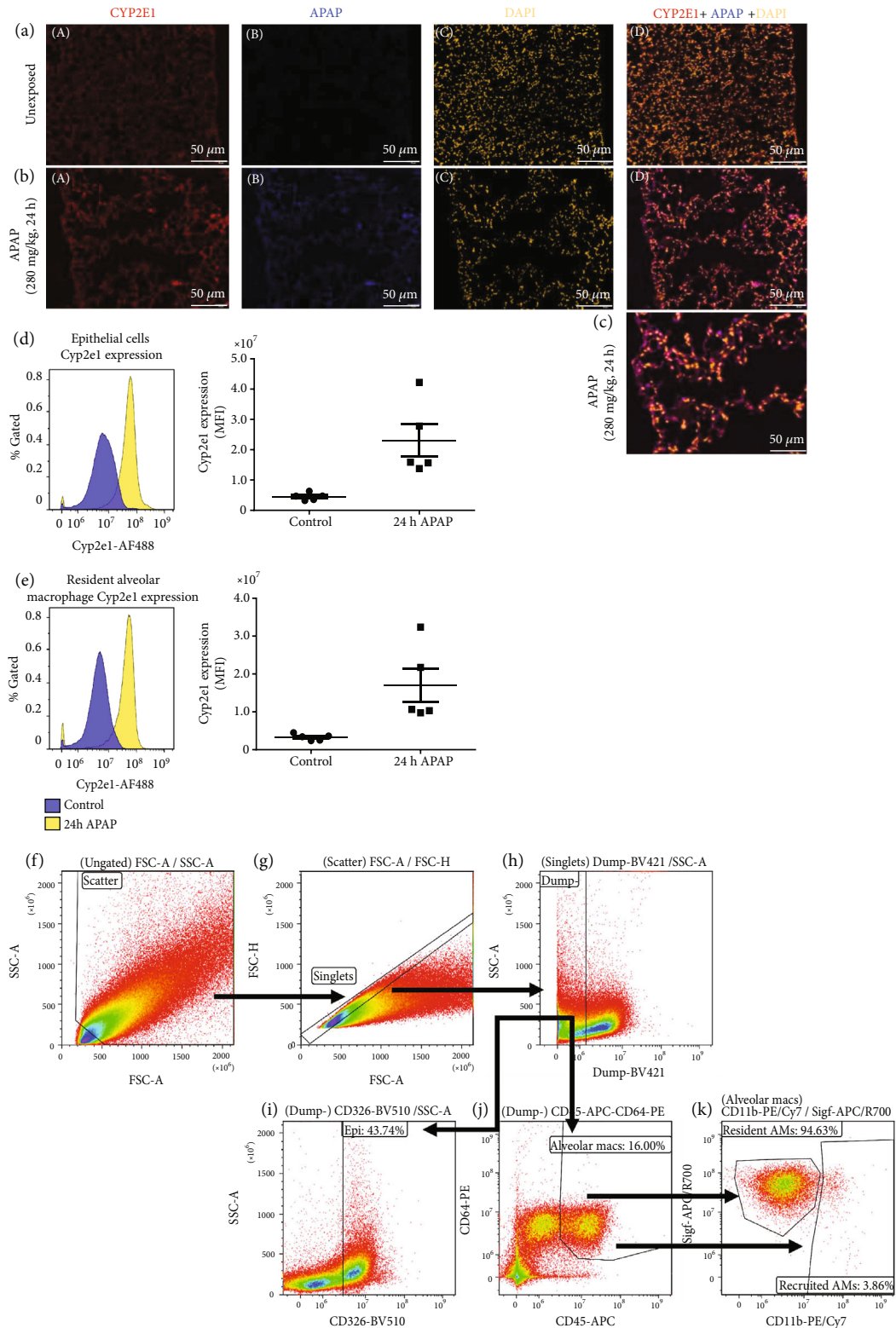


FIGURE 5: Toxic APAP metabolites accumulate in the distal lung. Representative immunofluorescence staining of the distal lung from (a) unexposed and (b and c) APAP-exposed (24 hours; 280 mg/kg, IP) adult male ICR mice. CYP2E1 was stained in red (a), APAP was stained in blue (b), and DAPI was stained in yellow (c). An overlay of all three stains (a, b, and c) is provided (d). Internal scale bar: 50 μm . Flow cytometric analysis demonstrates an induction of CYP2E1 expression in APAP-exposed mice when compared to unexposed controls in (d) epithelial cells and (e) resident alveolar macrophages. (f–k) Flow gating strategy. (f) Scatter cells are gated into (g) singlets, after which (h) neutrophils, B-cells, T-cells, and monocytes are excluded and the Dump⁻ gate is used to select for (i) epithelial (Dump⁻, CD326⁺) or (j) alveolar macrophages (Dump⁻, CD45⁺CD64⁺). (k) Resident (Dump⁻, CD45⁺CD64⁺Siglec-F^{Hi}CD11b^{Lo}) and recruited (Dump⁻, CD45⁺CD64⁺CD11b^{Hi}Siglec-F^{Lo}) alveolar macrophages are then segregated based on Siglec-F and CD11b.

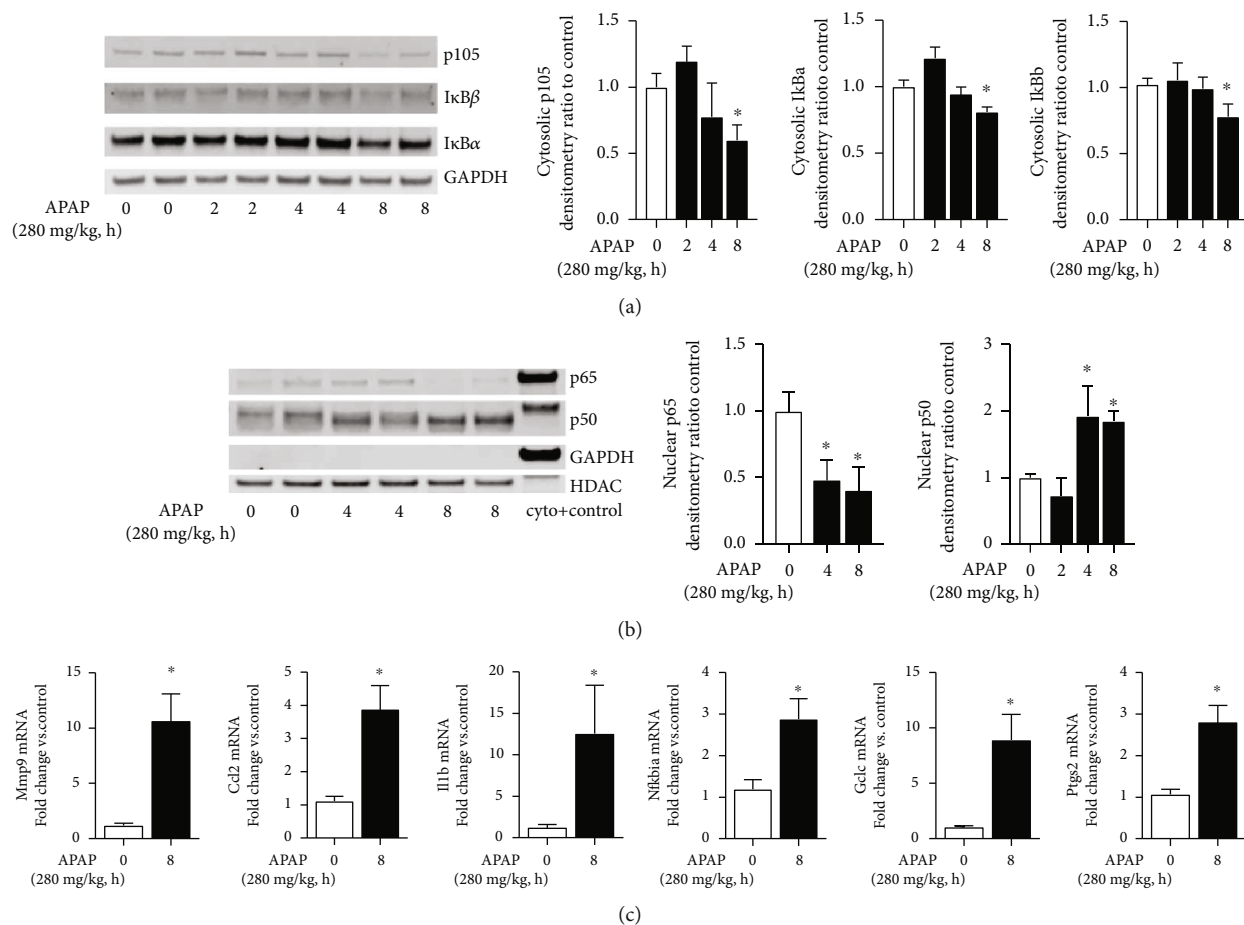


FIGURE 6: Toxic APAP exposure induces proinflammatory NF κ B signaling in the distal lung. (a) Representative Western blot and densitometric analysis of NF κ B inhibitory proteins p105, I κ B α , and I κ B β in distal lung cytosolic extracts after APAP exposure (2, 4, and 8 hours; 280 mg/kg, IP). GAPDH is shown as loading control. Data is expressed as mean \pm SEM ($N = 4-6$ per time point). * $p < 0.05$ vs. unexposed control. (b) Representative Western blot and densitometric analysis of NF κ B subunits p65 and p50 in distal lung nuclear extracts after APAP exposure (2, 4, and 8 hours; 280 mg/kg, IP). HDAC is shown as a loading control. GAPDH is shown to confirm the purity of the nuclear sample. Data is expressed as mean \pm SEM ($N = 4-6$ per time point). * $p < 0.05$ vs. unexposed control. (c) Fold change in NF κ B target gene mRNA expression: *Mmp9*, *Ccl2*, *Il1b*, *Nfkbia*, *Gclc*, and *Ptgs2* following APAP exposure (8 hours; 280 mg/kg, IP). Data expressed as mean \pm SEM ($N = 4-6$ per time point). * $p < 0.05$ vs. unexposed control.

within 24 hours of exposure. These histologic findings correspond with an increase in inflammatory cells in BALF obtained from APAP-exposed animals and a sustained depletion in the reduced glutathione in the lung. Furthermore, we demonstrate that the peripheral lung expresses CYP2E1, expression of CYP2E1 increases after APAP exposure, and that expression can be detected in alveolar macrophages and the pulmonary epithelium. We were able to detect the presence of APAP-protein adducts in the peripheral lung, as well as the activation of ER stress and proinflammatory signaling. Together, these results support the hypothesis that the lung is able to directly metabolize APAP, and that following a toxic exposure, there are measurable implications on oxidant, ER stress, and inflammatory stress signaling pathways. Activation of these responses are temporally related to proximal and distal lung injury. Further work is necessary to determine whether this injury can be prevented through pharmacologic interventions aimed precisely at the lung. However, although suggestive, whether

these mechanisms underlie the clinical relationship between APAP exposure and pulmonary dysfunction are unknown.

A large body of literature demonstrates that the lung is particularly sensitive to both acute toxic and chronic APAP exposure. In humans, acute overdose has been associated with ARDS [8], pneumonitis [39], and alveolar injury [40]. Both prenatal and early life exposures have been linked to the development of asthma [3, 5–7], while chronic exposure later in life has been associated with an increased risk of chronic obstructive pulmonary disease [4, 41]. Preclinical data across multiple species robustly support the association between APAP exposure and pulmonary injury. Toxic APAP exposure induces bronchiolar injury in rats and mice and induces an ARDS-like picture in pigs [10–14, 42]. Importantly, pulmonary injury appears to occur independently from (but concurrently with) hepatic injury. Firstly, while APAP-induced hepatic injury is dependent on the fasted status of the exposed animal, APAP-induced pulmonary injury is not [14]. Furthermore, despite a significant reduction in

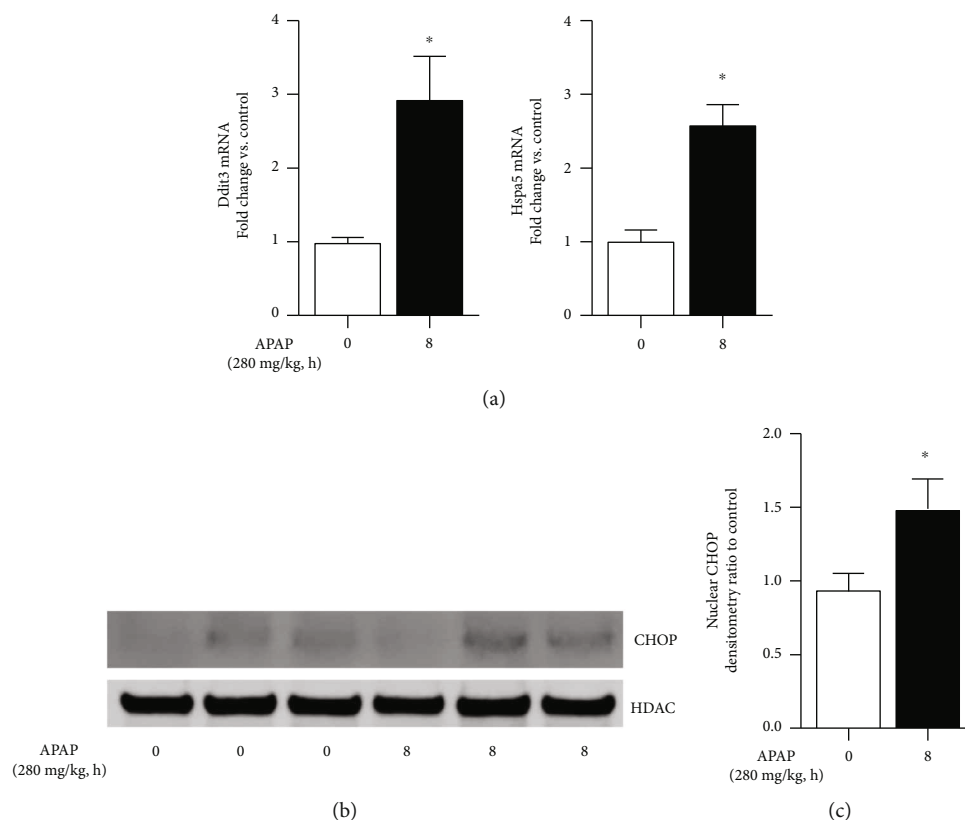


FIGURE 7: Toxic APAP exposure induces endoplasmic reticulum stress in the distal lung. (a) Fold change in mRNA expression of endoplasmic reticulum (ER) stress markers Ddit3 and Hspa5 in the distal lung after APAP exposure (8 hours; 280 mg/kg, IP). Data expressed as mean \pm SEM ($N = 4-6$ per time point). * $p < 0.05$ vs. unexposed control. (b) Representative Western blot and (c) densitometric analysis of CHOP in distal lung nuclear extracts after APAP exposure (2, 4, and 8 hours; 280 mg/kg, IP). Data expressed as mean \pm SEM ($N = 4-6$ per time point). * $p < 0.05$ vs. unexposed control.

APAP-induced liver injury in mice with a liver-specific knockout of NADPH-cytochrome P450 reductase, pulmonary injury remains consistent [13]. This observation is similar to those reported when APAP-exposed mice were pretreated with the mixed-function oxidase inhibitor piperonyl butoxide [15]. Although pretreatment largely abrogated APAP-induced hepatic injury, pulmonary injury remained consistent and significant [15].

There is biologic plausibility to the premise that the lung directly metabolizes APAP and that pulmonary injury occurs secondary to the accumulation of the toxic metabolites of APAP. The respiratory tract endures near continuous exposure to toxic xenobiotic compounds. As such, the expression of xenobiotic metabolizing enzymes, including CYP2E1 is believed to be quite important [19, 43, 44]. In humans, pulmonary CYP2E1 expression has been reported in the peripheral lung, including the alveolar epithelium and macrophages [25–27]. Interestingly, following APAP exposure, APAP-protein adducts can be detected in the areas of the lung that express CYP2E1 [11, 15, 18, 23, 24]. Of note, pulmonary CYP2E1 expression has been linked to pulmonary dysfunction induced by chronic alcohol ingestion [45]. Whether inhibiting pulmonary CYP2E1 expression would attenuate APAP-induced lung injury remains to be tested.

Recent reviews have confirmed that the mechanisms underlying APAP-induced lung injury are not well under-

stood and would benefit from further study [4]. Furthermore, while previous studies have clearly demonstrated the relationship between APAP-exposure and epithelium injury in the larger airways, very little information is known about the effect of APAP on the cells residing in the distal lung. Multiple potential mechanisms could explain how direct pulmonary metabolism of APAP injures the distal lung. These potential mechanisms include oxidative stress injury and activation of ER stress pathways. Our data support a role played by both oxidative and ER stress in the pathogenesis of APAP-induced lung injury.

Previous studies have shown that pulmonary CYP2E1 activity is a source of oxidative stress [20]. Following APAP exposure, we have shown that CYP2E1 expression increases in the distal lung, a potential source of damaging oxidative stress. Furthermore, we demonstrate that APAP exposure is associated with lung glutathione depletion and increased distal lung expression of the glutamate-cysteine ligase catalytic (GCLC) subunit. Previous studies have demonstrated that whole lung pulmonary glutathione decreases with toxic APAP exposure [12, 46]. Additionally, whole lung GCLC expression increases in response to toxic APAP exposure [47]. However, these data were interpreted with a focus on bronchiolar injury. Of note, GCLC overexpression attenuates APAP-induced liver injury [48], but whether this is true in the lung is unknown. Finally, we add *in vivo* data

to compliment previous *in vitro* studies demonstrating that APAP toxicity in isolated type II pulmonary epithelial cells and alveolar macrophages is associated with glutathione depletion [9, 28, 49]. Together, these data support the hypothesis that toxic APAP exposure induces oxidative stress in the distal lung, potentially contributing to injury and pulmonary dysfunction.

Recently, the role of ER stress has been implicated in APAP-induced hepatic injury [36, 38, 50]. However, whether toxic APAP exposure induces ER stress response pathways in the lung is unknown. We provide novel evidence that these pathways are in fact active in the distal lung. In the distal lung, toxic APAP exposure induces the expression of *Ddit3* (CHOP) and *Hspa5* (BIP), as well as CHOP nuclear translocation, all of which are markers of ER stress. While ER stress has been implicated in various lung diseases [51], this is the first report linking toxic APAP exposure to activation of ER stress pathways in the lung. More work needs to be done to understand the contribution of these pathways to the pathogenesis of APAP-induced pulmonary injury.

Our study has several limitations. We did not prove that the pulmonary CYP2E1 directly metabolizes APAP. It is possible that toxic APAP metabolites from the liver travel to the lung causing injury. More direct studies are needed, specifically testing whether pulmonary cell-specific CYP2E1 null models are resistant to APAP-induced lung injury. Previous reports have demonstrated sex-specific differences in APAP-induced hepatic and renal injury [52]. In the current study, we only evaluated pulmonary injury in male mice. Future studies are planned to evaluate whether female mice are equally susceptible to APAP-induced lung injury. Furthermore, we exposed mice to a single toxic dose of APAP, and more work needs to be done to evaluate the effect of repetitive, lower doses. Additionally, while we interrogated inflammatory, oxidant stress, and ER stress pathways, other potential mechanisms may underlie APAP-induced lung injury. Specifically, we did not test whether prostaglandin H synthase metabolism of APAP contributes to pulmonary injury [9, 28]. Finally, we used antibody-based approaches to detect CYP2E1 in the lung after APAP exposure using Western blot, immunostaining, and flow cytometry. Nonspecific binding of our antibody to non-CYP2E1 protein could make interpretation problematic. These limitations must be acknowledged. However, we have provided data to demonstrate that the antibody performs as expected with negative controls and positive controls and shows the appropriate expression pattern across organs and microsomal fractions.

In conclusion, toxic APAP exposure results in significant alveolar injury. This injury is associated with the upregulation of CYP2E1 in the resident macrophage and pulmonary epithelium, as well as the presence of APAP-protein adducts, indicative of direct pulmonary metabolism of APAP. Furthermore, toxic APAP exposure is associated with the activation of oxidant stress, ER stress, and inflammatory response pathways. These findings have clinical implications in our assessment of acute acetaminophen overdose, and require further study in the setting of chronic exposure.

Data Availability

The data used to support the findings of this study are included within the article.

Conflicts of Interest

The authors declare no potential financial or ethical conflicts of interest.

Authors' Contributions

CJW, JS, and SM contributed in the conception and design of the research; JS, AA, BB, CTP, RT, RD, LN, SM, and CJW performed experiments; JS, DJO, AA, BB, CTP, RT, RD, LN, SM, ENG, and CJW analyzed data; JS, DJO, AA, BB, CTP, RT, RD, LN, SM, ENG, and CJW interpreted the results of experiments; CJW drafted the manuscript; JS, DJO, AA, BB, CTP, LN, SM, and CJW prepared the figures; CJW edited and revised the manuscript; and JS, DJO, AA, BB, CJ, CTP, RT, RD, LN, SM, ENG, and CJW approved the final version of the manuscript.

Acknowledgments

This work was supported by NIH grant R01HL132941 to CJW, NIH grant R35HL139726 to ENG, and AHA grant 19POST34380396 to AA.

References

- [1] W. M. Lee, "Acetaminophen (APAP) hepatotoxicity—isn't it time for APAP to go away?," *Journal of Hepatology*, vol. 67, no. 6, pp. 1324–1331, 2017.
- [2] E. Yoon, A. Babar, M. Choudhary, M. Kutner, and N. Pypopoulos, "Acetaminophen-induced hepatotoxicity: a comprehensive update," *Journal of Clinical and Translational Hepatology*, vol. 4, no. 2, pp. 131–142, 2016.
- [3] J. C. McCrae, E. E. Morrison, I. M. MacIntyre, J. W. Dear, and D. J. Webb, "Long-term adverse effects of paracetamol—a review," *British Journal of Clinical Pharmacology*, vol. 84, no. 10, pp. 2218–2230, 2018.
- [4] S. Kennon-McGill and M. R. McGill, "Extrahepatic toxicity of acetaminophen: critical evaluation of the evidence and proposed mechanisms," *Journal of Clinical and Translational Research*, vol. 3, no. 3, pp. 297–310, 2018.
- [5] I. Eneli, K. Sadri, C. Camargo Jr., and R. Graham Barr, "Acetaminophen and the risk of asthma: the epidemiologic and pathophysiologic evidence," *Chest*, vol. 127, no. 2, pp. 604–612, 2005.
- [6] G. Fan, B. Wang, C. Liu, and D. Li, "Prenatal paracetamol use and asthma in childhood: a systematic review and meta-analysis," *Allergologia et Immunopathologia*, vol. 45, no. 6, pp. 528–533, 2017.
- [7] A. J. Henderson and S. O. Shaheen, "Acetaminophen and asthma," *Paediatric Respiratory Reviews*, vol. 14, no. 1, pp. 9–15, 2013.
- [8] S. V. Baudouin, P. Howdle, J. G. O'Grady, and N. R. Webster, "Acute lung injury in fulminant hepatic failure following paracetamol poisoning," *Thorax*, vol. 50, no. 4, pp. 399–402, 1995.

- [9] S. Dimova, P. H. Hoet, and B. Nemery, "Paracetamol (acetaminophen) cytotoxicity in rat type II pneumocytes and alveolar macrophages *in vitro*," *Biochemical Pharmacology*, vol. 59, no. 11, pp. 1467–1475, 2000.
- [10] M. E. Placke, D. S. Wyand, and S. D. Cohen, "Extrahepatic lesions induced by acetaminophen in the mouse," *Toxicologic Pathology*, vol. 15, no. 4, pp. 381–387, 1987.
- [11] S. G. Hart, R. W. Cartun, D. S. Wyand, E. A. Khairallah, and S. D. Cohen, "Immunohistochemical localization of acetaminophen in target tissues of the CD-1 mouse: correspondence of covalent binding with toxicity," *Fundamental and Applied Toxicology*, vol. 24, no. 2, pp. 260–274, 1995.
- [12] E. H. Jeffery and W. M. Haschek, "Protection by dimethylsulfide against acetaminophen-induced hepatic, but not respiratory toxicity in the mouse," *Toxicology and Applied Pharmacology*, vol. 93, no. 3, pp. 452–461, 1988.
- [13] J. Gu, H. Cui, M. Behr et al., "In vivo mechanisms of tissue-selective drug toxicity: effects of liver-specific knockout of the NADPH-cytochrome P450 reductase gene on acetaminophen toxicity in kidney, lung, and nasal mucosa," *Molecular Pharmacology*, vol. 67, no. 3, pp. 623–630, 2005.
- [14] S. B. Neff, T. A. Neff, S. L. Kunkel, and C. M. Hogaboam, "Alterations in cytokine/chemokine expression during organ-to-organ communication established via acetaminophen-induced toxicity," *Experimental and Molecular Pathology*, vol. 75, no. 3, pp. 187–193, 2003.
- [15] J. B. Bartolone, W. P. Beierschmitt, R. B. Birge et al., "Selective acetaminophen metabolite binding to hepatic and extrahepatic proteins: an in vivo and in vitro analysis," *Toxicology and Applied Pharmacology*, vol. 99, no. 2, pp. 240–249, 1989.
- [16] A. Ramachandran and H. Jaeschke, "Acetaminophen toxicity: novel insights into mechanisms and future perspectives," *Gene Expression*, vol. 18, no. 1, pp. 19–30, 2018.
- [17] M. Z. Yan, Y. Z. Huo, S. T. Yin, and H. B. Hu, "Mechanisms of acetaminophen-induced liver injury and its implications for therapeutic interventions," *Redox Biology*, vol. 17, pp. 274–283, 2018.
- [18] R. Nassini, S. Materazzi, E. Andrè et al., "Acetaminophen, via its reactive metabolite *N*-acetyl-*p*-benzo-quinoneimine and transient receptor potential ankyrin-1 stimulation, causes neurogenic inflammation in the airways and other tissues in rodents," *The FASEB Journal*, vol. 24, no. 12, pp. 4904–4916, 2010.
- [19] X. Ding and L. S. Kaminsky, "HUMANEXTRAHEPATICCYTOCHROMESP450: function in xenobiotic metabolism and tissue-selective chemical toxicity in the respiratory and gastrointestinal tracts," *Annual Review of Pharmacology and Toxicology*, vol. 43, no. 1, pp. 149–173, 2003.
- [20] J. Hukkanen, O. Pelkonen, and H. Raunio, "Expression of xenobiotic-metabolizing enzymes in human pulmonary tissue: possible role in susceptibility for ILD," *European Respiratory Journal*, vol. 32, pp. 122s–126s, 2001.
- [21] E. L. Crawford, D. A. Weaver, J. P. DeMuth et al., "Measurement of cytochrome P450 2A6 and 2E1 gene expression in primary human bronchial epithelial cells," *Carcinogenesis*, vol. 19, no. 10, pp. 1867–1871, 1998.
- [22] J. Hukkanen, O. Pelkonen, J. Hakkola, and H. Raunio, "Expression and regulation of xenobiotic-metabolizing cytochrome P450 (CYP) enzymes in human lung," *Critical Reviews in Toxicology*, vol. 32, no. 5, pp. 391–411, 2002.
- [23] K. Breen, J. C. Wandscheer, M. Peignoux, and D. Pessayre, "In situ formation of the acetaminophen metabolite covalently bound in kidney and lung. Supportive evidence provided by total hepatectomy," *Biochemical Pharmacology*, vol. 31, no. 1, pp. 115–116, 1982.
- [24] S. J. Bulera, S. D. Cohen, and E. A. Khairallah, "Acetaminophen-arylated proteins are detected in hepatic subcellular fractions and numerous extra-hepatic tissues in CD-1 and C57B1/6J mice," *Toxicology*, vol. 109, no. 2-3, pp. 85–99, 1996.
- [25] K. Mace, E. D. Bowman, P. Vautravers, P. G. Shields, C. C. Harris, and A. M. Pfeifer, "Characterisation of xenobiotic-metabolising enzyme expression in human bronchial mucosa and peripheral lung tissues," *European Journal of Cancer*, vol. 34, no. 6, pp. 914–920, 1998.
- [26] F. Botto, E. Seree, S. el Khyari et al., "Tissue-specific expression and methylation of the human CYP2E1 gene," *Biochemical Pharmacology*, vol. 48, no. 6, pp. 1095–1103, 1994.
- [27] J. Hukkanen, J. Hakkola, S. Anttila et al., "Detection of mRNA encoding xenobiotic-metabolizing cytochrome P450s in human bronchoalveolar macrophages and peripheral blood lymphocytes," *Molecular Carcinogenesis*, vol. 20, no. 2, pp. 224–230, 1997.
- [28] S. Dimova, P. H. Hoet, D. Dinsdale, and B. Nemery, "Acetaminophen decreases intracellular glutathione levels and modulates cytokine production in human alveolar macrophages and type II pneumocytes *in vitro*," *The International Journal of Biochemistry & Cell Biology*, vol. 37, no. 8, pp. 1727–1737, 2005.
- [29] B. V. Martin-Murphy, D. J. Kominsky, D. J. Orlicky, T. M. Donohue Jr., and C. Ju, "Increased susceptibility of natural killer T-cell-deficient mice to acetaminophen-induced liver injury," *Hepatology*, vol. 57, no. 4, pp. 1575–1584, 2013.
- [30] K. A. Michaelis, F. Agboke, T. Liu et al., "IKK β -mediated NF- κ B activation confers protection against hyperoxic lung injury," *American Journal of Respiratory Cell and Molecular Biology*, vol. 50, no. 2, pp. 429–438, 2014.
- [31] R. J. Good, L. Hernandez-Lagunas, A. Allawzi et al., "MicroRNA dysregulation in lung injury: the role of the miR-26a/EphA2 axis in regulation of endothelial permeability," *American Journal of Physiology-Lung Cellular and Molecular Physiology*, vol. 315, no. 4, pp. L584–L594, 2018.
- [32] O. Krenkel, J. C. Mossanen, and F. Tacke, "Immune mechanisms in acetaminophen-induced acute liver failure," *Hepatobiliary Surgery and Nutrition*, vol. 3, no. 6, pp. 331–343, 2014.
- [33] B. L. Woolbright and H. Jaeschke, "Role of the inflammasome in acetaminophen-induced liver injury and acute liver failure," *Journal of Hepatology*, vol. 66, no. 4, pp. 836–848, 2017.
- [34] B. Butler, R. De Dios, L. Nguyen, S. McKenna, S. Ghosh, and C. J. Wright, "Developmentally regulated innate immune NF κ B signaling mediates IL-1 α expression in the perinatal murine lung," *Frontiers in Immunology*, vol. 10, p. 1555, 2019.
- [35] G. Nagy, A. Szarka, G. Lotz et al., "BGP-15 inhibits caspase-independent programmed cell death in acetaminophen-induced liver injury," *Toxicology and Applied Pharmacology*, vol. 243, no. 1, pp. 96–103, 2010.
- [36] G. Nagy, T. Kardon, L. Wunderlich et al., "Acetaminophen induces ER dependent signaling in mouse liver," *Archives of Biochemistry and Biophysics*, vol. 459, no. 2, pp. 273–279, 2007.
- [37] D. Uzi, L. Barda, V. Scaiewicz et al., "CHOP is a critical regulator of acetaminophen-induced hepatotoxicity," *Journal of Hepatology*, vol. 59, no. 3, pp. 495–503, 2013.

- [38] F. Foufelle and B. Fromenty, "Role of endoplasmic reticulum stress in drug-induced toxicity," *Pharmacology Research & Perspectives*, vol. 4, no. 1, article e00211, 2016.
- [39] S. Akashi, M. Tominaga, K. Naitou et al., "Two cases of acetaminophen-induced pneumonitis," *Nihon Kyōbu Shikkan Gakkai zasshi*, vol. 35, no. 9, pp. 974–979, 1997.
- [40] L. M. Price, A. Poklis, and D. E. Johnson, "Fatal acetaminophen poisoning with evidence of subendocardial necrosis of the heart," *Journal of Forensic Sciences*, vol. 36, no. 3, pp. 930–935, 1991.
- [41] T. M. McKeever, S. A. Lewis, H. A. Smit, P. Burney, J. R. Britton, and P. A. Cassano, "The association of acetaminophen, aspirin, and ibuprofen with respiratory disease and lung function," *American Journal of Respiratory and Critical Care Medicine*, vol. 171, no. 9, pp. 966–971, 2005.
- [42] P. N. Newsome, N. C. Henderson, L. J. Nelson et al., "Development of an invasively monitored porcine model of acetaminophen-induced acute liver failure," *BMC Gastroenterology*, vol. 10, no. 1, 2010.
- [43] S. Anttila, H. Raunio, and J. Hakkola, "Cytochrome P450-mediated pulmonary metabolism of carcinogens: regulation and cross-talk in lung carcinogenesis," *American Journal of Respiratory Cell and Molecular Biology*, vol. 44, no. 5, pp. 583–590, 2011.
- [44] J. V. Castell, M. Teresa Donato, and M. J. Gómez-Lechón, "Metabolism and bioactivation of toxicants in the lung. The in vitro cellular approach," *Experimental and Toxicologic Pathology*, vol. 57, Supplement 1, pp. 189–204, 2005.
- [45] F. Romero, D. Shah, M. Duong et al., "Chronic alcohol ingestion in rats alters lung metabolism, promotes lipid accumulation, and impairs alveolar macrophage functions," *American Journal of Respiratory Cell and Molecular Biology*, vol. 51, no. 6, pp. 840–849, 2014.
- [46] T. S. Chen, J. P. Richie Jr., and C. A. Lang, "Life span profiles of glutathione and acetaminophen detoxification," *Drug Metabolism and Disposition*, vol. 18, no. 6, pp. 882–887, 1990.
- [47] G. J. Smith, J. A. Cichocki, B. J. Doughty, J. E. Manautou, S. E. Jordt, and J. B. Morris, "Effects of acetaminophen on oxidant and irritant respiratory tract responses to environmental tobacco smoke in female mice," *Environmental Health Perspectives*, vol. 124, no. 5, pp. 642–650, 2016.
- [48] D. Botta, S. Shi, C. C. White et al., "Acetaminophen-induced liver injury is attenuated in male glutamate-cysteine ligase transgenic mice," *The Journal of Biological Chemistry*, vol. 281, no. 39, pp. 28865–28875, 2006.
- [49] L. Micheli, D. Cerretani, A. I. Fiaschi, G. Giorgi, M. R. Romeo, and F. M. Runci, "Effect of acetaminophen on glutathione levels in rat testis and lung," *Environmental Health Perspectives*, vol. 102, Supplement 9, pp. 63–64, 1994.
- [50] L. Dara, C. Ji, and N. Kaplowitz, "The contribution of endoplasmic reticulum stress to liver diseases," *Hepatology*, vol. 53, no. 5, pp. 1752–1763, 2011.
- [51] S. J. Marciniak, "Endoplasmic reticulum stress in lung disease," *European Respiratory Review*, vol. 26, no. 144, article 170018, 2017.
- [52] D. J. Hoivik, J. E. Manautou, A. Tveit, S. G. Hart, E. A. Khairallah, and S. D. Cohen, "Gender-related differences in susceptibility to acetaminophen-induced protein arylation and nephrotoxicity in the CD-1 mouse," *Toxicology and Applied Pharmacology*, vol. 130, no. 2, pp. 257–271, 1995.

Research Article

Role of *HIF-1 α -miR30a-Snai1* Axis in Neonatal Hyperoxic Lung Injury

Yuhao Zhang, Xiaoyu Dong, and Krithika Lingappan 

Department of Pediatrics, Section of Neonatology, Texas Children's Hospital, Baylor College of Medicine, Houston, Texas, USA

Correspondence should be addressed to Krithika Lingappan; lingappa@bcm.edu

Received 21 April 2019; Revised 5 September 2019; Accepted 19 September 2019; Published 22 October 2019

Guest Editor: Lynette K. Rogers

Copyright © 2019 Yuhao Zhang et al. This is an open access article distributed under the Creative Commons Attribution License, which permits unrestricted use, distribution, and reproduction in any medium, provided the original work is properly cited.

Bronchopulmonary dysplasia (BPD) is characterized by a severe impairment in lung alveolarization and vascular development. We have previously shown that pulmonary angiogenesis is preserved in hyperoxia-exposed female mice accompanied by increased *miR-30a* expression, which is a proangiogenic miRNA. Also, *miR-30a* expression is decreased in human BPD. HIF-1 α plays an essential role in postnatal lung development, especially in recovery from hyperoxic injury. *Snai1* activation promotes pathological fibrosis through many mechanisms including Endo-MT, which may in turn adversely impact lung vascular development. Our objective was to test the hypothesis that higher *miR-30a* expression through *HIF-1 α* decreases *Snai1* expression in females and attenuates injury in the developing lung. Neonatal male and female mice (C57BL/6) were exposed to hyperoxia (P1-5, 0.95 FiO₂) and euthanized on P21. Neonatal human pulmonary microvascular endothelial cells (HPMECs; 18-24-week gestation donors; 3/group either sex) were subjected to hyperoxia (95% O₂ and 5% CO₂) or normoxia (air and 5% CO₂) up to 72 h. *Snai1* expression was measured in HPMECs *in vitro* and in neonatal mouse lungs *in vivo*. Also, *Snai1* expression was measured in HPMECs after *miR-30a* mimic and *miR-30a* inhibitor treatment. To further establish the potential regulation of *miR-30a* by *Hif-1 α* , *miR-30a* expression after Hif-1 α inhibition was measured in HPMECs. *In vivo*, *Snai1* expression was decreased in neonatal female lungs compared to males at P7. Increased *Snai1* expression was seen in male HPMECs upon exposure to hyperoxia *in vitro*. Treatment with the *miR-30a* mimic decreased *Snai1* expression in HPMECs, while *miR-30a* inhibition significantly increased *Snai1* expression in HPMECs. siRNA-mediated loss of *Hif-1 α* expression in HPMECs decreased *miR-30a* expression. *Hif-1 α* may lead to differential sex-specific *miR-30a* expression and may contribute to protection from hyperoxic lung injury in female neonatal mice through decreased *Snai1* expression.

1. Introduction

With the increasing survival of extremely premature babies, the incidence of bronchopulmonary dysplasia (BPD) has remained steady, despite the advances in neonatal intensive care. BPD is the cause of significant morbidity and leads to prolonged impairment in lung function in this group of patients. Many prenatal and postnatal factors are involved in the pathogenesis of BPD, and exposure to supraphysiological concentrations of oxygen contributes to its development. Murine models have utilized varying durations of postnatal hyperoxia exposure to simulate the human disease in neonatal mice [1, 2].

Bronchopulmonary dysplasia (BPD) is characterized mainly by an arrest in lung development with severe impair-

ment of alveolar septation and vascular development, and pathological fibrosis in severe cases [3–6]. Histopathological analysis in neonates with “new BPD” shows evidence of variable interstitial fibroproliferation compared to extensive fibroproliferation in “old BPD” [7]. BPD disproportionately affects male infants compared to females. The molecular mechanisms underlying this sex bias are not known. We have previously shown that alveolarization and pulmonary angiogenesis is preserved in hyperoxia-exposed female neonatal mice compared to males [8]. The protective effect in females is accompanied by an increase in pulmonary *miR-30a* expression in females [9]. *miR-30a* has proangiogenic, anti-inflammatory, and antifibrotic effects in many diseases processes [10–17], including those affecting the lung. Significantly, *miR-30a* expression is decreased in human patients

with BPD [9]. The upstream regulation of *miR-30a* leading to differential expression in males and females has not been elucidated. Previously published work has shown that *Hif-1 α* may increase *miR-30a* expression [18]. HIF-1 α plays a vital role in postnatal lung development [19], especially in recovery from hyperoxic injury [20] and acute lung injury [21]. Overexpression of *Hif-1 α* in hyperoxia-exposed neonatal mice attenuates lung injury [20]. *HIF-1 α* binding to its target genes is higher in female lungs after hyperoxia exposure [22]. Whether *HIF-1 α* increases *miR-30a* expression in the pulmonary microvascular endothelium is not known. *Snail* is a transcriptional repressor and a profibrotic molecule [23–28]. Studies have shown that *miR-30a* downregulates *Snail* [10, 14, 17].

However, the mechanistic role of the intersection between HIF-1 α , miR-30a, and *Snail* in neonatal hyperoxic lung injury has not been studied. Our objective was to test the hypothesis that HIF-1 α increases the miR-30a expression in females and decreases the *Snail* expression in the developing lung.

2. Methods

2.1. Animals. All experiments were performed per relevant guidelines and regulations. The care of animals was as per the 8th edition of the guide for the care and use of laboratory animals and other IACUC protocols. Timed pregnant C57BL/6J WT mice were obtained from Charles River Laboratories (Wilmington). The sex in neonatal mouse pups was determined as described before and with PCR analysis for the *Sry* gene [8].

2.1.1. Mouse Model of BPD. Mouse pups were exposed to normoxia (21% O₂) or hyperoxia (95% O₂), within 12 h of birth for five days. Neonatal mice are at the sacular stage of lung development during this period, equivalent to 26–36 weeks in human gestation. The dams were rotated between air- and hyperoxia-exposed litters every 24 hours to prevent oxygen toxicity in the dams. Oxygen exposure was conducted in plexiglass chambers as previously described [8]. Mice were euthanized on P7 and P21 (after recovery in room air). The mice were euthanized with sodium pentobarbital, 100 mg/kg, i.p. For the *in vivo* experiments, neonatal mice from different litters were randomly allocated to room air or hyperoxia. The experimental unit was a single neonatal mouse pup and data from 4–6 animals/group were used for analysis.

2.1.2. Cell Culture and Hyperoxia Treatment. Neonatal human pulmonary microvascular endothelial cells (HPMEC; male: #10885, #11367, and #10899; female: #5016, #10160, and #10169; 6 biological replicates in total) were purchased from ScienCell and maintained in Endothelial Cell Medium (Cat # 1001, ScienCell) at 37°C in 5% CO₂. The gestational age of the donors varied from 18 to 24 weeks. Male and female HPMECs were used from passages 3 to 5 to ensure their endothelial characteristics. Male or female HPMEC cells (1 × 10⁵) were seeded in a 6 mm dish. 24 h later, these cells were incubated at 37°C in room air condition (21% O₂, 5% CO₂) or in hyperoxia (95% O₂, 5% CO₂) as described

before for 72 h. For measuring *SNAIL* expression, both male and female HPMECs were used. For the rest of the *in vitro* experiments, female HPMECs were used as the miR-30a expression was increased only in female HPMECs [9].

2.1.3. miRNA and Plasmid Transfection in HPMECs. miR30a-5p mimic (HMI0454), miR30a-5p inhibitor (HSTUD0454), Hif-1 α -siRNA (3017635209), and negative control siRNA (NCSTUD001) were purchased from MilliporeSigma. Hif-1 α overexpression plasmid (#18948) was purchased from Addgene. pcDNA3.1 (V79020) plasmid was purchased from Thermo Fisher. MicroRNA negative control (30 pmol), miR30a-5p mimic (30 pmol), or miR30a-5p inhibitor (30 pmol) were used for HPMEC transfection separately using a Lipofectamine 2000 reagent (Cat #11668019; 6 μ l per well of a 6-well plate). Hif-1 α plasmid (2 μ g) with or without miR30a-5p inhibitor (60 pmol) was transfected using a Lipofectamine 2000 reagent (6 μ l per well of a 6-well plate). pcDNA3.1 plasmid (2 μ g/well) was transfected as a negative control of Hif-1 α . After six hours, fresh medium was added to the plate. After 48 h incubation in room air (21% O₂, 5% CO₂), cells were harvested for later use.

2.1.4. Quantitative PCR. Total RNA and microRNA was extracted from the lung tissues and cell lines using TRIzol (Cat #15596026, Thermo Fisher) and chloroform (Cat #C2432, Millipore-Sigma) and then treated with DNase I (Cat #K1622, Invitrogen). cDNA was prepared using a RevertAid Reverse Transcriptase (Thermo Fisher). MicroRNA cDNA was generated using a MystiCq microRNA cDNA Synthesis Mix (MilliporeSigma). Quantitative PCR was performed using the QuantStudio 7 Flex Real-Time PCR Detection System (Thermo Fisher) and SYBR Green (Cat #1725274, Bio-Rad). The thermal cycling conditions used were as follows: one cycle at 95°C for 1 min, 40 cycles at 95°C for 15 s, and one cycle at 60°C for 30 s. The primers used in the real-time PCR test were listed as follows: *Snail* (NM_005985, human) forward primer: GCGAGCTGCAG GACTCTAAT, reverse primer: GGACAGAGTCCCAGAT GAGC; *Snail* (NM_011427, mice) forward primer: CACC CTCATCTGGGACTCTC, reverse primer: GAGCTTTTG CCACTGTCCCTC; Hif-1 α (NM_001243084, human) forward primer: GATGTAATGCTCCCCTCACC, reverse primer: CTTGATTGAGTGCAGGGTCA; Hif-1 α (NM_001313919, mice) forward primer: ATTCTCCAAGCCCT CCAAGT, reverse primer: TCATCAGTGGTGGCAGTTG T; β -actin (NM_001101, human) forward primer: CATC GAGCACGGCATCGTCA, reverse primer: TAGCACAGC CTGGATAGCAAC; β -actin (NM_007393, mice) forward primer: GATCTGGCACCACACCTTCT, reverse primer: GGGGTGTTGAAGGTCTCAA; beta 2-microglobulin (NM_009735.3, mouse) forward primer: CTGACCGGCCT GTATGCTAT, reverse primer: CCGTTCTTACGATTT GGAT; and beta 2-microglobulin (NM_00408.3, human) forward primer: TGCTGTCTCCATGTTTGATGTATCT, reverse primer: TCTCTGCTCCCCACCTCTAAGT. miR30a-5p (MIRAP00079), MystiCq Universal PCR (MIRUP), and U6 (MIRCP00001) primers were purchased

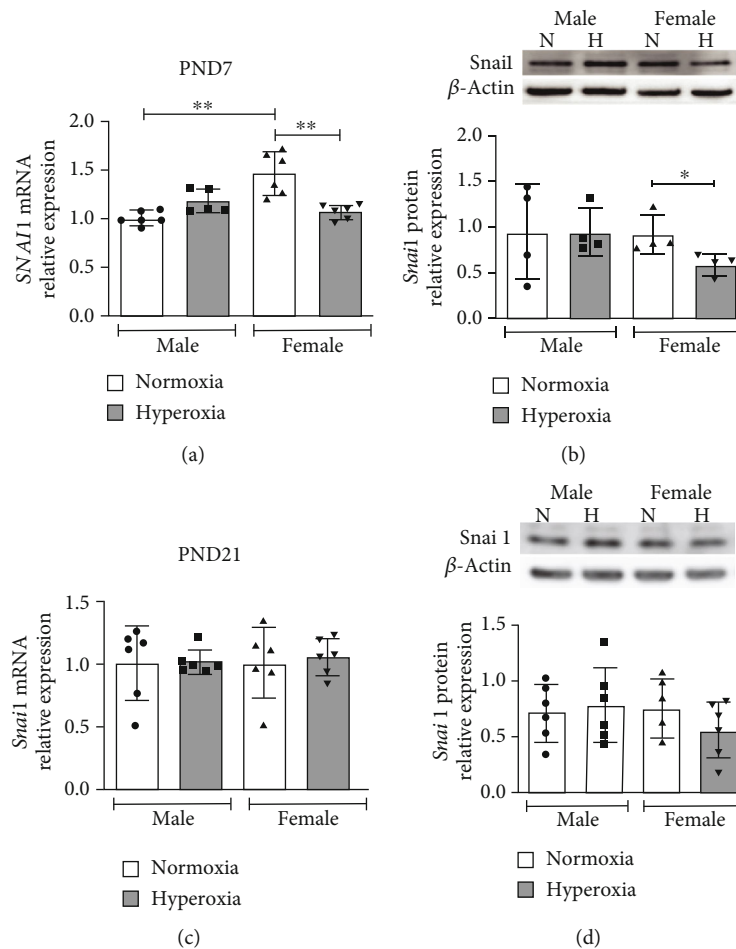


FIGURE 1: Differential sex-specific expression of *Snail* in neonatal mice after postnatal hyperoxia exposure: *Snail* mRNA (β -actin as housekeeping gene) and protein expression neonatal male and female mice exposed to hyperoxia (P1-5, 0.95 FiO₂) during the saccular stage of lung development. *Snail* mRNA (a, c) and protein expression (b, d) were measured in the lungs at P7 (a, b) immediately after hyperoxia exposure and at P21 (c, d) after recovery in normoxia. Values are means \pm SD. $n = 5 - 6$ mice per group. Significant differences between groups indicated by * $P < 0.05$ and ** $P < 0.01$.

from MilliporeSigma. Relative mRNA levels were calculated using the $2^{-\Delta\Delta CT}$ method and normalized by β -actin or beta 2-microglobulin in the same sample.

2.1.5. Western Immunoblotting. Protein was isolated from murine lung tissue and HPMECs using RIPA buffer (Thermo Fisher) containing protease mixture inhibitors (Thermo Fisher). Proteins were separated by 4–12% sodium dodecyl sulfate polyacrylamide gel electrophoresis, then transferred to a PVDF membrane using a Mini-PROTEAN Tetra Cell system (Bio-Rad). The following primary antibodies were used: goat anti-Snail1 (1:1000, Abcam, ab53519), rabbit anti- β -actin (1:5000, Cell Signaling, 4970), and rabbit anti-vinculin (1:1000, Cat#4650, Cell Signaling). Pierce ECL plus a Western blotting substrate (Cat #32132, Thermo Fisher) was used for visualizing immunoreactive protein bands. The protein bands were normalized by β -actin or vinculin on the same membrane.

2.1.6. Statistical Analysis. GraphPad version 7 was used for the analysis of our data. Data are expressed as means \pm SD.

Data were analyzed by two-way ANOVA to test for the independent effects of sex and hyperoxia and to look for any interaction (sex \times hyperoxia) or by Mann-Whitney U test. Multiple-comparison testing (Bonferroni) was performed if statistical significance ($P < 0.05$) was noted by ANOVA.

3. Results

3.1. Differential Sex-Specific Expression of *Snail* in Neonatal Mice after Postnatal Hyperoxia Exposure. WT male and female neonatal mice were exposed to hyperoxia (0.95 FiO₂ from P1-5) during the saccular stage of lung development, and *Snail* mRNA and protein expression were measured at P7 (early) and P21 (during recovery in normoxia) and compared to respective normoxic controls. *Snail* mRNA expression (β -actin as housekeeping gene) was decreased in female neonatal mice at P7 after hyperoxia exposure compared to female normoxic controls. No difference in expression was seen in males (Figure 1(a)). The results were similar with another housekeeping gene (β 2-microglobulin) as shown in Supp. Figure 1. Similarly, Snail

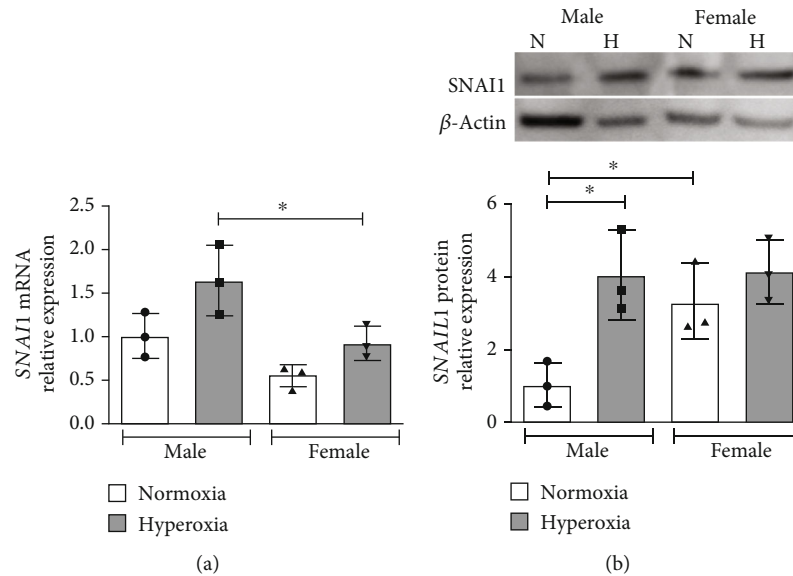


FIGURE 2: *Snail* mRNA and protein expression is increased in human pulmonary microvascular endothelial cells upon exposure to hyperoxia: *SNAIL* mRNA (a) and protein expression (b) were measured in neonatal human pulmonary microvascular endothelial cells exposed to normoxia or hyperoxia (0.95 FiO₂ up to 72 hrs). Values are mean \pm SD. $n = 3$ per group. Significant differences between indicated groups are indicated by * $P < 0.05$.

protein expression in the lungs was also decreased in females compared to female normoxic controls and compared to hyperoxia-exposed male mice (Figure 1(b)). *Snail* mRNA and protein expression did not show statistically different expression levels between any of the groups at P21 (Figures 1(c) and 1(d)). Protein expression was repeated with vinculin as the loading control; female mice tended to have lower *Snail* protein in the lungs at P7 compared to males, and in HPMECs, males tended to have a greater increase in *Snail* expression. These results however, were not statistically significant (Supp. Figure 1).

3.2. *Snail* mRNA and Protein Expression Are Increased in Male Human Pulmonary Microvascular Endothelial Cells upon Exposure to Hyperoxia. Next, we wanted to elucidate the response to hyperoxia in neonatal human pulmonary microvascular endothelial cells (HPMECs). These cells were exposed to hyperoxia (0.95 FiO₂) for up to 72 hours, and *SNAIL* mRNA (Figure 2(a)) and protein expression (Figure 2(b)) were measured. *SNAIL* mRNA expression was significantly higher in male HPMECs compared to female. Male HPMECs showed increased *SNAIL*1 protein upon exposure to hyperoxia, while female HPMECs did not show this change.

3.3. *Snail* Regulation by *miR-30a*. TargetScan reported *miR-30a* binding sites 630-637 bp in the 3'UTR of *SNAIL* (Figure 3(a)). *miR30a-5p* expression was increased in female HPMECs using the *miR30a-5p* mimic (Figure 3(b)). Following treatment with the mimic, *miR30-5p* expression was increased in female HPMECs. *SNAIL* mRNA (Figure 3(c)) and protein expression (Figure 3(d)) were decreased following *miR30a-5p* overexpression. In contrast, *SNAIL* protein expression was increased following treatment with a *miR30a-5p* inhibitor (Figure 3(e)).

3.3.1. Regulation of *miR30a-5p* by *HIF-1 α* . We have previously shown that *Hif-1 α* expression was increased in female mice at P7 and decreased in male mice at P21 after hyperoxia exposure [29] and that *HIF-1 α* binding to its target genes is more significant in female lungs after hyperoxia exposure [22]. *HIF-1 α* protein expression was decreased in both male and female HUVECs upon exposure to hyperoxia [29]. Motif analysis revealed a hypoxia response element (HRE) [AG]CGTG site 428 base pairs upstream of *miR-30a* (Figure 4(a)). To further establish the potential regulation of *miR-30a* by *Hif-1 α* , we used the siRNA-mediated loss of the *Hif-1 α* expression in female human pulmonary microvascular endothelial cells and its effect on *miR30a-5p* expression. Treatment of female HPMECs with *HIF-1 α* siRNA significantly decreased *HIF-1 α* expression (Figure 4(b)). Also, the expression of *miR30a-5p* was decreased in pulmonary microvascular endothelial cells transfected with *HIF-1 α* siRNA compared to cells treated with scrambled siRNA (Figure 4(c)).

3.3.2. *SNAIL* Expression following *HIF-1 α* Silencing in Female Human Pulmonary Microvascular Endothelial Cells. We next wanted to see if *HIF-1 α* played a role in regulating *SNAIL* expression in human pulmonary microvascular endothelial cells. Following the silencing of *HIF-1 α* in female HPMECs, *SNAIL* mRNA (Figure 5(a)) and protein expression (Figure 5(b)) were decreased in female HPMECs.

3.3.3. *SNAIL* Expression following *miR30a-5p* Inhibition, *HIF-1 α* Overexpression, or Both in Female HPMECs. Since both *miR30a-5p* and *HIF-1 α* had opposing effects on *SNAIL* expression, we wanted to determine the independent and additive effects of *miR30a-5p* inhibition and *HIF-1 α* overexpression in female HPMECs. *HIF-1 α* overexpression and *miR30a-5p* inhibition both independently increased *SNAIL* mRNA expression in female HPMECs (Figure 6(a)).

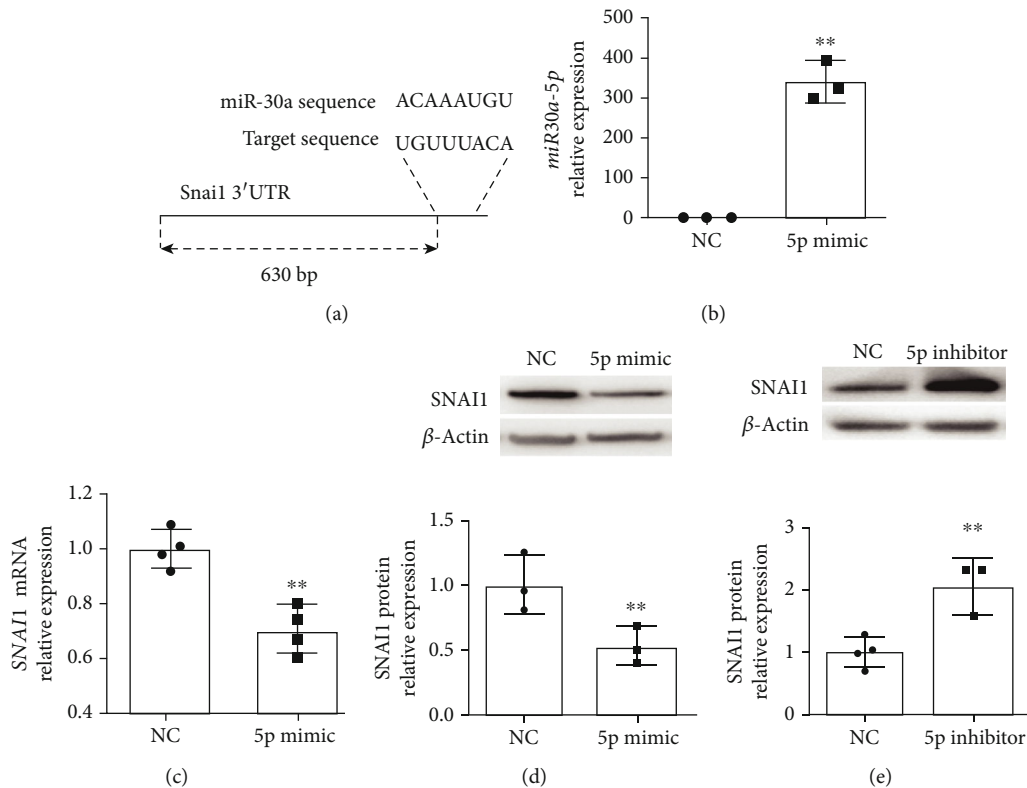


FIGURE 3: *miR30a-5p* decreases SNAIL expression in female neonatal human pulmonary microvascular endothelial cells: (a) TargetScan reported *miR-30a* binding sites 630-637 bp in the 3' UTR of SNAIL. Treatment with the *miR30a-5p* mimic increased the *miR30a-5p* expression (b) in HPMECs. SNAIL mRNA (c) and protein (d) expressions were decreased in neonatal HPMECs after *miR30a-5p* overexpression. In contrast, treatment with the *miR30a-5p* inhibitor increased SNAIL protein (e) expression ($n = 3-4$ experimental replicates/group). Values are means \pm SD. Significant differences between nontreated controls are indicated by * $P < 0.05$ and ** $P < 0.01$.

HIF-1 α overexpression had a more significant effect on SNAIL expression compared to *miR30a-5p* inhibition. Combined *HIF-1 α* overexpression and *miR30a-5p* inhibition increased SNAIL expression compared to controls, but there was no additive effect (Figure 6(a)). SNAIL protein was increased by *miR30a-5p* inhibition or *HIF-1 α* overexpression independently and by the combined treatment with *miR30a-5p* inhibition and *HIF-1 α* overexpression compared to controls. No statistically significant changes in protein levels were noted between the individual treatment groups (Figure 6(b)).

4. Discussion

Sex-specific differences exist in many neonatal morbidities including bronchopulmonary dysplasia (BPD), which adversely affects a significant number of extremely premature newborns. Elucidation of mechanisms responsible for the sex-specific differences in the development of this disease is critical for the development of individualized therapies. We identified miR-30a as a potential modulator of many of the genes differentially expressed in the angiogenesis pathway [9]. Interestingly, miR-30a expression was increased in the female lung after exposure to hyperoxia. These findings were replicated in neonatal human pulmonary microvascular endothelial cells (HPMECs), with higher miR-30a expression in female HPMECs upon exposure to hyperoxia. miR-30a

modulates many biological processes and has proangiogenic and antifibrotic properties. A miRNA can have many putative mRNA targets. *Snail* (a profibrotic gene) is a miR-30a target. We show that *Snail* expression is decreased in female neonatal mice *in vivo*. On the other hand, male HPMECs show increased SNAIL expression *in vitro* after exposure to hyperoxia. Also, we show that *Hif-1 α* could modulate miR-30a expression in HPMECs. Interestingly, *Hif-1 α* also increases *Snail* expression, and the net protective effect in females could be mediated through a *Hif-1 α* -mediated increase in the *miR-30a* expression which keeps the *Snail* expression in check during exposure to hyperoxia (Figure 7).

Snail (Snai Family Transcriptional Repressor 1) is a zinc finger transcriptional repressor protein and plays a central role in both epithelial to mesenchymal (EMT) [30] and endothelial to mesenchymal (Endo-MT) in many disease processes. Exposure to hyperoxia leads to a profibrotic phenotype leading to an increase in myofibroblasts [31-34]. Endo-MT is a complex biological process in which endothelial cells lose their surface expression of endothelial-specific markers (e.g., CD31 and vWF) and acquire a mesenchymal phenotype (elongated and fusiform) and express mesenchymal markers (like α -SMA and vimentin) [35]. The role of Endo-MT is known in lung diseases such as idiopathic pulmonary fibrosis (significant contribution to fibrosis and vascular regression) and pulmonary arterial hypertension (by

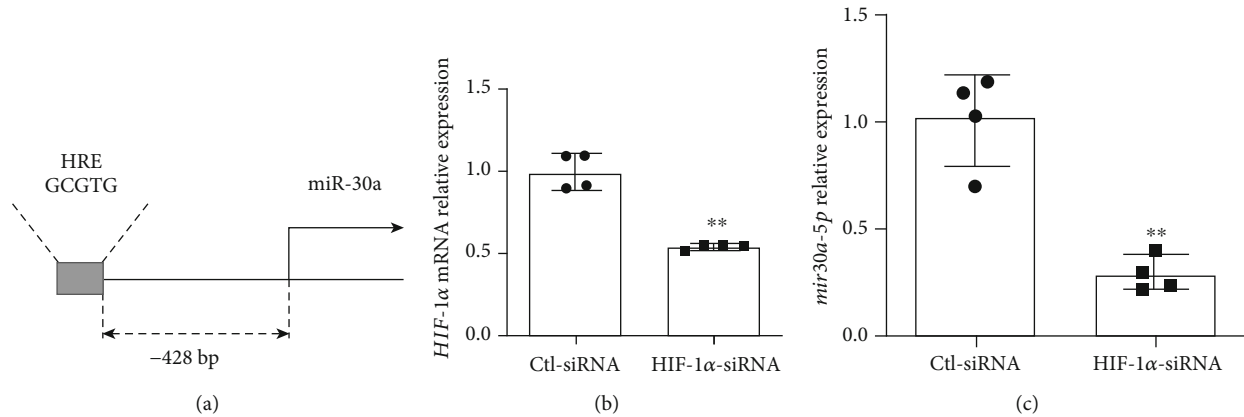


FIGURE 4: *miR-30a* regulation by HIF-1 α . (a) Motif search revealed a hypoxia response element [AG]CGTG site 428 base pairs upstream of *miR-30a*, based on the mm10 genome build. (b) *HIF-1α* mRNA expression in female HPMECs after *HIF-1α* knockdown using siRNA (Ctl-siRNA: control siRNA). (c) *mir30a-5p* expression in female HPMECs after *HIF-1α* knockdown. Values are expressed as mean \pm SD. $N = 4$ experimental replicates for each group in each test. Significant differences from baseline are indicated by ** $P < 0.01$.

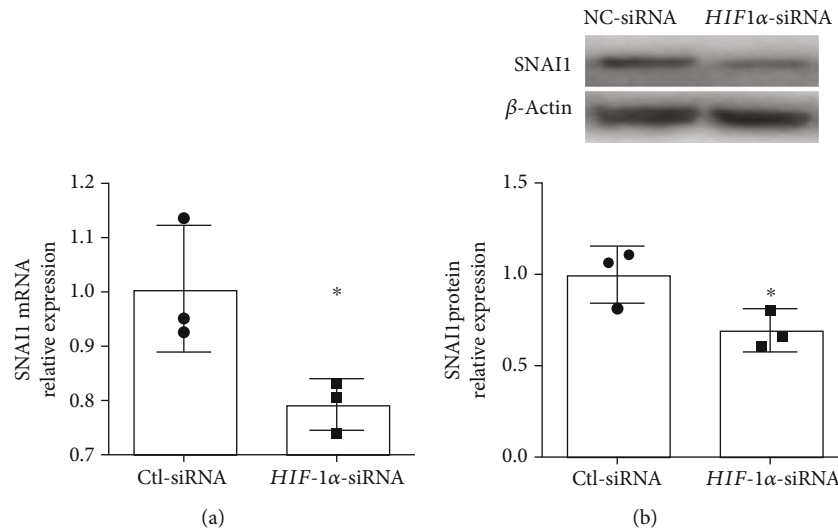


FIGURE 5: *HIF-1α* knockdown decreased *SNAIL1* mRNA and protein expression in neonatal female human pulmonary microvascular endothelial cells. *SNAIL1* mRNA (a) and protein (b) expression in HPMECs after *HIF-1α* knockdown using siRNA (Ctl-siRNA: control siRNA). Values are expressed as mean \pm SD. $N = 3$ experimental replicates for each group in each test. Significant differences from baseline are indicated by * $P < 0.05$.

causing pulmonary vascular remodeling and endothelial dysfunction) [36–38]. We have previously shown that male HPMECs show higher expression of α -SMA upon exposure to hyperoxia accompanied by a decrease in CD31 expression [39]. In this study, *SNAIL1* mRNA expression was significantly higher in male HPMECs compared to female. Male HPMECs showed increased *SNAIL1* protein upon exposure to hyperoxia, while female HPMECs did not show this change. In vivo, *Snail* expression was decreased in females immediately after (P7) hyperoxia exposure.

Since our group had discovered sex-specific differences in *miR-30a* expression with females showing higher expression than males [9], we wanted to elucidate the possible regulation of *SNAIL1* expression by *miR-30a* in female HPMECs. Other studies have shown *miR-30a* mediated downregulation of *Snail* [10, 14, 17]. Zhang et al. reported that *miR-30a*

targeted and downregulated *SNAIL1* in a diabetic cataract model *in vitro*. Similar antifibrotic effects were reported in non-small cell lung cancer [40], atrial fibrillation-induced myocardial fibrosis [14], and TGF- β 1-induced peritoneal fibrosis [10]. In female HPMECs, in the present study, we show decreased expression of *SNAIL1* with *miR-30a* overexpression and increased expression with *miR-30a* inhibition. To our knowledge, this is the first study to show that *miR-30a* targets *SNAIL1* in neonatal HPMECs.

Even though we had reported sex-specific differences in *miR-30a* expression [9], upstream modulation of *miR-30a* was not elucidated. *Hif-1α* is expressed in early lung development and slowly decreases expression as the lung matures, with a second transient peak at the alveolar stage of lung development around PND10 [20, 41]. Use of prolyl hydroxylase domain (PHD) inhibitors to increase HIF protein levels

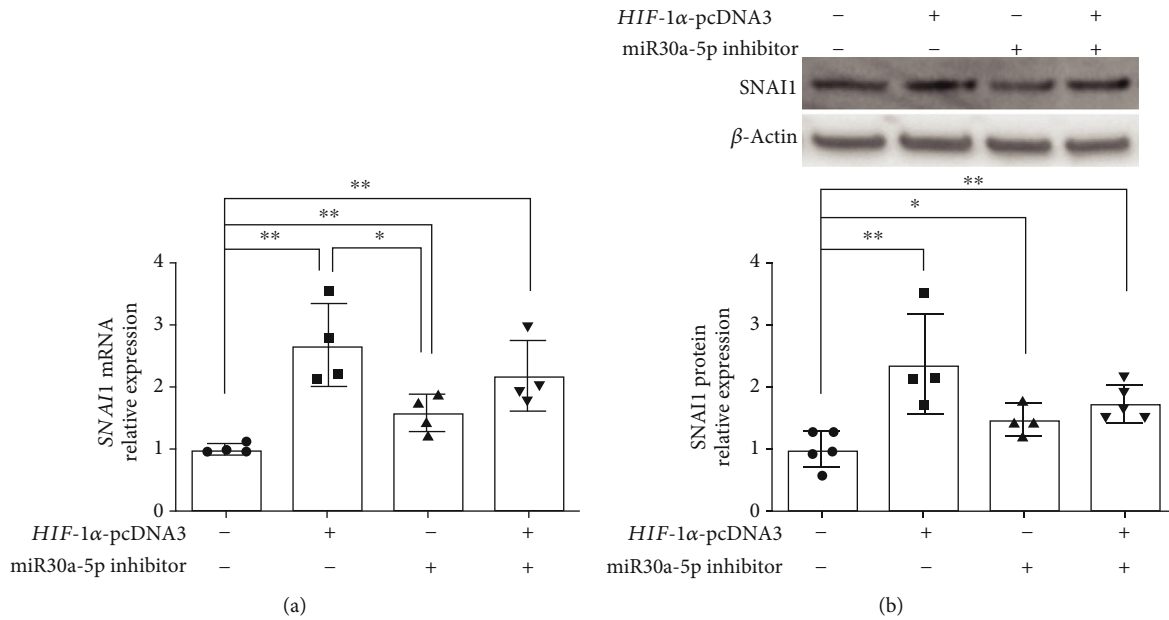


FIGURE 6: *SNAI1* expression following miR30a-5p inhibition, HIF-1 α overexpression, or both in female HPMECs: *SNAI1* mRNA (a) and protein (b) expression in female HPMECs transfected with HIF-1 α overexpression plasmid (*HIF-1 α -pcDNA3*), miR30a-5p inhibitor, or both. Values are expressed as mean \pm SD. $N = 4$ experimental replicates for each group. Significant differences between the indicated groups are shown by * $P < 0.05$ and ** $P < 0.01$.

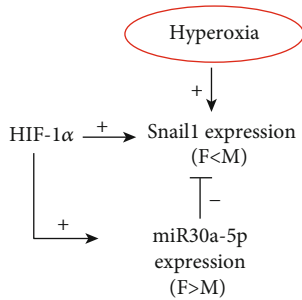


FIGURE 7: Overall schematic. Hyperoxia increases *SNAI1* expression *in vitro*, but females show decreased expression *in vivo*. miR-30a decreases *Snail* expression, and females show higher expression. HIF-1 α increases both the miR-30a and *Snail* expressions, but HIF-1 α -mediated miR-30a expression in females keeps the *Snail* expression in check upon exposure to hyperoxia.

improved lung growth in a preterm baboon model of BPD [42] Interestingly, *Hif-1 α* activity is increased, when human umbilical vein endothelial cells are returned to normoxic conditions after being exposed to hyperoxia [43]. We had previously reported that *HIF-1 α* binding to its target genes is more significant in female lungs after hyperoxia exposure [22]. In contrast to male mice, females did not show a decrease in *Hif-1 α* expression at PND21 after early hyperoxia exposure. Yang et al. showed that HIF-1 α inhibition abrogated *miR-30a* upregulation in cardiomyocytes [18]. In this study, we were able to show that the silencing of *HIF-1 α* in HPMECs significantly decreased *miR-30a* expression in HPMECs, thus postulating a role for *HIF-1 α* in increasing *miR-30a* expression in the hyperoxia model, especially during the normoxic recovery phase after exposure to hyperoxia.

Many factors including HIF-1 α , NFKB, STAT3, and NICD can induce *Snail* expression [30]. Xu et al. showed that *HIF-1 α* could induce *Snail*, independent of *TGF- β* , and that *SNAI1* is a direct target of *HIF-1 α* in human coronary endothelial cells [23]. We wanted to see if *HIF-1 α* modulated *SNAI1* expression in HPMECs. *HIF-1 α* knock-down in HPMECs decreased *SNAI1* mRNA and protein expression. Similar results were reported by Zhu et al. in pancreatic cancer cells [44]. Hypoxia-induced Endo-MT in a model of radiation-induced pulmonary fibrosis was mediated through *HIF-1 α* [45]. *HIF-1 α* may be thus inducing both profibrotic (*SNAI1*) and antifibrotic (*miR-30a*) pathways in HPMECs. The balance of expression between the two mediators may eventually predispose or protect the lung from pathologic fibrosis. In our study, *HIF-1 α* overexpression and *miR30a-5p* inhibition either separately or in combination increased *SNAI1* expression, but the combined treatment did not produce an additive effect in *SNAI1* expression.

We recognize the following limitations in this study. Our study only evaluated two time points *in vivo* after hyperoxia exposure during the saccular stage of lung development in mice. Later time points may have sustained differences in *Snail* expression, or these differences may be lost. Also, we used high oxygen concentration (0.95 FiO₂) for our hyperoxia exposure protocol based on the reproducible BPD-like phenotype produced in mice. Even though this limits hyperoxia exposure to the saccular stage of lung development, which equates to 26-36 weeks in human neonates, this oxygen concentration is much higher than what is used in the human NICU. Also, these results may be different from other models, where hyperoxia exposure is continued for longer durations [2]. We are also aware that findings in the murine

model may be strain-specific [46]. Our *in vivo* data is from whole lung tissue and does not show endothelial-specific expression. Our future studies will seek to validate the cell-specific expression of *Snail* in primary mouse endothelial cells and BPD and non-BPD patient samples. In conclusion, we show that the intersection between *HIF-1 α* , *miR-30a*, and *Snail* may play a role in driving sex-specific differences in after neonatal hyperoxic lung injury.

Data Availability

The data used to support the findings of this study are available from the corresponding author upon request.

Conflicts of Interest

The authors declare that there is no conflict of interest regarding the publication of this paper.

Acknowledgments

This work was supported by grants from NIH (K08-HL127103, R03-HL141572, and R01-HL144775 to KL).

Supplementary Materials

Supplementary Figure 1: *Snail* expression in vivo and in vitro: *Snail* mRNA (A–C) and protein (D–F) expression in neonatal male and female mice exposed to hyperoxia (P1-5, 0.95 FiO₂) during the saccular stage of lung development at P7 (A, D) and P21 (B, E) and in male and female neonatal human pulmonary microvascular endothelial cells (HPMECs) (C, F). Significant differences between the indicated groups is shown by **P* < 0.05. (Supplementary Materials)

References

- [1] C. Nardiello, I. Miřiková, D. M. Silva et al., “Standardisation of oxygen exposure in the development of mouse models for bronchopulmonary dysplasia,” *Disease Models & Mechanisms*, vol. 10, pp. 185–196, 2017.
- [2] J. Berger and V. Bhandari, “Animal models of bronchopulmonary dysplasia. I: the term mouse models,” *American Journal of Physiology-Lung Cellular and Molecular Physiology*, vol. 307, pp. L936–L947, 2014.
- [3] A. J. Jobe, “The new BPD: an arrest of lung development,” *Pediatric Research*, vol. 46, pp. 641–643, 1999.
- [4] C. D. Baker and C. M. Alvira, “Disrupted lung development and bronchopulmonary dysplasia: opportunities for lung repair and regeneration,” *Current Opinion in Pediatrics*, vol. 26, pp. 306–314, 2014.
- [5] C. D. Baker and S. H. Abman, “Impaired pulmonary vascular development in bronchopulmonary dysplasia,” *Neonatology*, vol. 107, pp. 344–351, 2015.
- [6] C. D. Baker, S. H. Abman, and P. M. Mourani, “Pulmonary hypertension in preterm infants with bronchopulmonary dysplasia,” *Pediatric Allergy, Immunology and Pulmonology*, vol. 27, pp. 8–16, 2014.
- [7] J. J. Coalson, “Pathology of new bronchopulmonary dysplasia,” *Seminars in Neonatology*, vol. 8, pp. 73–81, 2003.
- [8] K. Lingappan, W. Jiang, L. Wang, and B. Moorthy, “Sex-specific differences in neonatal hyperoxic lung injury,” *American Journal of Physiology-Lung Cellular and Molecular Physiology*, vol. 311, pp. L481–L493, 2016.
- [9] Y. Zhang, C. Coarfa, X. Dong et al., “MicroRNA-30a as a candidate underlying sex-specific differences in neonatal hyperoxic lung injury: implications for BPD,” *American Journal of Physiology-Lung Cellular and Molecular Physiology*, vol. 316, pp. L144–L156, 2018.
- [10] Q. Zhou, M. Yang, H. Lan, and X. Yu, “miR-30a negatively regulates TGF- β 1-induced epithelial-mesenchymal transition and peritoneal fibrosis by targeting *Snail*,” *The American Journal of Pathology*, vol. 183, pp. 808–819, 2013.
- [11] Y.-H. Chung, S. C. Li, Y. H. Kao et al., “miR-30a-5p inhibits epithelial-to-mesenchymal transition and upregulates expression of tight junction protein claudin-5 in human upper tract urothelial carcinoma cells,” *International Journal of Molecular Sciences*, vol. 18, p. 1826, 2017.
- [12] Z. Liu, K. Tu, and Q. Liu, “Effects of microRNA-30a on migration, invasion and prognosis of hepatocellular carcinoma,” *FEBS Letters*, vol. 588, pp. 3089–3097, 2014.
- [13] R. Peng, L. Zhou, Y. Zhou et al., “miR-30a inhibits the epithelial–mesenchymal transition of podocytes through downregulation of NFATc3,” *International Journal of Molecular Sciences*, vol. 16, pp. 24032–24047, 2015.
- [14] C.-T. Yuan, X. X. Li, Q. J. Cheng, Y. H. Wang, J. H. Wang, and C. L. Liu, “MiR-30a regulates the atrial fibrillation-induced myocardial fibrosis by targeting *snail 1*,” *International Journal of Clinical and Experimental Pathology*, vol. 8, pp. 15527–15536, 2015.
- [15] J. Chen, Y. Yu, S. Li et al., “MicroRNA-30a ameliorates hepatic fibrosis by inhibiting beclin1-mediated autophagy,” *Journal of Cellular and Molecular Medicine*, vol. 21, pp. 3679–3692, 2017.
- [16] C. Mao, J. Zhang, S. Lin et al., “miRNA-30a inhibits AECs-II apoptosis by blocking mitochondrial fission dependent on Drp-1,” *Journal of Cellular and Molecular Medicine*, vol. 18, pp. 2404–2416, 2014.
- [17] L. Zhang, Y. Wang, W. Li et al., “MicroRNA-30a regulation of epithelial-mesenchymal transition in diabetic cataracts through targeting *SNAIL1*,” *Scientific Reports*, vol. 7, article 1117, 2017.
- [18] Y. Yang, Y. Li, X. Chen, X. Cheng, Y. Liao, and X. Yu, “Exosomal transfer of miR-30a between cardiomyocytes regulates autophagy after hypoxia,” *Journal of Molecular Medicine*, vol. 94, pp. 711–724, 2016.
- [19] L. A. Shimoda and G. L. Semenza, “HIF and the lung: role of hypoxia-inducible factors in pulmonary development and disease,” *American Journal of Respiratory and Critical Care Medicine*, vol. 183, pp. 152–156, 2011.
- [20] A. Vadivel, R. S. Alphonse, N. Etches et al., “Hypoxia inducible factors promote alveolar development and regeneration,” *American Journal of Respiratory Cell and Molecular Biology*, vol. 50, pp. 96–105, 2014.
- [21] T. Eckle, K. Brodsky, M. Bonney et al., “HIF1A reduces acute lung injury by optimizing carbohydrate metabolism in the alveolar epithelium,” *PLoS Biology*, vol. 11, article e1001665, 2013.
- [22] C. Coarfa, Y. Zhang, S. Maity et al., “Sexual dimorphism of the pulmonary transcriptome in neonatal hyperoxic lung injury: identification of angiogenesis as a key pathway,” *American*

- Journal of Physiology-Lung Cellular and Molecular Physiology*, vol. 313, no. 6, pp. L991–L1005, 2017.
- [23] X. Xu, X. Tan, B. Tampe, E. Sanchez, M. Zeisberg, and E. M. Zeisberg, “Snail is a direct target of hypoxia-inducible factor 1 α (HIF1 α) in hypoxia-induced endothelial to mesenchymal transition of human coronary endothelial cells,” *Journal of Biological Chemistry*, vol. 290, pp. 16653–16664, 2015.
- [24] T. Kokudo, Y. Suzuki, Y. Yoshimatsu, T. Yamazaki, T. Watabe, and K. Miyazono, “Snail is required for TGF β -induced endothelial-mesenchymal transition of embryonic stem cell-derived endothelial cells,” *Journal of Cell Science*, vol. 121, pp. 3317–3324, 2008.
- [25] M. M. Mahmoud, J. Serbanovic-Canic, S. Feng et al., “Shear stress induces endothelial-to-mesenchymal transition via the transcription factor Snail,” *Scientific Reports*, vol. 7, p. 3375, 2017.
- [26] J.-X. Sun, T. F. Chang, M. H. Li et al., “SNAIL1, an endothelial-mesenchymal transition transcription factor, promotes the early phase of ocular neovascularization,” *Angiogenesis*, vol. 21, pp. 635–652, 2018.
- [27] C. Sahlgren, M. V. Gustafsson, S. Jin, L. Poellinger, and U. Lendahl, “Notch signaling mediates hypoxia-induced tumor cell migration and invasion,” *Proceedings of the National Academy of Sciences*, vol. 105, pp. 6392–6397, 2008.
- [28] Y. Matsuno, A. L. Coelho, G. Jarai, J. Westwick, and C. M. Hogaboam, “Notch signaling mediates TGF- β 1-induced epithelial-mesenchymal transition through the induction of Snail,” *The International Journal of Biochemistry & Cell Biology*, vol. 44, pp. 776–789, 2012.
- [29] Y. Zhang, W. Jiang, L. Wang, and K. Lingappan, “Sex-specific differences in the modulation of growth differentiation factor 15 (GDF15) by hyperoxia in vivo and in vitro: role of Hif-1 α ,” *Toxicology and Applied Pharmacology*, vol. 332, pp. 8–14, 2017.
- [30] S. Kaufhold and B. Bonavida, “Central role of Snail1 in the regulation of EMT and resistance in cancer: a target for therapeutic intervention,” *Journal of Experimental & Clinical Cancer Research*, vol. 33, p. 62, 2014.
- [31] L. G. Boros, J. S. Torday, W.-N. Paul Lee, and V. K. Rehan, “Oxygen-induced metabolic changes and transdifferentiation in immature fetal rat lung lipofibroblasts,” *Molecular Genetics and Metabolism*, vol. 77, pp. 230–236, 2002.
- [32] J. Ni, Z. Dong, W. Han, D. Kondrikov, and Y. Su, “The role of RhoA and cytoskeleton in myofibroblast transformation in hyperoxic lung fibrosis,” *Free Radical Biology & Medicine*, vol. 61, pp. 26–39, 2013.
- [33] D. Kondrikov, R. B. Caldwell, Z. Dong, and Y. Su, “Reactive oxygen species-dependent RhoA activation mediates collagen synthesis in hyperoxic lung fibrosis,” *Free Radical Biology & Medicine*, vol. 50, pp. 1689–1698, 2011.
- [34] J. M. S. Sucre, P. Vijayaraj, C. J. Aros et al., “Posttranslational modification of β -catenin is associated with pathogenic fibroblastic changes in bronchopulmonary dysplasia,” *American Journal of Physiology-Lung Cellular and Molecular Physiology*, vol. 312, pp. L186–L195, 2017.
- [35] S. Piera-Velazquez, F. A. Mendoza, and S. A. Jimenez, “Endothelial to mesenchymal transition (EndoMT) in the pathogenesis of human fibrotic diseases,” *Journal of Clinical Medicine*, vol. 5, p. 45, 2016.
- [36] Y. Li, K. O. Lui, and B. Zhou, “Reassessing endothelial-to-mesenchymal transition in cardiovascular diseases,” *Nature Reviews Cardiology*, vol. 15, pp. 445–456, 2018.
- [37] R. B. Good, A. J. Gilbane, S. L. Trinder et al., “Endothelial to mesenchymal transition contributes to endothelial dysfunction in pulmonary arterial hypertension,” *The American Journal of Pathology*, vol. 185, pp. 1850–1858, 2015.
- [38] N. Hashimoto, S. H. Phan, K. Imaizumi et al., “Endothelial-mesenchymal transition in bleomycin-induced pulmonary fibrosis,” *American Journal of Respiratory Cell and Molecular Biology*, vol. 43, pp. 161–172, 2010.
- [39] Y. Zhang, X. Dong, J. Shirazi, J. P. Gleghorn, and K. Lingappan, “Pulmonary endothelial cells exhibit sexual dimorphism in their response to hyperoxia,” *American Journal of Physiology-Heart and Circulatory Physiology*, vol. 315, pp. H1287–H1292, 2018.
- [40] R. Kumarswamy, G. Mudduluru, P. Ceppi et al., “MicroRNA-30a inhibits epithelial-to-mesenchymal transition by targeting Snail1 and is downregulated in non-small cell lung cancer,” *International Journal of Cancer*, vol. 130, pp. 2044–2053, 2012.
- [41] J. P. Bridges, S. Lin, M. Ikegami, and J. M. Shannon, “Conditional hypoxia inducible factor-1 α induction in embryonic pulmonary epithelium impairs maturation and augments lymphangiogenesis,” *Developmental Biology*, vol. 362, pp. 24–41, 2012.
- [42] T. M. Asikainen, L. Y. Chang, J. J. Coalson et al., “Improved lung growth and function through hypoxia-inducible factor in primate chronic lung disease of prematurity,” *The FASEB Journal*, vol. 20, pp. 1698–1700, 2006.
- [43] F. Cimino, C. Balestra, P. Germonpre et al., “Pulsed high oxygen induces a hypoxic-like response in human umbilical endothelial cells and in humans,” *Journal of Applied Physiology*, vol. 113, pp. 1684–1689, 2012.
- [44] G.-H. Zhu, C. Huang, Z.-Z. Feng, X.-H. Lv, and Z.-J. Qiu, “Hypoxia-induced snail expression through transcriptional regulation by HIF-1 α in pancreatic cancer cells,” *Digestive Diseases and Sciences*, vol. 58, pp. 3503–3515, 2013.
- [45] S.-H. Choi, Z.-Y. Hong, J.-K. Nam et al., “A hypoxia-induced vascular endothelial-to-mesenchymal transition in development of radiation-induced pulmonary fibrosis,” *Clinical Cancer Research*, vol. 21, pp. 3716–3726, 2015.
- [46] S. Leary, P. Das, D. Ponnalagu, H. Singh, and V. Bhandari, “Genetic strain and sex differences in a hyperoxia-induced mouse model of varying severity of bronchopulmonary dysplasia,” *The American Journal of Pathology*, vol. 189, pp. 999–1014, 2019.

Research Article

Cell Type- and Exposure-Specific Modulation of CD63/CD81-Positive and Tissue Factor-Positive Extracellular Vesicle Release in response to Respiratory Toxicants

Frank R. M. Stassen,¹ Pascale H. van Eijck,¹ Paul H. M. Savelkoul,^{1,2} Emiel F. M. Wouters,³ Gernot G. U. Rohde,^{3,4} Jacco J. Briedé,⁵ Niki L. Reynaert,³ Theo M. de Kok,⁵ and Birke J. Benedikter ^{1,3}

¹Department of Medical Microbiology, NUTRIM School of Nutrition and Translational Research in Metabolism, Maastricht University Medical Center, PO box 5800, 6202AZ Maastricht, Netherlands

²Department of Medical Microbiology & Infection Control, VU University Medical Center, P.O. Box 7057, 1007MB Amsterdam, Netherlands

³Department of Respiratory Medicine, NUTRIM School of Nutrition and Translational Research in Metabolism, Maastricht University Medical Center, PO box 5800, 6202AZ Maastricht, Netherlands

⁴Medical Clinic I, Department of Respiratory Medicine, Goethe University Hospital, Theodor-Stern-Kai 7, 60590 Frankfurt am Main, Germany

⁵Department of Toxicogenomics, GROW School for Oncology and Developmental Biology, Maastricht University, 6200 MD Maastricht, Netherlands

Correspondence should be addressed to Birke J. Benedikter; b.benedikter@maastrichtuniversity.nl

Received 5 March 2019; Revised 19 June 2019; Accepted 25 July 2019; Published 14 August 2019

Guest Editor: Jason Richardson

Copyright © 2019 Frank R. M. Stassen et al. This is an open access article distributed under the Creative Commons Attribution License, which permits unrestricted use, distribution, and reproduction in any medium, provided the original work is properly cited.

Chronic exposure to respiratory stressors increases the risk for pulmonary and cardiovascular diseases. Previously, we have shown that cigarette smoke extract (CSE) triggers the release of CD63⁺CD81⁺ and tissue factor (TF)⁺ procoagulant extracellular vesicles (EVs) by bronchial epithelial cells via depletion of cell surface thiols. Here, we hypothesized that this represents a universal response for different pulmonary cell types and respiratory exposures. Using bead-based flow cytometry, we found that bronchial epithelial cells and pulmonary fibroblasts, but not pulmonary microvascular endothelial cells or macrophages, release CD63⁺CD81⁺ and TF⁺ EVs in response to CSE. Cell surface thiols decreased in all cell types upon CSE exposure, whereas depletion of cell surface thiols using bacitracin only triggered EV release by epithelial cells and fibroblasts. The thiol-antioxidant NAC prevented the EV induction by CSE in epithelial cells and fibroblasts. Exposure of epithelial cells to occupational silica nanoparticles and particulate matter (PM) from outdoor air pollution also enhanced EV release. Cell surface thiols were mildly decreased and NAC partly prevented the EV induction for PM₁₀, but not for silica and PM_{2.5}. Taken together, induction of procoagulant EVs is a cell type-specific response to CSE. Moreover, induction of CD63⁺CD81⁺ and TF⁺ EVs in bronchial epithelial cells appears to be a universal response to various respiratory stressors. TF⁺ EVs may serve as biomarkers of exposure and/or risk in response to respiratory exposures and may help to guide preventive treatment decisions.

1. Introduction

The human lungs are covered with a vast epithelial surface, which makes them very efficient for gas exchange, but also highly vulnerable to inhaled exposures [1]. Such exposures include cigarette smoke, as well as gases, volatile compounds,

and particulates from outdoor and indoor sources of air pollution. Traffic emissions are major contributors to outdoor air pollution [2] whereas exposure to indoor air pollution is often occupational. For instance, workers of many industrial sectors are exposed to crystalline silica nanoparticles at their workplace [3]. Exposure to respiratory toxicants is

associated with several health consequences. Many respiratory exposures contribute to the development or aggravation of pulmonary diseases, such as chronic obstructive pulmonary disease (COPD) [4], (occupational) asthma [5, 6], or pneumoconiosis [7]. Moreover, respiratory exposures are associated with increased risks of lung cancer [8–10] and cardiovascular diseases (CVD) [11–13]. While the cellular and molecular mechanisms underlying the development of respiratory exposure-associated diseases are still incompletely understood, inflammation is known to play an important role.

Epithelial cells form a major cellular target for respiratory exposures as they cover the entire surface of the airways and alveoli [14]. Alveolar macrophages are additional targets due to their localization in the lung lumen. Moreover, both soluble and ultrafine particulate components of inhaled toxicants can translocate across the epithelial barrier or even disturb barrier integrity and interact with cell types located underneath the epithelium, such as fibroblasts and pulmonary microvascular endothelial cells [15–17]. When cells come into contact with environmental stressors, their behaviour is profoundly affected, including the release of extracellular vesicles (EVs) [18, 19]. These EVs are secreted membrane vesicles that carry a complex molecular cargo and exert versatile functions in cell-to-cell communication and in the extracellular space [20]. They are thought to be actively involved in the pathogenesis of several chronic inflammatory diseases, including CVD [21, 22]. We have previously shown that cigarette smoke extract (CSE) increases the amount of small (80–250 nm) CD63⁺CD81⁺ EVs released by bronchial epithelial cells [18]. These CSE-induced EVs were enriched in tissue factor (TF) compared to EVs secreted by unexposed cells [23]. Thus, they likely reflect epithelial activation and damage. Moreover, they exert a TF-dependent procoagulant activity and may thereby contribute to the elevated cardiovascular risk in smokers [23]. We further demonstrated that the EV induction by CSE depended on the oxidative depletion of cellular thiols and could be prevented by antioxidants, such as N-acetyl-L-cysteine (NAC) [18]. In the current study, we aimed to determine whether thiol-dependent EV induction is a universal response to respiratory exposures in different cell types and for different respiratory toxicants. We first investigated the effect of CSE on the EV release by bronchial epithelial cells, pulmonary fibroblasts, macrophages, and pulmonary microvascular endothelial cells. Secondly, we investigated whether respiratory exposures other than CSE also affect EV release by bronchial epithelial cells. For this purpose, cells were stimulated either with particulate matter (PM) from outdoor sources of air pollution or with crystalline silica particles. Total (CD63⁺CD81⁺) and procoagulant (TF⁺) EVs were detected using bead-based flow cytometry, a method that we and others have shown to be suitable for semiquantitative EV measurements [24–26].

2. Materials and Methods

2.1. Product Information. Detailed product information including catalogue numbers is provided in Supplementary Table 1.

2.2. Cell Culture. The bronchial epithelial cell line BEAS-2B (ATCC CRL-9609), the pulmonary fibroblast cell lines MRC-5 (ATCC CCL-171) and HEL-299 (ATCC CCL-137), the monocytic cell line THP-1, and the pulmonary microvascular endothelial cell line HPMEC-ST1.6R (a kind gift from Dr. C.J. Kirkpatrick, Institute for Pathology, University of Mainz, Germany [27]) were maintained at 5% CO₂ and 37°C. BEAS-2B cells were cultured as described previously [18]. Tests for mycoplasma contamination were performed regularly using the MycoAlert Mycoplasma Detection Kit (Lonza) according to the manufacturer's instructions, and all results were negative. MRC-5 and HEL-299 cells were cultured in a Minimal Essential Medium (MEM; Gibco) supplemented with 1% (v/v) 100x Non-Essential Amino Acids (Sigma-Aldrich), 2 mM L-glutamine, and 10% (v/v) foetal calf serum (FCS; Lonza). They were passaged once per week with a 1:2 split ratio and used for experiments between passages 20 and 30. THP-1 cells were cultured in RPMI-1640 (Gibco) supplemented with 50 μM β-mercaptoethanol (Sigma-Aldrich), 1 mM sodium pyruvate (Sigma-Aldrich), 12.5 mM glucose, and 10% (v/v) FCS. They were passaged once or twice per week with a split ratio of 1:5 to 1:20. HPMEC-ST1.6R cells were cultured as described previously in MCDB1 (Gibco) supplemented with 1 μg/ml hydrocortisone (Sigma-Aldrich), 10 ng/ml human recombinant epidermal growth factor (Sigma-Aldrich), 10% (v/v) FCS, and 1% (v/v) 100x penicillin and streptomycin (Gibco) [28]. They were subcultured twice per week with a split ratio of 1:4 to 1:8. Cell culture dishes were precoated with 2% (v/v) gelatin (Sigma-Aldrich) in MilliQ before HPMEC-ST1.6R cells were seeded.

For experiments, cells were seeded on 12- or 24-well plates. BEAS-2B and HPMEC-ST1.6R were seeded at 5×10^4 cells/cm² and allowed to attach overnight. MRC-5 and HEL-299 cells were seeded at 0.4×10^4 cells/cm² and grown until confluence (usually 72 h). THP-1 cells were seeded at 0.5×10^4 cells/cm² in a growth medium which was additionally supplemented with 200 nM phorbol 12-myristate 13-acetate (PMA; Sigma-Aldrich) to induce monocyte-to-macrophage differentiation. After 72 h, the PMA medium was replaced by a normal growth medium, followed by incubation for another 72 h.

For 2 h prior to exposure, cells were kept in a reduction medium. The reduction medium was DMEM-F12 without phenol-red (Gibco) supplemented with varying percentages of EV-depleted FCS depending on the cell line. For BEAS-2B and HPMEC-ST1.6R cells, the reduction medium was supplemented with 0.1% (v/v) EV-depleted FCS. For MRC-5 and HEL-299 cells, it was supplemented with 2% (v/v) EV-depleted FCS, and for THP-1 cells with 2% (v/v) EV-depleted FCS and 0.5 mM sodium pyruvate. EV-depleted FCS was prepared by 16 h centrifugation at 40,000 rpm (*average RCF* = 117,734 × *g*), in a fixed-angle Type 70Ti-rotor in an Optima L-90K preparative ultracentrifuge (Beckman-Coulter, Brea, CA, USA) as described previously [18].

2.3. Cell Exposures. CSE, bacitracin, and NAC solutions were prepared as described previously [18]. For CSE production, the smoke of one research reference cigarette without filter

(Type 3R4F, Tobacco Health Research, University of Kentucky) was drawn through 2 ml of PBS using a pump at constant speed. CSE was sterile-filtered and used within 15 min after production to avoid loss of unstable or volatile chemical species. CSE was only used when the smoking time was between 6 and 8 minutes and when the delta OD ($OD_{320\text{ nm}} - OD_{540\text{ nm}}$) was between 0.9 and 1.2. Silica particles were obtained from C&E Mineral Corp. and have been characterized previously [29]. Silica suspensions in PBS were prepared as described previously [29]. Particulate matter with an *aerodynamic diameter* $\leq 10\ \mu\text{m}$ (PM_{10}) and $\leq 2.5\ \mu\text{m}$ ($\text{PM}_{2.5}$) was sampled at three primary schools in Maastricht, Netherlands, as described previously [30]. For extraction of PM, filters were cut into pieces of approximately $1\ \text{cm}^2$ and incubated in 250 ml of dichloromethane overnight at room temperature on a shaker. Dichloromethane was then evaporated using a Rotavap rotational evaporator. The remaining dry material was resuspended in 5 ml methanol and transferred into a centrifuge tube. After 5 minutes of centrifugation at $300\ \times\ g$, the supernatant was transferred into a fresh recipient and evaporated using a Rotavap rotational evaporator. The remaining dry material was resuspended in methanol so that the particulate matter from $200\ \text{m}^3$ of air was suspended per ml. To obtain a suitable vehicle control, the extraction protocol was also applied to an unused PM_{10} filter. The resulting dry material was weight-matched to the PM_{10} extract and also suspended in methanol.

Prior to exposure, cells were washed twice with PBS followed by the addition of 1 ml of reduction medium. Different concentrations of CSE, NAC, bacitracin (Sigma-Aldrich), silica, PM_{10} , and $\text{PM}_{2.5}$ or the respective vehicle/solvent controls were then added, followed by 24 h incubation at 37°C and 5% CO_2 . CSE concentrations are given in % (v/v). Silica concentrations are given in $\times 10^6\ \mu\text{m}^2/\text{cm}^2$ (surface area of the silica particles/cell culture surface area), $150 \times 10^6\ \mu\text{m}^2/\text{cm}^2$ corresponds to $29.4\ \mu\text{g}/\text{cm}^2$ or $100\ \mu\text{g}/\text{ml}$. PM concentrations are given in m^3/ml (cubic meters of air filtered to obtain the PM/ml of a cell culture medium). The PM vehicle control was volume-matched to PM_{10} . The amount of PM per m^3 differed between the three sampling locations. Supplementary Table 2 gives a conversion of the PM concentrations used for cell stimulation from m^3/ml to micrograms per cell culture surface area ($\mu\text{g}/\text{cm}^2$).

2.4. Determination of Cell Metabolic Activity, EV Release, and Exofacial Thiols. Cell viability was assessed by the MTT assay as described previously [18]. Quantification of $\text{CD63}^+\text{CD81}^+$ EVs by bead-based flow cytometry of conditioned media was also done as described previously [18], except that $200\ \mu\text{l}$ of conditioned media were used instead of $400\ \mu\text{l}$. For the detection of $\text{CD63}/\text{CD81}/\text{CD9}^+\text{TF}^+$ EVs, the protocol was slightly adapted. In brief, 3.5×10^8 beads/ml ($4\ \mu\text{m}$ aldehyde/sulphate latex beads 5% (w/v); Molecular Probes, Life Technologies, Waltham, MA, USA) were coated with a mixture of $42\ \mu\text{g}/\text{ml}$ mouse anti-human CD81 antibody (Clone JS-81; BD Biosciences), $42\ \mu\text{g}/\text{ml}$ mouse anti-human CD63 antibody (Clone H5C6, BD Biosciences), and $42\ \mu\text{g}/\text{ml}$

mouse anti-human CD9 antibody (clone M-L13, BD Biosciences) by overnight incubation in MES buffer. Unconditioned (negative control) or conditioned media ($200\ \mu\text{l}$) were incubated overnight with the beads, followed by staining with $0.01\ \text{mg}/\text{ml}$ phycoerythrin- (PE-) labelled mouse anti-human TF antibody (Clone HTF-1; BD Biosciences) or PE-labelled IgG1,k isotype control (Clone MOPC-21, BD Biosciences). Measurements were performed on a BD FACSCanto II with FACSDiva V8.0.1 software. The PE-gate was set so that 2% of beads of the unconditioned medium control were PE-positive. Relative fluorescence units were then calculated by multiplying the % of positive beads with the mean fluorescence intensity. Supplementary Figure 1 shows the bead gating strategy (panel A) and the fluorescence intensity of EV samples and negative controls for the $\text{CD63}/\text{CD81}$ staining (panel B) or the TF staining (panel C).

Quantification of exofacial thiols was also performed as previously described [18] except that a different protocol was used for the detachment of adherent cells before staining. EDTA was added directly to the exposure medium to a final concentration of $10\ \text{mM}$. After incubating for 10 min at 37°C , cells were gently detached using the pipette tip and transferred to $1.5\ \text{ml}$ centrifuge tubes.

2.5. Electron Spin Resonance Spectroscopy. Electron spin resonance (ESR) spectroscopy was used to determine the generation of reactive oxygen species (ROS) as described previously [31]. In brief, $\text{PM}_{2.5}$ or PM_{10} filter pieces of $0.5\ \text{cm} \times 2\ \text{cm}$ were placed in a tissue cell (ER 162 TC-Q, Bruker BioSpin GmbH, Rheinstetten, Germany) and saturated with a solution of $70\ \mu\text{l}$ of $40\ \text{mM}$ Tris-HCl buffer supplemented with $100\ \text{mM}$ of the spin trap 5,5-dimethyl-1-pyrroline N-oxide (DMPO) and $13\ \mu\text{M}$ ascorbate. After sealing, the tissue cell with filter material was immediately placed in the resonator of the ESR spectrometer. ESR spectra were recorded at room temperature on a Bruker EMX 1273 spectrometer equipped with an ER 4119HS high-sensitivity resonator and $12\ \text{kW}$ power supply operating at X band frequencies. The modulation frequency of the spectrometer was $100\ \text{kHz}$. Instrumental conditions were as follows: center of magnetic field, $3490\ \text{G}$; scan range, $60\ \text{G}$; modulation amplitude, $1\ \text{G}$; receiver gain, 1×10^4 ; microwave frequency, $9.85\ \text{GHz}$; power, $50\ \text{mW}$; time constant, $40.96\ \text{ms}$; scan time, $20.97\ \text{s}$; and number of scans, 100. Spectra were quantified (in arbitrary units) by peak surface measurements using the WIN-EPR spectrum manipulation program.

2.6. Data Analysis. All values are expressed as percentages of the untreated control condition. Data were analysed using GraphPad Prism V5.03. All datasets were tested for normal distribution using the Kolmogorov-Smirnov test. For those datasets that passed the Kolmogorov-Smirnov test, a one sample *t*-test was used to test whether the mean of each measurement significantly differed from the control (100%). For those datasets that were not normally distributed, the Wilcoxon signed rank test was used. To test whether NAC significantly modified the effect of each

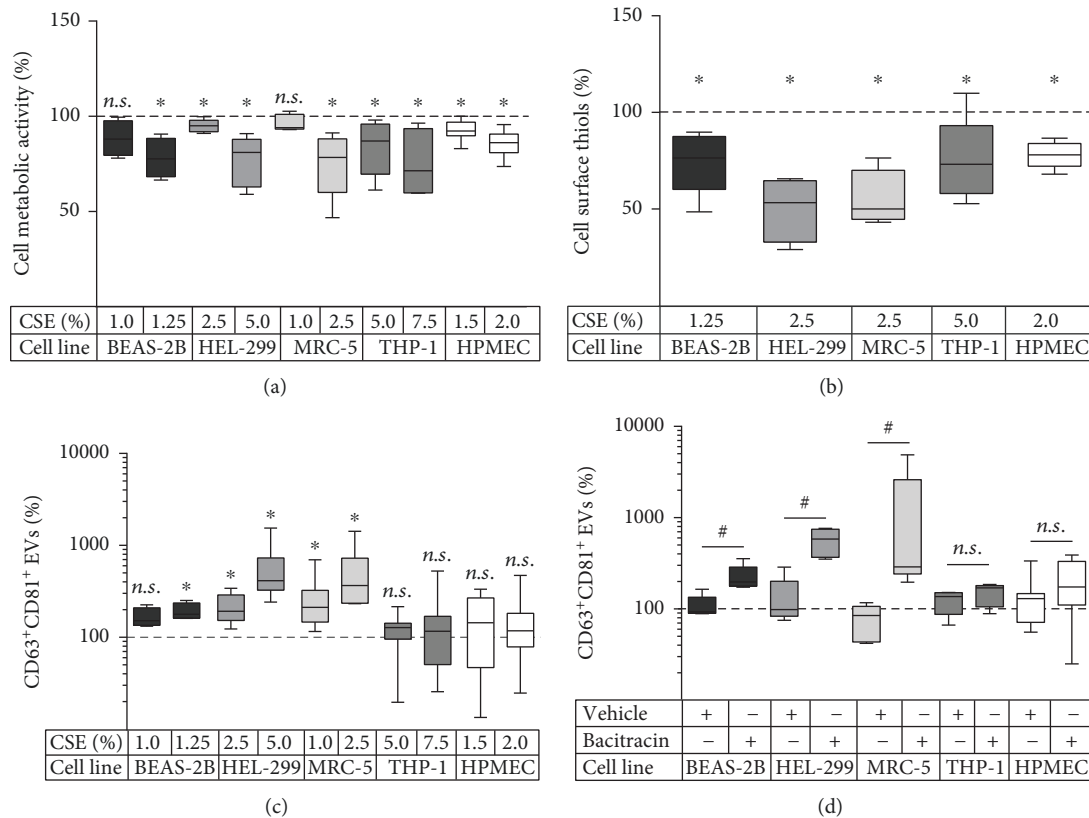


FIGURE 1: Effect of CSE and the thiol scavenger bacitracin on different pulmonary cell types. Effect of CSE exposure on (a) cell metabolic activity as determined by the MTT assay, $n=5-11$; (b) cell surface thiols, $n=4-6$; (c) release of CD63⁺CD81⁺ EVs determined by bead-based flow cytometry, $n=6-13$; (d) effect of 2.5 mM bacitracin on the release of CD63⁺CD81⁺ EVs, $n=5-9$. The box and whisker plots show the median (line in the box), 25th and 75th percentiles (outer lines of the box), and minimal and maximal values (whiskers). * $p < 0.05$ compared to the untreated control (100%), # $p < 0.05$ for bacitracin compared to the vehicle control. Cell lines: BEAS-2B: bronchial epithelial cells; HEL-299 and MRC-5: pulmonary fibroblast cell lines; THP-1: monocyte-derived macrophages; HPMEC: human pulmonary microvascular endothelial cell line.

exposure, a t -test was applied to compare the effect of treatment only to the treatment plus NAC. p values < 0.05 were considered statistically significant. All EV measurements are displayed on a Log10 scale, whereas cell metabolic activity, cell surface thiols, and ESR measurements are displayed on a linear scale.

3. Results

3.1. Effect of CSE on the EV Release by Different Cell Types. The first aim of this study was to investigate the effect of CSE on the EV release by different pulmonary cell types. Bronchial epithelial cells (BEAS-2B), pulmonary fibroblasts (HEL-299, MRC-5), monocyte-derived macrophages (THP-1), and pulmonary microvascular endothelial cells (HPMEC-ST1.6R, short HPMEC) were exposed to CSE for 24 h. According to the MTT assay, the used CSE concentrations decreased cell metabolic activity by no more than 25% (Figure 1(a)). We then assessed the effect of these CSE concentrations on cell surface thiols and on the release of CD63⁺CD81⁺ EVs. Despite a significant CSE-induced decrease in cell surface thiols for all cell types (Figure 1(b)), a concentration-dependent increase

in EV release was only observed in BEAS-2B, HEL-299, and MRC-5 cells, but not in THP-1 cells or HPMEC (Figure 1(c)). Likewise, the membrane impermeable thiol-blocking agent bacitracin was able to induce EV release by BEAS-2B, HEL-299, and MRC-5 cells, whereas no significant increase in EV release was observed for bacitracin-stimulated THP-1 and HPMEC cells (Figure 1(d)). Moreover, the thiol-antioxidant NAC inhibited the CSE-dependent EV induction in BEAS-2B, HEL-299, and MRC-5 cells, while it did not influence EV release by THP-1 cells and even slightly increased EV release in HPMEC cells (Figure 2(a)). Finally, we measured the quantity of the procoagulant protein TF on EVs released by the different cell types in response to CSE exposure in the presence or absence of NAC. EVs from BEAS-2B, HEL-299, and MRC-5 cells, but not THP-1 cells and HPMEC, showed an increased expression of TF when exposed to CSE, and this was preventable by NAC (Figure 2(b)). NAC was able to restore the cell metabolic activity during CSE exposure to approximately 100% for all cell types (Figure 2(c)).

Taken together, CSE enhanced the release of CD63⁺CD81⁺ EVs and TF⁺ EVs in bronchial epithelial cells and pulmonary fibroblasts, which was associated with a decrease

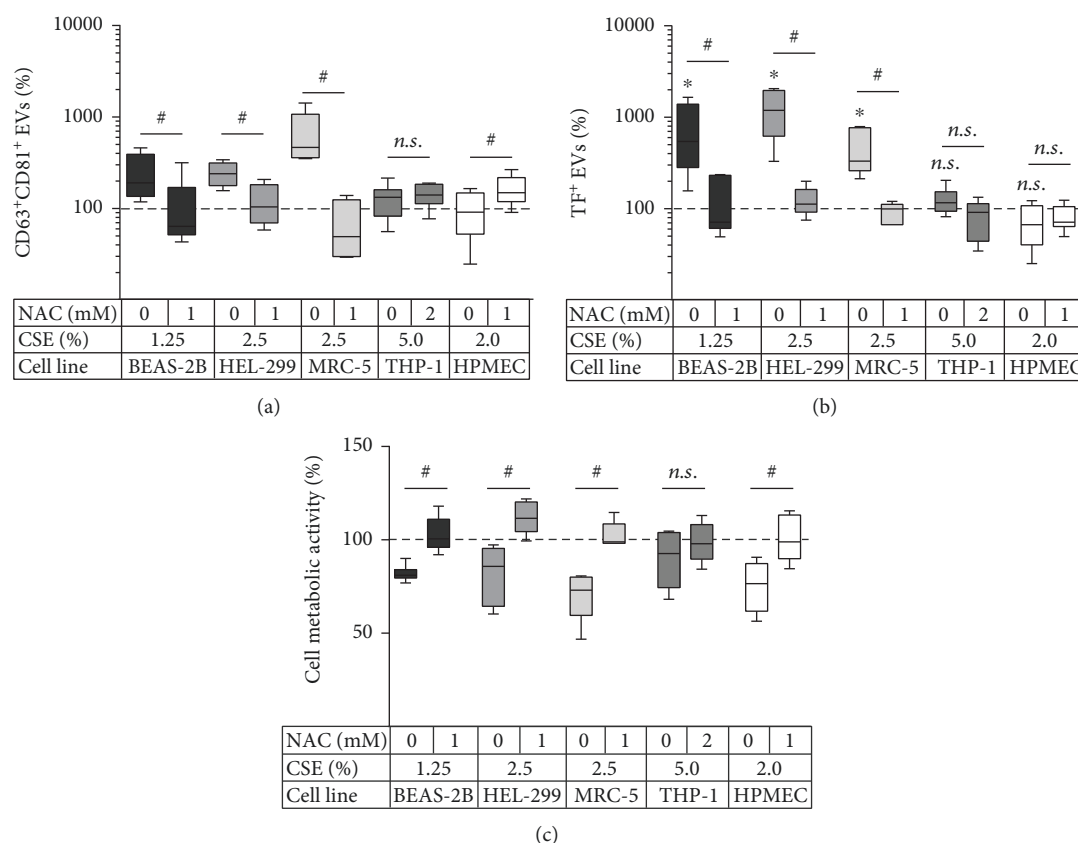


FIGURE 2: Effect of NAC on the EV release and cell metabolic activity during CSE exposure. Cells were exposed to CSE in the presence or absence of the thiol antioxidant NAC, and different readouts were performed. Concentration of (a) CD63⁺CD81⁺ EVs ($n = 5-9$) and (b) CD63/CD81/CD9⁺TF⁺ EVs ($n = 5-6$) as determined by bead-based flow cytometry. (c) Cell metabolic activity as determined by the MTT assay ($n = 5-11$). The box and whisker plots show the median (line in the box), 25th and 75th percentiles (outer lines of the box), and minimal and maximal values (whiskers). * $p < 0.05$ compared to the unexposed control (100%); # $p < 0.05$ for CSE alone compared to CSE with NAC. Cell lines: BEAS-2B: bronchial epithelial cells; HEL-299 and MRC-5: pulmonary fibroblast cell lines; THP-1: monocyte-derived macrophages; HPMEC: human pulmonary microvascular endothelial cell line.

in cell surface-exposed thiols. In these cells, the membrane impermeable thiol-blocking agent bacitracin also increased the EV release. Moreover, the CSE-induced release of CD63⁺CD81⁺ and TF⁺ EVs was preventable by the thiol-antioxidant NAC. In contrast, despite a significant depletion of cell surface thiols upon treatment with CSE, HPMEC and THP-1 cells did not show an enhanced EV release. In these cells, EV release could neither be triggered by bacitracin, nor was it decreased by NAC.

3.2. Effect of Different Respiratory Exposures on the EV Release by Bronchial Epithelial Cells. The second aim of this study was to investigate whether respiratory exposures such as crystalline silica particles or PM from air pollution affect the EV release by BEAS-2B bronchial epithelial cells similarly to CSE. Firstly, two concentrations of silica as well as PM_{2.5} and PM₁₀ were determined that decreased cell metabolic activity by at most 25% (Figure 3(a)). The concentration of cell surface thiols was not affected by silica or PM_{2.5} but was significantly decreased upon exposure to PM₁₀ (Figure 3(b)). To test whether the difference between PM_{2.5} and PM₁₀ could be attributed to differences

in their ROS-forming capacity, ROS generation for both PM types was assessed using ESR. PM samples were derived from three different sampling locations, and for each location, PM₁₀ had a higher ROS-generating capacity than PM_{2.5} (Figure 3(c)). All three exposure types (silica, PM_{2.5}, and PM₁₀), but not the vehicle control for PM, triggered an increase in CD63⁺CD81⁺ EVs (Figure 3(d)). NAC did not decrease the quantity of CD63⁺CD81⁺ EVs induced by silica or PM_{2.5}, but a trend for a decrease was observed for PM₁₀ ($p = 0.09$; Figure 4(a)). Importantly, TF⁺ EVs were also induced by all three stimuli (Figure 4(b)). Yet, NAC did not significantly decrease TF⁺ EVs for any of the exposures (Figure 4(b)). NAC treatment neither led to a significant recovery of the cell metabolic activity (Figure 4(c)).

To summarise, all tested respiratory stressors, namely, CSE (Figures 1 and 2), silica particles, PM_{2.5}, and PM₁₀, triggered total and TF⁺ EV release by bronchial epithelial cells. The EV induction could be entirely attributed to thiol-reactive species for CSE exposure and partly for the PM₁₀ exposure, whereas another mechanism appears to regulate the EV induction by PM_{2.5} and silica particles.

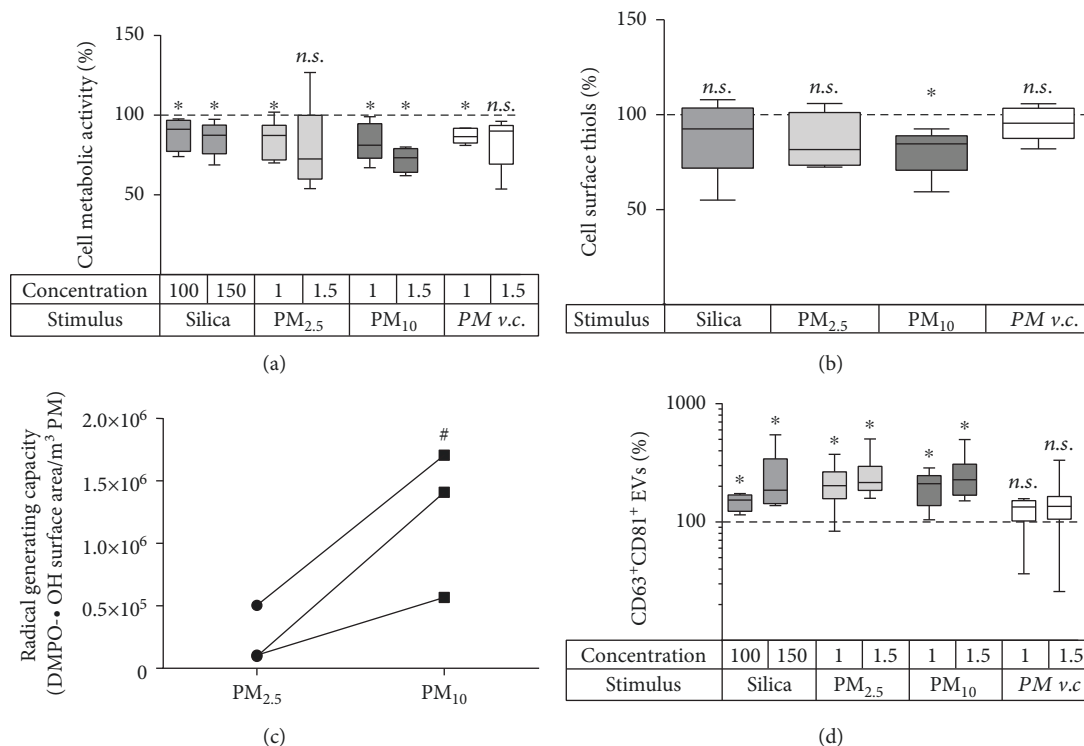


FIGURE 3: Effect of silica particles, PM_{2.5}, PM₁₀, and the PM vehicle control (v.c.) on bronchial epithelial cells. BEAS-2B cells were exposed for 24 h to different concentrations of the 4 stimuli. Silica concentrations are given in $\times 10^6 \mu\text{m}^2/\text{cm}^2$, and PM concentrations in m^3/ml . (a) Cell metabolic activity determined by the MTT assay, $n = 5-8$; (b) cell surface thiols after 24 h exposure to $100 \times 10^6 \mu\text{m}^2/\text{cm}^2$ silica or $1.5 \text{ m}^3/\text{ml}$ PM, $n = 5$. (c) ROS-generating capacity of PM_{2.5} and PM₁₀ as determined by ESR. Paired PM_{2.5} and PM₁₀ samples from the same sampling location are connected by a line. (d) Release of CD63⁺CD81⁺ EVs determined by bead-based flow cytometry, $n = 6-9$. * $p < 0.05$ compared to the unexposed control (100%); # $p < 0.05$ for PM₁₀ compared to PM_{2.5}.

4. Discussion

TF⁺ procoagulant EVs have been implicated as active contributors to thrombosis [32, 33] as well as pulmonary inflammation [34–37]. We have previously shown that exposure of bronchial epithelial cells to CSE causes an increase in total EV release and in TF-dependent procoagulant activity of these EVs [23]. Here, we extend these findings by showing that pulmonary fibroblasts also respond to CSE by releasing increased concentrations of EVs that express the exosome markers CD63 and CD81 as well as TF. Yet, no increased release of these EV populations was observed for monocyte-derived macrophages or pulmonary microvascular endothelial cells when stimulated with CSE. Moreover, the quantity of TF⁺ EVs released by unexposed cells was lower for endothelial cells and macrophages than for epithelial cells and fibroblasts (data not shown). This suggests that structural tissue cells may be the major source of TF⁺ EVs *in vivo*. Yet, others have reported that monocytes, macrophages, and endothelial cells respond to either CSE or PM exposure by releasing an increased quantity of TF⁺ EVs [19, 38, 39]. These divergent results may arise from the use of different cells (e.g., human umbilical vein endothelial cells) and/or cell culture conditions. Another likely explanation is the use of different methods for EV detection. While we detected TF⁺ EVs that were enriched in exosome markers

(CD63/CD81/CD9), the other studies based their findings on techniques that favour the detection of microvesicles. Thus, epithelial cells and fibroblasts may secrete TF in exosomes in response to CSE whereas macrophages and endothelial cells may secrete it in microvesicles. Side-by-side comparisons of exosome and microvesicle release by each cell type are required to investigate whether this is the case.

In the second part of this study, we investigated the effect of silica nanoparticles as well as small (PM_{2.5}) and larger (PM₁₀) particulates from outdoor air pollution on the release of EVs by bronchial epithelial cells. All three respiratory stressors triggered the release of CD63⁺CD81⁺ and TF⁺ EVs. Yet, they did not (silica, PM_{2.5}) or only mildly (PM₁₀) deplete cell surface thiols. Moreover, their effect on EV induction was not preventable by the antioxidant NAC (silica, PM_{2.5}) or the prevention did not reach statistical significance (PM₁₀, $p = 0.09$). This suggests that the EV induction by silica nanoparticles and PM_{2.5} is not mediated by oxidative thiol depletion and the EV induction by PM₁₀ is at most partly. A stronger contribution of oxidative mechanisms for PM₁₀ is supported by the observation that our PM₁₀ samples all had more radical-generating capacity than the paired PM_{2.5} samples.

Although PM has previously been shown to induce the release of TF⁺ microvesicles by endothelial cells *in vitro* [19], this is to our knowledge the first study reporting PM-induced EV release by epithelial cells. It is also the first study

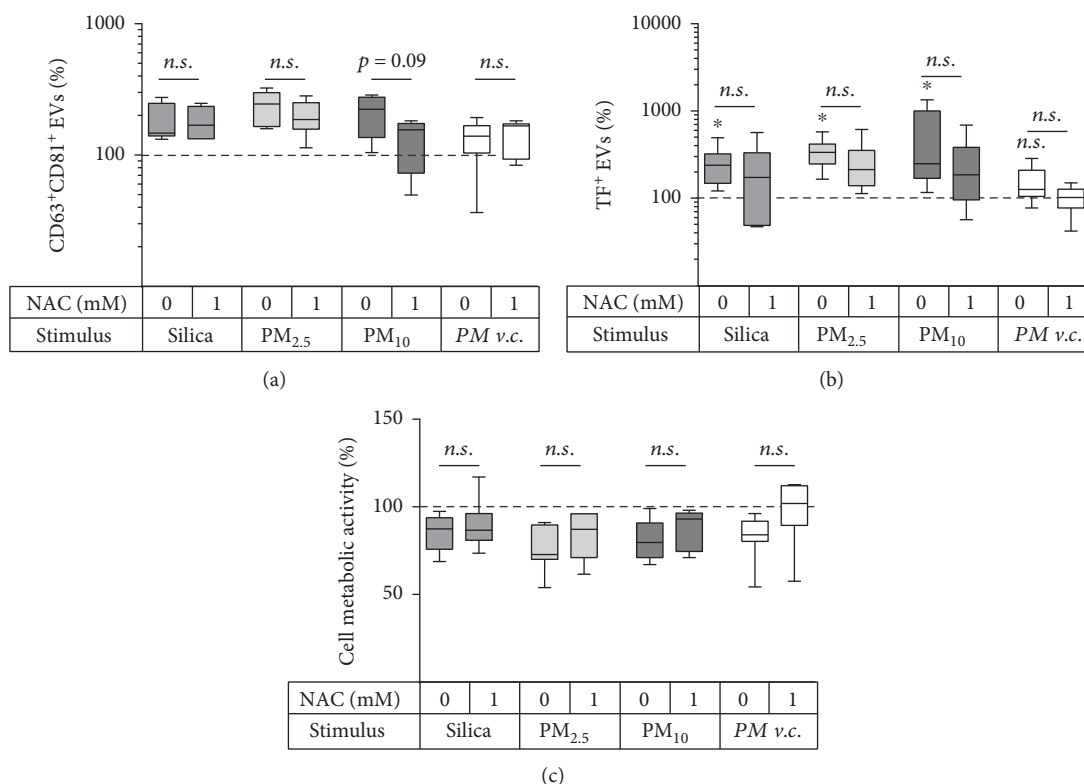


FIGURE 4: Effect of 1 mM NAC on EV release and cell metabolic activity during the exposure of BEAS-2B cells to silica ($100 \times 10^6 \mu\text{m}^2/\text{cm}^2$) or PM ($1.5 \text{ m}^3/\text{ml}$). Release of (a) CD63⁺CD81⁺ EVs, $n = 5-9$ and (b) CD63/CD81/CD9⁺TF⁺ EVs, $n = 6-7$. (c) Cell metabolic activity as determined by the MTT assay, $n = 5-8$. The box and whisker plots show the median (line in the box), 25th and 75th percentiles (outer lines of the box), and minimal and maximal values (whiskers). * $p < 0.05$ compared to the unexposed control (100%).

to report PM-induced release of TF on EVs that express exosome marker proteins and the first study to report that silica nanoparticles stimulate EV release. The finding that environmental as well as occupational air pollutants trigger the release of TF⁺ EVs is important as both types of exposures are associated with an increased risk for pulmonary [4–7] and cardiovascular disease [11–13] and exposure often cannot be avoided by at-risk individuals. Additional research should be performed to elucidate the cellular mechanisms that mediate the increased EV release in response to particulates, as this could allow identifying strategies for modulating particulate-induced changes in EV signalling.

This study was performed *in vitro* with immortalized cell lines and therefore has several inherent limitations. First, it is nearly impossible to accurately estimate which components of complex inhaled toxicants reach the respective target cells during real-life exposure and at what concentrations. Second, immortalized cell lines often exhibit a shift in dose response compared to primary cells. Third, cells underwent a single 24 h exposure, whereas real-life exposure to respiratory toxicants is usually chronic and/or repetitive over several years or even a lifetime. Therefore, the exposure conditions in this study cannot be directly compared to real-life exposures. Epidemiological and controlled animal or human exposure studies would be of great value to determine whether respiratory toxicants induce CD63⁺CD81⁺ and TF⁺ EVs *in vivo*. The assessment of EV concentrations in

the lung (e.g., bronchoalveolar lavage fluid) and blood specimen could be complemented by the detection of cell type-specific EV surface markers to estimate the relative contribution of different cell types to the *in vivo* EV pool.

5. Conclusions

In this study, we demonstrated that some pulmonary cell types (i.e., epithelial cells and fibroblasts), but not all, respond to CSE by releasing CD63⁺CD81⁺ and TF⁺ EVs. Moreover, CD63⁺CD81⁺ and TF⁺ EV induction in bronchial epithelial cells appears to be a universal response to various respiratory toxicants. Clinical studies are required to determine if these EV populations are associated with (1) the exposure to respiratory toxicants *in vivo* and (2) an elevated risk for cardiovascular or pulmonary disease development. If so, TF⁺ EVs might become useful biomarkers of exposure and/or risk and may help to guide preventive treatment decisions.

Data Availability

All data used to support the findings of this study are included within the article. Raw data used to generate the figures are available from the corresponding author upon request.

Disclosure

The current affiliation of Birke J. Benedikter is the Institute for Lung Research, Philipps-University Marburg, Hans-Meerwein-Straße 2, 35043 Marburg, Germany, Member of the German Center for Lung Research (DZL).

Conflicts of Interest

The authors declare that they have no conflicts of interest.

Acknowledgments

This project was funded by the Netherlands Organization for Scientific Research (NWO) under grant number 022.003.011 and by a Kootstra Talent Fellowship from the Center for Research Innovation, Support and Policy (CRISP) of Maastricht University Medical Center+, both awarded to BJB. The authors would like to thank Ingrid Dijkgraaf (Department of Biochemistry, Maastricht University) for her enthusiastic support with the Rotavap.

Supplementary Materials

Supplementary Figure 1: raw data of EV detection by bead-based flow cytometry. Representative flow cytometry plots are shown for an unconditioned medium control and conditioned medium samples of unexposed and CSE-exposed BEAS-2B cells. (A) Shows the gating strategy for the bead population. (B) Shows the specificity of fluorescence signal for the detection of the total EV population stained by antiCD63-coated beads and a PE-labelled anti-CD81 detection antibody, compared to a PE-labelled isotype control. (C) Shows the specificity of the fluorescence signal for the detection of the TF-positive EV population stained by beads coated with a mixture of anti-CD63, anti-CD81, and anti-CD9 antibodies and a PE-labelled anti-TF detection antibody, compared to a PE-labelled isotype control. Supplementary Table 1: overview of materials with the respective providers and catalogue numbers. Supplementary Table 2: table for unit conversion for the PM exposure. PM samples were collected at 3 different locations with different levels of air pollution. To reflect the real-life exposure at these locations, PM exposure was standardized per volume of filtered air rather than per weight of PM. (*Supplementary Materials*)

References

- [1] E. R. Weibel, "What makes a good lung?," *Swiss Medical Weekly*, vol. 139, no. 27-28, pp. 375-386, 2009.
- [2] R. N. Colvile, E. J. Hutchinson, J. S. Mindell, and R. F. Warren, "The transport sector as a source of air pollution," *Atmospheric Environment*, vol. 35, no. 9, pp. 1537-1565, 2001.
- [3] C. C. Leung, I. T. S. Yu, and W. Chen, "Silicosis," *Lancet*, vol. 379, no. 9830, pp. 2008-2018, 2012.
- [4] S. Salvi, "Tobacco smoking and environmental risk factors for chronic obstructive pulmonary disease," *Clinics in Chest Medicine*, vol. 35, no. 1, pp. 17-27, 2014.
- [5] M. Guarnieri and J. R. Balmes, "Outdoor air pollution and asthma," *Lancet*, vol. 383, no. 9928, pp. 1581-1592, 2014.
- [6] D. Harrison, H. Luo, and G. Friedman-Jimenez, "Occupational asthma and work-exacerbated asthma," *Seminars in Respiratory and Critical Care Medicine*, vol. 36, no. 03, pp. 388-407, 2015.
- [7] P. Cullinan and P. Reid, "Pneumoconiosis," *Primary Care Respiratory Journal*, vol. 22, no. 2, pp. 249-252, 2013.
- [8] K. Steenland and E. Ward, "Silica: a lung carcinogen," *CA: a Cancer Journal for Clinicians*, vol. 64, no. 1, pp. 63-69, 2014.
- [9] O. Raaschou-Nielsen, Z. J. Andersen, R. Beelen et al., "Air pollution and lung cancer incidence in 17 European cohorts: prospective analyses from the European Study of Cohorts for Air Pollution Effects (ESCAPE)," *The Lancet Oncology*, vol. 14, no. 9, pp. 813-822, 2013.
- [10] G. W. Warren and K. M. Cummings, "Tobacco and lung cancer: risks, trends, and outcomes in patients with cancer," *American Society of Clinical Oncology Educational Book*, vol. 33, pp. 359-364, 2013.
- [11] N. A. Rigotti and C. Clair, "Managing tobacco use: the neglected cardiovascular disease risk factor," *European Heart Journal*, vol. 34, no. 42, pp. 3259-3267, 2013.
- [12] B. A. Franklin, R. Brook, and C. Arden Pope III, "Air pollution and cardiovascular disease," *Current Problems in Cardiology*, vol. 40, no. 5, pp. 207-238, 2015.
- [13] T. Bourdrel, M. A. Bind, Y. Béjot, O. Morel, and J. F. Argacha, "Cardiovascular effects of air pollution," *Archives of Cardiovascular Diseases*, vol. 110, no. 11, pp. 634-642, 2017.
- [14] J. A. Whitsett and T. Alenghat, "Respiratory epithelial cells orchestrate pulmonary innate immunity," *Nature Immunology*, vol. 16, no. 1, pp. 27-35, 2015.
- [15] S. V. Raju, P. L. Jackson, C. A. Courville et al., "Cigarette smoke induces systemic defects in cystic fibrosis transmembrane conductance regulator function," *American Journal of Respiratory and Critical Care Medicine*, vol. 188, no. 11, pp. 1321-1330, 2013.
- [16] A. Shimada, N. Kawamura, M. Okajima, T. Kaewamatawong, H. Inoue, and T. Morita, "Translocation pathway of the intratracheally instilled ultrafine particles from the lung into the blood circulation in the mouse," *Toxicologic Pathology*, vol. 34, no. 7, pp. 949-957, 2006.
- [17] M. Aghapour, P. Raei, S. J. Moghaddam, P. S. Hiemstra, and I. H. Heijink, "Airway epithelial barrier dysfunction in chronic obstructive pulmonary disease: role of cigarette smoke exposure," *American Journal of Respiratory Cell and Molecular Biology*, vol. 58, no. 2, pp. 157-169, 2018.
- [18] B. J. Benedikter, C. Volgers, P. H. van Eijck et al., "Cigarette smoke extract induced exosome release is mediated by depletion of exofacial thiols and can be inhibited by thiol-antioxidants," *Free Radical Biology & Medicine*, vol. 108, pp. 334-344, 2017.
- [19] T. Neri, L. Pergoli, S. Petrini et al., "Particulate matter induces prothrombotic microparticle shedding by human mononuclear and endothelial cells," *Toxicology In Vitro*, vol. 32, pp. 333-338, 2016.
- [20] M. Yáñez-Mó, P. R. M. Siljander, Z. Andreu et al., "Biological properties of extracellular vesicles and their physiological functions," *Journal of Extracellular Vesicles*, vol. 4, no. 1, 2015.
- [21] E. I. Buzas, B. György, G. Nagy, A. Falus, and S. Gay, "Emerging role of extracellular vesicles in inflammatory diseases," *Nature Reviews Rheumatology*, vol. 10, no. 6, pp. 356-364, 2014.

- [22] X. Loyer, A. C. Vion, A. Tedgui, and C. M. Boulanger, "Microvesicles as cell-cell messengers in cardiovascular diseases," *Circulation Research*, vol. 114, no. 2, pp. 345–353, 2014.
- [23] B. J. Benedikter, F. G. Bouwman, A. C. A. Heinzmann et al., "Proteomic analysis reveals procoagulant properties of cigarette smoke-induced extracellular vesicles," *Journal of Extracellular Vesicles*, vol. 8, no. 1, 2019.
- [24] C. Volgers, B. J. Benedikter, G. E. Grauls, P. H. M. Savelkoul, and F. R. M. Stassen, "Bead-based flow-cytometry for semi-quantitative analysis of complex membrane vesicle populations released by bacteria and host cells," *Microbiological Research*, vol. 200, pp. 25–32, 2017.
- [25] B. J. Benedikter, F. G. Bouwman, T. Vajen et al., "Ultrafiltration combined with size exclusion chromatography efficiently isolates extracellular vesicles from cell culture media for compositional and functional studies," *Scientific Reports*, vol. 7, no. 1, 2017.
- [26] H. Suárez, A. Gámez-Valero, R. Reyes et al., "A bead-assisted flow cytometry method for the semi-quantitative analysis of extracellular vesicles," *Scientific Reports*, vol. 7, no. 1, 2017.
- [27] R. E. Unger, V. Krump-Konvalinkova, K. Peters, and C. J. Kirkpatrick, "In vitro expression of the endothelial phenotype: comparative study of primary isolated cells and cell lines, including the novel cell line HPMEC-ST1.6R," *Microvascular Research*, vol. 64, no. 3, pp. 384–397, 2002.
- [28] C. H. M. P. Willems, L. J. I. Zimmermann, P. J. L. T. Sanders et al., "Alveolocapillary model system to study alveolar re-epithelialization," *Experimental Cell Research*, vol. 319, no. 1, pp. 64–74, 2013.
- [29] T. N. Perkins, A. Shukla, P. M. Peeters et al., "Differences in gene expression and cytokine production by crystalline vs. amorphous silica in human lung epithelial cells," *Particle and Fibre Toxicology*, vol. 9, no. 1, p. 6, 2012.
- [30] J. G. F. Hogervorst, T. M. C. M. de Kok, J. J. Briedé, G. Wesseling, J. C. S. Kleinjans, and C. P. van Schayck, "Relationship between radical generation by urban ambient particulate matter and pulmonary function of school children," *Journal of Toxicology and Environmental Health. Part A*, vol. 69, no. 3, pp. 245–262, 2006.
- [31] J. J. Briedé, T. M. C. M. de Kok, J. G. F. Hogervorst, E. J. C. Moonen, C. L. B. op den Camp, and J. C. S. Kleinjans, "Development and application of an electron spin resonance spectrometry method for the determination of oxygen free radical formation by particulate matter," *Environmental Science & Technology*, vol. 39, no. 21, pp. 8420–8426, 2005.
- [32] N. van Es, S. Bleker, A. Sturk, and R. Nieuwland, "Clinical Significance of Tissue Factor-Exposing Microparticles in Arterial and Venous Thrombosis," *Seminars in Thrombosis and Hemostasis*, vol. 41, no. 07, pp. 718–727, 2015.
- [33] A. P. Owens and N. Mackman, "Microparticles in hemostasis and thrombosis," *Circulation Research*, vol. 108, no. 10, pp. 1284–1297, 2011.
- [34] J. A. Bastarache, R. D. Fremont, J. A. Kropski, F. R. Bossert, and L. B. Ware, "Procoagulant alveolar microparticles in the lungs of patients with acute respiratory distress syndrome," *American Journal of Physiology. Lung Cellular and Molecular Physiology*, vol. 297, no. 6, pp. L1035–L1041, 2009.
- [35] F. Novelli, T. Neri, L. Tavanti et al., "Procoagulant, tissue factor-bearing microparticles in bronchoalveolar lavage of interstitial lung disease patients: an observational study," *PLoS One*, vol. 9, no. 4, article e95013, 2014.
- [36] J. A. Park, A. S. Sharif, D. J. Tschumperlin et al., "Tissue factor-bearing exosome secretion from human mechanically stimulated bronchial epithelial cells in vitro and in vivo," *The Journal of Allergy and Clinical Immunology*, vol. 130, no. 6, pp. 1375–1383, 2012.
- [37] T. van der Poll, "Tissue factor as an initiator of coagulation and inflammation in the lung," *Critical Care*, vol. 12, Suppl 6, p. S3, 2008.
- [38] M. Li, D. Yu, K. J. Williams, and M. L. Liu, "Tobacco smoke induces the generation of procoagulant microvesicles from human monocytes/macrophages," *Arteriosclerosis, Thrombosis, and Vascular Biology*, vol. 30, no. 9, pp. 1818–1824, 2010.
- [39] C. Cordazzo, S. Petrini, T. Neri et al., "Rapid shedding of pro-inflammatory microparticles by human mononuclear cells exposed to cigarette smoke is dependent on Ca²⁺ mobilization," *Inflammation Research*, vol. 63, no. 7, pp. 539–547, 2014.

Research Article

Protection against Doxorubicin-Induced Cytotoxicity by Geniposide Involves AMPK α Signaling Pathway

Yan-Yan Meng,^{1,2,3} Yu-Pei Yuan,^{1,2,3} Xin Zhang,^{1,2,3} Chun-Yan Kong^{ID},^{1,2,3} Peng Song,^{1,2,3}
Zhen-Guo Ma^{ID},^{1,2,3} and Qi-Zhu Tang^{ID}^{1,2,3}

¹Department of Cardiology, Renmin Hospital of Wuhan University, Wuhan 430060, China

²Cardiovascular Research Institute of Wuhan University, Wuhan 430060, China

³Hubei Key Laboratory of Cardiology, Wuhan 430060, China

Correspondence should be addressed to Zhen-Guo Ma; zhengma@whu.edu.cn and Qi-Zhu Tang; qztang@whu.edu.cn

Received 27 February 2019; Revised 10 May 2019; Accepted 21 May 2019; Published 26 June 2019

Guest Editor: Lynette K. Rogers

Copyright © 2019 Yan-Yan Meng et al. This is an open access article distributed under the Creative Commons Attribution License, which permits unrestricted use, distribution, and reproduction in any medium, provided the original work is properly cited.

Oxidative stress and cardiomyocyte apoptosis play critical roles in the development of doxorubicin- (DOX-) induced cardiotoxicity. Our previous study found that geniposide (GE) could inhibit cardiac oxidative stress and apoptosis of cardiomyocytes but its role in DOX-induced heart injury remains unknown. Our study is aimed at investigating whether GE could protect against DOX-induced heart injury. The mice were subjected to a single intraperitoneal injection of DOX (15 mg/kg) to induce cardiomyopathy model. To explore the protective effects, GE was orally given for 10 days. The morphological examination and biochemical analysis were used to evaluate the effects of GE. H9C2 cells were used to verify the protective role of GE in vitro. GE treatment alleviated heart dysfunction and attenuated cardiac oxidative stress and cell loss induced by DOX in vivo and in vitro. GE could activate AMP-activated protein kinase α (AMPK α) in vivo and in vitro. Moreover, inhibition of AMPK α could abolish the protective effects of GE against DOX-induced oxidative stress and apoptosis. GE could protect against DOX-induced heart injury via activation of AMPK α . GE has therapeutic potential for the treatment of DOX cardiotoxicity.

1. Introduction

Doxorubicin (DOX) is an anthracycline that has been used to treat cancer for several decades and has potent broad-spectrum antineoplastic activity [1]. It has been used for the treatment of a variety of neoplasms including leukemia, lymphomas, thyroid cancer, ovarian cancer, and breast cancer [2–4]. However, its clinical application is largely limited by high incidence of irreversible side effects [5, 6]. Notably, the dose-dependent cardiotoxicity is the most dangerous complication of DOX which could eventually lead to fatal heart failure [7]. The mechanism involved in doxorubicin-induced cardiotoxicity is complex and multifactorial; nevertheless, accumulating evidences suggest that oxidative stress and apoptosis play pivotal roles [8, 9].

Cardiac tissue is especially vulnerable to free radicals induced by DOX because the hearts had a lot of mitochondria and cardiac antioxidant enzymes were relatively lower compared with other organs [10]. Previous studies have shown that increased levels of cardiac reactive oxygen species (ROS) were observed during the development of DOX-induced cardiomyopathy [11]. Excessive ROS accumulation caused lipid peroxidation, structural changes of biological macromolecules, and eventually result in cell apoptosis. Therefore, finding molecules that could inhibit oxidative stress and cardiomyocyte apoptosis would be of great significance for the prevention of DOX-related cardiac injury.

AMP-activated protein kinase α (AMPK α) plays a critical role in the process of various heart diseases [12–15]. It has been reported that the activation of AMPK α via

pharmacological approaches prevented pressure overload or obesity-induced cardiac remodeling in mice [16–18]. The results from our and other labs demonstrated that activation of AMPK α could attenuate high glucose-induced oxidative stress and cell apoptosis [19]. Hence, finding a positive regulator of AMPK α would be of great significance for DOX-induced cardiotoxicity.

Geniposide (GE), an iridoid glycoside derived from the gardenia plant, has a series of pharmacological effects, including antioxidative stress, antiapoptosis, anti-inflammatory, anti-ER stress, and other pharmacological effects [20–22]. Our previous study demonstrated that GE could attenuate the development of pressure overload-induced cardiac hypertrophy and prevent obesity-related cardiac complications via activation of AMPK α [16, 17]. However, it still remains unclear whether GE could defend against DOX-induced cardiotoxicity via AMPK α and the precise mechanisms. In the present study, we have found that GE improves cardiac function via the activation of AMPK α in DOX-induced cardiac injury.

2. Materials and Methods

2.1. Reagents. Geniposide (GE) was purchased from Shanghai Winherb Medical Science Co. (Shanghai, China). DOX (D1515) was purchased from Sigma-Aldrich (St. Louis, MO, USA). The purity of GE and DOX was above 98% as determined by HPLC analysis. Antibodies against T-AMPK α (#2603P, 1:1000), P-AMPK α (#2535, 1:1000), T-acetyl-CoA carboxylase (ACC, #3676, 1:1000), P-ACC (#3661S, 1:1000), Bcl-2 (#2870, 1:1000), Bax (#2772, 1:1000), cleaved caspase-3 (C-Caspase3, #9661, 1:1000), glyceraldehyde 3-phosphate dehydrogenase (GAPDH, #2118, 1:1000), and T-AMPK α 2 (#2757, 1:1000) were purchased from Cell Signaling Technology (Boston, MA, USA). The primary antibodies of nuclear factor erythroid-derived-like 2 (Nrf2, #ab31163, 1:1000), superoxide dismutase-1 (SOD1, #ab16831, 1:1000), and superoxide dismutase-2 (SOD2, #ab13533, 1:1000) were purchased from Abcam (Cambridge, UK). The cell counting kit-8 was purchased from Dōjindo Laboratories (Kumamoto, Japan). The bicinchoninic acid (BCA) protein assay kit was purchased from Pierce (Rockford, IL, USA).

2.2. Animals and Treatments. All animal experimental procedures were approved by the Guidelines for Animal Care and Use Committee of Renmin Hospital of Wuhan University, which is also in agreement with the Guidelines for the Care and Use of Laboratory Animals published by the United States National Institutes of Health (NIH Publication, revised 2011). Male C57BL/6 mice (8 to 10 weeks old; body weight: 25.5 ± 2 g) were obtained from the Institute of Laboratory Animal Science, Chinese Academy of Medical Sciences (Beijing, China). These mice were allowed free access to food and drinking water. They were fed in a house which the temperature (20–25°C) and humidity (50 \pm 5%) were under strict control and the light was kept at a 12h light-dark cycle. These mice were divided into four groups ($n = 10$ per group): saline group,

DOX group, DOX+GE (25 mg/kg) group, and DOX+GE (50 mg/kg) group, by a random number table. DOX was dissolved in normal saline. Mice in the DOX and DOX+GE groups were subjected to a single intraperitoneal injection of DOX (15 mg/kg). Correspondingly, equal volume of saline was given to the control mice according to our previous study [23]. Mice in the DOX+GE groups were orally given a dose of GE (25 or 50 mg/kg, 9:00 am) dissolved in sterile saline every day for 10 days beginning from three days before DOX injection. To clarify whether the cardiac protective effects of GE on DOX-induced cardiotoxicity were mediated by AMPK α , we used AMPK α 2 KO mice. The source of AMPK α 2 knockout mice was described in our previous article [16, 17]. Seven days later, the mice were sacrificed with an overdose of sodium pentobarbital (200 mg/kg; i.p.) to harvest the hearts and calculate the ratios, like heart weight (HW)/body weight (BW) and HW/tibia length (TL).

2.3. Echocardiography and Hemodynamics. Echocardiography and hemodynamics were performed as described previously [24, 25]. Briefly, a MyLab 30CV ultrasound (Esaote SpA, Genoa, Italy) with a 10 MHz linear array ultrasound transducer was used to obtain M-mode images at the papillary muscle level for measurement of systolic and diastolic function.

For the hemodynamic analysis, a 1.4-French Millar catheter transducer (SPR-839; Millar Instruments, Houston, TX) was inserted into the left ventricle via the right carotid artery to obtain invasive hemodynamic measurements. PVAN data analysis software was used to analyze all the data.

2.4. Western Blot. Proteins were extracted from heart tissues or cells with RIPA lysis buffer (Invitrogen, Carlsbad, CA, USA) on ice. Then, proteins were separated on 10% SDS-PAGE and transferred to polyvinylidene fluoride (PVDF) membranes (Millipore). Next, the membranes were blocked with 5% skim milk in Tris-buffered saline-Tween (TBST) for 1 h. Afterwards, the PVDF membranes were incubated with the indicated primary antibodies overnight at 4°C and with secondary antibodies for another 1 h at room temperature. Finally, these membranes were scanned, and the total protein levels were normalized to GAPDH. Phosphorylation was normalized to the matched total protein.

2.5. Total RNA Extraction and Quantitative Real-Time PCR. Trizol reagents were used to extract total RNA from heart tissue and cells. Reverse transcriptional reactions were performed using the Transcriptor First Strand cDNA Synthesis Kit (Roche Applied Science, USA). The target genes were amplified with the LightCycler 480 SYBR Green Master Mix (Roche, 04896866001). All the mRNA data were normalized to *Gapdh*.

2.6. Cell Culture. The H9C2 cardiomyocytes were purchased from the Cell Bank of the Chinese Academy of Sciences (Shanghai, China). All the cells were seeded in Dulbecco's modified Eagle's medium (DMEM) (GIBCO, C11995), supplemented with 10% fetal bovine serum (FBS) (Gibco,

10099), 100 U/ml penicillin, and 100 $\mu\text{g/ml}$ streptomycin (Gibco, 15140). Only cells below passage 10 were used in our study. Next, cells were divided into groups and given different stimuli. The five doses of GE were determined according to our previous studies [16, 17]. After being seeded onto 6-well for 48h, H9C2 were starved for another 16 hours and then were treated with DOX (1 $\mu\text{mol/l}$) or DOX+GE (1 $\mu\text{mol/l}$, 10 $\mu\text{mol/l}$, 25 $\mu\text{mol/l}$, 50 $\mu\text{mol/l}$, and 100 $\mu\text{mol/l}$) for 12 hours. To confirm our hypothesis that AMPK α is involved in GE-induced cardiac protective effects, adenoviral vectors carrying AMPK α 2 small hairpin RNAs (shAMPK α) or the scrambled shRNA were used to infect H9C2 cells at a MOI of 100 for 4h. The source of shAMPK α and the scrambled shRNA was described in our previous studies [16, 17]. To detect cell viability, the cells were seeded onto 96-well plates and were treated with DOX or DOX+GE (100 $\mu\text{mol/l}$) for 24 hours.

2.7. TUNEL Staining. TUNEL staining was performed as previously described [23]. Briefly, a TUNEL assay (Millipore, USA) was used according to the manufacturer's instructions. A fluorescence microscope (Olympus DX51) was used to evaluate apoptotic cells. Image-Pro Plus 6.0 was used to quantify all the images.

2.8. Measurement of Cardiac Troponin-I Levels. At three days after DOX injection, blood was collected from the retro-orbital plexus. Plasma was centrifuged for 10 min at 1000 g to obtain the supernatant. After that, a mouse cardiac troponin-I (cTnI) ELISA kit from Life Diagnostics Inc. (West Chester, PA) was used to detect the levels of troponin in mice.

2.9. Measurement of CK, LDH, GSH, Gpx, MDA, 4-HNE, and 3-NT Levels. At three days after DOX injection, blood samples were collected and centrifuged for plasma separation (1000 \times g, 10 minutes, 4°C). The levels of creatine kinase (CK) and lactate dehydrogenase (LDH) were detected using the commercial kits (Nanjing Jiancheng Bioengineering Institute, China) according to the instructions.

The heart tissues were placed in cold normal saline and homogenized. After that, the supernatant was obtained through centrifuging (10,000 \times g, 5 minutes, 4°C) to detect the glutathione (GSH), glutathione peroxidase (Gpx), malondialdehyde (MDA), 4-hydroxynonenal (4-HNE)-protein adducts, and 3-nitrotyrosine (3-NT) levels in heart tissues. 4-HNE and 3-NT ELISA Kits were provided by Abcam.

In vitro, the levels of LDH and MDA were also evaluated by corresponding kits and the treatment protocols were strictly carried out according to the manufacturer instructions.

2.10. Measurement of SOD and Caspase 3 Activities. The activities of total superoxide dismutase (SOD) and caspase 3 were assessed spectrophotometrically in the fresh heart samples and cell culture supernatants using commercial assay kits (Nanjing Jiancheng Bioengineering Institute, China) according to the provided instructions.

2.11. Measurement of Intracellular ROS. Intracellular ROS production was detected using 2,7-dichlorodihydrofluorescein diacetate (DCF-DA, Invitrogen) as an indicator according to a previous study [16]. In brief, H9c2 myocytes were cultured in 96-well plates and pretreated with GE and DOX for 2 hours. After that, the cells were incubated with DCFH-DA (10 μM) for 60 min in 37°C. The fluorescence was quantified using a spectrofluorometer with an excitation wavelength of 488 nm and emission at 525 nm.

2.12. Statistical Analysis. Quantitative data were presented as mean \pm standard deviation (SD). Comparisons between two groups were performed using Student's *t*-test. A one-way analysis of variance (ANOVA) followed by Tukey's post hoc test was used to analyze differences among groups. $P < 0.05$ was considered statistically significant.

3. Result

3.1. GE Improved Cardiac Function and Alleviated Cardiac Injury in Mice with DOX Injection. In the present study, 25 or 50 mg/kg of GE and 15 mg/kg of DOX were given according to our previous study [17, 23]. The injection of DOX obviously decreased body weight (BW), and GE at the dose of 25 or 50 mg/kg reduced weight loss during DOX treatment and restored body weight to the normal level (Figure 1(a)). Meanwhile, DOX also resulted in a decreased ratio of HW to TL, and conversely, GE could block this pathological decline (Figure 1(b)). DOX injection also led to a decrease in heart rate and blood pressure; however, there was no difference in the two between the DOX and DOX+GE groups (Figures 1(c) and 1(d)). Echocardiography and hemodynamics revealed that DOX treatment resulted in a reduction in ejection fraction (EF), maximal rate of the increase of left ventricular pressure (+dP/dt), and the maximal rate of the decrease of left ventricular pressure (-dP/dt) and GE significantly attenuated these pathological alterations in a dose-dependent manner (Figures 1(e)–1(g)). It also showed that 50 mg/kg of GE attenuated the level of brain natriuretic peptide (BNP) in mice with DOX injection (Figure 1(h)). Plasma cTnI is a well-established marker to reflect cardiac cell damage in patients with DOX. Therefore, we detected cTnI level in plasma of mice from four groups and found that cTnI concentrations were significantly higher in all DOX-treated mice compared with the saline group and mice from the DOX+GE25 and DOX+GE50 groups had relatively lower levels of cTnI (Figure 1(i)). CK and LDH levels in mice with DOX only were all obviously increased compared with the control groups; however, GE significantly decreased the CK and LDH levels (Figures 1(j) and 1(k)).

3.2. GE Protected against DOX-Induced Oxidative Damage In Vivo. To determine whether GE suppressed cardiac injury by inhibiting oxidative stress, we first examined levels of several antioxidant enzymes. As shown in Figure 2(a), DOX injection significantly downregulated the mRNA levels of SOD1, SOD2, and Gpx; however,

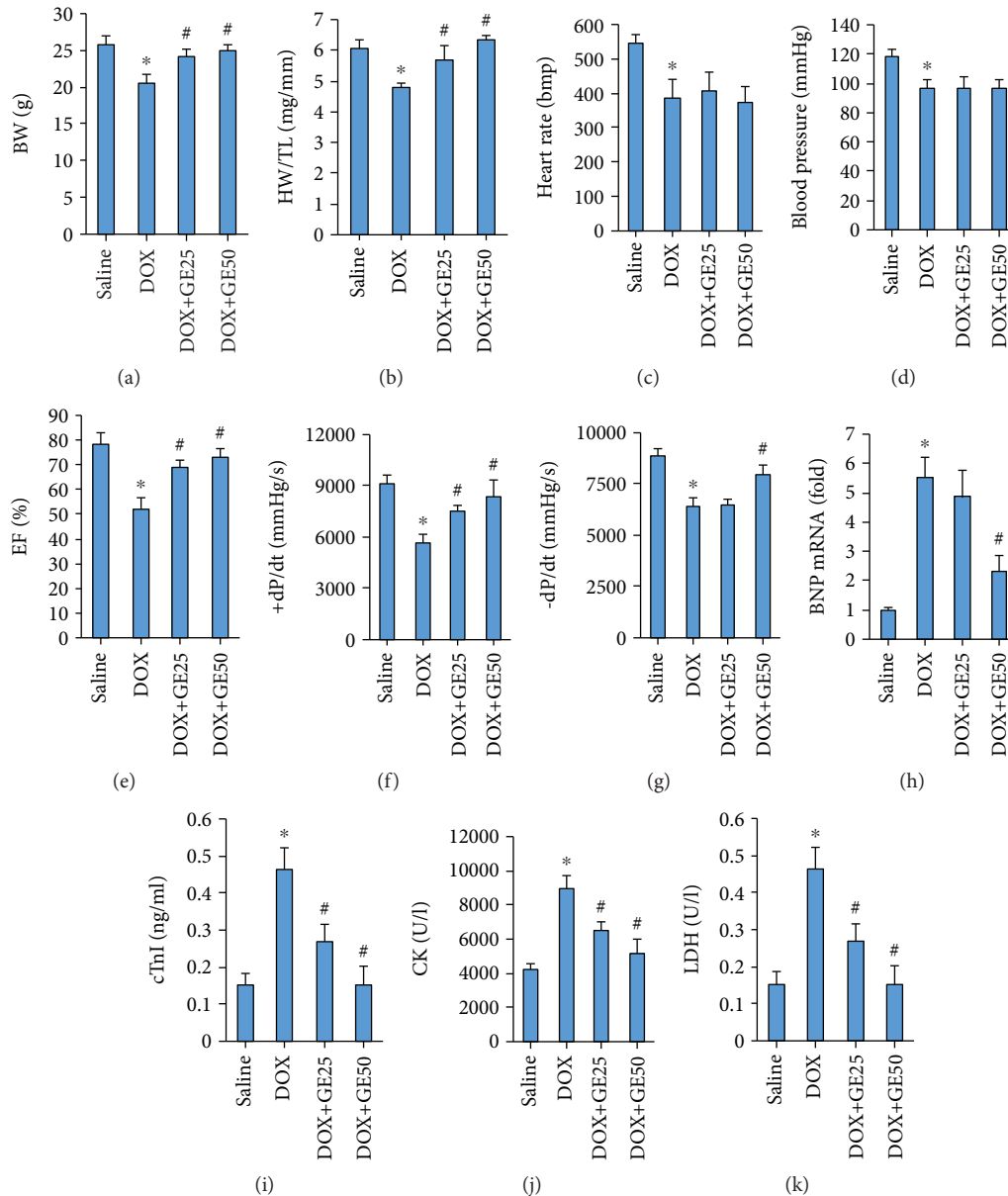


FIGURE 1: GE improved cardiac function and alleviated cardiac injury in mice with DOX treatment. (a) Body weight of four groups ($n = 10$). (b) Statistical results of the heart weight (HW)/tibia length (TL) ($n = 10$). (c) Heart rate of mice in four groups. (d) Maximum pressure. (e) Ejection fraction (EF) of mice ($n = 10$). (f, g) Hemodynamic analysis of mice with or without GE treatment ($n = 10$). (h) The mRNA expressions of hypertrophic markers ($n = 10$). (i) Plasma cardiac troponin-I (cTnI) levels. (j, k) Levels of creatine kinase (CK) and lactate dehydrogenase (LDH). Values represent the mean \pm SD. * $P < 0.05$ versus saline, # $P < 0.05$ versus DOX.

the treatment of GE (50 mg/kg) significantly upregulated the mRNA levels of these antioxidant enzymes in DOX-treated mice. Next, we measured the activity of total SOD and found that SOD activity in mice from the DOX+GE50 group was enhanced compared with that in mice from the DOX group (Figure 2(b)). GE treatment also increased level of GSH and the activity of Gpx in mice with DOX injection (Figures 2(c) and 2(d)). Next, we detected the level of MDA in the hearts and found that the abnormal accumulation of MDA in DOX-treated hearts was largely reduced by GE treatment in a dose-dependent manner (Figure 2(e)). 4-HNE is a by-product

of lipid peroxidation and is a stable marker of lipid peroxidation. 3-NT is a biomarker of protein oxidation produced upon the nitration of protein residues. The increased levels of 4-HNE and 3-NT could be observed in the hearts of mice with DOX only; however, after daily treatment of GE, these pathological upregulations were largely suppressed (Figures 2(f) and 2(g)). Western blot analyses were carried out to evaluate myocardial oxidative injury in mice with DOX injection. Nrf2 is an important transcription factor that regulates the cellular oxidative stress responses. Nrf2 can reduce the cell damage caused by reactive oxygen species. And the expression of Nrf2

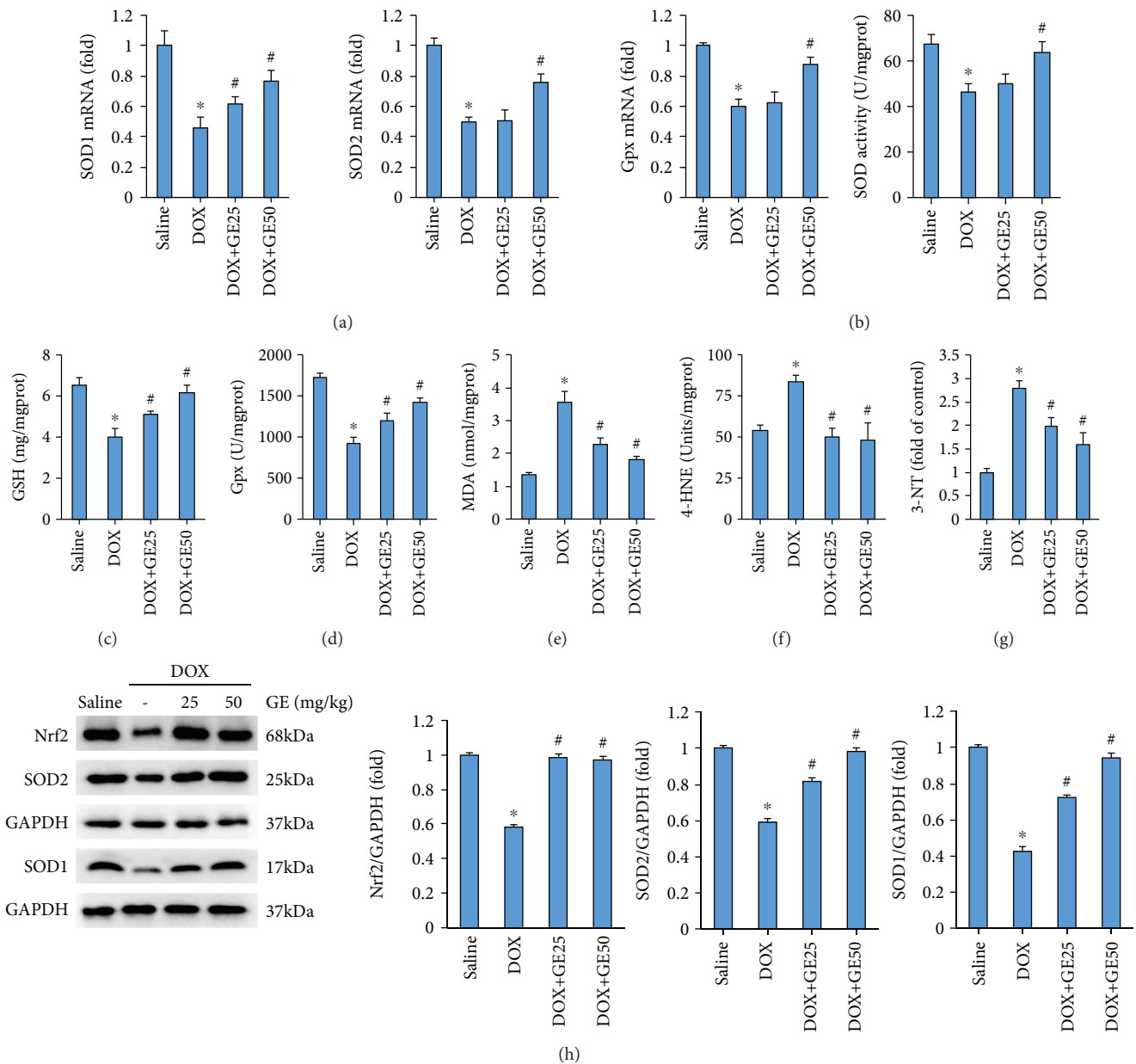


FIGURE 2: GE protected against DOX-induced oxidative damage in vivo. (a) The mRNA expressions of several antioxidant enzymes ($n = 10$). (b) Activity of superoxide dismutase (SOD) ($n = 10$). (c) Levels of glutathione (GSH) ($n = 10$). (d) Activity of glutathione peroxidase (Gpx) ($n = 10$). (e–g) Levels of malondialdehyde (MDA), 4-hydroxynonenal (4-HNE)-protein adducts, and 3-nitrotyrosine (3-NT) ($n = 10$). (h) Western blot and quantitative results in the indicated groups ($n = 10$). Values represent the mean \pm SD. * $P < 0.05$ versus saline, # $P < 0.05$ versus DOX.

was decreased in DOX-treated hearts, whereas the hearts from mice with DOX+GE showed increased level of Nrf2 (Figure 2(h)). Further detection of SOD1 and SOD2 expression also revealed that GE upregulated the expression of SOD1 and SOD2 in DOX-treated hearts (Figure 2(h)).

3.3. GE Attenuated DOX-Induced Cell Death In Vivo. Next, we investigated whether GE could attenuate DOX-induced cell apoptosis. DOX resulted in upregulation of Bax and downregulation of Bcl-2 in both mRNA level and protein level. However, after the intervention of GE,

these pathological alterations were almost completely blocked (Figures 3(a)–3(c)). The activity of caspase 3 was also increased in the DOX group, which was markedly inhibited by GE in a dose-dependent manner (Figure 3(d)). The antiapoptotic effects of GE were further confirmed by TUNEL staining, which showed that GE significantly reduced TUNEL-positive cells (Figure 3(e)).

3.4. GE Inhibited DOX-Induced Toxicity In Vitro. To further confirm the protective effects of GE in oxidative damage and apoptosis, we used H9C2 cardiomyocytes in vitro. H9C2 cells

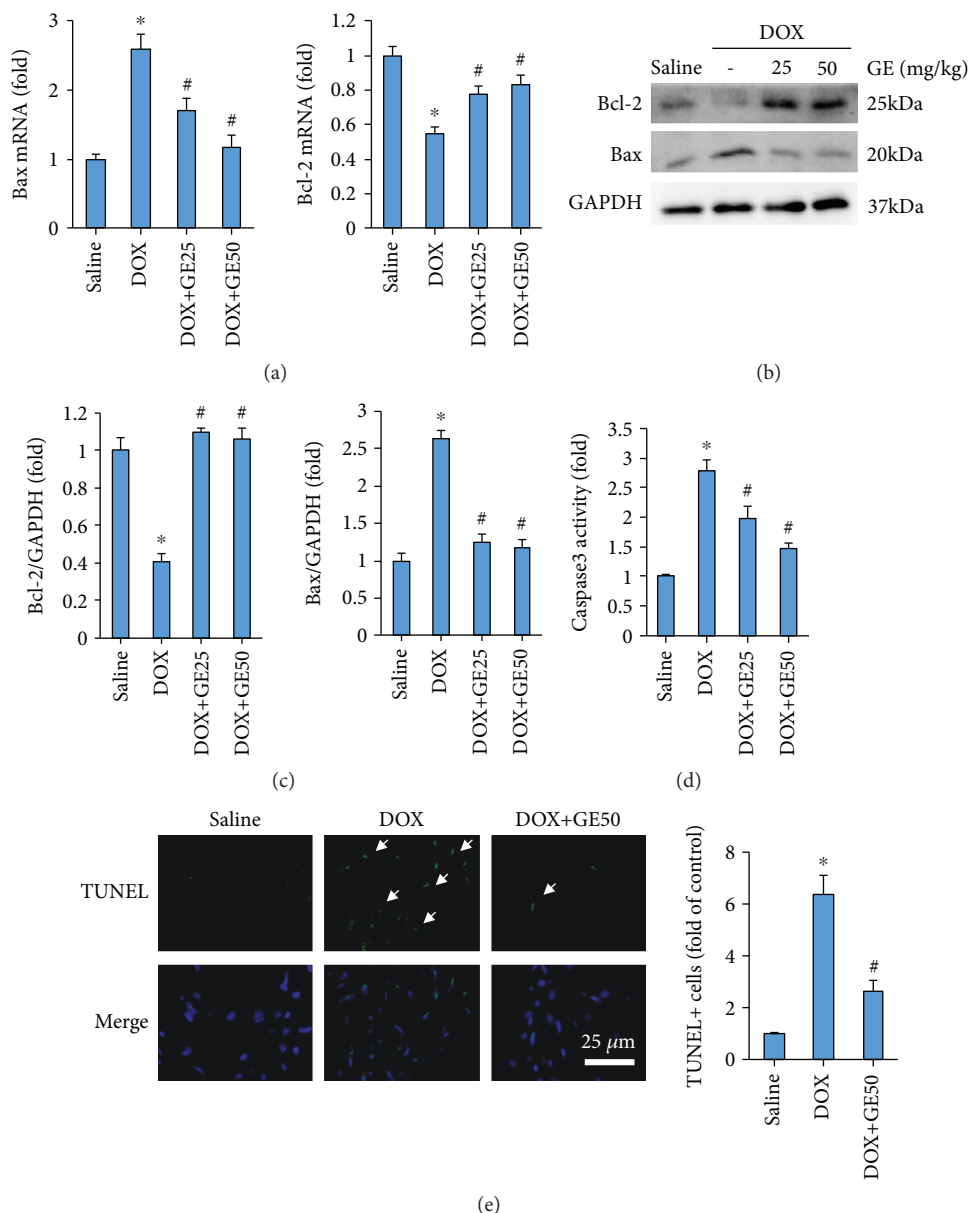


FIGURE 3: GE attenuated DOX-induced cell death in vivo. (a) The mRNA expressions of apoptosis markers ($n = 10$). (b, c) Western blot and quantitative results ($n = 10$). (d) Activity of caspase 3 of mice in four groups ($n = 10$). (e) Representative images of TUNEL and the quantitative results ($n = 10$). Arrows indicate TUNEL-positive cells. Values represent the mean \pm SD. * $P < 0.05$ versus saline, # $P < 0.05$ versus DOX.

treated with escalating doses of GE exhibited increased cell viability in a dose-dependent manner at all three treatment durations (Figure 4(a)). Next, we detected the release of LDH to reflect cardiomyocyte injury and found that GE could significantly attenuate the content of LDH in DOX-treated cardiomyocytes (Figure 4(b)). DOX treatment resulted in ROS accumulation in cardiomyocytes, while GE decreased ROS levels in DOX-treated cells (Figure 4(c)). GE also significantly enhanced the activity of SOD and reduced the level of MDA in vitro (Figures 4(d) and 4(e)). GE significantly suppressed the activity of caspase 3 in DOX-treated cardiomyocytes (Figure 4(f)).

3.5. GE Activated AMPK α to Prevent DOX-Induced Toxicity In Vitro. In previous investigation, we have indicated that GE could activate AMPK α to attenuate cardiac hypertrophy [17]. Therefore, we investigated in this study whether GE could attenuate cardiac injury induced by DOX via the activation of AMPK α . Western blot analysis revealed that phosphorylated AMPK α was remarkably decreased with the injection of DOX and restored after GE treatment in a dose-dependent manner (Figure 5(a)). Phosphorylation of ACC, a reflection of AMPK α activity, was also restored after GE treatment (Figure 5(a)). In agreement with this finding, we also found that GE increased expressions of p-AMPK α

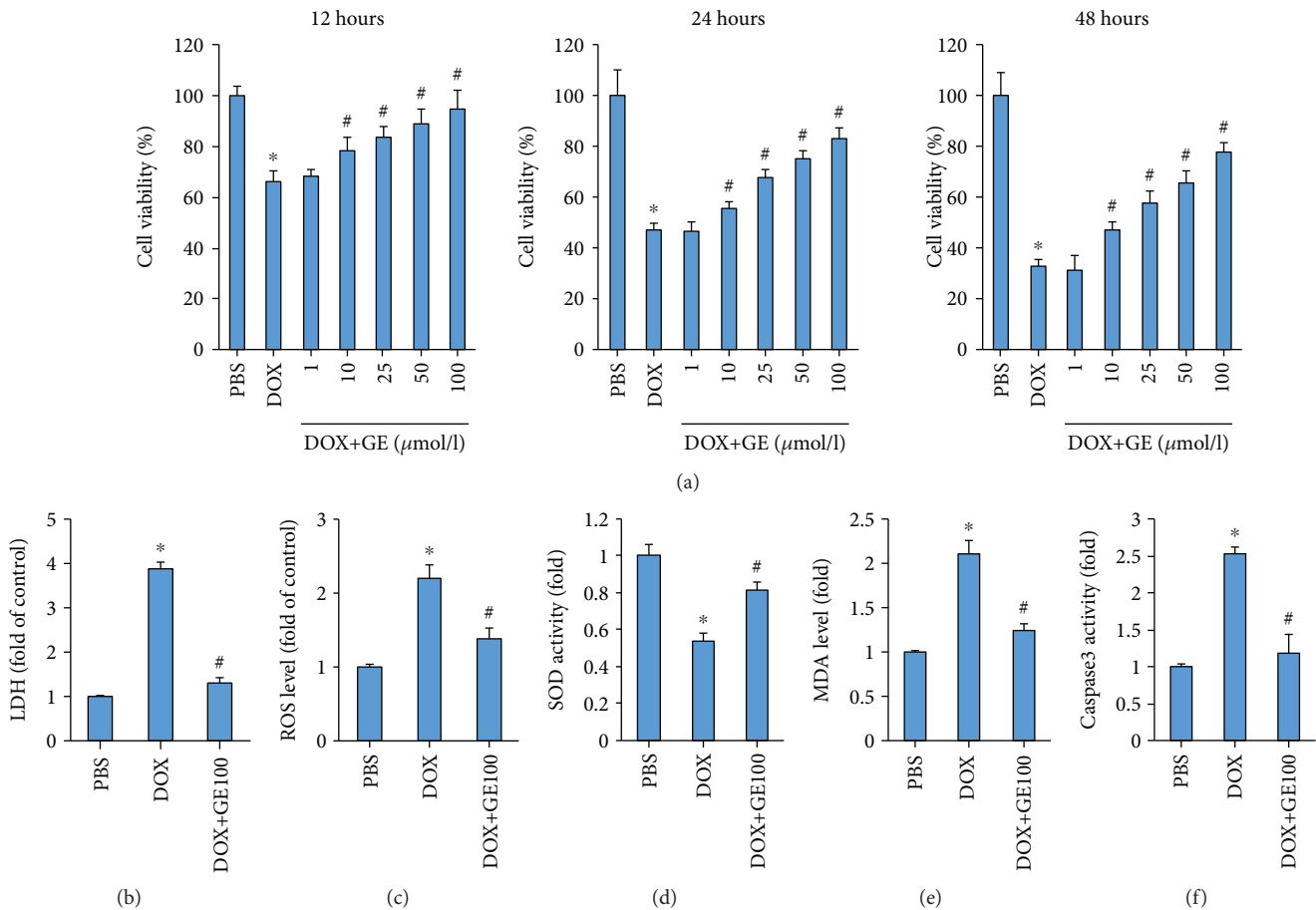


FIGURE 4: GE inhibited DOX-induced toxicity in vitro. (a) Cell viability after the treatment of DOX and GE with three different doses and durations ($n = 3$). (b) Levels of LDH in H9C2 cells ($n = 3$). (c) ROS level detected by DCF-DA in the indicated group ($n = 3$). (d) Activity of SOD in four groups ($n = 3$). (e) Levels of MDA ($n = 3$). (f) The activity of caspase 3 after GE (100 $\mu\text{mol/l}$) for 12 h ($n = 3$). Values represent the mean \pm SD. * $P < 0.05$ versus PBS, # $P < 0.05$ versus DOX.

and p-ACC in vitro (Figure 5(b)). To verify the hypothesis that GE activated AMPK α to protect against DOX-related cardiac injury, we used shAMPK α 2 to knock down AMPK α in H9C2 cells. The efficiency of shAMPK α 2 has been detected in our previous study [17]. As shown in TUNEL staining, GE (100 $\mu\text{mol/l}$) significantly inhibited DOX-induced cardiomyocyte apoptosis, and this effect of GE was abolished after AMPK α deficiency (Figure 5(c)). As shown in Figures 5(d) and 5(e), the protective effects of GE on cell viability and LDH release were completely offset after the infection of shAMPK α . GE also lost its protection against oxidative stress after AMPK α deficiency, as indicated by the elevated level of ROS and MDA (Figures 5(f) and 5(g)). Next, we detected whether the upregulation of Nrf2 by GE was also dependent on the activation of AMPK α . We found that and GE could increase Nrf2 expression even without any stimuli, and this effect was completely blocked by AMPK α deficiency (Figure 5(h)).

3.6. GE Lost Protection in Mice with AMPK α Deficiency. To further validate our finding, we used AMPK α 2 knockout mice. The protein levels of t-AMPK α 2 were detected by western blot in WT and AMPK α 2 KO mice (Figure 6(a)). GE lost

its protective effects against DOX-induced cardiac injury, as reflected by decreased EF and increased cTnI (Figures 6(b) and 6(c)). There was no difference between mice from the KO+DOX and KO+DOX+GE groups in 4-HNE level (Figure 6(d)). Further detection of C-Caspase3 expression and its activity revealed that AMPK α deficiency abolished the antiapoptosis effect of GE (Figures 6(e) and 6(f)).

4. Discussion

Here, we demonstrated for the first time that GE could improve cardiac function and alleviate cardiac injury induced by DOX. The major finding was that GE exerts antioxidative damage and antiapoptotic effects to attenuate DOX-induced cardiotoxicity via the activation of AMPK α from both in vivo and in vitro experiments. Moreover, AMPK α deficiency abolished GE-mediated cardiac protection against DOX-related cardiac injury. Our investigation provided a novel approach for the treatment of DOX-induced cardiac damage.

Oxidative stress is closely involved in the process of DOX-induced cardiac injury. DOX resulted in the accumulation of ROS, thus promoting the generation of by-product of lipid peroxidation via reacting with myocyte membranes [26]

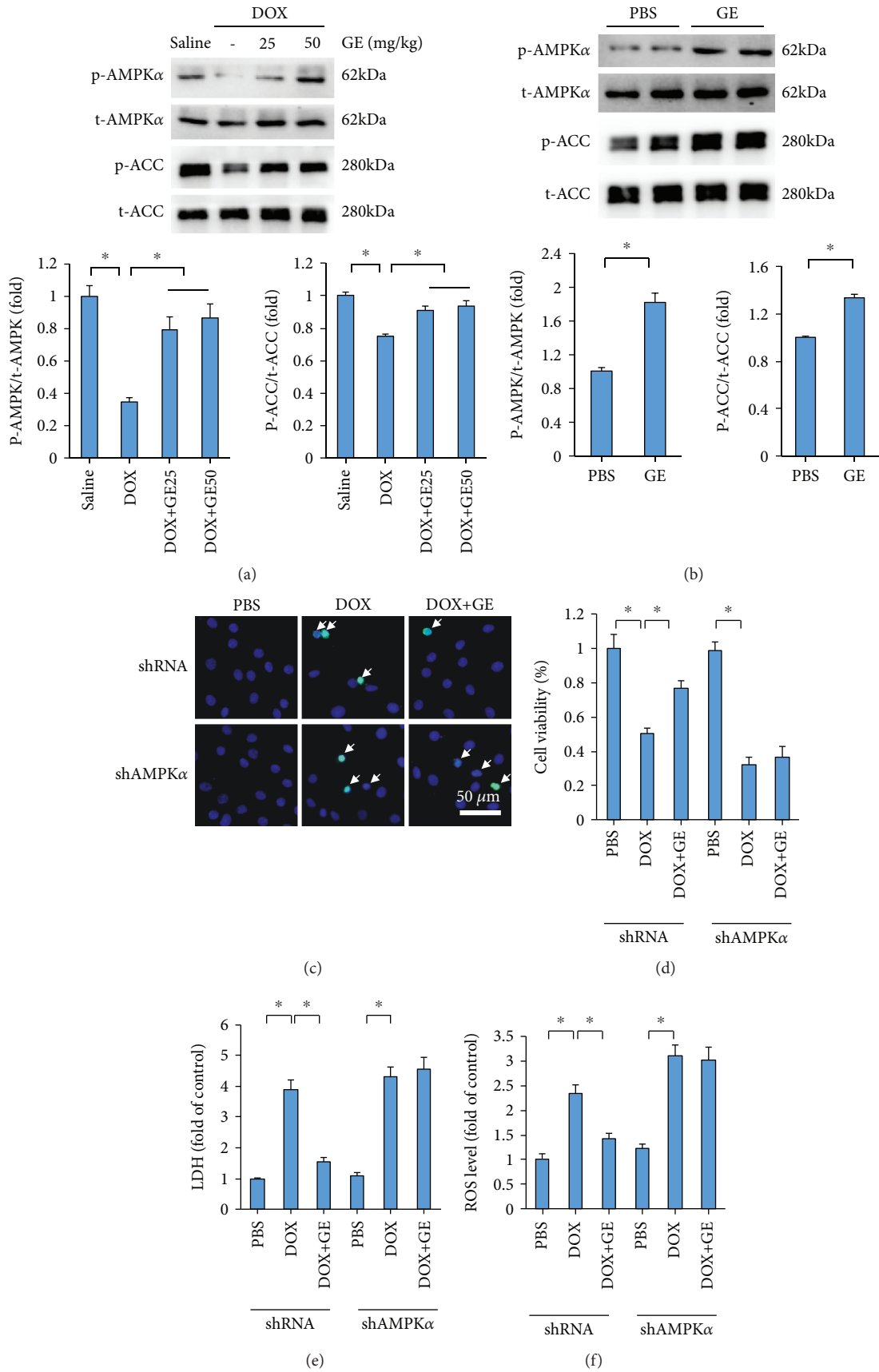


FIGURE 5: Continued.

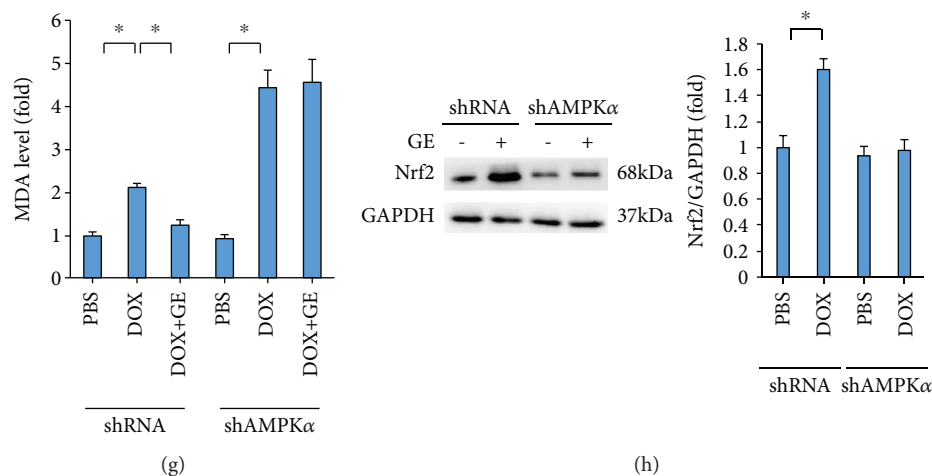


FIGURE 5: GE activated AMPK α to prevent DOX-induced toxicity in vitro. (a, b) Western blot and quantitative results in vivo ($n = 3$) and in vitro ($n = 3$). (c) Representative images of TUNEL and the quantitative results ($n = 3$). Arrows indicate TUNEL-positive cells. (d) Cell viability after GE ($100 \mu\text{mol/l}$) for 12 h ($n = 3$). (e) LDH levels of four groups ($n = 3$). (f) ROS level detected by DCF-DA in the indicated group ($n = 3$). (g) Levels of MDA ($n = 3$). (h) Western blot and quantitative results of Nrf2 and GAPDH in H9C2 cells ($n = 6$). Values represent the mean \pm SD. In (a), * $P < 0.05$ versus saline, # $P < 0.05$ versus DOX; in (b), * $P < 0.05$ versus PBS. In others, * $P < 0.05$ versus DOX.

and ultimately leading to cardiac dysfunction. It has been reported that 4-HNE could directly impair cardiac contractile function at cardiac myocyte level [27]. In view of the damage caused by oxidative stress, adjustment of this redox balance might attenuate DOX-induced injury. The data in our lab demonstrated that GE decreased the level of 4-HNE and MDA in isoprenaline-related cardiomyopathy [28]. Therefore, we investigated whether GE could inhibit DOX-induced oxidative damage. In our study, DOX challenge resulted in increased levels of 4-HNE, 3-NT, and MDA, accompanied by downregulation of Nrf2 and expressions and activities of SOD. All of the above alterations were alleviated by GE, suggesting that GE may correct DOX-induced disturbed redox status. Excessive oxidative stress resulted in cell apoptosis. GE attenuated cardiomyocyte apoptosis in high-fat diet-induced cardiac injury [17]. Consistent with this report, we demonstrated that GE inhibited DOX-induced cell loss in vivo and in vitro. We also found that GE largely attenuated DOX-related cardiac injury, as indicated by the release of cTnI, and improved cardiac function in DOX-treated mice.

Another question arises, that is, how GE exerted its protective effect. Accumulating evidence has shown that AMPK α is an indispensable regulator of a wide variety of physiological events, especially in cardiovascular diseases [29]. Abundant evidences illustrated the close association between AMPK α and DOX-induced heart injury. It has been reported that phosphorylation of AMPK α protein level was slightly increased after DOX treatment [30–32]. However, there sounds a quite different voice. Other studies found that DOX significantly decreased AMPK α expression [8, 33, 34]. Consistent with these studies, we also found that DOX treatment significantly attenuates the expression and activity of AMPK α in vivo. Moreover, GE could attenuate DOX-induced cardiac dysfunction via the activation of AMPK α and AMPK α deficiency abolished the GE-mediated protec-

tive effects both in vivo and in vitro, indicating that improved cardiac function caused by GE was at least partly mediated by AMPK α . Our previous study found that activation of AMPK α could inhibit oxidative stress and cell apoptosis [19]. Therefore, we verify whether the protection against oxidative stress and cell death provided by GE was also mediated by AMPK α . The data in our study demonstrated that the upregulation of Nrf2 caused by GE was inhibited by the knockdown of AMPK α in vitro. GE lost its inhibitory effect on ROS accumulation and production of lipid peroxidation in shAMPK α -infected cells after DOX injection. Using AMPK knockout mice, we found that GE cannot provide any protection against the production of 4-HNE after AMPK deficiency. Cell viability assay, TUNEL staining, and caspase 3 activity detection suggested that GE lost its inhibitory effects on cardiomyocyte apoptosis. The finding indicated that GE protected against DOX-related oxidative injury and cell apoptosis via activating AMPK α .

GE has been widely used in Asia and has extensive pharmacological actions for the treatment. Inchin-ko-to, a “magic pill” for jaundice, is mainly composed of an analogue of GE and has been clinically used in China and Japan for a long time [35]. In our previous study, we also found that mice treated with GE (50 mg/kg) exhibited no obvious change in hepatic morphology [16]. However, the attenuation of DOX-caused systematic injury (body weight loss) should not be all attributed to cardiac benefit provided by GE treatment. GE may also reduce the damage in other organs, which needs further investigation. Considering the translational potential of these findings, it was of importance to confirm that GE does not compromise therapeutic DOX levels or promote tumor growth. It has been reported that GE has been shown to inhibit DNA synthesis of tumor cells and inhibit cell cycle progression [36, 37]. However, there was no report on the effect of GE on the metastasis of tumor.

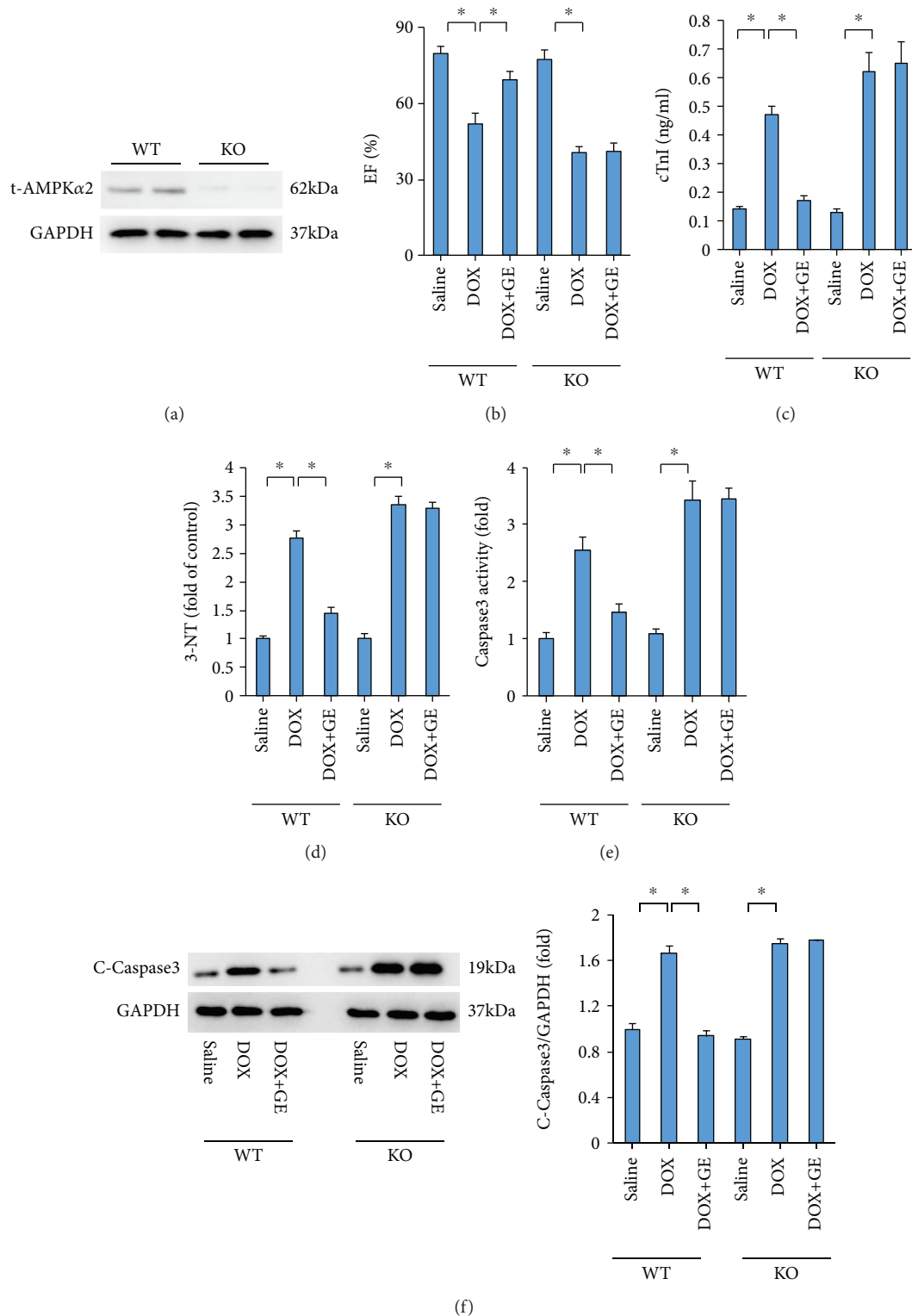


FIGURE 6: GE lost protection in mice with AMPK α deficiency. (a) The protein levels of t-AMPK α 2 of C57 and AMPK α 2 knockout mice ($n = 10$). (b) EF of mice ($n = 10$). (c, d) The levels of cTnI and 3-NT ($n = 10$) after the treatment of DOX and GE (50 mg/kg). (e) Activity of caspase 3 in the indicated group ($n = 10$). (f) The protein levels of caspase 3 and quantitative results ($n = 10$). Values represent the mean \pm SD. * P < 0.05 versus DOX.

Collectively, our present study demonstrated that GE could protect against DOX-induced cardiac toxicity, inhibiting oxidative stress and apoptosis of cardiomyocytes via the

activation of AMPK α . In addition, our findings provide a promising therapeutic approach to treat chemotherapeutic agent-induced cardiotoxicity.

Data Availability

The data used to support the findings of this study are available from the corresponding authors upon request.

Conflicts of Interest

The authors declare that they have no conflicts of interest.

Authors' Contributions

Yan-Yan Meng and Yu-Pei Yuan contributed equally to this work.

Acknowledgments

This work was supported by grants from the National Natural Science Foundation of China (No. 81700254), the Key Project of the National Natural Science Foundation (No. 81530012), the National Major Scientific Instrument and Equipment Development Projects (2013YQ03092306), and the Development Center for Medical Science and Technology National Health and Family Planning Commission of the People's Republic of China (the prevention and control project of cardiovascular disease, 2016ZX-008-01).




References

- [1] Y. Mai, J. J. Yu, B. Bartholdy et al., "An oxidative stress-based mechanism of doxorubicin cytotoxicity suggests new therapeutic strategies in ABC-DLBCL," *Blood*, vol. 128, no. 24, pp. 2797–2807, 2016.
- [2] I. Y. Zhitnyak, I. N. Bychkov, I. V. Sukhorukova et al., "Effect of BN nanoparticles loaded with doxorubicin on tumor cells with multiple drug resistance," *ACS Applied Materials & Interfaces*, vol. 9, no. 38, article 32498, 32508 pages, 2017.
- [3] Y. Zhang, M. Long, P. Huang et al., "Emerging integrated nanoclay-facilitated drug delivery system for papillary thyroid cancer therapy," *Scientific Reports*, vol. 6, no. 1, article 33335, 2016.
- [4] S. Wang, X. Liu, S. Chen et al., "Regulation of Ca²⁺ signaling for drug-resistant breast cancer therapy with mesoporous silica nanocapsules encapsulated doxorubicin/siRNA cocktail," *ACS Nano*, vol. 13, no. 1, pp. 274–283, 2018.
- [5] M. Li, V. Sala, M. C. de Santis et al., "Phosphoinositide 3-kinase gamma inhibition protects from anthracycline cardiotoxicity and reduces tumor growth," *Circulation*, vol. 138, no. 7, pp. 696–711, 2018.
- [6] J. Sun, Y. Wen, Y. Zhou et al., "p53 attenuates acetaminophen-induced hepatotoxicity by regulating drug-metabolizing enzymes and transporter expression," *Cell Death & Disease*, vol. 9, no. 5, p. 536, 2018.
- [7] H. K. Narayan, B. Finkelman, B. French et al., "Detailed echocardiographic phenotyping in breast cancer patients: associations with ejection fraction decline, recovery, and heart failure symptoms over 3 years of follow-up," *Circulation*, vol. 135, no. 15, pp. 1397–1412, 2017.
- [8] D. Liu, Z. Ma, S. Di et al., "AMPK/PGC1 α activation by melatonin attenuates acute doxorubicin cardiotoxicity via alleviating mitochondrial oxidative damage and apoptosis," *Free Radical Biology & Medicine*, vol. 129, pp. 59–72, 2018.
- [9] L. Huang, K. Zhang, Y. Guo et al., "Honokiol protects against doxorubicin cardiotoxicity via improving mitochondrial function in mouse hearts," *Scientific Reports*, vol. 7, no. 1, article 11989, 2017.
- [10] T. Li and P. K. Singal, "Adriamycin-induced early changes in myocardial antioxidant enzymes and their modulation by probucol," *Circulation*, vol. 102, no. 17, pp. 2105–2110, 2000.
- [11] D. McLaughlin, Y. Zhao, K. M. O'Neill et al., "Signalling mechanisms underlying doxorubicin and Nox2 NADPH oxidase-induced cardiomyopathy: involvement of mitofusin-2," *British Journal of Pharmacology*, vol. 174, no. 21, pp. 3677–3695, 2017.
- [12] R. W. Myers, H.-P. Guan, J. Ehrhart et al., "Systemic pan-AMPK activator MK-8722 improves glucose homeostasis but induces cardiac hypertrophy," *Science*, vol. 357, no. 6350, pp. 507–511, 2017.
- [13] Y. Kataoka, R. Shibata, K. Ohashi et al., "Omentin prevents myocardial ischemic injury through AMP-activated protein kinase- and Akt-dependent mechanisms," *Journal of the American College of Cardiology*, vol. 63, no. 24, pp. 2722–2733, 2014.
- [14] X. Tang, X. F. Chen, N. Y. Wang et al., "SIRT2 acts as a cardioprotective deacetylase in pathological cardiac hypertrophy," *Circulation*, vol. 136, no. 21, pp. 2051–2067, 2017.
- [15] Y.-C. Lai, D. M. Tabima, J. J. Dube et al., "SIRT3-AMP-activated protein kinase activation by nitrite and metformin improves hyperglycemia and normalizes pulmonary hypertension associated with heart failure with preserved ejection fraction," *Circulation*, vol. 133, no. 8, pp. 717–731, 2016.
- [16] Z. G. Ma, J. Dai, W. B. Zhang et al., "Protection against cardiac hypertrophy by geniposide involves the GLP-1 receptor / AMPK α signalling pathway," *British Journal of Pharmacology*, vol. 173, no. 9, pp. 1502–1516, 2016.
- [17] Z. G. Ma, C. Y. Kong, P. Song, X. Zhang, Y. P. Yuan, and Q. Z. Tang, "Geniposide protects against obesity-related cardiac injury through AMPK α - and Sirt1-dependent mechanisms," *Oxidative Medicine and Cellular Longevity*, vol. 2018, Article ID 6053727, 12 pages, 2018.
- [18] Z. G. Ma, J. Dai, W. Y. Wei et al., "Asiatic acid protects against cardiac hypertrophy through activating AMPK α signalling pathway," *International Journal of Biological Sciences*, vol. 12, no. 7, pp. 861–871, 2016.
- [19] Z. G. Ma, Y. P. Yuan, S. C. Xu et al., "CTRP3 attenuates cardiac dysfunction, inflammation, oxidative stress and cell death in diabetic cardiomyopathy in rats," *Diabetologia*, vol. 60, no. 6, pp. 1126–1137, 2017.
- [20] J. Tian, J. Zhu, Y. Yi et al., "Dose-related liver injury of geniposide associated with the alteration in bile acid synthesis and transportation," *Scientific Reports*, vol. 7, no. 1, p. 8938, 2017.
- [21] H. I. Cho, S. J. Kim, J. W. Choi, and S. M. Lee, "Genipin alleviates sepsis-induced liver injury by restoring autophagy," *British Journal of Pharmacology*, vol. 173, no. 6, pp. 980–991, 2016.
- [22] J. H. Peng, J. Leng, H. J. Tian et al., "Geniposide and chlorogenic acid combination ameliorates non-alcoholic steatohepatitis involving the protection on the gut barrier function in mouse induced by high-fat diet," *Frontiers in Pharmacology*, vol. 9, p. 1399, 2018.
- [23] Y. P. Yuan, Z. G. Ma, X. Zhang et al., "CTRP3 protected against doxorubicin-induced cardiac dysfunction, inflammation and cell death via activation of Sirt1," *Journal of Molecular and Cellular Cardiology*, vol. 114, pp. 38–47, 2018.

- [24] Z. G. Ma, J. Dai, Y. P. Yuan et al., "T-bet deficiency attenuates cardiac remodelling in rats," *Basic Research in Cardiology*, vol. 113, no. 3, p. 19, 2018.
- [25] Z. G. Ma, X. Zhang, Y. P. Yuan et al., "A77 1726 (leflunomide) blocks and reverses cardiac hypertrophy and fibrosis in mice," *Clinical Science (London, England)*, vol. 132, no. 6, pp. 685–699, 2018.
- [26] K. Uchida, "Role of reactive aldehyde in cardiovascular diseases," *Free Radical Biology & Medicine*, vol. 28, no. 12, pp. 1685–1696, 2000.
- [27] N. S. Aberle, M. J. Picklo, V. Amarnath, and J. Ren, "Inhibition of cardiac myocyte contraction by 4-hydroxy-trans-2-nonenal," *Cardiovascular Toxicology*, vol. 4, no. 1, pp. 21–28, 2004.
- [28] N. Li, H. Zhou, Z. G. Ma et al., "Geniposide alleviates isoproterenol-induced cardiac fibrosis partially via SIRT1 activation *in vivo* and *in vitro*," *Frontiers in Pharmacology*, vol. 9, p. 854, 2018.
- [29] R. Kjøbsted, J. R. Hingst, J. Fentz et al., "AMPK in skeletal muscle function and metabolism," *The FASEB Journal*, vol. 32, no. 4, pp. 1741–1777, 2018.
- [30] J. Zhao, J. Du, Y. Pan et al., "Activation of cardiac TrkB receptor by its small molecular agonist 7,8-dihydroxyflavone inhibits doxorubicin-induced cardiotoxicity via enhancing mitochondrial oxidative phosphorylation," *Free Radical Biology & Medicine*, vol. 130, pp. 557–567, 2019.
- [31] Y. Cao, T. Shen, X. Huang et al., "Astragalus polysaccharide restores autophagic flux and improves cardiomyocyte function in doxorubicin-induced cardiotoxicity," *Oncotarget*, vol. 8, no. 3, pp. 4837–4848, 2017.
- [32] X. Wang, X. L. Wang, H. L. Chen et al., "Ghrelin inhibits doxorubicin cardiotoxicity by inhibiting excessive autophagy through AMPK and p38-MAPK," *Biochemical Pharmacology*, vol. 88, no. 3, pp. 334–350, 2014.
- [33] C. Ni, P. Ma, R. Wang et al., "Doxorubicin-induced cardiotoxicity involves IFN γ -mediated metabolic reprogramming in cardiomyocytes," *The Journal of Pathology*, vol. 247, no. 3, pp. 320–332, 2019.
- [34] S. Wang, Y. Wang, Z. Zhang, Q. Liu, and J. Gu, "Cardioprotective effects of fibroblast growth factor 21 against doxorubicin-induced toxicity via the SIRT1/LKB1/AMPK pathway," *Cell Death & Disease*, vol. 8, no. 8, article e3018, 2017.
- [35] J. Shoda, T. Miura, H. Utsunomiya et al., "Genipin enhances Mrp2 (Abcc2)-mediated bile formation and organic anion transport in rat liver," *Hepatology*, vol. 39, no. 1, pp. 167–178, 2004.
- [36] Y. C. Chang, F. P. Chou, H. P. Huang, J. D. Hsu, and C. J. Wang, "Inhibition of cell cycle progression by penta-acetyl geniposide in rat C6 glioma cells," *Toxicology and Applied Pharmacology*, vol. 198, no. 1, pp. 11–20, 2004.
- [37] C. H. Peng, C. N. Huang, and C. J. Wang, "The anti-tumor effect and mechanisms of action of penta-acetyl geniposide," *Current Cancer Drug Targets*, vol. 5, no. 4, pp. 299–305, 2005.

Research Article

miR-25 Promotes Cell Proliferation, Migration, and Invasion of Non-Small-Cell Lung Cancer by Targeting the LATS2/YAP Signaling Pathway

Tangwei Wu,¹ Hui Hu,¹ Tianzhu Zhang,^{1,2} Liyuan Jiang,¹ Xiaoyi Li,¹ Shuyi Liu,³ Chao Zheng,¹ Ge Yan,^{1,2} Weiqun Chen,^{1,3,4,5} Yong Ning ,² Yong Li ,⁶ and Zhongxin Lu ^{1,2,3,4,5}

¹Department of Medical Laboratory, The Central Hospital of Wuhan, Tongji Medical College, Huazhong University of Science and Technology, Wuhan 430014, China

²School of Laboratory Medicine, Hubei University of Chinese Medicine, Wuhan 430065, China

³Cancer Research Institute of Wuhan, The Central Hospital of Wuhan, Tongji Medical College, Huazhong University of Science and Technology, Wuhan 430014, China

⁴Department of Central Laboratory, The Central Hospital of Wuhan, Tongji Medical College, Huazhong University of Science and Technology, Wuhan 430014, China

⁵Key Laboratory for Molecular Diagnosis of Hubei Province, The Central Hospital of Wuhan, Tongji Medical College, Huazhong University of Science and Technology, Wuhan 430014, China

⁶Department of Cancer Biology, Lerner Research Institute, Cleveland Clinic, Cleveland, OH 44195, USA

Correspondence should be addressed to Yong Li; liy2@ccf.org and Zhongxin Lu; lzx71@yahoo.com

Received 15 February 2019; Accepted 20 May 2019; Published 18 June 2019

Guest Editor: Bhagavatula Moorthy

Copyright © 2019 Tangwei Wu et al. This is an open access article distributed under the Creative Commons Attribution License, which permits unrestricted use, distribution, and reproduction in any medium, provided the original work is properly cited.

Metastasis is the leading cause of high mortality in lung cancer patients, and metastatic lung cancer is difficult to treat. miRNAs are involved in various biological processes of cancer, including metastasis. Our previous studies revealed that miR-25 promoted non-small-cell lung cancer (NSCLC) cell proliferation and suppressed cell apoptosis by directly targeting *TP53* and *MOAP1*. In this work, we further explored the miR-25 expression in NSCLC patients in the Cancer Genome Atlas (TCGA) database and measured the miR-25 expression levels in the tissues of NSCLC patients and cell lines. miR-25 was overexpressed in both NSCLC tissues and cell lines. NSCLC patients who expressed a higher level of miR-25 exhibited worse overall survival than those with a lower level of miR-25. Overexpression of miR-25 enhanced NSCLC cell migration and invasion, while the inhibition of miR-25 exhibited the opposite effects. We identified the large tumor suppressor homology 2 (*LATS2*) as a new target gene of miR-25 in lung cancer. The effects of miR-25 on promoting NSCLC cell migration and invasion were at least partially due to activation of the Hippo signaling pathway. Additionally, miR-25 antagomir inhibited xenograft tumor growth and metastasis by the upregulation of *LATS2*. Taken together, our findings demonstrate that miR-25 contribute to lung cancer cell proliferation and metastasis by targeting the *LATS2*/YAP signaling pathway, which implicate miR-25 as a promising therapeutic target for lung cancer metastasis. Given that oxidative stress induces the overexpression of miR-25 and plays a critical role in cancer progression, this study establishes miR-25 as an intermediate between oxidative stress and lung cancer metastasis.

1. Introduction

Lung cancer is the leading cause of cancer-related deaths in both developing and developed countries [1, 2]. Based on

the diverse pathobiological features, lung cancer can be divided into two major types: non-small-cell lung cancer (NSCLC) and small-cell lung cancer (SCLC). NSCLC accounts for approximately 80% of lung cancer. Despite

recent advances in treatments, the overall 5-year survival rate of patients with NSCLC remains less than 10% [3]. When diagnosed, most NSCLC patients are already at the metastatic stage with poor prognosis; metastasis in cancer is a tough in clinical care of NSCLC [4]. Oxidative stress plays important roles in the pathogenesis of lung cancer, including metastasis [5]. Yet the underlying mechanisms remain elusive.

MicroRNAs (miRNAs) are a group of ~22 nt endogenous noncoding small RNAs that play important roles in the pathogenesis of human diseases by targeting the 3'UTR of mRNAs for mRNA degradation or translational repression [6]. miRNAs are involved in a series of tumor biological processes, such as differentiation, proliferation, apoptosis, migration, invasion, and drug resistance [7–9]. Dysregulated miRNAs may act as tumor suppressors or oncogenes (oncomiRs). Combined serum levels of several miRNAs (miR-9-5p, miR-21-5p, and miR-223-3p) with existing tumor biomarkers offer better detection of NSCLC than the tumor biomarkers alone [10]. Functional studies of dysregulated miRNAs in cancer implicate miRNAs as attractive targets for novel therapeutic development [11, 12]. The anti-miR-122 reached the phase II trials for treating hepatitis [12]. The ongoing phase I trial MesomiR 1 (ClinicalTrials.gov NCT02580552) detected a case of partial response after eight weeks of treatment [13]. In addition, the miRagen company has developed an inhibitor for miR-155, MRG-106, for the treatment of hematologic tumor and is completing phase I clinical trials (<http://www.miragen.com/clinical-trials/>). Thus, further investigations on miRNA involved in tumor development and metastasis will offer new opportunities in cancer therapy.

miR-25, along with miR-93 and miR-106b, is a member of the miR-106b-25 cluster, which is located in the intron 13 of the minichromosome maintenance complex component 7 (*MCM7*) gene on chromosome 7q22.1. miR-25 is dysregulated in many human cancers with various functions [14]. In glioma, miR-25 promotes glioma cells proliferation by targeting *CDKN1C* [15]. In gastric cancer, miR-25 promotes cancer progression by directly downregulating *ERBB2* and is a noninvasive prognosis biomarker [16]. Colorectal cancer-derived exosomal miR-25 is involved in premetastatic niche formation and may be used as a blood-based biomarker for prediction of metastasis [17]. miR-25 principally functions as oncogene, but in some cases, it may be tumor suppressive. In cisplatin-resistant cervical cancer cells, miR-25 reverses epithelial-mesenchymal transition via targeting *Sema4C* [18]. miR-25 also modulates invasiveness and dissemination of human prostate cancer cells by targeting the proinvasive α v- and α 6-integrins [19].

Our previous studies revealed that miR-25 was elevated in the plasma of NSCLC patients and NSCLC cell lines, and miR-25 directly targeted and downregulated *TP53* and *MOAPI* in lung cancer and thereby reduced their downstream signaling to promote cell proliferation and suppress cell apoptosis [20, 21]. In this study, we measured the miR-25 expression levels in the tissues of NSCLC patients and NSCLC cell lines. miR-25 was involved in NSCLC cell proliferation, migration, invasion, and xenograft tumor

metastasis. Furthermore, we identified *LATS2* as a new target gene for miR-25 in NSCLC metastasis. As miR-25 is induced by oxidative stress [22], our study provides profound insights into the oncogenic role of miR-25 and implicates this miRNA as a link between oxidative stress and metastasis and a promising therapeutic target to suppress metastasis of NSCLC.

2. Materials and Methods

2.1. Clinical Specimens. Between June 2017 and June 2018, we collected fifteen paired NSCLC tissues and their adjacent normal lung tissues from the Central Hospital of Wuhan. All tissue specimens were frozen in the liquid nitrogen immediately or stored in the refrigerator at -80°C after surgical removal. None of the patients accepted any chemotherapy or radiotherapy prior to tumor resection. All patients received informed consent during enrollment. This research was approved by the Ethical and Scientific Committees of the Central Hospital of Wuhan.

2.2. The Cancer Genome Atlas (TCGA) Analysis. Data on miR-25 expression and clinical information of NSCLC patients were obtained from TCGA data set. miRNAs-seq data were downloaded from TCGA website (cancergenome.nih.gov/), `bcgsc.ca_LUAD.IlluminaHi-Seq_miRNASeq.Level_3.1.12.0`, `bcgsc.ca_LUSC.IlluminaGA_miRNASeq.Level_3.1.3.0`, and `bcgsc.ca_LUSC.IlluminaHiSeq_miRNASeq.Level_3.1.7.0`. For survival analysis, we then stratified the patients into two groups, high and low expressions, according to miR-25 expression using the median of miRNA abundance as the threshold and then conducted a two-sample Kolmogorov-Smirnov test (K-S test) and draw the K-M plot.

2.3. Cells and Cell Culture. The NSCLC cell lines, including H1299, A549, H23, H520, and the normal lung epithelial cell line BEAS-2B, and human embryonic kidney (HEK) 293T cells were all purchased from American Type Culture Collection (ATCC) [21]. Lung carcinoma 95-D cell line was obtained from the Cell Bank of the Chinese Academy of Sciences [21]. All cells were cultured with suggested media in a 5% CO_2 humidified incubator at 37°C as previously reported [21].

2.4. RNA Isolation and qRT-PCR. Total RNA was extracted from lung cancer tissues and cells using TRIzol reagent (Invitrogen, Carlsbad, CA, USA). The cDNA for target gene detection was synthesized from 1 μg total RNAs. The target miRNA or mRNA was measured using SYBR Green (Applied Biosystems, Carlsbad, CA, USA) in the CFX96 real-time detection system (Bio-Rad, Hercules, CA, USA). U6 and β -actin were used as an endogenous control, respectively, for miR-25 and *LATS2* detection. The miR-25 relative expression values were calculated using the $2^{-\Delta\text{Ct}}$ method for lung cancer tissues or using the $2^{-\Delta\Delta\text{Ct}}$ method for cells. The primers for the detection of the *LATS2* mRNA level were as follows: sense, TCC TGC CAC GAC TTA TTC, and anti-sense, GTG CCC GAT TCA TTA GC. *LATS2* mRNA relative values were calculated by using the $2^{-\Delta\Delta\text{Ct}}$ method.

2.5. Transient Transfection of pSIF-GFP-miR-25 or miRNA Inhibitors. The pSIF-GFP-miR-25 precursor plasmid and

the precursor control were gifts from professor Yong Li in Cleveland Clinic [20]. The transfection efficiency (>30%) of pSIF-GFP-miR-25 was checked based on GFP expression 24 h posttransfection by using a fluorescence microscope as reported in the previous study [21]. The miR-25 inhibitor and the negative control were purchased from GenePharm (Shanghai, China). The pSIF-GFP-miR-25 and the miR-25 inhibitor was used with a final concentration of 100 nM. The day before transfection, cells were plated to ensure ~70% cell confluence. Cell transfection was performed using Lipofectamine® LTX and Plus reagent (Invitrogen) following the manufacturer's protocol.

2.6. Colony Formation Assay. Cells were seeded into a 12-well plate (500 cells/well) and incubated for about ten days until colonies were apparent. The plate was then gently washed and stained with 0.1% crystal violet (Beyotime, Nantong, China). Colonies containing at least 50 cells were counted to observe the malignant viability of the single cell.

2.7. Wound Healing Assay. For cell mobility assay, cells were seeded onto 12-well plates (2×10^5 cells/well); 24 h after transfection, an artificial wound was created by scratching the confluent cell monolayer using a sterile 200 μ l pipette tip. Then, cells were washed twice with phosphate-buffered saline (PBS) and incubated in RPMI-1640 supplemented with 1% FBS. The wound healing images (magnification, $\times 100$) were taken at 0 h and 48 h after scratching. The wound healing rate was calculated by using the ImageJ software.

2.8. Invasion Assay. To investigate lung cancer cell invasion, transwell chamber (Corning, NY, USA) coated with Matrigel (BD Biosciences, CA, USA) was used. Twenty-four hours after transfection, cells were collected and suspended in 100 μ l serum-free medium. A total of 2×10^4 cells were seeded into the upper chamber, and the complete culture medium was added into the lower chamber. After incubation for 48 h, cells on the upper surface of the membrane were removed using cotton swabs. Cells located on the lower filter surfaces were fixed in 4% paraformaldehyde solution (Beyotime) and stained with 0.1% crystal violet (Beyotime). The number of invading cells was determined by evaluating 5 fields per membrane using an IX81 microscope (Olympus, Tokyo, Japan). Images were taken at magnification 100x.

2.9. Luciferase Reporter Assay. The LATS2 3'UTR containing the putative miR-25 recognition elements was amplified (sense, 5'-TAT CTA GAG GAC TCA GCA TCG CTT TCA AT-3', and antisense, 5'-ATG CGG CCG CTC ACA GCC ACA TCA TCA CCT T-3'). The mutated LATS2 3'UTR was also amplified (sense, 5'-TAT CTA GAG GAC TCA GCA TCG CTT TCA AT-3', and antisense, 5'-ATG CGG CCG CTT ACA TTC GCT ACG AGA GAT TTC-3'). The wild-type and mutated PCR products were respectively subcloned into the pRL-TK vector (Promega). Correct constructs were confirmed by sequencing. Luciferase reporter assays were carried out in HEK-293T, A549, and H1299 cells as previously described [21].

2.10. Western Blot. Western blot analysis was conducted as previously described [23]. The primary antibodies were used as follows: rabbit polyclonal anti-LATS2 (1:500, Proteintech, Rosemont, USA), rabbit polyclonal anti-YAP (1:500, Proteintech), rabbit monoclonal anti-phospho-YAP (Ser127, 1:1000, Cell Signaling Technology, Danvers, MA, USA), rabbit monoclonal anti-E-cadherin (1:1000, Cell Signaling Technology), rabbit monoclonal anti-Vimentin (1:1000, Cell Signaling Technology), and rabbit polyclonal anti-MMP9 (1:500, Proteintech). Mouse monoclonal anti- β -actin (1:1000, Sigma-Aldrich) was used as a reference.

2.11. LATS2 Overexpression. The pCneoMyc-LATS2 plasmid was a gift from Yutaka Hata (Addgene plasmid), which expressed Myc-tagged LATS2 in mammalian cells [24]. A549 cells were seeded in a 12-well plate (2×10^5 cells/well) and transfected with 2 μ g pSIF-GFP-miR-25 and/or 0.5 μ g pCneoMyc-LATS2 for 24 h. Transfected cells were then used for colony formation, wound healing, and invasion assays as described above.

2.12. Immunofluorescence Assay. For immunofluorescence assay, A549 cells were collected 48 h posttransfection and then seeded as 2×10^3 cells/well in eight-well chamber slide (Millipore, Darmstadt, Germany). After incubation for 24 h, cells were washed with PBS and fixed with -20°C pre-cooled methanol for 10 min at -20°C . Then, cells were washed with PBS and incubated in 0.2% Triton for 10 min at room temperature. Cells were blocked in 5% fetal bovine serum for 1 h at room temperature and incubated with rabbit polyclonal anti-YAP (1:50, Proteintech) over night at 4°C and shaking. Next, cells were washed with PBS and incubated in a secondary antibody for 45 min. At last, cells were washed and stained with DAPI for 10 min. The images were taken by using a fluorescence microscope (Olympus BX51, Tokyo, Japan). ImageJ software was used to calculate the colocalization rate.

2.13. In Vivo Assay. The miR-25 antagomir/control miR-Down™ was obtained from GenePharm (Shanghai, China) [21]. Five-week-old BALB/c nude mice were purchased from HFK Bio-Technology Co. Ltd. (Beijing, China). A total of 5×10^6 A549 cells, resuspended in Opti-MEM, were subcutaneously injected into the right flank of 6-week-old BALB/c nude mice ($n = 5$ for each group). The subsequent tumorigenesis experiments were performed as in the previous study [21]. For the tumor metastasis assay, a total of 2×10^6 A549 cells in OptiMEM were injected into the tail veins of nude mice ($n = 10$ for each group). One week later, the miR-25 antagomir or control (200 μ l, 375 μ g per mice) was injected into the tail veins once per week for 3 weeks. One month after the first injection of miR-25 antagomir or control, mice were sacrificed and lungs and livers were collected for further analyses.

2.14. Statistical Analysis. Independent *t*-test, paired *t*-test, and χ^2 test were carried out for statistical analysis using the SPSS 22.0 software. All experiments were repeated at least three times independently. *P* values less than 0.05 were

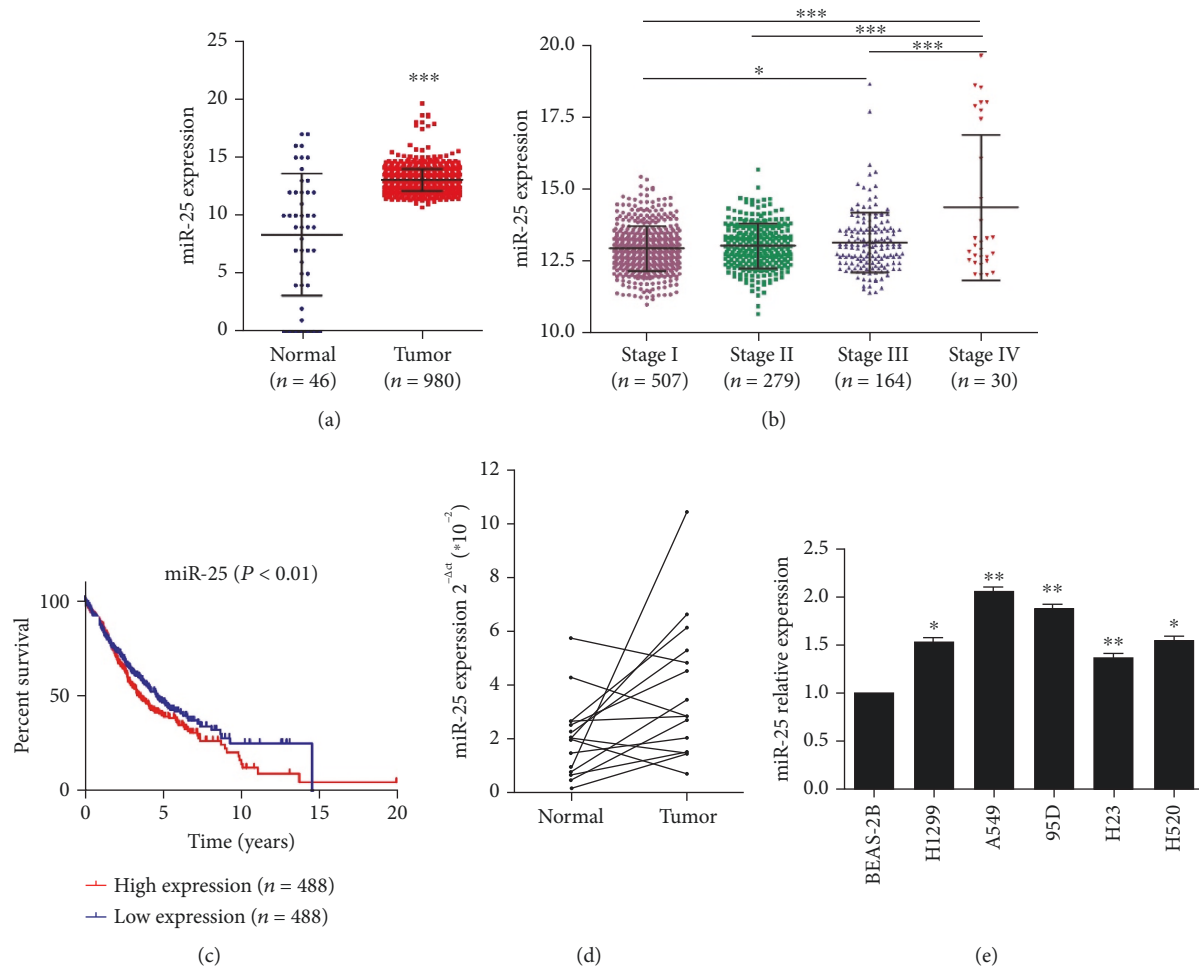


FIGURE 1: The expression of miR-25 in lung cancer tissues and cell lines. (a) miR-25 expression in the tumor tissues of NSCLC patients as compared to the control, noncancerous lung tissues from the TCGA database. (b) miR-25 expression in tumor tissues of NSCLC patients with different stages from the TCGA database. (c) In the TCGA database, the overall survival rate curves of NSCLC patients with high and low expression of miR-25 were shown. (d) The expression levels of miR-25 in 15 pairs of NSCLC tissues and the adjacent normal tissues by qRT-PCR. (e) The expression levels of miR-25 in NSCLC cell lines and the noncancerous lung epithelial cell line BEAS-2B. Results were presented as the mean \pm SD. * $P < 0.05$, ** $P < 0.01$, and *** $P < 0.001$.

considered to be statistically significant. * $P < 0.05$, ** $P < 0.01$, and *** $P < 0.001$.

3. Results

3.1. miR-25 Was Overexpressed in Both NSCLC Tissues and Cell Lines. To explore the role of miR-25 in NSCLC, we analyzed miR-25 expression in NSCLC patients in the TCGA database. As shown in Figure 1(a), miR-25 was significantly elevated in NSCLC tissues ($n = 980$) compared with the control, noncancerous lung tissues ($n = 46$). Moreover, miR-25 was gradually increased with NSCLC stages I to IV (Figure 1(b)). The levels of miR-25 were significantly higher in patients with stage IV than those with stage I, stage II, and stage III. There was also significant difference in miR-25 expression between the patients with stages I and III. Next, NSCLC patients ($n = 488$) with a high expression of miR-25 presented worse overall survival than the patients ($n = 488$) with a low expression of miR-25 (Figure 1(c)). We further

detected the expression of miR-25 in 15 pairs of paired NSCLC tissues and their adjacent normal lung tissues. The results showed that miR-25 was significantly upregulated in NSCLC tissues compared with their respective adjacent noncancerous tissues (Figure 1(d)). However, miR-25 was increased in 11/15 samples, suggesting that the upregulation of miR-25 occurred in approx. 2/3 of lung cancers, but not all (Figure 1(d)). Besides, qRT-PCR was used to evaluate the expression levels of miR-25 in various NSCLC cell lines and the normal lung epithelial cell line BEAS-2B. The results indicated that compared with noncancerous BEAS-2B cells, all five NSCLC cell lines expressed miR-25 at a higher level (Figure 1(e)). Because miR-25 expression was highest in metastatic cell line A549 and H1299 was a p53-null cell line which represents high malignancy, we chose these two lines as cell models in subsequent experiments.

3.2. miR-25 Enhanced NSCLC Cell Malignant Viability, Migration, and Invasion. The malignant viability of NSCLC

cells was evaluated by a colony formation assay. When transfected with the miR-25 precursor, there were much more colonies formed by A549 ($n = 124 \pm 8$) and H1299 ($n = 44 \pm 4$) cells than the controls, A549 ($n = 58 \pm 7$) and H1299 ($n = 29 \pm 2$) cells transfected with the precursor control (Figures 2(a) and 2(b)). Adversely, the numbers of colonies were markedly decreased in A549 ($n = 22 \pm 4$) and H1299 ($n = 13 \pm 3$) when the miR-25 inhibitor was introduced, compared with those in A549 ($n = 59 \pm 6$) and H1299 ($n = 29 \pm 6$) with the inhibitor control (Figures 2(a) and 2(b)). Next, the migration and invasion ability of NSCLC cells were assessed by wound healing and transwell assays. There was a significant higher wound healing rate in A549 cells with the miR-25 precursor (wound closure is $49.47 \pm 1.00\%$) than those with the control (wound closure is $29.50 \pm 3.99\%$; Figure 2(c)). Similarly, transfection with the miR-25 precursor in H1299 cells also resulted in an increase in the wound healing rate (wound closure is $82.70 \pm 4.42\%$) in comparison with the control (wound closure is $62.63 \pm 4.63\%$; Figure 2(d)). Inhibition of miR-25 decreased the wound closure rates in both A549 and H1299 (Figures 2(c) and 2(d)). For the transwell assay, as shown in Figure 2(e), the invaded cell number increased from 118 ± 6 to 170 ± 3 in A549 cells with the miR-25 precursor, whereas the invaded cell number decreased from 146 ± 5 to 88 ± 2 in A549 cells with the miR-25 inhibitor. Similar cell invasion effects were also observed when miR-25 was inhibited or overexpressed in H1299 cells (Figure 2(f)). The above results suggest that miR-25 enhanced lung cancer malignant viability, migration, and invasion. We further detected protein markers of cancer metastasis in A549 and H1299 cells. As shown in Figure 2(g), following the treatment of the miR-25 inhibitor, the level of the epithelial marker E-cadherin was upregulated, while the levels of the mesenchymal marker Vimentin and the cell matrix metalloproteinase MMP9 was downregulated in A549 and H1299 cells. These results indicate that the inhibition of miR-25 may suppress EMT and extracellular matrix degradation in NSCLC.

3.3. LATS2 Is a Direct Target of miR-25. Among the predicted targets of miR-25 in miRBase (version 21), *LATS2* located at chromosome 13q11-12 encodes the LATS2 protein, a Ser/Thr kinase regulating cell biological processes and a key component in the Hippo pathway. *LATS2* is reported as a target gene of miR-25 in ovarian cancer [25] and gastric cancer [26], yet such a relationship in lung cancer has not been established. There is a putative binding site for miR-25 in the 3' UTR of *LATS2* (Figure 3(a)). We used established procedures to determine whether *LATS2* is an authentic miR-25 target gene [21]. We first examined *LATS2* mRNA expression in 15 pairs of lung cancer tissues and their adjacent normal tissues by qRT-PCR. We found that *LATS2* levels were lower in lung cancer tissues than in adjacent normal tissues (Figure 3(b)). In addition, *LATS2* was reduced in NSCLC cell lines as compared to the noncancerous lung epithelial cell line BEAS-2B (Figure 3(c)). Data from the Cancer Genome Atlas (TCGA) indicated that lung cancer patients ($n = 573$) with a high expression of *LATS2* exerted higher overall survival rates than those ($n = 572$) with a low

expression of *LATS2* (Figure 3(d)), suggesting a tumor suppressive role for *LATS2* in lung cancer [21].

Next, we conducted luciferase reporter assays in HEK293T and H1299 cells by placing either the wild-type *LATS2* 3' UTR or a mutant lacking miR-25 binding sites (Figure 3(a)) downstream of the luciferase gene. We found that when miR-25 was upregulated, luciferase activities were decreased in cells carrying the luciferase gene with the wild-type 3' UTR, but not in those with the mutant 3' UTR (Figure 3(e)). Conversely, when miR-25 was downregulated, there was a significant increase in luciferase activities in HEK293T, A549, and H1299 cells with the wild-type 3' UTR but not in those with the mutant 3' UTR (Figures 3(f)–3(h)). We noted that the *LATS2* protein level was lower in both A549 and H1299 cells than in BEAS-2B cells (Figure 3(i)). When miR-25 was overexpressed, *LATS2* protein levels were significantly downregulated in A549 and H1299 cells; and *LATS2* protein levels were elevated when miR-25 was suppressed (Figure 3(j)).

3.4. miR-25 Promotes NSCLC Cell Malignant Viability, Migration, and Invasion by Targeting LATS2. To further explore whether miR-25 regulates NSCLC cell proliferation and metastasis by targeting *LATS2*, we transfected A549 cells with pCneoMyc-*LATS2* or the miR-25 precursor and evaluated the malignant phenotypes. As shown in Figure 4(a), the formed colonies of A549 cells was reduced from 58 ± 6 to 27 ± 3 following *LATS2* overexpression, while they were elevated from 58 ± 6 to 105 ± 11 when miR-25 was overexpressed. Yet, the overexpression of *LATS2* reversed the positive effects of miR-25 overexpression-mediated colony formation. As expected, the overexpression of *LATS2* markedly inhibited the wound closure rate and decreased the cell invasion of A549 cells, while overexpression of miR-25 exhibited the opposite effects (Figures 4(b) and 4(c)). Similarly, the miR-25-mediated enhanced migration and invasion of A549 cells were reversed by cotransfection with *LATS2* (Figures 4(b) and 4(c)). These results suggest that miR-25 promotes NSCLC cell malignant viability, migration, and invasion, at least partially, by targeting *LATS2*.

As a key serine/threonine kinase in the Hippo signaling pathway, *LATS2* phosphorylates the Hippo downstream effector YAP oncoprotein, reduces the level of YAP, and inhibits its shuttling from the cytoplasm to the nucleus, to exert its tumor-suppressive effects [27]. We detected the *LATS2*-related proteins in the Hippo pathway: YAP and phosphorylated YAP. As shown in Figure 4(d), when *LATS2* was overexpressed, the protein levels of phosphorylated YAP and E-cadherin were elevated, whereas YAP, Vimentin, and MMP9 were downregulated. Overexpression of miR-25 had opposite effects, including decreased *LATS2* expression, suppressed YAP phosphorylation and E-cadherin, and increased YAP, Vimentin, and MMP9 levels. The impact of miR-25 overexpression was partially reversed by coexpression of *LATS2*. Further, immunofluorescent staining was used to analysis the nuclear accumulation of YAP in A549 cells. As shown in Figure 4(e), *LATS2* overexpression inhibited the nuclear accumulation of YAP, whereas

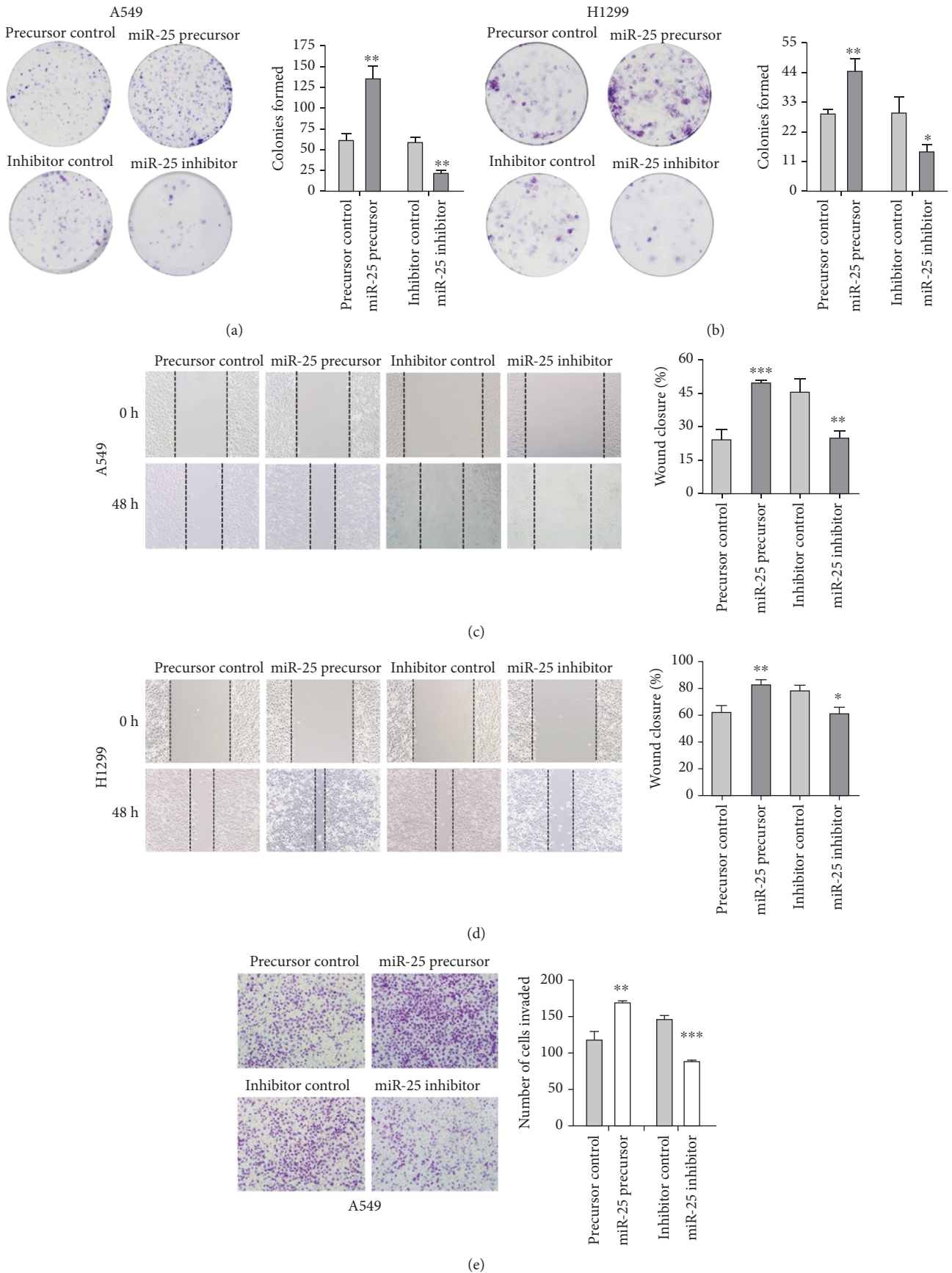


FIGURE 2: Continued.

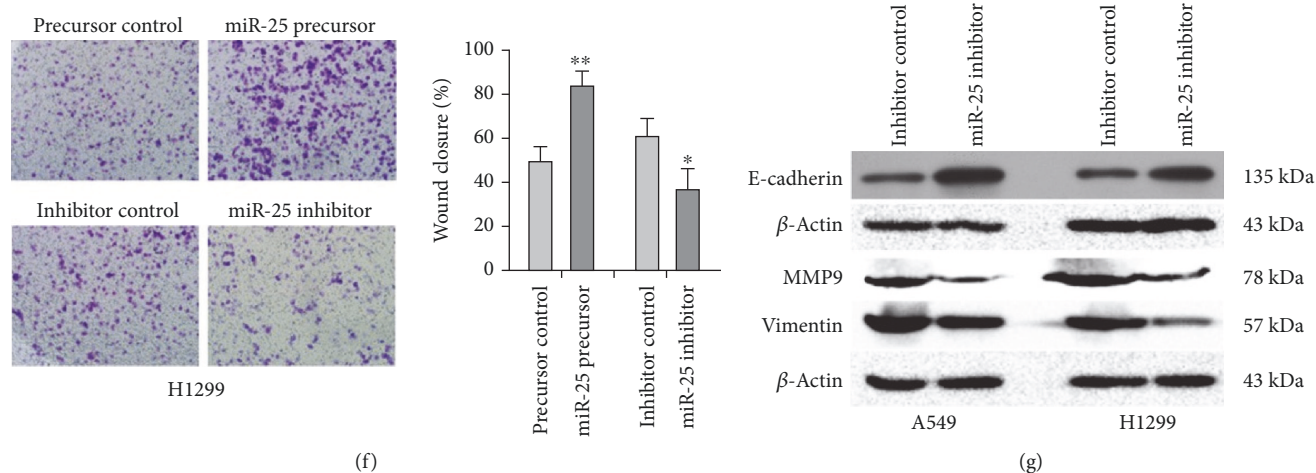


FIGURE 2: Overexpression or inhibition of miR-25 on cell proliferation, migration, and invasion in both A549 and H1299 cells. (a, b) Colony formation of cells transfected with the miR-25 precursor or the miR-25 inhibitor or with respective controls. (c, d) Wound healing assays for cell migration with altered miR-25 expression. (e, f) Transwell assays for cell invasion with altered miR-25 expression. (g) Western blot analyses of the expression of metastasis-related proteins, E-cadherin, Vimentin, and MMP9 in A549 and H1299 cells with altered miR-25 expression. Results were presented as mean \pm SD of three independent experiments. * $P < 0.05$, ** $P < 0.01$, and *** $P < 0.001$.

miR-25 overexpression promoted YAP protein nuclear localization. The miR-25-mediated enhanced nuclear accumulation of YAP in A549 cells was reversed by cotransfection with LATS2. These data support that LATS2 is a *bona fide* target of miR-25.

3.5. miR-25 Antagomir Inhibits Lung Tumor Growth and Metastasis In Vivo. To determine whether the inhibition of miR-25 affects lung tumorigenesis *in vivo*, we injected the miR-25 antagomir and control intratumorally when the tumors xenografted with A549 cells reached an average of 60 mm³ in immunodeficient mice. We found that tumors injected with the miR-25 antagomir exhibited slower growth than those with the control (Figure 5(a)). One month after the first dose of antagomir, tumor size (Figure 5(b)) and weight (Figure 5(c)) were significantly decreased. Next, we investigated whether the inhibition of miR-25 reduces lung cancer cell metastasis *in vivo* by injecting A549 cells through the tail vein. One week later, mice received the miR-25 antagomir or control. We examined the lungs and livers of the host mice one month after antagomir treatment (Figure 5(d)). As shown in Figures 5(e), 5(f), and 5(h), lung metastases were found in 100% of mice and liver metastases in 30% of mice in the control group; in the miR-25 antagomir group, 60% of lung metastases and 0% of liver metastases were observed. In addition, the 60% of lung metastases are micro metastases. The lung histology indicated that the number of metastases in the antagomir group was smaller than the control (Figure 5(g)). In addition, immunohistochemistry analysis showed that the expression of LATS2 and E-cadherin was noticeably higher, while that of Vimentin and MMP9 was lower in the lung metastases from mice treated with the miR-25 antagomir than from the control mice (Figure 5(i)). These results implicate that the inhibition of miR-25 significantly reduces tumor growth and metastasis of lung cancer by elevating LATS2 expression *in vivo*.

4. Discussion

Lung cancer is a major cause of cancer death worldwide [28]. Metastasis, for the most part, is responsible for the high mortality of lung cancer, underlying the urgency to find novel therapeutic targets for metastasis. Given that miRNAs are frequently dysregulated in cancer, more and more researchers are investigating oncogenic or tumor-suppressive miRNAs in lung cancer. The expression of miR-25, miR-26a, miR-127, and miR-134/miR-487b/miR-655 cluster was upregulated in lung cancer cells, and knock-down of these miRNAs suppressed cell proliferation and invasion [29–32]. For miR-218, miR-335, miR-200c, and miR-194 that were downregulated in lung cancer, their overexpression resulted in the reduced cell growth, migration, and invasion [33–36].

A previous report demonstrates that miR-25 is significantly upregulated by oxidative stress [22], supporting miR-25 as a potential drug target for antioxidative therapy. Our studies indicated that miR-25 was upregulated in the plasma of lung cancer patients and it promoted cell proliferation and inhibited apoptosis in lung cancer cells by targeting *TP53* and *MOAPI* [20, 21]. In the present study, we found that miR-25 expression was elevated in both the tissues of NSCLC patients and lung cancer cell lines. NSCLC patients with higher expression of miR-25 exhibited worse overall survival than those with lower expression of miR-25. Furthermore, the overexpression of miR-25 in A549 and H1299 cells enhanced cell viability, migration, and invasion, while the inhibition of miR-25 showed the opposite effects. Our results, in combination with previous studies, imply that miR-25 is an important biomarker for lung cancer diagnosis and a promising drug target for lung cancer metastasis.

To investigate the underlying mechanisms of miR-25 in enhancing lung cancer cell metastasis, we identified *LATS2* as a novel target of miR-25. *LATS2* plays a critical role in

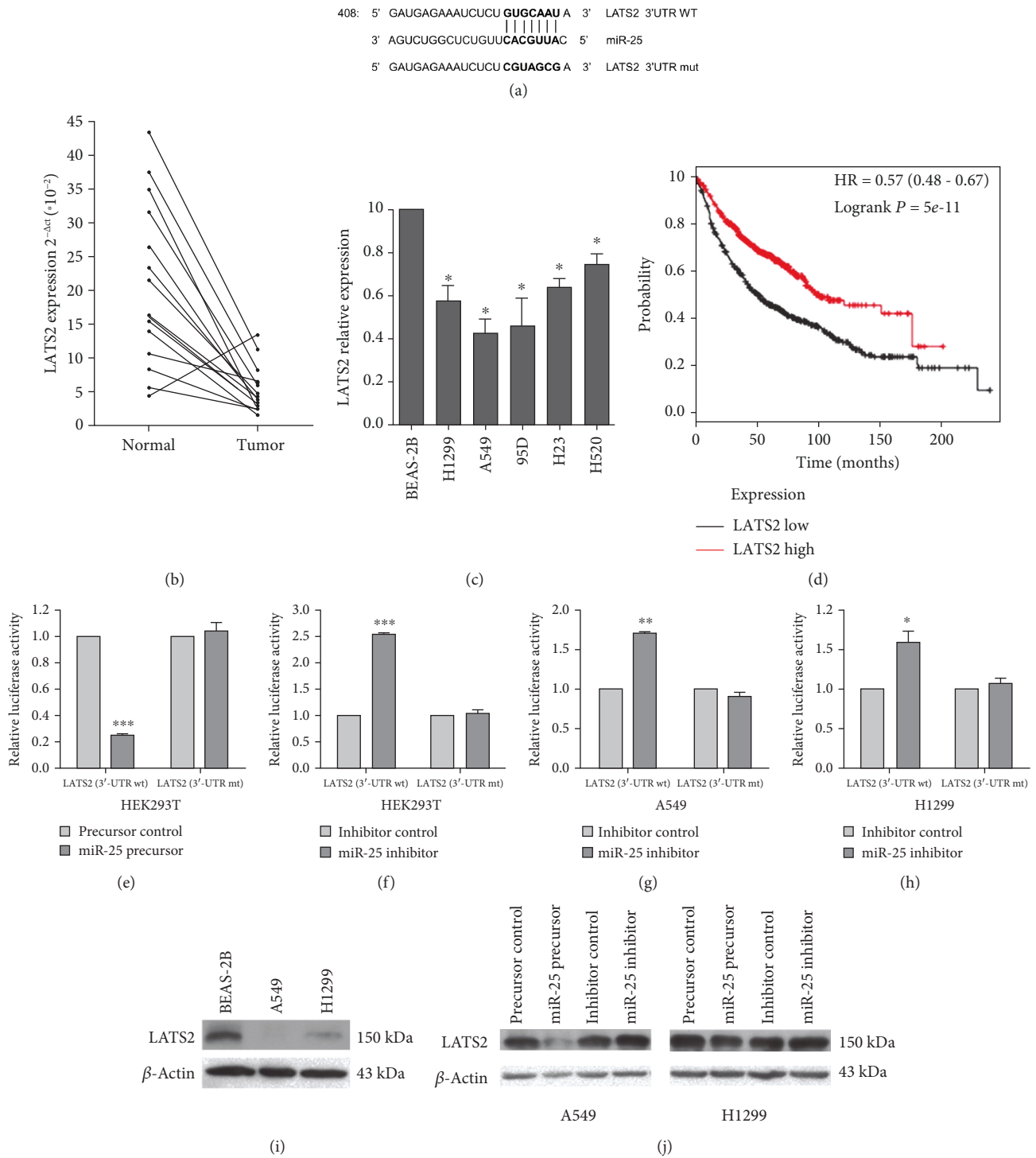


FIGURE 3: LATS2 is a target gene of miR-25 [21]. (a) The predicted binding site of miR-25 in the 3' UTR of LATS2 from miRBase. The mutated LATS2 3' UTR-binding site is indicated. (b) LATS2 expression in 15 pairs of NSCLC tissues and adjacent normal tissues by qRT-PCR. (c) LATS2 expression in NSCLC cell lines and the noncancerous lung epithelial cell line BEAS-2B. (d) Kaplan-Meier curve for overall survival in lung cancer patients with high or low LATS2 expression. Data were taken from TCGA. (e, f) Luciferase reporter assays in HEK-293 cells. (g, h) Luciferase reporter assays in H1299 cells. HEK-293T, A549, and H1299 cells were cotransfected with pRL-TK carrying a wild-type or mutant 3' UTR of LATS2 and the miR-25 precursor (60 ng) or the miR-25 inhibitor (10 pmol), and the luciferase activity was measured 48 h posttransfection. (i) Western blot assays for LATS2 in A549, H1299, and BEAS-2B cells. (j) Western blot analysis of LATS2 in A549 and H1299 cells transfected with miR-25 precursor or the miR-25 inhibitor. Experiments in this section were performed using our documented protocols [21]. Results were presented as the mean \pm SD. * $P < 0.05$ and *** $P < 0.001$.

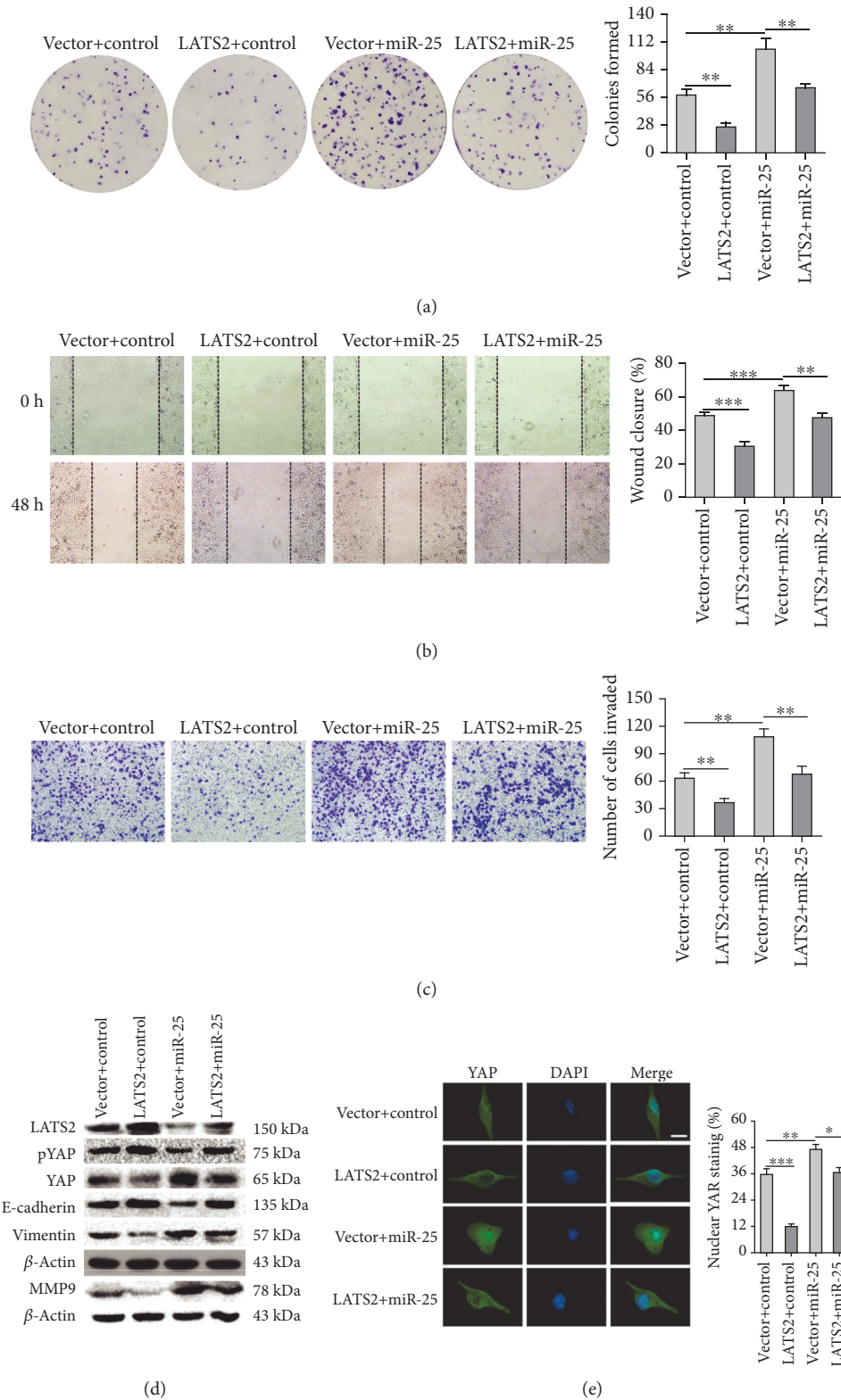
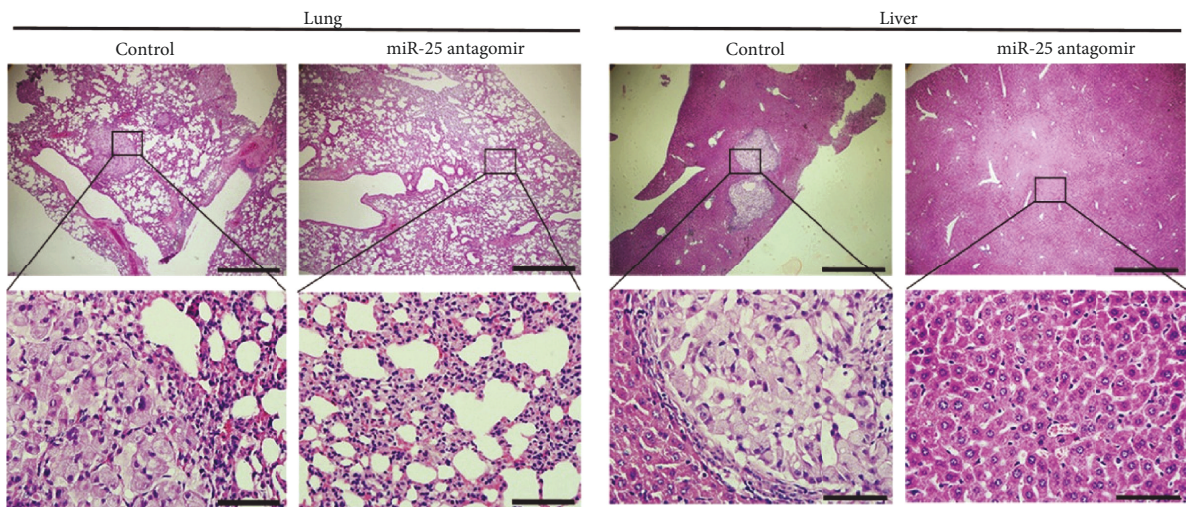
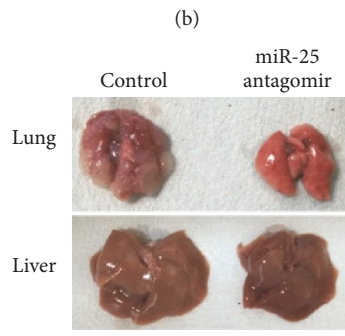
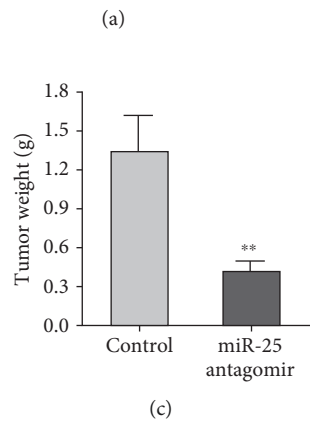
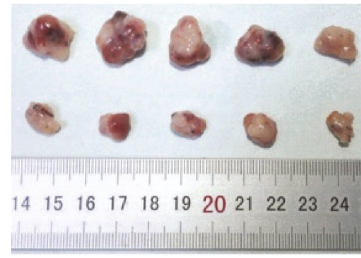
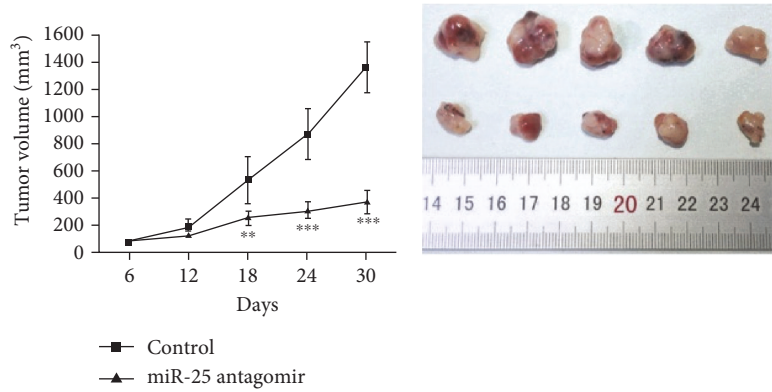
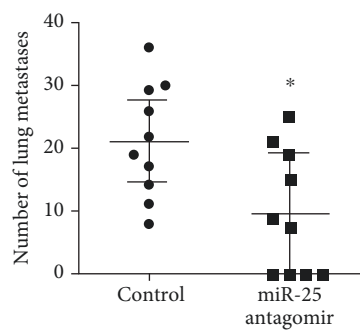


FIGURE 4: The effects of LATS2 expression on A549 cell proliferation, migration, and invasion. (a) Colony formation of A549 cells transfected with LATS2, miR-25, or the combination of both miR-25 and LATS2 plasmids. (b, c) Wound healing and transwell assays for migration and invasion capacities of A549 cells transfected with miR-25 and/or LATS2. (d) Western blot assays for LATS2, downstream effectors of the Hippo pathway (phosphorylated YAP and YAP), and metastasis-related proteins (E-cadherin, Vimentin, and MMP9) in A549 cells transfected with miR-25 and/or LATS2. Results were presented as the mean \pm SD. (e) Immunofluorescence assay for nuclear translocation of YAP protein. Representative immunofluorescent images of YAP staining were shown in the left panel (green: YAP; blue: nuclear; scale bar, 10 μ m). The nuclear localization of YAP is quantified in the right panel by ImageJ software. * $P < 0.05$, ** $P < 0.01$, and *** $P < 0.001$.



Group	Metastasis	P value
Control	10/10	
miR-25 antagonist	6/10	0.025



Group	Metastasis	P value
Control	3/10	
miR-25 antagonist	0/10	0.06

(f)

(g)

(h)

FIGURE 5: Continued.

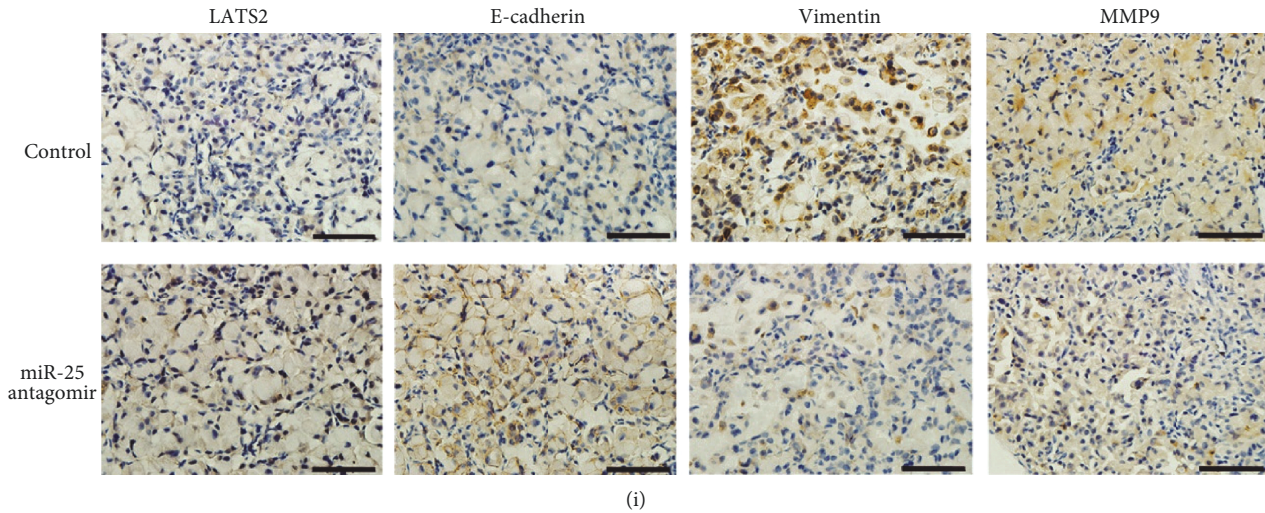


FIGURE 5: miR-25 antagomir inhibits lung cancer growth and metastasis in mouse xenografts. (a) Time course of tumor volumes from immunodeficient mice treated with the miR-25 antagomir or a control. Results were presented as the mean \pm SD. $**P < 0.01$ and $***P < 0.001$. (b, c) The image and the weight of xenograft tumors one month after the treatment. Mean \pm SD was shown. $**P < 0.01$. (d) Representative images of mouse lungs and livers. (e) Histological morphology of mouse lungs and livers by HE staining. The magnification of the upper row images was 40x, bar scale = 500 μ m. The magnification of the bottom row images was 400x, bar scale = 50 μ m. (f, h) The incidence of lung and liver metastasis in mice after tail intravenous injections with the miR-25 antagomir was shown in the table. (g) Quantification of the metastasis nodules in the lungs of each group ($n = 10$). $*P < 0.05$. (i) Representative images of immunohistochemical analysis of LATS2, E-cadherin, Vimentin, and MMP9 in lung metastasis (magnification, 400x, bar scale = 50 μ m). Brown represented the target protein in IHC, and blue represented nuclear staining.

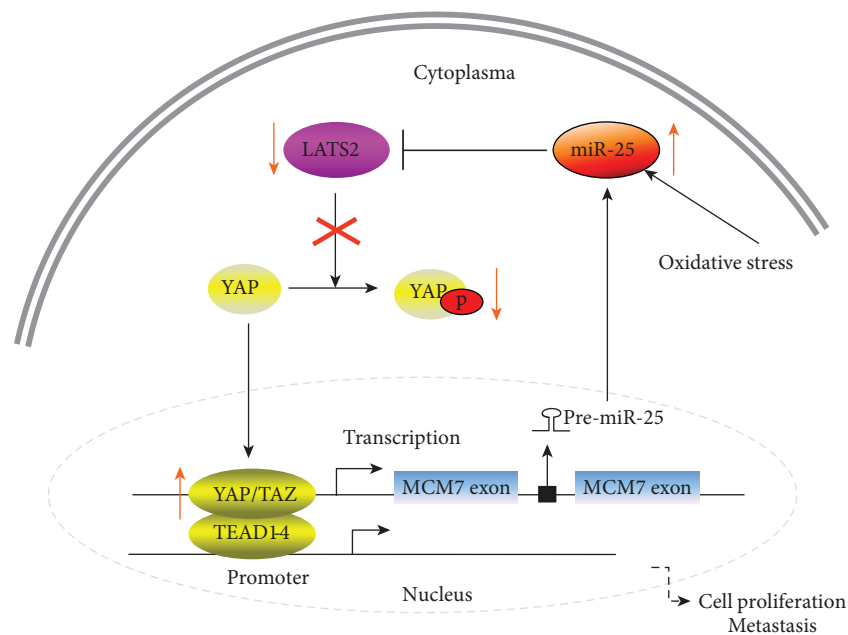


FIGURE 6: Schematic presentation of a positive feedback loop involving miR-25/LATS2/YAP/TAZ/TEAD/MCM7/miR-25 in lung cancer.

the Hippo signaling pathway [37]. Accumulating evidence supports that the LATS family of human tumor suppressors (LATS1 and LATS2) is a new governor of cell homeostasis [38] and LATS2 is downregulated in many cancers, such as prostate cancer [39] and colon cancer [40]. We showed that LATS2 was downregulated in tumor tissues of NSCLC patients and lung cancer cell lines, in agreement with a previ-

ous report [41]. As the mRNA levels of LATS2 and miR-25 expression were reversed in NSCLC, we further investigated the regulatory mechanism involved in them. As expected, a luciferase reporter assay and western blot analysis identified that LATS2 was a direct target gene of miR-25 in lung cancer. Overexpression of LATS2 reversed the effects of miR-25 on cell proliferation, migration, and invasion. More importantly,

the downstream effectors of LATS2 in the Hippo signaling pathway, YAP, phosphorylated YAP, E-cadherin, Vimentin, and MMP9 were all altered by modulating the expression of miR-25 and/or LATS2. Meanwhile, the enhanced nuclear accumulation of YAP by miR-25 overexpression in A549 cells was reversed by cotransfection with LATS2. In addition, the *in vivo* mouse xenograft experiments demonstrated that the inhibition of miR-25 suppressed tumor growth and lung cancer metastasis. Moreover, immunohistochemical analysis suggested that the slower tumor growth rate and the reduced metastasis by miR-25 inhibition were, at least in part, due to the upregulation of LATS2 and E-cadherin expression and the downregulation of Vimentin and MMP9. Collectively, these data support that miR-25 is an important regulator of the key kinase LATS2 in the Hippo pathway and provided new insights into the upstream regulation of Hippo signaling in lung cancer.

Previous reports showed that the host gene of miR-25, *MCM7*, was upregulated upon YAP or TAZ overexpression in MCF10A cells [42, 43]. *MCM7* was found to be a target of the Hippo pathway transcriptional coactivators YAP/TAZ by ChIP-seq in breast cancer cells [44]. In line with these results, YAP directly bound to the *MCM7* enhancer in NSCLC cells and elicited the oncogenic role of YAP/TAZ through modulation of a bioncogenic locus consisting of *MCM7* and its three hosted miRNAs [45]. In our study, we identified that LATS2 was a direct target of miR-25 in lung cancer. Given that LATS2 is an upstream regulator of YAP in the Hippo pathway, we summarize a positive feedback loop pathway in NSCLC (Figure 6); miR-25 overexpression, induced by oxidative stress in NSCLC, inhibits LATS2 expression, which reduces the phosphorylation of YAP, promoting the translocation of YAP oncoprotein from the cytoplasm to the nucleus. YAP/TAZ cooperates with the TEAD cotranscriptional activators in the nucleus and binds to a distal enhancer around the *MCM7* promoter. Upregulated *MCM7* and the miR-106b-25 cluster, in turn, inhibit the expression of LATS2. Additionally, excessive YAP/TAZ/TEAD cotranscriptional activators in the nucleus promote the transcription of genes involved in cell proliferation and metastasis. This positive feedback loop underscores the oncogenic role of miR-25 in promoting lung cancer cell proliferation and metastasis and may explain why miR-25 is upregulated in lung cancer.

Taken together, the present study demonstrate the oncogenic role of miR-25 in lung cancer. Oxidative stress-induced miR-25 overexpression promotes cell proliferation, migration, and invasion in NSCLC by directly inhibiting LATS2 and subsequently increasing downstream protein YAP nuclear translocation, constituting a positive feedback loop to regulate NSCLC metastasis. These findings implicate miR-25 as a promising therapeutic target for lung cancer metastasis.

Data Availability

The data used to support the findings of this study are available from the corresponding authors upon request.

Disclosure

The study sponsors do not take any role in the design of the study, data collection, analysis and interpretation, and the writing of the manuscript.

Conflicts of Interest

The authors declare no potential conflicts of interest.

Authors' Contributions

TW, HH, TZ, and LJ carried out the molecular biology analysis, participated in the design of the study and the clinical specimen collection, and drafted the manuscript. XL, SL, CZ, WC, GY, and YN carried out the clinical specimen collection, participated in the data analysis, and performed the statistical analysis. YL and ZL conceived and designed the study, participated in the data analysis and coordination, and helped in drafting the manuscript. All authors read and approved the final manuscript. Tangwei Wu, Hui Hu, Tianzhu Zhang, and Liyuan Jiang contributed equally to this work.

Acknowledgments

This project was supported by grants from the Yellow Crane Talent Plan Foundation, the Key Project of Natural Science Foundation of Hubei Province (2015CFA078), Research Fund of Wuhan Public Health Bureau (WX14C13, WX14B10, WX15A12, and WX18Y11), and Youth Foundation of Wuhan Central Hospital (YQ14A01 and YQ15A03).

References

- [1] R. L. Siegel, K. D. Miller, and A. Jemal, "Cancer statistics, 2018," *CA: A Cancer Journal for Clinicians*, vol. 68, no. 1, pp. 7–30, 2018.
- [2] L. A. Torre, F. Bray, R. L. Siegel, J. Ferlay, J. Lortet-Tieulent, and A. Jemal, "Global cancer statistics, 2012," *CA: A Cancer Journal for Clinicians*, vol. 65, no. 2, pp. 87–108, 2015.
- [3] Z. Chen, C. M. Fillmore, P. S. Hammerman, C. F. Kim, and K. K. Wong, "Non-small-cell lung cancers: a heterogeneous set of diseases," *Nature Reviews Cancer*, vol. 14, no. 8, pp. 535–546, 2014.
- [4] X. Wang and A. A. Adjei, "Lung cancer and metastasis: new opportunities and challenges," *Cancer and Metastasis Reviews*, vol. 34, no. 2, pp. 169–171, 2015.
- [5] E. Filaire, C. Dupuis, G. Galvaing et al., "Lung cancer: what are the links with oxidative stress, physical activity and nutrition," *Lung Cancer*, vol. 82, no. 3, pp. 383–389, 2013.
- [6] D. P. Bartel, "MicroRNAs: target recognition and regulatory functions," *Cell*, vol. 136, no. 2, pp. 215–233, 2009.
- [7] H. Chen, H. Pan, Y. Qian, W. Zhou, and X. Liu, "MiR-25-3p promotes the proliferation of triple negative breast cancer by targeting BTG2," *Molecular Cancer*, vol. 17, no. 1, p. 4, 2018.
- [8] C. W. Lin, Y. L. Chang, Y. C. Chang et al., "MicroRNA-135b promotes lung cancer metastasis by regulating multiple targets in the Hippo pathway and LZTS1," *Nature Communications*, vol. 4, no. 1, article 1877, 2013.

- [9] C. Kim, Y. Hong, H. Lee, H. Kang, and E. K. Lee, "MicroRNA-195 desensitizes HCT116 human colon cancer cells to 5-fluorouracil," *Cancer Letters*, vol. 412, pp. 264–271, 2018.
- [10] Y. Yang, K. Chen, Y. Zhou, Z. Hu, S. Chen, and Y. Huang, "Application of serum microRNA-9-5p, 21-5p, and 223-3p combined with tumor markers in the diagnosis of non-small-cell lung cancer in Yunnan in southwestern China," *Oncotargets and Therapy*, vol. 11, pp. 587–597, 2018.
- [11] R. Garzon, G. Marcucci, and C. M. Croce, "Targeting microRNAs in cancer: rationale, strategies and challenges," *Nature Reviews Drug Discovery*, vol. 9, no. 10, pp. 775–789, 2010.
- [12] R. Rupaimoole and F. J. Slack, "MicroRNA therapeutics: towards a new era for the management of cancer and other diseases," *Nature Reviews Drug Discovery*, vol. 16, no. 3, pp. 203–222, 2017.
- [13] S. C. Kao, M. Fulham, K. Wong et al., "A significant metabolic and radiological response after a novel targeted microRNA-based treatment approach in malignant pleural mesothelioma," *American Journal of Respiratory and Critical Care Medicine*, vol. 191, no. 12, pp. 1467–1469, 2015.
- [14] C. Caiazza and M. Mallardo, "The roles of miR-25 and its targeted genes in development of human cancer," *MicroRNA*, vol. 5, no. 2, pp. 113–119, 2016.
- [15] J. Zhang, X. Gong, K. Tian et al., "miR-25 promotes glioma cell proliferation by targeting CDKN1C," *Biomedicine & Pharmacotherapy*, vol. 71, pp. 7–14, 2015.
- [16] B. S. Li, Q. F. Zuo, Y. L. Zhao et al., "MicroRNA-25 promotes gastric cancer migration, invasion and proliferation by directly targeting transducer of ERBB2, 1 and correlates with poor survival," *Oncogene*, vol. 34, no. 20, pp. 2556–2565, 2015.
- [17] Z. Zeng, Y. Li, Y. Pan et al., "Cancer-derived exosomal miR-25-3p promotes pre-metastatic niche formation by inducing vascular permeability and angiogenesis," *Nature Communications*, vol. 9, no. 1, p. 5395, 2018.
- [18] J. Song and Y. Li, "miR-25-3p reverses epithelial-mesenchymal transition via targeting Sema4C in cisplatin-resistance cervical cancer cells," *Cancer Science*, vol. 108, no. 1, pp. 23–31, 2017.
- [19] E. Zoni, G. van der Horst, A. F. van de Merbel et al., "miR-25 modulates invasiveness and dissemination of human prostate cancer cells via regulation of α_v - and α_6 -integrin expression," *Cancer Research*, vol. 75, no. 11, pp. 2326–2336, 2015.
- [20] M. Kumar, Z. Lu, A. A. L. Takwi et al., "Negative regulation of the tumor suppressor p53 gene by microRNAs," *Oncogene*, vol. 30, no. 7, pp. 843–853, 2011.
- [21] T. Wu, W. Chen, D. Kong et al., "miR-25 targets the modulator of apoptosis 1 gene in lung cancer," *Carcinogenesis*, vol. 36, no. 8, pp. 925–935, 2015.
- [22] Q. Shi, W. Zhang, S. Guo et al., "Oxidative stress-induced overexpression of miR-25: the mechanism underlying the degeneration of melanocytes in vitiligo," *Cell Death & Differentiation*, vol. 23, no. 3, pp. 496–508, 2016.
- [23] T. Wu, W. Chen, S. Liu et al., "Huaier suppresses proliferation and induces apoptosis in human pulmonary cancer cells via upregulation of miR-26b-5p," *FEBS Letters*, vol. 588, no. 12, pp. 2107–2114, 2014.
- [24] Y. Bao, K. Nakagawa, Z. Yang et al., "A cell-based assay to screen stimulators of the Hippo pathway reveals the inhibitory effect of dobutamine on the YAP-dependent gene transcription," *Journal of Biochemistry*, vol. 150, no. 2, pp. 199–208, 2011.
- [25] S. Feng, W. Pan, Y. Jin, and J. Zheng, "MiR-25 promotes ovarian cancer proliferation and motility by targeting LATS2," *Tumor Biology*, vol. 35, no. 12, pp. 12339–12344, 2014.
- [26] M. Zhang, X. Wang, W. Li, and Y. Cui, "miR-107 and miR-25 simultaneously target LATS2 and regulate proliferation and invasion of gastric adenocarcinoma (GAC) cells," *Biochemical and Biophysical Research Communications*, vol. 460, no. 3, pp. 806–812, 2015.
- [27] J. S. Mo, H. W. Park, and K. L. Guan, "The Hippo signaling pathway in stem cell biology and cancer," *EMBO Reports*, vol. 15, no. 6, pp. 642–656, 2014.
- [28] W. Chen, R. Zheng, P. D. Baade et al., "Cancer statistics in China, 2015," *CA: A Cancer Journal for Clinicians*, vol. 66, no. 2, pp. 115–132, 2016.
- [29] X. Ding, T. Zhong, L. Jiang, J. Huang, Y. Xia, and R. Hu, "miR-25 enhances cell migration and invasion in non-small-cell lung cancer cells via ERK signaling pathway by inhibiting KLF4," *Molecular Medicine Reports*, vol. 17, no. 5, pp. 7005–7016, 2018.
- [30] G. Lin, B. Liu, Z. Meng et al., "MiR-26a enhances invasive capacity by suppressing GSK3 β in human lung cancer cells," *Experimental Cell Research*, vol. 352, no. 2, pp. 364–374, 2017.
- [31] L. Shi, Y. Wang, Z. Lu et al., "miR-127 promotes EMT and stem-like traits in lung cancer through a feed-forward regulatory loop," *Oncogene*, vol. 36, no. 12, pp. 1631–1643, 2017.
- [32] K. Kitamura, M. Seike, T. Okano et al., "MiR-134/487b/655 cluster regulates TGF- β -induced epithelial-mesenchymal transition and drug resistance to gefitinib by targeting MAGI2 in lung adenocarcinoma cells," *Molecular Cancer Therapeutics*, vol. 13, no. 2, pp. 444–453, 2014.
- [33] Y. Yang, L. Ding, Q. Hu et al., "MicroRNA-218 functions as a tumor suppressor in lung cancer by targeting IL-6/STAT3 and negatively correlates with poor prognosis," *Molecular Cancer*, vol. 16, no. 1, p. 141, 2017.
- [34] J. Liu, T. Bian, J. Feng et al., "miR-335 inhibited cell proliferation of lung cancer cells by target Tra2 β ," *Cancer Science*, vol. 109, no. 2, pp. 289–296, 2018.
- [35] J. Li, Q. Tan, M. Yan et al., "miRNA-200c inhibits invasion and metastasis of human non-small cell lung cancer by directly targeting ubiquitin specific peptidase 25," *Molecular Cancer*, vol. 13, no. 1, p. 166, 2014.
- [36] X. Wu, T. Liu, O. Fang, L. J. Leach, X. Hu, and Z. Luo, "miR-194 suppresses metastasis of non-small cell lung cancer through regulating expression of BMP1 and p27(kip1)," *Oncogene*, vol. 33, no. 12, pp. 1506–1514, 2014.
- [37] L. Hoa, Y. Kulaberoglu, R. Gundogdu et al., "The characterisation of LATS2 kinase regulation in Hippo-YAP signalling," *Cellular Signalling*, vol. 28, no. 5, pp. 488–497, 2016.
- [38] S. Visser and X. Yang, "LATS tumor suppressor: a new governor of cellular homeostasis," *Cell Cycle*, vol. 9, no. 19, pp. 3892–3903, 2010.
- [39] Y. Guo, J. Cui, Z. Ji et al., "miR-302/367/LATS2/YAP pathway is essential for prostate tumor-propagating cells and promotes the development of castration resistance," *Oncogene*, vol. 36, no. 45, pp. 6336–6347, 2017.
- [40] J. Li, X. Chen, X. Ding et al., "LATS2 suppresses oncogenic Wnt signaling by disrupting β -catenin/BCL9 interaction," *Cell Reports*, vol. 5, no. 6, pp. 1650–1663, 2013.
- [41] S. Y. Luo, K. Y. Sit, A. D. L. Sihoe et al., "Aberrant large tumor suppressor 2 (LATS2) gene expression correlates with EGFR

- mutation and survival in lung adenocarcinomas,” *Lung Cancer*, vol. 85, no. 2, pp. 282–292, 2014.
- [42] B. Zhao, X. Ye, J. Yu et al., “TEAD mediates YAP-dependent gene induction and growth control,” *Genes & Development*, vol. 22, no. 14, pp. 1962–1971, 2008.
- [43] H. Zhang, C. Y. Liu, Z. Y. Zha et al., “TEAD transcription factors mediate the function of TAZ in cell growth and epithelial-mesenchymal transition,” *Journal of Biological Chemistry*, vol. 284, no. 20, pp. 13355–13362, 2009.
- [44] F. Zanconato, M. Forcato, G. Battilana et al., “Genome-wide association between YAP/TAZ/TEAD and AP-1 at enhancers drives oncogenic growth,” *Nature Cell Biology*, vol. 17, no. 9, pp. 1218–1227, 2015.
- [45] F. Lo Sardo, M. Forcato, A. Sacconi et al., “MCM7 and its hosted miR-25, 93 and 106b cluster elicit YAP/TAZ oncogenic activity in lung cancer,” *Carcinogenesis*, vol. 38, no. 1, pp. 64–75, 2017.

Research Article

Thioredoxin Reductase-1 Inhibition Augments Endogenous Glutathione-Dependent Antioxidant Responses in Experimental Bronchopulmonary Dysplasia

Stephanie B. Wall,^{1,2} Rachael Wood,¹ Katelyn Dunigan,^{1,2} Qian Li,^{1,2} Rui Li,^{1,2} Lynette K. Rogers ³ and Trent E. Tipple ^{1,2}

¹Neonatal Redox Biology Laboratory, University of Alabama at Birmingham, Birmingham, AL, USA

²Division of Neonatology, University of Alabama at Birmingham, Birmingham, AL, USA

³Center for Perinatal Research, The Research Institute at Nationwide Children's Hospital, Columbus, OH, USA

Correspondence should be addressed to Trent E. Tipple; ttipple@peds.uab.edu

Received 20 October 2018; Accepted 25 November 2018; Published 21 January 2019

Academic Editor: Demetrios Kouretas

Copyright © 2019 Stephanie B. Wall et al. This is an open access article distributed under the Creative Commons Attribution License, which permits unrestricted use, distribution, and reproduction in any medium, provided the original work is properly cited.

Background. Aurothioglucose- (ATG-) mediated inhibition of thioredoxin reductase-1 (TXNRD1) improves alveolarization in experimental murine bronchopulmonary dysplasia (BPD). Glutathione (GSH) mediates susceptibility to neonatal and adult oxidative lung injury. We have previously shown that ATG attenuates hyperoxic lung injury and enhances glutathione- (GSH-) dependent antioxidant defenses in adult mice. **Hypothesis.** The present studies evaluated the effects of TXNRD1 inhibition on GSH-dependent antioxidant defenses in newborn mice *in vivo* and lung epithelia *in vitro*. **Methods.** Newborn mice received intraperitoneal ATG or saline prior to room air or 85% hyperoxia exposure. Glutamate-cysteine ligase (GCL) catalytic (Gclc) and modifier (Gclm) mRNA levels, total GSH levels, total GSH peroxidase (GPx) activity, and Gpx2 expression were determined in lung homogenates. *In vitro*, murine transformed club cells (mtCCs) were treated with the TXNRD1 inhibitor auranofin (AFN) or vehicle in the presence or absence of the GCL inhibitor buthionine sulfoximine (BSO). **Results.** *In vivo*, ATG enhanced hyperoxia-induced increases in Gclc mRNA levels, total GSH contents, and GPx activity. *In vitro*, AFN increased Gclm mRNA levels, intracellular and extracellular GSH levels, and GPx activity. BSO prevented AFN-induced increases in GSH levels. **Conclusions.** Our data are consistent with a model in which TXNRD1 inhibition augments hyperoxia-induced GSH-dependent antioxidant responses in neonatal mice. Discrepancies between *in vivo* and *in vitro* results highlight the need for methodologies that permit accurate assessments of the GSH system at the single-cell level.

1. Introduction

Bronchopulmonary dysplasia (BPD) is the most common respiratory morbidity of prematurity and is characterized by respiratory insufficiency. Although improvements have been made in the prevention and treatment of BPD, the pathophysiology is complex and involves activation of injury and repair pathways in developing lungs [1]. Infants with BPD have poor lung function due to inadequate alveolarization often resulting in lifelong decreases in pulmonary function [2]. Supplemental oxygen, while necessary to overcome

ventilation-perfusion mismatch, contributes to the development of BPD by damaging delicate lung tissues [3]. Premature infants are particularly vulnerable to oxygen toxicity due to poorly developed antioxidant systems [4–6].

Thioredoxin reductase-1 (TXNRD1) reduces oxidized thioredoxin-1 (Trx1). Previous studies from our group have demonstrated that TXNRD1 inhibition protects against the deleterious effects of hyperoxic exposure [7–9]. Our data have consistently indicated that activation of nuclear factor erythroid 2-related factor 2 (Nrf2) is a primary mechanism of protection afforded by TXNRD1 inhibitors, which is

consistent with other reports [10]. One cytoprotective pathway activated by Nrf2 promotes *de novo* synthesis of the antioxidant glutathione (GSH).

GSH is the most abundant low-molecular-weight antioxidant [11] and protects the lung from hyperoxic injury [12]. *De novo* GSH synthesis is controlled by the enzymes GSH synthetase and γ -glutamate cysteine ligase (GCL). GCL is a heterodimer consisting of catalytic (Gclc) and modifier (Gclm) subunits. GCL is the rate-limiting step in *de novo* GSH synthesis [13, 14]. Once produced, GSH serves many important intracellular and extracellular roles in the lung including acting as a cofactor for enzymatic antioxidant pathways in cells and epithelial lining fluid, scavenging free radicals, protecting against oxidative species, aiding metabolism of xenobiotics, and regulating inflammation [15]. Intracellularly, most GSH are either free or protein-bound. Free GSH, under normal conditions, is mostly reduced. Under highly oxidizing conditions, two GSH molecules become disulfide linked resulting in the formation of GSSG. GSSG can accumulate within tissues, and the ratio of GSH to GSSG is commonly employed as an index of redox status. Previous reports have established associations between decreased plasma and tracheal aspirate GSH/GSSG ratios and BPD incidence in human infants [16]. The majority of GSH-mediated reductive reactions involve catalysis. GSH peroxidases (GPx), of which there are at least 8 known isoforms, are selenoenzymes, so named due to the presence of an active site selenocysteine (Sec) residue. GPx catalyzes the reduction of peroxides by GSH resulting in the formation of GSSG. GPX2 is an inducible isoform that may be protective in settings of oxidative stress such as cigarette smoke exposure [17]. Furthermore, hyperoxia-induced increases in GPX2 are Nrf2-dependent in the murine lung [18].

Our group identified TXNRD1 inhibition as a novel strategy to prevent lung injury. Administration of the TXNRD1 inhibitor aurothioglucose (ATG) is protective in murine models of acute lung injury (ALI), and protection is associated with increases in GSH-dependent antioxidant defenses [7, 19]. More recently, our group demonstrated that ATG inhibited pulmonary TXNRD1 activity and significantly attenuated hyperoxic lung injury in a neonatal mouse model of BPD [9]. Given these collective findings, the present studies tested the hypothesis that ATG-mediated attenuation of murine neonatal hyperoxic lung injury correlates with enhanced GSH-dependent antioxidant defenses.

2. Methods

2.1. Animal Model. All mouse work was performed using protocols approved by the University of Alabama at Birmingham IACUC. Four time-dated pregnant C3H/HeN mice (Envigo) were allowed to undergo a natural delivery, and pups of both sexes from all litters were randomly mixed and equally distributed between dams. Within 12 h of birth, pups received either 25 mg/kg aurothioglucose (ATG) or saline (SA) intraperitoneally (i.p.). Pups were then exposed to either room air (RA, 21% O₂) or hyperoxia (85% O₂) for 24, 48, or 168 h which corresponds to postnatal days (d) 1, 3, and 7, respectively, with the day of birth being 0 d. We

previously reported the effects of hyperoxia and ATG on lung and body weights at day 7 in this model [9]. Hyperoxic exposures were performed in a custom-made plexiglass chamber with O₂ controlled using a BioSpherix ProOx P110 controller (Parish, NY). To avoid hyperoxic mortality, dams were rotated out of hyperoxia with a paired room air dam daily. Upon completion of exposure, pups were euthanized with ketamine/xylazine (200/20 mg/kg, i.p.) and lungs were collected within 5 min of euthanasia. Tissues were flash frozen in liquid nitrogen. For GSH assays, lungs were cardiac perfused with 10 ml of PBS before collection. Tissues were stored at -80°C until assessments were performed.

2.2. Cell Culture. Murine (mouse) transformed club cells (mtCCs, Dr. Francisco Demayo (NIH)) were maintained in DMEM supplemented with 10% FBS and 50 U/ml penicillin/streptomycin (Gibco). Cells were plated at equal densities and were treated at ~80-90% confluence with 0.5 μ M AFN (Sigma) or vehicle control (dimethyl sulfoxide, DMSO, Fisher) for up to 24 hr. Buthionine sulfoximine (BSO) was dissolved in sterile phosphate-buffered saline and used at a final concentration of 22.5 μ M in cell media.

2.3. Sample Preparation. Approximately, 10 μ g of tissue was homogenized (on ice, Dounce homogenizer) in 100 μ l of lysis buffer consisting of 10 mM Tris buffer (pH 7.4), containing 0.1% Triton X-100 and 100 μ M diethylenetriamine pentaacetic acid (DTPA) with protease inhibitors (Thermo Scientific). For cell culture experiments, cells were washed once in PBS and were lysed in the buffer described above. Tissue and cell lysates were centrifuged at 20,000 $\times g$ for 10 min, and supernatant was collected. Protein concentrations were determined by the bicinchoninic acid (BCA) assay (Pierce).

2.4. Western Blot. Samples were loaded onto 4-20% Criterion or Mini-PROTEAN TGX gels (Bio-Rad), transferred to PVDF membranes (Trans-Blot, Bio-Rad), blocked with 5% milk in Tris-buffered saline containing 0.05% Tween 20 (TBST), and probed with rabbit anti-GPX2 (ab137431, Abcam; 1:1000 in 5% milk in TBST) followed by a goat anti-rabbit IgG-HRP secondary antibody (sc-2004; Santa Cruz Biotechnology; 1:5000 in TBST). Membranes were developed using Clarity ECL Substrate (Bio-Rad) and imaged using a ChemiDoc System (Bio-Rad). For loading control, membranes were reprobed with a mouse anti- β -actin antibody (sc-47778, Santa Cruz; 1:1000 in milk in TBST) followed by an anti-mouse IgG-HRP secondary antibody (HAF007; R&D Systems; 1:5000 in TBST). Pixel density of GPX2 was normalized to the respective actin band density.

2.5. Quantitative Real-Time Polymerase Chain Reaction (qRT-PCR). Purified RNA (RNeasy and QIAcube; Qiagen, Valencia, CA) was reverse transcribed to cDNA using a PrimeScript RT Master Mix (Takara/Clontech, Mountain View, CA). PCR was performed using a Premix Ex Taq probe (Takara/Clontech) and Rotor-Gene Q instrument (Qiagen) with the primers for 18S (Hs99999901_s1), murine Gclc (Mm00802655_m1), and murine Gclm (Mm00514996_m1) (Applied Biosystems/Thermo Fisher; Foster City, CA). Cycle threshold (Δ CT) values were normalized to 18S, and then,

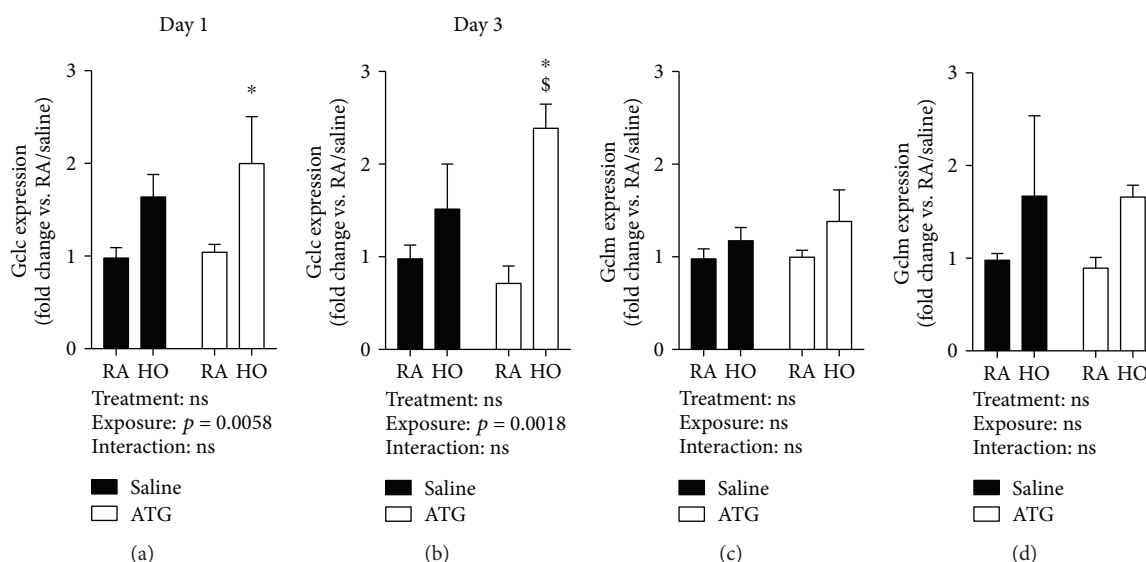


FIGURE 1: Lung Gclc and Gclm mRNA levels. Pups were dosed with saline or 25 mg/kg ATG and exposed to room air (RA) or 85% hyperoxia (HO) for 1 day (a, c) or 3 days (b, d) ($n = 3-6$). Data are expressed as fold change relative to saline/RA. * $p < 0.05$ vs. RA/saline; \$ $p < 0.01$ vs. RA/ATG.

fold changes were calculated relative to saline/room air (RA) using $2^{-\Delta\Delta CT}$.

2.6. GSH Recycling Assay. Total glutathione (expressed as GSH equivalents: $2\text{GSH} + \text{GSSG}$) levels were assessed in cellular lysates by the Tietze recycling assay [20]. Oxidized glutathione (GSSG) was measured by reacting samples with 2-vinylpyridine for 1 h. The reaction was then terminated with triethanolamine (TEA). 3 to 10 μg of tissue homogenate or cell lysate was loaded into a 96-well plate; no more than 20 μg was loaded for GSSG. Absorbance was monitored at 412 nm over 2 minutes in the presence of 0.5 mM dithionitrobenzene (DNTB), 0.24 mM NADPH, and GSH reductase (1:3000) in ammonium sulfate (G3664, Sigma). Standard curves were produced for both GSH and GSSG. Linear regression analysis was used to calculate GSH concentrations that were then normalized to the protein concentration.

2.7. GSH Peroxidase Activity. GPx activity in lung homogenates ($\sim 4-8 \mu\text{g}$) and cells ($\sim 50-70 \mu\text{g}$) was measured via the hydrogen peroxide-dependent consumption of NADPH at 340 nm over 5 minutes in the presence of 0.2 mM NADPH, 1.5 mM reduced GSH, 1.0 mM sodium azide, 0.5 mM DTPA, GSH reductase (1:427, Sigma), and 1.6 mM hydrogen peroxide (Fisher) in 50 mM Tris-HCl buffer at pH 7.0.

2.8. Statistics. Data (expressed as mean \pm SEM) were tested for homogeneity of variances, log-transformed when indicated, and analyzed by 2-way ANOVA (exposure and treatment as independent variables) followed by Tukey's multiple comparison tests using GraphPad Prism[®] 7.0. Significance was accepted at $p < 0.05$.

3. Results

3.1. ATG Enhances GCLC but Not GCLM mRNA Levels in the Lungs of Hyperoxia-Exposed Newborn Mice. ATG inhibits

TXNRD1 in the lungs of hyperoxia-exposed mice [9]. In an adult model of ALI, the protective effects of TXNRD1 inhibition correlated with increased Gclm mRNA levels [7]. Gclc and Gclm expression levels were measured in the lungs from day 1 and 3 pups to test the effects of hyperoxia and ATG on newborn lungs. Two-way ANOVA indicated an independent effect of hyperoxia on Gclc both at day 1 and day 3 (Figure 1). Post hoc analyses indicated significant increases in Gclc levels in the lungs from ATG/hyperoxia mice when compared to saline/RA controls at both 1 d (1.0 ± 0.1 vs. 2.0 ± 0.5 -fold, $p = 0.0456$) (Figure 1(a)) and 3 d (1.0 ± 0.1 vs. 2.4 ± 0.2 -fold, $p = 0.02$) (Figure 1(b)). There were no effects of hyperoxia or ATG on Gclm mRNA levels at either time point (Figures 1(c) and 1(d)).

3.2. Effects of ATG on Lung GSH Levels. ATG-mediated attenuation of lung injury in adult murine models is associated with enhanced lung GSH levels, and protection is GSH-dependent [7, 19]. To determine the effects of hyperoxia and ATG on lung GSH levels in our murine BPD model, tissue GSH and GSSG levels were measured following exposure and treatment as outlined above. At day 1, there were no effects of hyperoxia or ATG on total GSH levels (Figure 2(a)). By day 3, two-way ANOVA indicated independent effects of both hyperoxia and ATG (Figure 2(b)). GSH levels were significantly greater in the lungs from saline/hyperoxia mice ($32.6 \pm 3 \text{ pmol}/\mu\text{g}$) than from saline/RA controls ($18.25 \pm 1 \text{ pmol}/\mu\text{g}$, $p = 0.005$). Compared to saline/RA controls, total GSH levels were significantly greater in the lungs from ATG/hyperoxia mice ($42.3 \pm 3 \text{ pmol}/\mu\text{g}$, $p < 0.001$). Though GSH levels in the lungs from ATG/hyperoxia mice were greater than those in the lungs from hyperoxia/saline mice, the differences did not reach statistical significance ($p = 0.07$). At day 7, our analyses indicated only an independent effect of hyperoxia on lung GSH levels (Figure 2(c)). There were

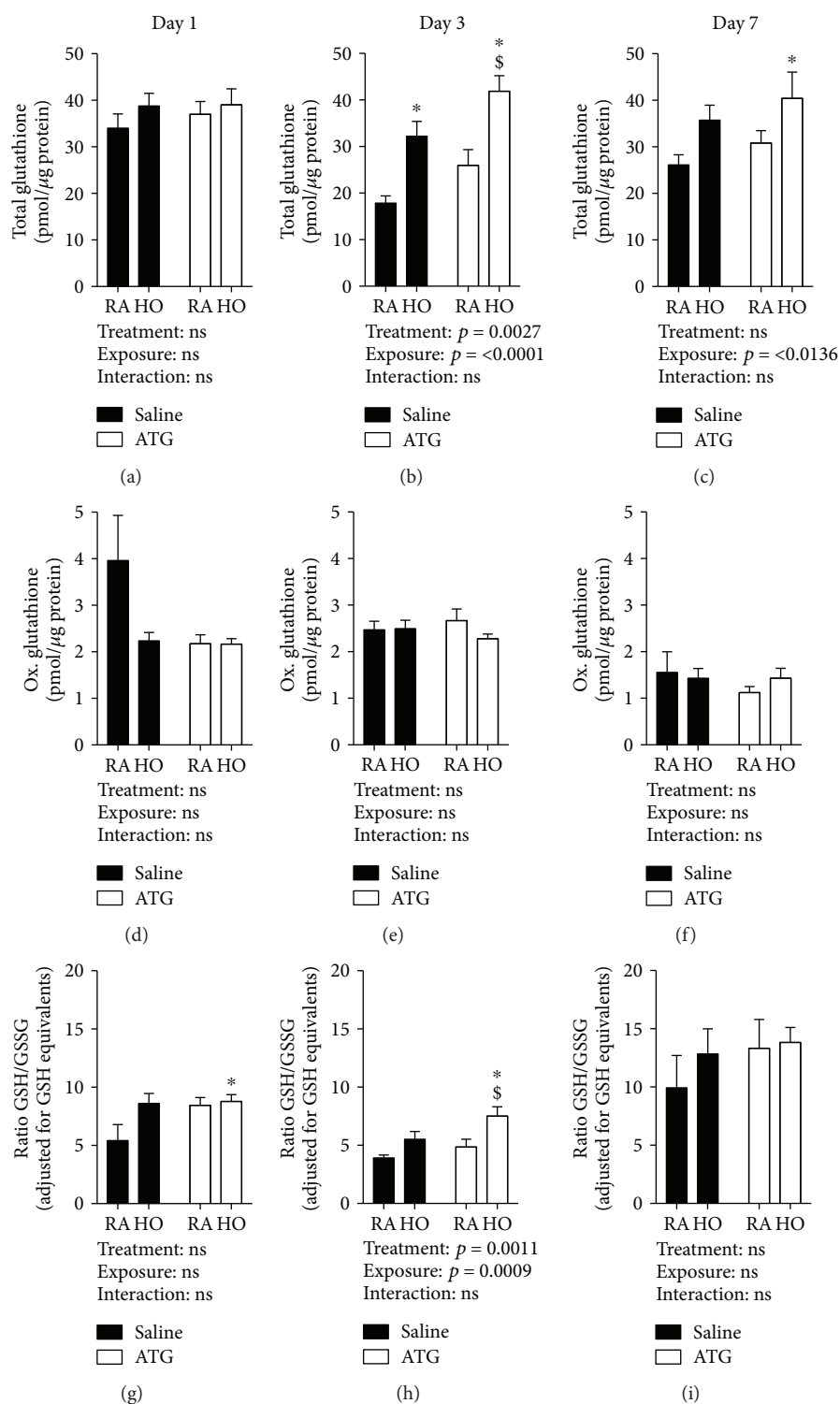


FIGURE 2: Lung glutathione levels. Pups were dosed with either saline or 25 mg/kg ATG and exposed to room air (RA) or hyperoxia (HO) for up to 7 days ($n = 4-6$). Total (a-c) and oxidized glutathione levels were determined (d, e) as described, and ratios of total to oxidized glutathione (adjusted for reduced glutathione equivalents) were calculated (g-i). * $p < 0.05$ vs. saline/RA; \$ $p < 0.05$ vs. ATG/RA.

no effects of hyperoxia exposure or ATG on lung GSSG levels at any time point (Figures 2(d)-2(f)).

GSH/GSSG ratios, commonly employed as an index of redox balance, were calculated and analyzed. Day 3 was the

only time point at which significant differences were identified (Figure 2(h)). Two-way ANOVA indicated effects of hyperoxia and ATG on GSH/GSSG ratios. Ratios were highest in the lungs from ATG/hyperoxia mice (7.7 ± 0.7), which

were significantly different from those in the lungs from saline/RA (4.1 ± 0.1 , $p = 0.001$) and ATG/RA (5.0 ± 0.5 , $p = 0.01$) mice. Calculated GSH/GSSG ratios were greater than those in the lungs from ATG/hyperoxia mice when compared to saline/hyperoxia mice (5.7 ± 0.5); however, the differences did not reach statistical difference ($p = 0.06$).

3.3. Hyperoxia Enhances Lung GPx Protein Expression and Activity. GPX2 is an oxidative stress-inducible GPx isoform in the lung [17]. Thus, we assessed GPX2 protein expression in the lungs from RA- or hyperoxia-exposed neonatal mice treated with saline or ATG. GPX2 expression was not different between groups after day 1 (Figure 3(a)). At day 3, however, two-way ANOVA indicated an independent effect of hyperoxia (Figure 3(b)). Specifically, GPX2 protein levels were approximately 5 times greater in both saline/hyperoxia and ATG/hyperoxia lungs when compared to saline/RA lungs. An independent effect of hyperoxia was also identified at 7 d (Figure 3(c)), and GPX2 protein levels remained 5 times greater in both saline groups.

We cannot exclude the presence of other GPx isoforms in the lung. Nevertheless, measurements of GPx protein expression alone do not directly correlate with total GPx activity. We therefore determined GPx activity in lung homogenates from all 4 groups at days 1, 3, and 7 (Figures 3(d)–3(f)). Developmentally, total lung GPx activity is greatest at day 7 (Figure 3(f)). Though there were no independent effects of hyperoxia or ATG on lung GPx activity at day 1 or 3, our data indicated an independent effect of hyperoxia on GPx activity at day 7 (Figure 3(f)). At this time point, absolute GPx activity was greatest in the lungs from ATG/hyperoxia mice.

3.4. TXNRD1 Inhibition Enhances *Gclm* mRNA Levels in Murine Lung Epithelial Cells. Lung tissue is comprised of more than 40 cell types, and homogenates contain traces of blood or serum even when lungs are perfused prior to harvest. Thus, data derived from lung homogenates may not accurately reflect processes within airway epithelial cells, the cells in which TXNRD1 is primarily expressed [8]. We therefore evaluated the effects of TXNRD1 inhibition on GSH-dependent responses using murine transformed club cells (mtCCs), an SV-40 transformed mouse lung epithelial cell line commonly used by our group. Cells were continuously cultured in the presence or absence of the TXNRD1 inhibitor auranofin (AFN, $0.5 \mu\text{M}$). Consistent with our previous findings in mtCCs in which we used brief treatment (1 h) with a higher AFN concentration ($1 \mu\text{M}$), TXNRD1 activity after 1 h of treatment was 87% lower in $0.5 \mu\text{M}$ AFN-treated cells when compared to vehicle-treated controls (Figure 4(a)). After 3 h of continuous AFN treatment, *Gclc* mRNA levels were increased by 1.8-fold ($p = 0.056$) and *GCLM* mRNA levels were increased by 2.5-fold (Figure 4(b)) when compared to those of vehicle- (DMSO) treated cells.

GSH levels were measured at 1, 6, and 24 h in cell lysates and at 6 and 24 h in media obtained from mtCCs continuously exposed to vehicle or $0.5 \mu\text{M}$ AFN. In vehicle-treated control mtCCs, lysate GSH levels were increased by 157% at 6 h and 128% at 24 h when compared to levels at 1 h

(Figure 5(a)). AFN treatment enhanced intracellular GSH levels by 122% at 6 h and 128% at 24 h when compared to respective vehicle-treated controls. Media GSH levels were not different between vehicle- and AFN-treated cells at 6 h (Figure 5(b)). In contrast, GSH levels were 2-fold greater in media from AFN-treated mtCCs at 24 h than from vehicle-treated controls.

To determine the impact of de novo GSH synthesis on changes in GSH contents, we utilized buthionine sulfoximine (BSO), a GCL inhibitor. mtCCs were cultured in the continuous presence or absence of $0.5 \mu\text{M}$ AFN and/or $22.5 \mu\text{M}$ BSO for 24 h. Thus, there were 4 experimental groups: vehicle, BSO, AFN, and BSO/AFN. At 24 h, our data revealed an independent effect of BSO on total GSH levels in cell lysate (Figure 5(c)) and media (Figure 5(d)). In lysates, BSO decreased total GSH levels to 13% of control values and 2.4% of control values in AFN-treated cells. In medium samples, BSO treatment in the absence or presence of AFN was associated with GSH concentrations that were approximately 20% compared to that of the DMSO-treated cells (Figure 5(d)).

In mtCCs treated with AFN for 24 h, we detected an independent effect of AFN on GPX2 protein levels (Figure 5(e)). Specifically, GPX2 expression was 2-fold greater in both AFN and BSO/AFN cells compared to vehicle or BSO groups alone. Similarly, our analyses indicated an independent effect of AFN on GPx activity in mtCCs. Compared to vehicle-treated controls, GPx activity was 2.5-fold greater in AFN-treated cells and 1.9-fold greater in BSO/AFN-treated cells than in controls (Figure 5(f)). GPx activity was 25% lower in BSO/AFN cells compared to cells cultured in the presence of AFN alone.

4. Discussion

GSH is the most abundant intracellular antioxidant and mediates susceptibility to and protection against neonatal and adult oxidative lung injury [11, 12, 15]. We previously demonstrated that ATG administered within 12 h of birth potently inhibits TXNRD1 and improves alveolarization in a murine BPD model [9]. The current manuscript extends our previous findings by demonstrating that TXNRD1 inhibition *in vivo* is associated with the following: (1) enhanced lung *Gclc* levels, increased total lung GSH levels, and elevated GSH/GSSG ratios in the lungs from hyperoxia-exposed mice at day 3 and (2) enhanced *Gclm* mRNA levels, increased intracellular and extracellular total GSH levels via enhanced de novo synthesis, and increased intracellular GPx activity in airway epithelial cells *in vitro*. Collectively, our data support a model in which TXNRD1 inhibition enhances pulmonary GSH-dependent antioxidant defenses promoting improved alveolarization.

In the current study, our data indicated that hyperoxia enhances *Gclc* but not *Gclm* expression in neonatal mouse lungs (Figure 1). Consistent with our findings with other Nrf2-regulated genes, the only significant increases in *Gclc* vs. control at d1 and d3 were detected in the ATG+hyperoxia group. This finding is suggestive of synergism between treatment and exposure on de novo GSH synthesis. Indeed, our

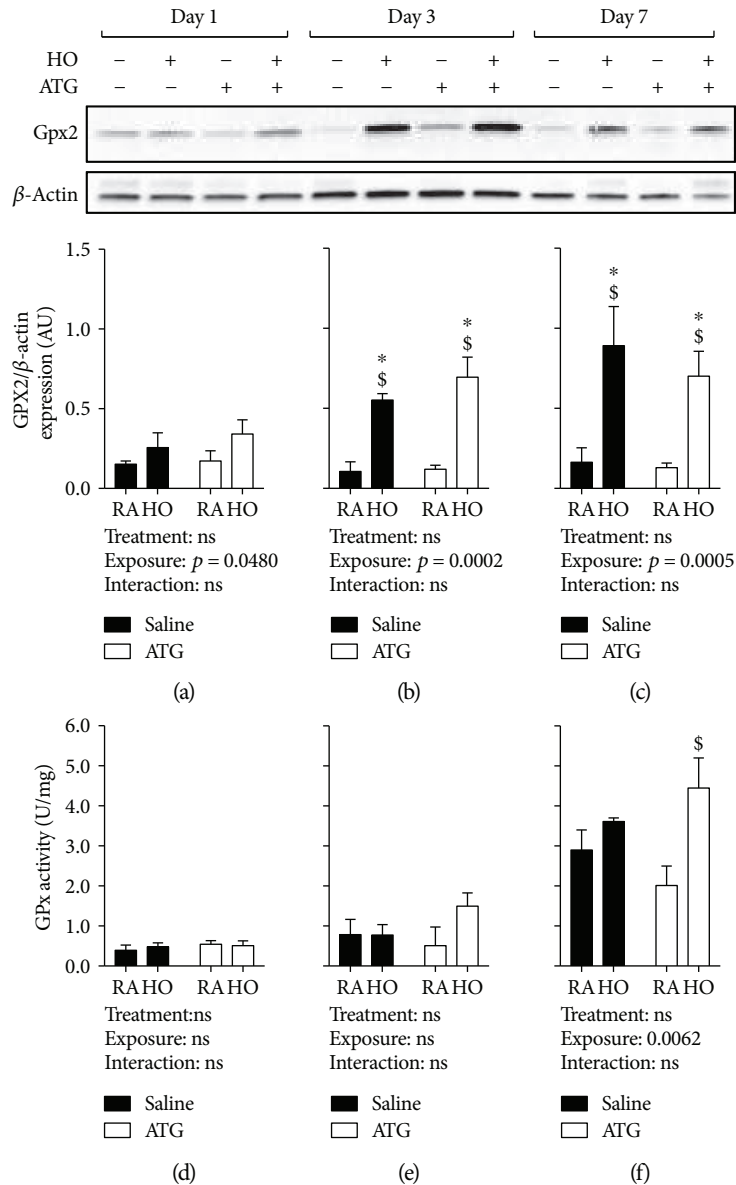


FIGURE 3: Lung glutathione peroxidase-2 expression and total GPx activity. Pups were dosed with either saline or 25 mg/kg ATG and exposed to either room air (RA) or hyperoxia (HO) for up to 7 days ($n = 3-5$). (a-c) Relative GPX2 density normalized to β -actin loading control. Total GPx activity (d-f). * $p < 0.05$ vs. saline/RA; $\$p < 0.05$ vs. ATG/RA.

data indicated independent effects of hyperoxia and ATG treatment on total lung GSH levels and GSH/GSSG ratios at d3 (Figures 2(b) and 2(e)). In absolute terms, the greatest levels of GSH and the highest GSH/GSSG ratios were found in the lungs from d3 ATG+hyperoxia mice.

Expression levels of both Gclc and Gclm are regulated by Nrf2. In our previous studies, we also identified a synergistic effect of ATG and hyperoxia on Nrf2-dependent pathways in the lungs from C3H/HeN mice [9]. One interpretation of these data is that TXNRD1 inhibition enhances Nrf2 dependent upon hyperoxic exposure resulting in proportionally greater induction of Nrf2-dependent pathways. The present data suggest that ATG enhances Nrf2-dependent de novo GSH synthesis by day 3. Importantly, day 3 immediately precedes initiation of the alveolar stage of development in the

murine lung. Thus, we speculate that hyperoxia, in combination with ATG, enhances lung GSH levels to preserve proalveolarization pathways that are interrupted by hyperoxia in the absence of ATG.

An essential caveat to these findings is that global assessments of GSH and GSSG levels in whole lung homogenates preclude the identification of treatment and exposure effects on individual cell types. Thus, the magnitude of differences are not likely to specifically reflect cell-specific effects of hyperoxia and TXNRD1 inhibition on lung GSH or GSSG levels. It is possible that our data underestimate the degree of enhanced *de novo* GSH synthesis in individual cell types. Given that TXNRD1 is most abundantly expressed in airway epithelia in newborn mouse lungs, we speculate that ATG enhances Nrf2-dependent responses, including enhancement

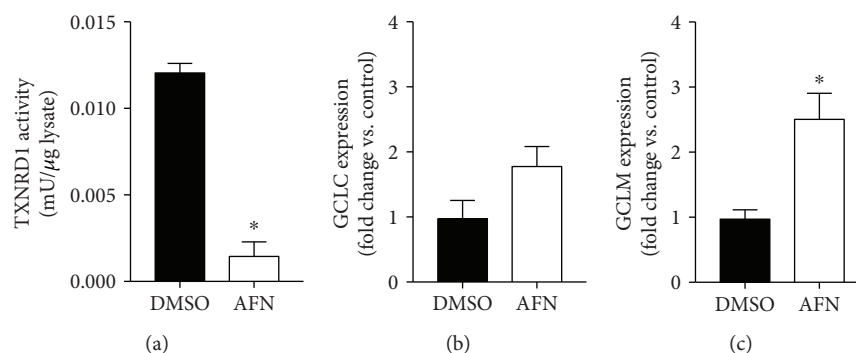


FIGURE 4: TXNRD1 activity and GCLC and GCLM expression in murine transformed club cells. mtCCs were treated with 0.5 μ M AFN or DMSO for 3 h ($n = 3-5$): (a) TXNRD1 activity and (b) GCLC and (c) GCLM mRNA expression. * $p < 0.003$.

of GSH levels, in this compartment [8]. Airway epithelia are also the primary source for the production of epithelial lining fluid (ELF). Should ATG treatment promote the *de novo* synthesis of GSH in airway epithelia, as we found in our studies *in vitro* (Figure 5), it is likely that GSH levels in ELF would also be enhanced in hyperoxia-exposed mice. In adult mice, Nrf2-dependent GSH modulated innate immune responses to bacterial infection [21]. Unfortunately, currently available methods in our laboratory do not permit us to accurately determine GSH levels in small volumes such as those obtained by bronchoalveolar lavage of neonatal mouse lungs. Additional studies are underway to define cell type specificity of Nrf2-dependent gene induction in ATG-treated mice; however, such studies are beyond the scope of the present manuscript.

We chose to also assess GPX2 expression and GPx activity because recent studies have indicated that GPX2, which is regulated by Nrf2, mediates responses to lung injury [22]. GPX2 protein expression was increased by hyperoxia at all three time points (Figures 3(a)–3(c)); however, our analyses did not identify an independent effect of ATG. We next tested total GPx activity in lung homogenates from all groups (Figures 3(d)–3(f)). GPx activity was not significantly altered by ATG or hyperoxia until day 7. It is important to note that ATG is capable of inhibiting other selenocysteine-containing proteins including GPx [23]. Our data indicated that ATG, at the doses used in the present studies, did not inhibit GPx activity in neonatal murine lungs. These data are in contrast to TXNRD1 inhibition and are consistent with previous reports [9, 23–25]. GPX2 expression and total GPx enzymatic activity in whole lung homogenates from hyperoxia-exposed pups were unaffected by ATG pretreatment. Given the enzymatic capacity of GPx family proteins to catalyze GSH-dependent reduction of hydroperoxides, it is possible that additional upregulation was unnecessary to facilitate catalysis at d3, the day at which we saw maximal increases in total GSH levels and GSH/GSSG ratios.

We have consistently utilized mtCCs as a model system to study the effects of TXNRD1 inhibitors. Club cells provide ELF antioxidants, and a subpopulation serves as progenitor cells in lung repair [26, 27]. In contrast to our previous studies [8], we decreased the concentration of AFN to 0.5 μ M and continuously exposed cells to AFN or vehicle to more closely mimic our studies *in vivo*. Importantly, we did not observe

evidence of AFN toxicity in the present studies which is in contrast to our previous studies with 1 μ M AFN (data not shown). TXNRD1 activity was inhibited by 87% in AFN-treated mtCCs in the present studies (Figure 4). AFN enhanced GCLM mRNA levels at 3 h; however, GCLC levels were not significantly different from each other ($p = 0.058$) by the statistical methods used.

In addition to measurements of intracellular GSH, we also sought to define the effects of TXNRD1 inhibition on extracellular GSH levels given the secretory property of club cells. Unsurprisingly, AFN enhanced total intracellular GSH levels by 6 h and differences were still present after 24 h of treatment (Figure 5(a)). Though not different at 6 h, AFN treatment also significantly enhanced GSH levels in the media at 24 h (Figure 5(b)). Extrapolation of these data suggest that TXNRD1 inhibition is likely to enhance ELF GSH levels which may, in part, contribute to its protective effects. Collectively, our data indicate a net increase of approximately 60% in total GSH contents (intracellular + extracellular) following TXNRD1 inhibition in mtCCs.

BSO alone significantly decreased intracellular GSH and medium GSH levels revealing the extent of basal GSH production under standard culture conditions (Figure 5(c)). The addition of BSO to AFN-treated cells prevented AFN-mediated increases in intracellular and extracellular GSH levels (Figures 5(c) and 5(d)). This indicates that AFN-mediated increases in GSH were mediated by *de novo* GSH synthesis. These and other studies indicate that *de novo* synthesis of GSH plays a major role in normal cell growth and proliferation [28, 29]. AFN treatment of mtCCs increased GPX2 levels by approximately 2-fold in the presence and absence of BSO (Figure 5(e)). GPx activity was also 2-fold greater following TXNRD1 inhibition in AFN-treated cells; however, concomitant BSO treatment significantly decreased GPx activity compared to AFN alone (Figure 5(f)). We interpret these findings to be reflective of cellular stress given observed morphological alterations in mtCCs concomitantly treated with AFN and BSO.

Therapeutic exogenous antioxidant administration has failed to prevent BPD [30]. Activation of endogenous antioxidant systems, such as that achieved by TXNRD1 inhibition, represents a novel approach to improving respiratory outcomes in premature infants. Our data suggest that augmentation of *de novo* GSH synthesis by therapeutic TXNRD1

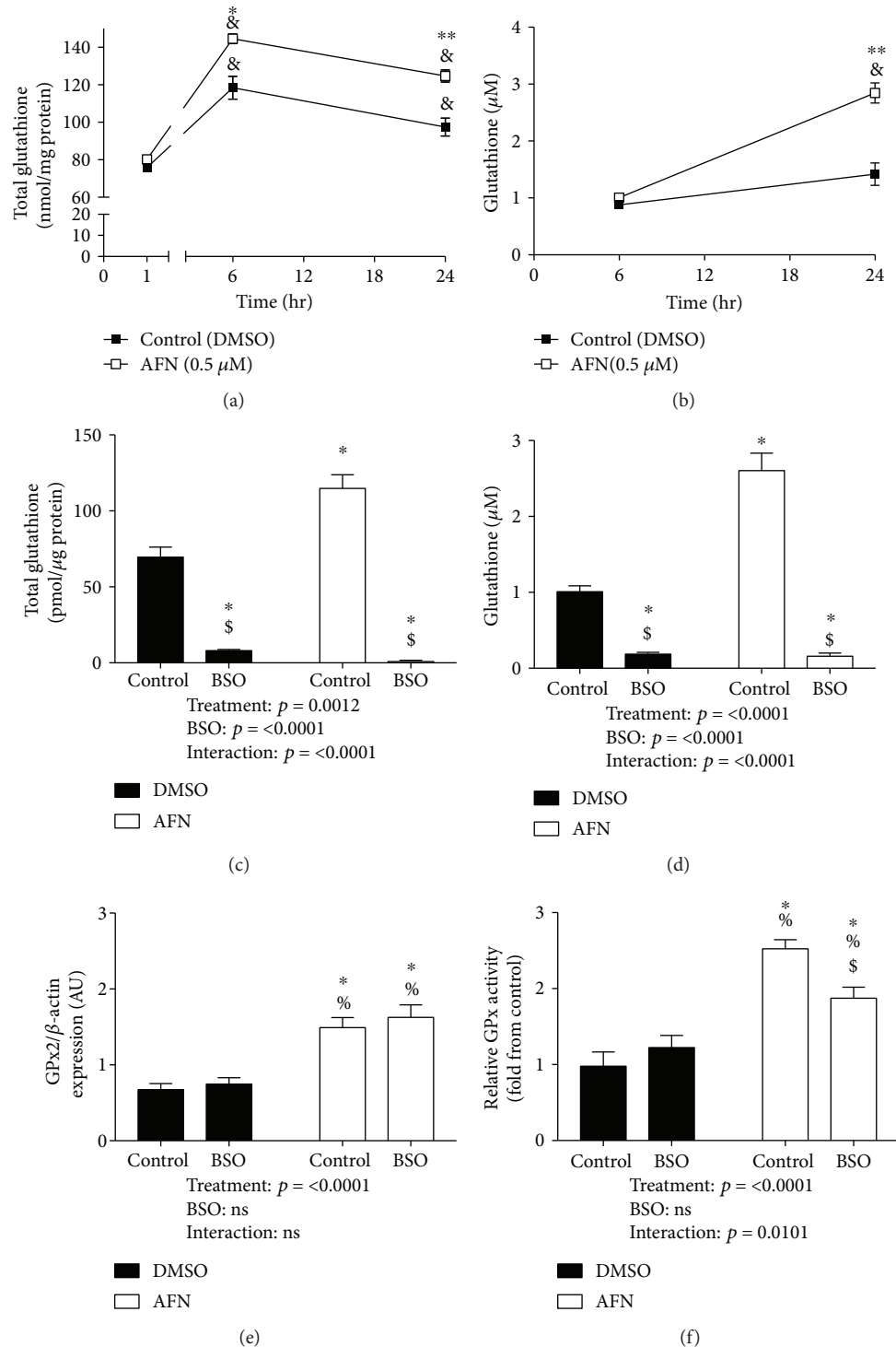


FIGURE 5: Total GSH levels and GPx activity in murine transformed club cells. mtCCs were treated with 0.5 μ M AFN (or vehicle, DMSO) for up to 24 h. Total GSH was measured at 1, 6, and 24 hr in the lysate (a) and at 6 and 24 hr in media (b). Data ($n = 3-9$) were analyzed by one-way ANOVA. In separate studies, mtCCs were treated with DMSO or 0.5 μ M AFN in DMSO in the presence or absence of buthionine sulfoximine (BSO). $^{\&}p < 0.05$ vs. 1 h control; $^*p < 0.05$ vs. 6 h control; $^{**}p < 0.05$ vs. 24 h control. Total GSH levels in lysate (c) and media (d) at 24 hr were determined. GPX2 expression (e) and total GPx activity (f) were also determined. Expression data is representative of 5-6 samples from two independent experiments, and activity data is $n = 3$ per one independent experiment. Data ($n = 3-6$) were analyzed by two-way ANOVA followed by Tukey's post hoc analysis. $^*p < 0.05$ vs. vehicle; $^{\&}p < 0.05$ vs. AFN; $^{\%}p < 0.05$ vs. BSO.

inhibition could be a mechanism leading to improved respiratory outcomes in prematurely born infants. It should be noted that *de novo* GSH synthesis requires adequate levels of cysteine [31, 32]. In addition, selenium is required for selenocysteine synthesis and both TXNRD1 and GPx require selenocysteine for optimal enzymatic activity [33]. The majority of these nutrients are transplacentally acquired during the third trimester [34]. This means that extremely premature infants are inherently deficient and currently employed perinatal nutritional strategies are often insufficient to correct these deficiencies. Thus, we speculate that augmentation of GSH-dependent antioxidant defenses by TXNRD1 inhibitors is likely to be influenced by the bioavailability of both cysteine and selenium.

In conclusion, our data are consistent with a model in which TXNRD1 inhibition enhances Nrf2-dependent augmentation of the GSH antioxidant system, including *de novo* GSH synthesis, elicited by hyperoxic exposure in neonatal mice. In contrast to previous approaches that utilized exogenous antioxidant administration to prevent BPD, the use of therapeutic TXNRD1 inhibition enhances endogenous Nrf2-dependent responses and is associated with improved lung development. Our lab is currently defining the impact of neonatal nutritional deficiencies in cysteine and/or selenium on pulmonary Nrf2-dependent responses and GSH-dependent antioxidant defenses which will likely influence the translation of our findings from bench to bedside.

Data Availability

No publicly available data were used for this manuscript.

Conflicts of Interest

The authors declare that there is no conflict of interest regarding the publication of this paper.

Authors' Contributions

SBW, RW, KD, QL, RL, LKR, and TET substantially contributed to the conception and design, acquisition of data, or analysis and interpretation of data. SBW and TET drafted the article or revised it critically for important intellectual content. SBW and TET are responsible for the final approval of the version to be published.

Acknowledgments

We thank Dr. Edward Schmidt, Dr. Justin Prigge, Dr. Changchun Ren, and Dr. Tamas Jilling for the assistance with reagents and advice on experimental design. This work is supported by a grant from the National Institutes of Health (R01HL119280) (TET).

References

- [1] E. Bancalari and D. Jain, "Bronchopulmonary dysplasia: can we agree on a definition?," *American Journal of Perinatology*, vol. 35, no. 6, pp. 537–540, 2018.
- [2] C. D. Baker and C. M. Alvira, "Disrupted lung development and bronchopulmonary dysplasia: opportunities for lung repair and regeneration," *Current Opinion in Pediatrics*, vol. 26, no. 3, pp. 306–314, 2014.
- [3] N. Ambalavanan and W. A. Carlo, "Bronchopulmonary dysplasia: new insights," *Clinics in Perinatology*, vol. 31, no. 3, pp. 613–628, 2004.
- [4] T. E. Tipple, "The thioredoxin system in neonatal lung disease," *Antioxidants & Redox Signaling*, vol. 21, no. 13, pp. 1916–1925, 2014.
- [5] T. M. Asikainen and C. W. White, "Pulmonary antioxidant defenses in the preterm newborn with respiratory distress and bronchopulmonary dysplasia in evolution: implications for antioxidant therapy," *Antioxidants & Redox Signaling*, vol. 6, no. 1, pp. 155–167, 2004.
- [6] T. M. Asikainen and C. W. White, "Antioxidant defenses in the preterm lung: role for hypoxia-inducible factors in BPD?," *Toxicology and Applied Pharmacology*, vol. 203, no. 2, pp. 177–188, 2005.
- [7] R. D. Britt Jr., M. L. Locy, L. K. Rogers, and T. E. Tipple, "The thioredoxin reductase-1 inhibitor aurothioglucose attenuates lung injury and improves survival in a murine model of acute respiratory distress syndrome," *Antioxidants & Redox Signaling*, vol. 20, no. 17, pp. 2681–2691, 2014.
- [8] M. L. Locy, L. K. Rogers, J. R. Prigge, E. E. Schmidt, E. S. J. Arnér, and T. E. Tipple, "Thioredoxin reductase inhibition elicits Nrf2-mediated responses in Clara cells: implications for oxidant-induced lung injury," *Antioxidants & Redox Signaling*, vol. 17, no. 10, pp. 1407–1416, 2012.
- [9] Q. Li, S. B. Wall, C. Ren et al., "Thioredoxin reductase inhibition attenuates neonatal hyperoxic lung injury and enhances nuclear factor E2-related factor 2 activation," *American Journal of Respiratory Cell and Molecular Biology*, vol. 55, no. 3, pp. 419–428, 2016.
- [10] M. Cebula, E. E. Schmidt, and E. S. J. Arnér, "TrxR1 as a potent regulator of the Nrf2-Keap1 response system," *Antioxidants & Redox Signaling*, vol. 23, no. 10, pp. 823–853, 2015.
- [11] A. Pompella, A. Visvikis, A. Paolicchi, V. D. Tata, and A. F. Casini, "The changing faces of glutathione, a cellular protagonist," *Biochemical Pharmacology*, vol. 66, no. 8, pp. 1499–1503, 2003.
- [12] S. G. Jenkinson, J. M. Jordan, and C. A. Duncan, "Effects of selenium deficiency on glutathione-induced protection from hyperbaric hyperoxia in rat," *American Journal of Physiology-Lung Cellular and Molecular Physiology*, vol. 257, no. 6, pp. L393–L398, 1989.
- [13] C. C. Franklin, D. S. Backos, I. Mohar, C. C. White, H. J. Forman, and T. J. Kavanagh, "Structure, function, and post-translational regulation of the catalytic and modifier subunits of glutamate cysteine ligase," *Molecular Aspects of Medicine*, vol. 30, no. 1–2, pp. 86–98, 2009.
- [14] S. C. Lu, "Glutathione synthesis," *Biochimica et Biophysica Acta (BBA) - General Subjects*, vol. 1830, no. 5, pp. 3143–3153, 2013.
- [15] I. Rahman, "Regulation of glutathione in inflammation and chronic lung diseases," *Mutation Research/Fundamental and Molecular Mechanisms of Mutagenesis*, vol. 579, no. 1–2, pp. 58–80, 2005.
- [16] S. E. Welty, "Is there a role for antioxidant therapy in bronchopulmonary dysplasia?," *The Journal of Nutrition*, vol. 131, no. 3, pp. 947S–950S, 2001.

- [17] A. Singh, T. Rangasamy, R. K. Thimmulappa et al., "Glutathione peroxidase 2, the major cigarette smoke-inducible isoform of GPX in lungs, is regulated by Nrf2," *American Journal of Respiratory Cell and Molecular Biology*, vol. 35, no. 6, pp. 639–650, 2006.
- [18] H.-Y. Cho, A. E. Jedlicka, S. P. M. Reddy et al., "Role of NRF2 in protection against hyperoxic lung injury in mice," *American Journal of Respiratory Cell and Molecular Biology*, vol. 26, no. 2, pp. 175–182, 2002.
- [19] T. E. Tipple, S. E. Welty, L. K. Rogers et al., "Thioredoxin-related mechanisms in hyperoxic lung injury in mice," *American Journal of Respiratory Cell and Molecular Biology*, vol. 37, no. 4, pp. 405–413, 2007.
- [20] I. Rahman, A. Kode, and S. K. Biswas, "Assay for quantitative determination of glutathione and glutathione disulfide levels using enzymatic recycling method," *Nature Protocols*, vol. 1, no. 6, pp. 3159–3165, 2006.
- [21] N. M. Reddy, V. Suryanarayana, D. V. Kalvakolanu et al., "Innate immunity against bacterial infection following hyperoxia exposure is impaired in NRF2-deficient mice," *The Journal of Immunology*, vol. 183, no. 7, pp. 4601–4608, 2009.
- [22] H. Y. Cho, B. van Houten, X. Wang et al., "Targeted deletion of *Nrf2* impairs lung development and oxidant injury in neonatal mice," *Antioxidants & Redox Signaling*, vol. 17, no. 8, pp. 1066–1082, 2012.
- [23] A. D. Smith, C. A. Guidry, V. C. Morris, and O. A. Levander, "Aurothioglucose inhibits murine thioredoxin reductase activity in vivo," *The Journal of Nutrition*, vol. 129, no. 1, pp. 194–198, 1999.
- [24] S. Gromer, L. D. Arscott, C. H. Williams Jr., R. H. Schirmer, and K. Becker, "Human placenta thioredoxin reductase. Isolation of the selenoenzyme, steady state kinetics, and inhibition by therapeutic gold compounds," *Journal of Biological Chemistry*, vol. 273, no. 32, pp. 20096–20101, 1998.
- [25] S. Gromer, H. Merkle, R. H. Schirmer, and K. Becker, "Human placenta thioredoxin reductase: preparation and inhibitor studies," *Methods in Enzymology*, vol. 347, pp. 382–394, 2002.
- [26] D. Zheng, B.-S. Soh, L. Yin et al., "Differentiation of club cells to alveolar epithelial cells in vitro," *Scientific Reports*, vol. 7, no. 1, article 41661, 2017.
- [27] W. Rokicki, M. Rokicki, J. Wojtacha, and A. Dzeljijli, "The role and importance of club cells (Clara cells) in the pathogenesis of some respiratory diseases," *Polish Journal of Cardio-Thoracic Surgery*, vol. 13, no. 1, pp. 26–30, 2016.
- [28] M. Poot, H. Teubert, P. S. Rabinovitch, and T. J. Kavanagh, "De novo synthesis of glutathione is required for both entry into and progression through the cell cycle," *Journal of Cellular Physiology*, vol. 163, no. 3, pp. 555–560, 1995.
- [29] S. Zheng, F. U. Yumei, and A. Chen, "De novo synthesis of glutathione is a prerequisite for curcumin to inhibit hepatic stellate cell (HSC) activation," *Free Radical Biology & Medicine*, vol. 43, no. 3, pp. 444–453, 2007.
- [30] S. K. Berkelhamer and K. N. Farrow, "Developmental regulation of antioxidant enzymes and their impact on neonatal lung disease," *Antioxidants & Redox Signaling*, vol. 21, no. 13, pp. 1837–1848, 2014.
- [31] Y. Liu, A. S. Hyde, M. A. Simpson, and J. J. Barycki, "Emerging regulatory paradigms in glutathione metabolism," *Advances in Cancer Research*, vol. 122, pp. 69–101, 2014.
- [32] J. I. Lee, J. Kang, and M. H. Stipanuk, "Differential regulation of glutamate-cysteine ligase subunit expression and increased holoenzyme formation in response to cysteine deprivation," *Biochemical Journal*, vol. 393, no. 1, pp. 181–190, 2006.
- [33] C. Kiermayer, B. Michalke, J. Schmidt, and M. Brielmeier, "Effect of selenium on thioredoxin reductase activity in *Txnrd1* or *Txnrd2* hemizygous mice," *Biological Chemistry*, vol. 388, no. 10, pp. 1091–1097, 2007.
- [34] R. Tindell and T. Tipple, "Selenium: implications for outcomes in extremely preterm infants," *Journal of Perinatology*, vol. 38, no. 3, pp. 197–202, 2018.